A MICROSTRUCTURAL INVESTIGATION OF RADIATION RECRYSTALLIZED SNOW LAYERS

by

David John Walters

A dissertation submitted in partial fulfillment
of the requirements for the degree

of

Doctor of Philosophy

in

Engineering

MONTANA STATE UNIVERSITY
Bozeman, Montana

August 2016

©COPYRIGHT

by

David John Walters

2016

All Rights Reserved

ACKNOWLEGMENTS

I am appreciative of the support I have received from Montana State University, the College of Engineering, and the Department of Civil Engineering. The independence and opportunity I have been afforded here has projected my research career forward while garnering widespread attention through public outreach, media inquiries, conference presentations, and publications.

Without the diligence of my research committee to secure funding, specifically Drs. Adams, Miller, McKittrick, and Edens, none of this work would have been possible. I am also grateful for the teaching opportunities afforded me by the department and Dr. Stephens to supplement my financial support and grow my skills as an instructor. I also want to specifically thank Dr. McKittrick for the endless efforts to maintain and operate the Subzero Science and Engineering Research Facility – a unique laboratory necessary for this research.

I am grateful to add to a solid foundation of snow and avalanche work laid by present and past colleagues. None of this is possible without the drive, passion, and independence instilled in me by my parents (and the occasional lift ticket). Lastly, my wife, Katie, deserves the biggest thanks for her unending patience and support that helps keep the important things in sight.

TABLE OF CONTENTS

1. INTRODUCTION 1

1.1 Motivation 1
1.2 Outline 3

2. AVALANCHES AND RADIATION RECRYSTALLIZED SNOW 6

2.1 Avalanches 6
2.2 Snow Metamorphism 7
2.3 Radiation Recrystallization 10

3. MICROMECHANICS AND EFFECTIVE STIFFNESS PROPERTIES 20

3.1 Micromechanics 20
3.1.1 Homogenization: Relating Micro to Macro 21
3.1.2 Localization-Voigt Approach 25
3.1.3 Summary of Micromechanics 27
3.2 Effective Elastic Stiffness 28
3.2.1 Localization Operation: Voigt's Hypothesis 30
3.2.2 Local Constitutive Behavior: Contact Law 31
3.2.3 Averaging: Love Operation 37
3.2.4 Effective Isotropic Stiffness Coefficients 38

4. FABRIC TENSORS AND DIRECTIONAL DATA 42

4.1 Fabric Tensors 42
4.1.1 The Contact Tensor 45
4.1.2 The MIL Fabric Tensor 54
4.2 Incorporating Fabric Tensors into Effective Elastic Stiffness 59
4.3 Summary of Fabric Tensors 66

5. EFFECTIVE MECHANICAL PROPERTIES: SHAPE FACTORS 67

5.1 Motivation 67
5.2 Scalar Shape Correction Factor 70

TABLE OF CONTENTS CONTINUED

5.3 Directional Correction Factor: Tensor Ratio 77
5.4 Summary of Shape Factors 87

6. FINITE ELEMENT MODELING 89

6.1 History 90
6.2 Formulation 94
6.2.1 Discretization 96
6.2.2 Material Parameters 102
6.2.3 Solution Technique 108
6.2.4 Shear Locking 113
6.3 Summary 122

7. METHODS AND EXPERIMENTS 123

7.1 Laboratory Procedures 123
7.1.1 Laboratory Specifications 123
7.1.2 Environmental Data 126
7.1.3 Snow Making Procedure 132
7.1.4 Metamorphism Procedures 135
7.1.5 Mechanical Testing Procedures 140
7.2 Microstructural Data Analysis 146
7.3 Tensor Analysis 150
7.3.1 Segmentation Software 150
7.3.2 Grain and Bond Properties 155
7.3.3 Tensor Computation 158

8. LABORATORY RESULTS 159

8.1 Initial Starting Snow 160
8.2 Radiation Recrystallization 165
8.2.1 Temperature and Vapor Pressure Gradients 165
8.2.2 Crystal Morphologies 174
8.2.3 Discussion 179
8.3 Macro-Scale Mechanical Test Results 186

TABLE OF CONTENTS CONTINUED

8.3.1 Mechanical Shear Test Results 186
New Snow Shear Tests. 187
Aged Snow Surface Shear Tests. 192
8.3.2 Previously Published Shear Test Results 198
8.3.3 Mechanical Compression Test Results 200
New Snow Compression Test. 200
One Week Old Snow Compression Test. 204
8.3.4 Previously Published Compression Test Results 208
8.3.5 Discussion 211
8.4 Summary 221

9. FABRIC TENSOR MODEL RESULTS 227

9.1 Fabric Tensor Validation 228
9.2 Radiation Recrystallized Results 235
9.2.1 Fabric Tensor Analysis 239
9.2.2 Effective Material Properties 248
Effective Properties Using Shertzer Model. 248
Effective Properties with the Scalar Shape Factor. 259
Effective Properties with Scalar Shape Factor and Tensor Ratio. 262
9.2.3 Discussion of Faceted Layer Tensor Results 264
Contact Tensor Results. 264
Sample 2W1 Discussion. 266
MIL Tensor Problems. 268
Volume Size Trouble. 274
9.2.4 Tensor Analyses of Sub-Faceted Layer 276
Tensor Analysis of the Sub-Facet Layer of Sample NS1. 277
Tensor Analysis of the Sub-Facet Layer of Sample NS2. 284
Tensor Analysis of the Sub-Facet Layer of Sample 1W3. 288
Summary of Cohesive Layer Tensor Analysis. 291
9.3 Summary 294

10. FINITE ELEMENT MODEL RESULTS 297

TABLE OF CONTENTS CONTINUED

10.1 Finite Element Analysis Results 298
10.1.1 New Snow Shear Tests 302
10.1.2 New Snow Compression Test 307
10.1.3 One Week Old Snow Shear Tests 310
10.1.4 One Week Old Snow Compression Test 315
10.1.5 Two Weeks Old Snow Shear Test 320
10.2 Discussion 325
10.2.1 Damaged Microstructures 326
10.2.2 Deviations from Absolute Experimental Values 328
Boundary Conditions. 328
Material Properties. 329
Element Formulation. 335
10.3 Summary 339

11. CONCLUSIONS AND RECOMMENDATIONS 342

11.1 Conclusions 342
11.2 Recommendations 349

REFERENCES CITED 353

APPENDICES 369

APPENDIX A: Mechanical Testing Data Acquisition Software 370
APPENDIX B: 3D Watershed Segmentation Matlab Code 373
APPENDIX C: Tensor Assembly Matlab Code 391
APPENDIX D: Mechanical Testing Results 456
APPENDIX E: Fabric Tensor Results 478
APPENDIX F: Finite Element Analysis Results 537

LIST OF TABLES

Table Page

6-1: Transversely isotropic stiffness coefficients for monocrystalline ice (Gammon et al., 1983; Petrenko and Whitworth, 1999). 103

7-1: Summary of chamber parameters for producing radiation recrystallized facets in the laboratory. 137

7-2: SkyScan 1173 scan settings used for all CT scans performed on cylindrical sample approximately 4 cm tall and 3 cm in diameter. The container is a plastic 35mm film canister. 140

7-3: SkyScan 1173 scan settings used for all snow samples collected during experimentation. These settings are sensitive to sample size and collection container which was consistent throughout testing. 148

7-4: Segmented bond and grain parameter descriptions. 156

8-1: Details of initial crystal types, sizes, and near surface densities of experimental samples following initial sintering period and prior to radiation recrystallization 163

8-2: Summary of shear modulus data for all shear experiments conducted. 198

8-3: Recomputed shear moduli for from Walters and Adams (2014b). 199

8-4: Summary of Young's modulus data for all compression experiments conducted. 207

8-5: Summary of compressive strength data for all compression experiments conducted. 208

LIST OF TABLES CONTINUED

Table Page

8-6: Compression test results reproduced from Walters and Adams (2014b, 2012). Young's moduli perpendicular to the snow surface ($E3$) and compressive strength (σs) are reported. The superscripts initial and RR refer to the initial configuration and the radiation recrystallized configuration. The results are computed from average strains from regions above and below the faceted layer. 209

8-7: Recomputed Young's moduli from Walters and Adams (2014b). 210

9-1: Thickness of CT analysis volumes for each experiment. 239

10-1: Summary of finite element data for each experimental sample and actual experimental results where available. (Surface parallel shear modulus = $G23$, surface normal Young's modulus = $E3$, peak shear stress = $\tau peak$, peak compressive axial stress = $\sigma peak$). The colors correspond to the colored data points utilized in the presentation of the FEA simulated stress and strains shown above. 324

LIST OF FIGURES

Figure Page

2-1: Schematic illustrating the near surface balances of incoming and outgoing short- and longwave radiation and the subsurface effects on the near surface region of the snowpack. 13

3-1: General homogenization scheme. 22

3-2: Specific homogenization scheme utilized here starting with global strains; scaling strains (kinematic variables) to local scale using the Voigt approximation as a localization operation; establishing a local constitutive law; then averaging the local stresses (static variables) to scale back up to global behavior. From here, the global constitutive behavior can be derived. 28

3-3: Undeformed idealized spherical contact geometry in two dimensions showing the local Cartesian coordinate system. Here, ρ represents the bond plane (contact) radius, R the grain radius, and $L\alpha$ the branch length connecting the centers of connected grains. 32

3-4: Deformed bonded grain pair geometry resulting from an axial load. The grey points represent the position of the undeformed branch vector whereas the black points show the incremental normal displacement of the contact area. 35

3-5: Deformed bonded grain pair geometry resulting from a shear load. 37

4-1: (a) Example 2-D section of snow microstructure obtained via μCT imaging. Ice grains are white, pores are black. Image is approximately 5mm square. (b) Example 3-D section of snow microstructure from which the 2-D section was extracted. 44

LIST OF FIGURES CONTINUED

Figure Page

4-2: A granular assembly showing example directional quantities. m, is a unit vector between centers of connected grains, and n, is a unit vector normal to a contact plane defining the bond between grains. 46

4-3: Hypothetical 2-D granular assembly consisting of 8 grains with 8 contact normal vectors. Half of the contact vectors ($n\alpha$) are oriented parallel to the $x1$ direction with the other half oriented parallel to the $x2$ direction. Red indicates the individual grains while the blue regions are the contact planes between connected grains. 48

4-4: Hypothetical 3-D granular assembly consisting of 8 grains connected in pairs at 4 distinct contact planes. All of the contact vectors ($n\alpha$) are oriented parallel to the $x1$ direction. Red indicates the individual grains while the blue regions are the contact planes between connected grains. 52

4-5: Hypothetical 2-D granular assembly consisting of 8 grains connected in pairs at 4 distinct contact planes. All of the contact vectors ($n\alpha$) are oriented at $+60°$ to the $x1$ direction. Red indicates the individual grains while the blue regions are the contact planes between connected grains. 53

4-6: A hypothetical 2-D microstructural data set with a grid of three test lines oriented at two distinct angles. The number of intersections at each test line is printed at the end of each line segment. At $\omega1$, few intersections are recorded as the test lines are mostly parallel with the microstructure. In contrast, a greater number of intersections are recorded at $\omega2$. 56

LIST OF FIGURES CONTINUED

Figure Page

4-7: Hypothetical 3-D MIL data represented in a pin-cushion plot. Each line segment is a vector oriented coincidentally with the MIL grid test angle ω and a magnitude equal to the MIL value at that specific angle. An ellipsoid can be fit using a least squares error method. The resulting eigenvectors from the anisotropy tensor $\boldsymbol{H}$ representing the equation of the ellipsoid shape are shown. Each vector is coincident with the major and minor axes of the ellipsoid shape. 58

4-8: Illustration of the shear stress τ and shear strain γ directions associated with the subscripts 23. 66

5-1: Plot of Shertzer's $E*$, Equation (3.21), as a function of density at constant values of bond radius to grain radius ratios (colored lines) against compiled measured data reproduced from Mellor (1975) (black outlined areas). 68

5-2: Configuration of two spherical grains contacting a spherical parent grain. The loading paths of the normal and shear components are shown on the right in addition to the distance from the center of the parent grain to the contact center. In the case of spheres, $r = d1 = d2$. 70

5-3: Illustration of the distance transform. The binary pixel values of the circle are shown on the left and the Euclidean distance transform values and image are shown on the right. 73

5-4: Configuration of three grains contacting a non-spherical parent grain. The loading paths of the normal and shear components are shown on the right. The dashed purple circle represents the spherical grain size. $d1, d2,$ and $d3$ are the distances from each bond center to the center of the largest sphere fit inside the parent grain. 74

LIST OF FIGURES CONTINUED

Figure Page

5-5: A hypothetical 3-D microstructure of ellipsoidal grains oriented with their major axes directed vertically. The middle row of grains is bonded laterally to each other. The top and bottom rows of grains are only bonded to the middle row of grains through nearly vertically oriented contacts. 79

5-6: A hypothetical 3-D microstructure of ellipsoidal grains oriented with their major axes directed horizontally. The middle column of grains is bonded laterally to each other. The left and right columns of grains are bonded to the middle of column of grains and vertically to each other. 81

5-7: Two dimensional bonded grain system in which the contact tensor remains constant for all microstructures ($F11 = 0, F22 = 1$) and the MIL tensor coefficients shift from an $x2$ preferred textural orientation with the leftmost bonded grain set, to an $x1$ preferred textural orientation with the rightmost bonded grain set. 84

6-1: Side-by-side view of two volumes of snow modeled with finite element methods. The sample on the left consists of an initially homogenous structure prior to recrystallization. The sample on the right contains a radiation recrystallized faceted layer buried by new snow. Each sample cross section is 5 mm × 5 mm. 96

6-2: Close up view of the raw surface mesh initially applied to the μCT imaged volume. Triangular elements are uniform in size with each side length equal to 29.76 μm. 99

6-3: Final volumetric mesh following mesh refinement procedures in Materialise Mimics ®. 101

6-4: Geometry of the homogeneous structural solid element SOLID185 (from: *ANSYS 14.5 APDL Element Reference*, 2012). 101

LIST OF FIGURES CONTINUED

Figure Page

6-5: Crystallographic planes of a single ice crystal (from: McClung and Schaerer, 2006). 103

6-6: Mohr-Coulomb failure surface (reproduced from Labuz and Zang, 2012). 108

6-7: Hypothetical column undergoing shear displacement. Boundary conditions are fixed at the bottom and periodic at the top. (a) Vertical axial stress: red is tension, blue compression, green is near zero stress. (b) Vertical displacement: red is up, blue is down, green is zero displacement. 111

6-8: Distribution of axial stress σzz of the microstructure subjected to $2 \times 10 - 5$ macroscopic vertical strain (from Hagenmuller et al., 2014). 113

6-9: Generic triangular constant strain element with 2 degrees of translational freedom at each node (reproduced from Cook et al., 2002). 114

6-10: Beam loaded in pure bending while meshed with 2-D triangular constant strain elements. Bottom image isolates the lower left element to examine the degrees of freedom (from Cook et al., 2002). 118

6-11: Full integration of a 3-D brick element showing accurate approximation of the bent shape. Notice the grid lines remain orthogonal – a requirement for no shear strain (*Abaqus 2016 Online Documentation*, 2015). 119

6-12: Full integration of a 3-D first order brick element. Shear locking occurs which introduces spurious shear strains as seen in the change in angles due to the edges not being able to assume a bent shape (*Abaqus 2016 Online Documentation*, 2015). 120

LIST OF FIGURES CONTINUED

Figure Page

6-13: Reduced integration of a 3-D first order brick element (single integration point). Shear locking is prevented since spurious shear strains are not produced, however, the grid lines in the deformed shape have not changed length (*Abaqus 2016 Online Documentation*, 2015)..... 121

7-1: Environmental chamber showing radiation and temperature instrumentation in place around a snow sample. The metal halide luminary is visible at the top center surrounded by the independently refrigerated ceiling..... 126

7-2: (Left) USGS Topographic map indicating the general location and altitude of the Yellowstone Club south field station (indicated by red marker). (Right) A satellite and digital terrain map obtained from Google Earth showing Pioneer Mountain and the location of the south field station at the Yellowstone Club. 127

7-3: Photo showing the meteorological station installed at the south field site. 127

7-4: Radiation recrystallized facets observed at the south field site at the Yellowstone Club on 3 January, 2011 at 13:30 (Photo Doug McCabe, YCSP). 129

7-5: Measured incoming longwave and shortwave radiation (normal to the slope) at the south field site at the Yellowstone Club for the 48 hour period on 2 January 2012 to 3 January 2011..... 130

7-6: Measured ambient air temperature and snow surface temperature at the south field site at the Yellowstone Club for the 48 hour period on 2 January 2012 to 3 January 2011..... 131

LIST OF FIGURES CONTINUED

Figure Page

7-7: Snowpack temperatures measured at 2 cm spatial intervals. The snow surface is indicated by the solid horizontal black line. Each curve represents 1 hour intervals beginning at 09:00 on 3 January 2011. A "knee temperature gradient" is observed to develop in the top 2-4 cm of the snow beginning at 11:00. 132

7-8: Snow making apparatus in the Cold and Hydrodynamics Chamber. 134

7-9: Example of time-lapsed photo of snow surface showing the approximate spatial scale. Photos are taken at this scale every 30 s for the duration of the experiment to examine the state of the snow surface during recrystallization. 138

7-10: Laser system for measuring small changes in snow surface height using triangulation. $Linitial$ and $hinitial$ are measured at the beginning of the experiment. dL is measured at intervals throughout the experiment for which values of dh can be derived. 139

7-11: Setting up a shear test. Here, the shear frame has been filled and surrounded by snow for sintering. 142

7-12: Sequence of images showing the cut-out process to remove excess snow from the buried shear frame. 142

7-13: Finished snow column preparation for shear experiments with LVDT mounted opposite the load actuator and contrasting paint pattern on the column face for optically measuring strain. 144

7-14: Empty 35mm film canister used for extracting and holding snow samples for μCT scanning. 147

7-15: 2-D Binary image for segmentation (from Mathworks, 2016). 152

LIST OF FIGURES CONTINUED

Figure Page

7-16: Image of the distance transform performed on the inverse of the binary image in Figure 7-15 (from Mathworks, 2016). 153

7-17: The segmented watershed transform of the objects shown in Figure 7-15 154

8-1: Dendritic crystals produced by the snow making apparatus. The background grid is 1mm square..... 160

8-2: Fragmented dendrites and rounded crystals representative of the surface and near surface of a snow sample following sieving new stellar dendrites through a 2mm grid and sintering for 12-24 hours. The grid in the background is 1mm square..... 162

8-3: Rounded fragment of a dendritic crystal found near the surface of a sample of snow sintered for 1 week. The grid in the background is 1mm square. 163

8-4: Volume rending of a sintered snow surface. The cross-section is 5 mm square by approximately 6 mm tall. 164

8-5: Temperature versus snow depth at 1 cm increments and 2 hour intervals for sample NS3. The actual snow surface is at 1 cm. 166

8-6: Temperature gradient in the top 1 cm of sample NS3 versus elapsed time. Ambient and near surface air temperatures are included on the secondary axis to show that the periodicity of the temperature gradient was related to the periodicity of the chamber air temperature. 167

8-7: Vapor pressure gradient with respect to time in the top 1 cm of sample NS3. 168

8-8: Temperature versus snow depth at 1 cm increments and 2 hour intervals for sample 1W1. The actual snow surface is at 1 cm. 169

LIST OF FIGURES CONTINUED

Figure Page

8-9: Temperature gradient in the top 2 cm of sample 1W1 versus elapsed time. Ambient and near surface air temperatures are included on the secondary axis to show the periodicity of the temperature gradient was related to the periodicity of the chamber air temperature. The near surface air temperature probe was improperly shaded and received direct sunlight causing readings above 0 °C. 170

8-10: Vapor pressure gradient with respect to time in the top 2 cm of sample 1W1. 171

8-11: Temperature versus snow depth at 1 cm increments and 2 hour intervals for sample 2W1. The actual snow surface is at 1 cm. 172

8-12: Temperature gradient in the top 2 cm of sample 2W1 versus elapsed time. Ambient and near surface air temperatures are included on the secondary axis to show the periodicity of the temperature gradient was related to the periodicity of the chamber air temperature. 173

8-13: Vapor pressure gradient with respect to time in the top 2 cm of sample 2W1. 173

8-14: Volume rending of the snow surface following 3 hours of metamorphism. The entire volume consists of coarser grains than those shown in Figure 8-4. The cross-section is 5 mm square by approximately 6 mm tall. 175

8-15: Photomicrograph of surface crystals of a new sample following 3 hours of radiation recrystallization. Small facets are observed growing off of the fragmented arms of decomposing dendritic crystals. The grid in the background is 1 mm square. 175

LIST OF FIGURES CONTINUED

Figure Page

8-16: MicroCT volume rendering of the surface and near surface of radiation recrystallized snow following 6 hours of metamorphism. Here, needle-like crystals begin to grow on the surface whereas faceted crystals continue to develop in size and organization in the middle of the sample. 176

8-17: Photomicrographs of disaggregated faceted and cup shaped crystals following 6 hours of recrystallization. The background grid is 2 mm square. 177

8-18: Micro-CT volume renderings of the top 6 mm of radiation recrystallized facets after 9 hours (left) and 12 hours (right). Here, needle-like crystals dominate the surface of each volume while vertically structured faceted and cup shape crystals permeate the midsection of each sample. 178

8-19: Photomicrographs of radiation recrystallized facets disaggregated from the surface and subsurface following 9 hours (left) and 12 hours (right) of metamorphism. Background grid is 1 mm square. 178

8-20: Profile cross-section of reconstructed CT scan containing a radiation recrystallized snow sample buried with new snow. The previous snow surface containing the elongated needle-like faceted crystals is indicated. Two distinct zones of unique faceted crystals exist following metamorphism. The approximate location of the average temperature gradient is positioned along the right side of the figure. 180

LIST OF FIGURES CONTINUED

Figure Page

8-21: Chains of radiation recrystallized faceted crystals similar to depth hoar formation. These crystals were extracted in-situ after sintering a layer of new snow over the top of a well-developed radiation recrystallized layer. The chain depicted here is parallel to the temperature gradient (perpendicular to the surface)..... 181

8-22: Long (4+ mm) faceted needle-like formation on the surface of radiation recrystallized snow following 12 hours of metamorphism. Background grid is 1 mm square. 182

8-24: Analysis of near surface density of experimental samples undergoing radiation recrystallization. Samples are analyzed using Micro-CT imaging..... 183

8-25: Measured changes in surface height for the duration of each radiation recrystallization experiment. 184

8-26: Shear strain distribution shown as an overlay on the actual sample. This test utilized an open faced shear frame being pushed from right to left relative to the image. 188

8-27: Non planar failure surface from the initial shear test on sample NS2 before radiation recrystallization. 189

8-28: Shear strain contours of sample NS2 containing a radiation recrystallized layer. Labeled points indicate the 3 distinct zones used for measuring shear moduli. The region of concentrated shear strain corresponds with the location of the radiation recrystallized facets. 190

LIST OF FIGURES CONTINUED

Figure Page

8-29: Shear stress and strain data for the initial and recrystallized state of experimental sample NS2. The slopes of the plotted lines represent the shear moduli of each layer examined. These are a first order fit to the stress and strain data in the presumed linear elastic region. 191

8-30: Shear strain distribution of the 1 week old surface of sample 1W1 prior to the growth of radiation recrystallization. Uniform strain distribution in the yellow and green contours corresponds with the 1 week old snow while the snow exhibiting less strain above is newly sintered snow added to support the shear frame (pushing right to left in this image). 194

8-31: The nearly planar fracture surface of the initial 1 week old snow sample (1W1) prior to radiation recrystallization. The fracture surface is approximately 2 cm below the old snow/new snow interface and at the base of the cutout column. Initial failure occurred in tension in the vertical direction at the base of the column on the right side. 195

8-32: Shear strain contours overlaid on profile images of sample 1W1 containing a radiation recrystallized layer. The stripe of concentrated shear strain also corresponds with the location of the faceted layer. The shear load is applied to the frame at the top of the image from right to left. 196

8-33: Shear stress and strain data for the initial and recrystallized state of experimental sample 1W1. The slopes of the plotted lines represent the shear moduli of each layer examined. These are a first order fit to the stress and strain data in the presumed linear elastic region. 197

LIST OF FIGURES CONTINUED

Figure Page

8-34: Minor strain (principal II) contours plotted on the vertical profile of sample NS3 undergoing compression testing prior to recrystallization. The plotted lines correspond to the strain value along each section line starting with $y = 0$ at the bottom of the sample. Minor strain direction was vertical (y-direction) in reference to this figure. 201

8-35: Minor strain (principal II) contours plotted on the vertical profile of sample NS3 undergoing compression testing following radiation recrystallization. The plotted lines correspond to the strain value along each section line starting with $y = 0$ at the bottom of the sample. 202

8-36: Comparison of stress/strain data for sample NS3 between the initial sample, the layer of radiation recrystallized facets and the consolidated layer of snow directly beneath the radiation recrystallized layer. 203

8-37: Minor strain contours (principal II) overlayed on the profile of a sample containing 1 week old snow buried by sintered new snow. The sample is being compressed in the vertical direction (y-axis). 205

8-38: Minor strain profile during compression of the buried radiation recrystallized layer of sample 1W3. Most strain is concentrated on the weak faceted portion of the sample, with more moderate strain occurring in the new snow located above the faceted layer. The least strain is observed in the consolidated snow below the faceted layer. Minor strain is oriented vertically in sections with non-zero strain. 206

LIST OF FIGURES CONTINUED

Figure Page

8-39: Comparison of stress/strain data for sample 1W3 between the initial sample, the layer of radiation recrystallized facets and the consolidated layer of snow directly beneath the radiation recrystallized layer. 207

8-40: Shear strain concentration on the radiation recrystallized layer of test 1W1 prior to failure. Localized heightened shear strain is the thickness of the radiation recrystallized faceted region. 211

8-41: Micrographs of cupped faceted crystals found on the lower (a) and upper (b) fracture surfaces following a shear test of a radiation recrystallized sample 1W1. The background grid is 1 mm square. 212

8-42: CT cross-section of surface needle crystals (a) before burial and (b) after burial of new snow crystals. 213

8-43: Free body diagram of an isolated column being loaded in shear. The external shear load applied to the shear frame produces the internal shear force V, and internal bending moment M. 217

8-44: Vertical displacement of an initial column of snow (no faceted layer) holding a right to left shear load. Upward displacement on the right edge with downward displacement on the left edge indicates rotation. 218

8-45: Example of major (tensile) strain immediately following initial fracture of the non-recrystallized column prior to full seperation. Indicates flexural strains prominent following the moment of failure. 218

LIST OF FIGURES CONTINUED

Figure Page

8-46: Vertical displacement of a column of snow containing a radiation recrystallized layer holding a right to left shear load. Upward displacement on the right edge with downward displacement on the left edge indicates rotation. 220

8-47: Example of major (tensile) strain immediately following initial fracture of the recrystallized column. Indicates flexural strains prominent following the moment of failure. Major strain is oriented vertically along the crack interface..... 220

9-1: Cubic volumes with a side length of 150 pixels. The volume on the left is artificially generated using random spheres. The volume on the right is of real snow. The solid volume fractions between the two volumes are similar (≈ 20%)..... 229

9-2: Possible plane fit orientations for bond areas represented by (a) only one pixel and (b) 2 pixels. Black squares represent the pixels identified as bonds. Similarly limited results would be expected in three dimensions. 230

9-3: Contact tensor for randomly generated microstructures varying in cubic side length from 25 pixels to 200 pixels. The contact orientation was computed via a plane fit method. 232

9-4: Contact tensor for randomly generated microstructures varying in cubic side length from 25 pixels to 200 pixels. The contact orientation was computed via a grain center-to-center method. 233

9-5: MIL tensor for randomly generated microstructures varying in cubic side length from 25 pixels to 150 pixels. 234

9-6: Tensor ratio for randomly generated microstructures varying in cubic side length from 25 pixels to 150 pixels. 235

LIST OF FIGURES CONTINUED

Figure Page

9-7: Coordinate system utilized by all CT-Scanned volumes. $x1$ and $x2$ establish a plane parallel to the snow surface. 236

9-8: Area fraction (density) of ice grains for a fully radiation recrystallized sample. The red line indicates the final height of the sample selected for fabric tensor analysis. Qualitative observations are made of the crystals near the boundaries of the selection for verification of the presence of desirable crystal morphologies. Cross-sectional images are parallel to the snow surface. 238

9-9: Average contact tensor coefficients of the three new snow experiments undergoing radiation recrystallization. Error bars represent the 95% confidence intervals. 240

9-10: Average MIL tensor coefficients of the three new snow experiments undergoing radiation recrystallization. Error bars represent the 95% confidence intervals. 241

9-11: Average tensor ratio in each axial direction of the three new snow experiments undergoing radiation recrystallization. Error bars represent the 95% confidence intervals..... 242

9-12: Average contact tensor coefficients of the three 1 week old snow experiments undergoing radiation recrystallization. Error bars represent the 95% confidence intervals..... 243

9-13: Average MIL tensor coefficients of the three 1 week old snow experiments undergoing radiation recrystallization. Error bars represent the 95% confidence intervals. 244

9-14: Average tensor ratio in each axial direction of the three 1 week old snow experiments undergoing radiation recrystallization. Error bars represent the 95% confidence intervals. 244

LIST OF FIGURES CONTINUED

Figure Page

9-15: Contact tensor coefficients of the single 2 weeks old snow experiment undergoing radiation recrystallization. Error bars represent the 95% confidence intervals. 246

9-16: MIL tensor coefficients of the single 2 weeks old snow experiment undergoing radiation recrystallization. Error bars represent the 95% confidence intervals. 246

9-17: Tensor ratio coefficients of the single 2 weeks old snow experiment undergoing radiation recrystallization. Error bars represent the 95% confidence intervals. 247

9-18: Computed effective Young's moduli using Shertzer's original formulation (2011) for sample NS1. $E*$ represents the scalar approximation of effective Young's modulus using microstructural variables. Ei represents effective Young's modulus in the ith axial direction using the contact tensor for directional data. 249

9-19: Computed effective shear moduli using Shertzer's original formulation (2011) for sample NS1. $G*$ represents the scalar approximation of effective shear modulus using microstructural variables. Gij represents effective shear modulus on the ith face in the jth direction using the contact tensor for directional data. 250

9-20: Evolution of ice volume fraction during recrystallization of sample NS1. 251

9-21: Mean 3-D bond radii, grain radii, and bond-to-grain radius ratio development during recrystallization of experiment NS-1. 252

9-22: Evolution of mean 3-D coordination number during recrystallization of experiment NS1..... 252

LIST OF FIGURES CONTINUED

Figure Page

9-23: Computed effective Young's moduli using Shertzer's original formulation (2011) for sample 1W3. $E*$ represents the scalar approximation of effective Young's modulus. Ei represents the effective Young's modulus in the ith axial direction using the contact tensor for directional data. 255

9-24: Computed effective shear moduli using Shertzer's original formulation (2011) for sample 1W3. $G*$ represents the scalar approximation of effective shear modulus. Gij represents the effective shear modulus on the ith face in the jth direction using the contact tensor for directional data. 255

9-25: Computed effective Young's moduli using Shertzer's original formulation (2011) for sample 2W1. $E*$ represents the scalar approximation of effective Young's modulus. Ei represents the effective Young's modulus in the ith axial direction using the contact tensor for directional data. 257

9-26: Computed effective shear moduli using Shertzer's original formulation (2011) for sample 2W1. $G*$ represents the scalar approximation of effective shear modulus. Gij represents the effective shear modulus on the ith face in the jth direction using the contact tensor for directional data. 257

9-27: Mean 3-D coordination number for experiment 2W1. Unlike other results, the connectivity increases during radiation recrystallization. 258

9-28: Mean bond radius and grain radius data for experiment 2W1. Unlike other experiments, the bond-to-grain radius ratio increases during radiation recrystallization. 259

LIST OF FIGURES CONTINUED

Figure Page

9-29: Scalar shape factor S for experimental sample NS1. Values of $S = 1$ correspond to perfectly spherical grains and $S = 0$ correspond to completely flattened grains (a line with no thickness). 260

9-30: Computed effective Young's moduli incorporating the scalar shape factor S for sample NS1. 261

9-31: Computed effective shear moduli incorporating the scalar shape factor S for sample NS1. 261

9-32: Computed effective Young's moduli incorporating the scalar shape factor S and the tensor ratio $\mathbf{\Gamma}$ for sample NS1. 263

9-33: Computed effective shear moduli incorporating the scalar shape factor S and the tensor ratio $\mathbf{\Gamma}$ for sample NS1. 264

9-34: Effective thermal conductivity of depth hoar being grown with a $100°\mathrm{C} \cdot \mathrm{m} - 1$ temperature gradient in the $x1$ direction (taken from: Shertzer and Adams, 2011). 265

9-35: Needle-like crystal forms near the surface of experimental sample NS3 after 12 hours of recrystallization. The $x1$-$x2$ plane is shown here (parallel to the snow surface). 271

9-36: MIL tensor coefficients for experimental sample NS3 demonstrating the coefficients in the $x1$ and $x2$ directions remain close to each other for the duration of the test. 271

9-37: MIL tensor coefficients for experimental sample 1W3 showing a clear preference to the $x1$ direction at both 6 hours and 12 hours. 272

LIST OF FIGURES CONTINUED

Figure Page

9-38: Needle-like crystal forms near the surface of experimental sample 1W3 after 12 hours of recrystallization. The $x1$-$x2$ plane is shown here (parallel to the snow surface). 273

9-39: Thin slice of homogeneous snow where the contact tensor and MIL tensor cannot analyze. 275

9-40: Contact tensor diagonal values for the coarsened layer of snow beneath the faceted layer of experimental sample NS1. 278

9-41: MIL tensor diagonal values for the coarsened layer of snow beneath the faceted layer of experimental sample NS1. 279

9-42: $x1$-$x3$ 2-D cross section of coarse layer grains from experiment NS1 after 12 hours of metamorphism. Inclusions of large ice grains from sieve spillover during sample preparation occasionally skew microstructural results. 280

9-43: Tensor ratio coefficients for the coarsened layer of snow beneath the faceted layer of experimental sample NS1. 280

9-44: Computed effective shear moduli for the coarsened base layer below the near surface facets in sample NS1 using the tensor ratio for directional data. 282

9-45: Mean 3-D coordination number for the coarsened base layer below the near surface facets in sample NS1..... 283

9-46: Mean 3-D bond radii and grain radii for the coarsened layer below the near surface facets of sample NS1..... 283

9-47: Tensor ratio coefficients for the sub-faceted layer of experimental sample NS2..... 285

LIST OF FIGURES CONTINUED

Figure Page

9-48: Computed effective shear moduli for the melt-freeze layer below the near surface facets in sample NS2 using the tensor ratio for directional data. 286

9-49: Computed effective Young's moduli for the melt-freeze layer below the near surface facets in sample NS2 using the tensor ratio for directional data. 287

9-50: Computed effective Young's moduli for the cohesive layer below the near surface facets in sample 1W3 using the tensor ratio for directional data. 290

9-51: MIL tensor diagonal values for the coarsened layer of snow beneath the faceted layer of experimental sample 1W3. 290

9-52: Tensor ratio coefficients for the sub-faceted layer of experimental sample 1W3. 291

10-1: Regions used for examining relative displacements within local regions of the microstructure. Average displacements are computed at the top and bottom edges of the boundaries for the entire cross-sectional plane defined at that boundary. The different colored regions define the top and bottom boundaries of the regions utilized in the results presented in this chapter. 301

10-2: FEA simulated average shear stress and strain for the initial snow surface and the radiation recrystallized faceted layer of experimental sample NS1. 303

10-3: FEA simulated average compressive stress and strain for the initial snow surface and the radiation recrystallized faceted layer of experimental sample NS1. 306

LIST OF FIGURES CONTINUED

Figure Page

10-4: FEA simulated effective compressive stress and strain for the initial snow surface and the radiation recrystallized faceted layer of experimental sample NS3. 309

10-5: FEA simulated effective shear stress and strain for the initial snow surface and the radiation recrystallized faceted layer of experimental sample NS3. 310

10-6: FEA simulated effective shear stress and strain for the initial snow surface and the radiation recrystallized faceted layer of experimental sample 1W1. 312

10-7: FEA simulated effective compressive stress and strain for the initial snow surface and the radiation recrystallized faceted layer of experimental sample 1W1. 314

10-8: FEA simulated effective compressive stress and strain for the initial snow surface and the radiation recrystallized faceted layer of experimental sample 1W3. 317

10-9: FEA simulated effective shear stress and strain for the initial snow surface and the radiation recrystallized faceted layer of experimental sample 1W3. 319

10-10: FEA simulated effective shear stress and strain for the initial snow surface and the radiation recrystallized faceted layer of experimental sample 2W1. 321

10-11: FEA simulated effective compressive stress and strain for the initial snow surface and the radiation recrystallized faceted layer of experimental sample 2W1. 323

LIST OF FIGURES CONTINUED

Figure Page

10-12: Volume rendering of a hexagonal cup/facet chain with the predominant crystal axis oriented vertically – parallel to the macro-scale temperature gradient (adapted from Adams and Walters, 2014). 332

10-13: Simulated shear stress and strain of the initial and faceted volumes of experimental sample 1W2. 334

10-14: Displacement in the x-direction (mm) overlaid on the deformed mesh (25x displacement) during the final load step of the simulated shear test on the faceted volume of sample 1W2. 335

10-15: Two dimensional analysis of a part with two sharp corners loaded horizontally in tension. Mesh refinement around sharp changes in geometry results in more accurate computation and distribution of stress. 337

10-16: Sample NS1 with simulated compression load in the vertical direction. Circled elements show areas with significant flexural stress and high stress gradients. 338

A-1: User interface for activating the virtual instrument, selecting the data filename and directory, and panel for live preview of data. 371

A-2: Main internal block diagram for sampling data, producing the live previews, and recording the data to a measurement file. 372

D-1: Shear stress and strain from the physical shear test of sample NS1. Includes data from the initial snow sample prior to recrystallization (blue) and data post recrystallization within the faceted layer (red) and below the faceted layer (black). Best fit lines are plotted to compute the shear modulus. 457

LIST OF FIGURES CONTINUED

Figure Page

D-2: Sequence of shear strain contours on sample NS1 of the initial non-recrystallized sample showing development of mostly uniform shear strain. Samples are loaded from right to left. The final image (Stage 70) is after failure of the sample has occurred. 458

D-3: Sequence of shear strain contours on sample NS1 of the radiation recrystallized sample showing development of localized shear strain in the faceted layer. Samples are loaded from right to left. The final image (Stage 62) is after partial failure of the sample has occurred. Failure continues across the plane defined by the area of increased shear strain. 459

D-4: Stage point locations used to query and average strain in regions of interest of sample NS1. Eight points (Stage point 0 through Stage point 7) are positioned within the faceted layer. Four points (Stage point 12 through Stage point 15) are positioned below the faceted layer. 460

D-5: Shear stress and strain from the physical shear test of sample NS2. Includes data from the initial snow sample prior to recrystallization (blue) and data post recrystallization within the faceted layer (red) and below the faceted layer (black). Best fit lines are plotted to compute the shear modulus. 460

D-6: Sequence of shear strain contours on sample NS2 of the initial non-recrystallized sample showing development of mostly uniform shear strain. Samples are loaded from right to left. The final image (Stage 71) is after failure of the sample has occurred. Although it appears a localized region of shear strain develops in the center, this is an artifact that became apparent after failure had occurred in the extreme lower right corner shown in Stage 71. 461

LIST OF FIGURES CONTINUED

Figure Page

D-7: Sequence of shear strain contours on sample NS2 of the radiation recrystallized sample showing development of localized shear strain in the faceted layer. Samples are loaded from right to left. The final image (Stage 43) is after failure of the sample has occurred. Failure occurred in a clean plane defined by the line of increased shear strain. 462

D-8: Stage point locations used to query and average strain in regions of interest of sample NS2. Eight points (Stage point 0 through Stage point 7) are positioned within the faceted layer. Four points (Stage point 12 through Stage point 15) are positioned below the faceted layer. 463

D-9: Compressive stress and strain from the physical compression test of sample NS3. Includes data from the initial snow sample prior to recrystallization (blue) and data post recrystallization within the faceted layer (red) and below the faceted layer (black). Best fit lines are plotted to compute the Young's modulus. 463

D-10: Sequence of minor strain contours on sample NS3 of the initial non-recrystallized sample showing development of mostly uniform minor strain. Minor strain is the minimum principal value of strain. In these images, the minor strain directions are oriented vertically (blue y-axis in the images). Samples are loaded in compression from top to bottom. The final image (Stage 59) is after failure of the sample has occurred. The failure plane was non-planar and only manifested in measurable minor strain on a small portion of the exposed column. Elastic strain recovery is exhibited in other portions of the sample. 464

LIST OF FIGURES CONTINUED

Figure Page

D-11: Sequence of minor strain contours on sample NS3 of the radiation recrystallized sample showing development of minor strain in a localized region coincident with the faceted layer. Minor strain is the minimum principal value of strain. In these images, the minor strain directions are oriented vertically in areas of non-zero strain (blue y-axis in the images). Samples are loaded in compression from top to bottom. The final image (Stage 38) is after failure of the sample has occurred. The failure plane was planar and eventually propagated across the entire faceted layer..... 465

D-12: Stage point locations used to query and average strain in regions of interest of sample NS3. Eight points (Stage point 0 through Stage point 7) are positioned within the faceted layer. Four points (Stage point 12 through Stage point 15) are positioned below the faceted layer. 466

D-13: Shear stress and strain from the physical shear test of sample 1W1. Includes data from the initial snow sample prior to recrystallization (blue) and data post recrystallization within the faceted layer (red) and below the faceted layer (black). Best fit lines are plotted to compute the shear modulus. 466

D-14: Sequence of shear strain contours on sample 1W1 of the initial non-recrystallized sample showing development of differing levels shear strain in the 1 week old snow (lower region with increased strain) and the new snow burying it (upper two thirds of the contours). Samples are loaded from right to left. The final image (Stage 44) is after failure of the sample has occurred. Failure of this sample occurred within the 1 week old snow approximately 2 cm below the old snow/new snow interface. 467

LIST OF FIGURES CONTINUED

Figure Page

D-15: Sequence of shear strain contours on sample 1W1 of the radiation recrystallized sample showing development of localized shear strain in the faceted layer. Samples are loaded from right to left. The final image (Stage 72) is after failure of the sample has occurred. Failure occurred along the plane defined by the area of increased shear strain. After separation, the upper slab seemed to get stuck and begin exhibiting increased uniform shear strain as the load actuator continued to push on the sample..... 468

D-16: Stage point locations used to query and average strain in regions of interest of sample 1W1. Eight points (Stage point 0 through Stage point 7) are positioned within the faceted layer. Four points (Stage point 12 through Stage point 15) are positioned below the faceted layer. 469

D-17: Shear stress and strain from the physical shear test of sample 1W2. Includes data from the initial snow sample prior to recrystallization (blue) and data post recrystallization within the faceted layer (red) and below the faceted layer (black). Best fit lines are plotted to compute the shear modulus. 469

D-18: Sequence of shear strain contours on sample 1W1 of the initial non-recrystallized sample showing development uniform levels shear strain. No discernable region in strain marks the interface between old snow and new snow. Samples are loaded from right to left. The final image (Stage 44) is after failure of the sample has occurred. Failure occurred at the base of the sample with the opening of a tensile crack in the lower right portion of the sample, similar to all other non-recrystallized shear tests. 470

LIST OF FIGURES CONTINUED

Figure Page

D-19: Sequence of shear strain contours on sample 1W2 of the radiation recrystallized sample showing development of localized shear strain in the faceted layer. Samples are loaded from right to left. The final image (Stage 71) is after failure of the sample has occurred. Failure occurred along the plane defined by the area of increased shear strain. 471

D-20: Stage point locations used to query and average strain in regions of interest of sample 1W2. Eight points (Stage point 0 through Stage point 7) are positioned within the faceted layer. Four points (Stage point 12 through Stage point 15) are positioned below the faceted layer. 472

D-21: Compressive stress and strain from the physical compression test of sample 1W3. Includes data from the initial snow sample before recrystallization (blue) and data post recrystallization within the faceted layer (red) and below the faceted layer (black). Best fit lines are plotted to compute Young's modulus. 472

D-22: Sequence of minor strain contours on sample 1W3 of the initial non-recrystallized sample showing development of differing levels shear strain in the 1 week old snow (lower region with increased strain) and the new snow burying it (upper region of the contours). Minor strain is the minimum principal value of strain. In these images, the minor strain directions are oriented vertically (blue y-axis in the images). Samples are loaded in compression from top to bottom. The final image (Stage 59) is after failure of the sample has occurred. Failure of this sample occurred within the 1 week old snow approximately 3 cm below the old snow/new snow interface. The failure plane was non-planar and only manifested in measurable minor strain on a small portion of the exposed column. Elastic strain recovery is exhibited in other portions of the sample. 473

LIST OF FIGURES CONTINUED

Figure Page

D-23: Sequence of minor strain contours on sample 1W3 of the radiation recrystallized sample showing development of minor strain in a localized region coincident with the faceted layer. Minor strain is the minimum principal value of strain. In these images, the minor strain directions are oriented vertically in areas of non-zero strain (blue y-axis in the images). Samples are loaded in compression from top to bottom. The final image (Stage 38) is after failure of the sample has occurred. The failure plane was planar and eventually propagated across the entire faceted layer..... 474

D-24: Stage point locations used to query and average strain in regions of interest of sample 1W3. Eight points (Stage point 0 through Stage point 7) are positioned within the faceted layer. Four points (Stage point 12 through Stage point 15) are positioned below the faceted layer. 475

D-25: Shear stress and strain from the physical shear test of sample 2W1. Includes data from the initial snow sample prior to recrystallization (blue) and data post recrystallization within the faceted layer (red) and below the faceted layer (black). Best fit lines are plotted to compute shear modulus. 475

D-26: Sequence of shear strain contours on sample 2W1 of the initial non-recrystallized sample showing development of differing levels shear strain in the 2 weeks old snow (lower region with increased strain) and the new snow burying it (upper two thirds of the contours). Concentration of strain occurs just below the new snow/old snow interface. Samples are loaded from right to left. The final image (Stage 43) is after failure of the sample has occurred. Failure of this sample occurred within the 2 weeks old snow approximately 1 cm below the old snow/new snow interface..... 476

LIST OF FIGURES CONTINUED

Figure Page

D-27: Stage point locations used to query and average strain in regions of interest of sample 2W1. Eight points (Stage point 0 through Stage point 7) are positioned within the faceted layer. Four points (Stage point 12 through Stage point 15) are positioned below the faceted layer. 477

E-1: Changes in volume fraction, ϕ, in the top 7.00 mm of sample NS1 associated with the faceted layer during the process of radiation recrystallization. 480

E-2: Changes in mean bond radius, ρ, and grain radius, R, in the top 7.00 mm of sample NS1 associated with the faceted layer during the process of radiation recrystallization. 481

E-3: Changes in mean 3-D coordination number, $\mathcal{N}$, in the top 7.00 mm of sample NS1 associated with the faceted layer during the process of radiation recrystallization. 481

E-4: Changes to the contact tensor diagonal coefficients aligned with the snow's coordinate system ($x3$ is vertical, normal to the snow surface) in the top 7.00 mm of sample NS1 associated with the faceted layer during the process of radiation recrystallization. 482

E-5: Changes to the MIL tensor diagonal coefficients aligned with the snow's coordinate system ($x3$ is vertical, normal to the snow surface) in the top 7.00 mm of sample NS1 associated with the faceted layer during the process of radiation recrystallization. 482

E-6: Changes to the tensor ratio diagonal coefficients aligned with the snow's coordinate system ($x3$ is vertical, normal to the snow surface) in the top 7.00 mm of sample NS1 associated with the faceted layer during the process of radiation recrystallization. 483

LIST OF FIGURES CONTINUED

Figure Page

E-7: Changes to the computed effective Young's moduli aligned with the snow's coordinate system in the top 7.00 mm of sample NS1 associated with the faceted layer during the process of radiation recrystallization. $E*$ represents the scalar computed effective Young's modulus. 483

E-8: Changes to the computed effective shear moduli aligned with the snow's coordinate system in the top 7.00 mm of sample NS1 associated with the faceted layer during the process of radiation recrystallization. $G*$ represents the scalar computed effective shear modulus. 484

E-9: Changes in volume fraction, ϕ, of sample NS1 associated with the layer below the faceted crystals during the process of radiation recrystallization. 484

E-10: Changes in mean bond radius, ρ, and grain radius, R, of sample NS1 associated layer below the faceted crystals during the process of radiation recrystallization. 485

E-11: Changes in mean 3-D coordination number, $\mathcal{N}$, of sample NS1 associated with the layer below the faceted crystals during the process of radiation recrystallization. 485

E-12: Changes to the contact tensor diagonal coefficients aligned with the snow's coordinate system ($x3$ is vertical, normal to the snow surface) of sample NS1 associated with the layer below the faceted crystals during the process of radiation recrystallization. 486

E-13: Changes to the MIL tensor diagonal coefficients aligned with the snow's coordinate system ($x3$ is vertical, normal to the snow surface) of sample NS1 associated with the layer below the faceted crystals during the process of radiation recrystallization. 486

LIST OF FIGURES CONTINUED

Figure Page

E-14: Changes to the tensor ratio diagonal coefficients aligned with the snow's coordinate system ($x3$ is vertical, normal to the snow surface) of sample NS1 associated with the layer below the faceted crystals during the process of radiation recrystallization. 487

E-15: Changes to the computed effective Young's moduli aligned with the snow's coordinate system of sample NS1 associated with the layer below the faceted crystals during the process of radiation recrystallization. $E*$ represents the scalar computed effective Young's modulus. 487

E-16: Changes to the computed effective shear moduli aligned with the snow's coordinate system of sample NS1 associated with the layer below the faceted crystals during the process of radiation recrystallization. $G*$ represents the scalar computed effective shear modulus. 488

E-17: Changes in volume fraction, ϕ, in the top 5.13 mm of sample NS2 associated with the faceted layer during the process of radiation recrystallization. 488

E-18: Changes in mean bond radius, ρ, and grain radius, R, in the top 5.13 mm of sample NS2 associated with the faceted layer during the process of radiation recrystallization. 489

E-19: Changes in mean 3-D coordination number, $\mathcal{N}$, in the top 5.13 mm of sample NS2 associated with the faceted layer during the process of radiation recrystallization. 489

E-20: Changes to the contact tensor diagonal coefficients aligned with the snow's coordinate system ($x3$ is vertical, normal to the snow surface) in the top 5.13 mm of sample NS2 associated with the faceted layer during the process of radiation recrystallization. 490

LIST OF FIGURES CONTINUED

Figure Page

E-21: Changes to the MIL tensor diagonal coefficients aligned with the snow's coordinate system ($x3$ is vertical, normal to the snow surface) in the top 5.13 mm of sample NS2 associated with the faceted layer during the process of radiation recrystallization. 490

E-22: Changes to the tensor ratio diagonal coefficients aligned with the snow's coordinate system ($x3$ is vertical, normal to the snow surface) in the top 5.13 mm of sample NS2 associated with the faceted layer during the process of radiation recrystallization. 491

E-23: Changes to the computed effective Young's moduli aligned with the snow's coordinate system in the top 5.13 mm of sample NS2 associated with the faceted layer during the process of radiation recrystallization. $E*$ represents the scalar computed effective Young's modulus. 491

E-24: Changes to the computed effective shear moduli aligned with the snow's coordinate system in the top 5.13 mm of sample NS2 associated with the faceted layer during the process of radiation recrystallization. $G*$ represents the scalar computed effective shear modulus. 492

E-25: Changes in volume fraction, ϕ, of sample NS2 associated with the layer below the faceted crystals during the process of radiation recrystallization. 492

E-26: Changes in mean bond radius, ρ, and grain radius, R, of sample NS2 associated layer below the faceted crystals during the process of radiation recrystallization. 493

E-27: Changes in mean 3-D coordination number, $\mathcal{N}$, of sample NS2 associated with the layer below the faceted crystals during the process of radiation recrystallization. 493

LIST OF FIGURES CONTINUED

Figure Page

E-28: Changes to the contact tensor diagonal coefficients aligned with the snow's coordinate system ($x3$ is vertical, normal to the snow surface) of sample NS2 associated with the layer below the faceted crystals during the process of radiation recrystallization. 494

E-29: Changes to the MIL tensor diagonal coefficients aligned with the snow's coordinate system ($x3$ is vertical, normal to the snow surface) of sample NS2 associated with the layer below the faceted crystals during the process of radiation recrystallization. 494

E-30: Changes to the tensor ratio diagonal coefficients aligned with the snow's coordinate system ($x3$ is vertical, normal to the snow surface) of sample NS2 associated with the layer below the faceted crystals during the process of radiation recrystallization. 495

E-31: Changes to the computed effective Young's moduli aligned with the snow's coordinate system of sample NS2 associated with the layer below the faceted crystals during the process of radiation recrystallization. $E*$ represents the scalar computed effective Young's modulus. 495

E-32: Changes to the computed effective shear moduli aligned with the snow's coordinate system of sample NS2 associated with the layer below the faceted crystals during the process of radiation recrystallization. $G*$ represents the scalar computed effective shear modulus. 496

E-33: Changes in volume fraction, ϕ, in the top 5.52 mm of sample NS3 associated with the faceted layer during the process of radiation recrystallization. 496

LIST OF FIGURES CONTINUED

Figure Page

E-34: Changes in mean bond radius, ρ, and grain radius, R, in the top 5.52 mm of sample NS3 associated with the faceted layer during the process of radiation recrystallization. 497

E-35: Changes in mean 3-D coordination number, $\mathcal{N}$, in the top 5.52 mm of sample NS3 associated with the faceted layer during the process of radiation recrystallization. 497

E-36: Changes to the contact tensor diagonal coefficients aligned with the snow's coordinate system ($x3$ is vertical, normal to the snow surface) in the top 5.52 mm of sample NS3 associated with the faceted layer during the process of radiation recrystallization. 498

E-37: Changes to the MIL tensor diagonal coefficients aligned with the snow's coordinate system ($x3$ is vertical, normal to the snow surface) in the top 5.52 mm of sample NS3 associated with the faceted layer during the process of radiation recrystallization. 498

E-38: Changes to the tensor ratio diagonal coefficients aligned with the snow's coordinate system ($x3$ is vertical, normal to the snow surface) in the top 5.52 mm of sample NS3 associated with the faceted layer during the process of radiation recrystallization. 499

E-39: Changes to the computed effective Young's moduli aligned with the snow's coordinate system in the top 5.52 mm of sample NS3 associated with the faceted layer during the process of radiation recrystallization. $E*$ represents the scalar computed effective Young's modulus. 499

LIST OF FIGURES CONTINUED

Figure Page

E-40: Changes to the computed effective shear moduli aligned with the snow's coordinate system in the top 5.52 mm of sample NS3 associated with the faceted layer during the process of radiation recrystallization. $G*$ represents the scalar computed effective shear modulus. 500

E-41: Changes in volume fraction, ϕ, of sample NS3 associated with the layer below the faceted crystals during the process of radiation recrystallization. 500

E-42: Changes in mean bond radius, ρ, and grain radius, R, of sample NS3 associated layer below the faceted crystals during the process of radiation recrystallization. 501

E-43: Changes in mean 3-D coordination number, $\mathcal{N}$, of sample NS3 associated with the layer below the faceted crystals during the process of radiation recrystallization. 501

E-44: Changes to the contact tensor diagonal coefficients aligned with the snow's coordinate system ($x3$ is vertical, normal to the snow surface) of sample NS3 associated with the layer below the faceted crystals during the process of radiation recrystallization. 502

E-45: Changes to the MIL tensor diagonal coefficients aligned with the snow's coordinate system ($x3$ is vertical, normal to the snow surface) of sample NS3 associated with the layer below the faceted crystals during the process of radiation recrystallization. 502

E-46: Changes to the tensor ratio diagonal coefficients aligned with the snow's coordinate system ($x3$ is vertical, normal to the snow surface) of sample NS3 associated with the layer below the faceted crystals during the process of radiation recrystallization. 503

LIST OF FIGURES CONTINUED

Figure Page

E-47: Changes to the computed effective Young's moduli aligned with the snow's coordinate system of sample NS3 associated with the layer below the faceted crystals during the process of radiation recrystallization. $E*$ represents the scalar computed effective Young's modulus. 503

E-48: Changes to the computed effective shear moduli aligned with the snow's coordinate system of sample NS3 associated with the layer below the faceted crystals during the process of radiation recrystallization. $G*$ represents the scalar computed effective shear modulus. 504

E-49: Changes in volume fraction, ϕ, in the top 7.00 mm of sample 1W1 associated with the faceted layer during the process of radiation recrystallization. 504

E-50: Changes in mean bond radius, ρ, and grain radius, R, in the top 7.00 mm of sample 1W1 associated with the faceted layer during the process of radiation recrystallization. 505

E-51: Changes in mean 3-D coordination number, $\mathcal{N}$, in the top 7.00 mm of sample 1W1 associated with the faceted layer during the process of radiation recrystallization. 505

E-52: Changes to the contact tensor diagonal coefficients aligned with the snow's coordinate system ($x3$ is vertical, normal to the snow surface) in the top 7.00 mm of sample 1W1 associated with the faceted layer during the process of radiation recrystallization. 506

E-53: Changes to the MIL tensor diagonal coefficients aligned with the snow's coordinate system ($x3$ is vertical, normal to the snow surface) in the top 7.00 mm of sample 1W1 associated with the faceted layer during the process of radiation recrystallization. 506

LIST OF FIGURES CONTINUED

Figure Page

E-54: Changes to the tensor ratio diagonal coefficients aligned with the snow's coordinate system ($x3$ is vertical, normal to the snow surface) in the top 7.00 mm of sample 1W1 associated with the faceted layer during the process of radiation recrystallization. 507

E-55: Changes to the computed effective Young's moduli aligned with the snow's coordinate system in the top 7.00 mm of sample 1W1 associated with the faceted layer during the process of radiation recrystallization. $E*$ represents the scalar computed effective Young's modulus. 507

E-56: Changes to the computed effective shear moduli aligned with the snow's coordinate system in the top 7.00 mm of sample 1W1 associated with the faceted layer during the process of radiation recrystallization. $G*$ represents the scalar computed effective shear modulus. 508

E-57: Changes in volume fraction, ϕ, of sample 1W1 associated with the layer below the faceted crystals during the process of radiation recrystallization. 508

E-58: Changes in mean bond radius, ρ, and grain radius, R, of sample 1W1 associated layer below the faceted crystals during the process of radiation recrystallization. 509

E-59: Changes in mean 3-D coordination number, $\mathcal{N}$, of sample 1W1 associated with the layer below the faceted crystals during the process of radiation recrystallization. 509

E-60: Changes to the contact tensor diagonal coefficients aligned with the snow's coordinate system ($x3$ is vertical, normal to the snow surface) of sample 1W1 associated with the layer below the faceted crystals during the process of radiation recrystallization. 510

LIST OF FIGURES CONTINUED

Figure Page

E-61: Changes to the MIL tensor diagonal coefficients aligned with the snow's coordinate system ($x3$ is vertical, normal to the snow surface) of sample 1W1 associated with the layer below the faceted crystals during the process of radiation recrystallization. 510

E-62: Changes to the tensor ratio diagonal coefficients aligned with the snow's coordinate system ($x3$ is vertical, normal to the snow surface) of sample 1W1 associated with the layer below the faceted crystals during the process of radiation recrystallization. 511

E-63: Changes to the computed effective Young's moduli aligned with the snow's coordinate system of sample 1W1 associated with the layer below the faceted crystals during the process of radiation recrystallization. $E*$ represents the scalar computed effective Young's modulus. 511

E-64: Changes to the computed effective shear moduli aligned with the snow's coordinate system of sample 1W1 associated with the layer below the faceted crystals during the process of radiation recrystallization. $G*$ represents the scalar computed effective shear modulus. 512

E-65: Changes in volume fraction, ϕ, in the top 7.00 mm of sample 1W2 associated with the faceted layer during the process of radiation recrystallization. 512

E-66: Changes in mean bond radius, ρ, and grain radius, R, in the top 7.00 mm of sample 1W2 associated with the faceted layer during the process of radiation recrystallization. 513

E-67: Changes in mean 3-D coordination number, $\mathcal{N}$, in the top 7.00 mm of sample 1W2 associated with the faceted layer during the process of radiation recrystallization. 513

LIST OF FIGURES CONTINUED

Figure Page

E-68: Changes to the contact tensor diagonal coefficients aligned with the snow's coordinate system ($x3$ is vertical, normal to the snow surface) in the top 7.00 mm of sample 1W2 associated with the faceted layer during the process of radiation recrystallization. 514

E-69: Changes to the MIL tensor diagonal coefficients aligned with the snow's coordinate system ($x3$ is vertical, normal to the snow surface) in the top 7.00 mm of sample 1W2 associated with the faceted layer during the process of radiation recrystallization. 514

E-70: Changes to the tensor ratio diagonal coefficients aligned with the snow's coordinate system ($x3$ is vertical, normal to the snow surface) in the top 7.00 mm of sample 1W2 associated with the faceted layer during the process of radiation recrystallization. 515

E-71: Changes to the computed effective Young's moduli aligned with the snow's coordinate system in the top 7.00 mm of sample 1W2 associated with the faceted layer during the process of radiation recrystallization. $E*$ represents the scalar computed effective Young's modulus. 515

E-72: Changes to the computed effective shear moduli aligned with the snow's coordinate system in the top 7.00 mm of sample 1W2 associated with the faceted layer during the process of radiation recrystallization. $G*$ represents the scalar computed effective shear modulus. 516

E-73: Changes in volume fraction, ϕ, of sample 1W2 associated with the layer below the faceted crystals during the process of radiation recrystallization. 516

LIST OF FIGURES CONTINUED

Figure Page

E-74: Changes in mean bond radius, ρ, and grain radius, R, of sample 1W2 associated layer below the faceted crystals during the process of radiation recrystallization. 517

E-75: Changes in mean 3-D coordination number, $\mathcal{N}$, of sample 1W2 associated with the layer below the faceted crystals during the process of radiation recrystallization. 517

E-76: Changes to the contact tensor diagonal coefficients aligned with the snow's coordinate system ($x3$ is vertical, normal to the snow surface) of sample 1W2 associated with the layer below the faceted crystals during the process of radiation recrystallization. 518

E-77: Changes to the MIL tensor diagonal coefficients aligned with the snow's coordinate system ($x3$ is vertical, normal to the snow surface) of sample 1W2 associated with the layer below the faceted crystals during the process of radiation recrystallization. 518

E-78: Changes to the tensor ratio diagonal coefficients aligned with the snow's coordinate system ($x3$ is vertical, normal to the snow surface) of sample 1W2 associated with the layer below the faceted crystals during the process of radiation recrystallization. 519

E-79: Changes to the computed effective Young's moduli aligned with the snow's coordinate system of sample 1W2 associated with the layer below the faceted crystals during the process of radiation recrystallization. $E*$ represents the scalar computed effective Young's modulus. 519

LIST OF FIGURES CONTINUED

Figure Page

E-80: Changes to the computed effective shear moduli aligned with the snow's coordinate system of sample 1W2 associated with the layer below the faceted crystals during the process of radiation recrystallization. $G*$ represents the scalar computed effective shear modulus. 520

E-81: Changes in volume fraction, ϕ, in the top 7.95 mm of sample 1W3 associated with the faceted layer during the process of radiation recrystallization. 520

E-82: Changes in mean bond radius, ρ, and grain radius, R, in the top 7.95 mm of sample 1W3 associated with the faceted layer during the process of radiation recrystallization. 521

E-83: Changes in mean 3-D coordination number, $\mathcal{N}$, in the top 7.95 mm of sample 1W3 associated with the faceted layer during the process of radiation recrystallization. 521

E-84: Changes to the contact tensor diagonal coefficients aligned with the snow's coordinate system ($x3$ is vertical, normal to the snow surface) in the top 7.95 mm of sample 1W3 associated with the faceted layer during the process of radiation recrystallization. 522

E-85: Changes to the MIL tensor diagonal coefficients aligned with the snow's coordinate system ($x3$ is vertical, normal to the snow surface) in the top 7.95 mm of sample 1W3 associated with the faceted layer during the process of radiation recrystallization. 522

E-86: Changes to the tensor ratio diagonal coefficients aligned with the snow's coordinate system ($x3$ is vertical, normal to the snow surface) in the top 7.95 mm of sample 1W3 associated with the faceted layer during the process of radiation recrystallization. 523

LIST OF FIGURES CONTINUED

Figure Page

E-87: Changes to the computed effective Young's moduli aligned with the snow's coordinate system in the top 7.95 mm of sample 1W3 associated with the faceted layer during the process of radiation recrystallization. $E*$ represents the scalar computed effective Young's modulus. 523

E-88: Changes to the computed effective shear moduli aligned with the snow's coordinate system in the top 7.95 mm of sample 1W3 associated with the faceted layer during the process of radiation recrystallization. $G*$ represents the scalar computed effective shear modulus. 524

E-89: Changes in volume fraction, ϕ, of sample 1W3 associated with the layer below the faceted crystals during the process of radiation recrystallization. 524

E-90: Changes in mean bond radius, ρ, and grain radius, R, of sample 1W3 associated layer below the faceted crystals during the process of radiation recrystallization. 525

E-91: Changes in mean 3-D coordination number, $\mathcal{N}$, of sample 1W3 associated with the layer below the faceted crystals during the process of radiation recrystallization. 525

E-92: Changes to the contact tensor diagonal coefficients aligned with the snow's coordinate system ($x3$ is vertical, normal to the snow surface) of sample 1W3 associated with the layer below the faceted crystals during the process of radiation recrystallization. 526

E-93: Changes to the MIL tensor diagonal coefficients aligned with the snow's coordinate system ($x3$ is vertical, normal to the snow surface) of sample 1W3 associated with the layer below the faceted crystals during the process of radiation recrystallization. 526

LIST OF FIGURES CONTINUED

Figure Page

E-94: Changes to the tensor ratio diagonal coefficients aligned with the snow's coordinate system ($x3$ is vertical, normal to the snow surface) of sample 1W3 associated with the layer below the faceted crystals during the process of radiation recrystallization. 527

E-95: Changes to the computed effective Young's moduli aligned with the snow's coordinate system of sample 1W3 associated with the layer below the faceted crystals during the process of radiation recrystallization. $E*$ represents the scalar computed effective Young's modulus. 527

E-96: Changes to the computed effective shear moduli aligned with the snow's coordinate system of sample 1W3 associated with the layer below the faceted crystals during the process of radiation recrystallization. $G*$ represents the scalar computed effective shear modulus. 528

E-97: Changes in volume fraction, ϕ, in the top 5.12 mm of sample 2W1 associated with the faceted layer during the process of radiation recrystallization. 528

E-98: Changes in mean bond radius, ρ, and grain radius, R, in the top 5.12 mm of sample 2W1 associated with the faceted layer during the process of radiation recrystallization. 529

E-99: Changes in mean 3-D coordination number, $\mathcal{N}$, in the top 5.12 mm of sample 2W1 associated with the faceted layer during the process of radiation recrystallization. 529

E-100: Changes to the contact tensor diagonal coefficients aligned with the snow's coordinate system ($x3$ is vertical, normal to the snow surface) in the top 5.12 mm of sample 2W1 associated with the faceted layer during the process of radiation recrystallization. 530

LIST OF FIGURES CONTINUED

Figure Page

E-101: Changes to the MIL tensor diagonal coefficients aligned with the snow's coordinate system ($x3$ is vertical, normal to the snow surface) in the top 5.12 mm of sample 2W1 associated with the faceted layer during the process of radiation recrystallization. 530

E-102: Changes to the tensor ratio diagonal coefficients aligned with the snow's coordinate system ($x3$ is vertical, normal to the snow surface) in the top 5.12 mm of sample 2W1 associated with the faceted layer during the process of radiation recrystallization. 531

E-103: Changes to the computed effective Young's moduli aligned with the snow's coordinate system in the top 5.12 mm of sample 2W1 associated with the faceted layer during the process of radiation recrystallization. $E*$ represents the scalar computed effective Young's modulus. 531

E-104: Changes to the computed effective shear moduli aligned with the snow's coordinate system in the top 5.12 mm of sample 2W1 associated with the faceted layer during the process of radiation recrystallization. $G*$ represents the scalar computed effective shear modulus. 532

E-105: Changes in volume fraction, ϕ, of sample 2W1 associated with the layer below the faceted crystals during the process of radiation recrystallization. 532

E-106: Changes in mean bond radius, ρ, and grain radius, R, of sample 2W1 associated layer below the faceted crystals during the process of radiation recrystallization. 533

E-107: Changes in mean 3-D coordination number, $\mathcal{N}$, of sample 2W1 associated with the layer below the faceted crystals during the process of radiation recrystallization. 533

LIST OF FIGURES CONTINUED

Figure Page

E-108: Changes to the contact tensor diagonal coefficients aligned with the snow's coordinate system ($x3$ is vertical, normal to the snow surface) of sample 2W1 associated with the layer below the faceted crystals during the process of radiation recrystallization. 534

E-109: Changes to the MIL tensor diagonal coefficients aligned with the snow's coordinate system ($x3$ is vertical, normal to the snow surface) of sample 2W1 associated with the layer below the faceted crystals during the process of radiation recrystallization. 534

E-110: Changes to the tensor ratio diagonal coefficients aligned with the snow's coordinate system ($x3$ is vertical, normal to the snow surface) of sample 2W1 associated with the layer below the faceted crystals during the process of radiation recrystallization. 535

E-111: Changes to the computed effective Young's moduli aligned with the snow's coordinate system of sample 2W1 associated with the layer below the faceted crystals during the process of radiation recrystallization. $E*$ represents the scalar computed effective Young's modulus. 535

E-112: Changes to the computed effective shear moduli aligned with the snow's coordinate system of sample 2W1 associated with the layer below the faceted crystals during the process of radiation recrystallization. $G*$ represents the scalar computed effective shear modulus. 536

F-1: FEA simulated average compressive stress and strain for the initial snow surface and the radiation recrystallized faceted layer of experimental sample NS1. 539

LIST OF FIGURES CONTINUED

Figure Page

F-2: FEA simulated average shear stress and strain for the initial snow surface and the radiation recrystallized faceted layer of experimental sample NS1. 539

F-3: FEA simulated average compressive stress and strain for the initial snow surface and the radiation recrystallized faceted layer of experimental sample NS2. 540

F-4: FEA simulated average shear stress and strain for the initial snow surface and the radiation recrystallized faceted layer of experimental sample NS2. 540

F-5: FEA simulated average compressive stress and strain for the initial snow surface and the radiation recrystallized faceted layer of experimental sample NS3. 541

F-6: FEA simulated average shear stress and strain for the initial snow surface and the radiation recrystallized faceted layer of experimental sample NS3. 541

F-7: FEA simulated average compressive stress and strain for the initial snow surface and the radiation recrystallized faceted layer of experimental sample 1W1. 542

F-8: FEA simulated average shear stress and strain for the initial snow surface and the radiation recrystallized faceted layer of experimental sample 1W1. 542

F-9: FEA simulated average compressive stress and strain for the initial snow surface and the radiation recrystallized faceted layer of experimental sample 1W2. 543

F-10: FEA simulated average shear stress and strain for the initial snow surface and the radiation recrystallized faceted layer of experimental sample 1W2. 543

LIST OF FIGURES CONTINUED

Figure Page

F-11: FEA simulated average compressive stress and strain for the initial snow surface and the radiation recrystallized faceted layer of experimental sample 1W3. 544

F-12: FEA simulated average shear stress and strain for the initial snow surface and the radiation recrystallized faceted layer of experimental sample 1W3. 544

F-13: FEA simulated average compressive stress and strain for the initial snow surface and the radiation recrystallized faceted layer of experimental sample 2W1. 545

F-14: FEA simulated average shear stress and strain for the initial snow surface and the radiation recrystallized faceted layer of experimental sample 2W1. 545

NOMENCLATURE

A	notation for a scalar
$\bar{A}, A_i$	notation for a vector, Cartesian components
$\boldsymbol{A}, A_{ij}$	notation for a 2nd order tensor, Cartesian components
$\mathbb{A}, A_{ijkl}$	notation for a 4th order tensor, Cartesian components
∇	del operator
$\cdot$	dot product
:	double dot product
$\otimes$	dyadic product
$\lfloor\ \rfloor$	interpolation function
δ_{ij}	Kronecker delta
$\langle\ \rangle$	volume average
exp( )	exponential (e^x)
A_c^{α}	area of contact α ($\mathrm{m}^2, \mathrm{mm}^2$)
$\mathbb{C}, C_{ijkl}$	4th order stiffness tensor, components (Pa)
$[C^*]$	effective stiffness coefficient in matrix form (Pa)
E_i	Young's modulus in axial direction x_1 (Pa)
E^*	effective scalar Young's modulus (Pa)

NOMENCLATURE CONTINUED

E_{ice}	Young's modulus of ice (GPa)
$\bar{F}$	general macro-scale homogenization flux term
$\boldsymbol{F}, F_{ij}$	2nd order contact tensor (-)
$\hat{F}_{ij}$	isotropic components of the contact tensor (-)
F'_{ij}	deviatoric components of the contact tensor (-)
G_{ij}	shear modulus on the x_i-x_j plane (Pa)
$\bar{G}$	general macro-scale homogenization gradient term
G_{ice}	shear modulus of ice (GPa)
G^*	effective second Lamé parameter/shear modulus (Pa)
$\boldsymbol{H}, H_{ij}$	MIL fabric tensor (-)
$I(\omega)$	number of test grid intersections at orientation ω (-)
$\boldsymbol{K}$	general proportionality constant
$\boldsymbol{K}^*$	general effective prop. constant derived from microstructure
L	total length of the test grid lines in MIL tensor analysis (m)
$\bar{L}^{\alpha}$	branch vector connecting centroids of bonded grains (-)
L_s	latent heat of sublimation for water ($2833\ \mathrm{kJ \cdot kg^{-1}}$)
LW_{in}	total incoming longwave radiation ($\mathrm{W \cdot m^{-2}}$)

NOMENCLATURE CONTINUED

$\boldsymbol{M}, M_{ij}$	inverse of the square of the mean intercept length tensor (m^{-2})
MIL	mean intercept length (m)
N	total number of contact vectors (-)
$\mathcal{N}$	mean 3-D coordination number (-)
N_{cp}	number of contact planes in a volume (-)
$\hat{R}$	mean grain radius (m)
R_v	gas constant for water vapor ($0.462\ \mathrm{kJ} \cdot (\mathrm{kg} \cdot \mathrm{K})^{-1}$)
S	mean scalar shape correction factor (-)
S_α	scalar shape correction factor for grain-bond pair α (-)
$[S^*]$	effective compliance coefficients in matrix form (Pa^{-1})
SW_{in}	total incoming shortwave radiation ($\mathrm{W} \cdot \mathrm{m}^{-2}$)
T	temperature (°C or K, as specified)
V	volume ($\mathrm{m}^3, \mathrm{mm}^3$, etc.)
a	grain number (-)
a_i	generic degrees of freedom at node i (-)
c_p	heat capacity at a constant pressure ($J \cdot K^{-1}$)
e	vapor pressure (Pa)
d^α	distance from the grain center to the center of bond α (m)

NOMENCLATURE CONTINUED

f	scalar isotropic value of a fabric tensor (1/2 in 2-D, 1/3 in 3-D)
$\bar{f}$	general micro-scale homogenization flux term
$\Delta\bar{f}^{\alpha}$	incremental change in force at contact α (N)
$\bar{g}$	general micro-scale homogenization gradient term
$k, \boldsymbol{k}$	thermal conductivity ($\mathrm{W} \cdot (\mathrm{m} \cdot K)^{-1}$)
k_n	normal stiffness of grain-to-grain contact ($\mathrm{N} \cdot \mathrm{m}^{-1}$)
k_s	shear stiffness of grain-to-grain contact ($\mathrm{N} \cdot \mathrm{m}^{-1}$)
$\bar{m}$	unit vector connecting the centers of bonded grains (-)
$\bar{n}$	unit vector normal to contact plane (-)
$\bar{q}$	general heat flux ($\mathrm{W} \cdot \mathrm{m}^{-2}$)
$\bar{q}_k$	heat flux due to conduction ($\mathrm{W} \cdot \mathrm{m}^{-2}$)
q_{LW}	net longwave radiation flux ($\mathrm{W} \cdot \mathrm{m}^{-2}$)
$\bar{q}_{swo}$	initial penetrating shortwave energy flux ($\mathrm{W} \cdot \mathrm{m}^{-2}$)
$\bar{q}_{sw}$	attenuated shortwave energy flux ($\mathrm{W} \cdot \mathrm{m}^{-2}$)
r_{eff}^{a}	effective spherical grain radius of grain a (m)
$\bar{s}, \bar{t}$	unit vectors tangent to contact plane (-)
t	time (sec., hrs.)
u, v	displacement in the horizontal and vertical directions (m)

NOMENCLATURE CONTINUED

$\Delta\bar{u}_a$	incremental displacement vector of particle a (m)
x_i	axial directions (-)
$\bar{x}_a$	position vector of particle a (-)
z	depth (m)
$\mathbf{E}$	macro-scale strain tensor (-)
$\mathbf{\Delta E}$	macro-scale strain increment tensor (-)
$\mathbf{\Gamma}, \Gamma_{ij}$	tensor ratio (-)
Ω_i	generic FEA field qunaitity (-)
$\boldsymbol{T}$	macro-scale stress tensor (Pa)
$\mathbf{\Delta}\boldsymbol{T}$	macro-scale stress increment tensor (Pa)
α	bond number (-)
$\bar{\delta}^{\alpha}$	micro-scale displacement at contact α (m)
$\Delta\bar{\delta}^{\alpha}$	incremental displacement at contact α (m)
$\boldsymbol{\varepsilon}, \varepsilon_{nn}$	normal strain, components (-)
$\boldsymbol{\gamma}, \gamma_{ns}$	shear strain, components (-)
κ	number density of grains (m^{-3})
λ^*	effective 1st Lamé parameter (Pa)
ν	Poisson's ratio (-)

NOMENCLATURE CONTINUED

ν^*	effective Poisson's ratio (-)
ω	test grid orientation angle for MIL tensor analysis (rad or °)
ϕ	ice volume fraction (-)
ρ	density ($\mathrm{kg} \cdot \mathrm{m}^{-3}$)
$\hat{\rho}$	mean bond radius (m)
$\boldsymbol{\sigma}, \sigma_{nn}$	normal stress, components (Pa)
σ_{ts}, σ_{cs}	uniaxial tensile and compressive strengths (Pa)
ς	albedo (-)
$\boldsymbol{\tau}, \tau_{ns}$	shear stress, components (Pa)
τ_s	shear strength (Pa)
ϑ	internal energy (J)
$\bar{\xi}$	heat flux across a boundary ($\mathrm{W} \cdot \mathrm{m}^{-2}$)
ζ	ratio of micro-scale shear stiffness to axial stiffness (-)

ABSTRACT

Radiation recrystallized snow is a pervasive weak layer of snow that, once buried, increases the threat of snow avalanches. While much is known about the conditions required to form radiation recrystallized snow layers, little is understood about the microstructural intricacies that develop resulting in decreased macro-scale mechanical stability. This study utilizes the Subzero Science and Engineering Research Facility at Montana State University to recreate clear daytime meteorological conditions to induce near surface metamorphism in snow. This metamorphic process develops radiation recrystallized layers of faceted crystals in the top 1-2 cm of snow over the course of 12 hours. Mechanical testing is performed before and after recrystallization to compute the relative change in mechanical properties of the recrystallized snow sample.

Near surface samples are also extracted and imaged at regular intervals using computed tomography. Imaging results in a 3-D reconstruction of representative snow microstructures recording the temporal evolution of faceted crystal formation. The microstructural data is utilized in two modeling approaches which seek to describe the macro-scale mechanical properties of the snow. A previously developed homogenization approach, which computes macro-scale effective stiffness properties using micromechanical interactions and texture, is enhanced by incorporating measures of individual grain shapes and differing textural measures. Another approach leverages the microstructure directly by simulating the response of macro-scale loads on a geometric mesh of the imaged microstructure using finite element methods.

Following recrystallization, physical mechanical testing demonstrated that the metamorphism process forms a stiff and strong sublayer capped by a weaker layer of faceted snow that is 75-80% less stiff in shear and 80-90% less stiff in compression than the strong layer below it. Microstructural analysis revealed multiple fine layers of unique crystal morphologies existing within the faceted region. Homogenization reflected reasonable trends in relative changes of effective stiffness properties but suffered from volumetric scale problems when analyzing the faceted layer. Finite element methods also reasonably computed the relative change in macro-scale effective properties as a result of changes to the microstructural geometry. Additionally, the finite element method estimates changes to effective strength and the location of mechanical failure within the faceted layers.

CHAPTER ONE

INTRODUCTION

"The scientist does not study nature because it is useful to do so. He studies it because he takes pleasure in it, and he takes pleasure in it because it is beautiful."
~ Henri Poincaré from Science et méthode (1908)

1.1 Motivation

Avalanches are a force of nature that have the power slow commerce to a halt, kill the unsuspecting winter recreationist, and even change the landscape of the mountains for a lifetime. Avalanches and snow are also interesting from an engineering perspective. The interplay of distinct layers within snow and their rapid metamorphism presents a unique challenge to describe the mechanical properties which lead to overall stability or instability leading to avalanches. Just as the thermal properties dictate the metamorphism process of the snows' microstructure, the mechanical properties of the snow either promote or hinder avalanche stability.

Comprehensive mechanical testing for properties of uniformly structured snow has been performed and compiled in several places (e.g., Mellor 1975; Föhn et al. 1998; Schweizer 1999; Stoffel 2005). An area lacking detail is directional properties for non-uniformly structured snow. The study presented here aims to

investigate the anisotropic properties of thin, metamorphosed layers of snow often responsible for avalanche initiation. A microstructural model first adapted by Shertzer (2011) and Shertzer and Adams (2011) forms the basis of this research. Modifications and additions to the model are proposed here to improve calculation of directional stiffness. In addition, a finite element approach is employed here to gain insight into the importance of the geometric layout of the ice network and their effect on macro-scale strength and stiffness.

To limit the scope of the study and to fit with ongoing research at Montana State University, radiation recrystallized snow is the chosen medium to study the mechanical effects of anisotropy. A case study by Birkeland (1998) indicated near-surface facet layers (which included radiation recrystallization) accounted for 59% of avalanches in southwest Montana, USA between the winter seasons of 1990-91 and 1995-96. Radiation recrystallized snow is composed of faceted snow crystals that are formed by crystal growth within the existing snow structure caused by near surface temperature gradients (Colbeck, 1989). These temperature gradients develop as a result of subsurface warming from incoming shortwave radiation and surface cooling due to outgoing longwave radiation (Colbeck, 1989). More recent investigations of radiation recrystallization have identified conducive conditions for radiation recrystallization and procedures for

reproducing these faceted layers in a laboratory setting (Morstad, 2004; Morstad et al., 2007, 2004; Slaughter, 2010; Slaughter et al., 2011, 2009, 2008). More detail will be provided in subsequent chapters.

1.2 Outline

This document is laid out in several major parts. The three main thrusts of this research are:

- to investigate the dynamic process of radiation recrystallization from a microstructural perspective,
- compute effective stiffness coefficients prior to and following radiation recrystallization using a microstructural based homogenization approach based on Shertzer's previous work (Shertzer and Adams, 2011; Shertzer, 2011), and
- compute effective stiffness coefficients and overall strength prior to and following radiation recrystallization using a microstructurally derived finite element modeling approach.

Chapter Two addresses necessary background information for developing radiation recrystallized facets. It reviews previous work and synthesizes important concepts used in the analysis of radiation recrystallized layers.

Chapter Three and Chapter Four review micromechanics and the homogenization approach developed by Shertzer (2011) and Shertzer and Adams (2011). This information provides a foundation for new additions to the homogenization approach in Chapter Five which seek to address the shortcomings of Shertzer's original approach by addressing grain shape and various textural parameters.

Chapter Six changes gears and provides necessary background information for the finite element technique proposed here. Following a review of previous work and background information, the analysis technique employed here is described in detail.

To provide appropriate data to feed the analysis techniques here, laboratory experiments are conducted and appropriate data is collected. Chapter Seven is flush with details regarding all aspects of the experimental program employed here as well as detailed data processing techniques.

The final chapters are devoted to results and discussion split into appropriate chapters defined by the three bulleted objectives described previously. Chapter Eight focuses on the laboratory results regarding the characteristics and observations of the radiation recrystallization experiments. It also presents the mechanical test results conducted on the various samples while

comparing to previous studies conducted prior to the present one. Chapter Nine is wholly focused on the results of the homogenization approach. Finally Chapter Ten is all about the results of the finite element analyses conducted on the microstructural geometry of the initial samples and radiation recrystallized samples.

Following a conclusion and overall summary in Chapter Eleven, several appendices follow which detail supplemental information such as extra results not presented in detail in the main body of this document and software source code developed for data processing and analysis.

CHAPTER TWO

AVALANCHES AND RADIATION RECRYSTALLIZED SNOW

> *"If I ask anybody who learned to ski after the age of five, they can remember their first day of skiing -- what the weather was like, who they went with, what they had for lunch. I believe that's because that first day on skis was the first day of total freedom in their life."*
> *~ Warren Miller*

2.1 Avalanches

Snow avalanches are a continuous threat to life and property in snow covered mountainous regions across the globe. According to *avalanche.org*, approximately 45 people per year are killed by avalanches in North America, and 150 per year worldwide at the present time. Most fatalities occur in uncontrolled backcountry terrain, however in-bounds ski area deaths are on the rise too (Stoffel et al., 2013). Ski areas attempt to artificially trigger avalanches to deal with the threat, often to a high degree of success. With backcountry use on the rise and ski area management pushing to expand into new, more hazardous terrain, avalanche fatalities are expected to continue to rise.

Additionally, commercial impacts of avalanches are on the rise as more goods and services are delivered along corridors affected by avalanche activity. A 2001 study estimated the hourly impact to regional commerce for closures on

Interstate-90 at Snoqualmie Pass in Washington State can exceed $750k per hour (Paulson, 2001). Like ski area management, departments of transportation actively control avalanche areas and often artificially trigger avalanches to decrease the imminent danger slides present to roadways and railways.

Whether ski patrollers or transportation technicians, avalanche control work is often completed based on accumulated experience and history of different types of avalanches triggered in different terrain types and snow types. Recognition of snowpack qualities such as layering within the snowpack influences the types and sizes of avalanches that are possible. Commonly, dry slab avalanches are triggered by a rapid increase in load which exceeds the strength of weakened layers of snow existing under harder slab layers.

Weak layers within the snow may be a result of different densities or crystal types resulting from storm snow or wind driven snow. Once on the ground, snow frequently changes its form and can result in various strong and weak layers within the snowpack.

2.2 Snow Metamorphism

Mountain snow cover is constantly changing once it lands on the ground. The environment in which the snowpack exists drives specific metamorphism

processes. Two main schemes of snow metamorphism occur: equi-temperature metamorphism and kinetic metamorphism (Adams and Miller, 2003; McClung and Schaerer, 2006; Miller et al., 2003; Tremper, 2001). Temperature gradients within the snowpack are one of the main indicators of the expected metamorphism scheme. It is generally agreed that equi-temperature metamorphism is dominant when $\nabla T < 10° \, \mathrm{C} \cdot \mathrm{m}^{-1}$ and kinetic metamorphism occurs at greater temperature gradients (Akitaya, 1974; Colbeck, 1983a, 1983b; McClung and Schaerer, 2006; Tremper, 2001). The type of metamorphism that occurs though is not binary between different temperature regimes but a smooth transition (Miller et al., 2003).

In equi-temperature metamorphism, microstructural changes are driven by the shapes of the grains themselves. Atmospheric snow crystals are only able to continue to grow or maintain their shape in environments with high vapor super-saturation (McClung and Schaerer, 2006). Once on the ground, overall vapor super-saturation can fall below 1% within a dry snowpack (McClung and Schaerer, 2006). In general, new snow forms are highly unstable due to their high surface area to volume ratio and generally degrade to more rounded forms in the absence of sufficient vapor saturation (McClung and Schaerer, 2006). Vapor pressures are higher over sharp convex surface than concave surfaces

(McClung and Schaerer, 2006; Miller et al., 2003). This tends to drive local vapor pressure gradients promoting sublimation away from sharp features and filling in shallow concave surfaces. The rate of metamorphism substantially increases as internal snowpack temperatures increase as well (McClung and Schaerer, 2006; Miller et al., 2003).

As macro scale temperature gradients increase, vapor pressure gradients also increase. Rate of metamorphism ultimately depends on the magnitude of the temperature gradient, vapor pressure gradient, and size of the pore space. In the warm region of the temperature gradient, sublimation increases to the point where vapor begins diffusing to other regions of the snowpack where it accumulates (Colbeck, 1983b; Miller et al., 2003; Staron et al., 2014, 2012). To compute the vapor pressure gradient in a snow pack, the vapor pressure at specific temperatures in the snowpack (e_i) is estimated using the Clausius-Clapeyron equation:

$$e_i = e_0 \cdot \exp\left(\frac{L_s}{R_v}\left(\frac{1}{T_0} - \frac{1}{T_i}\right)\right). \tag{2.1}$$

This equation is derived for vapor pressure over flat surfaces consisting of H_2O. In this equation, e_0 and T_0 are the reference pressure (0.402 kPa) and temperature ($-5°\,\mathrm{C}$) used here. R_v is the gas constant for water vapor ($R_v = 0.462\ \mathrm{kJ} \cdot$

$(\mathrm{kg} \cdot \mathrm{K})^{-1}$), and L_s is the latent heat of sublimation ($L_s = 2833\ \mathrm{kJ} \cdot \mathrm{kg}^{-1}$). Faceted forms of snow generally become prevalent at vapor pressure gradients of $\nabla e_i \geq 0.5\ \mathrm{kPa} \cdot \mathrm{m}^{-1}$ (Armstrong, 1985).

Generally, equi-temperature microstructures form strong cohesive sintered snow packs consisting of mostly rounded grains. Alternatively, kinetic metamorphism is usually associated with mechanically weak microstructures consisting of poorly bonded, faceted crystals. Significantly developed microstructures can also exhibit distinct patterns of grain arrangement that contribute to distinctive mechanical and thermal qualities. Typical forms of kinetic growth metamorphism are depth hoar and near surface facets.

2.3 Radiation Recrystallization

Radiation recrystallized snow is a special class of temperature gradient metamorphism and a sub-class of near surface facets. The temperature gradient is established through a radiation balance at the surface and near surface of the snow across a wide spectrum of electromagnetic radiation. The effects of this radiation generate rapid metamorphism in the top 10-20 mm of the snowpack. The thinness of this region often makes this type of layer much more difficult to

detect in stability assessment and field study profiles than other common weak layers such as depth hoar and surface hoar.

Several previous studies that observed radiation recrystallized snow formation (Akitaya and Shimizu, 1987; Armstrong, 1985; LaChapelle and Armstrong, 1977; LaChapelle, 1970). However, Colbeck (1989) conducted one of the first studies to explicitly examine near-surface faceting. Colbeck (1989) observed radiation recrystallized facets approximately 0.1 m below the surface of the snow when solar radiation peaked at 126 $\mathrm{W \cdot m^{-2}}$ and 30° C air temperature swings occurred. Colbeck (1989) began to establish some of the necessary conditions for near-surface facet growth, especially when diurnal temperature effects are couple with absorbed solar radiation.

Later on Fukuzawa and Akitaya (1993) found magnitudes of temperature gradients of $|\overline{\nabla}T| = 100 - 300\ \mathrm{°C \cdot m^{-1}}$ and lower density snow overlaying an older dense layer contributed to the formation near surface facets. Fierz (1998) corroborated those conditions after observing $1.5 - 2$ mm facets formed under a thin crust after 11 cm of lower density snow fell atop a denser snow pack following days of clear weather. Detailed studies in the mountains of southwest Montana observed the formation of radiation recrystallized facets and diurnal recrystallized facets given large temperature swings between night and day and

ample solar shortwave radiation (Birkeland et al., 1998, 1996; Birkeland, 1998). As a result of the near surface radiation balance and diurnal air temperature changes, temperature gradients in the upper 5 cm of the snow pack were observed with magnitudes between $|\overline{\nabla}T| = 100 - 250\ ^{\circ}\mathrm{C} \cdot \mathrm{m}^{-1}$ (Birkeland et al., 1996; Birkeland, 1998).

Other investigations continued to support near surface temperature gradients propagated by the longwave and shortwave radiation balance in the top few centimeters of the snowpack (Cooperstein et al., 2004; Hardy et al., 2001; Höller, 2004). Morstad (2004) and Morstad et al. (2007) performed the first detailed laboratory study of radiation recrystallized snow pinpointing the necessary conditions required to recreate layers in a laboratory setting. Field and lab studies that followed determined the most important factors toward the formation of radiation recrystallized snow both in the field and in the laboratory (McCabe et al., 2008; Slaughter, 2010; Slaughter et al., 2011, 2009, 2008).

Summarizing the work of previous research, temperature and vapor pressure gradients are responsible for the metamorphism that occurs during radiation recrystallization – often in a matter of hours. Temperatures within the snowpack are a function of the heat flux in and out of the control volume. These fluxes are established by a balance of incoming and outgoing radiation in the

near surface region of the snowpack (top 5-10 cm) in addition to latent heat exchange and heat conduction within the snowpack, and convection at the surface if significant wind is present. These modes of energy transfer are displayed in the schematic in Figure 2-1.

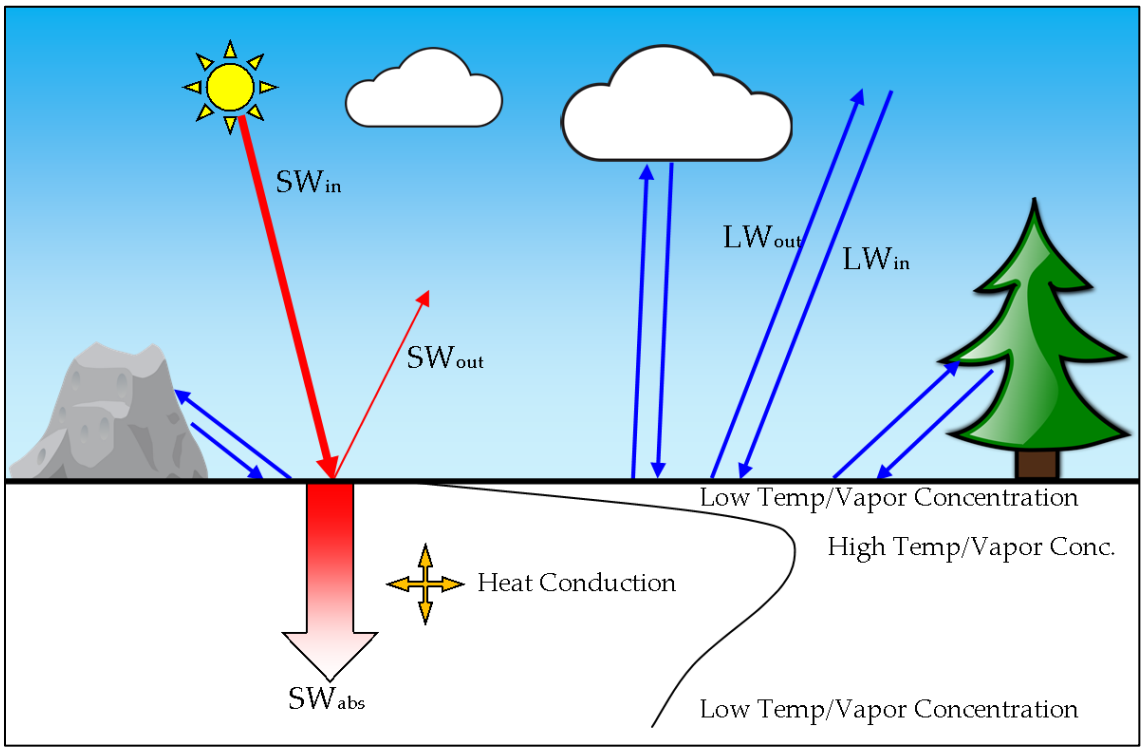


Figure 2-1: Schematic illustrating the near surface balances of incoming and outgoing short- and longwave radiation and the subsurface effects on the near surface region of the snowpack.

The balance of energy within the snowpack is governed by the First Law of Thermodynamics. In its general form, the First Law of Thermodynamics is written as:

$$\frac{d}{dt}(KE + E) = W + Q, \tag{2.2}$$

where KE is macroscale kinetic energy, E is the internal energy, W is the rate of work imparted on the system, and Q is the rate of heat moving into the system. For the purposes of examining near surface metamorphism, the system is stationary allowing kinetic energy to be neglected. Mechanical work is also negligible on the system during the metamorphism process.

Heat input, Q, can be split into two parts: heat fluxing across the boundary of the control volume, and heat generated within the control volume. As a mathematical expression, the two parts are:

$$Q = \oint_{CS} -\bar{\xi} \cdot \hat{n} dA + \int_{CV} \rho h dV. \tag{2.3}$$

The first term is a surface integral computing the sum of the heat flux, $\bar{\xi}$, entering the control surface, CS, normal to the boundary, $\hat{n}$. The second term represents internal heat generation governed by the volumetric sum of product of the material density ρ and the specific heat supply, h.

Working with the left hand side of Equation (2.2), the internal energy is described as:

$$\frac{d}{dt}E = \frac{d}{dt}\int_{CV} \rho \vartheta dV, \tag{2.4}$$

where ϑ is the specific internal energy. Assembling the expanded terms in Equations (2.3) and (2.9) with the previously mentioned assumptions yields:

$$\frac{d}{dt}\int_{CV}\rho\vartheta dV = \oint_{CS} -\bar{\xi}\cdot\hat{n}dA + \int_{CV}\rho h dV. \tag{2.5}$$

The specific internal energy, ϑ, is assumed to be a continuous and differentiable function. This enables the use of the Reynolds Transport Theorem, bringing the time derivative inside the integral of the term on the left hand side of Equation (2.13) as:

$$\frac{d}{dt}\int_{CV}\rho\vartheta dV = \int_{CV}\frac{d}{dt}\rho\vartheta dV. \tag{2.6}$$

Another transformation can be made utilizing Gauss' Theorem. Gauss' Theorem allows surface integrals to be expressed as volume integrals through the generic relationship given as:

$$\oint_{CS}\bar{b}\cdot\hat{n}dA = \int_{CV}\overline{\nabla}\cdot\bar{b}dV, \tag{2.7}$$

where $\bar{b}$ is some arbitrary vector. Gauss' Theorem transforms the middle term of Equation (2.5) to:

$$\oint_{CS} -\bar{\xi}\cdot\hat{n}dA = \int_{CV} -\overline{\nabla}\cdot\bar{\xi}dV. \tag{2.8}$$

Now all of the terms can be collected under one common volume integral as:

$$\int_{CV}\left[\frac{d}{dt}\rho\vartheta + \overline{\nabla}\cdot\bar{\xi} - \rho h\right]dV = 0. \tag{2.9}$$

To be valid for any arbitrary control volume, the integrand of Equation (2.9) must be equal to zero. This produces the local form of the First Law of Thermodynamics which neglects external kinetic energy and mechanical work terms. The relationship is:

$$\frac{d}{dt}\rho\vartheta + \overline{\nabla}\cdot\bar{\xi} - \rho h = 0. \tag{2.10}$$

This equation includes three main terms in the summation: internal energy per unit mass ($\frac{d}{dt}\rho\vartheta$), surface flux terms ($\overline{\nabla}\cdot\bar{\xi}$), and source terms ($\rho h$). The internal energy component can be expressed as:

$$\frac{d}{dt}\rho\vartheta = \rho c_p\frac{\partial T}{\partial t}, \tag{2.11}$$

which is a function of the density ρ, the heat capacity at constant pressure c_p, and the time rate of change of temperature T. The heat flux across the control surface is defined as:

$$\bar{\xi} = \bar{q}_k + \bar{q}, \tag{2.12}$$

where $\bar{q}_k$ is the heat flux as a result of conduction and $\bar{q}$ is a sum of all other heat fluxes including radiation heat transfer. Since source terms such as radiation heat transfer are included in the surface flux term, ρh in Equation (2.10) is 0.

Conduction in the snow is computed using Fourier's Law of heat conduction (e.g. Incropera et al., 2007):

$$\bar{q}_k = -\boldsymbol{k}\bar{\nabla}T, \tag{2.13}$$

where $\boldsymbol{k}$ is defined as the thermal conductivity tensor for snow. Recent studies by Shertzer (2011) and Shertzer and Adams (2011) describe how to compute the effective thermal conductivity of snow utilizing microstructural data. Other flux terms are defined by the incoming and outgoing radiation as well as latent heat exchange as a result of phase change.

Shortwave energy (mostly originating from the sun) comprises of some of the near ultra violet and all visible and near infra-red spectrums of light (0.28-2.8 μm). The heat flux into the snowpack resulting from shortwave energy is only made up of absorbed shortwave radiation. Much of the incoming shortwave energy is reflected according to the albedo ς of the snow. The total penetrating flux of energy is:

$$\bar{q}_{swo} = SW_{in}(1-\varsigma). \tag{2.14}$$

Once penetrating the snowpack, shortwave energy is attenuated at an exponential rate as in:

$$\bar{q}_{sw} = \bar{q}_{swo}\exp(-k_s z), \tag{2.15}$$

where $\bar{q}_{swo}$ is the initial surface penetrating shortwave flux, z is the depth below the surface, and k_s is a wavelength dependent extinction coefficient (Bohren and Barkstrom, 1974; Curl et al., 1972; Curley, 2015; Curley et al., 2014; Fierz et al., 2008; Grenfell and Perovich, 1981; Schwerdtfeger and Weller, 1971; Warren et al., 2006).

Longwave radiation is defined within the infrared spectrum. Snow is a nearly perfect blackbody radiator at this spectrum with an emissivity $\varepsilon = 0.988$ (Gray and Male, 1981). Long wave energy is emitted and absorbed by all surfaces, where the total amount of energy emitted is determined by the surface temperature of an object. The net flux of longwave radiation at the surface of the snow is defined according to the Stefan-Boltzman law as (e.g. Incropera et al., 2007):

$$q_{LW} = LW_{in} - \varepsilon\sigma T_s^4, \tag{2.16}$$

where LW_{in} is the total incoming longwave radiation, and the Stefan-Boltzman constant is $\sigma = 5.670 \times 10^{-8} W \cdot (m^2 \cdot K^4)^{-1}$. In this case, if q_{LW} is negative this term is producing a cooling effect – positive, a warming effect.

Latent and sensible heat exchanges take place between the snow surface and air, and between the pore space and ice network microscopically. Approximations and derivations accounting for the flux associated with these

terms are discussed in detail in other bodies of work (Adams and Sato, 1993; Fierz and Lehning, 2001; Lehning et al., 2002; Staron et al., 2014).

All of these terms add up to contribute to a temperature gradient profile in the near surface region of the snowpack termed the knee-temperature gradient (Slaughter, 2010; Slaughter et al., 2011). Knee-temperature gradient describes the near surface warming that occurs 1-3 cm at depth located between significantly colder temperatures at the surface and generally cooler temperatures at depth. This temperature profile is shown in Figure 2-1. Temperature gradients beyond $500° \, C \cdot m^{-1}$ have been observed in the top 1-2 cm of the snowpack on clear sunny days when slope normal incoming shortwave radiation exceeds $500 \, W \cdot m^{-2}$ and incoming longwave radiation below $300 \, W \cdot m^{-2}$ (McCabe et al., 2008; Morstad, 2004; Morstad et al., 2007, 2004; Slaughter, 2010; Slaughter et al., 2011, 2009, 2008). These temperature gradients directly drive the vapor pressure gradient responsible for the movement of water vapor according to the Clausius-Clapeyron relationship previously listed in Equation (2.1). To date, it is unknown if any comprehensive microstructure based constitutive efforts have taken place investigating the thermodynamic environment of radiation recrystallized snow.

CHAPTER THREE

MICROMECHANICS AND EFFECTIVE STIFFNESS PROPERTIES

"Phenomena unfold on their own appropriate scales of space and time and may be invisible in our myopic world of dimensions assessed by comparison with human height and times metered by human lifespans. So much of accumulating importance at earthly scales […] is invisible by the measuring rod of a human life. So much that matters to particles in the microscopic world of molecules […] either averages out to stability at our scale or simply stands below our limits of perception."
~ Stephen Jay Gould (American Paleontologist)

3.1 Micromechanics

Snow exhibits much more variation in mechanical and thermal properties than density alone can account for. For this reason, the microstructural arrangement is thought to play a major role in the effective properties attributed to snow. Utilizing micromechanical methods to describe snow's mechanical behavior is an obvious next step. Similar methods have been utilized to study effective behavior of other engineering materials such as composites, solid foams, bones, and polycrystals.

Since the motivation for this aspect of the research is to improve on the development by Shertzer (2011) and Shertzer and Adams (2011) rather than an alternative approach, micromechanical techniques pertaining to Shertzer's

contact tensor model will be reviewed here. Several alternative approaches are discussed within Chapter 2 of Shertzer's dissertation (2011).

3.1.1 Homogenization: Relating Micro to Macro

The selection of an appropriate spatial scale is important for using microstructural modeling to describe the effective properties of snow. For example, at a spatial scale on the order of several meters, snow appears as a single homogeneous material. At an intermediate scale around a meter or less, distinct layers in the snow appear. Describing properties at this scale is desirable since most avalanche problems and field observations of mechanical properties of snow are observed at this scale. Often, observers take an even closer look at the snow to determine the crystalline nature of the snow. At this scale, the individual constituents of ice and air are revealed. It is important to note that at this micro-scale, the basis for the macro-scale properties are determined by the specific arrangement of individual grains of snow (ice) and their relationship to neighboring grains of snow.

The appropriate scale is determined when selecting a Representative Volume Element (RVE) (Shertzer, 2011). In the case of investigating the microstructure of snow, an appropriate RVE scale is on the order of millimeters (~10^{-3} m). Central to selecting an RVE of this size is to develop a relationship for

describing behavior between the micro- and macro-scales. This development is termed homogenization (Cambou, 1998; Oda and Iwashita, 1999).

Homogenization, as depicted in Figure 3-1, takes macro-scale observable properties such as a flux term, $\bar{F}$ or a gradient term, $\bar{G}$; localizes the behavior to describe the micro-scale properties, $\bar{f}$ and $\bar{g}$; utilizes a known local constitutive law; then averages the result to move back to the unknown macro-scale quantity. By traveling either clockwise or counter-clockwise around the flowchart in Figure 3-1 starting with either macro-scale quantity, the development of an effective relationship between macro-scale properties based on the known microstructural interactions can be established. In materials with a periodic or

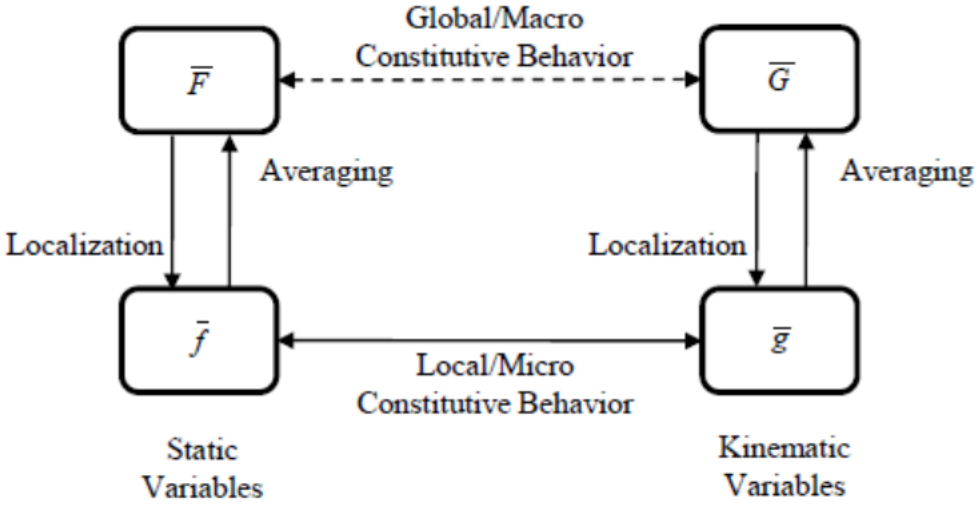


Figure 3-1: General homogenization scheme.(Figure from: Shertzer, 2011)

predictable microstructural arrangement, the link between macro-scale observations and micro-scale properties is based on solutions to partial differential equations. A thorough explanation of periodic microstructures is available by Hollister and Kikuehi (1992) and Hornung (1997). However, snow microstructure is not a periodic material with predictable perturbations.

Observation of most types of snow on a microscopic level reveals the mostly random nature of the arrangement of grains of ice. Although microstructural patterns may develop following extensive recrystallization, a mean field theory for randomly distributed media is much better suited to describe macro-scale behavior using microscopic field quantities that may be unknown and not well-behaved (Shertzer, 2011). This method utilizes volume averaging methods applied to microscopic fields to produce the corresponding macroscopic fields.

First order linear approximations are commonly used to relate generic macroscale quantities such as $\bar{F}$ and $\bar{G}$ through some proportionality constant $\boldsymbol{K}$ in the form of:

$$\bar{F} = \boldsymbol{K} \cdot \bar{G}. \tag{3.1}$$

During Shertzer's development of a constitutive law, heat transfer was the primary objective (Shertzer and Adams, 2011; Shertzer, 2011). In this sense,

Equation (3.1) can describe the vector quantities of temperature gradient ($\bar{G}$) and heat flux ($\bar{F}$) through a second order tensor of thermal conductivity ($-\boldsymbol{K}$, note: negative sign for thermal conductivity is standard convention for conduction heat transfer) using Fourier's Law. The sign of the proportionality constant is related to the physical problem described by the general relationship expressed in Equation (3.1). In the case of this study, which examines snow's mechanical properties, second order tensor quantities of strain ($\bar{G}$) and stress ($\bar{F}$) are described using a fourth order stiffness coefficient ($\boldsymbol{K}$) using linear Hooke's Law.

In the case of solid mechanics, if material testing were conducted at the macro-scale, both strain ($\bar{G}$) and stress ($\bar{F}$) are observed quantities allowing the stiffness coefficient ($\boldsymbol{K}$) to be established directly from the mechanical test. However, in cases where mechanical testing is insufficient or impossible, one can utilize the homogenization scheme depicted in Figure 3-1 to establish a linear coefficient $\boldsymbol{K}$. Using the mean field theory approach (Eshelby, 1957; Hill, 1963; Nemat-Nasser and Hori, 1999; Oda and Iwashita, 1999) macro-scale quantities, $\bar{F}$ and $\bar{G}$, are defined as the mean of the microscopic field variables, $\bar{f}$ and $\bar{g}$ (Shertzer, 2011). The averaging process as shown in Figure 3-1 is,

$$\bar{F} = \langle \bar{f} \rangle = \frac{1}{V} \int \bar{f} dV \qquad \bar{G} = \langle \bar{g} \rangle = \frac{1}{V} \int \bar{g} dV. \tag{3.2}$$

These volume averaged quantities, effectively moving from micro- to macro-scales, smooth over microscopic field variations (Hornung, 1997). Now using the volume average across the entire RVE of the volume averaged microscopic variables, $\langle \bar{f} \rangle$ and $\langle \bar{g} \rangle$, in Equation (3.2), the link between them can be described as,

$$\langle \bar{f} \rangle = \boldsymbol{K}^* \cdot \langle \bar{g} \rangle, \tag{3.3}$$

where $\boldsymbol{K}^*$ is the now an effective material property based on the volume average of microstructural variables (Shertzer, 2011).

Since the homogenization process always starts with a global variable, whether it be $\bar{G}$ or $\bar{F}$, a localization parameter must be established. However, localization operations for a randomly distributed media like snow are not well defined (Shertzer, 2011) and present the greatest difficulty in the homogenization approach (Cambou and Dubujet, 2001; Oda and Iwashita, 1999).

3.1.2 Localization-Voigt Approach

Since localization operations in randomly distributed media are difficult, approximations and assumptions need to be made (Shertzer, 2011). One such approximation is the Voigt approximation (Voigt, 1889). In an effort to apply macro-scale behavior to the microstructure, the Voigt approximation applies a uniform strain increment to all micro-scale constituents to approximate the

global behavior (Voigt, 1889). As a consequence of this approximation, the effective stiffness in the RVE is greater than the actual stiffness of the global body due to the Principle of Minimum Potential Energy. Similar concepts can be used for problems in thermal conductivity and vapor diffusion as outlined in Chapter 3 of Shertzer's dissertation (2011).

The Principle of Minimum Potential Energy states that only the deformed configuration of a solid which satisfies the equilibrium equations governing displacement is given by the minimum value of potential energy (Cook et al., 2002, p. 138; Kim and Sankar, 2009, p. 133). By applying a uniform strain to the entire microstructure, greater strain energy is produced than the minimum potential energy solution would suggest at the RVE scale. As a consequence of the increased strain energy, the mean stress must also increase above that of the RVE observed stress, thus resulting in an overestimate of stiffness.

While the Voigt approximation provides an upper bound estimate of stiffness (Voigt, 1889), alternatively the Reuss approximation provides a lower bound estimate of stiffness (Reuss, 1929). Instead of supplying a uniform strain increment to the entire microstructure, the Reuss approximation applies a uniform stress increment. Converse to the Voigt approximation, complimentary strain energy would be minimized when presented with a macroscopic stress

field. However, the Reuss approximation produces greater complimentary strain energy at the microstructural level. In order to produce the increase in complimentary strain energy, additional strain must occur within the RVE than the larger body. Increased strain results in greater compliance, or less stiffness, thus providing a lower bound estimate of stiffness (Hollister and Kikuchi, 1992).

3.1.3 Summary of Micromechanics

Although a great number of methods for dealing with micro to macro relationships have been developed, only the pertinent information for dealing with Shertzer's model is presented here. The intent of this study is to make useful additions and validations to Shertzer's model rather than dramatically change its foundation. For this reason, the overall homogenization scheme presented by Shertzer (2011) is followed.

Homogenization begins at the macro-scale with the kinematic variables (in this case strain or displacement). The Voigt approximation (Voigt, 1889) is used as a localization scheme to shift from macro-scale strain to micro-scale strain. A local constitutive law is proposed (discussed later) to relate micro-scale strains to micro-scale stresses. Finally an averaging operation is undertaken, as described by Equation (3.2), to scale micro-scale stresses back up the macro-scale. Once this operation (summarized in Figure 3-2) is completed, a relationship

describing the macro-scale stress and strain is complete yielding an effective material property (in this case stiffness).

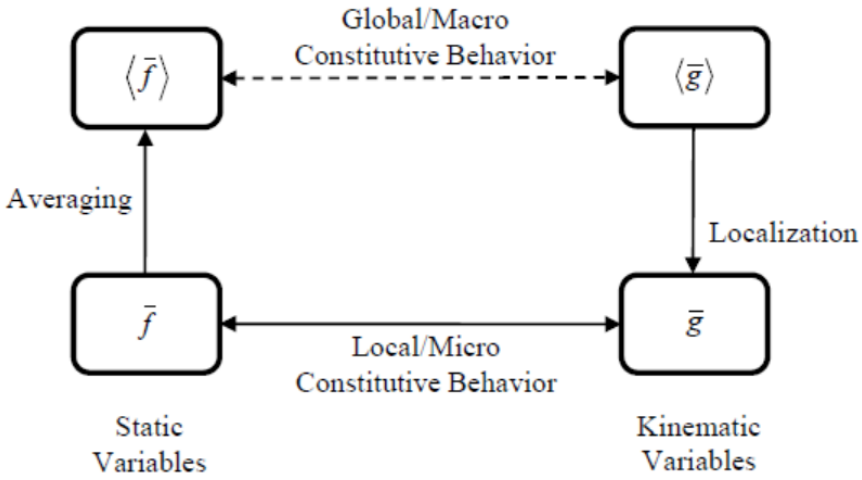


Figure 3-2: Specific homogenization scheme utilized here starting with global strains; scaling strains (kinematic variables) to local scale using the Voigt approximation as a localization operation; establishing a local constitutive law; then averaging the local stresses (static variables) to scale back up to global behavior. From here, the global constitutive behavior can be derived. (Figure from: Shertzer, 2011)

3.2 Effective Elastic Stiffness

In his dissertation, Shertzer (2011) makes an initial attempt to describe the elastic stiffness properties at the macro-scale using microstructural parameters. Mechanical stiffness is described using the 4th order stiffness tensor, $\mathbb{C}$. This would represent the proportionality constant, $\boldsymbol{K}$, in Equation (3.1). Also referring to Equation (3.1), the global stress tensor, **T**, and global strain tensor, **E**, represent $\bar{F}$ and $\bar{G}$ respectively. In the simplest case of isotropy, two independent material

properties exist (e.g. Shames and Cozzarelli, 1997). In the development that follows, the initial constitutive model assumes a microstructure comprised of spherical constituents. Problems arise with this assumption since elastic properties (having two independent parameters) are not robust to deviations away from a spherical microstructure (Kachanov and Sevostianov, 2005). Spherical grains are used however since the initial motivation for this microstructural approach by Shertzer (2011) was for snow's effective thermal properties (Shertzer and Adams, 2011; Shertzer et al., 2010): which are robust to deviations from idealized spherical grains due to the existence of only one independent material property in isotropy (Kachanov and Sevostianov, 2005).

In the following sub-sections, Shertzer's (2011) development of a linear elastic model is presented. As is commonly done when working with the 4th order stiffness tensor $\mathbb{C}$ in its isotropic configuration, Lamé's parameters (λ^* and G^*) are used. The star on each variable indicates it is an effective property since it has its basis in terms of the microstructure but is valid at the macroscale. The approach borrows heavily from other similar analytical microstructural approaches done previously (Cambou et al., 1995; Chang and Liao, 1994; Chang and Lun, 1992; Emeriault and Cambou, 1996; Liao et al., 1997; Rahmoun et al.,

2009). New work addressing deviations away from an idealized geometry of spherical grains is addressed in Chapter Five.

3.2.1 Localization Operation: Voigt's Hypothesis

The first step in developing a linear elastic relationship is to start with the macroscopic quantity of strain $\mathbf{E}$ and relate that to the micro-scale contact displacements $\bar{\delta}^{\alpha}$. What follows describes the specific detail which relates the operation depicted going from the upper-right to lower-right in Figure 3-2. Invoking Voigt's hypothesis, the mean displacement field of the granular assembly is described by

$$\Delta\bar{u}^{a} = \bar{x}^{a} \cdot \mathbf{\Delta E}, \tag{3.4}$$

where $\Delta\bar{u}^{a}$ is the displacement vector of particle a, $\bar{x}^{a}$ is the position vector of particle a, and $\mathbf{\Delta E}$ is the macroscopic strain increment tensor (Liao et al., 1997; Voigt, 1889). However, the relative displacement between grains connected by a bond, α, is critical for further development of this mechanical relationship (Shertzer, 2011). According to Chang and Lun (1992), this change is simply accomplished by replacing $\Delta\bar{u}^{a}$ with $\Delta\bar{\delta}^{\alpha}$, the relative displacement of the centroids of two grains connected by bond α, and $\bar{x}^{a}$ with $\bar{L}^{\alpha}$, the position vector connecting the centroids of grains joined by bond α, resulting in

$$\Delta\bar{\delta}^{\alpha} = \bar{L}^{\alpha} \cdot \mathbf{\Delta E}. \tag{3.5}$$

In these equations, the quantity $\Delta\bar{\delta}^{\alpha}$ is referred to as the incremental contact displacement since all of the deformation of the grain bond system is assumed in the bonds, thus leaving the grains rigid (Shertzer, 2011). In this scheme, axial deformation is permitted even though it seems inconsistent with the lack of a physical dimension axially on the bond plane. To aid in visualization of axial deformation of the bonds with rigid grains, a small neck connecting grains along branch vector $\bar{L}^{\alpha}$ is permitted and the bond plane is on the plane of minimum diameter within the neck between grains (Alley, 1986; Edens and Brown, 1995; Nicot, 2004). An example of this is shown in Figure 3-3.

3.2.2 Local Constitutive Behavior: Contact Law

The next step in the homogenization process is to describe the micro-scale mechanical behavior. In this case, it describes the contact behavior between connected grains. This operation is depicted on the bottom portion of the homogenization scheme shown in Figure 3-2.

Shertzer (2011) begins with a simple linear elastic stiffness relationship between connected grains:

$$\Delta\bar{f}^{\alpha} = -\boldsymbol{K} \cdot \Delta\bar{\delta}^{\alpha}, \tag{3.6}$$

where $\Delta\bar{f}^{\alpha}$ and $\Delta\bar{\delta}^{\alpha}$ are the incremental change in force and displacement of contact α respectively, and $\boldsymbol{K}$ is the contact "spring" stiffness. This type of contact law has been used previously to develop macroscopic constitutive relationships (Cambou et al., 1995; Chang and Liao, 1994; Chang et al., 1995; Walton, 1987). Direction of the stiffness parameter is related to the local orientation of each contact. Relative to the contact orientation, unit vector $\bar{n}$ defines the normal to a contact plane connecting grains. Continuing with a Cartesian basis, $\bar{s}$ and $\bar{t}$ are orthogonal to each other and $\bar{n}$. Figure 3-3 shows the local coordinate system of each bond plane in 2-dimensions where the $\bar{t}$ direction points into the page.

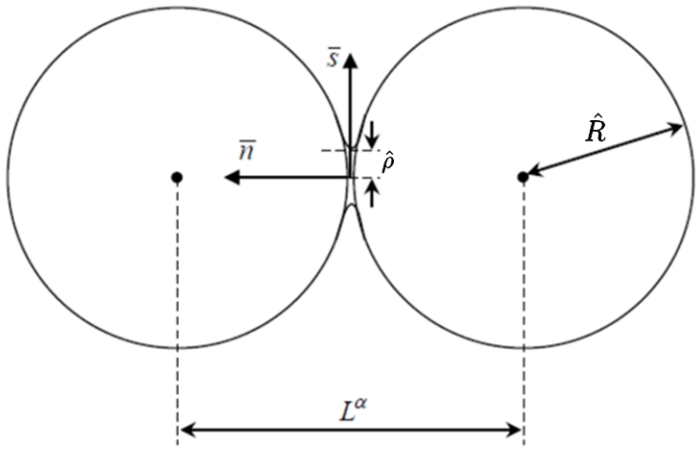


Figure 3-3: Undeformed idealized spherical contact geometry in two dimensions showing the local Cartesian coordinate system. Here, $\hat{\rho}$ represents the bond plane (contact) radius, $\hat{R}$ the grain radius, and L^{α} the branch length connecting the centers of connected grains. (from Shertzer, 2011).

When grains are approximated as idealized spheres, the resulting bond between them is a circular plane. The proportionality constant $\boldsymbol{K}$ in Equation (3.6) can describe independent stiffnesses in different axial directions. The axisymmetric bond plane requires two stiffnesses to describe the elastic behavior of the bond (Shertzer, 2011). Normal to the bond plane ($\bar{n}$ direction in Figure 3-3), k_n represents the resistance to axial deformation, and parallel to the bond plane (plane defined by $\bar{s}$ and $\bar{t}$ in Figure 3-3), k_s represents the resistance to shear deformation of the bond between the two planes (Shertzer, 2011). The expansion of the "spring" stiffness coefficient $\boldsymbol{K}$ is,

$$K_{ij} = \begin{bmatrix} k_n & 0 & 0 \\ 0 & k_s & 0 \\ 0 & 0 & k_s \end{bmatrix} \tag{3.7}$$

To describe k_n, the axial stiffness of the contact area, Shertzer (2011) utilizes simple linear elastic Hooke's law so that,

$$\Delta\sigma_{\mathrm{nn}} = E_{\mathrm{ice}}\Delta\varepsilon_{\mathrm{nn}}, \tag{3.8}$$

where $\Delta\sigma_{nn}$ and $\Delta\varepsilon_{nn}$ are the incremental axial stress and strain at the bond respectively and E_{ice} is the Young's modulus of ice. Some further simplifications can be made by assuming the local incremental stress is an average axial stress. Using basic mechanics, stress can be redefined in terms of incremental force at the bond, Δf_n^{α}, and contact area, A_c^{α}, as:

$$\Delta\sigma_{nn} = \Delta f_n^{\alpha} / A_c^{\alpha} \, . \tag{3.9}$$

Similarly, strain can be redefined in terms of incremental axial displacement of the bond, $\Delta\delta_n^{\alpha}$, and the branch length (original undeformed length of the bond), L^{α}, as:

$$\Delta\varepsilon_{nn} = \Delta\delta_n^{\alpha} / L^{\alpha}. \tag{3.10}$$

Using the idealized geometry as a guide, further redefinition of some terms is achieved. Recognizing the contact is circular between two spherical grains, the area of the contact is defined as:

$$A_c^{\alpha} = \pi\hat{\rho}^2, \tag{3.11}$$

where $\hat{\rho}$ is the mean radius of the circular contact area of the bonds (Shertzer, 2011). Also, the branch length can be simplified as:

$$L^{\alpha} = 2\hat{R} \tag{3.12}$$

where $\hat{R}$ is the mean grain radius of the idealized spherical grains (Shertzer, 2011). It should be noted that the neck shown in Figure 3-3 and subsequent figures is a visual aid with no significant length along the branch length vector.

Collecting the terms in Equations (3.9) through (3.12) and inserting them into Equation (3.8) results in:

$$\Delta f_n^{\alpha} = \left(\frac{\pi\hat{\rho}^2 E_{ice}}{2\hat{R}}\right)\Delta\delta_n^{\alpha}, \tag{3.13}$$

where the term inside the parentheses represents the axial stiffness term, k_n (Shertzer, 2011). Equation (3.13) relates the incremental contact normal displacement to the accompanying incremental normal force for any bond in the microstructure (Shertzer, 2011). The relationship in Equation (3.13) is similar to other developments (Cambou et al., 1995; Chang and Liao, 1994; Chang et al., 1995; Nicot, 2004; Walton, 1987). The deformed geometry of a bonded grain pair resulting from a normal load is shown in Figure 3-4. It also shows the relevant geometric quantities supporting the above equations.

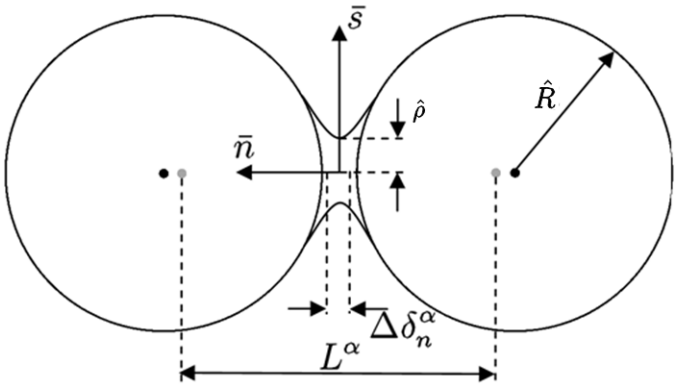


Figure 3-4: Deformed bonded grain pair geometry resulting from an axial load. The grey points represent the position of the undeformed branch vector whereas the black points show the incremental normal displacement of the contact area. (from Shertzer, 2011).

Shear deformation is handled in a similar manner. Shear deformation takes place in a plane containing the $\bar{s}$ and $\bar{t}$ axes. This relationship is defined as:

$$\Delta\tau_{ns} = G_{ice}\Delta\gamma_{ns}, \tag{3.14}$$

where $\Delta\tau_{ns}$ and $\Delta\gamma_{ns}$ are the shear stress and strain at the contact between two grains (Shertzer, 2011). Figure 3-5 below shows the configuration of a pair of grains that have undergone shear deformation. Using average stress, the stress variable becomes:

$$\Delta\tau_{ns} = \Delta f_s^{\alpha}/A_c, \tag{3.15}$$

with Δf_s^{α} being the incremental shear force acting on the contact between the bonded pair of grains in Figure 3-5 (Shertzer, 2011). Similarly, strain becomes:

$$\Delta\gamma_{ns} = 2\delta_s^{\alpha}/L^{\alpha}. \tag{3.16}$$

The variables in Equation (3.16) are depicted in Figure 3-5 (Shertzer, 2011). Equation (3.16) also utilizes the small strain approximation commonly used in basic mechanics of materials.

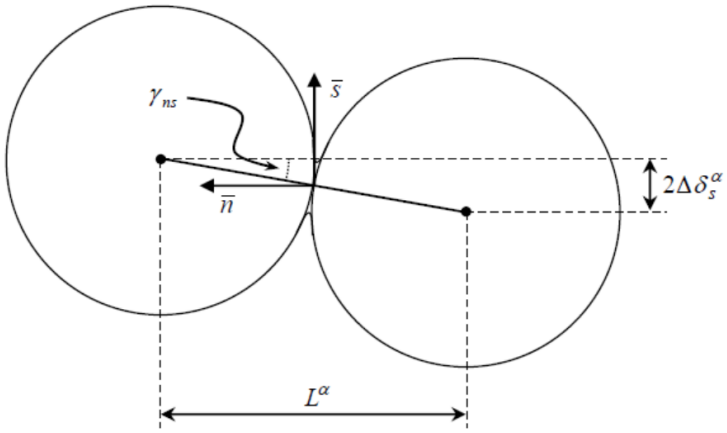


Figure 3-5: Deformed bonded grain pair geometry resulting from a shear load. (from Shertzer, 2011).

Gathering the terms in Equations (3.15) and (3.16) and substituting them into Equation (3.14) results in:

$$\Delta f_s^\alpha = \left(\frac{\pi\hat{\rho}^2 G_{ice}}{2\hat{R}}\right) 2\Delta\delta_s^\alpha, \tag{3.17}$$

where the term inside of the parentheses represents the shear spring stiffness, k_s (Shertzer, 2011).

3.2.3 Averaging: Love Operation

The aim of averaging is to effectively establish the global stress field resulting from the volume average of all local stresses. Here, the Love operation utilizes contact forces between individual grains (Love, 1927):

$$\boldsymbol{\Delta T} = \langle \Delta\bar{f}^\alpha \otimes \bar{L}^\alpha \rangle. \tag{3.18}$$

The incremental global stress, $\boldsymbol{\Delta T}$, is the volume average of the dyadic product of the incremental contact forces and branch vectors across all α bonds (Love, 1927). Although Equation (3.18) is regarded as a fundamental equation in granular mechanics (Cambou, 1998; Christoffersen et al., 1981; Mehrabadi and Nemat-Nasser, 1982; Oda and Iwashita, 1999), Shertzer (2011) provides a detailed proof of the formula using a strain energy density formulation.

3.2.4 Effective Isotropic Stiffness Coefficients

The homogenization scheme has been completed. Figure 3-2 offers a reminder of the specific steps in developing a macro-scale constitutive relationship using the microstructural properties of the granular material: snow. The localization operation from a global strain increment to local displacements is given in Equation (3.5). At the microstructural level, the relationship between local contact displacement and contact force is given as Equation (3.6) where the contact stiffness is described in Equation (3.7). Finally, a volume average of the local contact forces is computed in the Love operation using Equation (3.18) resulting in a global stress increment. These operations allow for the derivation of a global constitutive relationship based on microstructural properties.

Shertzer (2011) presents a derivation for the isotropic effective stiffness coefficients borrowing from other successful derivations utilizing

microstructures composed on uniformly sized spheres and contacts (Cambou et al., 1995; Chang and Liao, 1994; Chang et al., 1995; Walton, 1987). When reduced to two independent coefficients representing an isotropic medium, some common representations are (Shertzer, 2011):

$$\begin{aligned} E^* &= \frac{4k_n N_{cp}\hat{R}^2}{3V}\left(\frac{2+3\zeta}{4+\zeta}\right), \\ \nu^* &= \frac{1-\zeta}{4+\zeta}, \\ \lambda^* &= \frac{4k_n N_{cp}\hat{R}^2}{15V}(1-\zeta), \\ G^* &= \frac{2k_n N_{cp}\hat{R}^2}{15V}(2+3\zeta). \end{aligned} \tag{3.19}$$

E^* and ν^* are effective Young's modulus and Poisson's ratio respectively. λ^* and G^* are Lamé parameters. Within the Equations above, V is the total representative volume, N_{cp} is the total number of bonds (contact planes) within V, and ζ is the ratio of the shear stiffness to the axial stiffness (Shertzer, 2011):

$$\zeta = k_s/k_n = G_{ice}/E_{ice}. \tag{3.20}$$

Although the variables in Equation (3.19) now fully reflect microstructural variables, not all of them are readily measurable. It is useful to make substitutions such that the variables represented are readily measurable. Some substitutions include:

- Volume fraction of spherical ice grains: $\phi = \frac{4}{3}\pi\hat{R}^3\kappa$,
- Number density of grains; number of grains within the volume: $\kappa = \frac{P}{V}$,
- 3-D coordination number; number of contacts per particle: $\mathcal{N} = \frac{N_{cp}}{P}$.

Using the above relationships, and replacing the bond stiffness parameter, k_n, from the expression in Equation (3.13), more useful representations of the expressions of Equation (3.19) are:

$$
\begin{aligned}
E^* &= \frac{1}{2}\left(\frac{\hat{\rho}}{\hat{R}}\right)^2 \phi\mathcal{N}E_{ice}\left(\frac{2+3\zeta}{4+\zeta}\right),^{1} \\
\nu^* &= \left(\frac{1-\zeta}{4+\zeta}\right), \\
\lambda^* &= \frac{1}{20}\left(\frac{\hat{\rho}}{\hat{R}}\right)^2 \phi\mathcal{N}E_{ice}(1-\zeta), \\
G^* &= \frac{1}{40}\left(\frac{\hat{\rho}}{\hat{R}}\right)^2 \phi\mathcal{N}E_{ice}(2-3\zeta).
\end{aligned}
\tag{3.21}
$$

The above equations assume a randomly configured spherical grain microstructure without addressing the orientations of individual grain contacts with respect to the volumes' global coordinate system. Hence, the above equations are only capable of estimating effective properties as scalar value (representing isotropy), even when it is known a sample is anisotropic. The chapters that follow highlight how anisotropic behavior can be incorporated

[1] Note: Shertzer lists this equation as $E^* = \frac{1}{4}\left(\frac{\hat{\rho}}{\hat{R}}\right)^2$ ... (Eqn 4.15 in Shertzer 2011). Working through the formulations preceding this result, it should, instead, be recorded as shown above in Equation (3.21).

through the use of directional data using a fabric tensor. In addition, measurable correction factors are proposed for modifying the effective properties just described for when a spherical microstructure is not apparent.

CHAPTER FOUR

FABRIC TENSORS AND DIRECTIONAL DATA

"Efforts and courage are not enough without purpose and direction."
~John F. Kennedy

4.1 Fabric Tensors

All of the work in the previous chapter regarding the development of a micromechanical approach to describing the macroscopic mechanical behavior of snow has been independent of any structural anisotropy exhibited by the snow microstructure. In situations where the snowpack is well sintered and composed of mostly rounded grains of snow, the microstructure is mostly isotropic and scalar effective material properties may be sufficient by themselves. However anisotropy in the microstructure is introduced during temperature gradient metamorphism (which includes radiation recrystallization). Often, temperature gradient metamorphism develops a transversely isotropic structure composed of highly faceted, poorly bonded crystals (Kry, 1975; Schneebeli and Sokratov, 2004; Shertzer and Adams, 2011; Shertzer, 2011; Shertzer et al., 2010; Srivastava et al., 2010; Sturm et al., 1997).

Since anisotropic materials have more unknown material properties than can be measured with a single mechanical test, employing a fabric tensor in combination with microstructural variables can estimate these unknown material properties including directionality imposed by the microstructure. A fabric tensor is a mathematical entity which quantifies the alignment of either the solid grains or void pore spaces – "… the fabric of the microstructure" (Shertzer, 2011). The use of fabric tensors is diverse. Their use has application in fields such as granular materials (Christoffersen et al., 1981; Mehrabadi and Nemat-Nasser, 1982; Nemat-Nasser and Mehrabadi, 1983; Satake, 1983), bone mechanics (Cowin, 1986, 1985; Kabel et al., 1999; Turner and Cowin, 1987) and damage mechanics (Kachanov, 1980; Lubarda and Krajcinovic, 1993; Voyiadjis et al., 2007; Zysset and Curnier, 1995). In each case, fabric tensors describe the alignment and arrangement of pertinent structural parameters including grain orientation, fiber direction, crack arrangement, etc.

For snow mechanics, the most pertinent directional data comes from the arrangement of the grains making up the microstructure. Snow's microstructure may be examined using images containing data from 2-D slices of snow obtained via sectioning techniques or X-ray Computed Tomography (CT) analysis as shown in Figure 4-1a, or 3-D data from CT analysis as shown in Figure 4-1b.

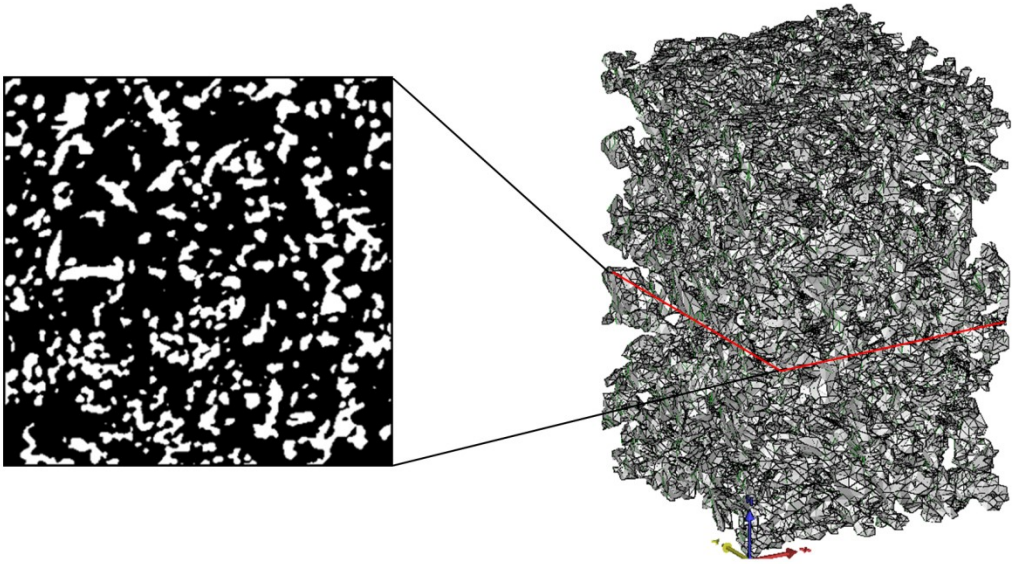


Figure 4-1: (a) Example 2-D section of snow microstructure obtained via μCT imaging. Ice grains are white, pores are black. Image is approximately 5mm square. (b) Example 3-D section of snow microstructure from which the 2-D section was extracted.

Several studies have successfully utilized micro Computed Tomography (μCT) imaging to analyze snow microstructure (Chandel et al., 2014; Lundy et al., 2002; Schneebeli and Sokratov, 2004; Shertzer and Adams, 2011; Shertzer, 2011; Shertzer et al., 2010; Srivastava et al., 2010). Using the data obtained from either technique, various directional quantities (fabric tensors) can be obtained. One such quantity is the contact tensor which describes the inter-granular bond plane orientations in a volume (Christoffersen et al., 1981; Kanatani, 1984; Mehrabadi and Nemat-Nasser, 1982; Oda et al., 1985; Shertzer and Adams, 2011; Shertzer, 2011; Shertzer et al., 2010). Another quantity that will prove useful is the Mean

Intercept Length (MIL) fabric tensor. This quantity describes the directional preference of either the solid materials or pore spaces that make up a volume (Harrigan and Mann, 1984). Both of these quantities will be discussed in further detail.

4.1.1 The Contact Tensor

In the previous chapter, the constitutive relationship developed for the effective stiffness of a granular assembly focused on the contact interface between connected grains. It assumed the grains were rigid with all of the local deformation concentrated at the bonds. From Figure 4-1, it is also apparent that the main bodies of grains are significantly larger than the constricted regions connecting grains – the bonds. Thus, forces transmitted by the microstructure should cause stress concentrations at these constrictions highlighting how important the bonds are within the microstructure (Hagenmuller et al., 2014; Walters and Adams, 2014a). Others have shown that internal forces are transmitted along the unit normal vectors to the plane connecting two grains (Batchelor and O'Brien, 1977; Chang and Liao, 1994)

By utilizing the bonded areas as a source of directional data, different definitions of how to define directional data arise. Focusing on the example granular assembly in Figure 4-2, directions approximating the orientation of the

bonds are defined as $\bar{n}$, the unit normal vector perpendicular to the bond plane or $\bar{m}$, the unit normal vector connecting the centers of two bonded grains (Shertzer and Adams, 2011; Shertzer, 2011). In the case of assuming spherical grains, the vectors $\bar{m}$ and $\bar{n}$ become coincident (Shertzer and Adams, 2011; Shertzer, 2011).

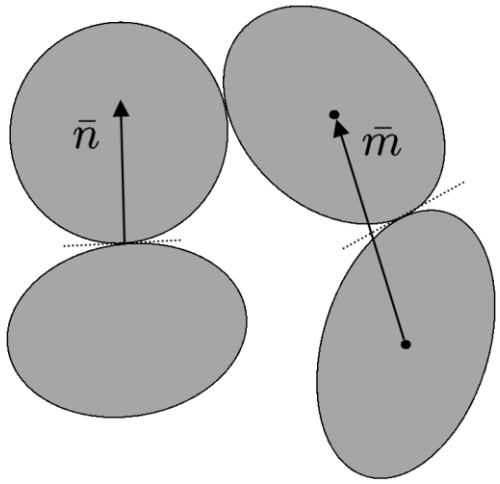


Figure 4-2: A granular assembly showing example directional quantities. $\bar{m}$, is a unit vector between centers of connected grains, and $\bar{n}$, is a unit vector normal to a contact plane defining the bond between grains.

The contact tensor, labeled $\boldsymbol{F}$, is built from the distribution of contact normal vectors $\bar{n}$ or $\bar{m}$ (Shertzer and Adams, 2011; Shertzer, 2011). The coefficients of $\boldsymbol{F}$ are computed using a global reference coordinate system. In index notation, computation of the coefficients of $\boldsymbol{F}$ is given in Kanatani (1984) as:

$$F_{ij} = \frac{1}{N}\sum_{\alpha=1}^{N} n_i^{\alpha} n_j^{\alpha}, \tag{4.1}$$

where N is the total number of contact vectors, $\bar{n}$. n_i^{α} are the components of the unit vectors $\bar{n}$ with respect to the principal axis x_i in a Cartesian coordinate system of contact plane α. Equation (4.1) is sufficient for describing the use of the contact tensor in this study, however much work has been completed in describing the details of the contact tensor and its statistical relevance to the distribution density of population of contact normal vectors (Christoffersen et al., 1981; Kanatani, 1984; Mehrabadi and Nemat-Nasser, 1982; Oda et al., 1985; Shertzer, 2011).

Additionally, the contact tensor may be reoriented into its principal orientation. In its principal orientation, the physical definition of the contact tensor is revealed. In this orientation, the diagonal coefficients of $\boldsymbol{F}$ represent the fractions of bonds in a given volume of snow with contact plane normal projections oriented parallel to the principal axes (Shertzer and Adams, 2011; Shertzer, 2011).

Borrowing from examples set forth by Shertzer et al. (2010), Shertzer and Adams (2011), and Shertzer (2011), the following will illustrate the construction of the contact tensor using 2-D and 3-D hypothetical cases. In the first example

illustrated below in Figure 4-3, eight grains connected in pairs in two dimensions contain $N = 8$ contact normal vectors – half oriented parallel with the x_1 axis and the other half parallel with the x_2 axis.

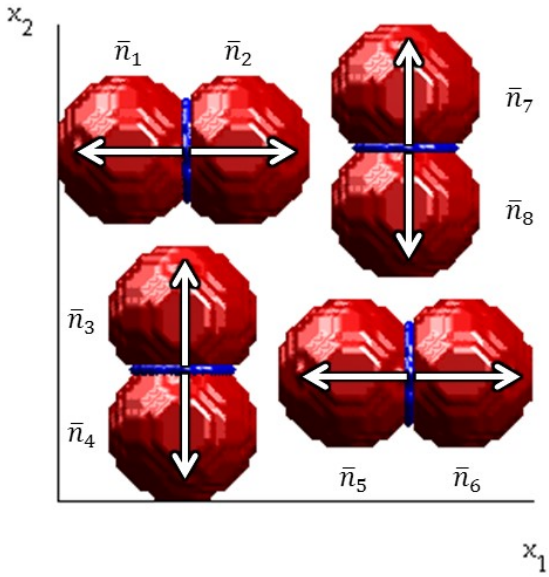


Figure 4-3: Hypothetical 2-D granular assembly consisting of 8 grains with 8 contact normal vectors. Half of the contact vectors ($\bar{n}^{\alpha}$) are oriented parallel to the x_1 direction with the other half oriented parallel to the x_2 direction. Red indicates the individual grains while the blue regions are the contact planes between connected grains.

The grain contacts pictured in Figure 4-3 produce the following 2nd order contact tensor coefficients using Equation (4.1) (Shertzer and Adams, 2011; Shertzer, 2011; Shertzer et al., 2010):

$$F_{ij} = \frac{1}{8}\begin{bmatrix} n_1^1 n_1^1 + \cdots + n_1^8 n_1^8 & n_1^1 n_2^1 + \cdots + n_1^8 n_2^8 \\ n_2^1 n_1^1 + \cdots + n_2^8 n_1^8 & n_2^1 n_2^1 + \cdots + n_2^8 n_2^8 \end{bmatrix}, \tag{4.2}$$

$$F_{ij} = \frac{1}{8}\begin{bmatrix}(-1\cdot -1+\cdots+0\cdot 0) & (-1\cdot 0+\cdots+0\cdot -1)\\ (0\cdot -1+\cdots+-1\cdot 0) & (0\cdot 0+\cdots+-1\cdot -1)\end{bmatrix},$$

$$F_{ij} = \frac{1}{8}\begin{bmatrix}4 & 0\\ 0 & 4\end{bmatrix} = \begin{bmatrix}1/2 & 0\\ 0 & 1/2\end{bmatrix}.$$

Notice how in the final formulation, the coefficient $F_{11} = 1/2$ means half of the bonds exhibit an orientation parallel to the x_1 axis while $F_{22} = 1/2$ states the other half of the elements are oriented parallel to the x_2 axis.

In addition, note the symmetry of the pairs of vectors at each contact plane. Each vector is parallel but pointing in the opposite direction. Due to the nature of how the contact tensor is calculated, only one vector is necessary per contact plane (Shertzer, 2011). When analyzing real data, analysis algorithms (described later) are limited to choosing one normal vector per identified contact to make use of this symmetry property and save computation time.

To further analyze anisotropic features (or isotropic) of the textural data, the contact tensor F_{ij} is decomposed into the sum of its isotropic, $\hat{F}_{ij}$, and deviatoric, F'_{ij} parts. This is done (in 3-D) using the operation (Reddy, 2008):

$$F_{ij} = \hat{F}_{ij} + F'_{ij} = \frac{1}{3}F_{kk}\delta_{ij} + F'_{ij}, \tag{4.3}$$

where δ_{ij} is the Kronecker delta. Here, another useful property of the contact tensor presents itself. Since in its principal orientation the contact tensor represents the fractions of bond plane normal vectors oriented parallel to each

principal axis, the trace or first invariant of the tensor always equals 1 ($F_{kk} = 1$). This reduces Equation (4.3) to:

$$F_{ij} = \frac{1}{3}\delta_{ij} + F'_{ij} = f\delta_{ij} + F'_{ij}. \tag{4.4}$$

Equation (4.4) introduces f as the scalar isotropic value of the tensor – an important quantity that will be used later in incorporating the contact tensor into the effective stiffness of a granular material. While in 3-D, $f = 1/3$, the same operation can be done on any second order tensor resulting in $f = 1/2$ for the 2-D case.

Using Equation (4.4) the data presented in Figure 4-3 is written in isotropic and deviatoric form as:

$$F_{ij} = \frac{1}{2}\begin{bmatrix} 1 & 0 \\ 0 & 1 \end{bmatrix} + \begin{bmatrix} 0 & 0 \\ 0 & 0 \end{bmatrix}. \tag{4.5}$$

In this case, the deviatoric part contains only zeros indicating textural isotropy or no directional preference of bonds (Shertzer and Adams, 2011; Shertzer, 2011). One might say that the configuration of grains in Figure 4-3 is not isotropic but shows directional preference to the x_1 and x_2 axes. This is a limitation of using a 2nd order tensor which, in 2-D, only has two principal directions (Shertzer and Adams, 2011; Shertzer, 2011).

In three dimensions, the full capabilities of the 2nd order contact tensor are realized. Figure 4-4 shows a hypothetical 3-D arrangement of 8 grains: all oriented with their contact normal vectors ($\bar{n}^{\alpha}$) parallel to the x_1 axis. Utilizing Equation (4.1) and making use of the symmetry of the contact normal vectors such that $N = 4$, the contact tensor in the 3-D case is:

$$F_{ij} = \frac{1}{4}\begin{bmatrix} 4 & 0 & 0 \\ 0 & 0 & 0 \\ 0 & 0 & 0 \end{bmatrix} = \begin{bmatrix} 1 & 0 & 0 \\ 0 & 0 & 0 \\ 0 & 0 & 0 \end{bmatrix}. \tag{4.6}$$

Splitting the equation into its isotropic and deviatoric parts results in:

$$F_{ij} = \frac{1}{3}\begin{bmatrix} 1 & 0 & 0 \\ 0 & 1 & 0 \\ 0 & 0 & 1 \end{bmatrix} + \begin{bmatrix} 2/3 & 0 & 0 \\ 0 & -1/3 & 0 \\ 0 & 0 & -1/3 \end{bmatrix}. \tag{4.7}$$

The deviatoric part in Equation (4.7) clearly shows the departure from isotropy exhibited in the hypothetical microstructure in Figure 4-4 . In this case since two values are repeated, a transversely isotropic structure is present. It also represents the extreme of a transversely isotropic texture since all of the directional data is oriented in one direction. Should all three principal values of the contact tensor differ, an orthotropic structure is present (Shertzer and Adams, 2011; Shertzer, 2011). Since a second order tensor in 3-D cannot have more than

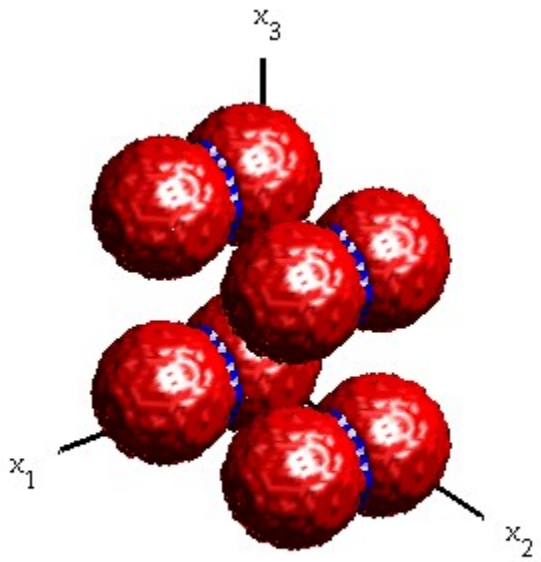


Figure 4-4: Hypothetical 3-D granular assembly consisting of 8 grains connected in pairs at 4 distinct contact planes. All of the contact vectors ($\bar{n}^{\alpha}$) are oriented parallel to the x_1 direction. Red indicates the individual grains while the blue regions are the contact planes between connected grains.

three distinct principal values, a 4th order or higher order tensor is required to capture a more complex texture than orthotropic symmetry (Shertzer, 2011). Although the 4th order contact tensor can be easily calculated, it is unnecessary as the 2nd order tensor should be sufficient in characterizing anisotropy in snow (Shertzer, 2011).

In each of the previous cases (Figures 4-3 and 4-4), the textural data aligned with the global coordinate systems thus producing contact tensors already oriented in their principal directions. A final hypothetical configuration

is presented in Figure 4-5 such that all of the contact normal vectors ($\bar{n}^{\alpha}$) are angled +60° away from the x_1 axis. The contact tensor produced from Equation (4.1) is:

$$F_{ij} = \frac{1}{4}\begin{bmatrix} 4(1/2 \cdot 1/2) & 4\left(1/2 \cdot \sqrt{3}/2\right) \\ 4\left(\sqrt{3}/2 \cdot 1/2\right) & 4\left(\sqrt{3}/2 \cdot \sqrt{3}/2\right) \end{bmatrix},$$
$$F_{ij} = \begin{bmatrix} 1/4 & \sqrt{3}/4 \\ \sqrt{3}/4 & 3/4 \end{bmatrix}. \tag{4.8}$$

The lack of zero values in the non-diagonal terms in Equation (4.8) indicate the coordinate system of x_1 and x_2 in Figure 4-5 is not in the principal orientation.

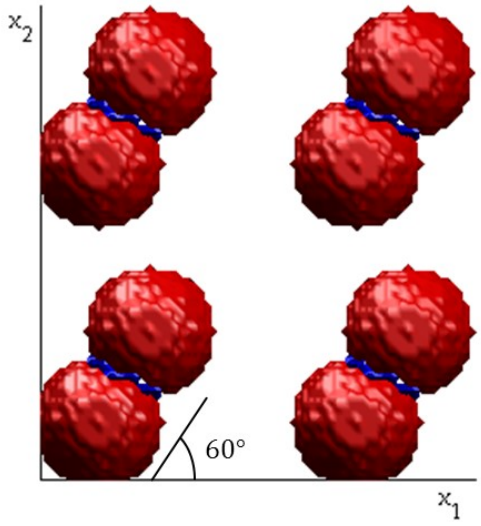


Figure 4-5: Hypothetical 2-D granular assembly consisting of 8 grains connected in pairs at 4 distinct contact planes. All of the contact vectors ($\bar{n}^{\alpha}$) are oriented at +60° to the x_1 direction. Red indicates the individual grains while the blue regions are the contact planes between connected grains.

It is also clear qualitatively from Figure 4-5 that the contact tensor should be transversely isotropic with the unique value oriented 60° counter-clockwise to the x_1 axis. This is shown quantitatively by solving an eigenvalue problem to attain the principal values and orientation (e.g. Reddy, 2008). As expected, the contact tensor in its principal orientation is:

$$F_{ij}^{(p)} = \begin{bmatrix} 0 & 0 \\ 0 & 1 \end{bmatrix}. \tag{4.9}$$

The direction of the non-zero value of $F_{ij}^{(p)}$ in reference to the axes provided in Figure 4-5 is:

$$\bar{n}^{(p)} = \frac{1}{2}\hat{\imath} + \frac{\sqrt{3}}{2}\hat{\jmath}. \tag{4.10}$$

These operations show the contact tensor can be computed from any arbitrary reference coordinate system (Shertzer, 2011).

4.1.2 The MIL Fabric Tensor

Another useful way to analytically describe the anisotropy of a microstructural sample is using the Mean Intercept Length (MIL) fabric tensor. While the contact tensor describes the overall orientation of the contact (bond) interfaces between grains, the MIL tensor describes the orientation of the overall structure itself – independent of the contact orientation. The MIL tensor

describes this anisotropy using an intersection counting technique (Odgaard, 1997; Odgaard et al., 1997).

In this technique, a linear grid is superimposed over the microstructural data in question (2D or 3D) and the number of intersections with the solid/void interface is counted (Bruker-microCT, 2012; Harrigan and Mann, 1984; Odgaard, 1997; Odgaard et al., 1997; Underwood, 1970; Whitehouse, 1974). Variable $I(\omega)$ is the number of intersections the test grid makes with the solid/void interface at each grid angle ω. This is repeated for several angles of ω to develop a full picture of the overall orientation of a microstructural sample. These come together to define the MIL at various angles as:

$$MIL(\omega) = \frac{L}{I(\omega)}, \tag{4.11}$$

where L is the total length of the test lines (Odgaard, 1997).

To visualize what is occurring in Equation (4.11), Figure 4-6 shows a hypothetical 2-D microstructure with a grid of test lines angled at two distinct orientations. At each orientation, the length of the three lines is totaled. The total number of intersections is also recorded. In this scheme, only entrance into a solid constituent is counted (Bruker-microCT, 2012). This same sequence is repeated at other orientations to obtain MIL values at various orientations. Other algorithms count both entrances and exits from the solid constituents. However,

this only affects the MIL value by a scalar value and has no effect on the representation of the directional data (Odgaard, 1997).

The total MIL at each angle ω is then plotted as a vector whose magnitude is the MIL value and the angle is ω (Bruker-microCT, 2012; Harrigan and Mann, 1984). After plotting each vector for every tested angle ω, a pin cushion diagram is created that represents all of the MIL vectors as seen in Figure 4-7.

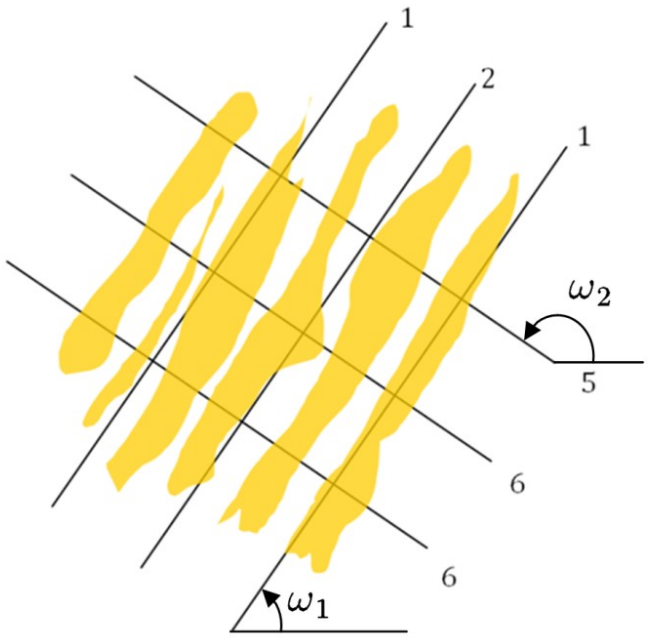


Figure 4-6: A hypothetical 2-D microstructural data set with a grid of three test lines oriented at two distinct angles. The number of intersections at each test line is printed at the end of each line segment. At ω_1, few intersections are recorded as the test lines are mostly parallel with the microstructure. In contrast, a greater number of intersections are recorded at ω_2. (adapted from Bruker-microCT, 2012).

In 2-D, an ellipse can be fitted to the data using a least squares error method similar to that outlined in Kanatani (1984). In 3-D, the same method produces a least squares fit ellipsoid. To make the data more useful for tensor analysis, Harrigan and Mann (1984) showed a method for representing the equation for an ellipse or ellipsoid using a 2nd order tensor. The relationship for the least squares fit distribution of MIL and the 2nd order tensor $\boldsymbol{M}$ is:

$$\frac{1}{\left(MIL(\bar{o})\right)^2} \approx \bar{o} \cdot \boldsymbol{M} \cdot \bar{o} = M_{ij} o_i o_j, \tag{4.12}$$

where $\bar{o}$ is a unit vector in the direction of the test line (Harrigan and Mann, 1984; Shertzer, 2011). The 2nd order tensor $\boldsymbol{M}$ is shown as the inverse of the square of the mean intercept length. This means larger MIL measurements correspond to smaller coefficients in the anisotropy tensor $\boldsymbol{M}$ (refer to Equation (4.11)).

Customarily though, larger coefficients are associated with preferential microstructural orientation. Therefore, the MIL fabric tensor $\boldsymbol{H}$ is taken as (Cowin, 1986, 1985; Odgaard et al., 1997; Srivastava et al., 2010),

$$\boldsymbol{H} = \boldsymbol{M}^{-1/2}. \tag{4.13}$$

The eigenvectors of $\boldsymbol{H}$ are oriented along the major and minor axes of the ellipse or ellipsoid approximation with the eigenvalues representing their

magnitude. An example of the 3-D pin-cushion with eigenvectors is shown in Figure 4-7.

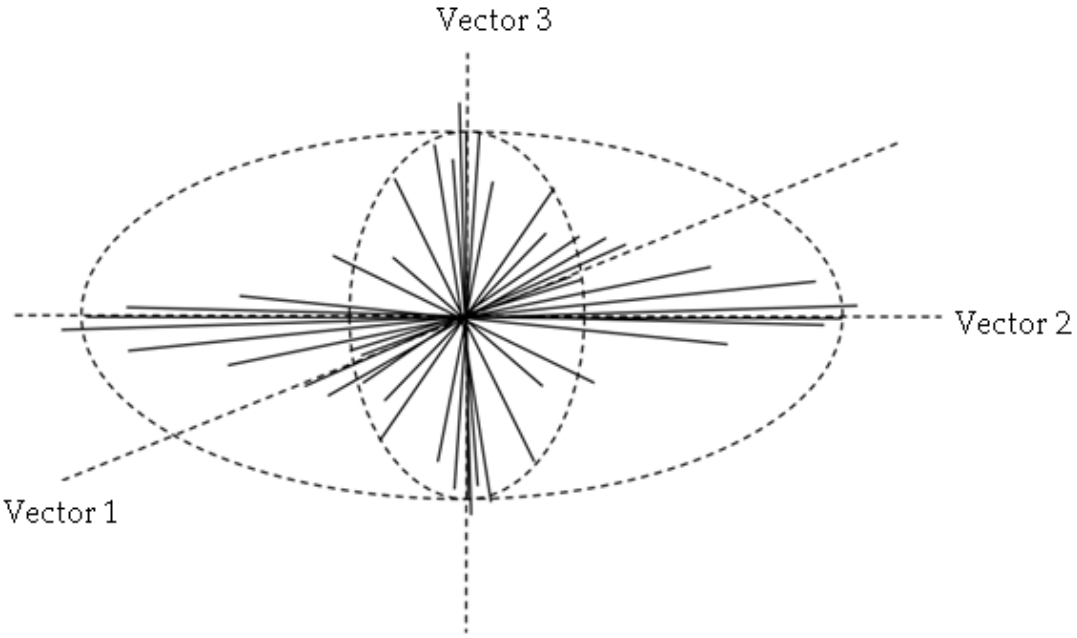


Figure 4-7: Hypothetical 3-D MIL data represented in a pin-cushion plot. Each line segment is a vector oriented coincidentally with the MIL grid test angle ω and a magnitude equal to the MIL value at that specific angle. An ellipsoid can be fit using a least squares error method. The resulting eigenvectors from the anisotropy tensor $\boldsymbol{H}$ representing the equation of the ellipsoid shape are shown. Each vector is coincident with the major and minor axes of the ellipsoid shape.

One problematic feature of $\boldsymbol{H}$ is the fact that it has dimensions of length. Additionally, unlike the contact tensor $\boldsymbol{F}$, the first invariant varies as the microstructural texture of a sample changes. To overcome this, $\boldsymbol{H}$ is often normalized to force its first invariant to be equal to one (Cowin, 1986, 1985;

Odgaard et al., 1997; Srivastava et al., 2010). Normalization also renders $\boldsymbol{H}$ dimensionless, similar to $\boldsymbol{F}$.

The MIL fabric tensor is an alternative way to describe the textural anisotropy of snow microstructure. It provides fundamentally different directional data than the contact tensor. However, when used in conjunction with the contact tensor, the MIL tensor can provide useful supplementary information about the microstructure's mechanical properties as will be described in the next chapter.

4.2 Incorporating Fabric Tensors into Effective Elastic Stiffness

The contact tensor $\boldsymbol{F}$ can be joined to the effective stiffness development described in Equation (3.21). Although this development will show how $\boldsymbol{F}$ computes the anisotropic component of effective stiffness, any second order tensor describing anisotropy can be used (such as $\boldsymbol{H}$). Mechanical stiffness is generally described using a 4^{th} order tensor (e.g. Shames and Cozzarelli, 1997). After incorporating the contact tensor, tensor products between 2^{nd} order tensors such as $\boldsymbol{F}$ maintains a stiffness tensor of 4^{th} order (Shertzer, 2011). While the proper components have already been developed (scalar stiffness relation Equation (3.21), and the contact tensor Equation (4.1)), it is useful to start at the

beginning of the development of Hooke's law. What follows is a review of generalized Hooke's law for linear elastic materials and its reduction down to isotropic Hooke's law using the framework of Shames and Cozzarelli (1997) and Reddy (2008).

In macroscale, the generalized Hooke's law in tensor notation is given as,

$$\mathbf{T} = \mathbb{C} : \mathbf{E}, \tag{4.14}$$

where $\mathbf{T}$ is the 2nd order stress tensor, $\mathbb{C}$ is the 4th order stiffness tensor, and $\mathbf{E}$ is the 2nd order strain tensor. Evaluating the double-dot product, Equation (4.14) in index notation is,

$$\mathrm{T}_{ij} = C_{ijkl}\mathrm{E}_{kl}. \tag{4.15}$$

In general terms and in three dimensions, C_{ijkl} has 81 independent coefficients.

Symmetry of the stress tensor ($\mathrm{T}_{ij} = \mathrm{T}_{ji}$) and of the strain tensor ($\mathrm{E}_{kl} = \mathrm{E}_{lk}$) also requires symmetries in the stiffness tensor such as:

$$C_{ijkl} = C_{jikl}$$

$$\text{and} \tag{4.16}$$

$$C_{ijkl} = C_{ijlk}.$$

These symmetries reduce the stiffness tensor from 81 independent coefficients to 36 independent coefficients. The stiffness tensor itself is symmetric resulting in:

$$C_{ijkl} = C_{klij}, \tag{4.17}$$

further reducing the number of independent coefficients to 21. Using Voigt notation, the stiffness tensor can be displayed in a two-dimensional matrix as:

$$[C] = \begin{bmatrix} C_{1111} & C_{1122} & C_{1133} & C_{1123} & C_{1113} & C_{1112} \\ 0 & C_{2222} & C_{2233} & C_{2223} & C_{2213} & C_{2212} \\ 0 & 0 & C_{3333} & C_{3323} & C_{3313} & C_{3312} \\ 0 & 0 & 0 & C_{2323} & C_{2313} & C_{2312} \\ 0 & 0 & 0 & 0 & C_{1313} & C_{1312} \\ 0 & 0 & 0 & 0 & 0 & C_{1212} \end{bmatrix}. \tag{4.18}$$

Stress and strain are column vectors with 6 elements such that:

$$\{\mathrm{T}\} = [C]\{\mathrm{E}\}. \tag{4.19}$$

Taking note of material symmetries along different axial directions and performing the rotations and reflections required to reflect that material symmetry as outlined in Shames and Cozzarelli (1997) and Reddy (2008) the isotropic stiffness matrix is obtained:

$$[C] = \begin{bmatrix} (\lambda + 2\mathrm{G}) & \lambda & \lambda & 0 & 0 & 0 \\ \lambda & (\lambda + 2\mathrm{G}) & \lambda & 0 & 0 & 0 \\ \lambda & \lambda & (\lambda + 2\mathrm{G}) & 0 & 0 & 0 \\ 0 & 0 & 0 & 2\mathrm{G} & 0 & 0 \\ 0 & 0 & 0 & 0 & 2\mathrm{G} & 0 \\ 0 & 0 & 0 & 0 & 0 & 2\mathrm{G} \end{bmatrix}, \tag{4.20}$$

where λ and G are the 1st and 2nd Lamé constants. Written in index notation, the stiffness matrix is:

$$C_{ijkl} = \lambda\delta_{ij}\delta_{kl} + 2G\delta_{ik}\delta_{jl}, \tag{4.21}$$

where δ is the Kronecker delta.

At this point, incorporation of the contact tensor begins. Modification of Equation (4.21) allows for inclusion of the contact tensor. First, the Lamé parameters are replaced with their effective constants λ^* and G^* - from Equation (3.21) (Shertzer, 2011). Next, the second order contact tensor (F_{ij}) is incorporated by the following substitution based on Equation (4.4) (Shertzer, 2011):

$$\delta_{ij} \Leftrightarrow \frac{1}{f} F_{ij}. \tag{4.22}$$

In this equation and the equation that follows, f is the contact tensor's isotropic value allowing the relationship in Equation (4.22) to become the identity tensor for isotropic microstructures. Using these substitutions, Equation (4.21) becomes (Shertzer, 2011):

$$C^*_{ijkl} = \frac{1}{f^2}\left(\lambda^* F_{ij}F_{kl} + 2G^* F_{ik}F_{jl}\right). \tag{4.23}$$

If the contact tensor is isotropic, Equation (4.23) becomes identical to Equation (4.21) – isotropic Hooke's Law.

It is necessary for the contact tensor to be oriented in its principal direction (Shertzer, 2011). This assures that the material symmetry reflected in the effective stiffness matrix aligns with the textural symmetry exhibited by the

microstructure on which the material stiffness is based (Odgaard et al., 1997; Satyawali et al., 2008; Shertzer, 2011; Srivastava et al., 2010). Equation (4.23) in matrix form is:

$$[C^*] = \begin{bmatrix} (\lambda^* + 2G^*)\left(\frac{F_{11}}{f}\right)^2 & \lambda^*\frac{F_{11}F_{22}}{f^2} & \lambda^*\frac{F_{11}F_{33}}{f^2} & 0 & 0 & 0 \\ \lambda^*\frac{F_{22}F_{11}}{f^2} & (\lambda^* + 2G^*)\left(\frac{F_{22}}{f}\right)^2 & \lambda^*\frac{F_{22}F_{33}}{f^2} & 0 & 0 & 0 \\ \lambda^*\frac{F_{33}F_{11}}{f^2} & \lambda^*\frac{F_{33}F_{22}}{f^2} & (\lambda^* + 2G^*)\left(\frac{F_{33}}{f}\right)^2 & 0 & 0 & 0 \\ 0 & 0 & 0 & 2G^*\frac{F_{22}F_{33}}{f^2} & 0 & 0 \\ 0 & 0 & 0 & 0 & 2G^*\frac{F_{33}F_{11}}{f^2} & 0 \\ 0 & 0 & 0 & 0 & 0 & 2G^*\frac{F_{11}F_{22}}{f^2} \end{bmatrix} \quad (4.24)$$

The starred coefficients in the above equations are calculated using microstructural parameters according to Equation (3.21). These represent the scalar effective stiffness parameters. Anisotropy is captured by the contact tensor coefficients F_{ij}. In the isotropic case, $F_{11} = F_{22} = F_{33} = f$ and the scalar effective stiffness properties are returned unchanged. In cases of textural anisotropy, the contact tensor values deviate away from their isotropic values and that anisotropy is reflected through the matrix represented in Equation (4.24).

When performing laboratory experiments, parameters such as Young's modulus E, shear modulus G, and Poisson's ratio ν are measured directly. For the isotropic case, E and ν are related to the Lamé paramters via:

$$E = \frac{G(3\lambda + 2G)}{\lambda + G}, \qquad \nu = \frac{\lambda}{2(\lambda + G)}. \tag{4.25}$$

It is useful to rewrite Equation (4.24) in terms of E, G, and ν for direct comparison with mechanical test results. After making the substitutions outlined in Equation (4.25), the stiffness matrix becomes a large "messy" equation. The cleanest form to work with is the compliance matrix $[S^*]$ which is the inverse of the stiffness matrix $[S^*] = [C^*]^{-1}$. This matrix is given as:

$$[S^*] = \begin{bmatrix} \frac{1}{E^*}\left(\frac{f}{F_{11}}\right)^2 & \frac{\nu^*}{E^*}\frac{f^2}{F_{11}F_{22}} & \frac{\nu^*}{E^*}\frac{f^2}{F_{11}F_{33}} & 0 & 0 & 0 \\ \frac{\nu^*}{E^*}\frac{f^2}{F_{22}F_{11}} & \frac{1}{E^*}\left(\frac{f}{F_{22}}\right)^2 & \frac{\nu^*}{E^*}\frac{f^2}{F_{22}F_{33}} & 0 & 0 & 0 \\ \frac{\nu^*}{E^*}\frac{f^2}{F_{33}F_{11}} & \frac{\nu^*}{E^*}\frac{f^2}{F_{33}F_{22}} & \frac{1}{E^*}\left(\frac{f}{F_{33}}\right)^2 & 0 & 0 & 0 \\ 0 & 0 & 0 & \frac{1}{2G^*}\frac{f^2}{F_{22}F_{33}} & 0 & 0 \\ 0 & 0 & 0 & 0 & \frac{1}{2G^*}\frac{f^2}{F_{33}F_{11}} & 0 \\ 0 & 0 & 0 & 0 & 0 & \frac{1}{2G^*}\frac{f^2}{F_{11}F_{22}} \end{bmatrix}. \tag{4.26}$$

The total value in each position of matrix $[S^*]$ is used to directly compute the anisotropic stiffness value occupied by the appropriate position within the matrix. For example, calculating the Young's modulus E_1 in the x_1 direction of the material's coordinate system is:

$$E_1 = \left[\frac{1}{E^*}\left(\frac{f}{F_{11}}\right)^2\right]^{-1}. \tag{4.27}$$

Similar macroscale values for shear modulus can be obtained with care in how it is used. For example, one shear modulus value is:

$$\frac{1}{2}G_{23} = \left[\frac{1}{2G^*}\frac{f^2}{F_{22}F_{33}}\right]^{-1}, \tag{4.28}$$

where G_{23} is the shear modulus on the x_2 oriented face pointing in the x_3 direction. Shear strain and stress directions relating to this shear modulus quantity are illustrated in Figure 4-8. The quantity in the S_{44} matrix position is only half of the total shear modulus since during the formulation, the factor of 2 often associated with the tensor definition of shear strain ($\varepsilon_{ij}, i \neq j$) in Hooke's Law was brought inside the stiffness matrix as shown in Equations (4.20) and (4.21). When applying Hooke's law for shear stress and strain, one must be careful to use the appropriate shear strain value:

$$\tau_{ij} = G_{ij}(\gamma_{ij}) = G_{ij}(2\varepsilon_{ij}), \text{where } i \neq j, \tag{4.29}$$

γ_{ij} is the engineering definition of shear strain, and ε_{ij} is the tensor definition of shear strain. Engineering strain is depicted in Figure 4-8.

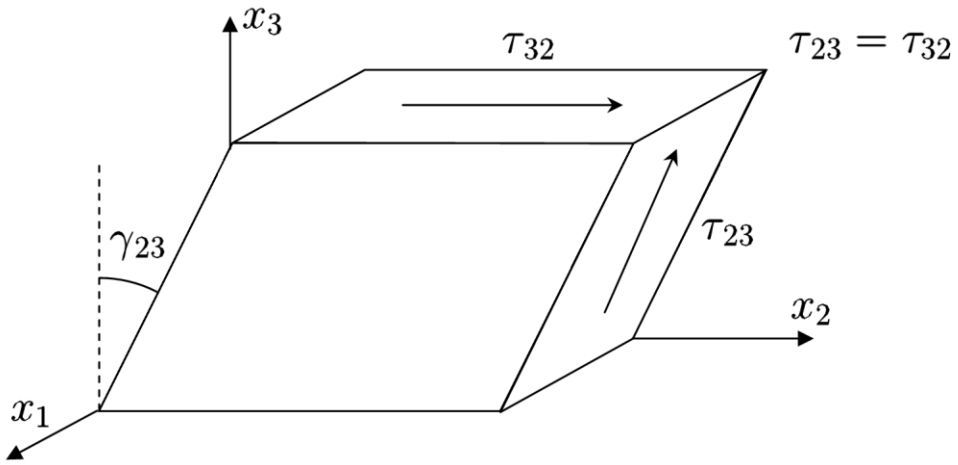


Figure 4-8: Illustration of the shear stress τ and shear strain γ directions associated with the subscripts 23.

4.3 Summary of Fabric Tensors

A fabric tensor offers a mathematical way to describe anisotropy within a material. Here, two different candidates of fabric tensors for use on snow microstructure are reviewed – the contact tensor and the MIL tensor. Using techniques described above, any second order directional fabric tensor can be incorporated into the effective stiffness as long as it is oriented in its principal direction.

CHAPTER FIVE

EFFECTIVE MECHANICAL PROPERTIES: SHAPE FACTORS

"Ut tensio, sic vis." (As the extension, so the force)
~Robert Hooke (1678)

5.1 Motivation

If dealing with spherical particles of snow, Shertzer's (2011) formulation for effective mechanical stiffness of snow outlined in the previous two chapters would be sufficient. However, the ice particles that comprise snow, in its infinite forms, are almost never spherical, and even less likely that an entire snowpack would consist of all spherical grains. As was previously mentioned, the microstructural model outlined previously is not robust to deviations away from the spherical assumption of particles (Kachanov and Sevostianov, 2005). This thought is reinforced by investigating calculated values of scalar Young's modulus, E^*, using equation (3.21):

$$E^* = \frac{1}{2}\left(\frac{\hat{\rho}}{\hat{R}}\right)^2 \phi \mathcal{N} E_{ice}\left(\frac{2+3\zeta}{4+\zeta}\right). \tag{3.21}$$

Here, E^* is computed and plotted for constant values of bond radius to grain radius ratios, $\hat{\rho}/\hat{R}$, and as a function of density or volume fraction, ϕ. The

coordination number, $\mathcal{N}$ is estimated and computed using volume fraction through the relationship given by Adams and Sato (1993):

$$\mathcal{N} = 3.565 - 7.435\phi + 24.825\phi^2. \tag{5.1}$$

This produces a plot of possible values for E^* shown in Figure 5-1. Also included in Figure 5-1 are the ranges of compiled measured Young's modulus data reproduced from Mellor (1975). Until a density of 600 $\mathrm{kg \cdot m^{-3}}$, values of Young's modulus are overestimated except for unrealistically low values of $\hat{\rho}/\hat{R}$.

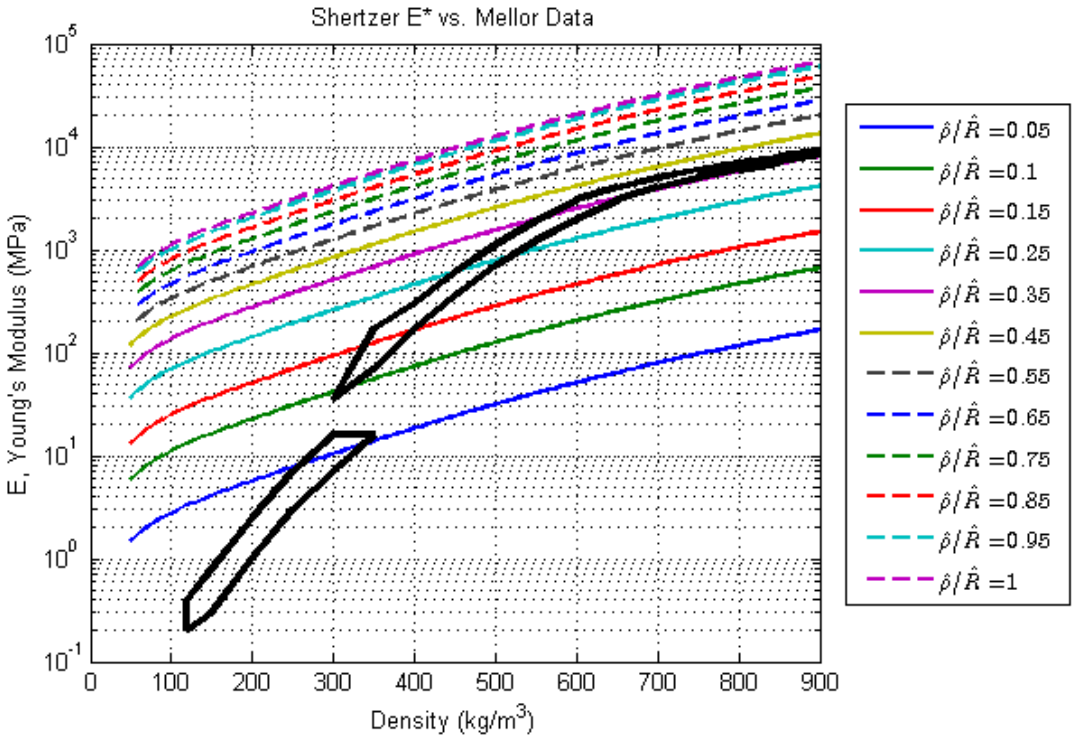


Figure 5-1: Plot of Shertzer's E^*, Equation (3.21), as a function of density at constant values of bond radius to grain radius ratios (colored lines) against compiled measured data reproduced from Mellor (1975) (black outlined areas).

Two possible explanations for overestimating Young's modulus are offered. One possibility lies at the core of the development of the homogenization scheme used to develop the constitutive model in use here. As discussed earlier, the localization scheme to apply macro-scale conditions on the microstructure was the Voigt approximation (Shertzer and Adams, 2011; Shertzer, 2011; Voigt, 1889). The Voigt approximation inherently overestimates macro-scale stiffness. Abandoning the Voigt approximation to avoid its overestimate of stiffness would require creating a new constitutive model rather than working with the one proposed by Shertzer (2011).

Another possibility to address overestimation of stiffness is the significant effect of irregularly shaped snow crystals on intergranular mechanics and their effective stiffnesses in relation to spheres. It has been shown in discrete element modeling that elliptical particles with a large enough aspect ratio actually decrease the effective macro scale stiffness (Emeriault and Claquin, 2004). Two shape correction factors have been developed in this presentation to address deviations away from spherical particles and the affect the orientation of these irregularities may have on the overall stiffness of the snow microstructure.

5.2 Scalar Shape Correction Factor

The spherical grain assumption used to develop Shertzer's (2011) scalar constitutive relationship described earlier, while effective for describing heat transfer properties, is generally inadequate when describing mechanical properties. Examining the configuration of the contact between spherical grains, independent of the size of the contacts, shows a simple geometric relationship that only depends on the parent grain's radius and the position of the contacting grain's center as illustrated in Figure 5-2.

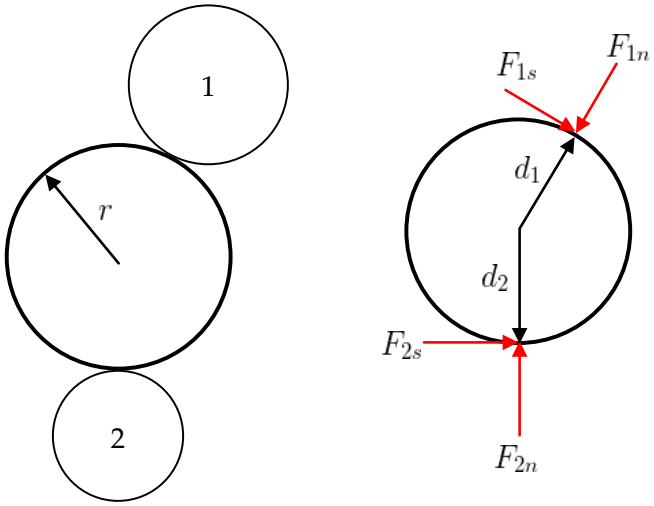


Figure 5-2: Configuration of two spherical grains contacting a spherical parent grain. The loading paths of the normal and shear components are shown on the right in addition to the distance from the center of the parent grain to the contact center. In the case of spheres, $r = d_1 = d_2$.

The distance from the center of the parent grain to any point of contact on the boundary has a constant value equal to the parent grain's radius. In addition, when inspecting the force components of each contacting grain, the normal force's line of action is always directed through the center of the parent grain. This, in effect, guarantees that all of the compressive forces from one spherical grain to another are directed through the maximum amount of material, thus producing the stiffest response. Since directed through the geometric center of the grain, the normal component of the contact force also produces an axial deformation on the parent grain. The orientation of the contact forces are already addressed through the incorporation of the contact tensor.

Effective spherical grain radii are identified following what is termed a segmentation process. The segmentation algorithm implemented to identify individual grains and bonds, whether done in 2D (Edens and Brown, 1995; Edens, 1997; Lundy et al., 2002) or 3D (Meyer, 1994) for example, utilizes Euclidean distance transforms to measure structure thickness. The Euclidean distance transform calculates the distance between each non-zero binary pixel and the nearest zero binary pixel. This distance may be parallel to the grid, or the hypotenuse distance to the nearest zero binary pixel. The distance transform is illustrated in Figure 5-3.

Using Figure 5-3, the distance transform values of 1 (as shown on the right) around the edge of the binary circle are a result of having a shared edge with a zero value pixel (as shown on the left). Therefore the nearest zero-valued pixel is only 1 pixel away, hence a distance transform of 1. The next highest valued distance transforms (1.41) result from non-zero valued pixels touching zero valued pixels on a corner. This distance is the hypotenuse of a 45° triangle where the base legs are 1 pixel each. Using the center pixel, to arrive at the nearest zero-valued pixel, one must travel (for example) two pixels to the right and one pixel up. The hypotenuse formed by these base legs of travel is 2.24. Three other acceptable directions of travel exist for the center pixel which produces the same distance transform value of 2.24.

The effective spherical grain radius is the largest distance transform value within a grain with its center located at the pixel or voxel containing the largest distance transform. Using Figure 5-3, the grain radius would be 2.24 pixels, with its center at coordinates (4, 4).

0	0	0	0	0	0	0
0	0	0	1	0	0	0
0	0	1	1	1	0	0
0	1	1	1	1	1	0
0	0	1	1	1	0	0
0	0	0	1	0	0	0
0	0	0	0	0	0	0

Circle

0	0	0	0	0	0	0
0	0	0	1	0	0	0
0	0	1	1.41	1	0	0
0	1	1.41	2.24	1.41	1	0
0	0	1	1.41	1	0	0
0	0	0	1	0	0	0
0	0	0	0	0	0	0

Distance Transform of Circle



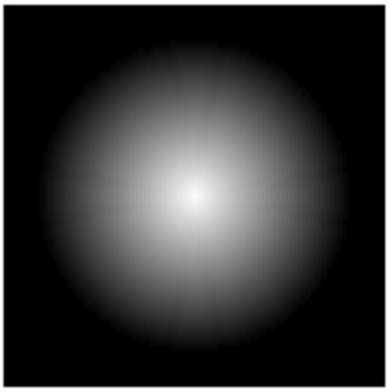


Figure 5-3: Illustration of the distance transform. The binary pixel values of the circle are shown on the left and the Euclidean distance transform values and image are shown on the right.

Although examining contact between non-spherical grains is already done using effective spherical grain radii, the contact is more complex than the spherical configuration in Figure 5-2. Figure 5-4 illustrates a hypothetical grain scale interaction between a non-spherical parent grain and three contacting grains. The effective spherical grain radius is depicted as the purple dashed circle in Figure 5-4, which is the largest inscribed sphere that could fit inside an individual grain. Each of the three contacts have different distances from their

bond centers to the effective spherical center as noted by $d_1, d_2,$ and d_3. Additionally, if the normal and shear components of contact force are aligned normal to and tangent to the grain surface respectively, the normal forces' lines of action may not necessarily be directed through the effective spherical center of the grain.

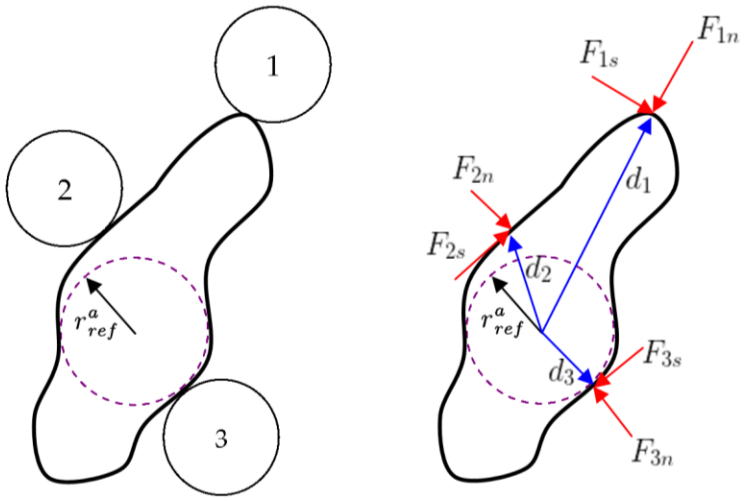


Figure 5-4: Configuration of three grains contacting a non-spherical parent grain. The loading paths of the normal and shear components are shown on the right. The dashed purple circle represents the spherical grain size. $d_1, d_2,$ and d_3 are the distances from each bond center to the center of the largest sphere fit inside the parent grain.

As a consequence of differing distances between the effective grain center and bond centers, the amount of material along the lines of action of the contact normal forces also varies – affecting the effective stiffness. Since the line of action of the contact normal force may not be directed through the geometric center of

the grain, flexural deformation may become significant through increased bending moments as off axis loading becomes significant. Additionally, stability of loading may be called into question in regards to bonds positioned far away from the effective grain center. In a full assembly of ice grains, the effective stiffness could be compromised if some of the grains internally have buckled.

With Euler buckling, the critical stress for a structure is related to the slenderness ratio, L/r (column length divided by radius of gyration) (e.g. Chap. 16 in Philpot, 2013). Emeriault and Claquin (2004) showed through discrete element modeling and statistical homogenization that 2-D microstructures made up of ellipses generally decreased in effective stiffness as the aspect ratio (major axis to minor axis dimensions) increased. Each of these aspect ratio approaches inspired the calculation of a new aspect ratio based scalar shape factor.

The scalar shape factor developed here makes use the effective spherical grain radius and its location calculated during the segmentation routine as well as the location of each contact on the grain boundary. The scalar shape correction factor is calculated for each grain-bond pair as:

$$S_\alpha = \frac{r_{eff}^a}{d^\alpha} \tag{5.2}$$

where r_{eff}^a is the effective spherical grain radius of grain a and d^α is the distance from the grain center to the center of bond α on the parent grain's boundary. Equation

(5.2) is arranged in a way to scale the effective stiffness response of individual grains in proportion to its deviation away from a spherical shape. As the distance between the center of the grain and center of the bond (d^{α}) increases, the potential for increased flexural deformation of the grain bond pair also increases through potentially increased bending moments and decreased buckling stability. As the influence of flexural deformation of bonded grain pairs increases, the effective macroscale stiffness should decrease.

To incorporate the scalar shape correction factor into the constitutive relationship, S_{α} is obtained for each grain-bond pair then averaged to produce a global scalar shape correction factor S:

$$S = \frac{1}{N}\sum_{\alpha=1}^{N} S_{\alpha}. \tag{5.3}$$

N is the total number of grain-bond pairs. The volume averaged shape factor S is incorporated into the scalar elastic coefficients as a multiplicative factor:

$$\begin{aligned} E^{*} &= \frac{1}{2} S \left(\frac{\hat{\rho}}{\hat{R}}\right)^{2} \phi \mathcal{N} E_{ice} \left(\frac{2+3\zeta}{4+\zeta}\right) \text{ and} \\ G^{*} &= \frac{1}{40} S \left(\frac{\hat{\rho}}{\hat{R}}\right)^{2} \phi \mathcal{N} E_{ice} (2-3\zeta). \end{aligned} \tag{5.4}$$

According to Emeriault and Claquin (2004), an ellipse-like aspect ratio does not have a significant effect on the effective Poisson's ratio. Therefore, Poisson's ratio, ν^*, remains unaffected here by the S.

The incorporation of shape factor S as a multiplicative factor reduces the effective mechanical stiffnesses when analyzing micro-structures with non-spherical grains. However, an important property of this shape factor is its value when spherical constituents are being analyzed. For spheres, $S = 1$ and does not have an effect on Equation (5.4), reducing it to the form found in Equation (3.21), which is based on spherical particles.

5.3 Directional Correction Factor: Tensor Ratio

In the previous chapter, two different fabric tensors were reviewed which mathematically describe anisotropies in the microstructure of snow. The contact tensor provides the proportion of contact normal vectors at the bonds between individual grains oriented in the material's principal direction. The MIL tensor describes the overall material orientation of the microstructure, without the necessity of calculating locations of individual bonds and grains. In calculation, each of these quantities are independent of each other; although may be related via the physical process of the formation of the microstructure.

Choosing the appropriate quantity to describe the anisotropic qualities of a snow's microstructure is challenging. Choosing the contact tensor makes sense from a mechanics standpoint since stress and strain concentrations are most significant in regions of reduced areas – the bonds (Walters and Adams, 2014a). The MIL tensor however is generally an available quantity without needing to identify bonds and grains. By describing the overall orientation of the material making up the texture of the microstructure, the effect on mechanics should be obvious. Loading a series of columns along their axes behaves differently than if loaded transverse to their axes.

Using these two quantities together can be an even more powerful tool in fully describing the mechanical anisotropy. To help explain the development of combining these two tensor quantities, two different hypothetical microstructures comprised of 3-D ellipsoids of uniform size are presented. In one sample shown in Figure 5-5, ellipsoids are oriented with their major axes pointed vertically. The middle row of ellipsoids are bonded laterally (in the x and y directions). The remaining sets of grains are only bonded to the middle row through nearly vertically oriented bonds.

Analyzing the volume of grains in Figure 5-5 produced a contact tensor (calculated from Equation (4.1)) with coefficients of $F_{11} = 0.2693, F_{22} =$

0.2692, and $F_{33} = 0.4615$. In terms of the contacts, this represents a transversely isotropic microstructure with the preferential bonding direction oriented vertically (the x_3 direction). The normalized MIL tensor values (calculated from Equation (4.13)) are $H_{11} = 0.2359, H_{22} = 0.2332$, and $H_{33} = 0.5184$. The diagonal values of $\boldsymbol{H}$ do not add up to 1 due to the statistical uncertainty of the small sample size. These values indicate more of the geometry of the sample also preferentially oriented in the vertical direction and also nearly transversely isotropic in texture.

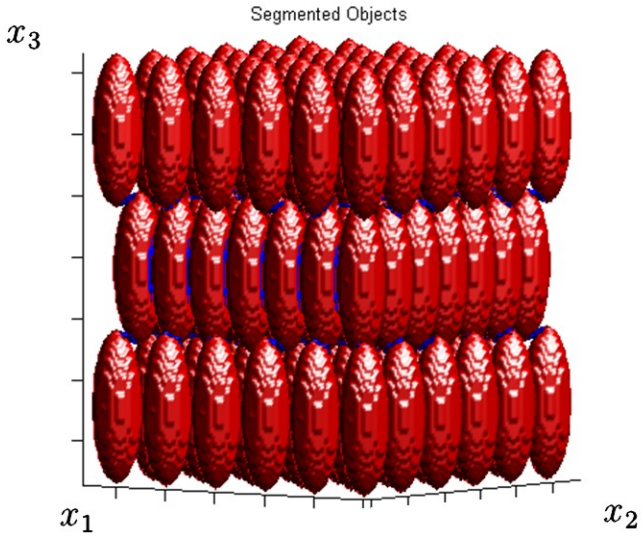


Figure 5-5: A hypothetical 3-D microstructure of ellipsoidal grains oriented with their major axes directed vertically. The middle row of grains is bonded laterally to each other. The top and bottom rows of grains are only bonded to the middle row of grains through nearly vertically oriented contacts.

The contact tensor and MIL both have transversely isotropic configurations with a vertical preference. In this sense, calculating effective mechanical properties as described in previous chapters would produce similar results regardless of whether the contact tensor or the MIL tensor is used.

However, if the configuration of grains were changed, the disadvantages of using each tensor value singly become apparent. In the next configuration shown in Figure 5-6, the same size grains are arranged similar to those in Figure 5-5 except the long axes lay horizontally. The contacts between grains are arranged in a way such that they are still predominantly oriented vertically.

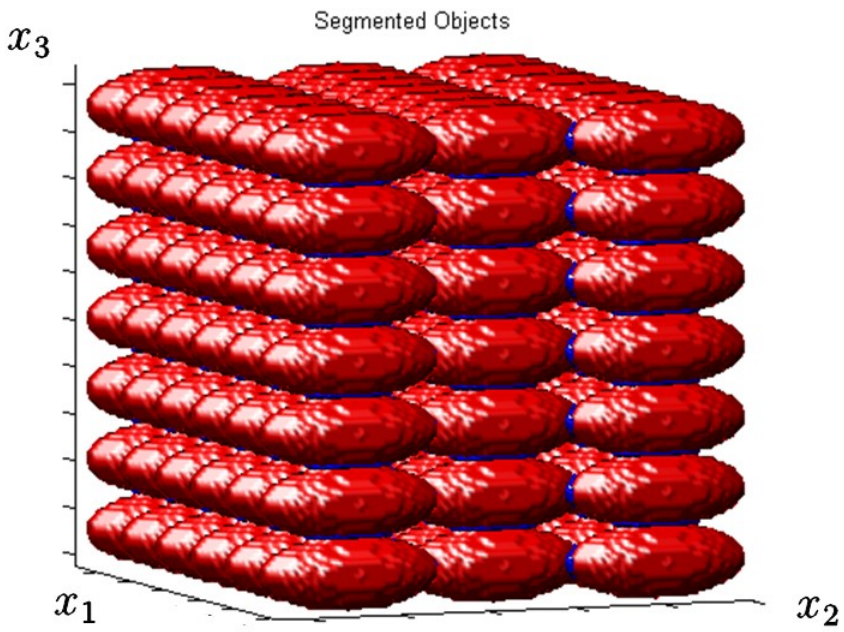


Figure 5-6: A hypothetical 3-D microstructure of ellipsoidal grains oriented with their major axes directed horizontally. The middle column of grains is bonded laterally to each other. The left and right columns of grains are bonded to the middle of column of grains and vertically to each other.

In this particular case, the contact tensor shows the contacts as still being predominantly vertical with $F_{11} = 0.1766, F_{22} = 0.3352,$ and $F_{33} = 0.4682$. Transverse isotropy is lost due to the way in which the bonds are arranged amongst the grains, however the objective was to still achieve preferential bonding in the vertical direction. The MIL tensor values for this orientation paint a different picture with $H_{11} = 0.2495, H_{22} = 0.4692,$ and $H_{33} = 0.2801$. The values here have similar magnitudes to the contact tensor; however, the preferential direction is rotated 90° into the x_2 direction.

If utilizing the contact tensor, the calculated effective stiffness would be increased above the scalar E^* value in the vertical direction of the sample in Figure 5-6, while decreasing the effective stiffness in each of the horizontal directions. However, if the MIL tensor is selected, stiffness is enhanced in the x_2 direction while decreasing in the others.

When comparing between samples, the contact tensor F_{33} for the vertically oriented ellipses in Figure 5-5 and the horizontally oriented ellipses in Figure 5-6 is approximately the same. Thus using this value to alter the effective stiffness in each of these samples would produce the same effective stiffness in the vertical direction. However, qualitatively, each of these samples should produce vastly different mechanical behavior in response to vertical loads due to the stability of the arrangement of grains.

It is proposed here to address the differences and effects of structural stability among connected grains by considering a ratio of the two different tensor quantities termed the tensor ratio. The tensor ratio takes into account similarities or differences between the contact tensor and the MIL tensor. The tensor ratio is formulated as:

$$\Gamma_{11} = \frac{F_{11}}{H_{11}}, \Gamma_{22} = \frac{F_{22}}{H_{22}}, \text{and } \Gamma_{33} = \frac{F_{33}}{H_{33}}, \tag{5.5}$$

where Γ_{ii} are the tensor ratio diagonal coefficients, F_{ii} are the diagonal contact tensor coefficients, and H_{ii} are the normalized diagonal MIL tensor coefficients. This equation assumes the principal orientations of the contact and MIL tensors are coincident.

The terms in the tensor ratio are arranged in this fashion to due to the effect each fabric tensor has on the mechanical performance of the microstructure in question. The contact tensor, $\boldsymbol{F}$, appears in the numerator of Equation (5.5) due to the direct relationship to mechanical performance. If deformation and stress is assumed to concentrate in the bonded regions of the snow microstructure, having a higher number of contact surfaces in a particular direction should produce a stiffer response as stresses can be more evenly distributed. In directions with few bonds, stress concentrations are more pronounced, leading to increased compliance and decreased effective stiffness.

In contrast to that, the MIL tensor coefficients may have an inverse relationship to mechanical stiffness. Using the simple bonded grain sets in Figure 5-7, the contact tensor remains unchanged for each arrangement while the MIL tensor shifts from an x_2 preferred textural orientation with the leftmost bonded grain set, to an x_1 preferred textural orientation with the rightmost bonded grain set. Under axial loads directed in the x_2 direction, according to the

concept of Euler buckling, the leftmost microstructure in Figure 5-7 presents the least stable configuration. Progressing to the right in Figure 5-7, the mechanical stability in response to vertically directed loads increases. Decreased stability in a particular direction on the microstructural level leads to increased compliance and decreased stiffness in the same direction at the macroscopic level. The combined effect of the contact tensor and the proposed inverse relationship of the MIL tensor on the mechanical stability is assembled into the tensor ratio relationship found here in Equation (5.5).

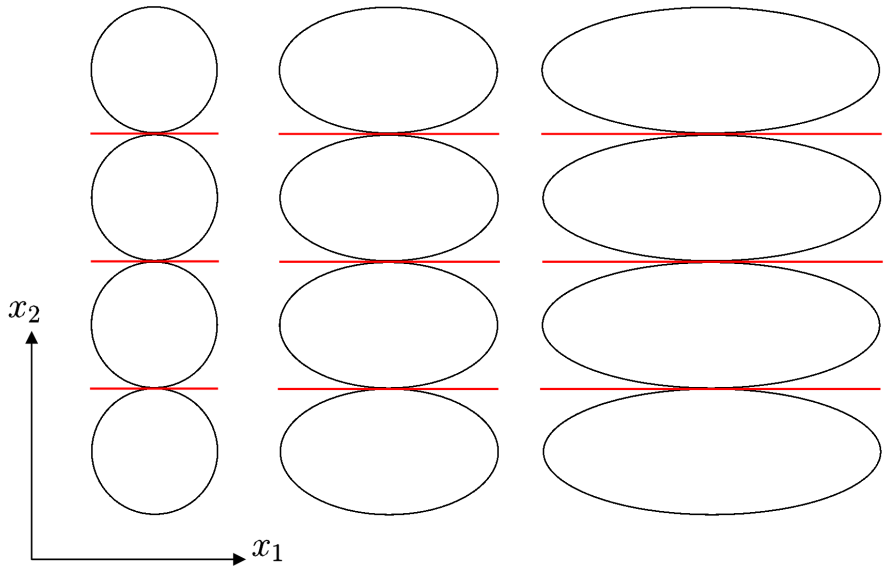


Figure 5-7: Two dimensional bonded grain system in which the contact tensor remains constant for all microstructures ($F_{11} = 0, F_{22} = 1$) and the MIL tensor coefficients shift from an x_2 preferred textural orientation with the leftmost bonded grain set, to an x_1 preferred textural orientation with the rightmost bonded grain set.

Another justification for the arrangement of the tensor ratio in Equation (5.5) comes from an extreme hypothetical case. If the microstructure in question is a fluid with suspended solids, it would imply no bonding exists between the solid constituents. In the absence of contacts, all coefficients of the contact tensor would be zero. However, the MIL tensor would still have non-zero coefficients as intercepts through the suspended solids would still be counted. By definition, a Newtonian fluid is unable to support shear stresses in static equilibrium. This definition requires the shear modulus to be zero. When using the homogenization framework presented here, the tensor ratio as defined in Equation (5.5) would be zero: rendering the shear modulus as zero. If the proposed definition of the tensor ratio is inverse to Equation (5.5), the tensor ratio would be mathematically undefined when any contact tensor coefficient is zero.

The tensor ratio is a directional shape factor accounting for both the arrangement of bonds and the geometric arrangement of grains. Since the tensor ratio is also a second order tensor, much like the contact tensor $\boldsymbol{F}$ and the MIL tensor $\boldsymbol{H}$, it is incorporated into the microstructural stiffness model in Equations (4.23), (4.24), and (4.26) in the same way. Using the index notation of Equation (4.23) and substituting in the tensor ratio gives:

$$C^*_{ijkl} = \left(\lambda^* \Gamma_{ij} \Gamma_{kl} + 2G^* \Gamma_{ik} \Gamma_{jl}\right). \tag{5.6}$$

Since computing the tensor ratio $\boldsymbol{\Gamma}$ already utilizes the normalized contact tensor $\boldsymbol{F}$ and MIL tensor $\boldsymbol{H}$, the $1/f^2$ term found in Equation (4.23) is unnecessary. Equation (5.6) is more useful in matrix form when inverted into the compliance matrix for easy access to the effective Young's modulus and shear modulus in each material direction. Using a process similar to obtaining Equation (4.26), the compliance matrix with the tensor ratio gives:

$$[S^*] = \begin{bmatrix} \frac{1}{E^*}\left(\frac{1}{\Gamma_{11}}\right)^2 & \frac{\nu^*}{E^*}\frac{1}{\Gamma_{11}\Gamma_{22}} & \frac{\nu^*}{E^*}\frac{1}{\Gamma_{11}\Gamma_{33}} & 0 & 0 & 0 \\ \frac{\nu^*}{E^*}\frac{1}{\Gamma_{22}\Gamma_{11}} & \frac{1}{E^*}\left(\frac{1}{\Gamma_{22}}\right)^2 & \frac{\nu^*}{E^*}\frac{1}{\Gamma_{22}\Gamma_{33}} & 0 & 0 & 0 \\ \frac{\nu^*}{E^*}\frac{1}{\Gamma_{33}\Gamma_{11}} & \frac{\nu^*}{E^*}\frac{1}{\Gamma_{33}\Gamma_{22}} & \frac{1}{E^*}\left(\frac{1}{\Gamma_{33}}\right)^2 & 0 & 0 & 0 \\ 0 & 0 & 0 & \frac{1}{2G^*}\frac{1}{\Gamma_{22}\Gamma_{33}} & 0 & 0 \\ 0 & 0 & 0 & 0 & \frac{1}{2G^*}\frac{1}{\Gamma_{33}\Gamma_{11}} & 0 \\ 0 & 0 & 0 & 0 & 0 & \frac{1}{2G^*}\frac{1}{\Gamma_{11}\Gamma_{22}} \end{bmatrix}. \tag{5.7}$$

In situations where the contact tensor $\boldsymbol{F}$ and the MIL tensor $\boldsymbol{H}$ hold the same value, the tensor ratio $\boldsymbol{\Gamma}$ becomes an identity matrix and isotropy is implied. The tensor ratio quantity then drops out of Equation (5.7) to return the isotropic configuration of the compliance matrix. Extracting material properties

for specific directions from Equation (5.7) uses the same methods described in the previous chapter.

5.4 Summary of Shape Factors

Assuming all snow grain types as spheres on a microstructural level significantly restricts the accuracy of a microstructural based model. Here, grain shape can be addressed on a scalar level using a measurable aspect ratio which corrects for deviations away from spherical shapes. This scalar factor is arranged in an aspect ratio which accounts for increased flexural deformation of bonded grain pairs. The increased flexure could result from the possibility of significant bending moments and decreased structural stability developing as crystals elongate away from spherical shapes.

In terms of directional quantities, tensors such as the contact tensor and MIL tensor provide different, but complimentary insights into the arrangement of grains. The tensor ratio utilizes these two values to quantify the combined effect both tensors have on the overall macroscale stiffness of the snow. Just as the scalar shape factor handles the overall deviations of the shapes away from a simple spherical shape (independent of orientation), the tensor ratio and

underlying fabric tensors used in computation account for the specific arrangement and distribution of grains throughout the microstructure.

In the chapters that follow, the feasibility of each of these shape factors will be put to use on real, lab-grown radiation recrystallized samples to investigate the evolution of mechanical properties of a developing radiation recrystallized snow layer.

CHAPTER SIX

FINITE ELEMENT MODELING

"Nature uses only the longest threads to weave her patterns, so each small piece of her fabric reveals the organization of the entire tapestry."
~ Dr. Richard Feynman 1965

Finite element modeling is a useful numerical technique for analyzing field problems (solid mechanics, heat transfer, electro-magnetism). In this case, the field problem is the determination of the stress and strain response of a snow structure before and after radiation recrystallization. Finite element analysis is often employed when no closed-form analytical solution is available or is difficult to solve. The complexities of the problem inhibiting analytical solutions can arise from a number of places including material properties, boundary conditions, structure geometry, etc. In the case of modeling the mechanical response of snow to a load or displacement, material parameters are too difficult to measure to produce an accurate modeled response.

Here, the effective material properties such as stiffness and strength will be derived from the stress/strain response of a microstructural model of the snow. Material parameters for ice are known with much greater precision than for snow. Using μCT scans of the microstructure of snow, the solid volumetric

representation is converted to a discretized finite element mesh. Ice material parameters are applied to the snow's microstructural network of ice grains. The overall mechanical response is used to derive effective material properties with relative changes to the effective properties presumably based on the microstructural configuration of the snow sample. Any microstructural arrangement is able to be analyzed and thus can provide comparisons between separate microstructures pre- and post-recrystallization.

6.1 History

Finite element modeling has been utilized numerous times in studying the mechanical response of snow to a load. Early adopters of finite element models utilized a continuum approach: modelling snow as a continuous material. Stoffel and Bartelt (2003) and later Stoffel (2005) utilized 2-D and 3-D meshes with weak interfaces defined between solid elements to model avalanche release in elastic and viscoelastic situations. Additionally, Stoffel (2005) included terrain effects in the geometry of the continuum model to simulate avalanche release in real topographic environments. An attempt at modeling weak layer interaction with slab layers was also taken by Scapozza and Bartelt (2003). Modeling was carried out in two dimensions and mostly focused on the viscoelastic response. A

similar study was undertaken by Navarre et al. (2007) which expanded to three dimensions.

All of these previous modelling attempts (and others not included here) relied heavily on accurate material parameters or constitutive models to describe the material behavior. The continuum approach allowed the inclusion of several parameters including damage criteria, viscosity terms, and layered structuring, which makes analytical solutions difficult or impossible. However, each model was only able to perform as well as the material parameters used for input.

More recent attempts to describe the mechanical response of snow to a prescribed load delved into the microstructure. Schneebeli (2004) first attempted a basic approach using 3-D microstructures derived from μCT imaging to create a model. The ice network geometry was meshed and loaded directly in a finite element simulation using linear elastic parameters for ice. The simulation results produced an effective elastic modulus for snow 3–100 times larger than previously published measurements of elastic moduli (Schneebeli, 2004). It was conjectured this was related to strain rate effects since the deformation of ice is significantly affected by the loading rate (Schneebeli, 2004).

Little work was published on finite element modeling using the microstructure until 2010 when Srivastava et al. (2010) published work on

analyzing the temporal evolution of temperature gradient metamorphism using a hybrid approach combining directional fabric data with a voxel based approach developed by Garboczi (1998). Details were sparse in Srivastava et al. (2010) and it was unclear which approach was utilized since several models were presented in Garboczi (1998). Regardless, Srivastava et al. (2010) showed a similar microstructural evolution of the texture of the snow as observed in this study and others (Schneebeli and Sokratov, 2004; Shertzer and Adams, 2011; Shertzer, 2011; Shertzer et al., 2010). Like the Schneebeli study (2004), computed effective Young's moduli for snow were one to two orders of magnitude higher than published values (e.g. Mellor, 1975).

Around the same time, other studies were trying to utilize the information obtained from computed tomography and simplify it into readily usable forms. Yuan et al. (2010) compared the results of a finite element analysis of the real microstructure of snow to a microstructural volume of a statistically generated geometry used to simulate a snow microstructure. The main purpose was to investigate the viability of stochastically generated microstructures. Numerical simulation was employed to evaluate the effectiveness (Yuan et al., 2010). In a separate approach Theile et al. (2011) tried to utilize beam elements to discretize the 3-D microstructure of snow. It was argued that most of the deformation

occurs at the boundaries between grains and a 3-D microstructure composed of beam elements could significantly reduce model complexity and improve computation time (Theile et al., 2011).

More recent publications align closer to the finite element work undertaken here. Chandel et al. (2014) performed a volume sensitivity study using the finite element method simulating mechanical response of the snow using the 3-D microstructure of snow obtained through μCT imaging. A single volume of snow was tested mechanically and imaged using μCT. Compression was simulated on sub-volumes taken from the original sample and an elasto-plastic constitutive law incorporating damage accumulation was employed (Chandel et al., 2014). An actual mechanical test was also conducted on the sample that was analyzed in the study and the data matched remarkably well. It was found that moving from a cubic volume with a side length of 1.791 mm (5.745 mm^3) to a side length of 3.582 mm (45.96 mm^3) reduced the error in calculation of the Young's modulus from 44% to 18% compared to the experimentally measured value (Chandel et al., 2014). Reasonable approximations of the effective compressive strength were also achieved (Chandel et al., 2014).

Hagenmuller et al. (2014) also performed a finite element analysis directly on the microstructure derived from μCT imaging. The size of the volumes were consistent with those used in the Chandel et al. study (2014). Hagenmuller et al. (2014) utilized sample densities around $350\ \mathrm{kg \cdot m^{-3}}$, much more dense than the snow utilized in this study. Hagenmuller et al. (2014) were also able to utilize a simpler failure criteria to simulate localized material failure. They employed Rankine criteria with a simple rectangular failure surface defined by the maximum and minimum principal stresses in principal stress space. Element failure was determined through an iterative approach (Hagenmuller et al., 2014).

Snow samples utilized by Chandel et al. (2014) and Hagenmuller et al. (2014) only represented well sintered homogeneous samples of snow. Neither has applied their technique to highly faceted weak layers of snow. The insights from these two studies are quite influential in the development of the finite element approach employed here.

6.2 Formulation

Here, two separate samples are collected from each experiment for μCT imaging for use specifically in the finite element analysis. The first sample contains the initial snow surface prior to recrystallization capped by newly

sieved snow. This procedure ensures the imaged sample of snow contains approximately the same stratigraphy present in the mechanical test performed on the non-radiation recrystallized samples. Three types of initial surface snow were tested: one containing a sintered new snow surface (< 48 hours old), one that has been sintering for 1 week, and another sintering for 2 weeks. All types of initial snow surfaces were capped by sieved fresh snow and allowed to sinter for 12 hours prior to the mechanical test. This procedure is detailed in Chapter Seven. The sample collected for 3-D imaging is also capped by new snow and allowed to sinter for the same amount of time before imaging.

The second sample is collected following the conclusion of creating a near surface faceted layer through radiation recrystallization. Again, the near surface portion is extracted from the sample and capped by sieved snow following the same procedure for the initial sample of snow. In this way, the microstructures of the old and new snow are captured as well as the microstructural interaction of these two distinct crystal morphologies. Examples of the two different microstructures are illustrated in Figure 6-1 below.

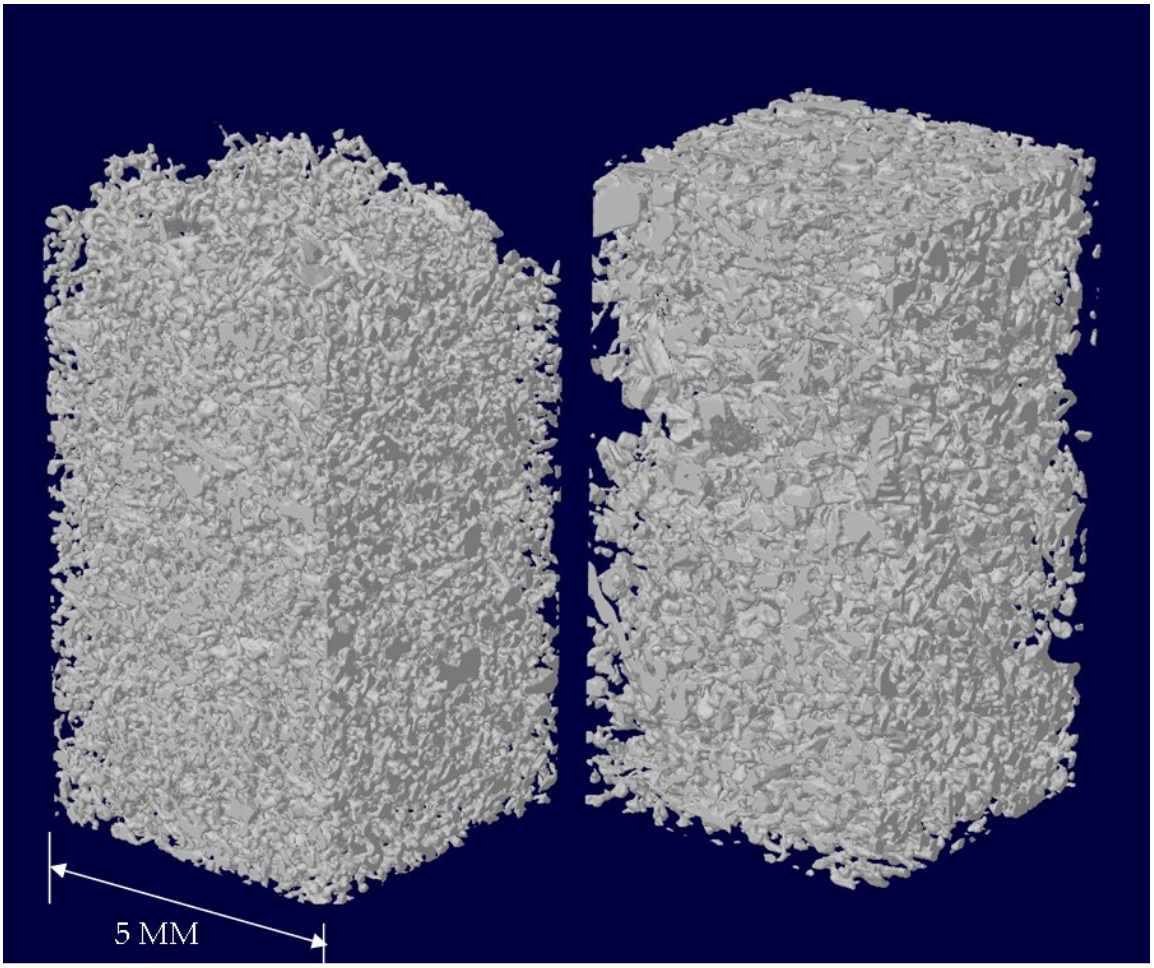


Figure 6-1: Side-by-side view of two volumes of snow modeled with finite element methods. The sample on the left consists of an initially homogenous structure prior to recrystallization. The sample on the right contains a radiation recrystallized faceted layer buried by new snow. Each sample cross section is 5 mm × 5 mm.

6.2.1 Discretization

Samples are scanned and reconstructed to form a 3-D image stack according to the procedures outlined in Section 7.2. Once the volumes have been reconstructed and binarized to distinguish between solid ice and air pore spaces, a sub volume is selected which contains the layered snow interface of interest. A

separate image stack containing the binarized images is saved for use in a program specially designed for converting CT voxel data to usable finite element meshes.

Materialise Mimics ® is a software suite originally intended for the biomedical engineering field to model real human anatomy and its interaction with artificial structural implants and prosthetics. This program has found a wider audience recently to mechanists interested in utilizing complex microstructural geometries in finite element analyses and computational fluid dynamics. Materialise Mimics ® is employed here to operate on the 3-D volumetric data of the microstructure of snow for the purpose of refining μCT data into a usable form for finite element analysis.

The initial surface mesh generated directly from the 3D voxels is a triangular mesh of uniform size with base edge dimensions equivalent to the scan resolution. The voxel size utilized in this study was 14.88 μm, but the resolution was halved to accommodate a large enough volume of snow. The voxel binning process leaves the voxel size for generating a surface mesh of 29.76 μm. This voxel size provided comparable resolution with those used in recent studies (Chandel et al., 2014; Hagenmuller et al., 2014). With this voxel size, the total number of surface elements initially can range from 5 million to 8 million

triangular surface elements. A close up of the unmodified surface mesh is shown in Figure 6-2. The goal of discretization is to reduce the complexities in areas that do not need a detailed mesh while maintaining a fine mesh in areas with rapidly changing topography. Additionally, software licensing limits in ANSYS Mechanical (FEA package utilized in this study) required models with fewer than 250k elements and/or nodes.

Within the program, several tools exist to reduce the number of triangles, smooth the mesh and perform remesh operations with quality controls such as element aspect ratios and max/min angles within elements. In most situations, elements perform best where the external surfaces/edges form a nearly equilateral geometry (Cook et al., 2002). For triangular elements, that means the ideal shape is an equilateral triangle. For quad elements, squares are best. To help maintain appropriate detail in thin sections of the geometry, element growth control is also applied to limit large size discrepancies between adjacent elements. Materialise Mimics ® also includes tools for fixing common errors that occur during the mesh regenerating process such as overlapping edges, inverted faces (elements that face the wrong direction), planar holes, and noise shells. Noise shells are pieces of the mesh that get cut off from the main body volume during remeshing operations. The goal is to export a volume mesh containing

one fully connected volume. Additional floating volumes cause problems later on during the analysis.

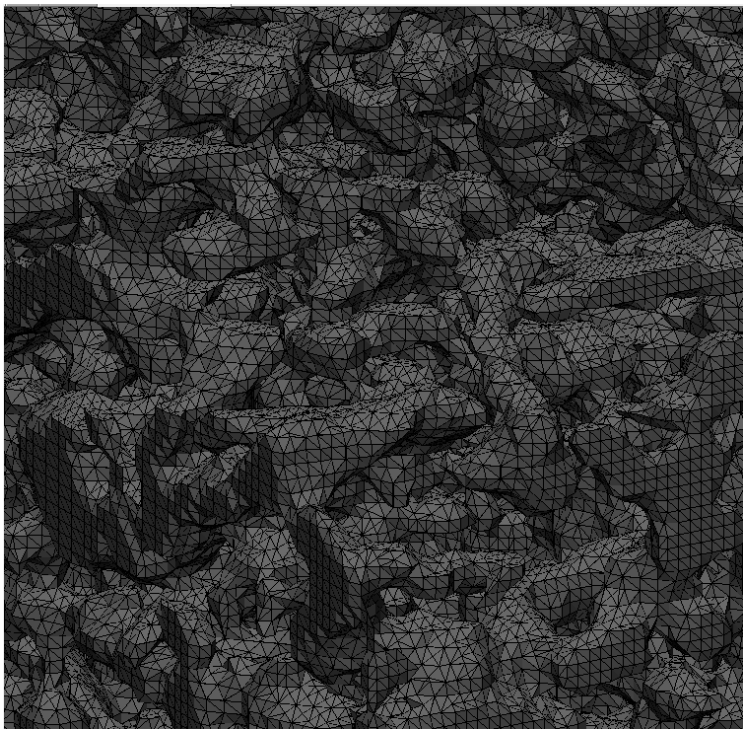


Figure 6-2: Close up view of the raw surface mesh initially applied to the μCT imaged volume. Triangular elements are uniform in size with each side length equal to 29.76 μm.

Following the conclusion of remeshing operations on the surface, a volumetric mesh is mapped inside the surface mesh. Tetrahedral elements are generated since they best handle the complex geometry associated with the microstructural ice network. In order to stay under the node limit of ANSYS Academic, tet4 elements were used (linear, constant strain elements). It is also possible to utilize the higher order tet10 element with midside nodes. Tet10

elements are not utilized here since generating volumetric meshes with sufficient detail creates too many nodes. The disadvantages of using linear tetrahedral elements will be discussed later.

After the mesh refinement procedure, the final meshes tend to utilize approximately 180k to 250k solid linear tetrahedral elements, depending on the total volume and complexity of the microstructure. An example of a final volume mesh is shown in Figure 6-3.

Upon import into ANSYS Mechanical, the volumetric mesh is assigned SOLID185 elements. As shown in Figure 6-4 below, SOLID 185 is normally an 8 node brick element with 3 degrees of freedom at each node. The element can be degenerated into a tetrahedron by grouping nodes M,N,O, and P at the top, and nodes K, and L and the bottom as shown in Figure 6-4. SOLID 285 is another element considered since it is natively a tet4 element. However, the notes for SOLID 285 recommend utilizing SOLID 185 instead since SOLID285 elements are not computationally efficient with compressible materials (*ANSYS 14.5 APDL Element Reference*, 2012). SOLID 185 allows for element birth and death which is a critical feature utilized in the implementation of this model. Although the tetrahedral degeneration of SOLID185 is not recommended, the list of available elements is small due to the restrictions imposed by the complex geometry and

node/element limitations of the available software. Accounting for the shortcomings of the chosen element type is discussed later in Subsection 6.2.4.

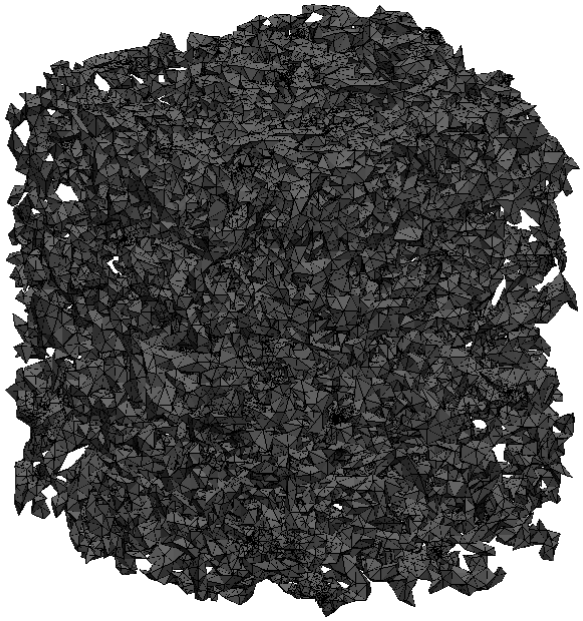


Figure 6-3: Final volumetric mesh following mesh refinement procedures in Materialise Mimics ®.

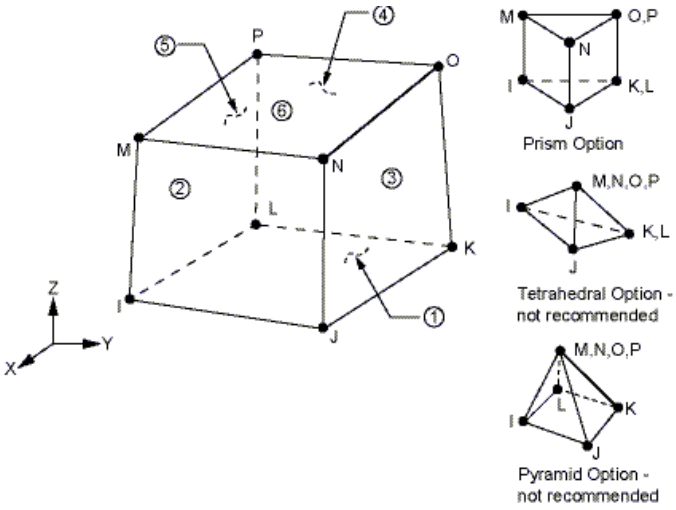


Figure 6-4: Geometry of the homogeneous structural solid element SOLID185 (from: *ANSYS 14.5 APDL Element Reference,* 2012).

6.2.2 Material Parameters

Selecting the appropriate material parameters for ice is not trivial for proper performance of the model. Several modelling efforts have cited the texts of Petrenko and Whitworth (1999) and Schulson and Duval (2009) for properties of ice. Each list the isotropic Young's modulus of polycrystalline ice at 9.3 GPa and 9.5 GPa respectively. The Poisson's ratio for isotropic polycrystalline ice is given as 0.325 (Petrenko and Whitworth, 1999). Polycrystalline ice is often considered isotropic when single ice crystals are randomly oriented in a matrix of ice grains.

Single ice crystals themselves are highly anisotropic and yield transversely isotropic properties with 5 independent stiffness coefficients. Ice crystals are hexagonal with a basal plane defined by the c-axis, and 6 a-axes extending through the hexagonal vertices of the crystal. The crystallographic planes are illustrated in Figure 6-5 (McClung and Schaerer, 2006). The transversely isotropic stiffness coefficients are listed in Table 6-1 below. In the case of transverse isotropy employed here, the stiffness coefficient C_{33} is collinear with the c-axis of the single crystal orientation. The stiffness coefficients of a transversely isotropic structure are given as:

$$[C] = \begin{bmatrix} C_{11} & C_{12} & C_{13} & 0 & 0 & 0 \\ C_{12} & C_{11} & C_{13} & 0 & 0 & 0 \\ C_{13} & C_{13} & C_{33} & 0 & 0 & 0 \\ 0 & 0 & 0 & C_{44} & 0 & 0 \\ 0 & 0 & 0 & 0 & C_{44} & 0 \\ 0 & 0 & 0 & 0 & 0 & (C_{11} - C_{12})/2 \end{bmatrix}. \quad (6.1)$$

Table 6-1: Transversely isotropic stiffness coefficients for monocrystalline ice (Gammon et al., 1983; Petrenko and Whitworth, 1999).

Parameter	Value (GPa)
C_{11}	13.67
C_{12}	6.83
C_{13}	5.51
C_{33}	14.76
C_{44}	3.01

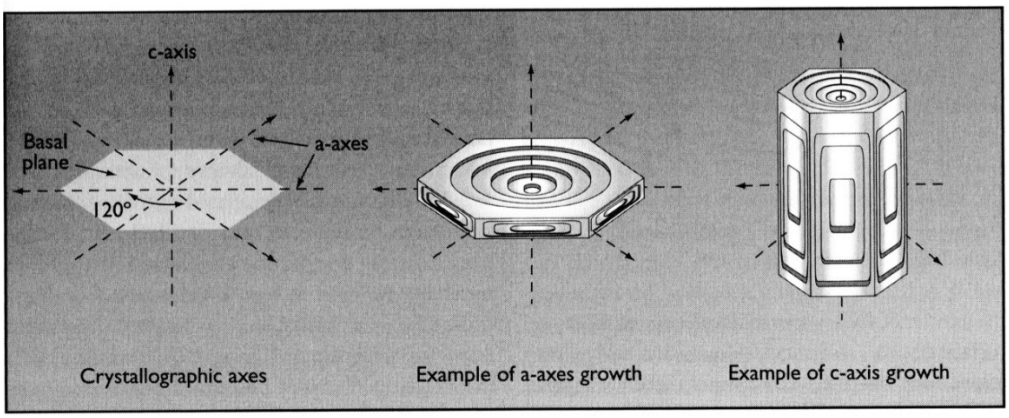


Figure 6-5: Crystallographic planes of a single ice crystal (from: McClung and Schaerer, 2006).

Working with the isotropic coefficients from Petrenko and Whitworth (1999) in the model produced overly stiff results relative to mechanical results reported in this study and elsewhere (e.g. Mellor, 1975). According the literature, the values by Petrenko and Whitworth (1999) and Schulson and Duval

(2009) represent the upper edge of material properties for ice used in finite element models for snow (Chandel et al., 2014). Most measurements on the stiffness coefficients for ice are performed on freshwater ice frozen from the liquid phase of water.

Kermani et al. (2008) offers Young's modulus measurements for atmospherically formed ice, or ice accumulated from a super-cooled state and vapor state. Kermani et al. (2008) lists the isotropic Young's modulus of ice at 1 GPa. Testing was performed at a strain rate of $2 \times 10^{-3}\ \mathrm{s}^{-1}$ at temperatures of $-3°\ \mathrm{C}, -10°\ \mathrm{C}$, and $-\ 20°\ \mathrm{C}$. The Young's modulus was nearly constant across all of these temperatures. The tested strain rate and temperature ranges are similar enough to the mechanical experiments performed on this test. Chandel et al. (2014) utilized the data from Kermani et al. (2008) and later revised their Young's modulus to 0.95 GPa to better fit with experimental tests.

Finite element models used here only consider the isotropic parameters of polycrystalline ice. Holding the material parameters constant between different volumes of snow isolates the effect of the microstructure on the effective mechanical response of the snow. The assumption of having a sufficiently random orientation of ice grains in all situations is challenged by recent work by Riche et al. (2013).

Riche et al. (2013) found preferred crystal orientations in microstructures of temperature gradient metamorphism. Following several weeks or metamorphism within a temperature gradient of $|\overline{\nabla}T| = 50° \, \mathrm{C} \cdot \mathrm{m}^{-1}$ and an average temperature of $-20° \, \mathrm{C}$, grains had a tendency toward horizontally oriented c-axes (transverse to the temperature gradient) (Riche et al., 2013). In their discussion, Riche et al. (2013) admitted the favored crystallographic orientation strongly depends on the temperature and vapor saturation but could also be triggered by the configuration of the base crystals and pore spaces (Adams and Miller, 2003).

Although significant crystal orientation patterns may develop as a result of radiation recrystallized metamorphism, no feasible way to assess crystal orientation was available at the time of this study. Adding in the effects of preferred crystal orientation may be a future consideration.

Material failure criteria are also necessary to implement a basic damage model to assess effective strength of the snow sample. Hagenmuller et al. (2014) employs a simple Rankine criteria which specifies a maximum and minimum principal stress as failure. If either value is exceeded, element failure has occurred. Maximum normal stress theories are generally prescribed for brittle materials (Vable, 2002). Chandel et al. (2014) employ a more sophisticated

element failure model which degrades the initial stiffness of an element to zero over time. This damage model is based on Von-Mises J2 plasticity (Chandel et al., 2014).

The approach employed here to detect material failure lies in the middle of those used by Hagenmuller et al. (2014) and Chandel et al. (2014). Initially, a Tresca failure criterion was employed as a simplistic approach to detecting material failure. The Tresca failure theory is also referred to as the maximum shear stress theory. It is traditionally utilized for ductile materials (Vable, 2002). Ice can exhibit significant ductile deformation prior to failure depending on strain rate.

Using ordered principal stresses ($\sigma_1 > \sigma_2 > \sigma_3$), failure stress is defined as:

$$\frac{1}{2}(\sigma_1 - \sigma_3) \leq \tau_s, \tag{6.2}$$

where τ_s is defined as the shear strength and $\tau_s = \frac{1}{2}\sigma_{ts}$ (Tresca, 1864). σ_{ts} is the uniaxial tensile strength. Tresca failure theory assumes the tensile strength σ_{ts} and the compressive strength σ_{cs} are equal in magnitude (Tresca, 1864).

However, Kermani et al. (2007) lists separate strengths for tension and compression: 3.0 MPa and 5.5 MPa respectively. In order to handle different axial strength magnitudes in tension and compression, the Mohr-Coulomb failure theory is used. The Mohr-Coulomb theory reduces to the Tresca criteria if

the magnitudes of the compressive and tensile strengths are the same. Mohr-Coulomb theory also provides equal weight to brittle failure (axial stress) and ductile failure (shear stress). A form of Mohr-Coulomb theory can be written in terms of tensile strength and compressive strength if the principal stresses are ordered as previously mentioned (Labuz and Zang, 2012):

$$\frac{m+1}{2}\left(\sigma_1 - \sigma_3 + K(\sigma_1 + \sigma_3)\right) \leq \sigma_{cs},$$

$$m = \frac{\sigma_{cs}}{\sigma_{ts}}, \text{and} \tag{6.3}$$

$$K = \frac{m-1}{m+1}.$$

If after assessing σ_1 and σ_3 the left side of Equation (6.3) is greater than σ_{cs}, the material has failed. The failure surface is shown in Figure 6-6 reproduced from Labuz and Zang (2012). Detection for element failure will be described in the following section. Element failure is implemented over yield behavior since the assumed localized strain rates dictate mostly brittle failure in ice: making yield and failure occur at the same stress.

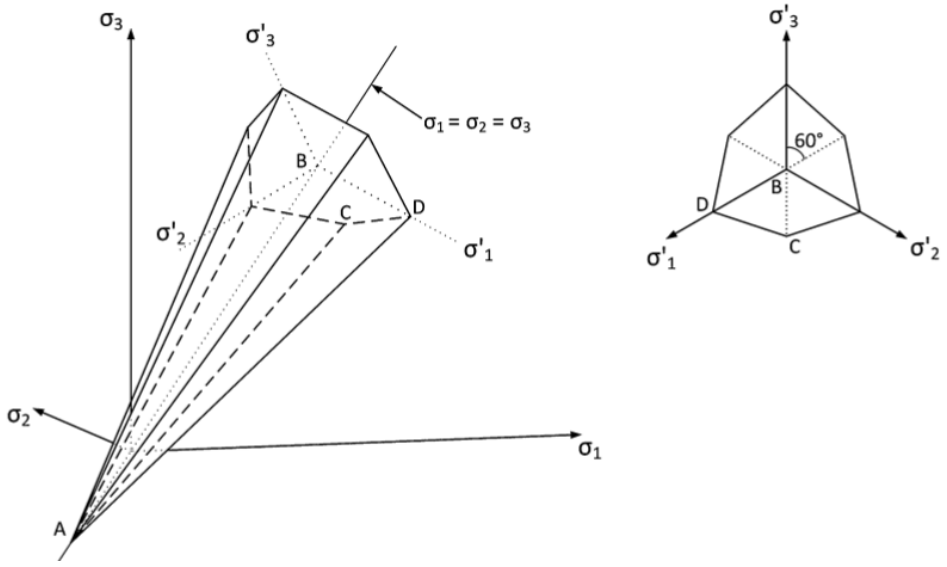


Figure 6-6: Mohr-Coulomb failure surface (reproduced from Labuz and Zang, 2012).

6.2.3 Solution Technique

Following the import of the volumetric mesh and setting of the material properties, boundary conditions were applied to the sample. Two test modes were utilized: one in compression and one in shear. For both modes, the nodes in the bottom 0.25 mm of the sample are fixed ($U_x = U_y = U_z = 0$). This is to assure an adequate grip on the sample to appropriately distribute the internal forces through most of the sample. Non-zero displacement boundary conditions are applied to the top 0.5 mm of the sample (again to assure an adequate grip of the material).

If only the boundary nodes are supplied with boundary conditions (top or bottom), inadequate distribution of internal forces may occur on some meshes.

Meshing operations sometimes leaves isolated branches of the geometry as the only material that extends to the top or bottom boundary of the volume representation. Applying a displacement to a singly connected branch of the microstructure is not realistic when considering the multiple connections likely present before artificially isolating a sub-volume from a larger sample.

Displacement is specified in increments of 0.001 mm to 0.005 mm per equilibrium iteration. This parameter is adjusted as needed to aid in convergence of the model. In shear, the top nodes are prescribed horizontal displacement. In compression, vertical displacement is specified.

The shear case also has a vertical nodal force that is applied in compression to the top nodes to simulate the overburden pressure resulting from the combined weight of the snow and shear frame. The combined mass of the frame and the snow it contains (estimated at a density of $150\ \mathrm{kg \cdot m^{-3}}$) produces a total compressive stress of approximately 215 Pa. This stress is converted back to an appropriate force for the size of the cross-section and is equally distributed as nodal force across the constrained nodes at the top of the sample.

Periodic symmetry conditions were considered along the lateral boundaries and the top of the sample however their use was abandoned after unpredictable and undesirable behavior. Periodic boundary conditions along the

lateral faces of the sample produced unrealistic displacements in the microstructure attached to the boundary since the random nature of the geometry and connectivity to other grains was not well translated. By imposing periodic boundary conditions on the top surface, 2 significant regions of bending stress develop as seen in the example in Figure 6-7 below, rather than just one. Bending stresses are a part of the mechanical experiment performed in the laboratory however, in the lab the top of the sample is able to freely move vertically, allowing for expansion or collapse of the microstructure imposed by a shear load. By specifying periodic boundary conditions to the top surface, collapse or expansion in the vertical direction could be unrealistically restricted.

A static analysis setup is implemented iteratively. To account for the possibility of significant changes to local regions of the geometry, non-linear large strain approximations were used to characterize the finite strain exhibited by each element. To handle the nonlinear behavior of the large strain formulation, the Newton-Raphson solver is switched to full. In the full Newton-Raphson procedure, the full stiffness matrix is updated at every equilibrium iteration (*ANSYS 14.5 APDL Structural Analysis Guide*, 2012). This does require significant computational time but, it is necessary for proper convergence. The solver was also set to output data to accommodate full frame restarts.

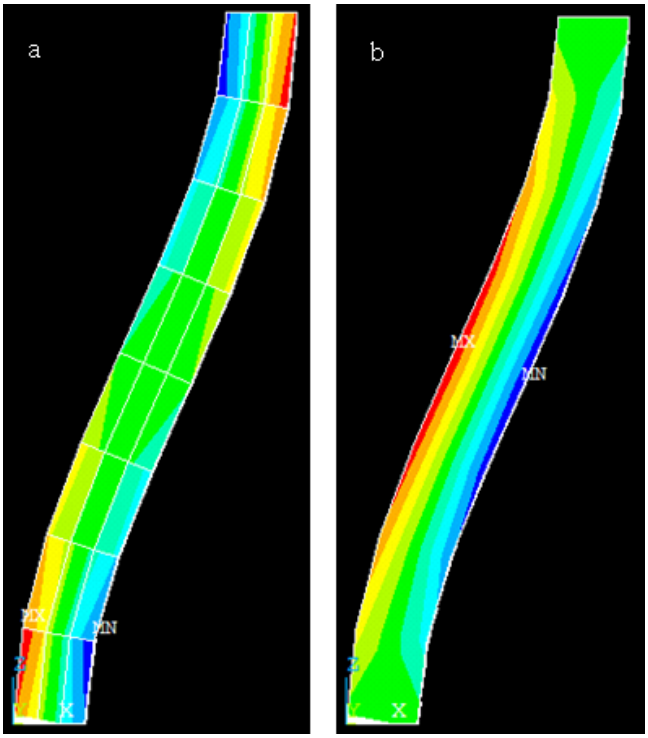


Figure 6-7: Hypothetical column undergoing shear displacement. Boundary conditions are fixed at the bottom and periodic at the top. (a) Vertical axial stress: red is tension, blue compression, green is near zero stress. (b) Vertical displacement: red is up, blue is down, green is zero displacement.

Solving the problem is accomplished through an iterative process. Following the completion of each load step, principal stresses are stored for each element. The Mohr-Coulomb failure theory is evaluated for each of the elements. Elements that have exceeded the failure criteria are "killed" from the analysis. Element death switches the stiffness of an element to zero. In this way, it remains connected to the remainder of the mesh and maintains its position in the global stiffness matrix, but does not contribute to computation of nodal reaction forces. This iterative approach effectively and simplistically handles localized

element failure simulating macro-scale damage accumulation. The analysis is performed until convergence fails, or 25 full iterations have been completed.

Contact between elements on either side of a killed element is not enforced. Given the total amount of strain in the sample, especially during the elastic portion of loading, it is not expected that deformation will result in significant contribution of contact forces that would develop between dead elements. For a porous medium like snow, it is reasonable to assume failed material would be able move into the pore spaces with little or no resistance following failure. Automatically detecting contact between unpredictable surfaces is difficult to implement and computationally more expensive than current resources allow.

Using this iterative technique, reaction forces on the bottom constrained nodes are recorded for the duration of the experiment. Post processing allows for the computation of the effective stress and strain utilizing the total cross sectional area of the control volume independent of the microstructure contained within. Using this information, effective stiffness and strength properties can be extracted as well as any plastic deformation effects occurring during macroscopic failure of the sample.

6.2.4 Shear Locking

As previously mentioned, the use of constant strain tetrahedral elements is not the recommended option due to element behavior under bending conditions. Hagenmuller et al. (2014) demonstrated in their model that bond regions between grains can undergo significant bending deformation (see Figure 6-8). Shear locking occurs when elements generate conditions too stiff for proper bending applications.

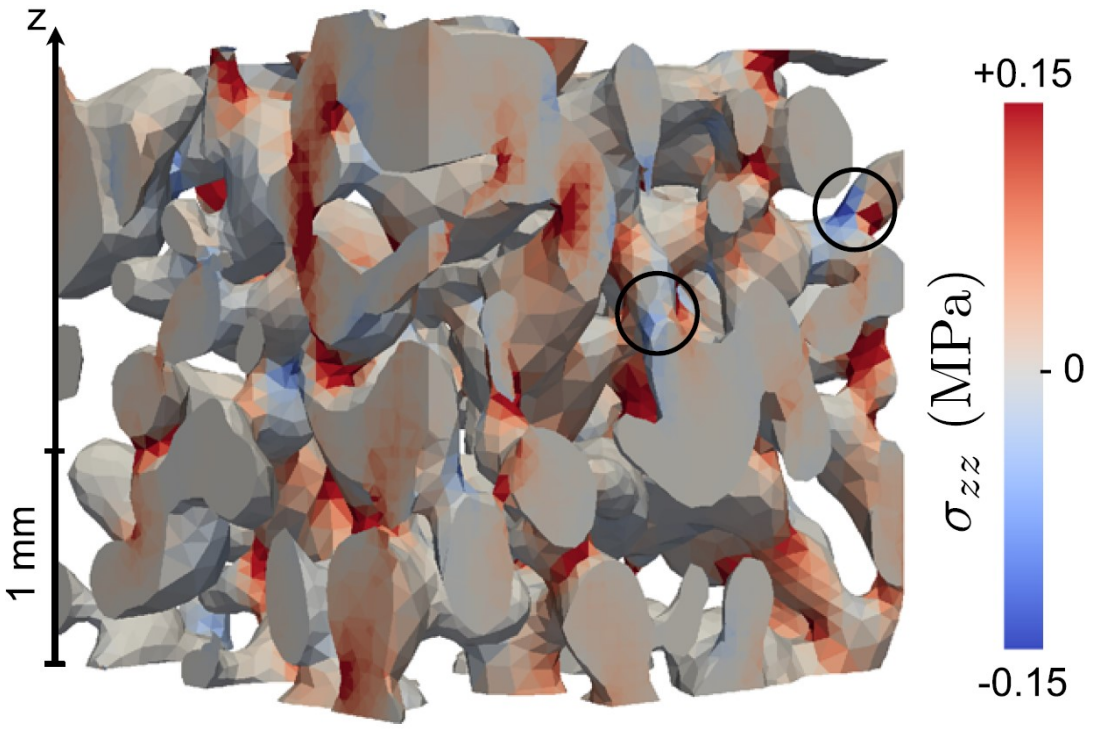


Figure 6-8: Distribution of axial stress σ_{zz} of the microstructure subjected to 2×10^{-5} macroscopic vertical strain (from Hagenmuller et al., 2014).

An example of shear locking will be demonstrated by analyzing a single two dimensional triangular element experiencing bending deformation. The demonstration here is borrowed heavily from Cook et al. (2002). First we will start by setting up a linearly interpolated shape function for the element to analyze some generic field quantity Ω. If the element is configured as the one in Figure 6-9 the degrees of freedom a_i are interpolated over the element as,

$$\begin{Bmatrix}\Omega_1\\ \Omega_2\\ \Omega_3\end{Bmatrix} = [1\ x\ y]\begin{Bmatrix}a_1\\ a_2\\ a_3\end{Bmatrix} = \begin{bmatrix}1 & 0 & 0\\ 1 & x_2 & 0\\ 1 & x_3 & y_3\end{bmatrix}\begin{Bmatrix}a_1\\ a_2\\ a_3\end{Bmatrix}. \tag{6.4}$$

The a_i coefficients are easily solved using the back substitution technique associated with Gauss elimination. Since the matrix is already triangularized, the coefficients are simply computed as:

$$\begin{aligned} a_1 &= \Omega_1, \\ a_2 &= \frac{\Omega_2 - a_1}{x_2}, \text{ and} \\ a_3 &= \frac{\Omega_3 - x_3 a_2 - a_1}{y_3}. \end{aligned} \tag{6.5}$$

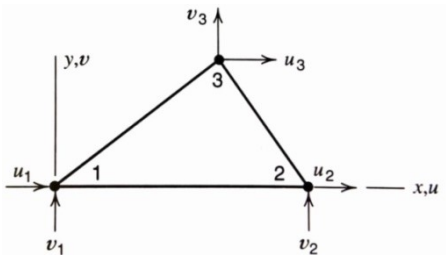


Figure 6-9: Generic triangular constant strain element with 2 degrees of translational freedom at each node (reproduced from Cook et al., 2002).

Making substitutions for similar terms in Equation (6.5) gives the final form based on the nodal positions and field quantities as:

$$\begin{gathered} a_1 = \Omega_1, \\ a_2 = \frac{\Omega_2 - \Omega_1}{x_2}, \text{ and} \\ a_3 = \frac{\Omega_1(x_3 - x_2)}{x_2 y_3} - \frac{x_3 \Omega_2}{x_2 y_3} + \frac{\Omega_3}{y_3}. \end{gathered} \tag{6.6}$$

If the field quantities of interest are displacements (such as those shown in Figure 6-9), then direction needs to be accounted for since in 2D there are 2 degrees of freedom per node. The expansion to 2 degrees of freedom per node is accomplished by:

$$u = \lfloor 1 \; x \; y \rfloor \begin{Bmatrix} a_1 \\ a_2 \\ a_3 \end{Bmatrix} \text{ and } v = \lfloor 1 \; x \; y \rfloor \begin{Bmatrix} a_4 \\ a_5 \\ a_6 \end{Bmatrix}. \tag{6.7}$$

In this case, the degrees of freedom are defined as:

$$\begin{gathered} a_1 = u_1, \\ a_2 = \frac{u_2 - u_1}{x_2}, \\ a_3 = \frac{\mathrm{u}_1(x_3 - x_2)}{x_2 y_3} - \frac{x_3 u_2}{x_2 y_3} + \frac{u_3}{y_3}, \\ a_4 = v_1, \\ a_5 = \frac{v_2 - v_1}{x_2}, \text{ and} \\ a_6 = \frac{v_1(x_3 - x_2)}{x_2 y_3} - \frac{x_3 v_2}{x_2 y_3} + \frac{v_3}{y_3}. \end{gathered} \tag{6.8}$$

The interpolated displacement field is given as:

$$D = \begin{bmatrix} 1 & 0 & 0 & 0 & 0 & 0 \\ -\frac{1}{x_2} & 0 & \frac{1}{x_2} & 0 & 0 & 0 \\ \frac{x_3 - x_2}{x_2 y_3} & 0 & -\frac{x_3}{x_2 y_3} & 0 & \frac{1}{y_3} & 0 \\ 0 & 1 & 0 & 0 & 0 & 0 \\ 0 & -\frac{1}{x_2} & 0 & \frac{1}{x_2} & 0 & 0 \\ 0 & \frac{x_3 - x_2}{x_2 y_3} & 0 & -\frac{x_3}{x_2 y_3} & 0 & \frac{1}{y_3} \end{bmatrix} \begin{Bmatrix} u_1 \\ v_1 \\ u_2 \\ v_2 \\ u_3 \\ v_3 \end{Bmatrix}. \tag{6.9}$$

The 6×6 square matrix in Equation (6.9) is termed the $[\boldsymbol{A}]^{-1}$ displacement matrix. In order to compute strains using the degrees of freedom shown, a displacement gradient matrix must be assembled where:

$$\begin{Bmatrix} \varepsilon_x \\ \varepsilon_y \\ \gamma_{xy} \end{Bmatrix} = [\boldsymbol{B}] \begin{Bmatrix} u_1 \\ v_1 \\ u_2 \\ v_2 \\ u_3 \\ v_3 \end{Bmatrix} \text{ and}$$

$$[\boldsymbol{B}] = \begin{Bmatrix} \frac{\partial u}{\partial x} \\ \frac{\partial v}{\partial y} \\ \frac{\partial u}{\partial y} + \frac{\partial v}{\partial x} \end{Bmatrix} [1 \; x \; y][\boldsymbol{A}]^{-1}. \tag{6.10}$$

Further expansion of $[\boldsymbol{B}]$ in Equation (6.10) expands to:

$$[\boldsymbol{B}] = \begin{bmatrix} 0 & 1 & 0 & 0 & 0 & 0 \\ 0 & 0 & 0 & 0 & 0 & 1 \\ 0 & 0 & 1 & 0 & 0 & 1 \end{bmatrix} [\boldsymbol{A}]^{-1}. \tag{6.11}$$

Plugging $[\boldsymbol{B}]$ into the first expression of Equation (6.10) produces the elemental strain equation as a function of nodal position and displacement:

$$\begin{Bmatrix} \varepsilon_x \\ \varepsilon_y \\ \gamma_{xy} \end{Bmatrix} = \underbrace{\begin{bmatrix} -\frac{1}{x_2} & 0 & \frac{1}{x_2} & 0 & 0 & 0 \\ 0 & \frac{x_3 - x_2}{x_2 y_3} & 0 & -\frac{x_3}{x_2 y_3} & 0 & \frac{1}{y_3} \\ \frac{x_3 - x_2}{x_2 y_3} & -\frac{1}{x_2} & -\frac{x_3}{x_2 y_3} & \frac{1}{x_2} & \frac{1}{y_3} & 0 \end{bmatrix}}_{[\boldsymbol{B}]} \begin{Bmatrix} u_1 \\ v_1 \\ u_2 \\ v_2 \\ u_3 \\ v_3 \end{Bmatrix}. \tag{6.12}$$

The beam in Figure 6-10 is loaded in pure bending. A closer examination of the single element located in the lower left corner of the beam will be analyzed. In this setup of pure bending, all stresses and strains should be axial in nature. No shear stress or strain should develop as determined by the analytical solution of the beam loaded in pure bending.

Utilizing the strain/displacement relationship in Equation (6.12) and nodal positions of the single element in Figure 6-10, the strain on the element can be computed. Using the nodal configuration in Figure 6-10, $x_2 = a, x_3 = 0$, and $y_3 = a$. Additionally, the only non-zero degrees of freedom are u_2 and v_2. Computing the strains gives:

$$\varepsilon_x = \frac{u_2}{a},\ \varepsilon_y = 0, \text{and}$$
$$\gamma_{xy} = \frac{v_2}{a}. \tag{6.13}$$

Given the state of the load in Figure 6-10, the transverse shear strain should be zero. The constant strain element employed creates a spurious shear strain which absorbs energy (Cook et al., 2002). To achieve a prescribed deformation, more load would need to be applied than is correct leading to excessive stiffness. This excessive stiffness is what is described as shear locking.

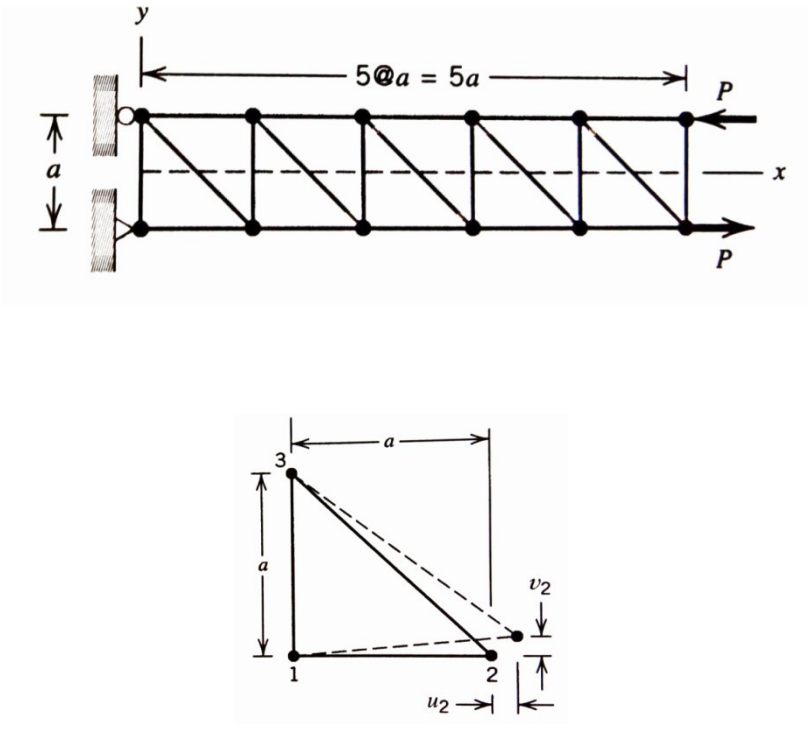


Figure 6-10: Beam loaded in pure bending while meshed with 2-D triangular constant strain elements. Bottom image isolates the lower left element to examine the degrees of freedom (from Cook et al., 2002).

To avoid shear locking, a higher order element is recommended. In this case, switching from tet4 elements to tet10 elements would be the recommendation. However, due to current software licensing limits, the node count required to produce a quality mesh using tet10 elements would be above the 250k node/element limit of ANSYS Academic.

Another possibility to reduce the effects of shear locking is to change from full integration of individual elements to a reduced integration scheme. A first order 3-D brick element is used for easy visualization however; the same concepts are applicable to first order tetrahedral elements too. When using full integration with 2nd order or higher elements, bending modes are captured accurately without any creation of spurious shear strains as seen in Figure 6-11.

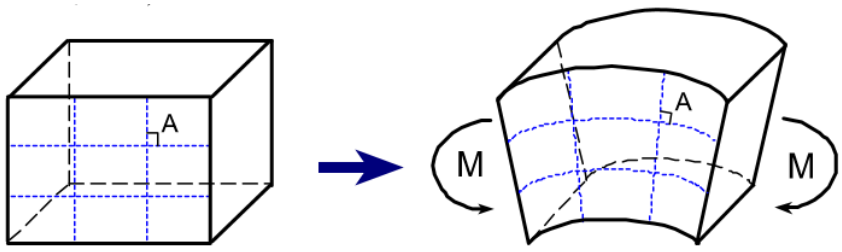


Figure 6-11: Full integration of a 3-D brick element showing accurate approximation of the bent shape. Notice the grid lines remain orthogonal – a requirement for no shear strain (*Abaqus 2016 Online Documentation*, 2015).

However, as explained previously, shear locking can occur when using first order elements producing spurious shear strain to develop in constant strain

elements as seen in Figure 6-12. In Figure 6-12, shear strain is easily detected by the angular deviation of the test grid superimposed on the element experiencing pure bending conditions.

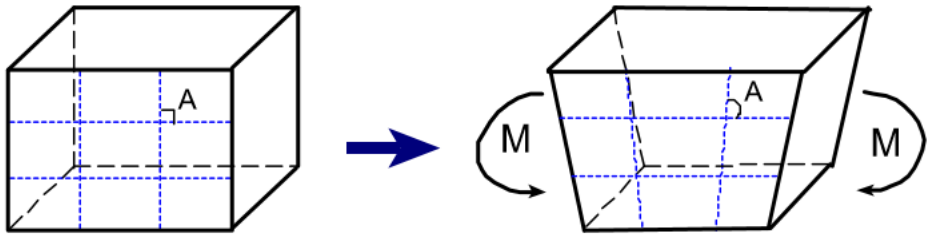


Figure 6-12: Full integration of a 3-D first order brick element. Shear locking occurs which introduces spurious shear strains as seen in the change in angles due to the edges not being able to assume a bent shape (*Abaqus 2016 Online Documentation*, 2015).

Reduced integration is a technique that not only speeds up computation time, but also prevents shear locking. For a first order 3-D element, this reduces the number of integration points to one. As seen in Figure 6-13, the problem of shear locking is solved, however a new problem is introduced – hourglassing.

Hourglassing is a problem opposite of shear locking. It produces elements with too much flexibility. Inspecting Figure 6-13, shear locking is appropriately prevented; however the vertical and horizontal test lines remain unchanged in length. Computationally, this produces a deformed element with no change in strain energy. This zero-energy deformation mode is a non-

physical response which can propagate when coarse meshes are used. This results in excess structural flexibility when significant bending modes are introduced.

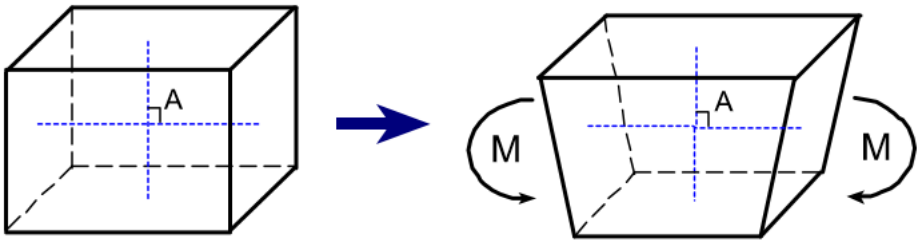


Figure 6-13: Reduced integration of a 3-D first order brick element (single integration point). Shear locking is prevented since spurious shear strains are not produced, however, the grid lines in the deformed shape have not changed length (*Abaqus 2016 Online Documentation*, 2015).

ANSYS Mechanical APDL provides element technology for SOLID185 elements to reduce the effects of hourglassing. By enabling KEYOPT(2)=1, which enforces uniform reduced integration, hourglass stiffness parameters are added to each element to reasonably prevent elemental hourglass modes (*ANSYS 14.5 APDL Element Reference*, 2012). Hourglass stiffness parameters introduce a small amount of artificial strain energy. However, as long as the ratio of artificial strain energy to total strain energy remains less than 5%,

$$\frac{\text{artificial energy}}{\text{total energy}} \leq 5\%, \tag{6.14}$$

the solution is generally acceptable (*Abaqus 2016 Online Documentation*, 2015, *ANSYS 14.5 APDL Element Reference*, 2012).

6.3 Summary

Microstructural based finite element analysis will be iterative in nature. Adequate tetrahedral meshes can be generated directly from the geometry produced through μCT imaging. Appropriate material properties for polycrystalline ice will be applied to a non-faceted and faceted microstructure model. Localized damage is governed by the iterative process of inspecting elements that have exceeded the Mohr-Coulomb failure criteria and "killing" them from the analysis. Results of this portion of the study are examined in Chapter Ten.

CHAPTER SEVEN

METHODS AND EXPERIMENTS

"Things do not happen. Things are made to happen."
~ John F. Kennedy

A laboratory experimental program is implemented to support the analytical work described previously. The laboratory facilities at Montana State University enable simulation of the mountain environment conducive to the formation of radiation recrystallized snow. What follows are the general laboratory procedures and methods for collecting, manipulating, and analyzing relevant data to support the tensor based constitutive model and the finite element model.

7.1 Laboratory Procedures

7.1.1 Laboratory Specifications

Laboratory experiments took place in the Subzero Science and Engineering Research Facility (SSERF) at Montana State University. In particular, two chambers were used primarily to conduct this research – the Cold Hydrodynamics Chamber and the Environmental Chamber.

The Cold Hydrodynamics Chamber is where atmospherically similar snow is manufactured for use with experiments. This chamber is capable of maintaining air temperatures down to −25° C. In addition, a plumbing system provides access to liquid water controlled up to a temperature of +20° C. During snow making operations, this room is outfitted with an apparatus that utilizes the liquid water capabilities to produce snow. This process will be described below in sub-section 7.1.3.

The Environmental Chamber is used for inducing snowpack metamorphism using realistic mountain environment parameters. This environment is achieved through specialized equipment installed with the chamber. Air temperatures can be controlled to a minimum temperature of −40° C. In addition, the ceiling of the chamber can be refrigerated to a temperature of −50° C – independent of the air temperature. This equipment allows for simulation of the effective temperature of the sky whether the simulated sky is cloudy or clear. A metal halide luminary is also installed in the center of the ceiling offering the same wavelengths and similar intensity delivered by the sun.

An array of instrumentation is utilized inside the lab to obtain measurements inside the snowpack and the environment surrounding the

snowpack during metamorphism. Instrumentation inside the lab that were used for these experiments and shown in Figure 7-1 includes:

- several thermocouple sensors mounted to the walls and ceiling to obtain boundary temperatures of the chamber,
- a thermocouple array containing 20 thermocouples spaced 0.5 cm apart to obtain near surface temperature gradients in the snow,
- an Eppley Labs PSP Pyranometer for measuring incoming shortwave radiation (Spectral Range 295-2800 nm),
- an Eppley Labs PIR Infrared Radiometer for measuring incoming longwave radiation (Spectral Range 4-50 μm),
- an Everest Interscience Model 4000-4ZL non-contact infrared sensor for measuring snow surface temperature remotely,
- and a Vaisala INTERCAP Humidity and Temperature Probe HMP60 for measuring ambient temperature and relative humidity.

All of these instruments were fed to an Agilent 34970A Data Logger in which each data channel was read every 30 seconds for the duration of a metamorphism experiment.



Figure 7-1: Environmental chamber showing radiation and temperature instrumentation in place around a snow sample. The metal halide luminary is visible at the top center surrounded by the independently refrigerated ceiling.

7.1.2 Environmental Data

Environmental parameters for input into the laboratory control system for the growth of radiation recrystallized facets originate from field stations located at the Yellowstone Club in southwest Montana. The primary field site for studying radiation recrystallized snow is located outside the official ski area boundary at an elevation of 2747 m, a slope aspect of 187°, and latitude-longitude coordinates of 45.230133°N and 111.442248°W. The general elevation and location of the site is shown in Figures 7-2 and 7-3.



Figure 7-2: (Left) USGS Topographic map indicating the general location and altitude of the Yellowstone Club south field station (indicated by red marker). (Right) A satellite and digital terrain map obtained from Google Earth showing Pioneer Mountain and the location of the south field station at the Yellowstone Club.



Figure 7-3: Photo showing the meteorological station installed at the south field site.

The field site is equipped with a meteorological station (see Figure 7-3) measuring ambient air temperature, relative humidity, snow depth, snow surface temperature, near surface snowpack temperatures at 2 cm vertical spacing, incoming slope normal solar shortwave radiation, reflected slope normal shortwave radiation, and incoming slope normal longwave radiation. The slope angle at the meteorological station is approximately 30°. Conditions at this site are read at 3 minute intervals with the average of each 3 minute reading recorded every half hour.

In addition to meteorological data, field notes, snow pit profiles, and photomicrographs of snow crystals are collected frequently by the members of the Yellowstone Club Ski Patrol. A database of meteorological data, notes, and photomicrographs exists back to the 2005-2006 winter season. The database has been utilized in numerous studies investigating radiation recrystallized snow and the conditions that form them (Curley et al., 2014; McCabe et al., 2008; Slaughter, 2010; Slaughter et al., 2011, 2009, 2008; Staples, 2008; Staples et al., 2006).

For the sake of repeatability in the lab, one day that was conducive to radiation recrystallization development was selected out of the database of field conditions for use with all laboratory experiments conducted in this study.

Conditions on 3 January, 2011 produced radiation recrystallized facets of 0.5 mm (Figure 7-4). Previously, 2.5 cm of new snow had fallen overnight with about 7.5 cm of new snow in the preceding 24 hours as noted by the daily report by the YCSP. The facets formed on 0.5mm decomposing stellar crystals resulting from the new snow overnight.

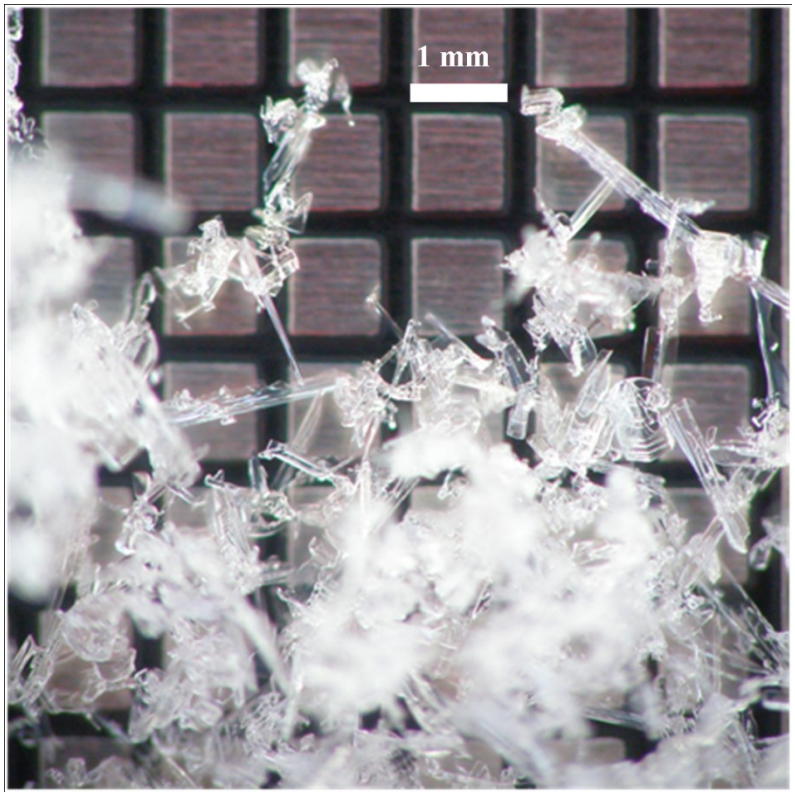


Figure 7-4: Radiation recrystallized facets observed at the south field site at the Yellowstone Club on 3 January, 2011 at 13:30 (Photo Doug McCabe, YCSP).

By 13:30, when the observation was made, incoming shortwave radiation peaked near 1,000 $W \cdot m^{-2}$, and incoming longwave radiation varied between 215

and 315 $W \cdot m^{-2}$. The measured incoming radiation curves are plotted for 3 January, 2011 and the 24 hours prior in Figure 7-5. The ambient air temperature rose to $-6.5°$ C from $-16°$ C before sunrise. The snow surface temperature started off significantly colder than the air temperature at nearly $-24°$ C coinciding with the morning low air temperature. At the peak air temperature and incoming solar radiation, the snow surface temperature briefly rose above the recorded air temperature to $-5.1°$ C. Most of the time however, the snow surface temperatures remained colder than the ambient air temperature as shown in Figure 7-6.

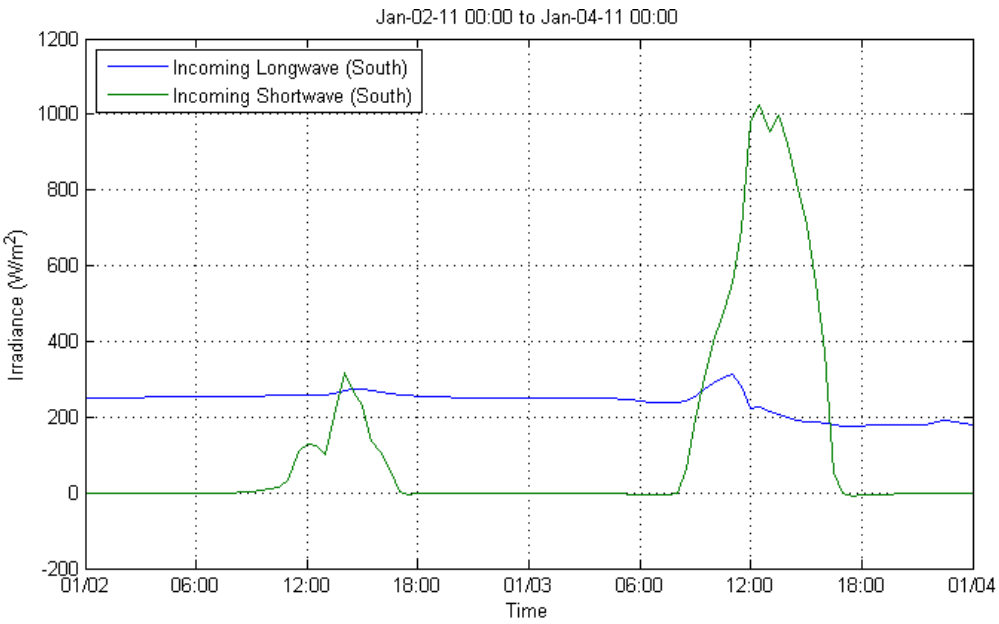


Figure 7-5: Measured incoming longwave and shortwave radiation (normal to the slope) at the south field site at the Yellowstone Club for the 48 hour period on 2 January 2012 to 3 January 2011.

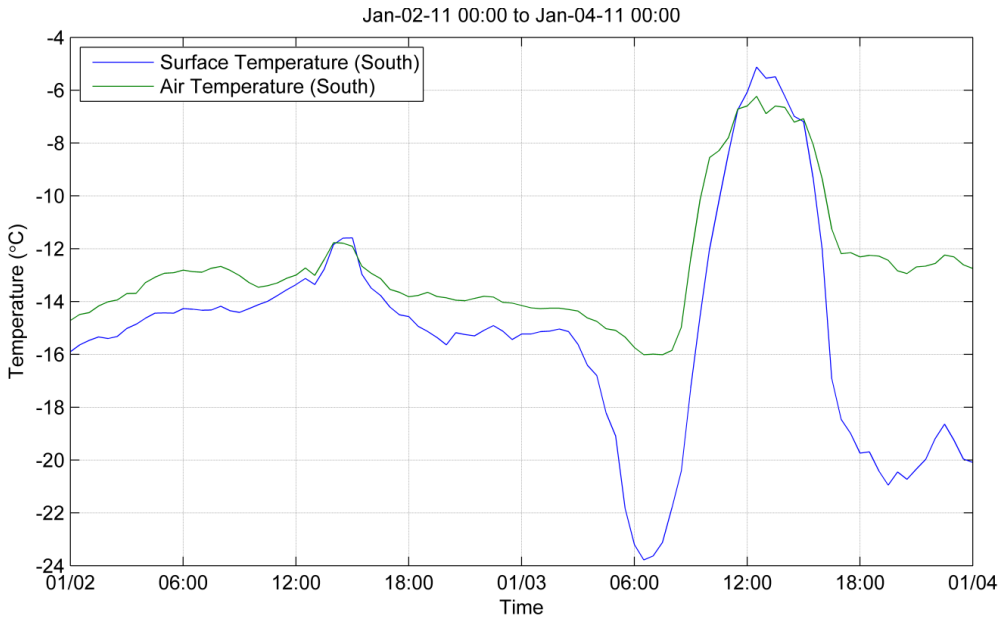


Figure 7-6: Measured ambient air temperature and snow surface temperature at the south field site at the Yellowstone Club for the 48 hour period on 2 January 2012 to 3 January 2011.

In-situ measurements of the near surface temperature gradient are difficult to measure since the thermocouples used to measure snow temperatures at 2 cm intervals are not shielded from direct sunlight and absorb significant amounts of solar radiation. This causes erroneous temperature values of temperatures at depth. Regardless, a "knee temperature gradient," (Curley et al., 2014; Morstad, 2004; Morstad et al., 2007; Slaughter, 2010) was still observed to develop starting around 11:00 and continuing through 15:00 as seen in Figure 7-7. Facet formation was observed at 13:30.

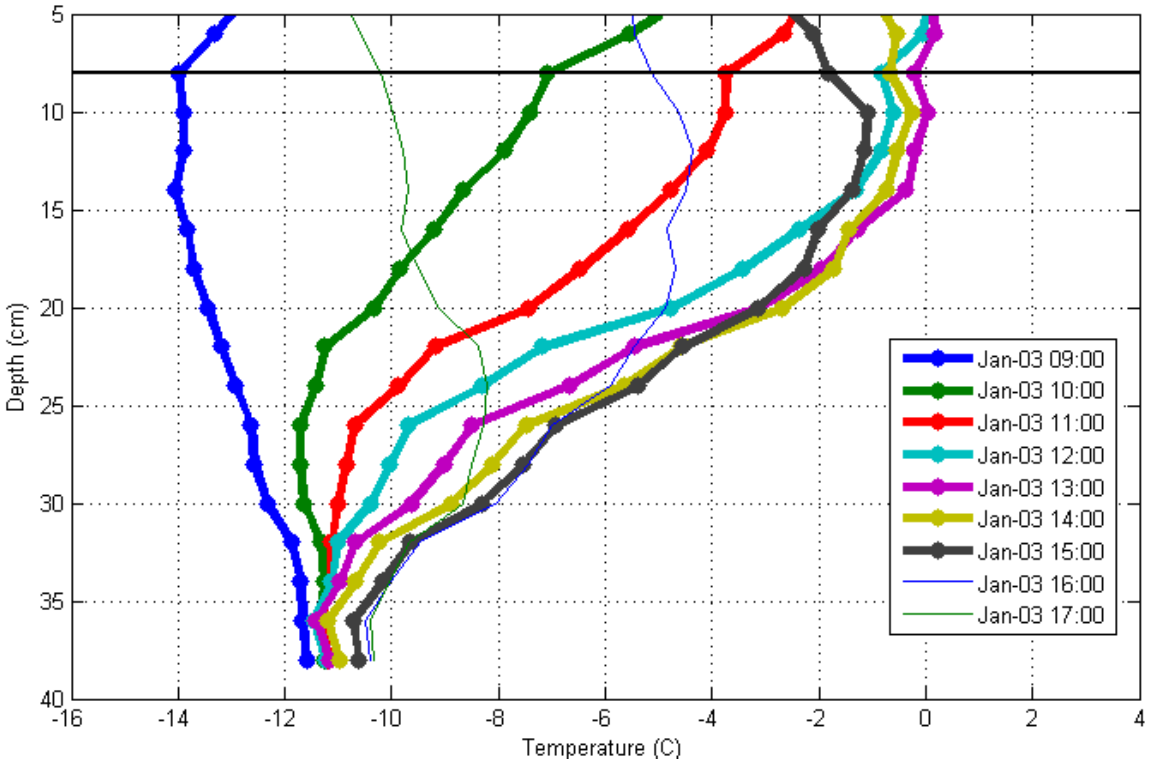


Figure 7-7: Snowpack temperatures measured at 2 cm spatial intervals. The snow surface is indicated by the solid horizontal black line. Each curve represents 1 hour intervals beginning at 09:00 on 3 January 2011. A "knee temperature gradient" is observed to develop in the top 2-4 cm of the snow beginning at 11:00.

7.1.3 Snow Making Procedure

Manufacturing atmospherically representative snow is useful for control over the initial state of snow in all experiments. The process in use today in the SSERF is the result of an iterative design process. Bones and Adams (2009) developed a table top snowmaker citing information from Libbrecht (2003), Nakamura (1978), Nakaya (1954), and Schneebeli (n.d.). The production of snowflakes was scaled up through several iterations by high school research

interns associated with the Army Educational Outreach Program's Research & Engineering Apprenticeship Program.

In its current version, the apparatus is situated in the Cold and Hydrodynamics Chamber as shown below in Figure 7-8. To maximize production, the air temperature of the chamber is maintained at −25° C while the supplied liquid water is maintained at +20°C. Shown in Figure 7-8, the louvers from the evaporator fans are directed toward the ceiling of the chamber. This creates a cyclic wind environment where air flows across the ceiling toward the front of the room and returns to the back along the floor. The apparatus on the floor is designed to humidify the air. The goal is to precipitate snowflakes from supersaturated air.

The air is humidified at the front of the apparatus by liquid water dripping a mesh suspended across the opening. The air is forced into the front of the apparatus by the air current described above. This humidification process warms the air slightly. Excess liquid water is allowed to drain away and recirculate. As the now saturated air flows through the horizontal tunnel of the apparatus, it begins cooling back toward the ambient temperature of the whole chamber. Upon entering the vertical section of the apparatus, the air has sufficiently cooled to become super-saturated. The suspended strings in this

section provide nucleation sites for snow crystals to form from the super-saturated flow of air. Snow is collected in the container under the vertical section and stored for later use.



Figure 7-8: Snow making apparatus in the Cold and Hydrodynamics Chamber.

7.1.4 Metamorphism Procedures

After snow is collected from the snowmaker, it is sieved through a mesh grid with 2 mm openings to achieve a nearly uniform snow crystal size $\leq$ 2 mm. The snow surface is manually smoothed intermittently in between adding sieved snow to achieve a planar snow surface mimicking the natural snow accumulation process. After this process, the samples are divided into three different groups to investigate the effects of snow surface age on the recrystallization process: new snow, 1 week old snow, and 2 weeks old snow. The samples that require 1-2 weeks of aging and sintering are covered and stored at a temperature of $-15°$ C. After storage for the appropriate amount of time, the aged samples are treated to the same mechanical testing and metamorphism procedures as the new snow.

The samples are prepared for a mechanical test to analyze the initial state of mechanical properties. The mechanical test setup procedure is described in the following subsection. To allow adequate time to complete the mechanical testing, the start of radiation recrystallization begins 36-48 hours after the initial snow surface is sieved and placed in the testing chamber.

Following the mechanical test, the instrumentation described previously is setup around and in the snow sample as seen in Figure 7-1. Since the

pyranometer and radiometer measuring incoming radiation are installed near the side of the sample, radiation values measured by these sensors for the duration of the test will be slightly different than the radiation directed at the snow surface centered under the lamp. To achieve desired radiation values initially, the sensors are positioned directly under the solar lamp. The solar lamp is set to maximum power and the height of the sample box is adjusted. When the snow surface is approximately 113.5 cm from the floor of the chamber, the incoming shortwave radiation is initially at $750\ \mathrm{W \cdot m^{-2}}$. The ambient air temperature is held at $-15°$ C. With the ceiling refrigerated to $-50°$ C and swept to clear frost formation, the incoming longwave is usually between $210 - 230\ \mathrm{W \cdot m^{-2}}$.

In order to achieve the field measured incoming shortwave radiation value of 1,000 $\mathrm{W \cdot m^{-2}}$, the snow box would need to be positioned closer to the solar source. At this position, the incoming longwave radiation is significantly higher since the sky-view of the snow sample is dominated by the warm lamp window while minimizing the view of the refrigerated ceiling. Also, the observed peak of incoming shortwave radiation value at 1,000 $\mathrm{W \cdot m^{-2}}$ only lasted for 2 hours. Instead of a rising and falling intensity of shortwave radiation, the snow ample is subjected to a constant $750\ \mathrm{W \cdot m^{-2}}$ for 12 hours. As

will be described in the following chapter, this produced similar crystal formations as observed in the field. In addition, the absorption of solar radiation at the snow surface produces a similar air temperature rise near the snow sample as was observed in the field. A summary of chamber parameter set points are provided below in Table 7-1.

Table 7-1: Summary of chamber parameters for producing radiation recrystallized facets in the laboratory.

Parameter	Value	Units
Ambient Air Temperature	-15	°C
Incoming Shortwave Radiation	750	W m^{-2}
Incoming Longwave Radiation	210-230	W m^{-2}
Sky Temperature (Cold Ceiling)	-50	°C
Duration	12	hrs

In addition to the automated measurements taken in and around the sample for the duration of the experiment, some manual observations are also taken during the process of radiation recrystallization. A camera outfitted with a macro-lens is used to record time-lapse photos of the state of the snow surface throughout the experiment. Photos are taken at 30 s intervals. A scale is included in the first image for spatial reference as seen in Figure 7-9. Time-lapse photo series for each experiment reference the scale initially photographed at the beginning of each experiment

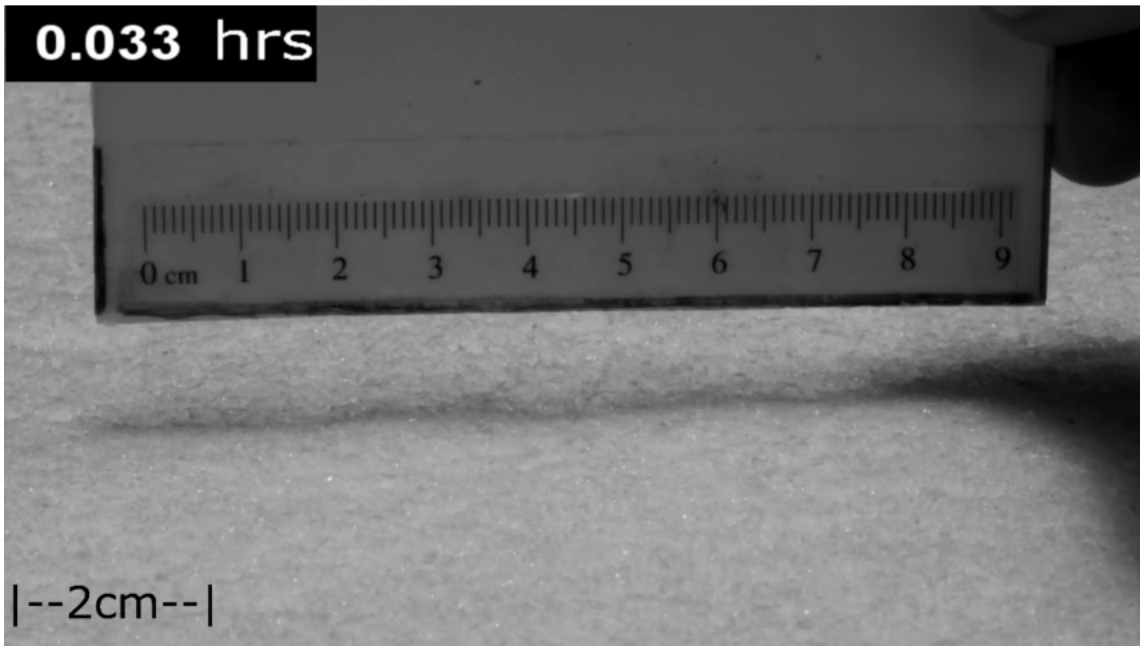


Figure 7-9: Example of time-lapsed photo of snow surface showing the approximate spatial scale. Photos are taken at this scale every 30 s for the duration of the experiment to examine the state of the snow surface during recrystallization.

In an effort to measure the combined effects of snow compaction and mass loss out the surface of the snow, a simple laser measurement system was also set up. A laser pointer was positioned at the side of the box as seen in Figure 7-10 with a known height above the initial snow surface. The horizontal distance of the laser spot was measured by establishing a triangulated reference of the snow surface in relation to the laser position. At 3 hour intervals, the horizontal distance of where the laser spot intersects the snow surface is taken, giving a precise way of measuring small changes in height of the snow surface throughout the experiment.

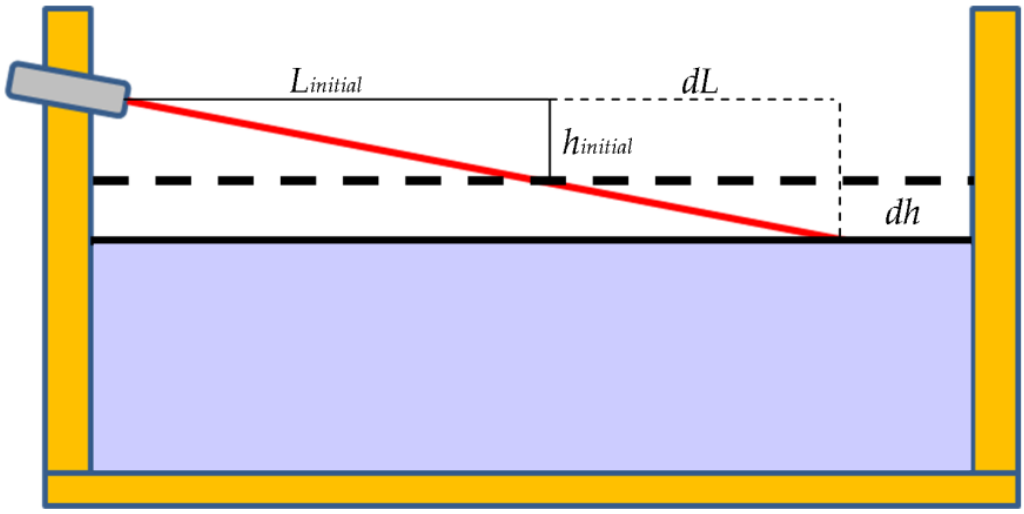


Figure 7-10: Laser system for measuring small changes in snow surface height using triangulation. $L_{initial}$ and $h_{initial}$ are measured at the beginning of the experiment. dL is measured at intervals throughout the experiment for which values of dh can be derived.

To obtain microstructure data, small samples representative of the volume are taken from the top approximately 4 cm of snow. These are collected in a cylindrical plastic container formerly used as packaging for 35mm rolls of film. Samples are obtained at 3 hour intervals (at the same time the laser measurements described above are taken). The same container is used throughout every experiment so Computed Tomography (CT) scan settings and exposures can all be compared relative to a single reference sample. Samples are scanned in a SkyScan 1173 micro-CT scanner maintained at similar subzero temperatures as the experimental sample. Scans are conducted using the settings

in Table 7-2 below. Further details regarding scan settings and digital reconstruction of the microstructural data will be discussed further in section 7.2.

Table 7-2: SkyScan 1173 scan settings used for all CT scans performed on cylindrical sample approximately 4 cm tall and 3 cm in diameter. The container is a plastic 35mm film canister.

Parameter	Value	Units
Voltage	42	kV
Current	190	μA
Exposure Time	1000	ms
Voxel Size	14.88	μm

7.1.5 Mechanical Testing Procedures

Mechanical tests on the macroscale are performed on the snow sample prior to and following metamorphism of the snow sample via radiation recrystallization. The mechanical test setup is identical in procedure on samples containing no recrystallized layer and samples containing a radiation recrystallized layer. Due to the size of the samples utilized in the lab, only one mode of testing could be completed per sample – compression or shear. In all cases, loading is applied using displacement rate control through a modified soil testing apparatus, the GeoTac – GeoJac. For shear experiments, the actuator is coupled to the side of a welded frame with internal support fins. The cross sectional area of the frame is 250 cm^2. The frame is consistent with shear frames

specified in the official avalanche observation guide for avalanche programs in the United States (Greene et al., 2010). For compression experiments, the actuator is reconfigured to supply a compressive load to a metal plate with the same cross sectional area: 250 cm^2.

For shear testing, approximately 5 mm to 10 mm of snow are initially sifted onto the existing snow surface. This first layer is used to prevent the metal shear frame from cutting into or directly impacting the initial surface of the snow. This avoids directly applying a stress concentration to the radiation recrystallized layer. At this point, the shear frame is placed gently onto the newly sifted snow. More snow is sieved into and around the frame to completely bury the frame under the new snow (Figure 7-11). The buried frame is allowed to sinter overnight for a period of 12-24 hours so the new snow added can gain structural integrity.

After a period of sintering, the snow is cut carefully using a sharp instrument and removed from around the perimeter of the frame. The cuts

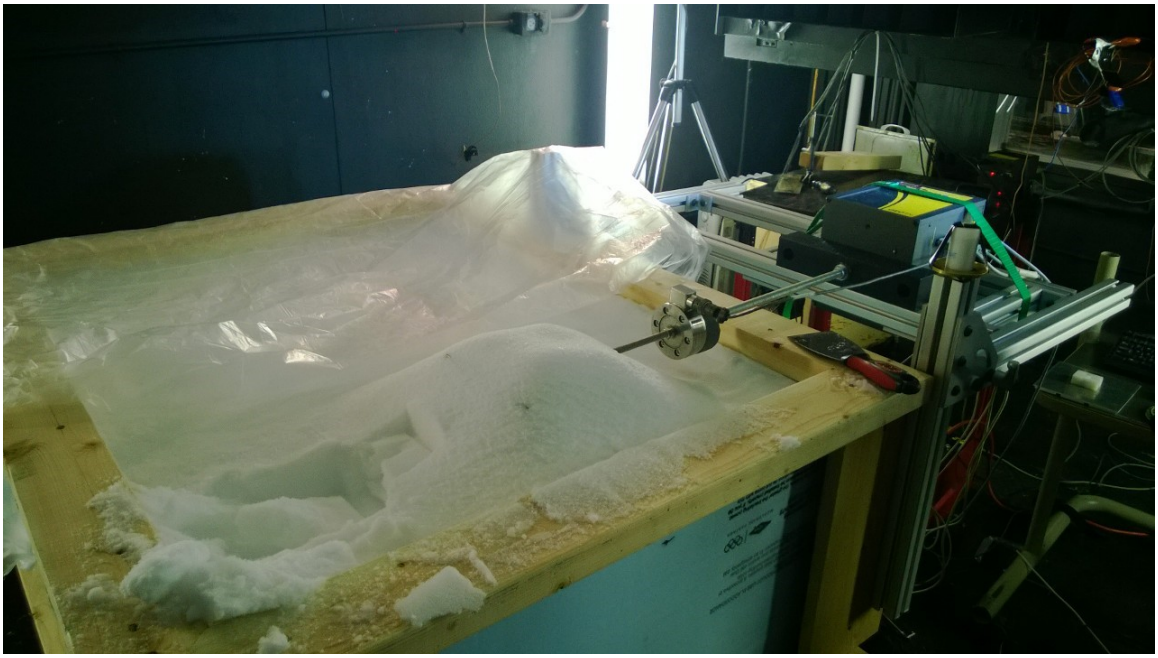


Figure 7-11: Setting up a shear test. Here, the shear frame has been filled and surrounded by snow for sintering.

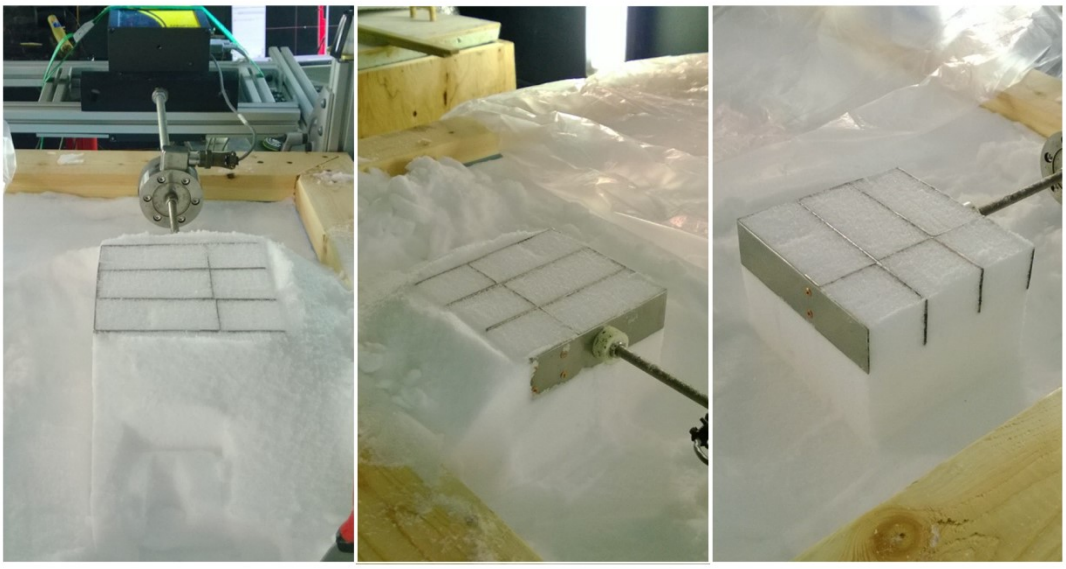


Figure 7-12: Sequence of images showing the cut-out process to remove excess snow from the buried shear frame.

plunge to a depth of 1-2 cm below the faceted layer (if the sample contains one). This leaves an exposed column beneath the shear frame between 5 cm and 7 cm. Figure 7-12 shows the sequence of cutting a neat and exposed column under the shear frame.

Following the isolation of a column of snow, one surface is painted with a fine, random contrasting paint for use with an optical strain measuring system (particle image velocimetry) called ARAMIS. This system, along with other instrumentation used in the mechanical testing process is described later. In addition, an LVDT is placed in the snow opposite the actuator to record a backup record of total displacement of the frame. The painted column and LVDT setup is depicted in Figure 7-13.

The test is ready to commence once the ARAMIS system is placed. For shear experiments, the displacement rate is set for 0.2 mm/s. This produces an average shear strain rate between $2.9 \times 10^{-3}\ s^{-1}$ to $3.6 \times 10^{-3}\ s^{-1}$(depending on the height of the isolated column). These strain rates are near the cutoff for brittle elastic behavior for snow (Föhn et al., 1998; Reiweger et al., 2010). Since the ARAMIS system employed here has a capture limit of 15 frames/sec, straining the samples any faster often resulted in the ARAMIS system missing

the elastic portion of the loading event. Samples are loaded at this constant rate until failure.

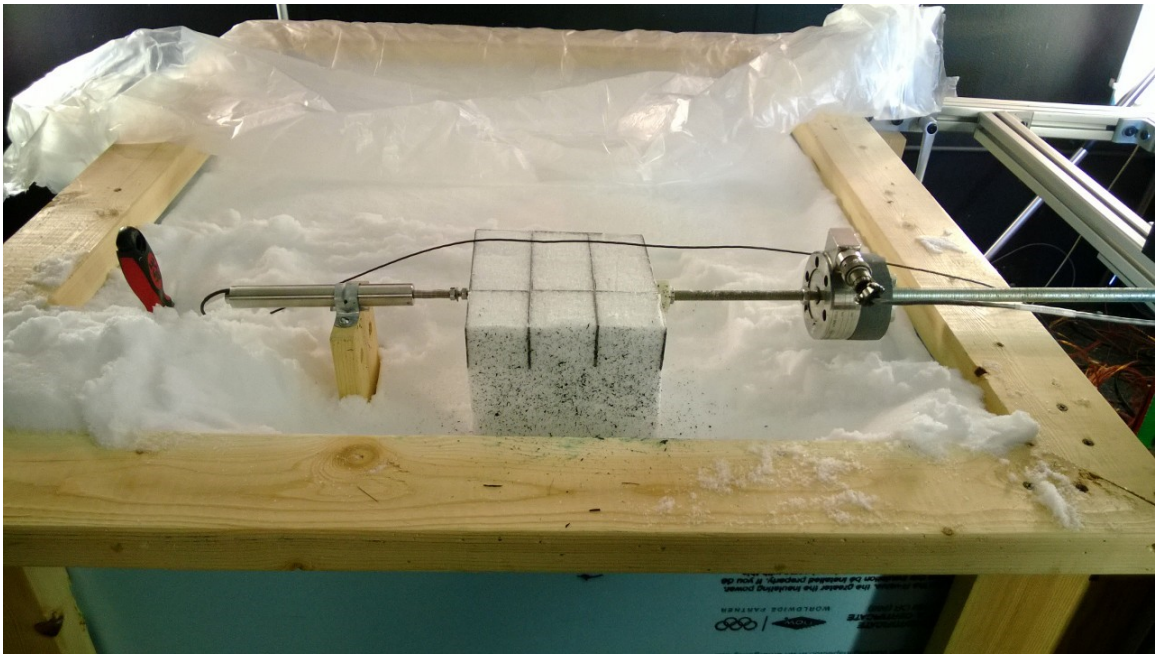


Figure 7-13: Finished snow column preparation for shear experiments with LVDT mounted opposite the load actuator and contrasting paint pattern on the column face for optically measuring strain.

Compression samples are prepared in nearly the same way as shear samples with some changes. First, the entire shear frame is not necessary. Instead, transmission of the compressive load to the snow sample is conducted through a sturdy aluminum plate with the same cross-sectional area of 250 cm^2. When the initial snow surface is buried, snow is sieved to a total depth equal to that used for the shear tests (including the depth of the now excluded shear frame). After sintering for the same amount of time, an isolated column is cut in

the same fashion as shown in Figure 7-12 using the perimeter of the load plate as a guide. In the compression test, the load actuator is also positioned over the sample to provide force normal to the snow surface. The displacement rate is the same as before, 0.2 mm/s, producing similar average axial strain rates as the shear test.

Three main groups of instrumentation are in use during the mechanical tests. The GeoJac actuator is operated from its own computer system. This system is strictly for operation of the actuator and does not record any data. Another computer system operates a National Instruments data acquisition system recording at 1000 Hz. This system monitors a load cell rated for 100 lb. (≈ 444.8 N) placed in series with the actuator, an LVDT placed to measure the overall displacement of the shear frame or compression cap, and a "sense" line originating from a third system.

The third system is ARAMIS, an optical strain measuring device that operates using Particle Image Velocimetry (PIV) techniques. Previous studies have successfully employed PIV techniques for measuring strain in snow samples (e.g. Gleason, 2006; Reiweger and Schweizer, 2010; Reiweger et al., 2010; Walters and Adams, 2012; Walters et al., 2010). This system takes 5 megapixel images of the painted surface at a rate of 15 frames per second. Proprietary

software algorithms measure relative motion between individual paint particles across the whole painted face to produce a continuous plot of displacement and strain. This system can record displacements down to 10-20 μm. When ARAMIS is triggered to start taking images, an output line is programmed to produce a 5V analog pulse when it is taking images and returns to 0V when the image taking sequence is stopped. This analog signal is read into the National Instruments DAQ system described previously as a trigger to sync the clock between the load monitoring and strain monitoring systems. The LabView code associated with operating the DAQ is included in Appendix A.

7.2 Microstructural Data Analysis

Throughout the course of the experiment, small subsamples of snow are collected from the main sample for imaging in the micro Computed Tomography (μCT) scanner. An initial sample of snow is collected prior to the first mechanical test which does not contain faceted crystals. Samples are then collected from the top 4.5 cm – 5 cm of snow prior to the beginning of recrystallization and every three hours until completion of the radiation recrystallization process. A final sample is taken which contains the radiation recrystallized layer capped by a new layer of sintered snow obtained prior to the final mechanical test. Samples

are extracted using the open end of a 35 mm film storage container (dimensions, 5 cm in height and 3 cm in diameter for a total volume of approximately 35 cm^3) shown in Figure 7-14.



Figure 7-14: Empty 35mm film canister used for extracting and holding snow samples for μCT scanning.

Once a subsample is extracted for scanning, it is mounted to a sample plate for placement on the imaging stage of a SkyScan 1173 μCT scanner in a room maintained below $0° C$. Using the control software, the sample is centered in the camera image to achieve a voxel size of 14.88 μm. Through a process of trial and error, the scanner settings listed in Table 7-3 below were found to provide adequate contrast between ice and air while minimizing noise. Once samples are scanned, they are discarded. To help identify types of crystals present near the surface of the representative samples, crystals are also collected, disaggregated, and photographed under an optical microscope.

Table 7-3: SkyScan 1173 scan settings used for all snow samples collected during experimentation. These settings are sensitive to sample size and collection container which was consistent throughout testing.

Parameter	Value	Units
Voltage	42	kV
Current	190	μA
Exposure Time	1000	ms
Voxel Size	14.88	μm
Rotation Step	0.700	degrees
Frame Averaging	3	-

The scanner produces a series of shadow projection images, one for each rotated position of the sample. These shadow projections are reconstructed into a stack of cross-section images via the Feldkamp Algorithm (Feldkamp et al., 1984) using the program NRecon maintained by Bruker microCT. A reference scan originally used to set the scan settings is also used to set the grayscale thresholds for reconstruction. In addition, 3 levels of Gaussian smoothing are applied. Together, smoothing and grayscale thresholds eliminate most image noise on each cross-section. Beam hardening correction (Casteele et al., 2004; Van Gompel et al., 2011) and ring artifact reduction (Jha et al., 2014; Sijbers and Postnov, 2004) are also applied for the reference sample. Each of these reconstruction settings are maintained for all samples so comparative analyses can be made amongst all samples. Misalignment correction is applied individually to each sample as this correction is unique to each scan.

Upon successful completion of reconstruction, the image stack is opened in the DataViewer program, also maintained by Bruker microCT, to check alignment of the sample with the coordinate system established by the orientation of the image stack. It is desirable for the vertical direction of the image stack (x_3 direction) be parallel with a vector normal to the snow surface. Since sub-volumes are extracted manually for scanning, misalignment of the sample within the container is common. The DataViewer program allows for samples to be reoriented so the surface normal and global $x_3$axis are parallel. A new image stack is generated following this reorientation.

The realigned image stack is loaded into a final Bruker microCT program: CTAn. Within this program, a volume of interest is selected and binarized for further analysis. Binary thresholding is performed to distinguish which voxels are associated with ice, and which voxels are associated with the pore spaces based on each voxel's gray scale intensity. To determine the correct binary threshold for the sample, the threshold is fine tuned to obtain the correct ice volume fraction. The density of the reference sample used to obtain all of the previous analysis settings is measured macroscopically. Using the scan settings in Table 7-3, and the same reconstruction settings every time, setting the low binary threshold to 26 and the high threshold to 255 produces appropriate ice

volume fractions of the binarized images. The binarized volume of interest is saved as a stack of binary images for further analysis.

7.3 Tensor Analysis

The information presented in the previous section is about capturing the 3-D microstructure and refining it to the point where the snow's microstructure is represented accurately in a digital format. Next, the digital volumes of snow need to be processed separately to determine grain and bond properties as well as directional quantities such as the contact tensor or the MIL tensor. Determining grain and bond properties for the contact tensor requires separate custom software to segment the 3-D volume into individual grains and bonds. The MIL tensor does not require segmentation and can be processed in the CTAn software already discussed.

7.3.1 Segmentation Software

Segmentation is the process which computationally separates individual grains and the bonds that connect them. Previous work of segmenting 3-D CT scans of snow relied on 2-D stereology: identifying grains and bond planes on 2-D planes in the image stack and statistically computing the 3-D parameters from these 2-D calculations (Edens and Brown, 1995; Edens, 1997; Lundy et al., 2002;

Shertzer and Adams, 2011; Shertzer, 2011; Shertzer et al., 2010). To reduce statistical uncertainty, it is desirable to operate directly on the 3-D volume rather than 2-D cross-sections of the 3-D volume.

A technique by Meyer (1994) called watershed segmentation allows for computation of individual grains and bonds directly from the 3-D binary image stack. A technical article by Mathworks in 2002 discusses the implementation of Meyer's algorithm (1994) using Matlab image processing tools (Eddins, 2002). Borrowing from the Eddins (2002) article, a 2-D binary image (Figure 7-15) is segmented, however this technique works in the same way with 3-D binary voxel images. In the following series, white pixels are represented by 1's and black pixels represented by 0's. The pixels' spatial position in the image is representative of its position within a 2-D binary array.

The goal is to process each of the two circles in Figure 7-15 to find the separator between the two circles. One way is to consider each circular object as a catchment basin, or individual watershed. The imaginary ridge that separates these two catchment basins forms a line that separates or segments these two objects. To accomplish this, the distance transform of this image is performed. The distance transform produces a matrix whose values represent the distance from each non-zero pixel to the nearest zero pixel value in the image. An

example of the distance transform is illustrated previously in 5-3 (and reproduced here for convenience).

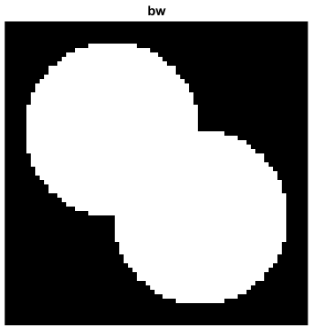


Figure 7-15: 2-D Binary image for segmentation (from Mathworks, 2016).

0	0	0	0	0	0	0
0	0	0	1	0	0	0
0	0	1	1	1	0	0
0	1	1	1	1	1	0
0	0	1	1	1	0	0
0	0	0	1	0	0	0
0	0	0	0	0	0	0

Circle

0	0	0	0	0	0	0
0	0	0	1	0	0	0
0	0	1	1.41	1	0	0
0	1	1.41	2.24	1.41	1	0
0	0	1	1.41	1	0	0
0	0	0	1	0	0	0
0	0	0	0	0	0	0

Distance Transform of Circle



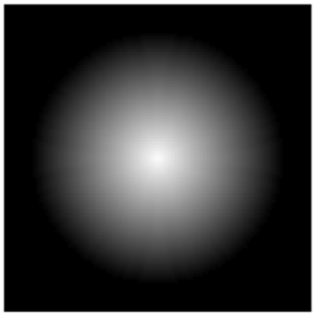


Figure 5-3: Illustration of the distance transform. The binary pixel values of the circle are shown on the left and the Euclidean distance transform values and image are shown on the right.

The distance transform of the objects in Figure 7-15 produces the image in Figure 7-16, where the pixel greyscale value represents the distance transform value of each pixel from the original image.

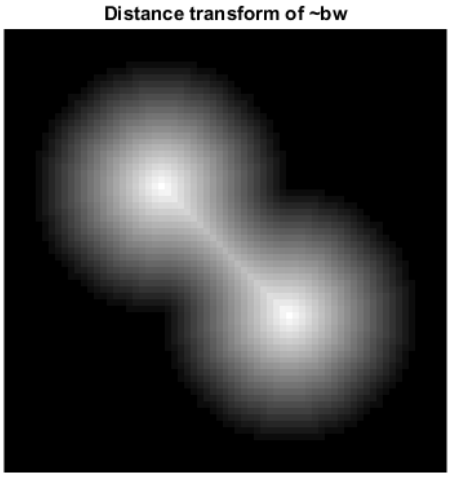


Figure 7-16: Image of the distance transform performed on the inverse of the binary image in Figure 7-15 (from Mathworks, 2016).

At this point, the watershed function is called. The watershed function processes the inverse of Figure 7-16. The Meyer (1994) algorithm starts by identifying local minimum pixel values (greyscale values from 0 to 1) of the inverse distance transform. These local minima are identified by finding pixels entirely surrounded by greyscale values greater than it. Each local minimum identifies a unique catchment basin. Greyscale values of the inverted distance transform are analogous to topographic elevations: low values are low elevation,

high values, high elevation. The watershed routine starts at the lowest valued minimum and begins to virtually "flood" the inverse distance transform image. Flood boundaries of each catchment basin are tracked. Where the flood boundaries join together, a segmentation line is created. The algorithm enacts the flooding by labeling pixels from Figure 7-16 with their respective watershed number or catchment basin number. Pixels which are labeled 0 do not belong to a watershed and become the segmentation lines. In this way, individual catchment basins or objects are identified and analyzed separately. Figure 7-17 below shows the segmented objects from this example.

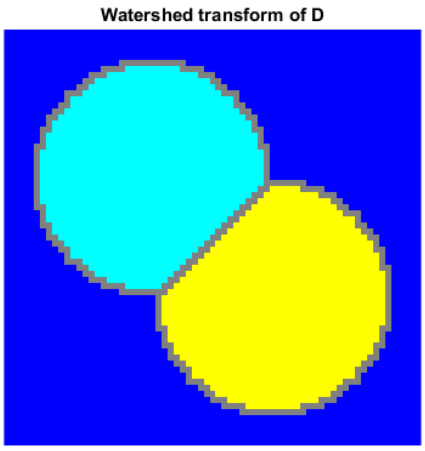


Figure 7-17: The segmented watershed transform of the objects shown in Figure 7-15. (from Mathworks, 2016).

Following watershed segmentation, separate arrays with bond information and connected grain information are exported for further processing

in Matlab. Segmentation code development was first undertaken locally by Anthony LeBaron at Montana State University and further refined by this author. The Matlab code performing watershed segmentation and subsequent bond and grain analysis is attached in Appendix B.

7.3.2 Grain and Bond Properties

An additional software component was developed here to make use of the segmented data resulting from watershed segmentation. Using the connected grains and bonds arrays created during watershed segmentation, the effective grain radii, the bond sizes, and coordinate positions of each grain center and bond center can be determined. All of these parameters are useful for analysis of the inputs of the constitutive model described in Chapter Three and Chapter Four.

The effective grain radius is measured using the distance transform function described previously. In analyses done here as well as previous CT studies by Shertzer and Adams (2011), the effective spherical grain radius is described as the largest sphere that can be inscribed inside an individual grain. The distance transform effectively measures this value. Using the connected grains array, each grain is analyzed for the location and value of the maximum

distance transform. The magnitude of the maximum distance transform is the effective spherical grain radius, and its location is noted for further use.

The next subroutine identifies connected grain pairs and the individual bond with which they are associated. Once connected grains are identified, a plane fit routine is performed on the bond to determine the "best fit" bond orientation. The center coordinates of the bond plane between connected grains is identified as well as the area of the bond between connected grains.

A final data array is assembled which disseminates the pertinent microstructural data in tabular form. Table 7-4 below describes the output data array and the definition of each parameter. This data is used for calculating the contact tensor and related microstructural parameters.

Table 7-4: Segmented bond and grain parameter descriptions.

Parameter	Description
Bond (Idx)	Bond number identified through watershed segmentation
BCx (pix)	Bond centroid x-coordinate (units: pixels)
BCy (pix)	Bond centroid y-coordinate (units: pixels)
BCz (pix)	Bond centroid z-coordinate (units: pixels)
BA (pix^2)	Bond area (units: square pixels)
BNx	Unit normal vector defining bond plane (x-direction)
BNy	Unit normal vector defining bond plane (y-direction)
BNz	Unit normal vector defining bond plane (z-direction)
G1 (Idx)	Grain number of the first grain connected to the numbered bond
G1Cx (pix)	Grain 1 of bonded pair mass centroid x-coord (units: pixel)
G1Cy (pix)	Grain 1 of bonded pair mass centroid y-coord (units: pixel)
G1Cz (pix)	Grain 1 of bonded pair mass centroid z-coord (units: pixel)

Table 7-4 continued

G1Rad (pix)	Grain 1 of bonded pair effective spherical grain radius (unit: pixel)
G1RCx (pix)	Grain 1 of bonded pair, center of largest inscribed sphere (x-coord)
G1RCy (pix)	Grain 1 of bonded pair, center of largest inscribed sphere (y-coord)
G1RCz (pix)	Grain 1 of bonded pair, center of largest inscribed sphere (z-coord)
G2 (Idx)	Grain number of the second grain connected to the numbered bond
G2Cx (pix)	Grain 2 of bonded pair mass centroid x-coord (units: pixel)
G2Cy (pix)	Grain 2 of bonded pair mass centroid y-coord (units: pixel)
G2Cz (pix)	Grain 2 of bonded pair mass centroid z-coord (units: pixel)
G2Rad (pix)	Grain 2 of bonded pair effective spherical grain radius (unit: pixel)
G2RCx (pix)	Grain 2 of bonded pair, center of largest inscribed sphere (x-coord)
G2RCy (pix)	Grain 2 of bonded pair, center of largest inscribed sphere (y-coord)
G2RCz (pix)	Grain 2 of bonded pair, center of largest inscribed sphere (z-coord)
Row (Idx)	Array row number used for debugging purposes

From this data array, parameters needed for Equation (3.21) are able to be calculated for the entire volume. These parameters include:

- Average grain radius, $\hat{R}$ (taken from G1Rad and G2Rad)
- Average bond radius, $\hat{\rho}$ (taken from BA and approximated as a circular radius)
- Coordination number, $\mathcal{N}$ (average number of times a grain ID number is connected to a unique bond)

Volume fraction of ice, ϕ, is already provided from the analysis in CTAn as well as mapping pixel size to real world dimension.

7.3.3 Tensor Computation

The contact tensor utilizes the segmented data described previously. Bond orientation data is either used directly from the plane fit data generated for each bond, or computed from grain center to grain center of the bonded pairs of grains. The latter is useful for when bond sizes are relatively small in relation to the pixel resolution. Low resolution data only allows for a limited number of orientations to be computed directly from plane fitting, which sometimes produces erroneous contact orientations. The computed contact orientations are converted to vector form and assembled into the contact tensor using Equation (4.1).

The MIL tensor is computed in the CTAn program using the same volume of interest as the contact tensor. This is obtained through the advanced stereological analysis. The principle MIL lengths are the diagonal values of the second order MIL tensor as described earlier in Section 4.1.2. The MIL tensor is normalized against its trace so its diagonal is equal to 1.

From here, the MIL tensor and contact tensor can be compared directly and used to compute the tensor ratio. The Matlab code supporting the assembly of the tensors is included in Appendix C.

CHAPTER EIGHT

LABORATORY RESULTS

"You can observe a lot by just watching."
~Yogi Berra

A series of laboratory experiments were conducted at the Subzero Science and Engineering Research Facility at Montana State University. These experiments were designed to mimic the environmental conditions which produce radiation recrystallized layers of snow in mountain snow covers. Studying the growth and formation of these layers in a laboratory setting allows for a detailed investigation of the growth process as well as the change in the mechanical characteristics of the near surface region of the snow during and following recrystallization.

The chapters that follow will describe and discuss results and observations from these experiments. This chapter will focus on the direct observations of the environment near and inside the snowpack and the evolution of crystal morphologies during and following the experiment. In addition, macro-scale mechanical testing prior to and following recrystallization will also be discussed. In Chapter Nine, the focus will shift to the microstructural results regarding fabric tensor and in Chapter Ten the finite element analysis results.

8.1 Initial Starting Snow

The snow used for all experiments was manufactured using the procedure described previously in section 7.1.3. The chamber producing the snow operated with an air temperature of $-25°$ C. Unfortunately, no data recording equipment was present during the production of snow. Dendritic crystals such as those in Figure 8-1 were primarily produced by the apparatus and collected for use in all experiments.

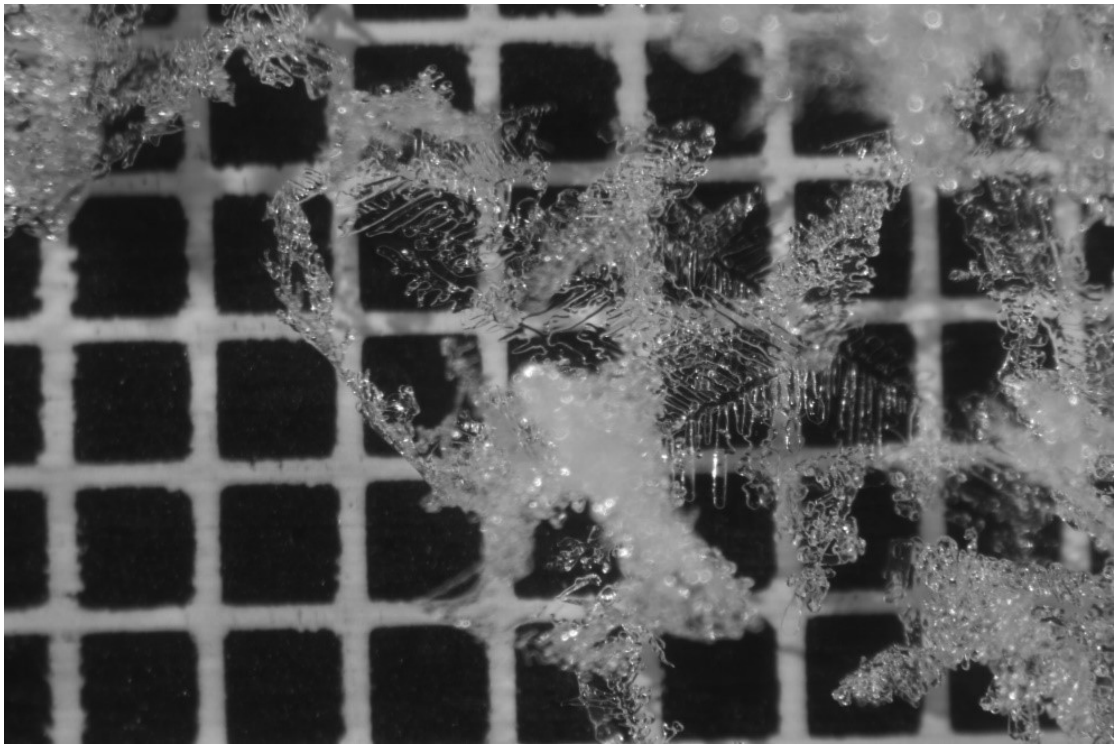


Figure 8-1: Dendritic crystals produced by the snow making apparatus. The background grid is 1mm square.

The manufactured snow is sieved into the sample containers through a 2mm grid and left to sinter for the appropriate amount of time. As highlighted in the previous chapter, sinter times for the samples were subdivided into three different categories: new snow surface (sinter 12-24 hours), 1 week old surface, and 2 weeks old snow surface. Three experiments were completed on the new snow surface, three on the 1 week old surface, and one on the 2 weeks old surface. All samples were allowed to sinter covered (not sealed) at an air temperature of −15° C.

After sintering for 12-24 hours, the three new snow surface experiments exhibited similar crystal characteristics. The sieve produced generally uniform results in terms of crystal sizes. Crystal types present in the surface and near surface were dominated by fragmented and rounding dendritic crystals. An example of the crystals present is shown in Figure 8-2. Individual crystal morphologies, crystal sizes, and sample densities of the initial snow samples prior to recrystallization are summarized in Table 8-1 below. Also refer to Table 8-1 for abbreviated naming convention of each sample used throughout the remaining text.

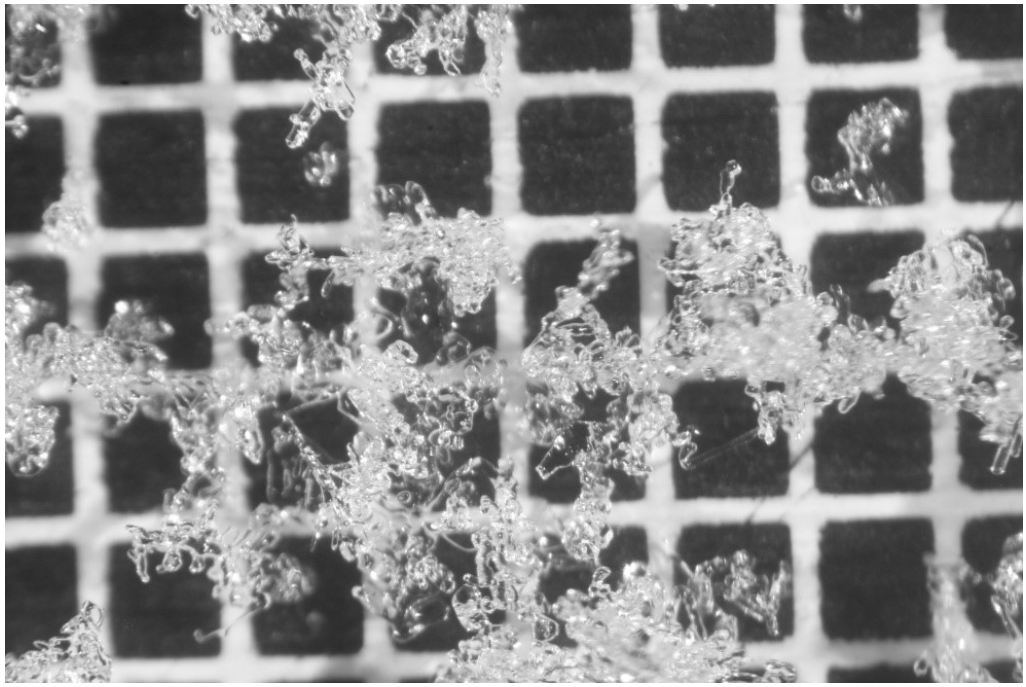


Figure 8-2: Fragmented dendrites and rounded crystals representative of the surface and near surface of a snow sample following sieving new stellar dendrites through a 2mm grid and sintering for 12-24 hours. The grid in the background is 1mm square.

The samples that were prepared to sinter for 1 week and 2 weeks to simulate older snow surfaces produced similar results. Most of the snow was dominated by rounded grains, but as evidenced by the photomicrograph in Figure 8-3, some highly decomposed dendrites were still present. Although the boxes were covered during sintering, they were not sealed and some sublimation subsequently occurred over the duration of the sintering process. Crystal morphologies, grain sizes, and sample densities of these initial samples are also detailed in Table 8-1 below.

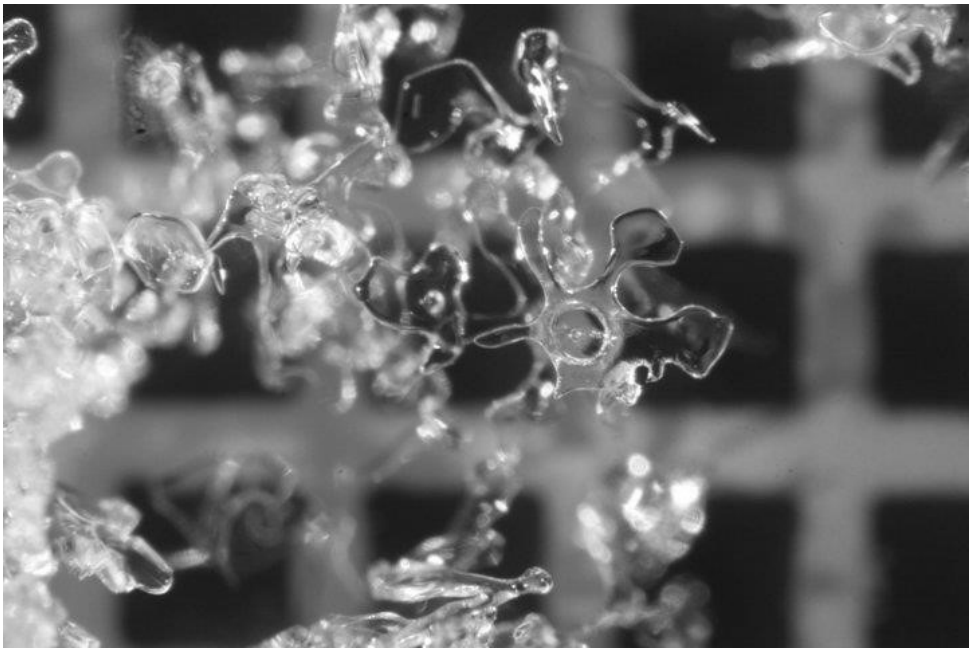


Figure 8-3: Rounded fragment of a dendritic crystal found near the surface of a sample of snow sintered for 1 week. The grid in the background is 1mm square.

Table 8-1: Details of initial crystal types, sizes, and near surface densities of experimental samples following initial sintering period and prior to radiation recrystallization

Sample	Primary Crystal Type	Avg. Crystal Size (mm)	Near Surface Density (kg m^{-3})
New Snow 1 (NS1)	Fragmented Dendrites	0.75	178
New Snow 2 (NS2)	Fragmented Dendrites	1.00	120
New Snow 3 (NS3)	Fragmented Dendrites	0.75	178
1 Week Old 1 (1W1)	Rounded Grains/ Decomposed Dendrites	0.80	170
1 Week Old 2 (1W2)	Rounded Grains/ Decomposed Dendrites	0.70	194
1 Week Old 3 (1W3)	Rounded Grains/ Decomposed Dendrites	0.50	235
2 Weeks Old (2W1)	Rounded Grains	1.00	129

Using the micro-CT scanner, the three dimensional arrangement and shapes of grains becomes apparent. In Figure 8-4, most of the grains appear rounded and randomly distributed throughout the volume. Qualitatively, little difference is noticed in the 3-D volume renderings across all of the experimental samples, regardless of snow surface age. A more detailed microstructural analysis is discussed in the following chapter.

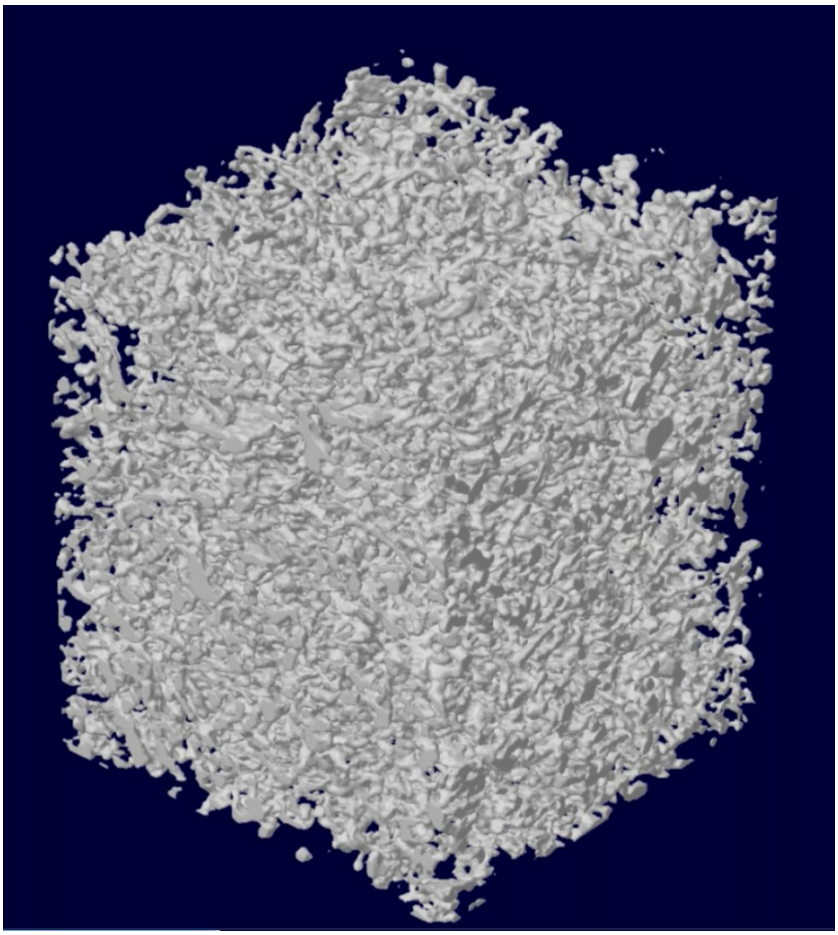


Figure 8-4: Volume rending of a sintered snow surface. The cross-section is 5 mm square by approximately 6 mm tall.

8.2 Radiation Recrystallization

Although the initial state of each experiment was split into three different categories (based on the age of the sintered snow surface), they were all subjected to the same environmental conditions. Despite the differences in the initial age of the snow surface, most experiments displayed similar results in terms of temperature and vapor pressure gradients that developed as well as crystal morphologies.

8.2.1 Temperature and Vapor Pressure Gradients

Temperature gradients and subsequently vapor pressure gradients are some of the primary metrics calculated when investigating the rate and extent of kinetic growth metamorphism. Maximum temperature gradients exceeding $300\,°\mathrm{C}\cdot\mathrm{m}^{-1}$ in magnitude were observed in all experiments, which is in agreement with past observations and investigations of near surface facet growth (Adams and Walters, 2014; Birkeland et al., 1998, 1996; Birkeland, 1998; Fukuzawa and Akitaya, 1993; McCabe et al., 2008; Morstad, 2004; Morstad et al., 2007, 2004; Slaughter et al., 2011, 2009, 2008; Slaughter, 2010). In most experiments, it took approximately 5 to 7 hours for the temperature gradient to settle at a maximum value. Beyond this time, temperature gradients seemed to

hold steady although temperature gradient data becomes suspect beyond about 8 hours due to melting and sublimation around the thermocouple array.

Temperature profiles displaying snow temperature versus snow depth at 2 hour intervals are shown in Figure 8-5 for sample NS3 (refer to Table 8-1 for sample name abbreviations). Due to the position of the thermocouple array measuring snowpack temperatures, the snow surface was located near 1 cm in depth in Figure 8-5. The steepest temperature gradient in this sample was located in the top 1 cm of the snowpack and is plotted separately in Figure 8-6.

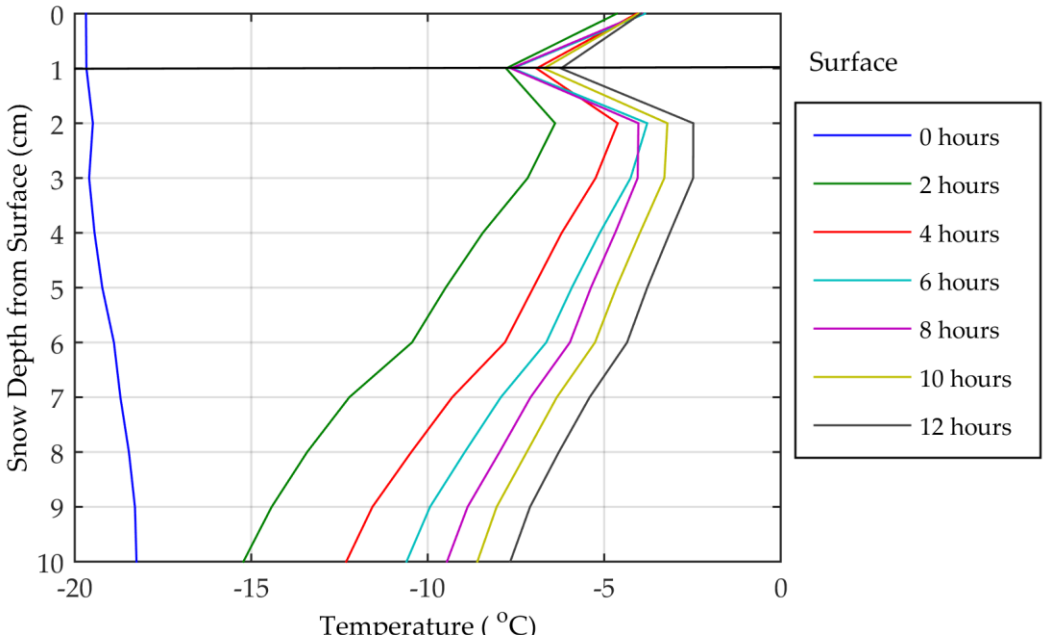


Figure 8-5: Temperature versus snow depth at 1 cm increments and 2 hour intervals for sample NS3. The actual snow surface is at 1 cm.

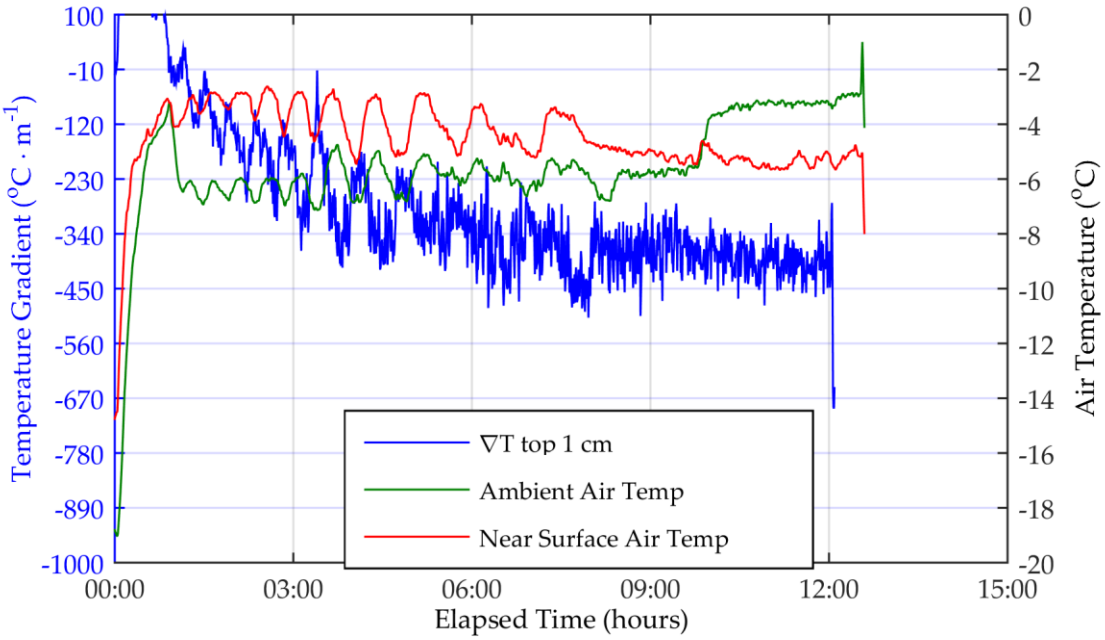


Figure 8-6: Temperature gradient in the top 1 cm of sample NS3 versus elapsed time. Ambient and near surface air temperatures are included on the secondary axis to show that the periodicity of the temperature gradient was related to the periodicity of the chamber air temperature.

The temperature gradient reached the value of $-100\,°\mathrm{C}\cdot\mathrm{m}^{-1}$ after approximately 1.5 hours, and increased in magnitude to a steady value around $-350\,°\mathrm{C}\cdot\mathrm{m}^{-1}$ at approximately 7 hours. The periodicity observed in the temperature gradient plot is related to the ambient air temperature in the environmental chamber (also plotted in Figure 8-6). This is due to $\pm 1\,°C$ sensitivity in the laboratory's air temperature control.

Using the Clausius-Clapeyron equation to compute the vapor pressure values at each thermocouple in the array, a vapor pressure gradient could be

plotted for the region with the highest temperature gradient. Since directly related to the temperature gradient in Figure 8-6, the vapor pressure gradient in the top 1 cm of sample NS3 takes on the same shape as seen in Figure 8-7. The steady state value of approximately $-12\,\mathrm{kPa}\cdot\mathrm{m}^{-1}$ after 7 hours exceeds previously reported values of $-2.5\,\mathrm{kPa}\cdot\mathrm{m}^{-1}$ responsible for diurnal near surface facet growth in the field in 36 hours (Birkeland et al., 1998). Here, near surface facet growth occurred in less than 12 hours.

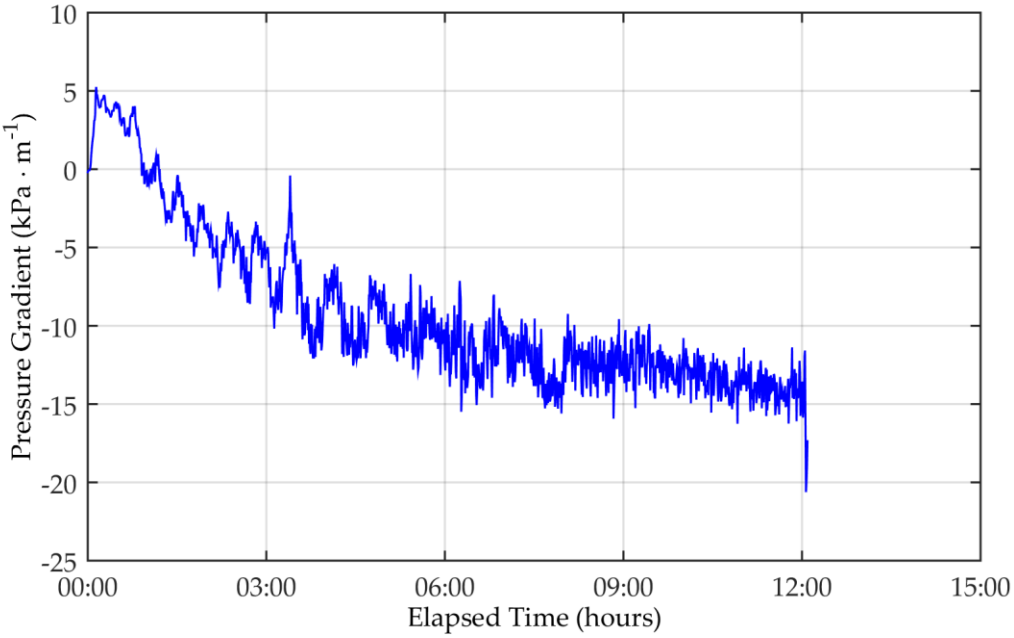


Figure 8-7: Vapor pressure gradient with respect to time in the top 1 cm of sample NS3.

The 1 week old surface samples produced similar results for temperature and vapor pressure gradients. The temperature profiles versus depth for sample

1W1 are shown below in Figure 8-8. Similar to the temperature profiles in Figure 8-5, the snow surface is located at 1 cm.

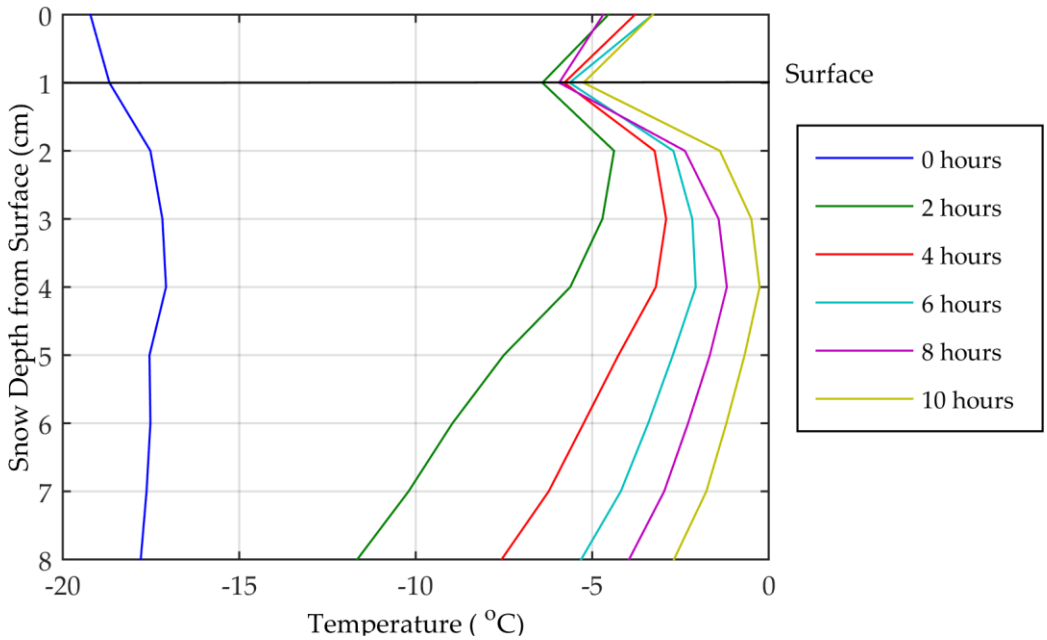


Figure 8-8: Temperature versus snow depth at 1 cm increments and 2 hour intervals for sample 1W1. The actual snow surface is at 1 cm.

For this sample, the near surface temperature gradients are computed for the top 2 cm of the sample and plotted with respect to time in Figure 8-9. The same periodic behavior as shown in Figure 8-6 was observed here due to the control parameters of the chamber air temperature. The near surface air temperature in Figure 8-9 rose above 0 °C due to improper shielding of the probe from simulated sunlight. The steady state temperature gradient settled out to approximately $-400\,°\mathrm{C}\cdot\mathrm{m}^{-1}$ before increasing in magnitude toward the end.

This late increase is unreliable due to melting and sublimation occurring around the thermocouple array used to measure near surface snow temperatures.

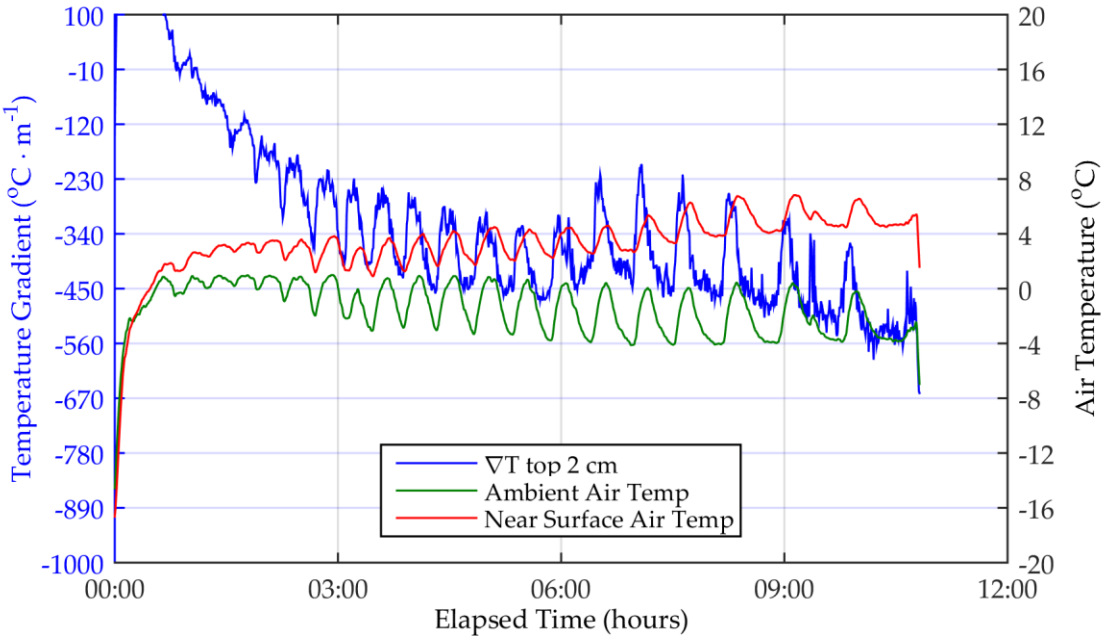


Figure 8-9: Temperature gradient in the top 2 cm of sample 1W1 versus elapsed time. Ambient and near surface air temperatures are included on the secondary axis to show the periodicity of the temperature gradient was related to the periodicity of the chamber air temperature. The near surface air temperature probe was improperly shaded and received direct sunlight causing readings above 0 °C.

The vapor pressure gradient followed the same trend as the temperature gradient in the top 2 cm of the snowpack. In Figure 8-10, the vapor pressure gradient is shown increasing in magnitude to approximately $-15\,\mathrm{kPa}\cdot\mathrm{m}^{-1}$ and leveling off after 6 hours. It is presumed the vapor pressure gradient remained

at steady state since the source temperature data was suspect for the remainder of the experiment.

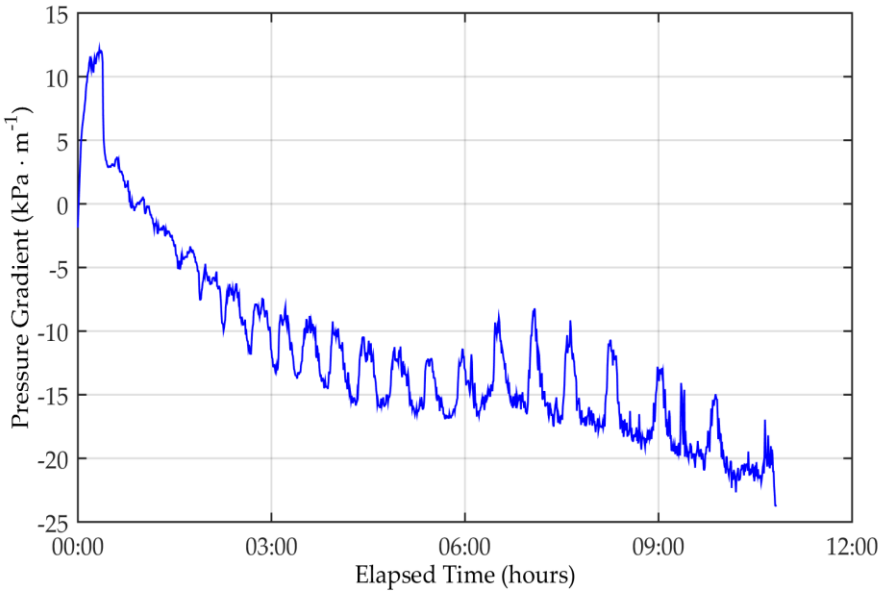


Figure 8-10: Vapor pressure gradient with respect to time in the top 2 cm of sample 1W1.

The lone sample with a 2 week old snow surface, 2W1, showed similar temperature profiles (Figure 8-11), temperature gradients in the top 2 cm (Figure 8-12), and vapor pressure gradients in the top 2 cm (Figure 8-13). The temperature gradient in the top 2 cm of the snow sample settled around $-340\ °C \cdot m^{-1}$ after 6 hours. The vapor pressure gradient in the top 2 cm of the sample in this case did not reach a steady state value – like the temperature

gradient. Regardless, vapor pressure gradients of $-10\ \mathrm{kPa \cdot m^{-1}}$ to $-15\ \mathrm{kPa \cdot m^{-1}}$ beyond 6 hours (Figure 8-13) fit with the rest of the experiments.

These three sets of data are representative of all the laboratory experiments conducted here. All experiments had temperature gradients exceed $300\ \mathrm{°C \cdot m^{-1}}$ and vapor pressure gradients exceed $10\ \mathrm{kPa \cdot m^{-1}}$ in the near surface region of the snowpack. The similarity of conditions resulted in similar crystal morphologies throughout the samples too.

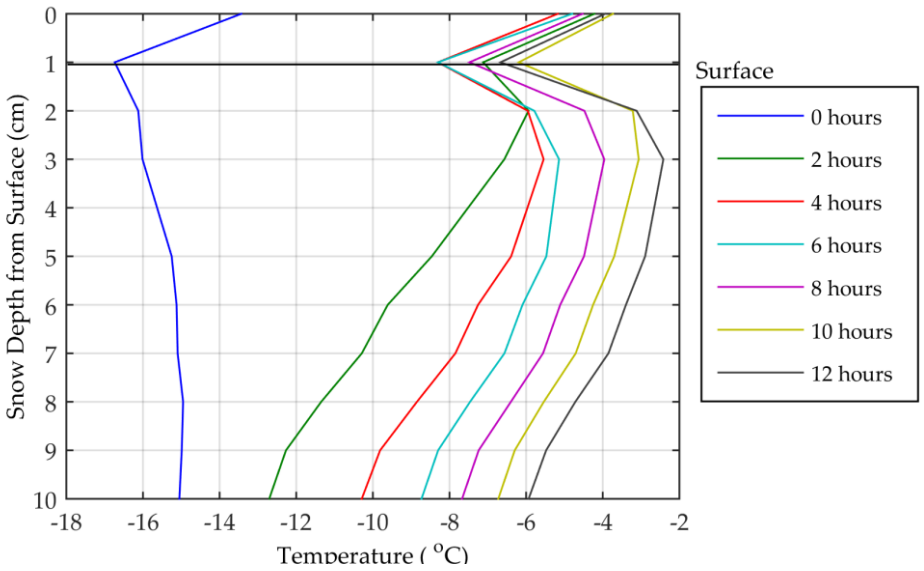


Figure 8-11: Temperature versus snow depth at 1 cm increments and 2 hour intervals for sample 2W1. The actual snow surface is at 1 cm.

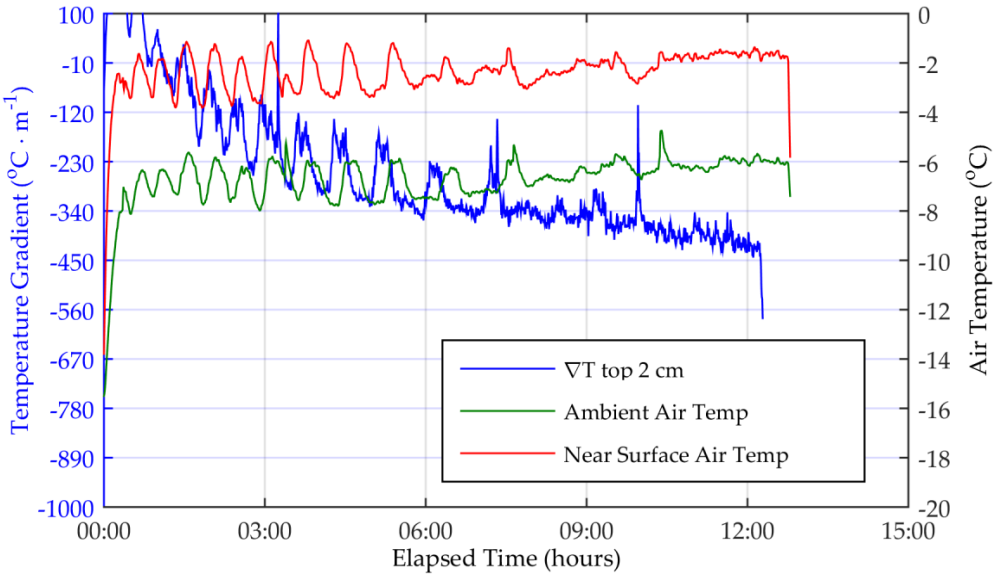


Figure 8-12: Temperature gradient in the top 2 cm of sample 2W1 versus elapsed time. Ambient and near surface air temperatures are included on the secondary axis to show the periodicity of the temperature gradient was related to the periodicity of the chamber air temperature.

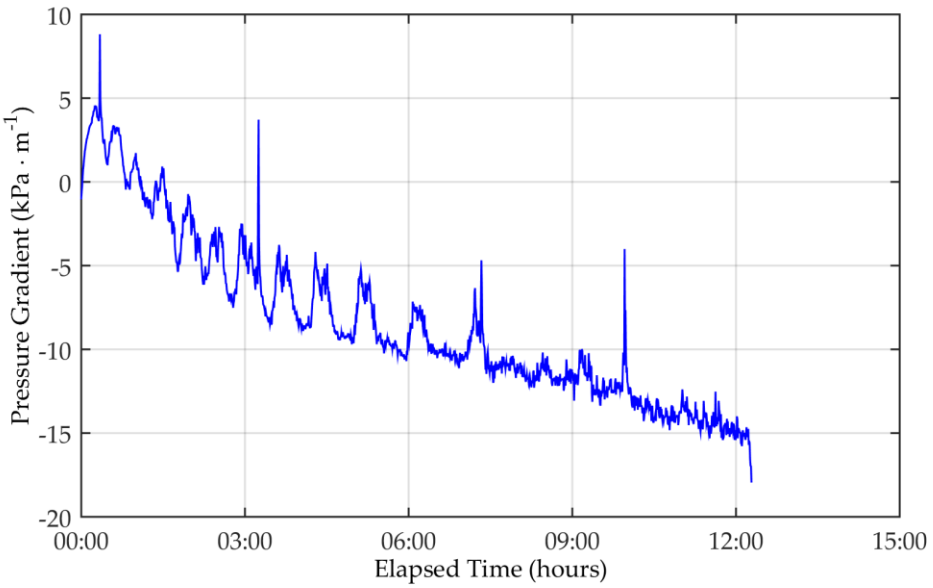


Figure 8-13: Vapor pressure gradient with respect to time in the top 2 cm of sample 2W1.

8.2.2 Crystal Morphologies

The temperature gradient and vapor pressure gradient data suggests rapid facet growth. A combination of tools is used to examine the changes in the near surface structure of the snowpack. Microscopy and Computed Tomography are used to characterize grain scale structure and crystal types and sizes. Time lapse photography and laser assisted measurements of surface height changes are used to examine surface effects during metamorphism. These tools are described in further detail in Section 7.1.4.

Beyond the differences in the initial structure previously described, metamorphism progressed in a similar fashion for all tests. After 3 hours of metamorphism, the volume rendering of the near surface region in Figure 8-14 shows a slightly coarser configuration of grains from its initial state shown in Figure 8-4. Using microscopy, remnants of the original sintered crystals are apparent, however small facet growth is already occurring as seen in Figure 8-15.

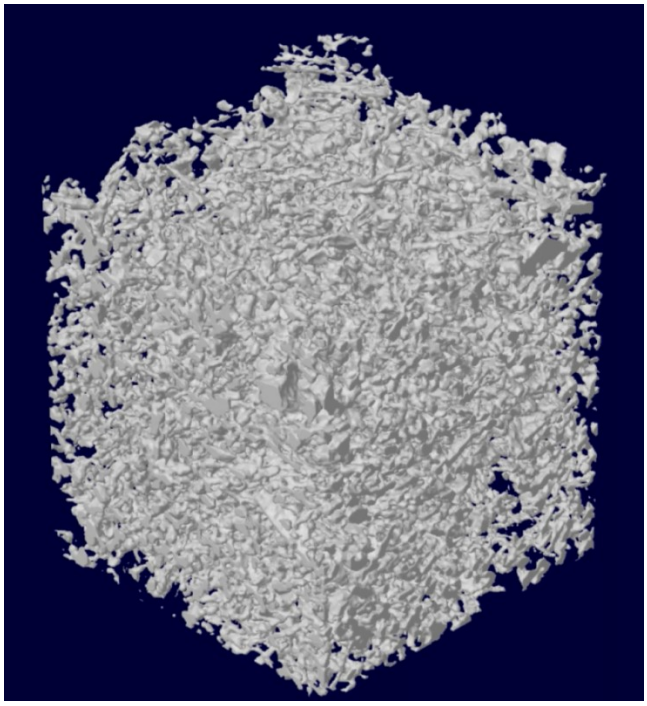


Figure 8-14: Volume rending of the snow surface following 3 hours of metamorphism. The entire volume consists of coarser grains than those shown in Figure 8-4. The cross-section is 5 mm square by approximately 6 mm tall.

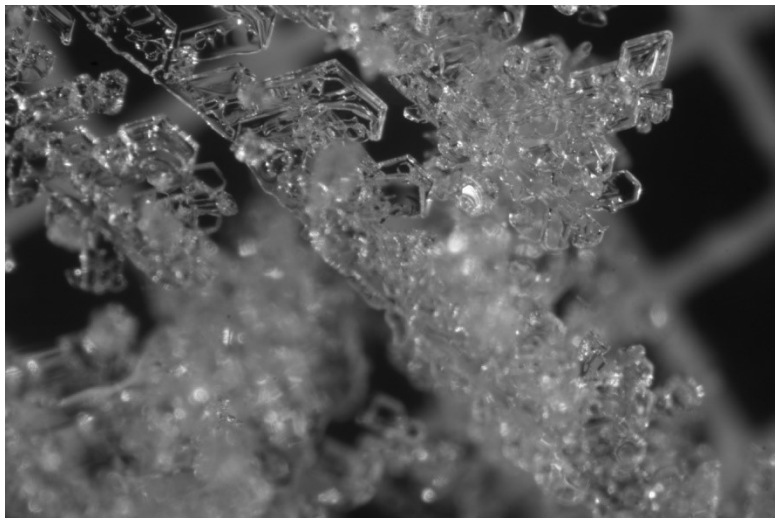


Figure 8-15: Photomicrograph of surface crystals of a new sample following 3 hours of radiation recrystallization. Small facets are observed growing off of the fragmented arms of decomposing dendritic crystals. The grid in the background is 1 mm square.

After 6 hours, facet growth is more evident in both the volume rendering from the micro-CT scan and microscopy. Using the CT scanner, small elongated, needle like crystals are visible on the surface of the snow while small facet like grains exist near the surface (Figure 8-16). The faceted crystals below the surface are discernable in photomicrographs of disaggregated crystals (Figure 8-17). Small faceted crystals and cup shaped crystals smaller than 1 mm prevail.

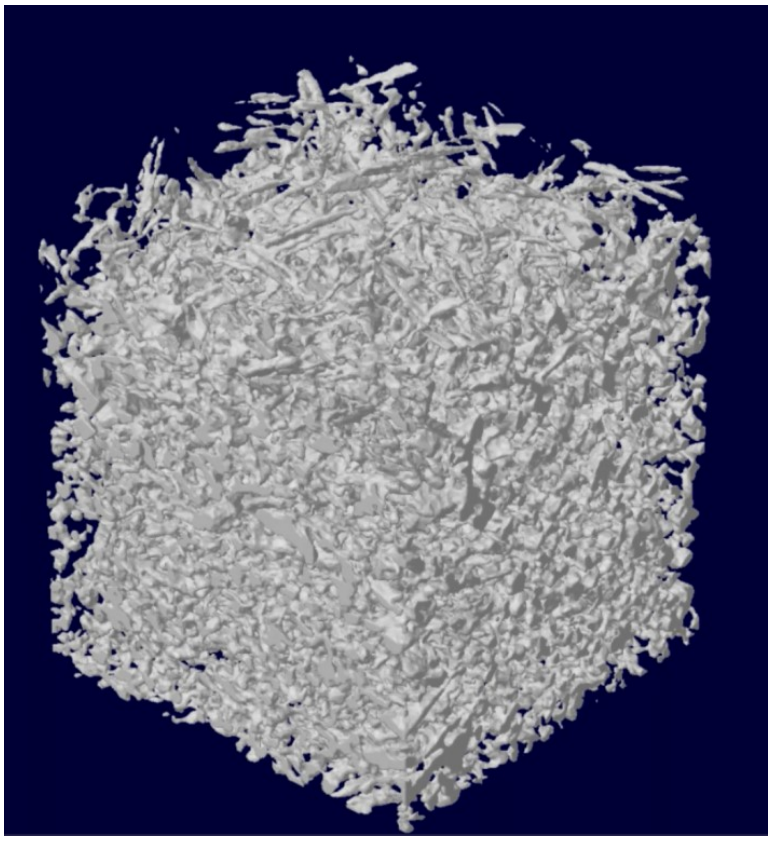


Figure 8-16: MicroCT volume rendering of the surface and near surface of radiation recrystallized snow following 6 hours of metamorphism. Here, needle-like crystals begin to grow on the surface whereas faceted crystals continue to develop in size and organization in the middle of the sample.

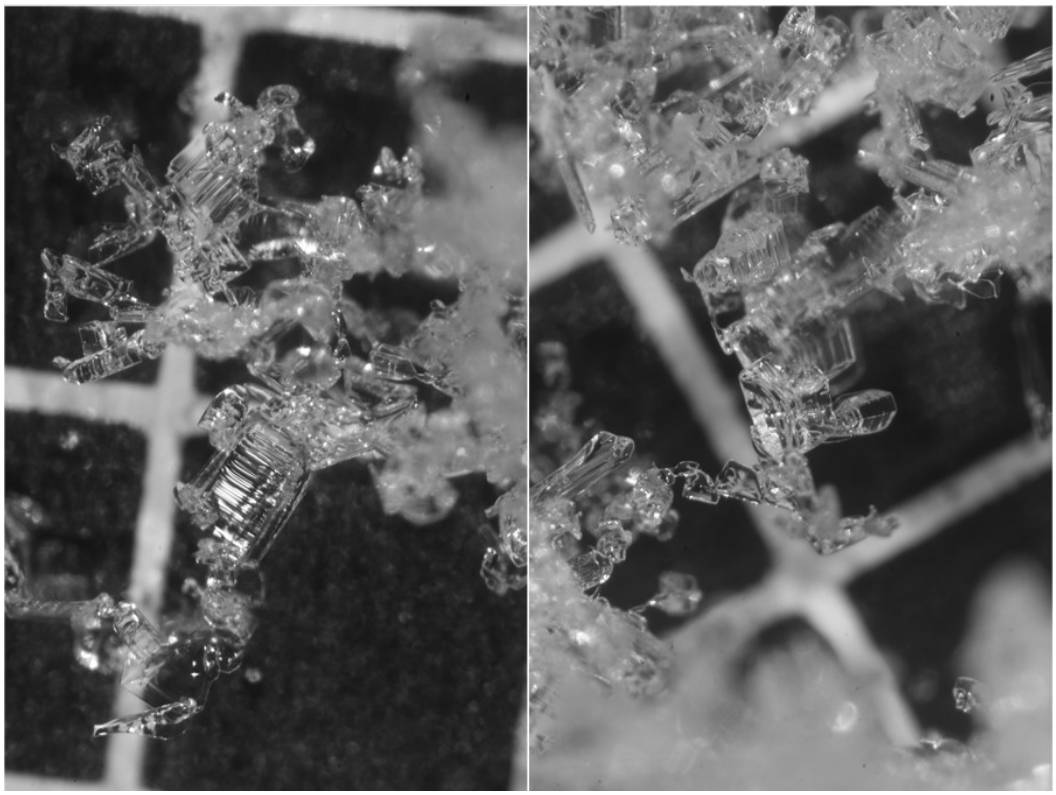


Figure 8-17: Photomicrographs of disaggregated faceted and cup shaped crystals following 6 hours of recrystallization. The background grid is 2 mm square.

After 9 hours and 12 hours of metamorphism, surface crystals become more developed as elongated and needle like crystals and facets prevail. Sub surface facet growth appears to reach a steady state with small depth hoar like faceted and cup shaped crystals. Not much difference is observed in the crystals between 9 hours and 12 hours as seen in side-by-side views of microCT scans in Figure 8-18 and photomicrographs in Figure 8-19.

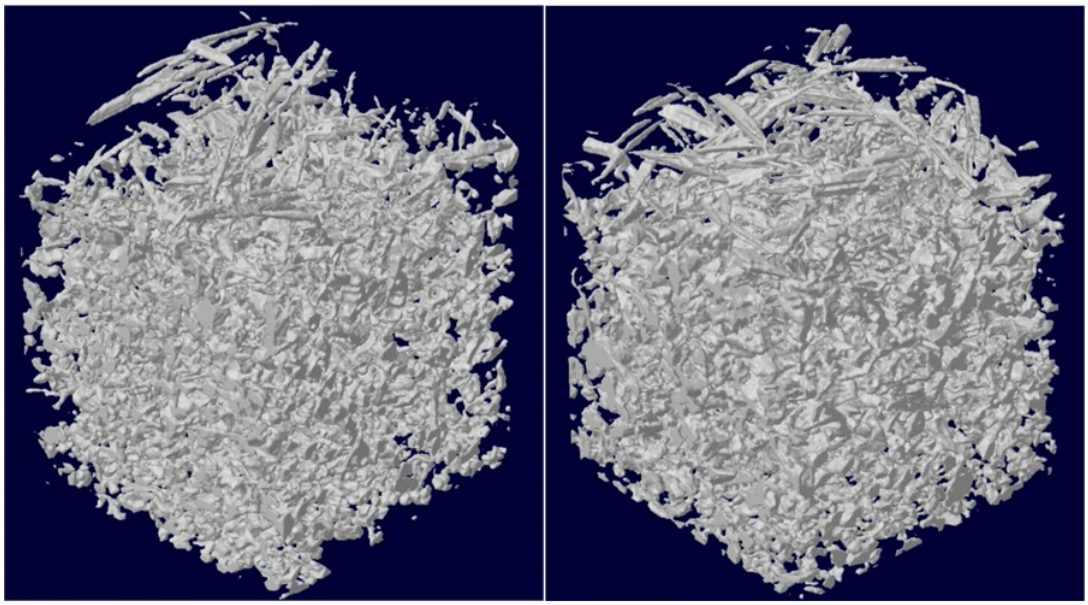


Figure 8-18: Micro-CT volume renderings of the top 6 mm of radiation recrystallized facets after 9 hours (left) and 12 hours (right). Here, needle-like crystals dominate the surface of each volume while vertically structured faceted and cup shape crystals permeate the midsection of each sample.

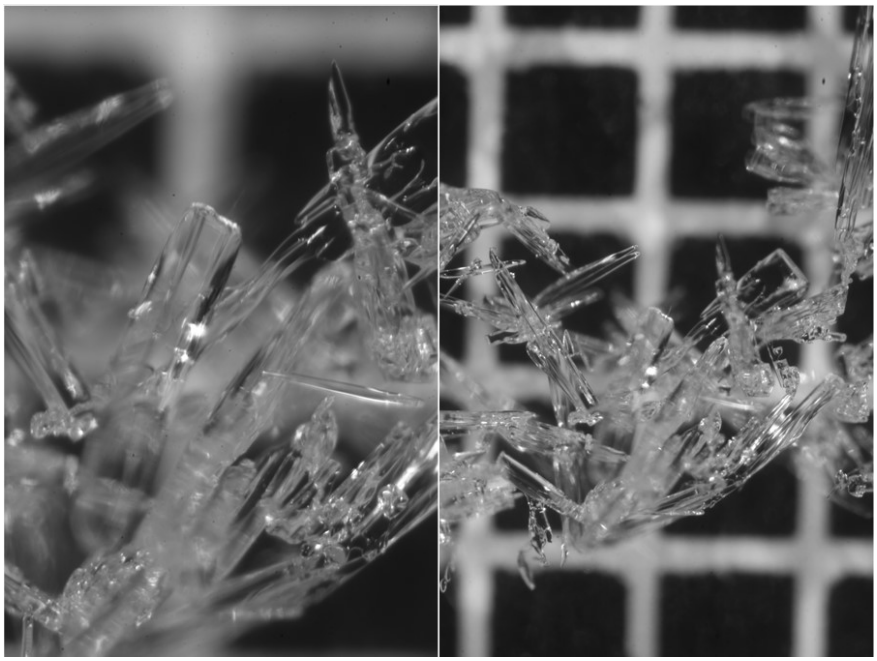


Figure 8-19: Photomicrographs of radiation recrystallized facets disaggregated from the surface and subsurface following 9 hours (left) and 12 hours (right) of metamorphism. Background grid is 1 mm square.

8.2.3 Discussion

Following recrystallization, three distinct zones of unique crystals exist near the surface of the snow. Long needle like facet growth dominates the top 0.5 mm of the sample. These elongated facet crystals typically do not become present until after 6 to 7 hours of metamorphism. Immediately below this surface layer, small hexagonal and rectangular faceted and cup shape crystals dominate the pattern. This intermediate zone was observed to be between 5 mm and 10 mm thick. The facet growth below the surface seemed to steadily increase throughout the first half of the experiment then slow for the remainder of the experiment. Below this layer, a bed surface of coarse rounded grains exists if temperatures stayed below freezing, or melt-freeze grains developed if subsurface temperatures reached 0 °C. In the case where melt-freeze occurred, the snow above this region remained dry from the radiative cooling occurring at the surface. A qualitative view of this layering is apparent in a depth profile cross-section taken from reconstructed CT images shown in Figure 8-20.

The intermediate layer of recrystallized snow contained hexagonal and rectangular faceted and cup shaped crystals. This growth resembles small scale growth of depth hoar crystals. This type of growth is consistent with general temperature gradient metamorphism. In this regime, water vapor diffuses

through the pore spaces by following the vapor pressure gradient that develops as a result of sublimation and accumulation of H_2O in accordance with the temperature gradient. These grains, although small, even develop similar chain like structures to those observed in well-developed depth hoar (Staron et al., 2014, 2012). The chains of facets from the radiation recrystallized experiment are shown in Figure 8-21.

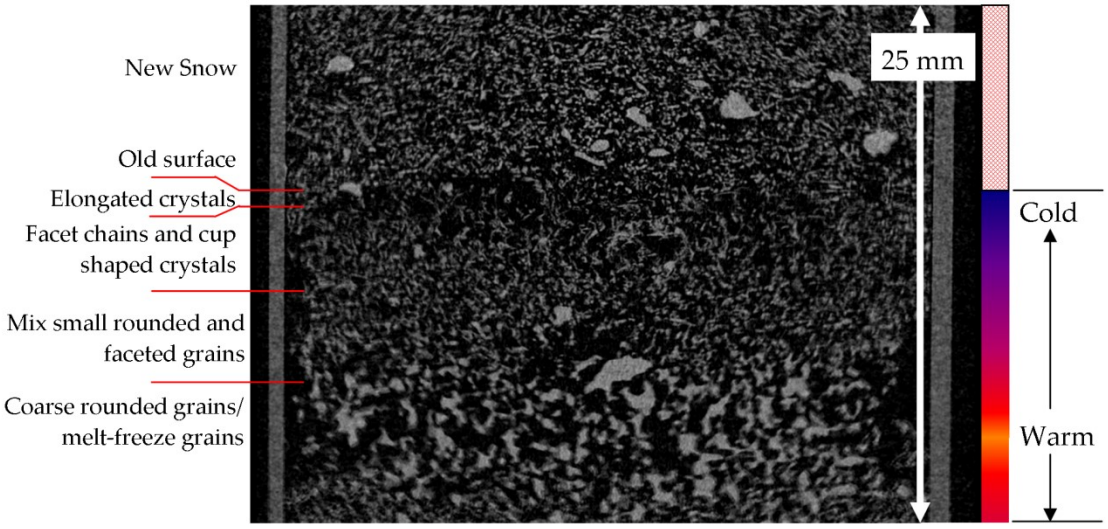


Figure 8-20: Profile cross-section of reconstructed CT scan containing a radiation recrystallized snow sample buried with new snow. The previous snow surface containing the elongated needle-like faceted crystals is indicated. Two distinct zones of unique faceted crystals exist following metamorphism. The approximate location of the average temperature gradient is positioned along the right side of the figure.

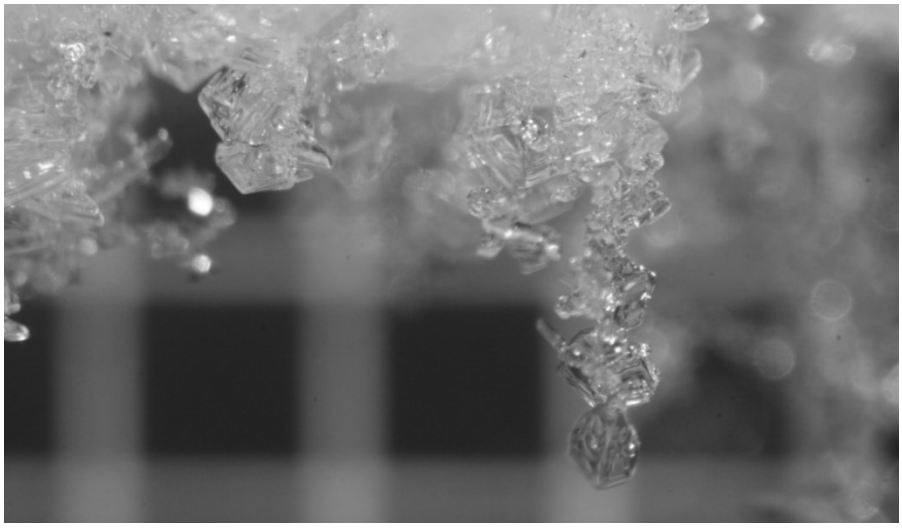


Figure 8-21: Chains of radiation recrystallized faceted crystals similar to depth hoar formation. These crystals were extracted in-situ after sintering a layer of new snow over the top of a well-developed radiation recrystallized layer. The chain depicted here is parallel to the temperature gradient (perpendicular to the surface).

In contrast to the intermediate faceted layer, slender needle-like formations appear on the surface of the snow beginning after the six to seven hour point in the experiment. The crystals can exceed 4 mm in length and generally start off in faceted form (Figure 8-22) before sublimating due to intense solar radiation. These surface formations were unexpected and did not manifest themselves until the last 5-6 hours of the metamorphism portion of the experiments. These types of surface forms were present in all experiments with formation occurring in similar time frames.

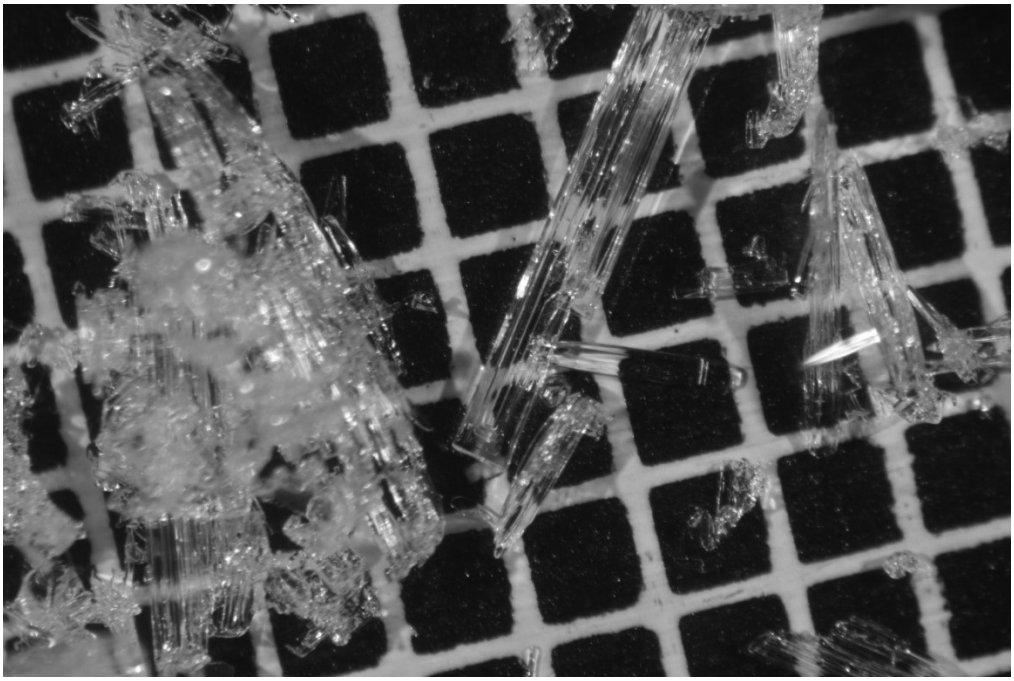


Figure 8-22: Long (4+ mm) faceted needle-like formation on the surface of radiation recrystallized snow following 12 hours of metamorphism. Background grid is 1 mm square.

The scheme for growing these surface crystals is different than those that are subsurface. Similar growths were observed in the Antarctic region termed sublimation crystals (Gallet et al., 2014). Gallet et al. (2014) found, on sunny days, surface hoar like formations growing in clusters. Further observation showed an environment near the surface reaching supersaturation supporting faceted crystal growth. However, modeling efforts only predicted sublimation crystal growth resulting from atmospheric vapor content for some of the days. On other days where sublimation crystal growth was observed, the model pointed to insufficient vapor content in the surrounding atmosphere. Gallet et al.

(2014) concluded the vapor source must originate from the snowpack resulting from subsurface sublimation due to near surface warming – similar to the temperature profiles observed in the experiments reported here.

MicroCT data analyzing the surface density of each experimental sample along with snow surface height measurements also support the idea of vapor fluxing to the surface to form what Gallet et al. (2014) termed sublimation crystals. Analysis of the density of the top 5 mm to 10 mm of each snow sample at 3 hour intervals is shown in Figure 8-23. In most experiments, density is mostly stable through 3 hours, declines through 6 hours and 9 hours, and levels off for the remainder of the experiment.

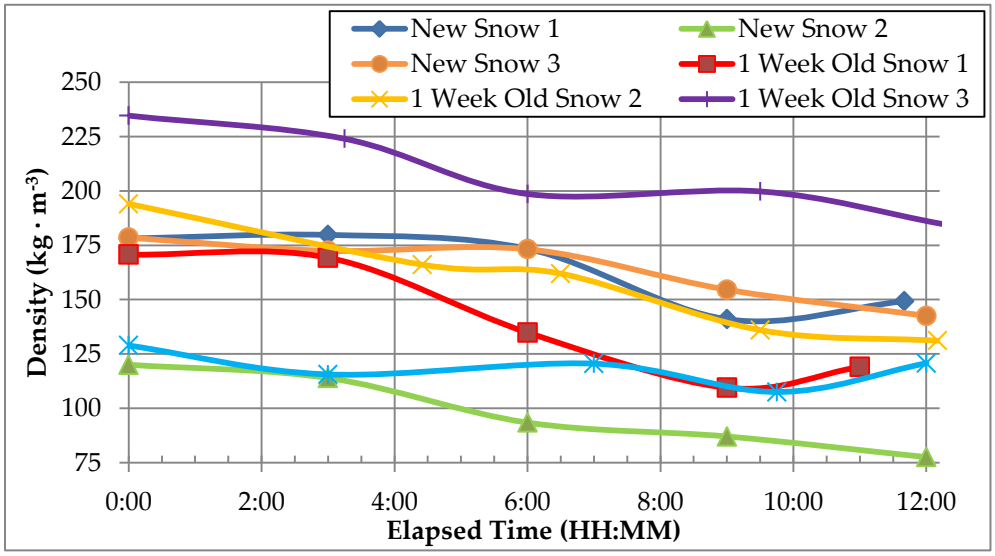


Figure 8-23: Analysis of near surface density of experimental samples undergoing radiation recrystallization. Samples are analyzed using Micro-CT imaging.

Figure 8-24 shows the change in surface height of the snow using laser measurements described in Section 7.1.4. In all experiments except NS2, surface height changes were negligible until after the 6 hour point of each experiment. Sample NS2 is thought to have accelerated surface height changes due to a significantly lower initial sample density as seen in Figure 8-23. Beyond six hours, changes in surface height accelerate downward for the duration of the experiment.

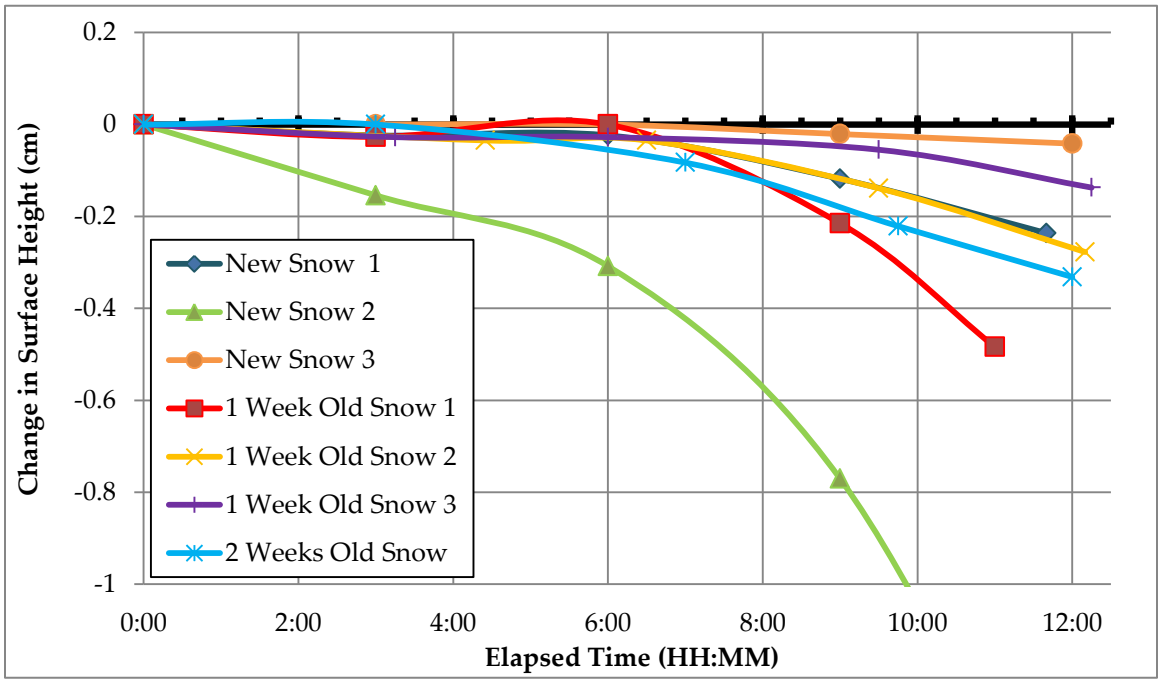


Figure 8-24: Measured changes in surface height for the duration of each radiation recrystallization experiment.

Using the near surface density data in Figure 8-23 and the change in surface height data in Figure 8-24, the first six hours of radiation recrystallization

were likely dominated by diffuse temperature gradient metamorphism. This rearrangement of the microstructure could result in changes in near surface density as mass is redistributed in the snow sample, but not lost out of the surface of the snow. Beyond six hours, it is thought that the metamorphism occurring below the surface results in a microstructure conducive to supporting movement of water vapor in the pore spaces of the metamorphosed snow vigorous enough to flux through the surface of the snow sample. The water vapor that breaks free of the surface could then leave the snowpack entirely, or redeposit on the surface forming sublimation crystals. The calm wind conditions in the laboratory would support large amounts of vapor remaining near the surface of the snow sample available for deposition onto the surface. On nearly calm days, less prolific needle like formation has been observed at the Yellowstone Club south study site as well.

More detailed study on vapor movement within temperature gradient metamorphosed snow is required to confirm temperature and vapor pressure gradient driven fluid flow. The data here is merely suggestive of this regime considering the two distinct stages of recrystallization during the metamorphic process.

8.3 Macro-Scale Mechanical Test Results

While the crystal morphologies and resulting microstructure form the foundation for changes within the near surface region of the snow, changes in mechanical properties are the direct connection to the formation of avalanches. Macroscale testing is conducted prior to and following radiation recrystallization to determine changes in strength and stiffness both temporally and spatially. Here, detailed results from one sample of each surface age category are discussed with synthesized data shown for each test. Detailed data of each test is listed in Appendix D.

8.3.1 Mechanical Shear Test Results

Shear testing was performed on two new snow samples, two 1 week old samples, and one 2 week old sample. All shear tests conducted included physical testing prior to and following radiation recrystallization. In each case, new snow was sintered over the previous surface using procedures outlined in Section 7.1.5. All samples were subjected to a constant displacement rate parallel to the snow surface at $0.2\,\mathrm{mm}\cdot\mathrm{s}^{-1}$. Depending on the height of the isolated column of snow, the shear strain rate resulting from the constant displacement rate was between $2.9\times10^{-3}\,\mathrm{rad}\cdot\mathrm{s}^{-1}$ and $3.6\times10^{-3}\,\mathrm{rad}\cdot\mathrm{s}^{-1}$. The design of the test – pushing transversely on an isolated column of snow – allows for flexural

stress to develop in addition to shear stress. Thus, the stress at failure is only a minimum shear strength value. In each test, measurable flexural deformation occurred which could have resulted in regions of tension/compression failure prior to reaching the maximum shear strength.

New Snow Shear Tests. Samples NS1 and NS2 were tested in shear. Each sample had significant differences in surface densities initially and throughout the duration of the recrystallization as seen previously in Figure 8-23. Prior to recrystallization, this large difference in density manifested itself in large differences in measured shear modulus and minimum shear strength as is summarized later in Table 8-2. Only one test will be discussed in detail here.

Sample NS2 had an initial shear modulus of 0.291 MPa and initial minimum shear strength of 0.882 kPa. All new snow samples tested in shear exhibited a nearly linear stress strain profile with minimal strain softening occurring near the point of failure. The shear stress and strain profile with a linear fit computing the shear modulus is plotted later in Figure 8-28 alongside the shear stress and strain data of the measured moduli of the layered radiation recrystallized sample. Shear strain in the initial sample was distributed nearly uniformly throughout the sample as indicated by the strain overlays in Figure 8-25. In Figure 8-25 and subsequent plots of shear strain, the shear strain data

represented is engineering shear strain, γ_{xy}, even though the analysis program used to generate the figure titles this measure Epsilon XY.

In both new snow cases, the samples failed near the base of the isolated column with opening of a tensile crack. This is indicative of a flexural failure occurring prior to the maximum shear strength being reached. Additionally, the failure surface was rough and non-planar as indicated by Figure 8-26.

Following metamorphism, a layer of near surface facets exists in the top 1 to 2 cm of the snow. Metamorphism also took place below the layer of near surface facets leaving a generally coarsened arrangement of large rounded

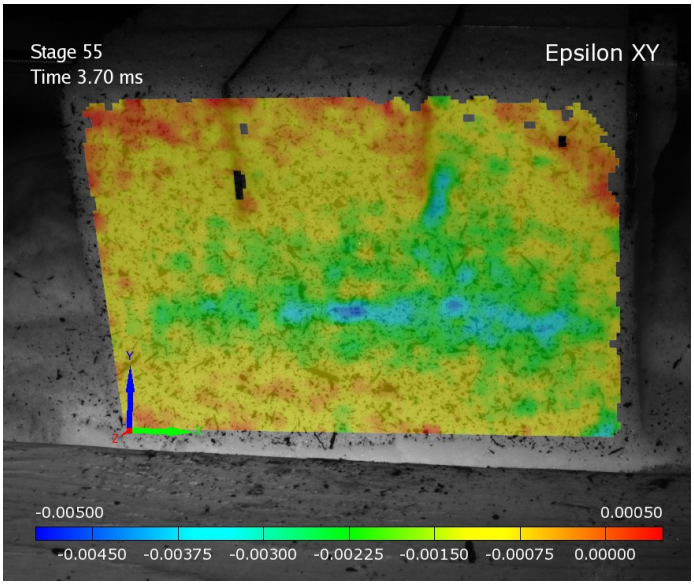


Figure 8-25: Shear strain distribution shown as an overlay on the actual sample. This test utilized an open faced shear frame being pushed from right to left relative to the image.



Figure 8-26: Non planar failure surface from the initial shear test on sample NS2 before radiation recrystallization.

grains. Measurements of the shear moduli are conducted in the layer below the near surface facets, and within the faceted layer.

Using the sample NS2, the shear strain contours in Figure 8-27 show a region of concentrated local strain in the same location as the radiation recrystallized layer as well as different fields of shear strain above and below the faceted layer. The labeled points in Figure 8-27 indicate the points used for measuring the shear modulus. In Figure 8-27, the radiation recrystallized layer contains the highest magnitude of shear strain. The snow below the radiation recrystallized layer contains the least amount of strain.

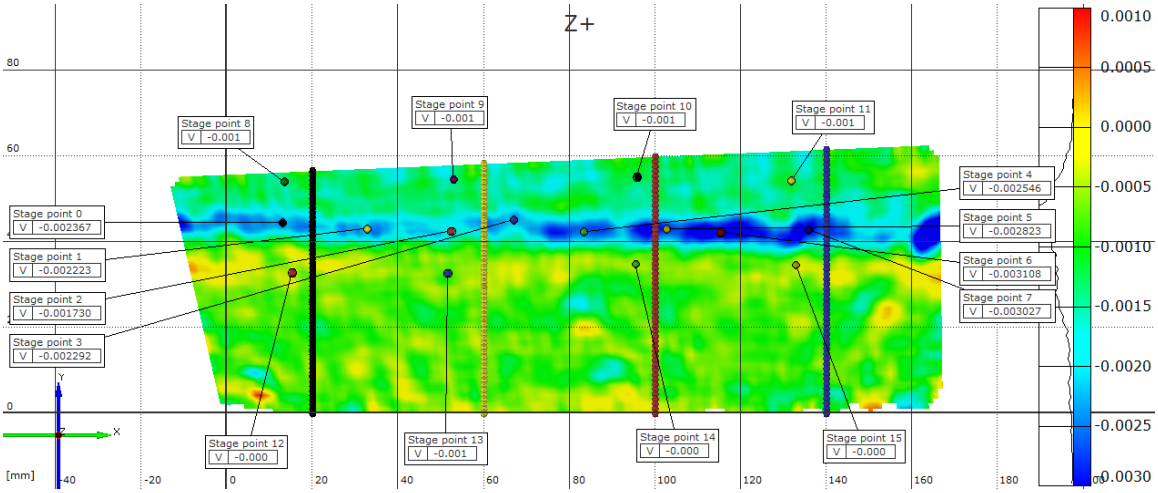


Figure 8-27: Shear strain contours of sample NS2 containing a radiation recrystallized layer. Labeled points indicate the 3 distinct zones used for measuring shear moduli. The region of concentrated shear strain corresponds with the location of the radiation recrystallized facets.

Three comparisons of shear moduli can be made within the same experimental sample: initial snow state versus the radiation recrystallized layer of snow; initial snow state versus the snow beneath the radiation recrystallized layer; and the radiation recrystallized layer of snow versus the snow beneath the radiation recrystallized layer (both layers following radiation recrystallization). Each of these comparisons can be made using the stress and strain profiles plotted in Figure 8-28.

When comparing the initial state of snow to the radiation recrystallized layer, the shear modulus increased by 44.7% from 0.291 MPa to 0.421 MPa. Comparing the initial state of snow to the consolidated snow beneath the radiation recrystallized layer, the shear modulus increased by 579% from 0.291

MPa to 1.97 MPa. Sample NS2 did experience significant subsurface melt freeze due to the initially low density.

Using the final recrystallized state, the shear moduli of the faceted layer and the layer below the facets are compared. The shear modulus of the radiation recrystallized layer was 78.7% lower than the shear modulus of the snow immediately below it. All of these comparisons are illustrated in Figure 8-28 below.

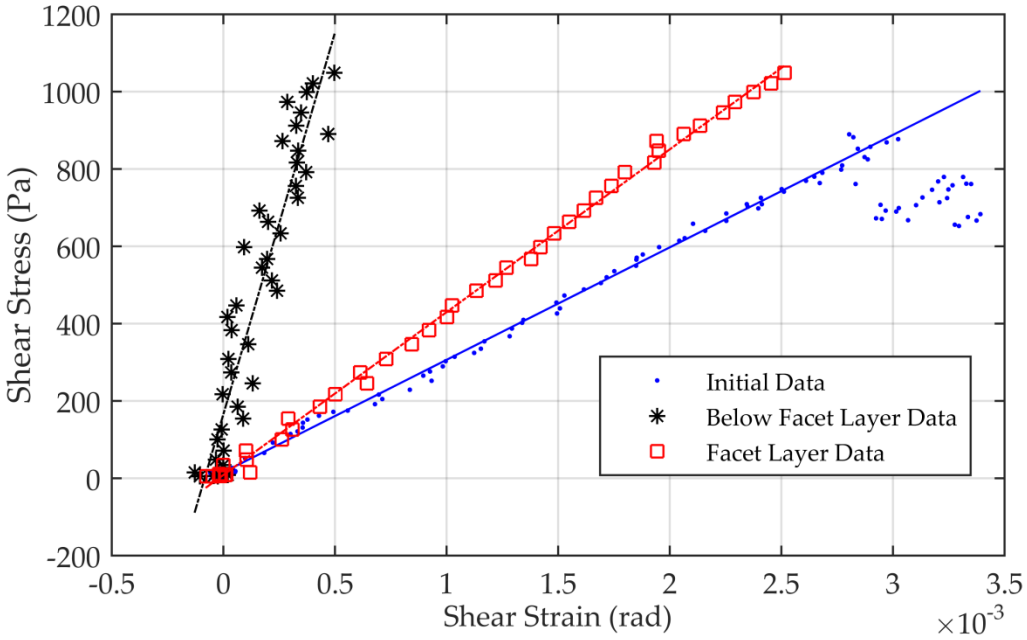


Figure 8-28: Shear stress and strain data for the initial and recrystallized state of experimental sample NS2. The slopes of the plotted lines represent the shear moduli of each layer examined. These are a first order fit to the stress and strain data in the presumed linear elastic region.

The maximum shear stress achieved by sample NS2 following radiation recrystallization was 1.08 kPa: a 20% increase from the initial sample absent radiation recrystallized facets. Due to the nature of the loading setup (which contains flexural stresses), the change in shear strength is not accurately represented by this test as will be discussed later. All results discussed here are summarized in Table 8-2.

Aged Snow Surface Shear Tests. The samples containing a 1 week old snow surface (1W1 and 1W2) and a 2 week old snow surface (2W1) were also tested in shear and exhibited similar results. Every effort was made to ensure stable storage temperatures were provided for the preparations for these samples. Unfortunately, sample 1W1 and 2W1 experienced small changes in temperature ($\pm 5° C$) as the preparation chamber is multipurpose and used by multiple research groups. During their storage, the air temperature in the chamber was warmed or cooled for other uses before returning to $-15° C$. These temperature variations were not recorded. Although the density was unaffected, the surface texture felt less cohesive than sintered new snow when manipulating the snow surface in preparation for initial mechanical tests.

When subsequently buried by new snow and allowed to sinter, sample 1W1 and 2W1 allowed more strain in the aged snow below the new snow,

indicating less shear stiffness relative to the added new snow. This is clearly shown in Figure 8-29 which shows the shear strain profile for sample 1W1 prior to the growth of radiation recrystallized facets. Since the aged snow is of interest, stress and strain measurements are taken from the section corresponding to the older snow surface. Sample 1W2 was not subjected to temperature changes and thus did not exhibit different behavior from the new snow tests. This seems to indicate significant sintering takes place in the first several hours of snowfall, then progresses slowly at greater durations given equi-temperature conditions.

Like the new snow shear tests, a plot of the stress and strain profile will be shown collectively with data from radiation recrystallized layered sample in Figure 8-32. The shear modulus for the 1 week old snow for 1W1 is 0.314 MPa. The minimum shear strength value of this older layer of snow is 0.668 kPa.

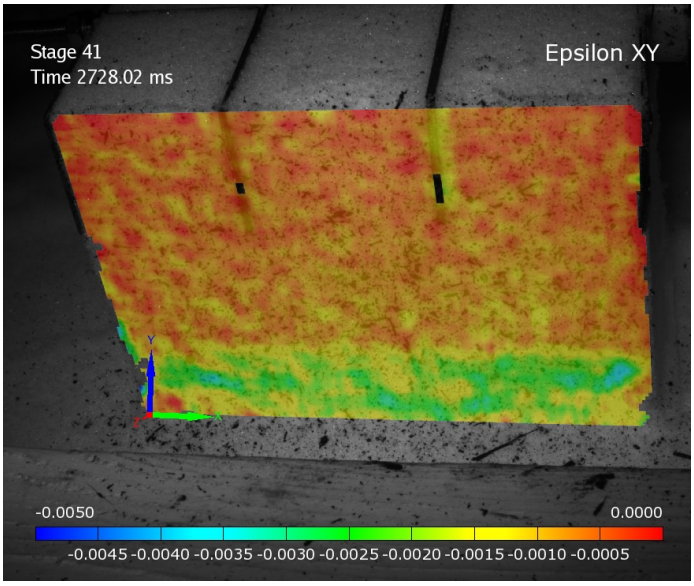


Figure 8-29: Shear strain distribution of the 1 week old surface of sample 1W1 prior to the growth of radiation recrystallization. Uniform strain distribution in the yellow and green contours corresponds with the 1 week old snow while the snow exhibiting less strain above is newly sintered snow added to support the shear frame (pushing right to left in this image).

The sample appeared to fail with opening of a tensile crack at the base of the column – consistent with the other tests not containing a radiation recrystallized layer. Unlike the other tests, a nearly planar surface was left behind as shown in Figure 8-30. The fractured surface was located approximately 2 cm below the old snow/new snow interface. The location and quality of the fracture surface was unexpected and unexplainable.



Figure 8-30: The nearly planar fracture surface of the initial 1 week old snow sample (1W1) prior to radiation recrystallization. The fracture surface is approximately 2 cm below the old snow/new snow interface and at the base of the cutout column. Initial failure occurred in tension in the vertical direction at the base of the column on the right side.

Following the growth of radiation recrystallized facets, the same comparisons of shear moduli are made as previously discussed. The comparisons are illustrated in Figure 8-32. Continuing with sample 1W1, the shear modulus of the radiation recrystallized layer decreased 34.7% from the initial 1 week old layer of snow – from 0.314 MPa to 0.205 MPa. The shear modulus of the snow underneath the radiation recrystallized layer increased 847% when compared to the initial 1 week old snow surface – from 0.314 MPa to 2.98 MPa. In Figure 8-32, the scatter in the stress strain data for the snow directly under the faceted layer is a result of very small strains being measured. The

shear strain contours overlaid on images of sample 1W1 containing a buried radiation recrystallized layer are shown in Figure 8-31. Here, the radiation recrystallized layer appears as the obvious stripe of concentrated shear strain with minimal shear strain directly below this layer.

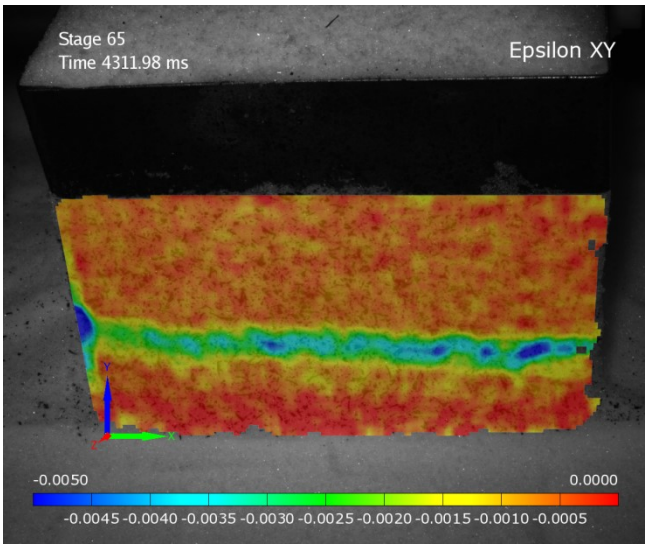


Figure 8-31: Shear strain contours overlaid on profile images of sample 1W1 containing a radiation recrystallized layer. The stripe of concentrated shear strain also corresponds with the location of the faceted layer. The shear load is applied to the frame at the top of the image from right to left.

Within the radiation recrystallized sample itself (1W1), the radiation recrystallized layer was 93.1% less stiff than the consolidated snow found directly beneath the radiation recrystallized layer. A comparison of the stress/strain curves for these samples is shown in Figure 8-32.

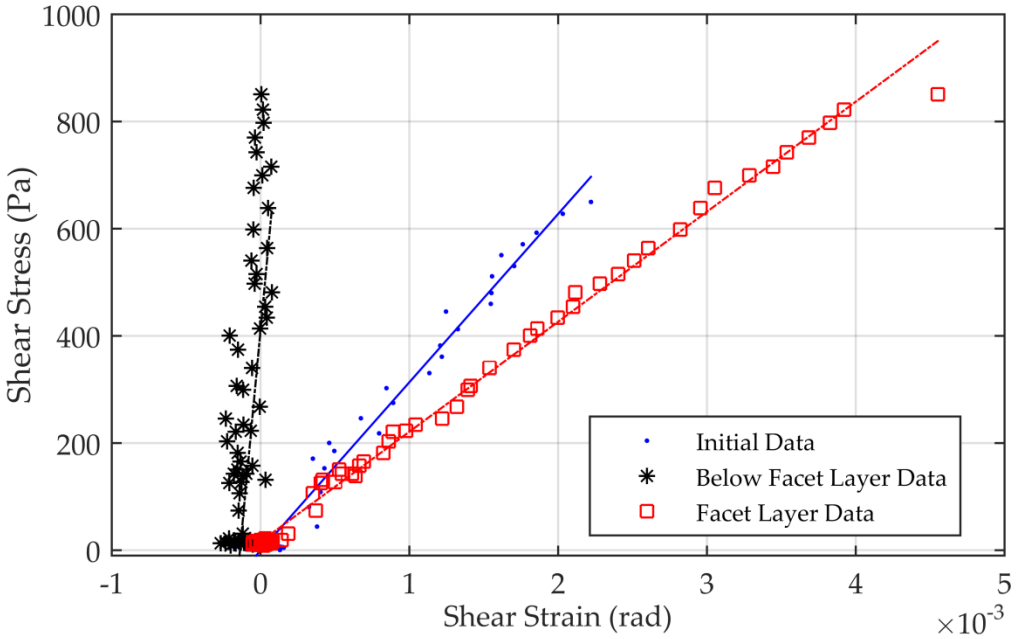


Figure 8-32: Shear stress and strain data for the initial and recrystallized state of experimental sample 1W1. The slopes of the plotted lines represent the shear moduli of each layer examined. These are a first order fit to the stress and strain data in the presumed linear elastic region.

The maximum shear stress achieved by the radiation recrystallized sample was 0.864 kPa - a 22.2% increase over the initial 1 week old snow surface. The comparison of shear strength numbers, as previously mentioned, is inconclusive on the actual change in shear strength. This will be discussed later.

The second 1 week old snow surface sample did not experience the temperature fluctuations during storage the other 2 aged samples received. Subsequently, there was no discernable difference in mechanical properties during the initial shear test that contained the 1 week old and sintered new snow

interface. As previously mentioned, rapid sintering may occur in the first several hours of snow accumulation with minimal or slow additional sintering taking place later. A more detailed study of sintering times and mechanical properties would need to be conducted to conclusively determine effective sintering rates. The remainder of the experiments exhibited similar comparisons as the other aged samples between the initial state of snow and the radiation recrystallized state. Table 8-2 summarizes the measured shear moduli from the entire set of shear tests conducted.

Table 8-2: Summary of shear modulus data for all shear experiments conducted.

Sample	Initial Shear Mod. (MPa)	Below Facets (Base) Shear Mod. (MPa)	Facet Layer Shear Mod. (MPa)	% Change Init. to Base	% Change Init. to Facets	% Change Base to Facets
NS1	1.25	1.67	0.417	+33.5%	-66.6%	-75.0%
NS2	0.291	1.97	0.421	+579%	+44.7%	-78.7%
1W1	0.314	2.98	0.205	+847%	-34.7%	-93.1%
1W2	0.405	2.96	0.625	+630%	+54.3%	-78.9%
2W1	0.338	1.24	0.315	+267%	-6.86%	-74.6%

8.3.2 Previously Published Shear Test Results

Prior to the present study, four shear test experiments were performed on radiation recrystallized snow formed from new snow surfaces (Walters and Adams, 2014b). In this study, only mechanical test results are presented for shear moduli in the location of the faceted layer. The results were reexamined to

more precisely measure shear strain within the faceted layer as well as shear strain in the sub-faceted region, similar to the experiments conducted in the present study. Table 8-3 below shows the re-tabulated results from Walters and Adams (2014b).

Table 8-3: Recomputed shear moduli for from Walters and Adams (2014b).

Sample (from prev. study)	**Initial Shear Mod. (MPa)**	**Below Facets (Base) Shear Mod. (MPa)**	**Facet Layer Shear Mod. (MPa)**	**% Change Init. to Base**	**% Change Init. to Facets**	**% Change Base to Facets**
1	1.24	2.03	0.338	+63.7%	-72.7%	-83.3%
2	1.03	1.78	0.372	+72.8%	-63.9%	-79.1%
3	0.784	4.95	0.990	+531%	+26.3%	-80.0%
4	1.12	5.21	1.27	+365%	+13.4%	-75.6%

The results in Table 8-3 follow a similar pattern to those presented in this study in Table 8-2. The sub-faceted layer generally increases significantly from the initial state of the snow. The faceted layer however continues with unpredictable changes, sometimes increasing and sometimes decreasing from the initial configuration of snow. Consistently, like the present tests, is observed in the relative change in shear moduli between the final sub-faceted and faceted layers following metamorphism. The behavior of the shear tests presented in Walters and Adams (2014b) is similar to those conducted in this study.

8.3.3 Mechanical Compression Test Results

Two of the seven experimental samples were mechanically tested in compression. This pair of tests consisted of one new snow sample (NS3) and one 1 week old snow sample (1W3). The isolated column heights were approximately the same as used for the shear tests described previously. The constant displacement rate of $0.2\ \mathrm{mm \cdot s^{-1}}$ produced similar compressive strain rates between $2.6 \times 10^{-3}\ \mathrm{s^{-1}}$ and $3.6 \times 10^{-3}\ \mathrm{s^{-1}}$, depending on the column height. In addition, compressive strengths measured from this test setup are relevant due to the nature of loading, unlike shear strength values.

New Snow Compression Test. Starting with the new snow sample NS3, the initial compression test showed linear stress/strain behavior up to the point of failure. The stress/strain curve for sample NS3 prior to recrystallization is shown in Figure 8-35 along with the stress and strain/strain data from the radiation recrystallized layered sample. The measured Young's modulus is 1.51 MPa and the ultimate compressive strength is 3.83 kPa.

The isolated column of snow showed a nearly uniform distribution of compressive axial strain along the axis of loading as seen in Figure 8-33. Minor strain is plotted in Figure 8-33. The minor strain directions are nearly vertical across the face of the sample. Strain transverse to the axis of loading was below

the threshold of detection making calculation of Poisson's ratio unfeasible. The sample failed on a ragged, non-planar surface near the base of the sample.

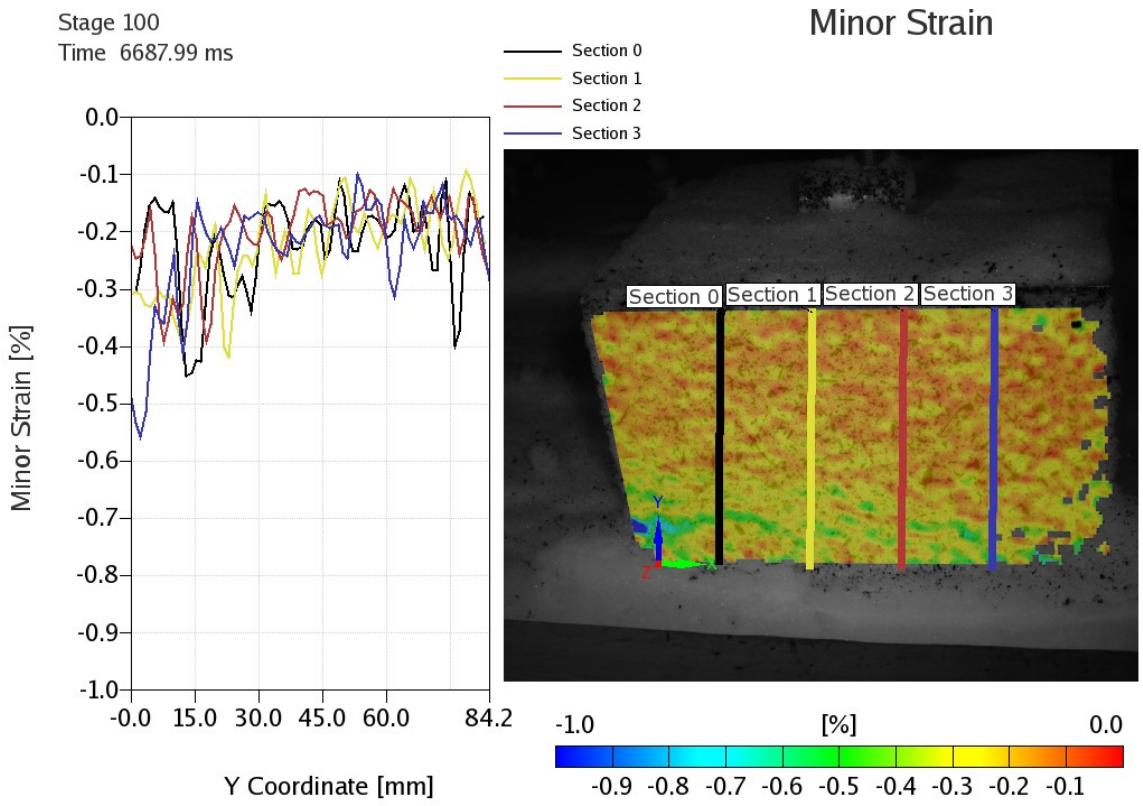


Figure 8-33: Minor strain (principal II) contours plotted on the vertical profile of sample NS3 undergoing compression testing prior to recrystallization. The plotted lines correspond to the strain value along each section line starting with $y = 0$ at the bottom of the sample. Minor strain direction was vertical (y-direction) in reference to this figure.

Following radiation recrystallization and subsequent burial of the faceted layer with new snow, the sample was tested again in the same way. Comparisons of the mechanical properties between the initial state of snow, the faceted layer of snow, and the consolidated layer of snow directly beneath the

faceted layer of snow are made. These comparisons are illustrated in Figure 8-35. Compressive axial strain became highly concentrated along the location of the radiation recrystallized layer as seen in Figure 8-34.

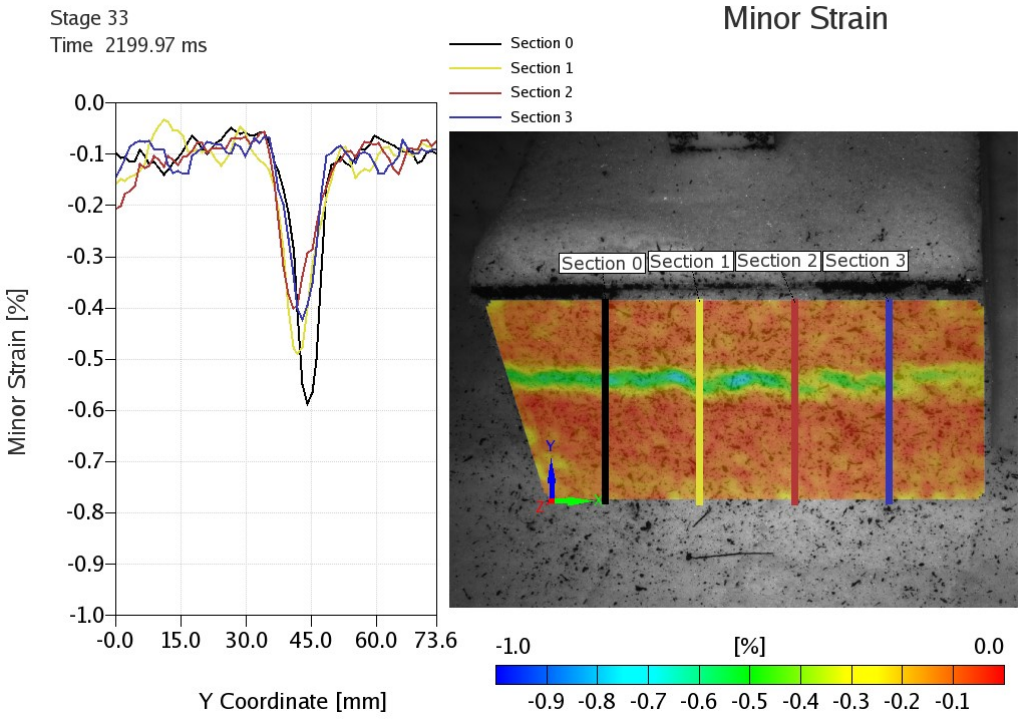


Figure 8-34: Minor strain (principal II) contours plotted on the vertical profile of sample NS3 undergoing compression testing following radiation recrystallization. The plotted lines correspond to the strain value along each section line starting with $y = 0$ at the bottom of the sample.

Compared to the initial state of snow, the buried radiation recrystallized layer of snow was 59.4% less stiff – a change from 1.51 MPa down to 0.615 MPa. The sample also failed in a clean plane along the faceted layer producing a compressive strength in the vertically oriented principal direction of 2.50 kPa, a

decrease of 34.8% from the initial state of snow. The Young's modulus for consolidated snow directly beneath the layer of radiation recrystallized facets increased from the initial state of new snow by 191% - from 1.51 MPa to 4.03 MPa.

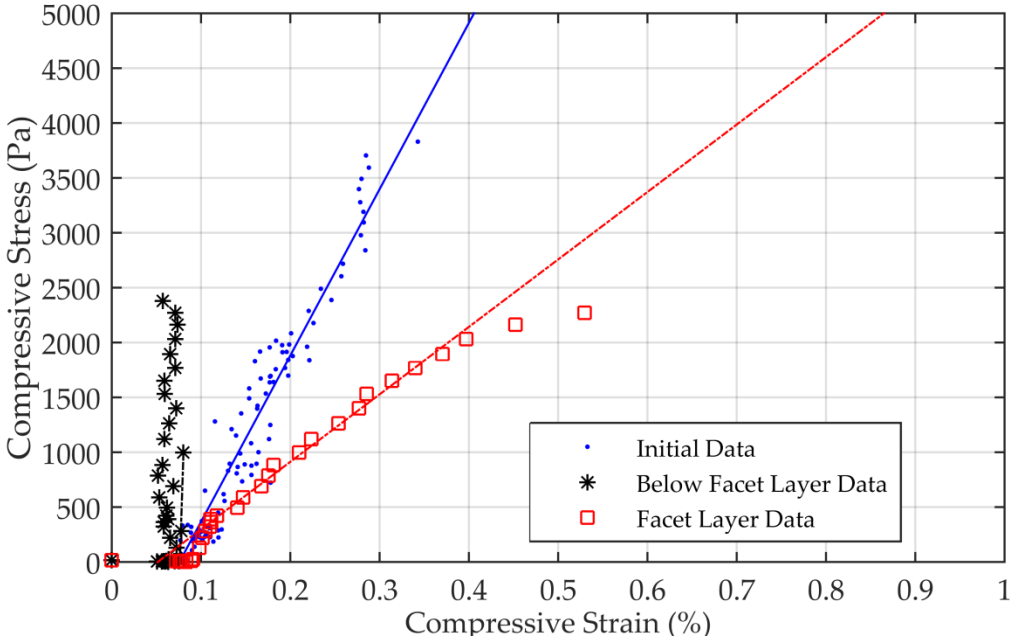


Figure 8-35: Comparison of stress/strain data for sample NS3 between the initial sample, the layer of radiation recrystallized facets and the consolidated layer of snow directly beneath the radiation recrystallized layer.

The final comparison for sample NS3 is between the layer of radiation recrystallized facets and the layer of snow below the faceted layer. The Young's modulus for the faceted layer was 84.7% less than the Young's modulus the snow below it. A visual comparison of all of this data is shown in Figure 8-35.

One Week Old Snow Compression Test. The other compression test was conducted on a sample that started with a 1 week old snow surface prepared in the same manner as those used in the shear tests. Sample 1W3 experienced the same small temperature changes during storage some of the other samples received. Again, this resulted in a surface texture with less cohesion than well sintered new snow. Following burial with new snow that was allowed to sinter, the sample was compressed. The strain results in Figure 8-36 verify the difference in stiffness properties between the 1 week old snow and the sintered new snow.

Focusing on the 1 week old layer of snow, the stress/strain profile was similarly linear to all of the previously examined mechanical tests. The stress/strain curve is shown in Figure 8-38 along with the stresses and strains from the radiation recrystallized sample. The Young's modulus for the initial 1 week old snow surface is 2.28 MPa. The sample also failed in a non-uniform manner at a compressive strength of 5.24 kPa.

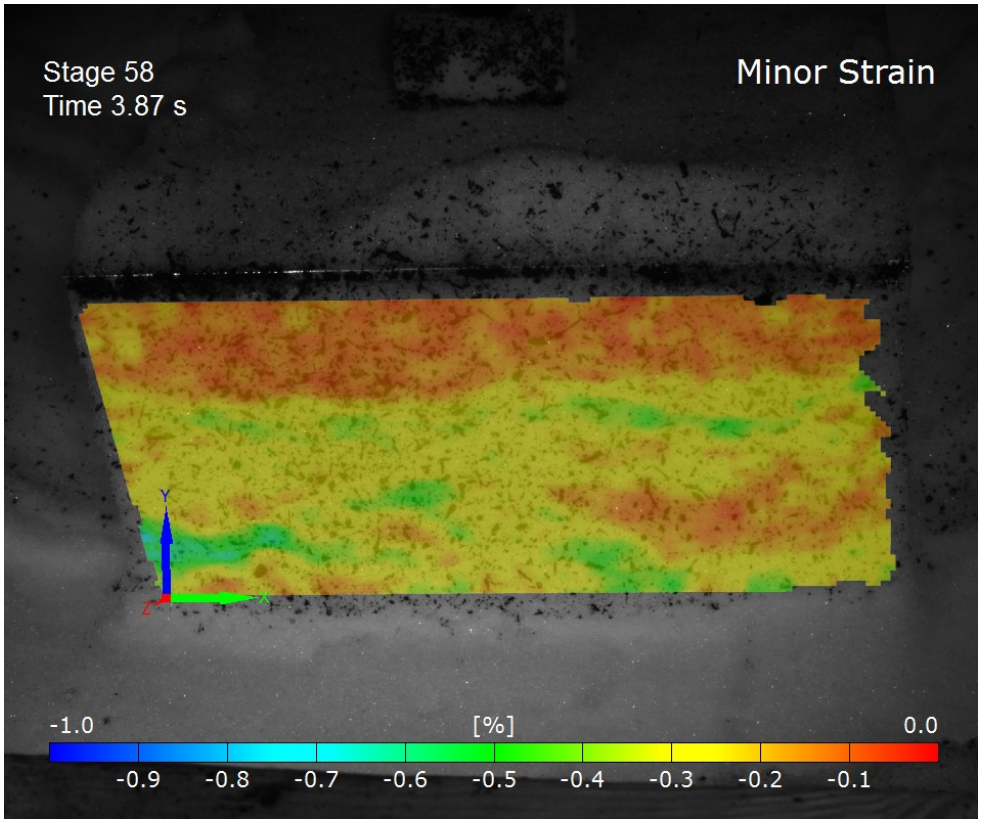


Figure 8-36: Minor strain contours (principal II) overlayed on the profile of a sample containing 1 week old snow buried by sintered new snow. The sample is being compressed in the vertical direction (y-axis).

Comparing the initial 1 week old snow to the radiation recrystallized facet layer, the Young's modulus normal to the snow surface decreased by 78.3%, to 0.494 MPa. The radiation recrystallized sample failed definitively in the faceted layer with a compressive strength 54.2% less than that of the original 1 week old layer at 2.40 kPa. In contrast, the snow immediately below the radiation recrystallized layer became more consolidated with a stiffness increase of 102% from the initial state of snow. The measured Young's modulus of this lower

layer was 4.61 MPa. The different stiffnesses of the new snow, buried faceted layer, and consolidated stiffer snow are clearly evident in strain profile shown in Figure 8-37 and the stress and strain comparisons in Figure 8-38.

Similar to the previous tests, the faceted layer of snow located directly above the consolidated base of snow, both formed during recrystallization, was 89.3% less than the consolidated layer.

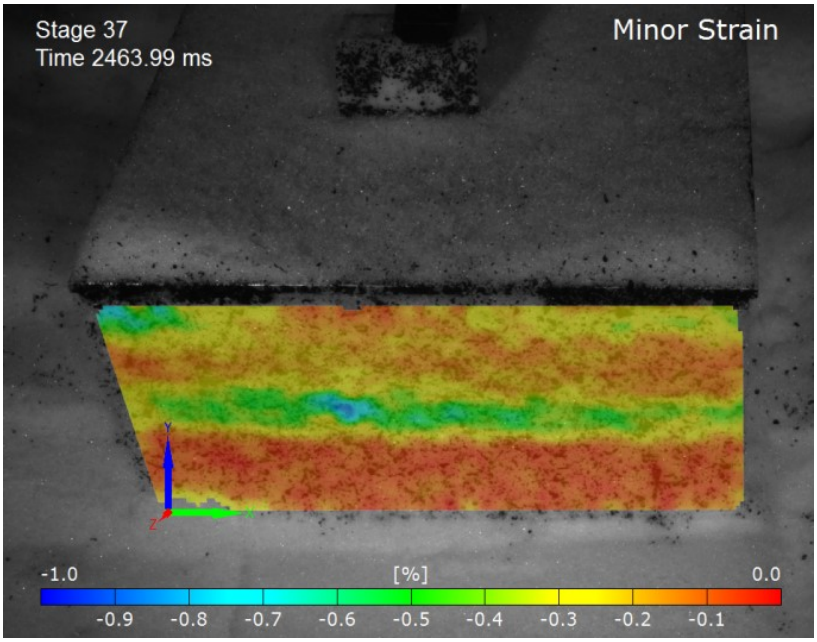


Figure 8-37: Minor strain profile during compression of the buried radiation recrystallized layer of sample 1W3. Most strain is concentrated on the weak faceted portion of the sample, with more moderate strain occurring in the new snow located above the faceted layer. The least strain is observed in the consolidated snow below the faceted layer. Minor strain is oriented vertically in sections with non-zero strain.

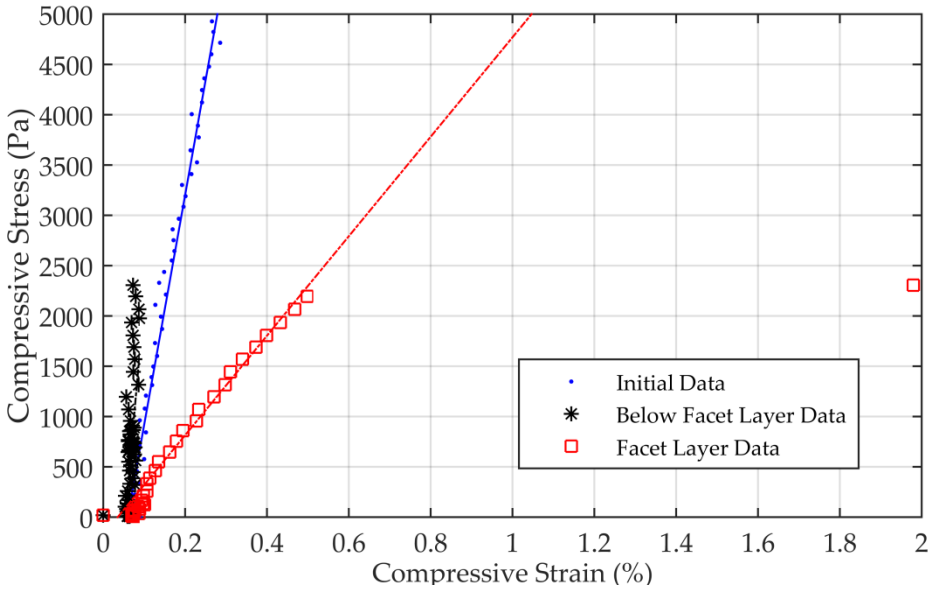


Figure 8-38: Comparison of stress/strain data for sample 1W3 between the initial sample, the layer of radiation recrystallized facets and the consolidated layer of snow directly beneath the radiation recrystallized layer.

Young's modulus results of the compression test experiments are summarized in Table 8-4 below. Since the compression tests also resulted in accurate readings of compressive strength values normal to the surface of the snow, strength results are summarized in Table 8-5 below.

Table 8-4: Summary of Young's modulus data for all compression experiments conducted.

Sample	Initial Young's Mod. (MPa)	Below Facets (Base) Young's Mod. (MPa)	Facet Layer Young's Mod. (MPa)	% Change Init. to Base	% Change Init. to Facets	% Change Base to Facets
NS3	1.39	4.03	0.530	+191%	-61.7%	-86.8%
1W3	2.28	4.61	0.494	+102%	-78.3%	-89.3%

Table 8-5: Summary of compressive strength data for all compression experiments conducted.

Sample	Initial Compressive Strength (kPa)	Faceted Layer Compressive Strength (kPa)	% Change (Initial to Facets)
NS3	3.83	2.50	-34.8%
1W3	5.25	2.40	-54.2%

8.3.4 Previously Published Compression Test Results

After reviewing the small set of compression test results performed here, it may seem like the results contradict previously published results by Walters and Adams (2014b, 2012). In these previous works, four samples of radiation recrystallized snow were tested in compression and their Young's moduli were compared to an initial configuration of sieved snow using similar procedures employed in the current study. These test results predated μCT capabilities at Montana State University and therefore microstructural data does not exist for these samples. Nonetheless, the Young's moduli reported in Walters and Adams (2014b, 2012) appeared to show significant increases following radiation recrystallization as shown in Table 8-6 reproduced from these works below (here samples 5 through 8 represent compression tests whereas samples 1 through 4 were shear tests).

Table 8-6: Compression test results reproduced from Walters and Adams (2014b, 2012). Young's moduli perpendicular to the snow surface (E_3) and compressive strength (σ_s) are reported. The superscripts initial and RR refer to the initial configuration and the radiation recrystallized configuration. The results are computed from average strains from regions above and below the faceted layer.

Sample	Density $(\mathbf{kg \cdot m^{-3}})$	$E_3^{initial}$ MPa	E_3^{RR} MPa	$\sigma_s^{initial}$ kPa	σ_s^{RR} kPa
5	190	1.24	5.94	1.96	1.11
6	180	1.03	3.47	2.52	1.00
7	150	0.784	2.09	1.51	1.67
8	147	1.12	3.91	5.00	5.31

However, while not reported in error, analysis of these samples naively consisted of average axial strains across a region which included the new snow burying the faceted layer, the faceted layer itself, and the cohesive snow found beneath the faceted layer. Preparation techniques for implementing the optical strain measuring system (ARAMIS) were not as well practiced during these previous experiments resulting in lower quality images used for computing strain.

Regardless, these previous samples were reanalyzed using what is known now about the nature of the fine structured layering found in radiation recrystallized faceted snow. Analysis of the previous data was refined to only query strain in the known location of the weak layer. Using this point data is bound to have a higher degree of uncertainty and merely represents an estimate

of the stiffness of the faceted layer. Using this technique, Young's moduli for just the faceted layer are quite different from the originally published values in Table 8-6. The updated values shown in Table 8-7 align closely with the values reported in the present study (in Table 8-4 and Table 8-5).

Table 8-7: Recomputed Young's moduli from Walters and Adams (2014b).

Sample (from prev. study)	Initial Young's Mod. (MPa)	Below Facets (Base) Young's Mod. (MPa)	Facet Layer Young's Mod. (MPa)	% Change Init. to Base	% Change Init. to Facets	% Change Base to Facets
5	1.24	2.20	0.444	+77.4%	-64.2%	-79.8%
6	1.03	2.45	0.412	+138%	-86.2%	-94.2%
7	0.784	0.983	0.114	+25.4%	-85.5%	-88.4%
8	1.12	7.08	1.07	+532%	-4.46%	-84.9%

The data reported in Walters and Adams (2014b, 2012) bolsters support for the data reported in the present study. The previously reported data included snow from the layer immediately beneath the faceted layer. The large increases associated with the previously averaged data are consistent with the increases in Young's moduli observed in the present study for the cohesive layer found immediately beneath the faceted layer.

8.3.5 Discussion

Following radiation recrystallization, all of the mechanical experiments showed a concentration of strain in the general location of the radiation recrystallized facet layer – regardless of whether tested in shear or compression. The localized strain concentration appears to show the entire thickness of the recrystallized layer experiencing heightened strain relative to the other layers as shown in Figure 8-39.

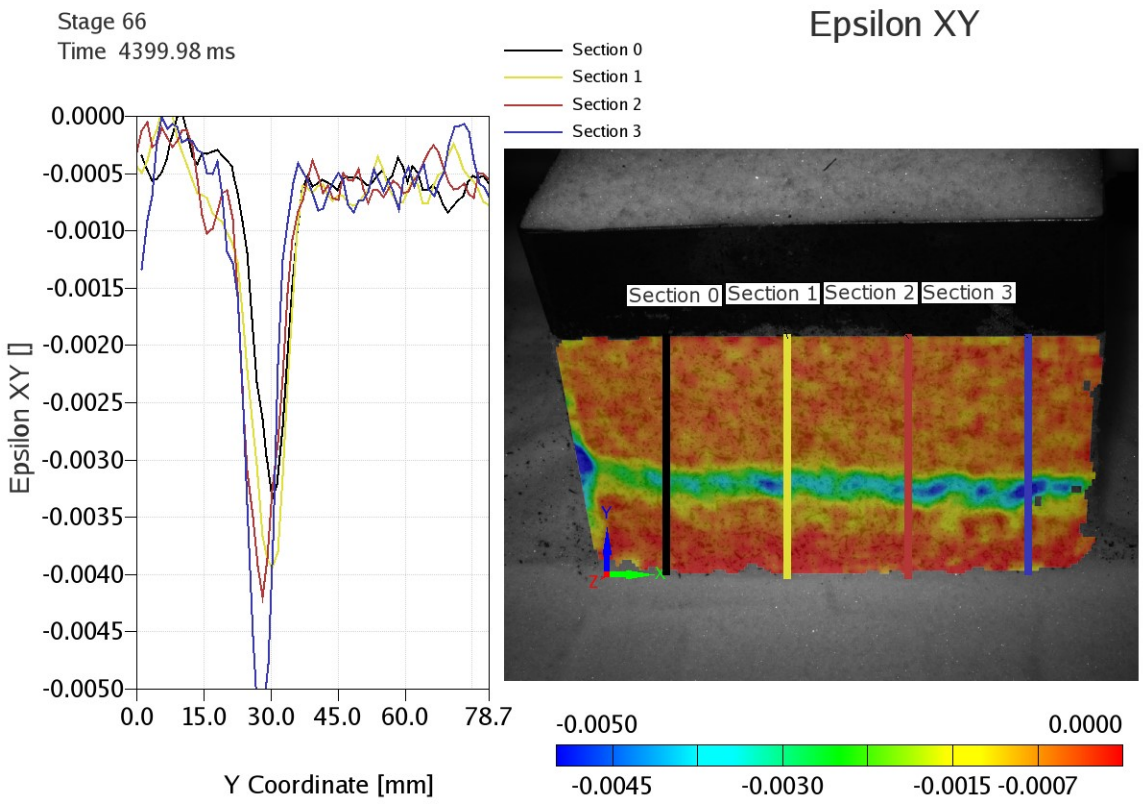


Figure 8-39: Shear strain concentration on the radiation recrystallized layer of test 1W1 prior to failure. Localized heightened shear strain is the thickness of the radiation recrystallized faceted region.

Upon failure of the sample, the upper and lower slabs of snow are carefully separated to expose the fractured surfaces. Crystal samples are extracted from each surface for inspection under the microscope. Microscopy reveals cup shaped crystals on either side of the fracture surface (example, Figure 8-40). Needle shaped crystals formed at the surface of the radiation recrystallized formation were not present in any of the photomicrographs of the fractured surfaces. This suggests the weakest portion of the radiation recrystallized layer lies within the depth-hoar-like cupped facet formation layer.

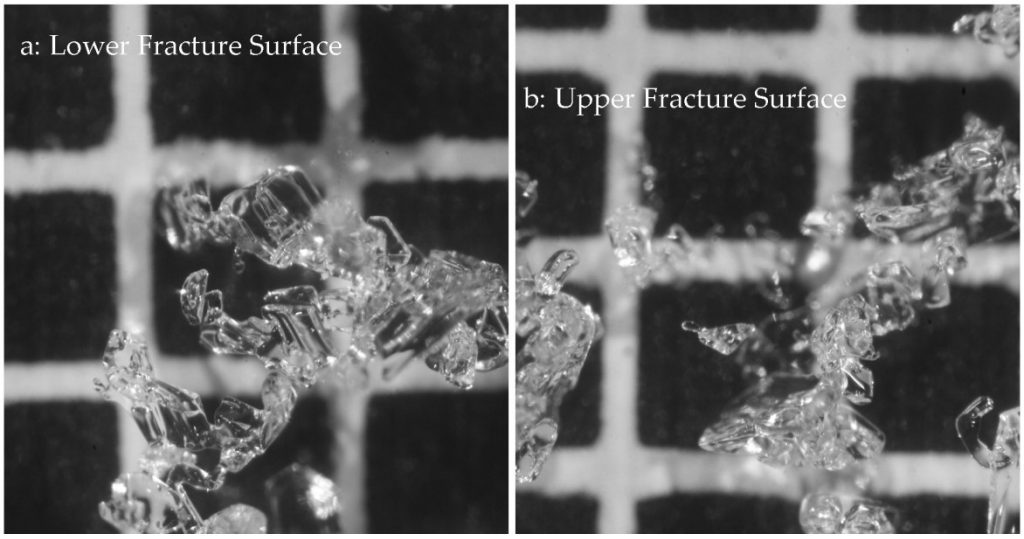


Figure 8-40: Micrographs of cupped faceted crystals found on the lower (a) and upper (b) fracture surfaces following a shear test of a radiation recrystallized sample 1W1. The background grid is 1 mm square.

Additionally, the extremely porous nature of the surface needle-like formations are quickly filled in by new snow as seen in CT cross-sections before

and after burial (Figure 8-41). This "locks-up" the surface layer by the introduction of new snow grains. Unlike the shear tests, inspection of the fracture surfaces of the compression tests would be impractical since the faceted layer implodes as the slab layers are forced together.

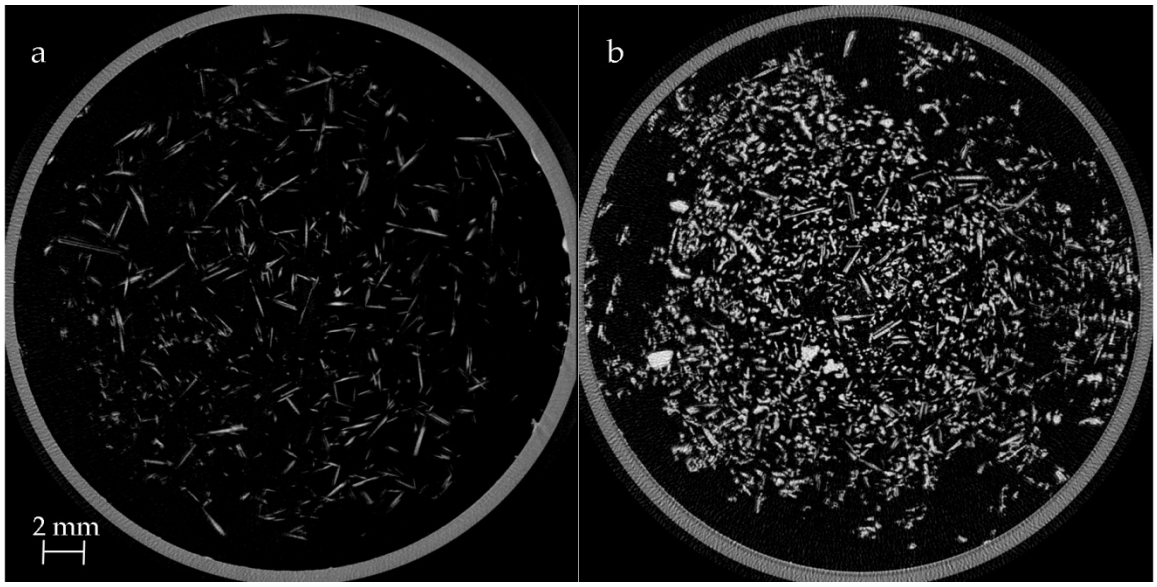


Figure 8-41: CT cross-section of surface needle crystals (a) before burial and (b) after burial of new snow crystals.

The changes to the snow's structure underneath the faceted layer are also interesting. In most cases, both the shear modulus (see Table 8-2) and Young's modulus (see Table 8-4) increased dramatically following recrystallization. The process of forming radiation recrystallized facets is also responsible for creating a cohesive bed surface immediately below the faceted crystals. This has the potential to promote changes in the fracture propagation quality and distance

(Habermann et al., 2008). The significant rise in stiffness of the sub-faceted layer is attributed to the warm temperatures (relative to melting) and minimal temperature gradients (as seen in Figures 8-5, 8-8, and 8-11) promoting vigorous sintering to take place.

The degree to which the snow below the faceted layer gained stiffness (whether shear or compression) affected whether the faceted layer decreased or increased in stiffness from its original configuration. When looking at Table 8-2, samples NS2 and 1W2 saw an increase in stiffness of the base layer below the radiation recrystallized facets of 653% and 844% respectively. The significantly stiffened base layer resulted in the stiffness of the faceted crystals actually increasing from their original configurations. In effect, the entire near surface of the snow became stiffer during radiation recrystallization, albeit not uniformly.

The three other samples that were shear tested also increased in shear stiffness below the faceted layer, although not as significant as the two previously mentioned. This resulted in modest decreases in shear stiffness between the faceted layer and the initial configurations. Subtle differences in surface preparation may have resulted in significant post-recrystallization differences in mechanical properties. All surfaces are prepared by hand with the

assistance of hand tools. It is unrealistic to expect complete uniformity of surface preparation between independent experiments.

The most striking commonality between all of the shear tests is the difference in shear stiffnesses of the two different layers of snow that exist in the final recrystallized state. Most samples tested showed the faceted layers were between 80%-88% less stiff than the snow found immediately below the faceted layers.

With the information from the tests performed in this study, and revision of previous results, the compressive stiffnesses between layers in the final recrystallized state showed similar results. Additionally, the compression tests mostly showed a decrease in compressive strength normal to the surface of the snow as previously discussed.

The mismatch of material properties in such a small spatial region provides a path for focused fracture initiation and propagation. This study intended to focus on the changes to the faceted region of radiation recrystallized layers. In hindsight, detailed data collection and sampling on the microstructure should have also occurred on the cohesive sub-faceted layer as macro-scale mechanical testing showed significant changes in mechanical performance both within and below the faceted region. The process of radiation recrystallization,

as demonstrated for the first time here, generates adjacent layers with significantly mismatched stiffness properties promoting easy failure initiation and fracture propagation.

On the subject of strength, it was expected that the shear strength of the radiation recrystallized facet layer would also decrease from its initial state prior to recrystallization. Initially, this hypothesis seemed incorrect. The way in which the shear test is setup, however, has a significant impact on how samples fail when loaded in shear.

Unlike the testing apparatus used by McClung (1977) and Schweizer (1998), which limits the failure region to a small horizontal zone, the setup here is intended to allow the sample to fail in a non-prescribed region. The apparatus is similar in concept to that used by Fukuzawa and Narita (1992). The one used here is described in detail in Section 7.1.5. A consequence of the setup used here and in Fukuzawa and Narita (1992) is the introduction of flexure forces within the isolated column. A free body diagram in Figure 8-42 and subsequent analysis shows maximum axial forces from internal bending moments occur at the base of the column while internal shear forces remain constant.

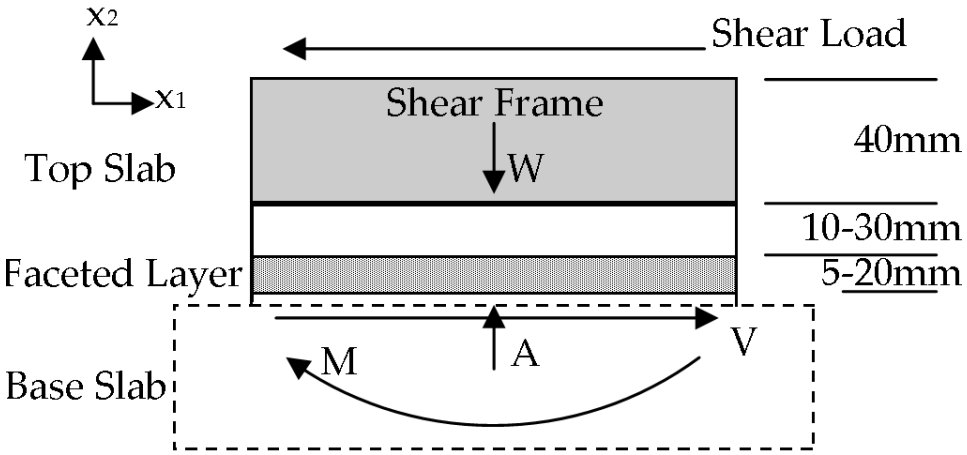


Figure 8-42: Free body diagram of an isolated column being loaded in shear. The external shear load applied to the shear frame produces the internal shear force V, and internal bending moment M.

These flexure forces and deformations manifested themselves significantly in every shear test performed. In samples not containing a radiation recrystallized layer (the initial testing phase), rotation of the column was measurable using the ARAMIS optical strain system. Rotation of the column is evident in overlays showing vertical displacement contours (example Figure 8-43). In every case with the initial non-recrystallized column, a tensile crack opened at the base of the column as a result of flexural deformation. Maximum tensile strain contours confirm this immediately following failure (Figure 8-44).

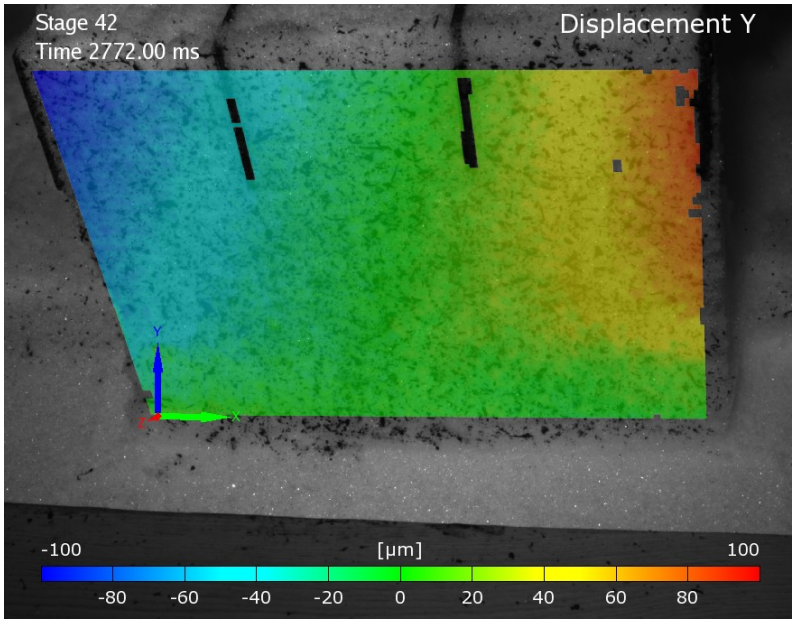


Figure 8-43: Vertical displacement of an initial column of snow (no faceted layer) holding a right to left shear load. Upward displacement on the right edge with downward displacement on the left edge indicates rotation.

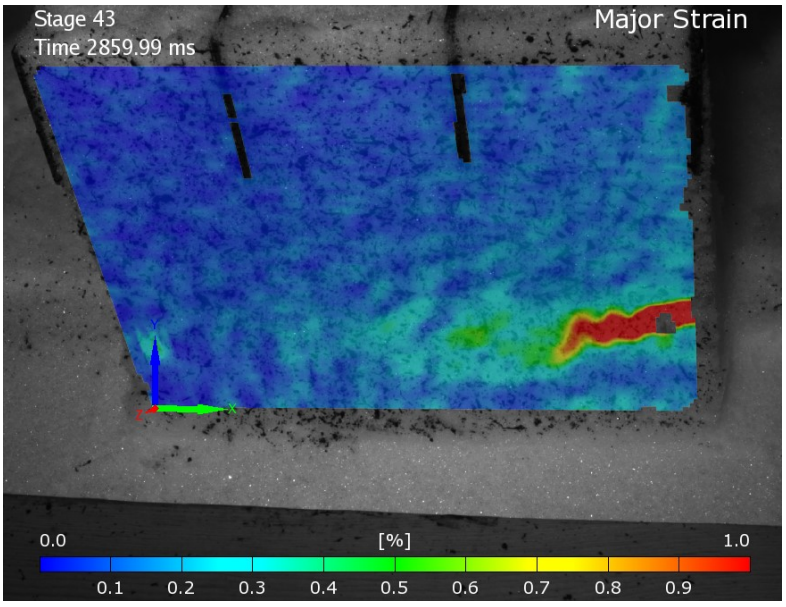


Figure 8-44: Example of major (tensile) strain immediately following initial fracture of the non-recrystallized column prior to full seperation. Indicates flexural strains prominent following the initiation of failure.

Prior to the point of failure, the column is adequately supporting both shear and flexure stresses. However, the primary strain direction immediately following failure of the non-recrystallized column is in tension. The frame rate of the ARAMIS system is not fast enough to determine the failure mode at the point of fracture propagation. However, from a strength of materials approach, it seems the tensile strength of the column was exceeded prior to exceedance of the shear strength. For this reason, the peak shear stress measured on all of the initial columns of snow is merely a minimum value for shear strength since it is unknown whether the maximum shear stress was ever achieved.

A similar result is observed in the shear test results of the samples containing a radiation recrystallized layer. Figure 8-45 shows rotation of the column is subtle, but still detectable in layered samples. Here shear strain is localized on the radiation recrystallized layer (see Figures 8-27 and 8-31). However, immediately following failure, evidence of significant tensile strain is visible post failure in Figure 8-46.

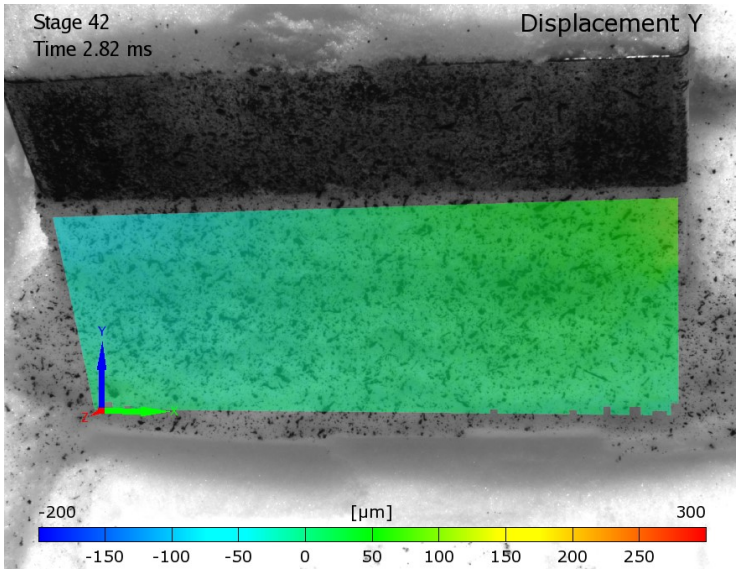


Figure 8-45: Vertical displacement of a column of snow containing a radiation recrystallized layer holding a right to left shear load. Upward displacement on the right edge with downward displacement on the left edge indicates rotation.

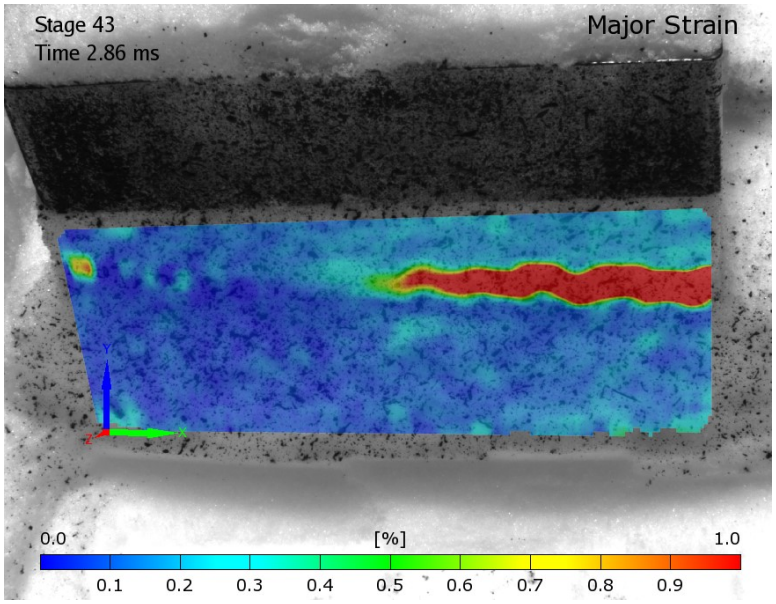


Figure 8-46: Example of major (tensile) strain immediately following initial fracture of the recrystallized column. Indicates flexural strains prominent following the moment of failure. Major strain is oriented vertically along the crack interface

Due to the presence of significant flexure strains, once again the peak shear stress values recorded merely represent the minimum shear strength values of the radiation recrystallized layer. In addition, the location of the faceted layer (where failure occurs) affects the magnitude of the bending moment contributing to failure than the non-layered columns. This does not allow for relative comparisons before and after recrystallization has taken place.

While the testing apparatus employed here helped test for stiffness properties of a stratified sample, it is inadequate for determining accurate shear strength values or comparisons of shear strength values. To investigate relative differences in shear strength values, a setup similar to that used by McClung (1977) and Schweizer (1998) needs to be employed.

8.4 Summary

Previous research established the conditions necessary to study radiation recrystallized weak layers in a laboratory environment (Morstad, 2004; Morstad et al., 2007; Slaughter et al., 2009; Walters and Adams, 2014b). In the present study, these techniques were leveraged to launch a detailed study into the microstructural qualities of radiation recrystallized layers.

Several new insights regarding the formation process and final crystalline structure of radiation recrystallized snow layers were gained through deploying unique instrumentation and analytical techniques. μCT imaging revealed several different crystal morphologies never before seen developing in a spatial region as small as 5-10 mm. By sampling representative volumes of near surface snow at regular intervals throughout the recrystallization process, the timing of the presence of unique crystal morphologies could also be ascertained.

Although the environmental parameters applied externally to the snow samples were constant, the recrystallization process associated with the faceted region consistently split into 2 different crystal growth regimes dictated by the behavior of the near surface temperature and vapor pressure gradients. Through the first 5-7 hours of metamorphism, the vertical temperature gradient in the top 1-2 cm of snow smoothly increased to a magnitude between 300 and 500 $°\mathrm{C} \cdot \mathrm{m}^{-1}$ with the vapor pressure gradient developing in the same way to a magnitude between 10 and 15 $\mathrm{kPa} \cdot \mathrm{m}^{-1}$. Using optical microscopy and μCT imaging, recrystallization was slow and dominated by near surface cup and facet like growth. Time lapse macro-photography and physical observation of the snow surface showed minimal change to the surface crystal morphologies during this

period of metamorphism. Precise surface measurements also detected minimal changes in surface height of the snow relative to the sample container.

After 5-7 hours of metamorphism, the temperature gradients and vapor pressure gradients achieved a steady state value. Interestingly, new crystal growth patterns developed coincidental with the steady state temperature and vapor pressure gradients. Near surface faceted crystals appear more organized with chain like vertical structuring similar to well-developed surface hoar – but with smaller crystals. Elongated surface crystals also begin to propagate during this time resembling needle-like surface hoar growth. During this time, the surface height of the samples also begins accelerating downward signifying either significant subsurface compaction or significant mass-loss. Similar near surface conditions and surface crystal growth analyzed by Gallet et al. (2014) suggest surface hoar like growth resulting from supersaturation of the surface from a subsurface vapor source. This raises an interesting question about vapor movement through the pore spaces at various stages of temperature gradient metamorphism. Does the combination of severe temperature gradients and vertically oriented structuring of the snow microstructure allow convective vapor flow to develop in the pore spaces; and in this case lead to significant water vapor breaking free of the surface?

Mechanical testing of the radiation recrystallized layers of snow emphasized the significance of the fine structured layering that exists following metamorphism. The initial focus of mechanical testing rested on the faceted region of the radiation recrystallized samples early on in this study and in previous studies (Walters and Adams, 2014b, 2012; Walters et al., 2010). Regardless of the initial starting state of the snow (new snow, 1 week old, or 2 weeks old), shear testing showed the relative change in measured shear moduli between the initial sample and the recrystallized sample behaved erratically: sometimes increasing in shear stiffness or sometimes decreasing.

By using particle image velocimetry (PIV) techniques for measuring mechanical strain, any portion of the prepared snow column could be analyzed for deformation during mechanical testing. In addition to isolating strain in the location of the faceted layers, strain was also measured for the snow beneath the faceted layers following recrystallization. In this region, the snow consistently increased in shear stiffness following metamorphism – up to 850% stiffer. Analyzing the faceted layers and sub-faceted regions separately following recrystallization showed a consistent separation in shear stiffnesses. The faceted layer of snow was consistently 75-90% less stiff in shear than the sub-faceted layer below. Previously published data in Walters and Adams (2014b) was

reexamined to include separate measurements of the sub-faceted region. The results of this reanalysis show consistent results to the most recent tests performed as a part of this study.

Compression testing revealed similar but more consistent results to those conducted in shear. The Young's moduli between the initial state of snow and the sub-faceted region increased up to 500% when including reanalyzed data from Walters and Adams (2014b). Following recrystallization, the relative difference in Young's moduli spatially between the faceted layer and the sub-faceted layer exhibited similar characteristics to the shear modulus results. The faceted layer was generally 80-90% less stiff axially than the sub-faceted layer.

Using the mechanical testing results, multiple conclusions can be made regarding radiation recrystallized snow. Using the vertical temperature profiles measured by thermocouple arrays (as in Figure 8-5), the generally warm conditions present at 2-4 cm in depth, coupled with minimal temperature gradients, promotes vigorous sintering and coarsening of that region of the snow resulting in a significant increase in shear and axial stiffness. Coupled with the kinetic metamorphism found above this warm region, abrupt changes in mechanical properties form as a result of radiation recrystallization.

The implications of this are significant. From a material failure standpoint, abrupt changes in mechanical properties have the ability to focus fracture propagation due to the potentially significant mismatches in mechanical strain when deformed by a mechanical load. Additionally, the near surface region as a whole does not necessarily need to become weaker to promote the formation of a dangerous avalanche layer. Through laboratory testing, metamorphism as a result of radiation recrystallization is able to generate stout cohesive layers of snow simultaneously with thin faceted layers of snow – which are consistently less stiff and strong than the stiffer layers formed via the same process.

CHAPTER NINE

FABRIC TENSOR MODEL RESULTS

"In nature, when you conduct science, it is the natural world that is the ultimate decider in what is true and what is not."
~ Neil deGrasse Tyson

Detailed microstructural analysis of all of the experimental samples was conducted. CT scans obtained at regular intervals during the recrystallization process are used to compute the changes to the effective stiffness properties temporally using microstructure based scalar and directional properties described in Chapters Three through Five. The fabric tensor based effective properties are compared to measured macroscale results.

Representative samples from the top 10 mm to 20 mm of the snow were extracted at approximately 3 hour intervals for each radiation recrystallization experiment. Each sample was scanned in the μCT scanner using the settings described in Section 7.2. Since analyzing the full volume of the CT scan is prohibitively expensive computationally, smaller sub-volumes are analyzed. In order to assure the volume sizes chosen are representative of the larger volume from which they are extracted, the fabric tensor model was validated using artificially generated 3-D volumes. These randomly generated volumes also help

validate other aspects and computation options of the fabric tensor model other than appropriate sample size.

9.1 Fabric Tensor Validation

The accuracy of the tensor calculations, whether the contact tensor, $\boldsymbol{F}$ or the MIL tensor, $\boldsymbol{H}$, are sensitive to the volume on which it operates. Too few grains in the analysis results in statistically insignificant results that are not representative of the larger volume. To analyze the sensitivity of each fabric tensor to sample volume size, artificial microstructures resembling snow are generated and analyzed.

To approximate the microstructure of snow, volumes containing randomly sized spheres placed in random locations are generated. Maximum and minimum sphere sizes as well as the number of spheres in a volume are controlled to achieve reasonable approximations of solid volume fractions, grain sizes, and contact areas to real snow samples. Using a volume of $(150 \text{ pixel})^3$, an artificially generated volume of spheres is qualitatively comparable to a sample of real sintered snow as seen in Figure 9-1.

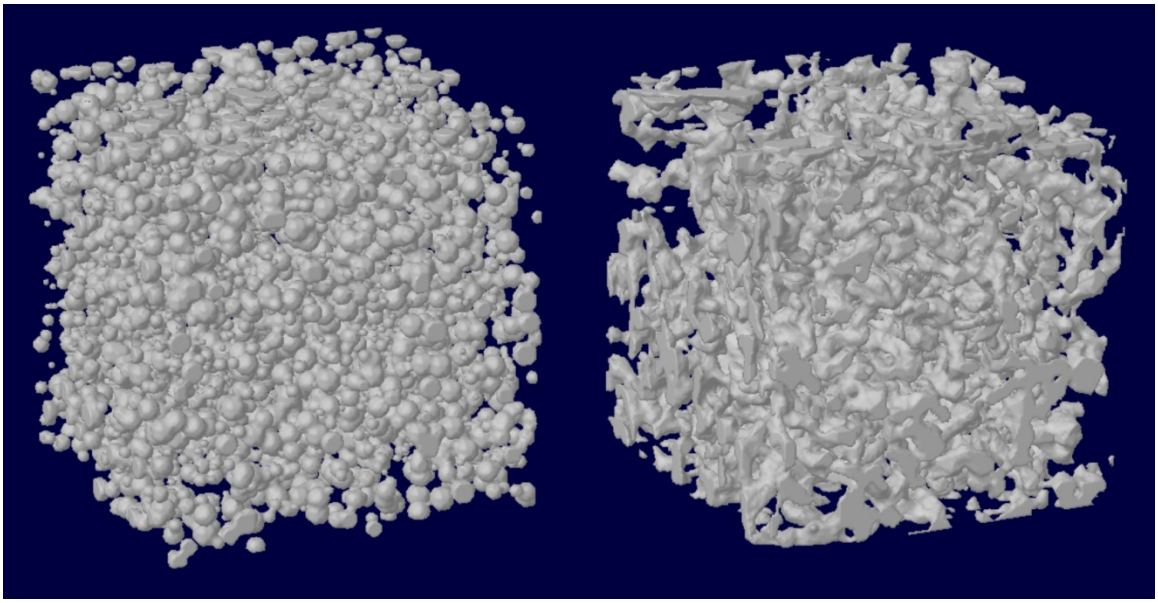


Figure 9-1: Cubic volumes with a side length of 150 pixels. The volume on the left is artificially generated using random spheres. The volume on the right is of real snow. The solid volume fractions between the two volumes are similar ($\approx 20\%$).

The random nature of the size and location of the spheres should generate a uniform microstructure of bonded spherical grains with an isotropic "fabric" – both $\boldsymbol{F}$ and $\boldsymbol{H}$ should be isotropic. Total volume can be adjusted to test the significance of sample size on the variance of $\boldsymbol{F}$ and $\boldsymbol{H}$. Cubic volumes with side lengths of 25 pixels through 200 pixels in intervals of 25 pixels are generated. Ten volumes of each are generated. In each case, the fabric tensor, $\boldsymbol{F}$, MIL tensor, $\boldsymbol{H}$, and tensor ratio, $\boldsymbol{\Gamma}$ are evaluated and averaged.

These artificial microstructures also help choose the most accurate way to calculate the contact tensor based on the mean size of the microstructural

geometry. The orientation of individual contact planes can be calculated using two different techniques. One technique performs a least squares plane fit on the voxels generated as the bond surface. When bond planes are small, only a limited number of plane fit orientations exist. Figure 9-2 shows in 2-D that bond areas represented by only 1 pixel can only have 2 possible plane fit orientations. Bond areas represented by 2 pixels only have 3 possible plane fit orientations.

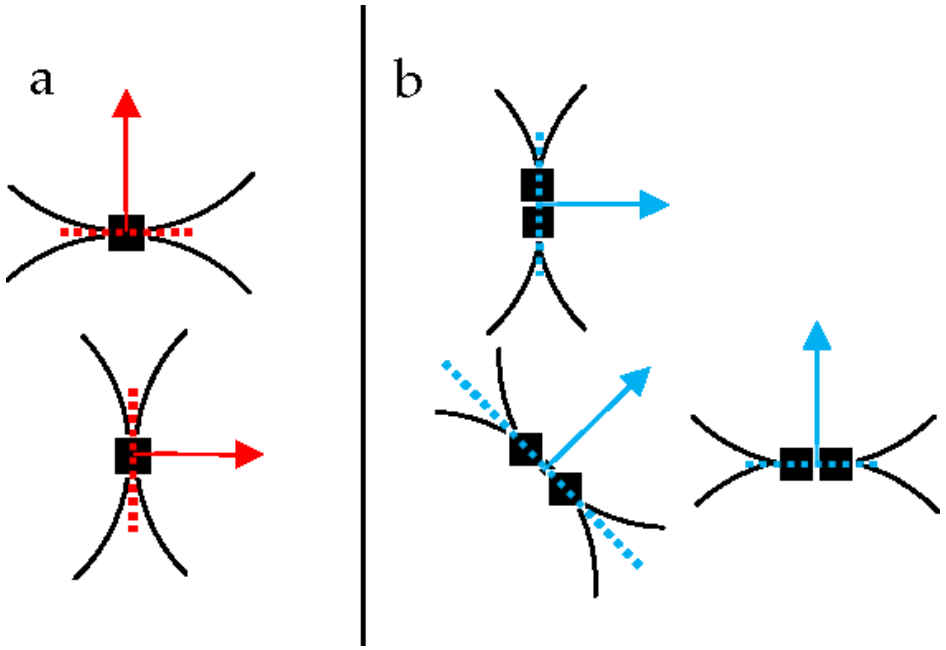


Figure 9-2: Possible plane fit orientations for bond areas represented by (a) only one pixel and (b) 2 pixels. Black squares represent the pixels identified as bonds. Similarly limited results would be expected in three dimensions.

Another technique determines the vector orientation connecting the geometric centers of a bonded pair of grains. This vector is used as the bond plane orientation. For bonded spheres, this technique and the plane fit technique

for determining the contact orientation produce identical results. Here, the center-to-center orientation allows for more possibilities of contact orientation to be utilized with less sensitivity to the resolution of the volumetric data.

Utilizing the average contact tensor values for the artificially generated volumes shows a clear choice in the appropriate method for computing the orientation of individual contacts. When constructing the contact tensor using the plane fit orientations of the individual contacts, anisotropy is clearly indicated for all artificially generated volume sizes as seen in Figure 9-3. A 3-D volume consists of a stack of two dimensional planar images. Given enough randomly generated volumes, the distribution should show near isotropy every time. The unchanging anisotropy in the contact tensor as calculated by the plane-fit routine is a clear indication the grain and bond sizes are too small to allow diverse plane fit orientations. This situation is likely described by the limitations of small bonds illustrated in Figure 9-2.

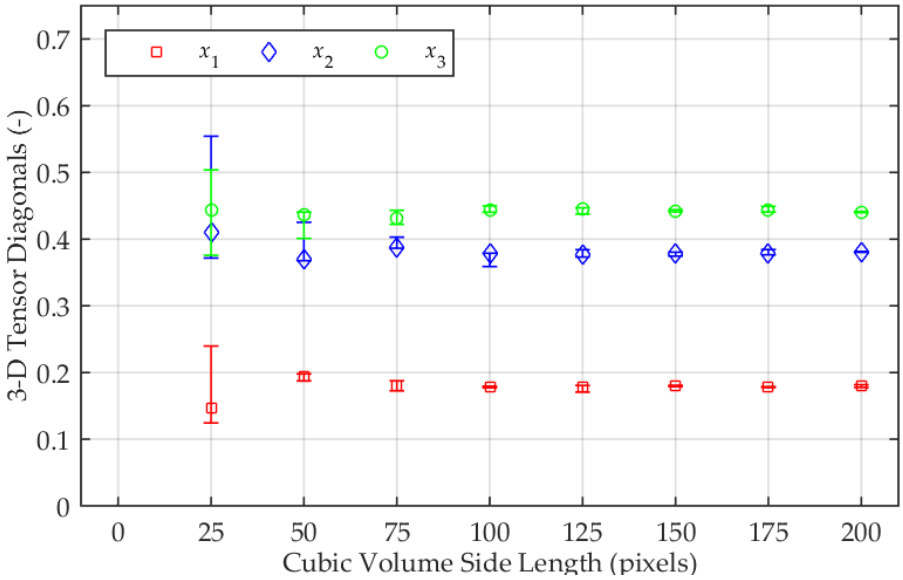


Figure 9-3: Contact tensor for randomly generated microstructures varying in cubic side length from 25 pixels to 200 pixels. The contact orientation was computed via a plane fit method.

Using the exact same volumes used to generate the plane fit calculated contact tensor in Figure 9-3, the contact tensor can be generated using a grain-center-to-grain-center method as previously described. As expected, the contact tensor using this center-to-center orientation to define individual contact orientations is much closer to an isotropic configuration as seen in Figure 9-4 below. Again, only 10 microstructures of each volume are generated. With more runs and computation time, it is expected near perfect isotropy would be generated.

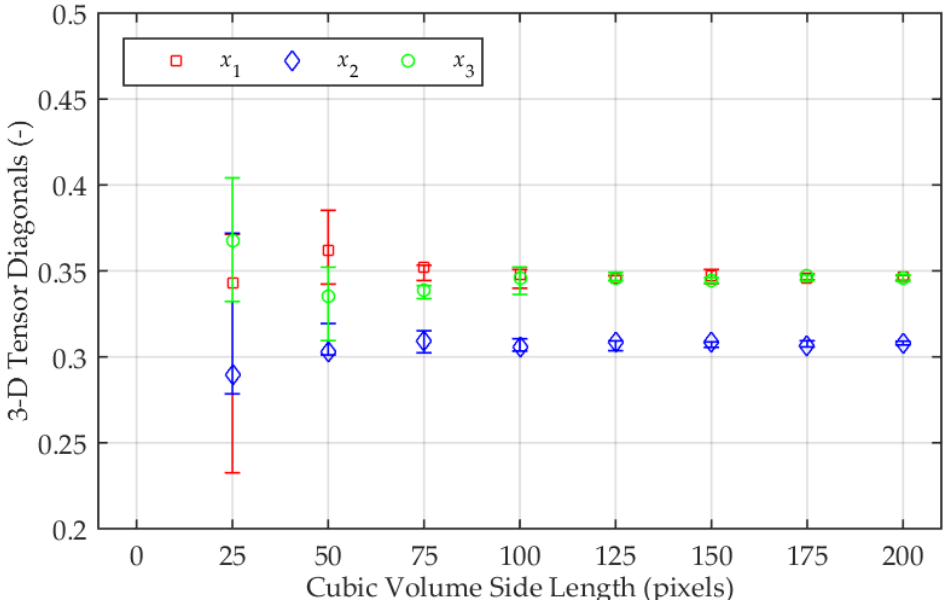


Figure 9-4: Contact tensor for randomly generated microstructures varying in cubic side length from 25 pixels to 200 pixels. The contact orientation was computed via a grain center-to-center method.

Continuing with the same randomly generated microstructures, the MIL tensor could also be computed for each sized volume. The average MIL tensor coefficients (shown in Figure 9-5) of 10 volumes of each size (same volumes as those used in computing the contact tensor) show a nearly isotropic geometric structure for almost all volumes. However, unlike the contact tensor, the uncertainty remains high with the 95% confidence intervals showing wide variation. This demonstrates the MIL tensor requires a volume of sufficient dimension to accurately compute the degree of anisotropy with high certainty.

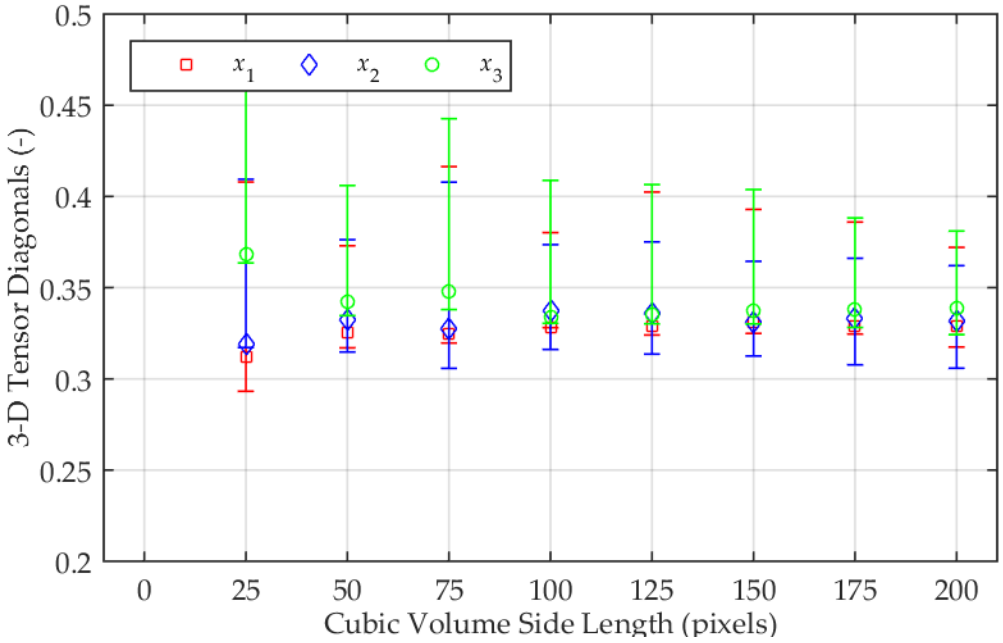


Figure 9-5: MIL tensor for randomly generated microstructures varying in cubic side length from 25 pixels to 150 pixels.

For CT scans of snow microstructures with average grain sizes ranging from 2-10 voxels in size, it is recommended the contact tensor is computed using the bonded grain center to grain center orientation for computation of individual contact orientations. Additionally, the contact tensor is able to compute directional quantities with higher confidence on smaller volumes than MIL tensor as shown by the results using artificial microstructures above. Regardless, using randomly generated microstructures should produce isotropic properties with regards to contact directions and geometric layout. This is reflected through the computation of the tensor ratio using the contact tensors and MIL

tensors from the previously mentioned randomly generated samples. The average tensor ratio for each volume in each coordinate direction is nearly 1 for almost all configurations. This is also expected since the microstructures were constructed using spherical grains. The average tensor ratio coefficients for each axial direction are plotted in Figure 9-6.

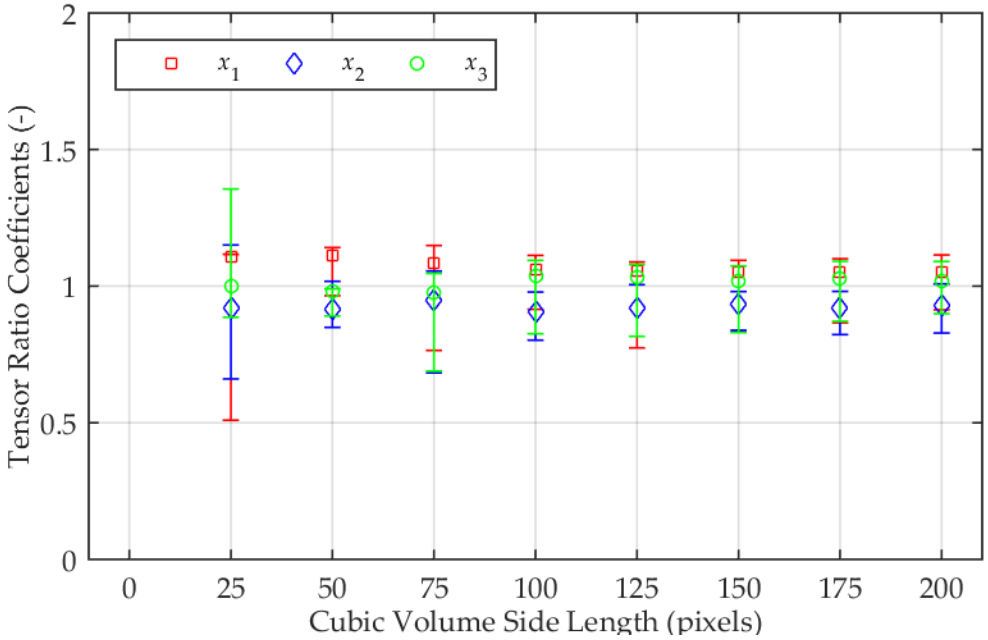


Figure 9-6: Tensor ratio for randomly generated microstructures varying in cubic side length from 25 pixels to 150 pixels.

9.2 Radiation Recrystallized Results

Each sample from the radiation recrystallized experiments was scanned according to the parameters discussed in Section 7.2. A Cartesian coordinate system is established for use with all systems. The x_1 and x_2 axial directions form

a plane parallel with the snow surface while the positive x_3 axis is normal to the snow surface (pointing in the direction of the atmosphere, see Figure 9-7). CT volume information is stored in image stacks containing cross-section data parallel to the x_1-x_2 plane and stacked in the x_3 direction. The cross-sectional dimensions of all samples are 340×340 pixels with the x_3 dimension set based on the final thickness of the faceted layer of each radiation recrystallization experiment (always ≥ 340 pixels). Using a consistent voxel resolution of $14.88\,\mu m$ for all scans produces images with a surface parallel cross-section of $5 \times 5\,mm$. As detailed in the previous section, a volume of this size should be more than sufficient for fabric tensor analysis. Conveniently, volumes of this size are also sufficient for use with finite element analyses (discussed in the next chapter) and exceed the recommended volume size established by Chandel et al. (2014).

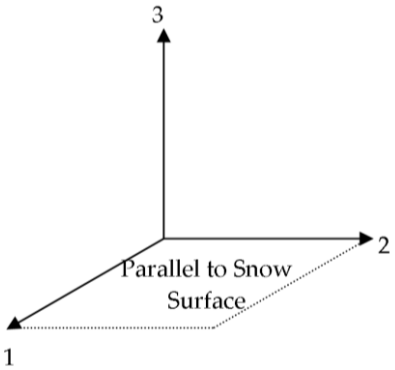


Figure 9-7: Coordinate system utilized by all CT-Scanned volumes. x_1 and x_2 establish a plane parallel to the snow surface.

Determining the appropriate height of each sample is accomplished through a combination of density analysis and visual inspection of the crystals of the final CT scan following recrystallization. Analyzing the density, the area fraction of solid objects for each 2-D cross sectional image is computed. This produces data showing how the area fraction (density) changes with respect to depth. An example of how density changes with respect to depth is illustrated in Figure 9-8. After examining the density profile for pattern changes, the crystal forms are manually inspected at areas of interest to determine the existence of faceted or rounded crystals at certain depths. Once the height of the final sample is determined using this technique, the same volume of interest is utilized for all volumes collected throughout the recrystallization of an individual experiment.

The final thickness of the faceted layers as determined by this technique is tabulated below in Table 9-1. These thicknesses represent the total thickness of all faceted crystal layers regardless of whether the dominate crystal morphologies change in distinct sub-layers as discussed earlier in Section 8.2. As will be discussed later, analysis of individual sub-layers is not possible using the fabric tensor technique employed here.

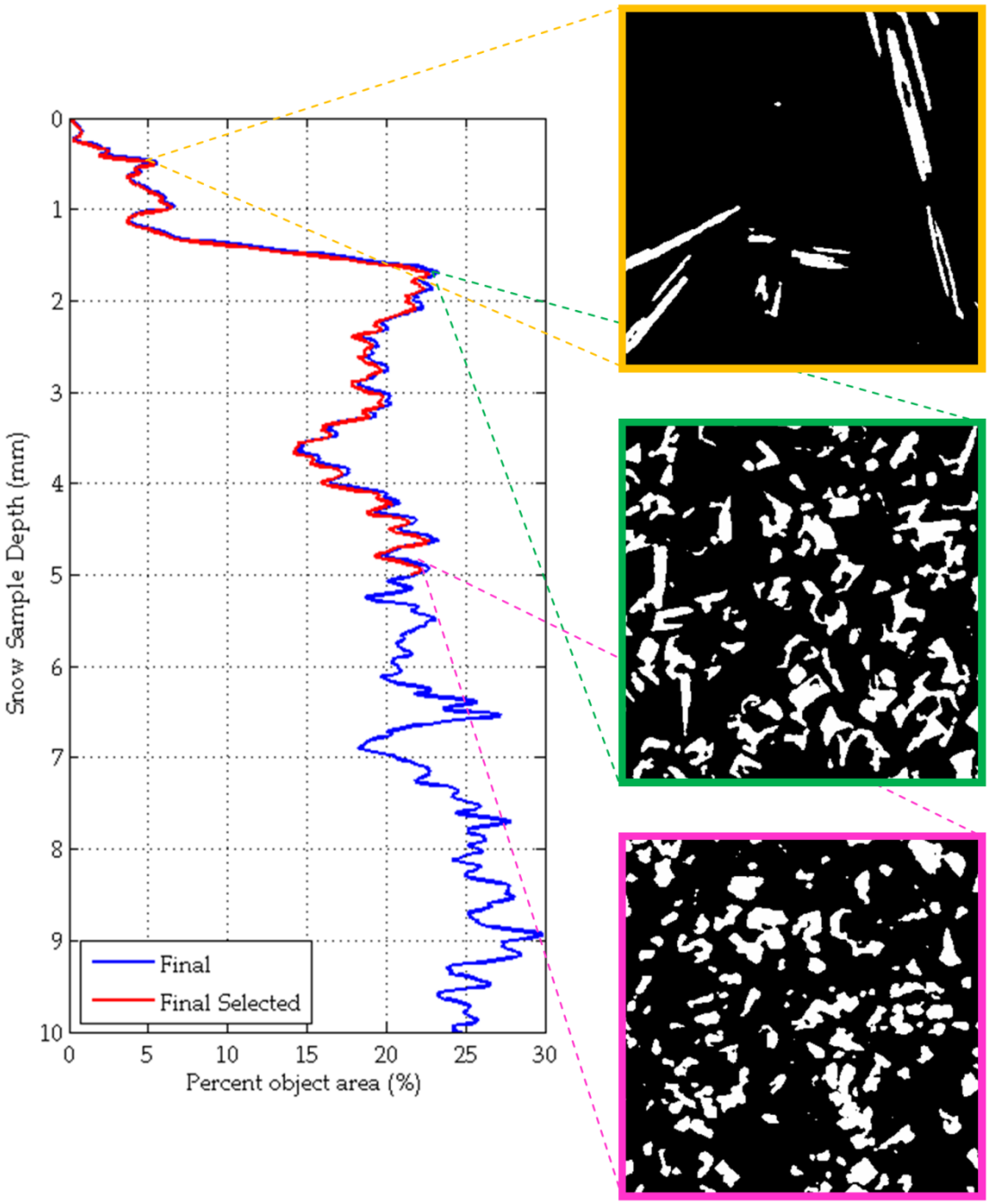


Figure 9-8: Area fraction (density) of ice grains for a fully radiation recrystallized sample. The red line indicates the final height of the sample selected for fabric tensor analysis. Qualitative observations are made of the crystals near the boundaries of the selection for verification of the presence of desirable crystal morphologies. Cross-sectional images are parallel to the snow surface.

Table 9-1: Thickness of CT analysis volumes for each experiment.

Experimental Sample	Analysis Thickness (mm)
New Snow 1 (NS1)	7.00
New Snow 2 (NS2)	5.13
New Snow 3 (NS3)	5.52
1 Week Old 1 (1W1)	7.00
1 Week Old 2 (1W2)	5.01
1 Week Old 3 (1W3)	7.95
2 Weeks Old 1 (2W1)	5.12

9.2.1 Fabric Tensor Analysis

Since the contact tenor, MIL tensor, and tensor ratio values are normalized values, it is appropriate to present average results from each type of experiment (new snow, 1 week old, 2 weeks old). However, when discussing the effective stiffness of the samples, each experiment contains a unique microstructure producing distinct effective properties. In the next subsection, calculated effective stiffnesses will be compared directly to the experimentally obtained stiffnesses presented in Section 8.3.

Starting with the new snow sample set (NS1, NS2, and NS3), the contact tensor was evaluated for each near surface sample at 3 hour intervals during the process of radiation recrystallization. The average contact tensor coefficients in the $x_1, x_2,$ and x_3 directions for all of the new snow tests are plotted in Figure 9-9. The initial microstructures were transversely isotropic with respect to the contact

tensor in the x_1-x_2 plane with more bond orientation components tending to align along the plane of isotropy rather than vertically. After 3 hours little has changed. At 6 hours and beyond, the fractions of contact orientation components converge toward isotropy at 12 hours.

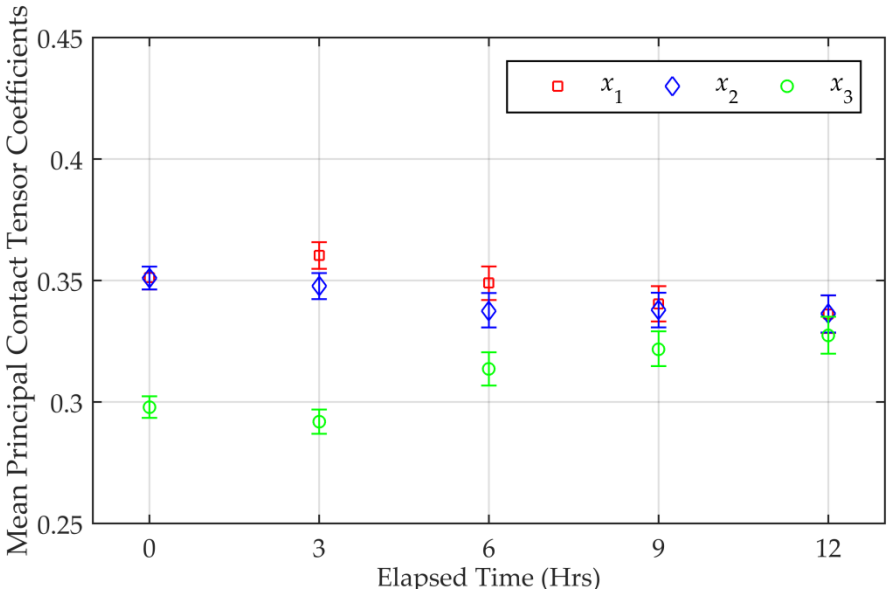


Figure 9-9: Average contact tensor coefficients of the three new snow experiments undergoing radiation recrystallization. Error bars represent the 95% confidence intervals.

The averages of the MIL tensor coefficients show isotropy or near isotropy throughout the duration of recrystallization (Figure 9-10). Although the total control volume bounding the measurement of the MIL tensor remains the same for the duration of each experiment, the 95% confidence intervals expand in the latter half of the experiments. This is likely due to the decrease in the total

number of grains inside the control volume later in the experiment to due decreases in near surface density (see Figure 8-23).

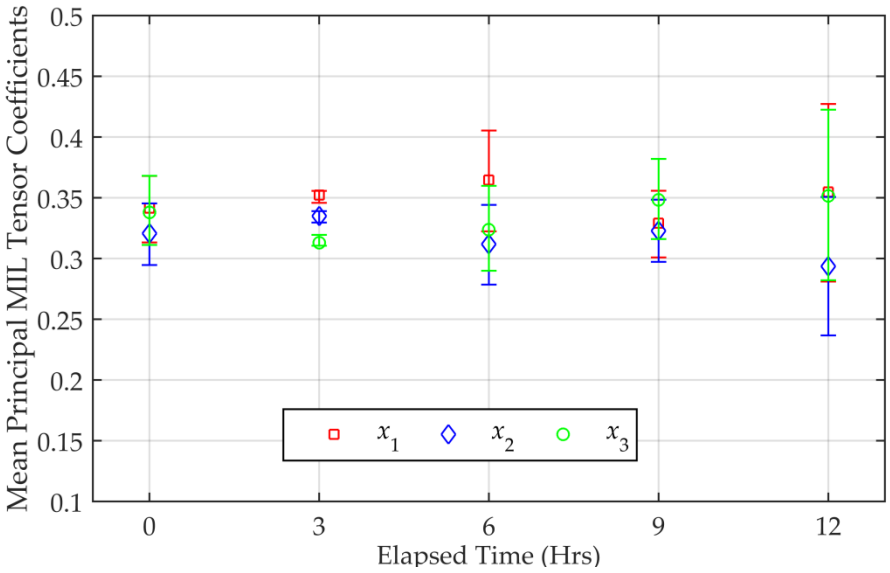


Figure 9-10: Average MIL tensor coefficients of the three new snow experiments undergoing radiation recrystallization. Error bars represent the 95% confidence intervals.

Using the computed contact tensor coefficients and MIL tensor coefficients, the tensor ratio is computed for each test and averaged to produce the result illustrated in Figure 9-11. The combined effects of the MIL tensor and contact tensor result in an initially weakly anisotropic tensor ratio that converges to isotropy about halfway through the radiation recrystallization process. However, the wider confidence intervals associated with the MIL tensor limits the statistical independence of most of the tensor ratio coefficients.

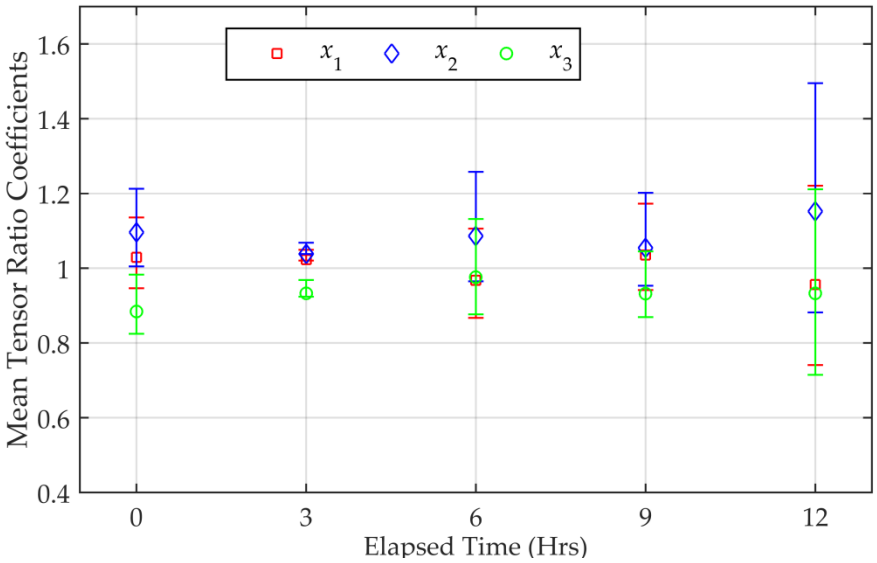


Figure 9-11: Average tensor ratio in each axial direction of the three new snow experiments undergoing radiation recrystallization. Error bars represent the 95% confidence intervals.

The group of three radiation recrystallization experiments conducted on a 1 week old snow surface exhibited similar results to the new snow samples. Again, the individual fabric tensor results are averaged and presented here. The contact tensor coefficients showed a nearly transversely isotropic structure initially, diverged away from transverse isotropy after 3 hours, and began converging slowly toward isotropy at 12 hours. The average contact tensor coefficients for the 1 week old snow surface are shown in Figure 9-12.

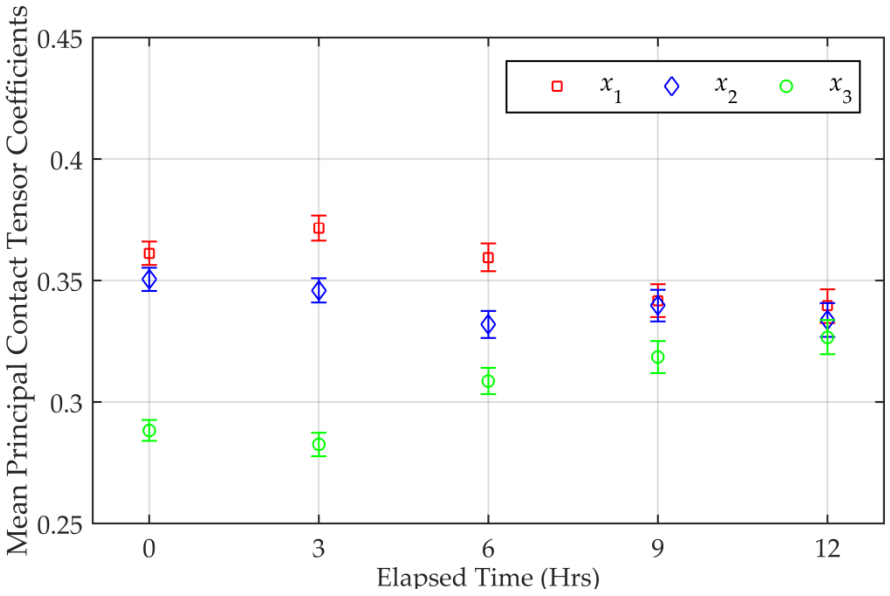


Figure 9-12: Average contact tensor coefficients of the three 1 week old snow experiments undergoing radiation recrystallization. Error bars represent the 95% confidence intervals.

The average MIL tensor diagonal coefficients shown in Figure 9-13 remain nearly isotropic throughout the duration of the test. Similar to the new snow samples, the spread of the 95% confidence intervals widen as near surface metamorphism progresses. The tensor ratio coefficients also look similar to the new snow experiments. Movement from a slightly non-isotropic tensor ratio to a final isotropic configuration is driven mostly by changes in the contact tensor. The average tensor ratio coefficients for the 1 week old snow samples are shown in Figure 9-14.

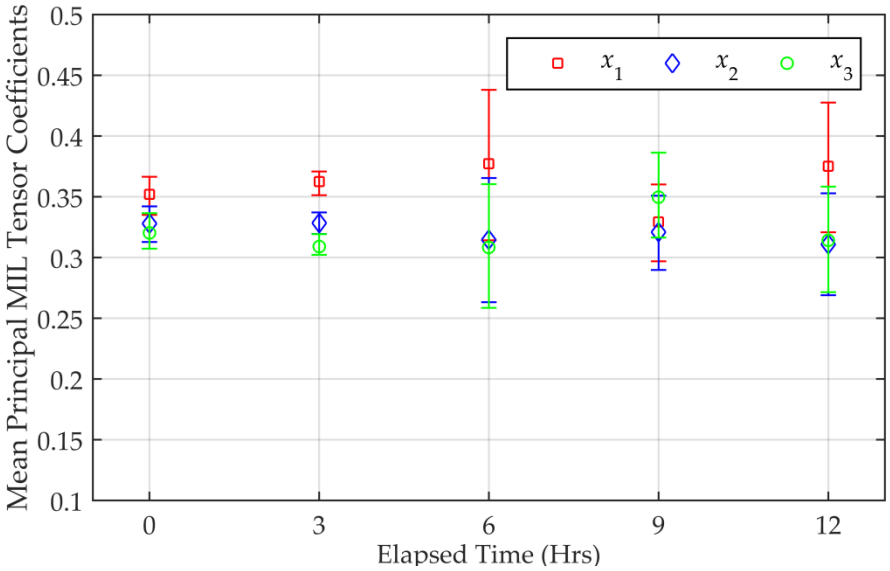


Figure 9-13: Average MIL tensor coefficients of the three 1 week old snow experiments undergoing radiation recrystallization. Error bars represent the 95% confidence intervals.

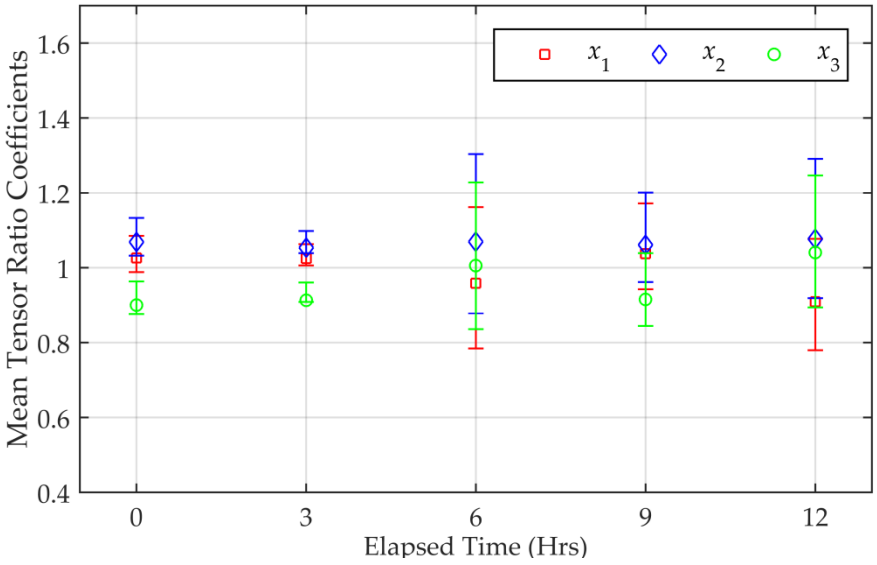


Figure 9-14: Average tensor ratio in each axial direction of the three 1 week old snow experiments undergoing radiation recrystallization. Error bars represent the 95% confidence intervals.

Only one 2 weeks old snow sample was tested experimentally due to its similarity to the other 1 week old samples. The results for the single test 2 weeks old test are presented here. As with the other tests, the contact tensor exhibited initial anisotropy that converged toward isotropy in the latter half of the recrystallization process. It is not known why the initial computation of the contact tensor did not show any transverse isotropy like other tests, but independent coefficients indicative of orthotropic symmetry. A higher order contact tensor would be required to capture more degrees of anisotropy (Shertzer, 2011). The progression of the contact tensor of the near surface during recrystallization is shown in Figure 9-15.

The MIL tensor coefficients are plotted in Figure 9-16. The MIL tensor coefficients also start off nearly isotropic through 3 hours of recrystallization. The next two intervals during recrystallization (6.5 hrs. and 9.5 hrs.) show slight preference of MIL tensor values in the x_1 direction, although edges of the confidence intervals still overlap with the edges of other coefficients' intervals. The final scan at 12 hours recovers an isotropic configuration, but with a wider spread of confidence intervals. Interpretation of this will be discussed later.

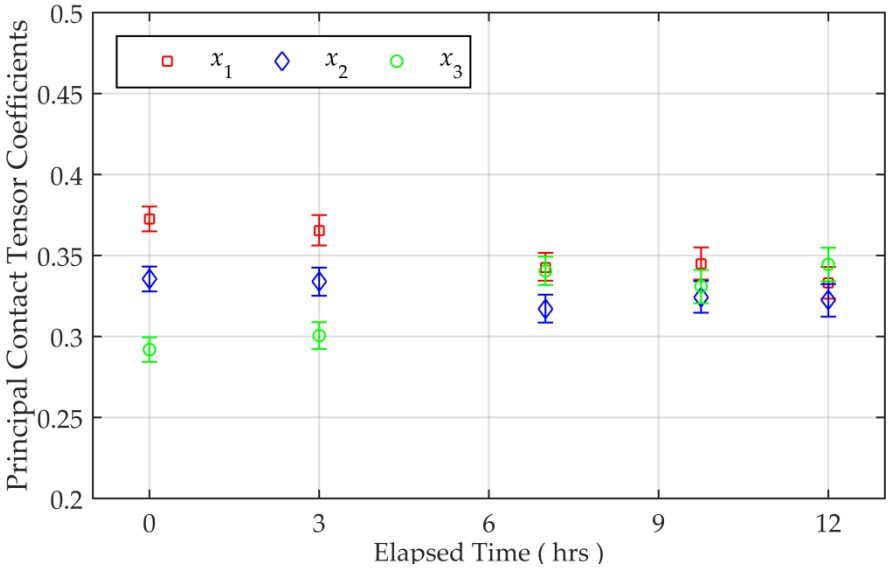


Figure 9-15: Contact tensor coefficients of the single 2 weeks old snow experiment undergoing radiation recrystallization. Error bars represent the 95% confidence intervals.

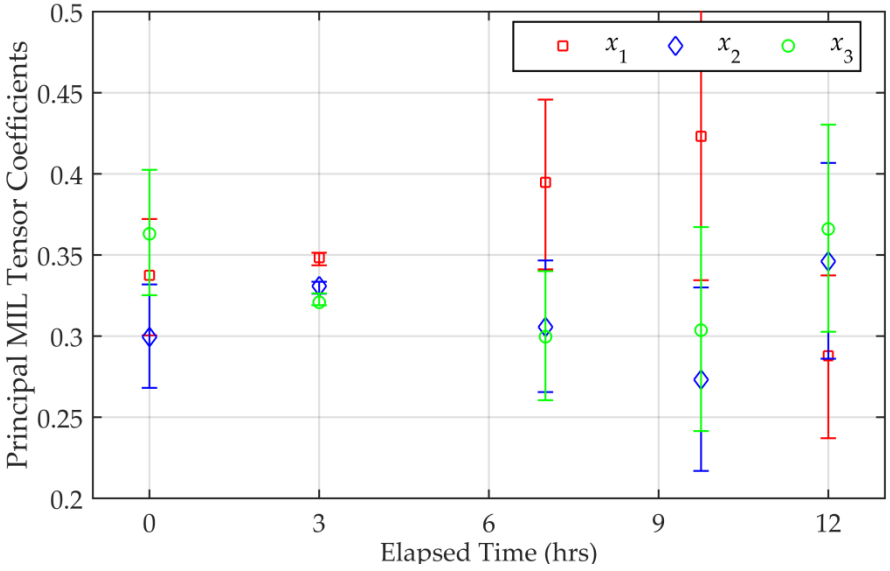


Figure 9-16: MIL tensor coefficients of the single 2 weeks old snow experiment undergoing radiation recrystallization. Error bars represent the 95% confidence intervals.

The tensor ratio starts off transversely isotropic with preference to the isotropic x_1-x_2 plane. The x_3 tensor ratio coefficient increases for the first half of the experiment then settles back toward 1 at the conclusion of the experiment. As with other experimental results, the final configuration was isotropic with wide confidence intervals in the latter half of the experiment. The tensor ratios for the 2 weeks old surface during recrystallization are plotted in Figure 9-17. Interpretation of the fabric tensor values will be discussed in subsection 9.2.3 following the presentation of calculated effective stiffness properties.

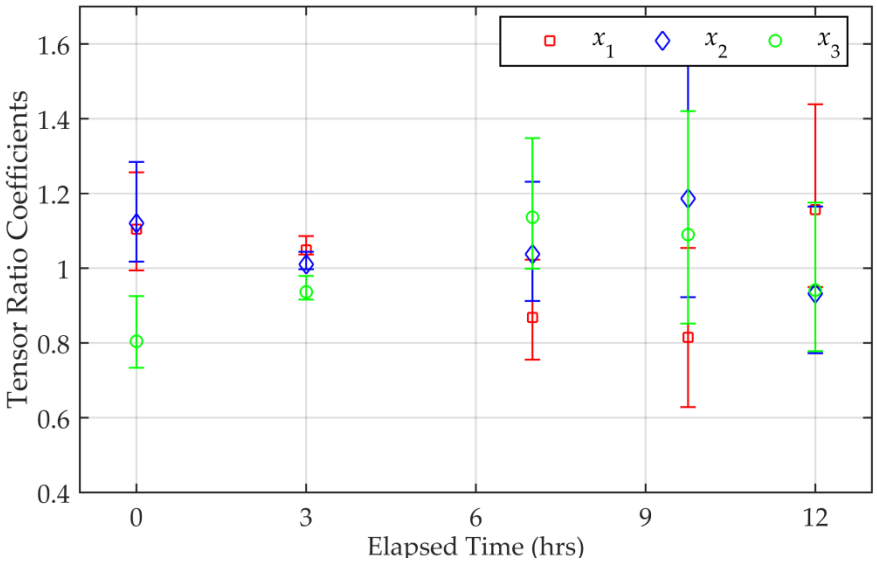


Figure 9-17: Tensor ratio coefficients of the single 2 weeks old snow experiment undergoing radiation recrystallization. Error bars represent the 95% confidence intervals.

9.2.2 Effective Material Properties

Each experiment produced unique results with several similarities and differences across the complete set of experiments. Effective material properties are computed using Shertzer's original model (2011), using the inclusion of the scalar shape factor (developed in Section 5.2), and finally using the inclusion of both the scalar shape factor and use of the tensor ratio for directional data (developed in Section 5.3). Additional pertinent microstructural information is also provided for further explanation in the discussion.

Effective Properties Using Shertzer Model. General results using Shertzer's original formulation (2011) are presented here using sample NS1 as an example. Several experiments showed similar trends and results. Experiments with key differences will be discussed separately. Sample NS1 is used to present effective properties when incorporating the scalar shape factor and tensor ratio in subsections that follow this. Individual fabric tensor computations for each experiment are presented with the mechanical testing data in Appendix F.

Sample NS1 started with a new snow surface which underwent 12 hours of radiation recrystallization. The sample was shear tested. The initial shear modulus (G_{23}) was measured as 1.34 MPa, and the final shear modulus of the radiation recrystallized layer (G_{23}) was 0.399 MPa for a total change of -70%.

Using the contact tensor as directional data, the temporal changes in effective Young's moduli and shear moduli are shown in Figures 9-18 and 9-19 respectively.

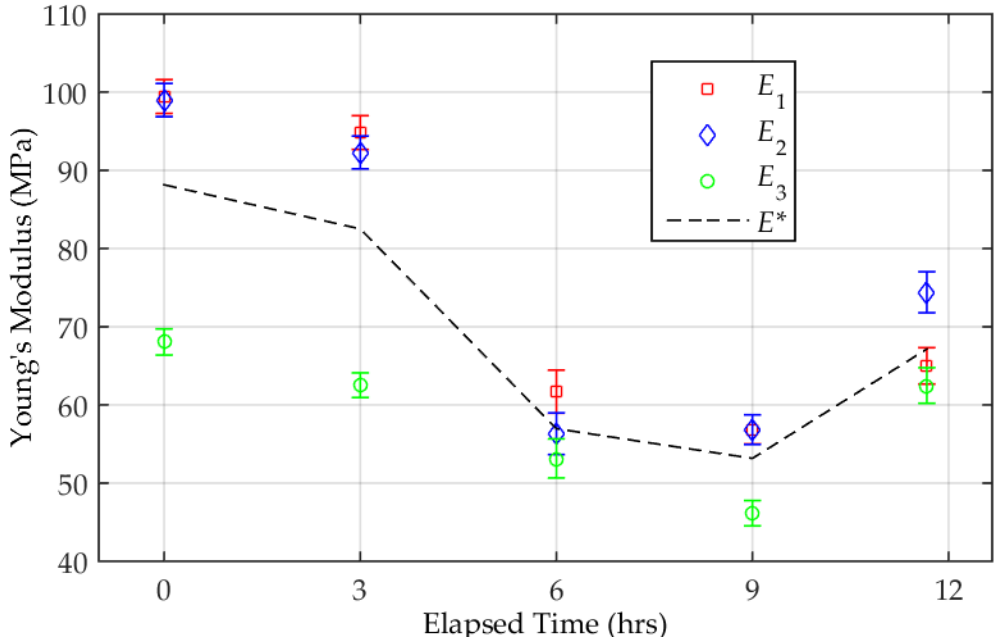


Figure 9-18: Computed effective Young's moduli using Shertzer's original formulation (2011) for sample NS1. E^* represents the isotropic approximation of effective Young's modulus using microstructural variables. E_i represents effective Young's modulus in the i^{th} axial direction using the contact tensor (Equation (4.27)) for directional data.

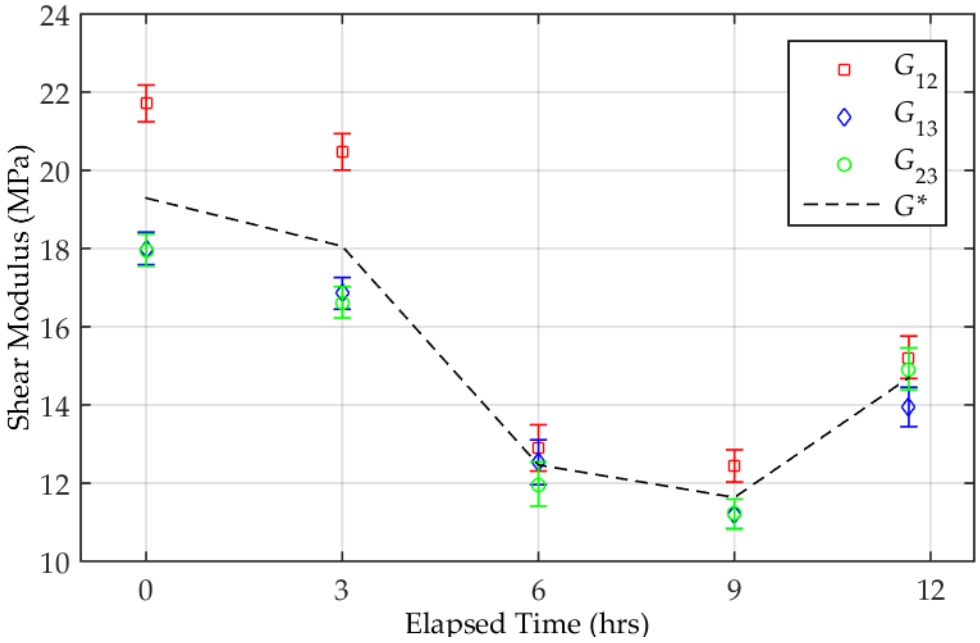


Figure 9-19: Computed effective shear moduli using Shertzer's original formulation (2011) for sample NS1. G^* represents the isotropic approximation of effective shear modulus using microstructural variables. G_{ij} represents effective shear modulus on the i^{th} face in the j^{th} direction using the contact tensor (Equation (4.28)) for directional data.

In both of the above figures, the starred value (e.g. E^*) represents the scalar approximation of the respective stiffness value as computed by Equation (3.21). This equation alone does not take into account any directionality of the grains or bonds and thus can only represent a non-directional scalar quantity. The colored coefficients in the figures depart from the scalar value using directional data and are computed as in Equations (4.27) and (4.28). Starting with the scalar values in both figures above, changes are driven by 3 quantities:

ice volume fraction ϕ, bond radius to grain radius ratio $\hat{\rho}/\hat{R}$, and mean 3-D coordination number $\mathcal{N}$.

The ice volume fraction versus time is plotted in Figure 9-20. The volume fraction holds steady near 20% before decreasing to 15% after 9 hours and holding steady at the final scan. The changes in volume fraction are minor contributions to the changes in effective moduli. The mean bond radii, grain radii, and bond-to-grain radius ratios are plotted in Figure 9-21. The bond-to-grain radius ratio holds steady just below 0.6 and does not contribute significantly to the change in effective properties for experiment NS1.

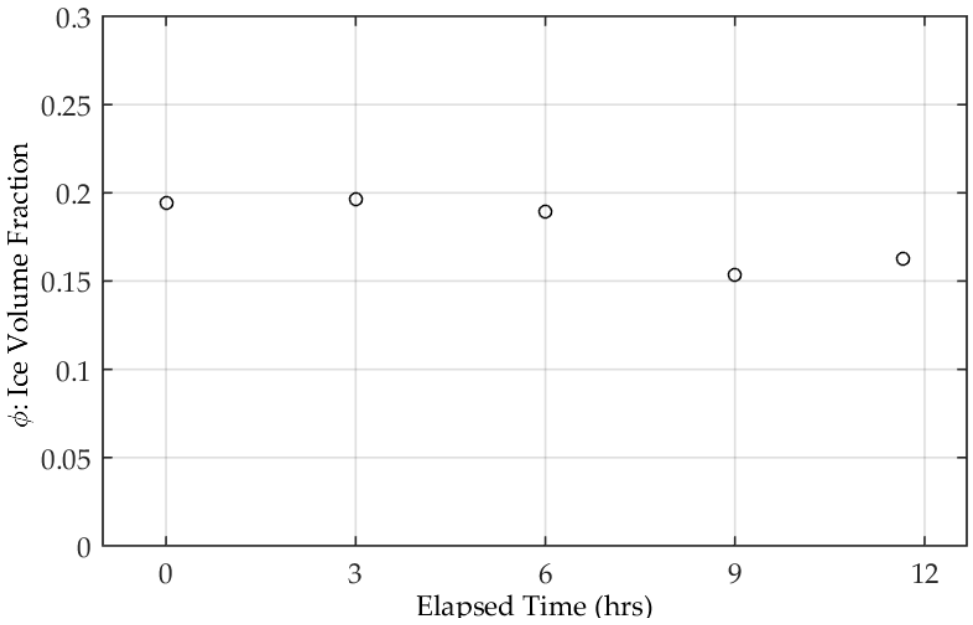


Figure 9-20: Evolution of ice volume fraction during recrystallization of sample NS1.

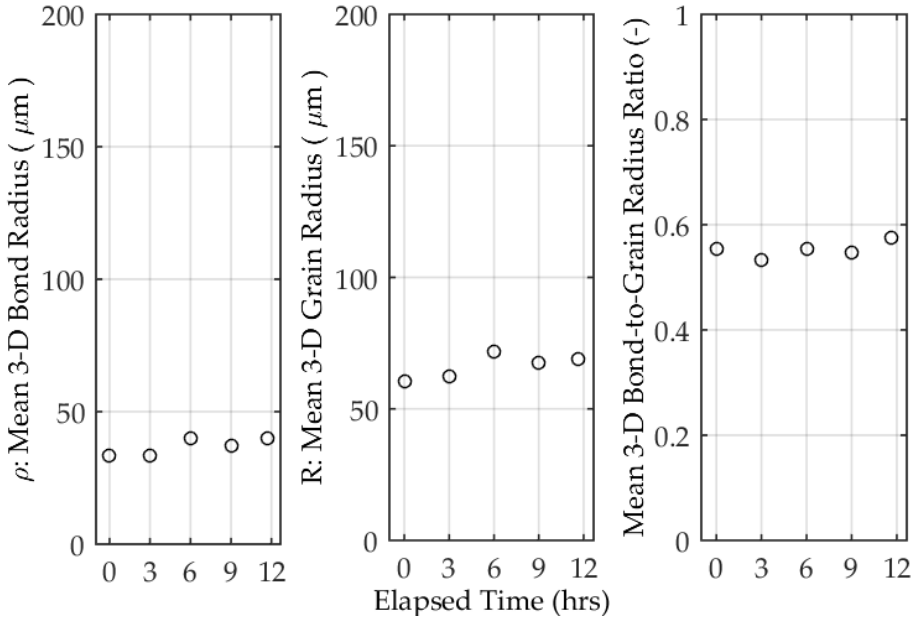


Figure 9-21: Mean 3-D bond radii, grain radii, and bond-to-grain radius ratio development during recrystallization of experiment NS-1.

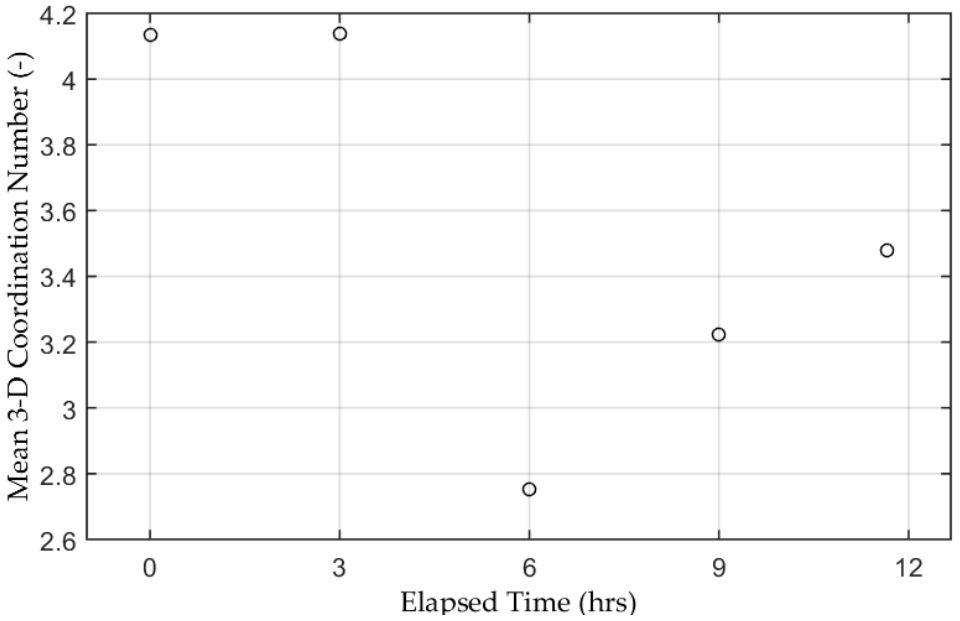


Figure 9-22: Evolution of mean 3-D coordination number during recrystallization of experiment NS1.

The mean 3-D coordination number, indicating the average number of bonds per grain, is plotted above in Figure 9-22. $\mathcal{N}$ drops significantly from 3 hours to 6 hours then rises again for the remainder of the experiment. Trends for the mean coordination number were difficult to establish as this measure behaved erratically across all experiments. Regardless, the sharp drop and slow increase of $\mathcal{N}$ along with changes in ϕ combine to cause the decline then upturn in the E^* and G^* values in Figures 9-18 and 9-19.

The departures from the isotropic values are driven by the changes in the contact tensor $\boldsymbol{F}$ over time. Observing the average contact tensor values for new snow experiments shown in Figure 9-9, preference is given to the isotropic plane parallel to the snow surface leading to E_1 and E_2 values above the scalar E^* value and E_3 computed well below the E^* value. Although the computed value for E^* changes over time, the separate Young's moduli slowly converge toward that value, indicating an evolution toward isotropy. Similar behavior is observed in the shear modulus data. Using the MIL tensor for directional data instead of the contact tensor would have produced values that tracked closely with the scalar effective properties due to the nearly constant isotropic texture expressed by the MIL tensor.

The computed shear modulus using Shertzer's model is an order of magnitude higher than the measured shear modulus (G_{23}) both at the initial time step (17.96 MPa compared to 1.34 MPa measured) and the final time step (14.91 MPa compared to 0.399 MPa measured). Regardless of the absolute values computed by Shertzer's original model, the relative change from beginning to end was only -17%: far from the -70% in the measured results. Samples NS2, 1W1, and 1W2 all produced similar results.

Samples NS3 and 1W3 showed decreasing effective scalar properties (E^* and G^*) for the duration of the experiment with no upturn at the end – unlike previously described tests. Using the results from sample 1W3, the effective Young's moduli and shear moduli are plotted in Figures 9-23 and 9-24 respectively.

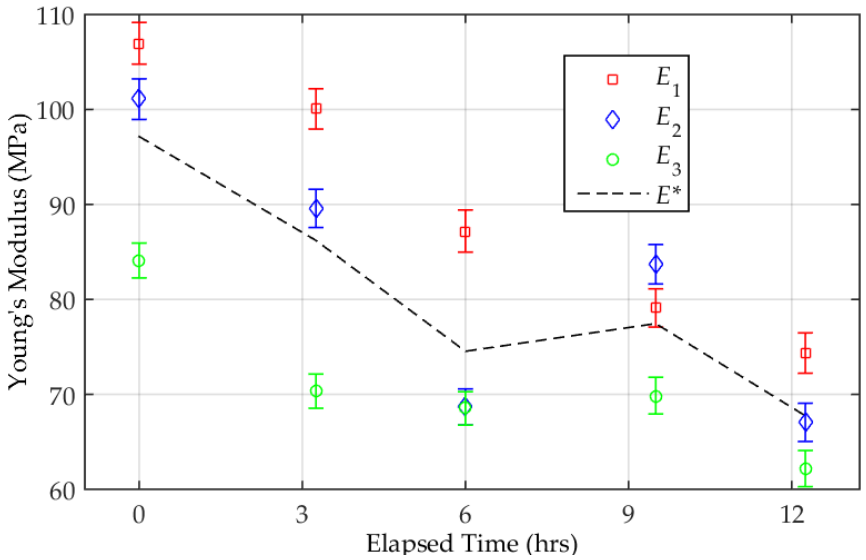


Figure 9-23: Computed effective Young's moduli using Shertzer's original formulation (2011) for sample 1W3. E^* represents the isotropic approximation of effective Young's modulus. E_i represents the effective Young's modulus in the i^{th} axial direction using the contact tensor for directional data.

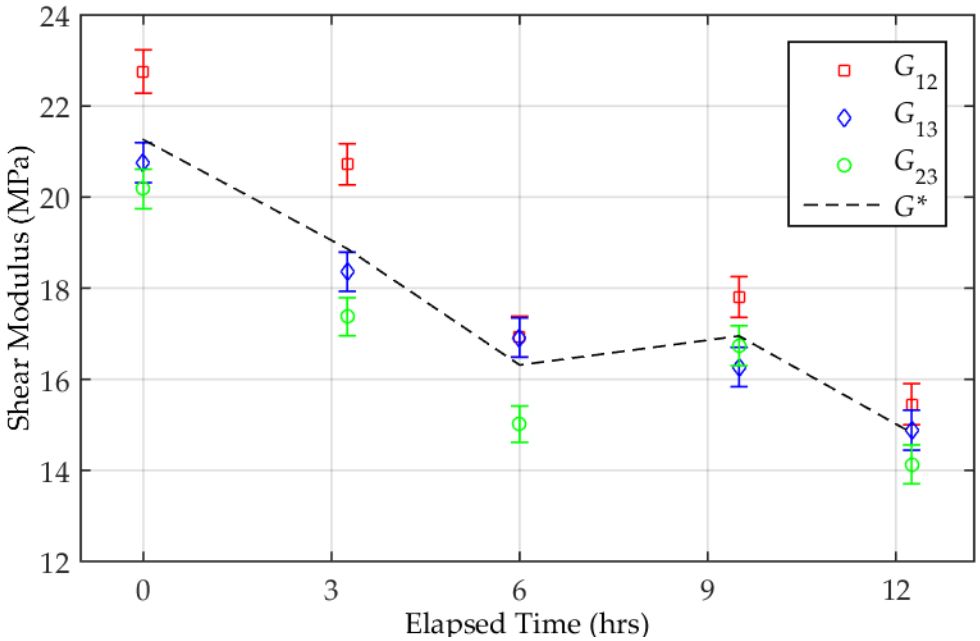


Figure 9-24: Computed effective shear moduli using Shertzer's original formulation (2011) for sample 1W3. G^* represents the isotropic approximation of effective shear modulus. G_{ij} represents the effective shear modulus on the i^{th} face in the j^{th} direction using the contact tensor for directional data.

Regardless of the slightly different microstructural makeup at the end of the experiment for samples NS3 and 1W3, the deficiencies in Shertzer's original formulation when applied to mechanical properties remain the same as the previously presented experiments. In the case of sample 1W3, the Young's modulus in the x_3 direction was measured directly with a laboratory mechanical test. E_3 was measured initially as 2.28 MPa – nearly two orders of magnitude less than the computed value of 84.11 MPa from Figure 9-23. The final Young's modulus in the x_3 direction measured in the lab was 0.529 MPa. The computed value using microstructural parameters unaltered from Shertzer's formulation was 62.13 MPa.

One experiment that produced fabric tensor results unlike any other experiment was sample 2W1 (the 2 weeks old snow surface). Macroscale testing did not suggest any discernable differences following radiation recrystallization when compared to other experimental samples. However, the microstructural results show contradictions with other experiments with regards to effective Young's moduli and shear moduli increasing for the duration of the radiation recrystallization experiment. The effective Young's moduli are plotted in Figure 9-25 with the effective shear moduli following in Figure 9-26.

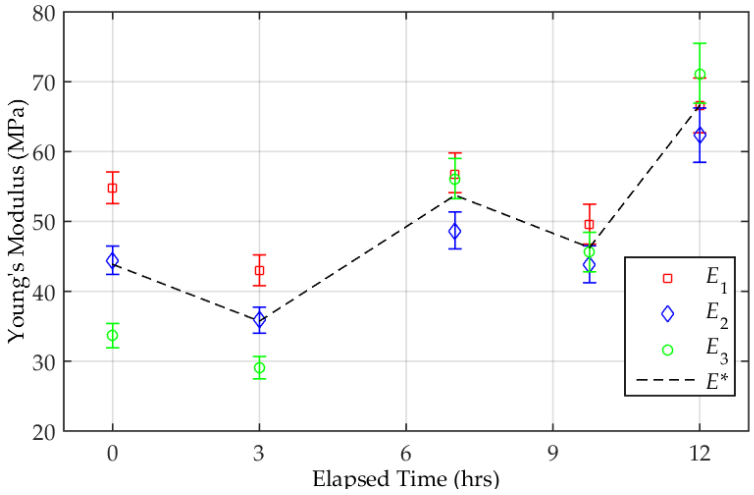


Figure 9-25: Computed effective Young's moduli using Shertzer's original formulation (2011) for sample 2W1. E^* represents the scalar approximation of effective Young's modulus. E_i represents the effective Young's modulus in the i^{th} axial direction using the contact tensor for directional data.

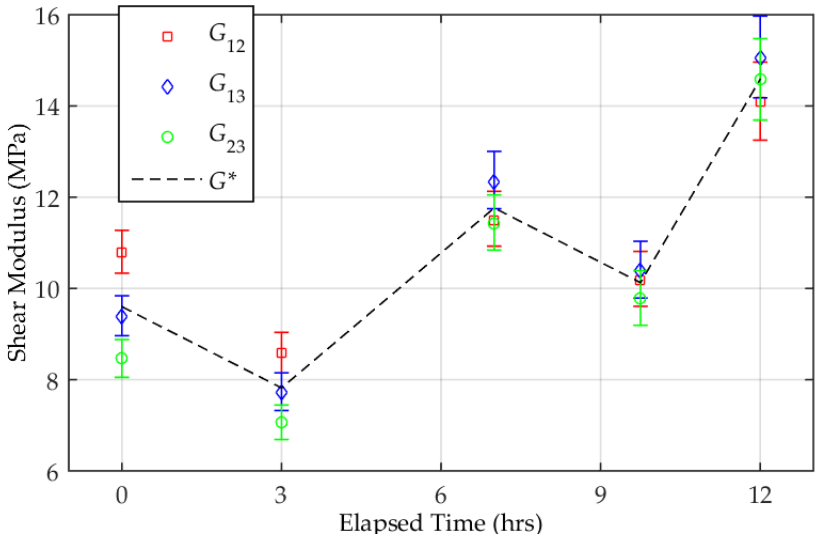


Figure 9-26: Computed effective shear moduli using Shertzer's original formulation (2011) for sample 2W1. G^* represents the scalar approximation of effective shear modulus. G_{ij} represents the effective shear modulus on the i^{th} face in the j^{th} direction using the contact tensor for directional data.

The evolution of the fabric tensor coefficients is similar to the other tests as illustrated in the previous section (Figures 9-15 through 9-17). However, unlike other experiments, the mean 3-D coordination number $\mathcal{N}$ increased for the duration of the experiment (Figure 9-27) as did the mean bond-to-grain radius ratio $\hat{\rho}/\hat{R}$ (Figure 9-28). Both of these values combined produced the upturn in effective moduli illustrated in the figures below. The coordination number was initially much lower than the other experiments. Other differences and anomalies with this particular experiment will be discussed separately in the discussion subsection that follows.

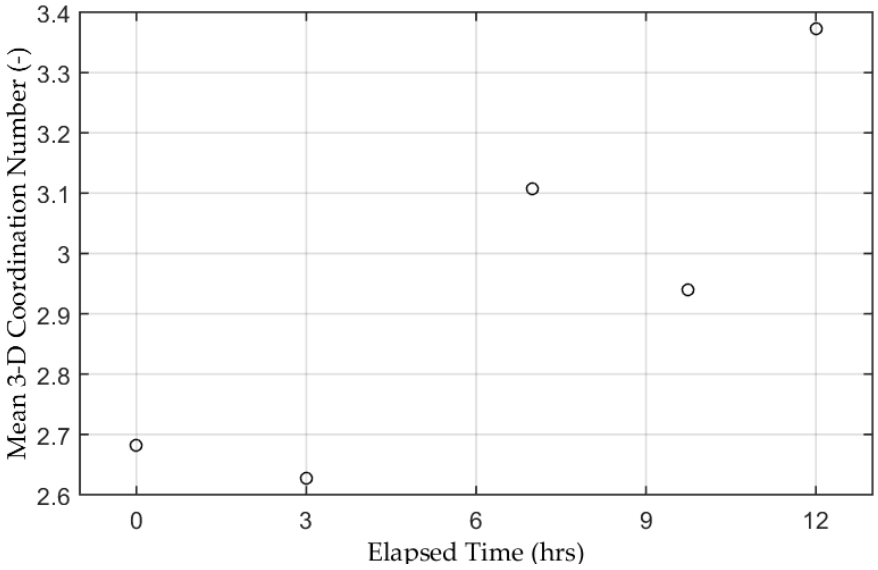


Figure 9-27: Mean 3-D coordination number for experiment 2W1. Unlike other results, the connectivity increases during radiation recrystallization.

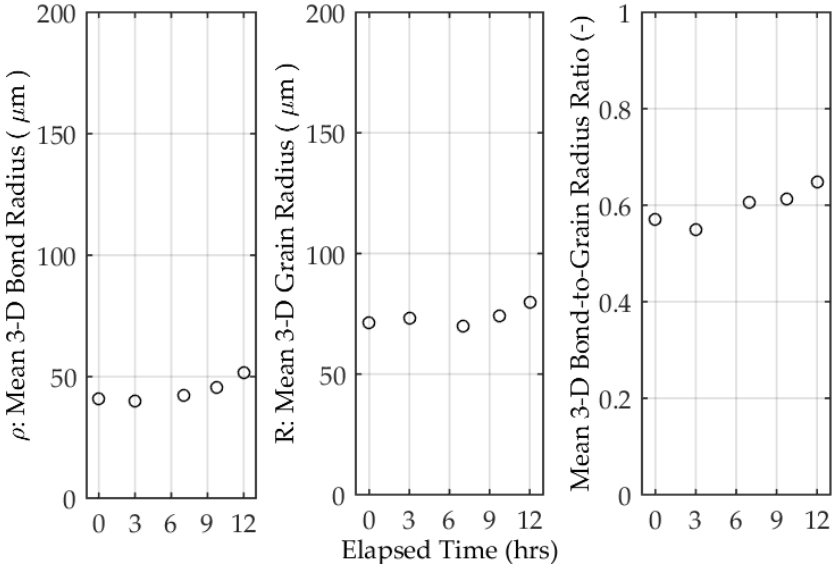


Figure 9-28: Mean bond radius and grain radius data for experiment 2W1. Unlike other experiments, the bond-to-grain radius ratio increases during radiation recrystallization.

Effective Properties with the Scalar Shape Factor. The scalar shape factor S is developed in detail in Section 5.2. The scalar shape factor only adjusts the computed effective coefficients by a scalar value as seen in Equation (5.4). Continuing with experimental sample NS1, the scalar shape factor S is plotted versus time in Figure 9-29 below. A shape factor value of $S = 1$ corresponds to spherical grains whereas $S = 0$ corresponds to a completely flattened grain (ellipsoid flattened to a line). The plotted values of S for sample NS1 suggest highly elliptical grains and thus reduce the overall stiffness of the sample both axially and in shear.

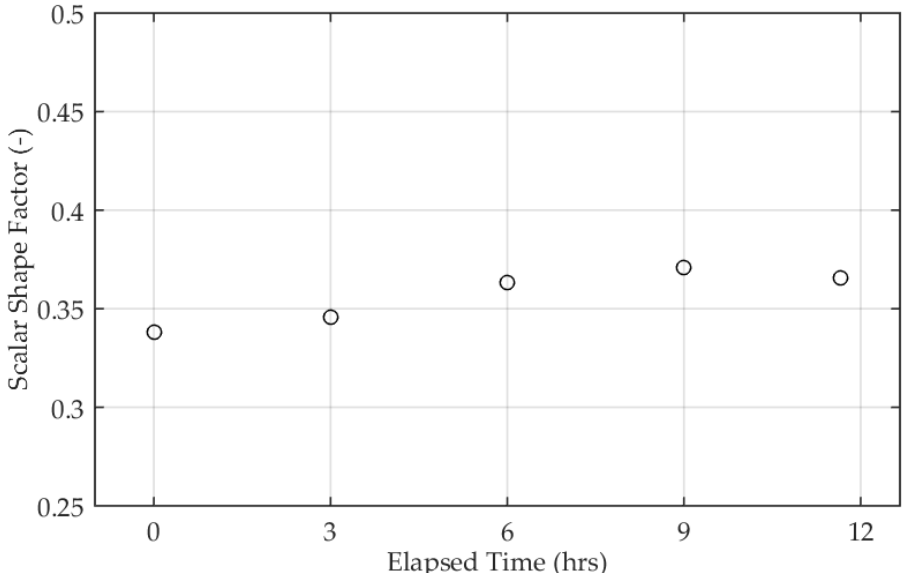


Figure 9-29: Scalar shape factor S for experimental sample NS1. Values of $S = 1$ correspond to perfectly spherical grains and $S = 0$ correspond to completely flattened grains (a line with no thickness).

The adjusted values for Young's moduli and shear moduli are plotted in Figures 9-30 and 9-31 respectively. The plots here look very similar in shape to Figures 9-18 and 9-19 because the computed effective moduli only vary by a scalar factor, S. The scalar shape factor brought the calculated effective shear modulus G_{23} closer to agreement with the experimentally tested results. Now the initial shear modulus is calculated as 6.07 MPa compared to 1.34 MPa experimentally, and the final shear modulus calculated as 5.45 MPa compared to 0.399 MPa experimentally.

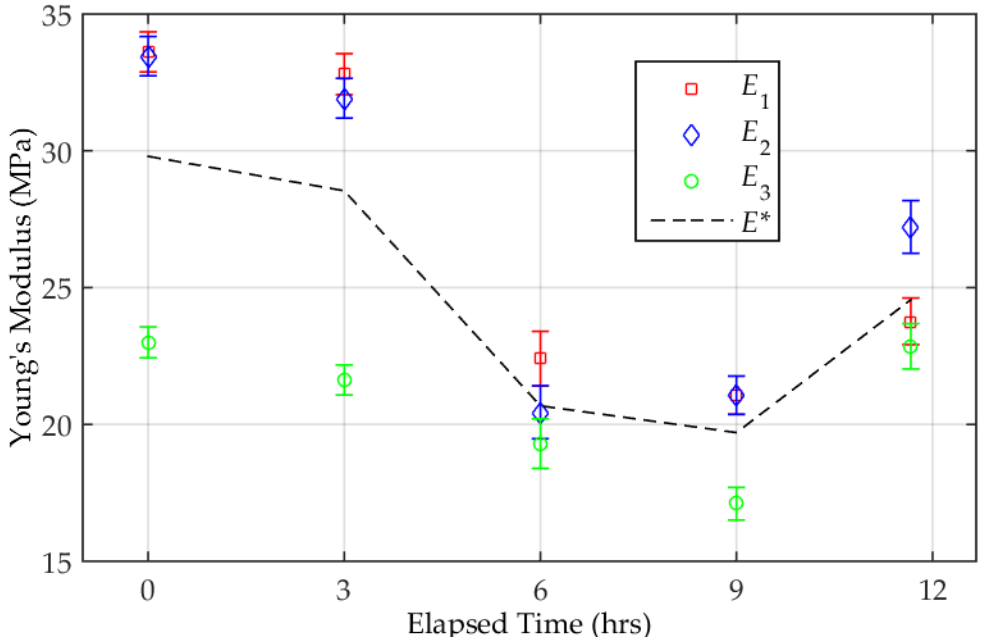


Figure 9-30: Computed effective Young's moduli incorporating the scalar shape factor *S* for sample NS1.

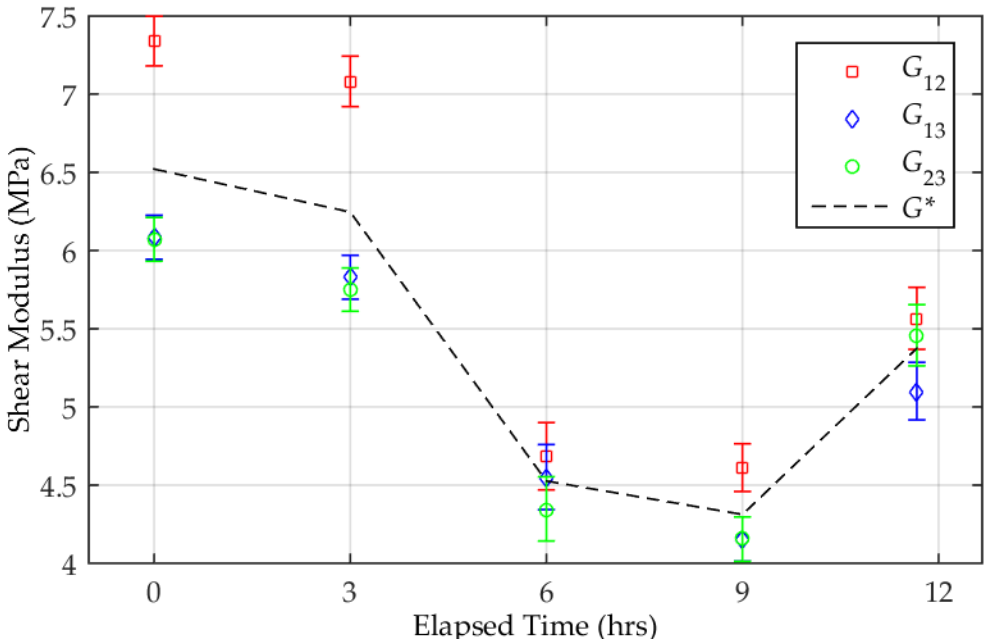


Figure 9-31: Computed effective shear moduli incorporating the scalar shape factor *S* for sample NS1.

The remaining 6 experimental samples not discussed here had similar distributions of scalar shape factors as those in Figure 9-29 and varied between 0.3 and 0.4. The shapes of the distributions remained unchanged and only the magnitudes of computed moduli were reduced by the amount of the computed shape factors for each experimental sample at each sampling time. The relative difference between anisotropic stiffness coefficients and the computed scalar isotropic value remains unchanged as well. A complete set of figures for each individual experiment is provided in Appendix E.

Effective Properties with Scalar Shape Factor and Tensor Ratio. The introduction of the tensor ratio $\boldsymbol{\Gamma}$ as a second order fabric tensor offers a way to relate the similarities or differences between two other fabric tensors: the contact tensor $\boldsymbol{F}$ and the MIL tensor $\boldsymbol{H}$. Development of the tensor ratio is detailed in Section 5.3. The tensor ratio, being a directional quantity, will only affect the computation of the anisotropic stiffness coefficients relative to the computed scalar value.

Using experimental sample NS1 as an example, the effective Young's moduli and shear moduli, as computed using the scalar shape factor S and the tensor ratio $\boldsymbol{\Gamma}$, are illustrated in Figures 9-32 and 9-33 below. Using the tensor ratio for directional data, G_{13} and G_{23} remain nearly identical reflecting the

isotropic plane of the transversely isotropic microstructure. However, due to the statistical uncertainty associated with the MIL tensor, the confidence intervals at all time steps are wide and overlap indicating statistically the microstructure remains nearly isotropic. Little change is observed in the effective shear moduli in the isotropic plane: initially at 6.20 MPa and finally at 5.21 MPa. These results are quite similar to those computed using just the scalar shape factor.

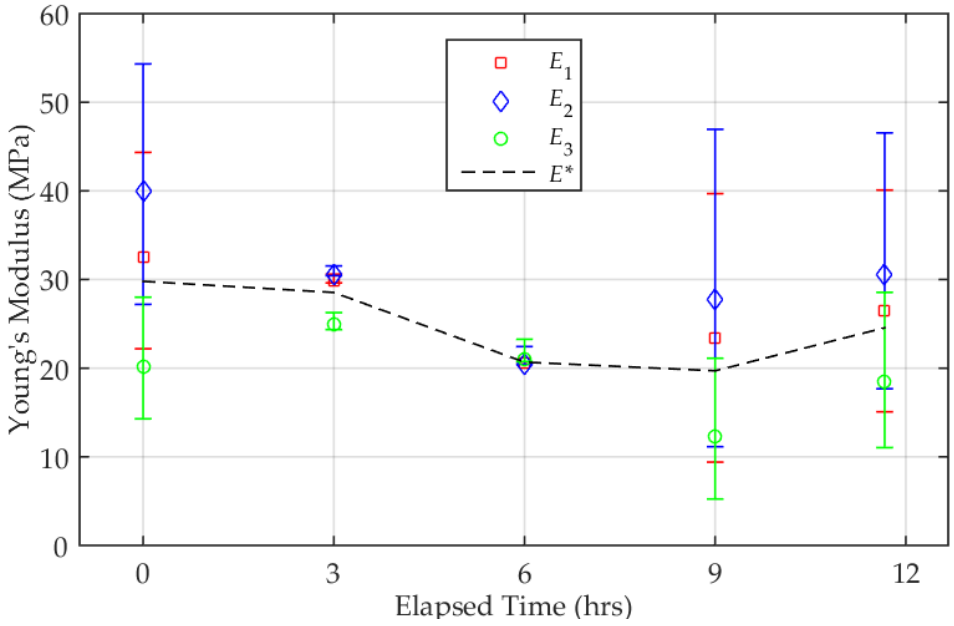


Figure 9-32: Computed effective Young's moduli incorporating the scalar shape factor S and the tensor ratio $\boldsymbol{\Gamma}$ for sample NS1.

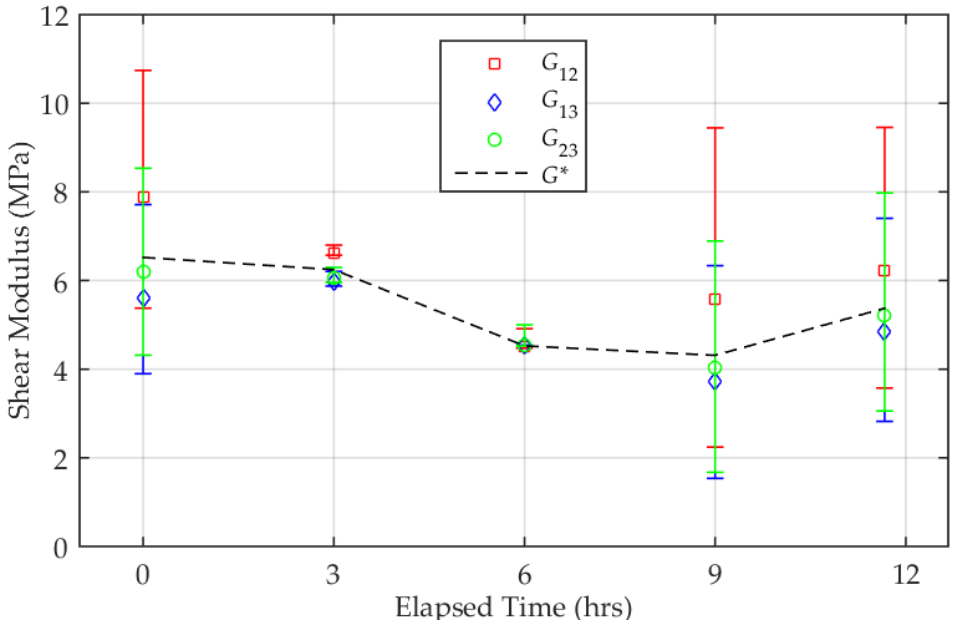


Figure 9-33: Computed effective shear moduli incorporating the scalar shape factor S and the tensor ratio $\boldsymbol{\Gamma}$ for sample NS1.

Performance of the tensor ratio is similar across all experimental samples. Computed values of the elastic moduli using the tensor ratio are sensitive to the amount of error introduced by the MIL tensor. Individual results for each experiment are listed in Appendix E.

9.2.3 Discussion of Faceted Layer Tensor Results

Contact Tensor Results. The trends showed in the evolution of the contact tensor are encouraging. Radiation recrystallized snow is a specialized form of temperature gradient metamorphism. Shertzer and Adams (2011) and Shertzer et al. (2010) utilized the contact tensor to investigate anisotropic changes in

thermal conductivity. In their study, Shertzer and Adams (2011) used CT scans from Schneebeli and Sokratov (2004) taken every 8 hours during the growth of depth hoar. The temperature gradient was positioned parallel to the x_1 axis in their study. Figure 9-34 below is reproduced from Shertzer and Adams (2011). Although it shows the effective thermal conductivity, it also reflects the relative computed values of the contact tensor. Initially, it shows a slightly anisotropic initial structure that converges to isotropy after approximately 1.5 days, and then develops into a strong preference for the x_1 direction. Here, the temperature gradient was a constant $100°\mathrm{C} \cdot \mathrm{m}^{-1}$.

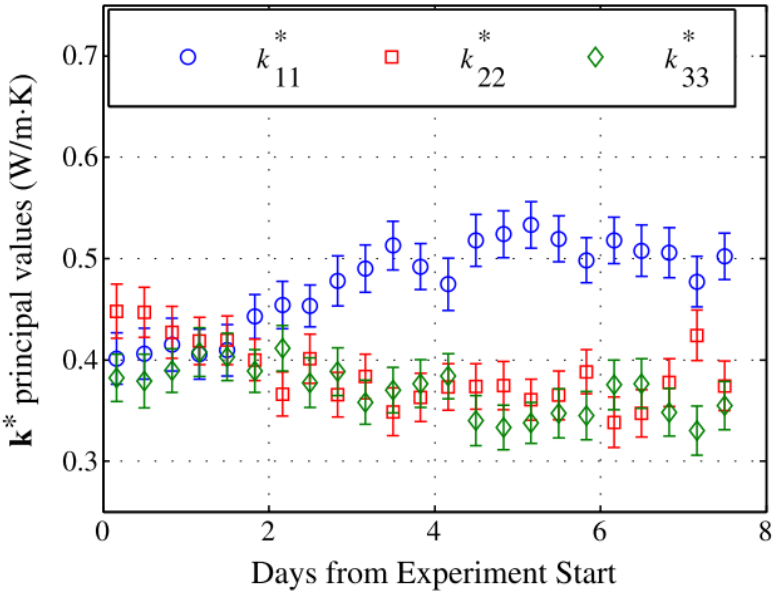


Figure 9-34: Effective thermal conductivity of depth hoar being grown with a $100°\mathrm{C} \cdot \mathrm{m}^{-1}$ temperature gradient in the x_1 direction (taken from: Shertzer and Adams, 2011).

In experiments conducted here, the temperature gradients were generally $\nabla T > 300°\mathrm{C} \cdot \mathrm{m}^{-1}$. It is expected that metamorphism would occur at an accelerated rate given the higher temperature gradient. Plots of the of the contact tensors in Figures 9-9, 9-12, and 9-15 show a similar evolution of the microstructure as the Shertzer and Adams study (2011) – at least to the convergence of isotropy. In the experiments here, the temperature gradient is parallel to the x_3 axis instead of the x_1 axis in the Shertzer and Adams study (2011).

Although the evolution of the contact tensor for the early stages of depth hoar development appears similar to the evolution for the radiation recrystallized layers, nothing can be said conclusively between these two studies regarding the contact tensor. As will be discussed later, the contact tensor (as well as other fabric tensors) may not accurately reflect the true textural anisotropy of the radiation recrystallized layers.

Sample 2W1 Discussion. Experimental sample 2W1 (2 weeks old snow surface) produced anomalous effective stiffness coefficients using the homogenization approach. Macroscale mechanical testing in shear showed a decrease in shear modulus ($G_{23} = G_{13}$) of approximately 17.7% from the initial configuration to the faceted configuration. However, using homogenization, the

shear modulus G_{23} increased from its initial configuration 44.5% using the tensor ratio for directional data and the scalar shape factor. This was the only experiment to show an overall increase in stiffness as calculated by microstructural variables even though the actual mechanical test results showed a decrease in stiffness.

As previously reported, the mean 3-D coordination number $\mathcal{N}$ generally increased throughout the duration of the experiment as captured by CT scans obtained every 3 hours (see Figure 9-27). All other experiments saw a general decrease in coordination number and all others started with coordination numbers $\mathcal{N} > 3$. The coordination number was the most influential parameter in causing an increase in the effective stiffness coefficients.

Additionally, the volume fraction of the near surface remained steady between 11% and 14% — significantly lower than other experiments. To investigate the abnormally low density in the CT scans obtained during recrystallization process, the initial CT scan was compared to a separate CT scan obtained prior to the initial mechanical test. The 2 separate scans were conducted on two separate sub volumes of the same sample at the same stage of metamorphism. The CT scan obtained prior to the macroscale mechanical test showed a volume fraction of 27%. The volume fraction of the sample obtained at

the beginning of the radiation recrystallization experiment (following the mechanical test) had a measured volume fraction of 14%.

Samples taken at the same stage of metamorphism but from separate regions of the snow sample should show approximately the same microstructure. When different densities and microstructures are recorded, it is suspected that deficiencies in the preparation of this sample occurred. Because of these recorded differences, it is unknown whether the macroscale mechanical tests or the microstructural analysis offer a valid investigation of the changes in mechanical properties for this particular experiment. Although some data from this experiment appears usable, the unexplainable differences between the macroscale test and the microstructural results render the results of this particular sample invalid.

MIL Tensor Problems. Introducing the scalar shape factor S had a significant positive impact on the computation of effective stiffness coefficients. While not perfect, most computed values were within an order of magnitude of the measured value from physical mechanical tests. Additionally, when looking over the individual tests' data, the microstructurally computed stiffness coefficients were correctly positioned with respect to each other. For example, if 3 different samples had actual Young's moduli of $E^{A}_{Actual} > E^{B}_{Actual} > E^{C}_{Actual}$, the

microstructural approach correctly computed the relative order of the Young's moduli: $E^{A}_{Micro} > E^{B}_{Micro} > E^{C}_{Micro}$. This signifies the constitutive relationship is reasonably reflecting differences in microstructure that affect macroscale performance.

It was hypothesized that the introduction of the tensor ratio **Γ** would further improve the accuracy of the computed effective stiffness coefficients. Here, the MIL tensor $\boldsymbol{H}$ plays an equal role to the contact tensor $\boldsymbol{F}$ in the computation of **Γ**. As demonstrated in Section 9.1, the MIL tensor requires larger volumes for accuracy in computing directional coefficients than the contact tensor. When anisotropy is present or expected, the appropriate volume required for accurate and predictable computation of the MIL tensor grows larger than those required for homogeneous volumes. Figures 9-10, 9-13, and 9-16 clearly show that when the MIL tensor coefficients diverge from an isotropic configuration, the ranges of the 95% confidence intervals also grow. This growth in the MIL tensor confidence intervals is similarly reflected in the computation of the tensor ratio coefficients.

The MIL tensor coefficients representative of an entire volume are also sensitive to local microstructural patterns within the volume being analyzed. As explained in Section 8.2, needle-like forms begin to dominate the surface

microstructure of the radiation recrystallized samples. In some cases, such as experimental sample NS3, the x_1-x_2 plane distribution of needle-like crystals are nearly uniform as seen in Figure 9-35 below. The remainder of the sample also does not appear to qualitatively have any directional preference of the crystals in the x_1 or the x_2 direction throughout the remainder of the depth of the sample. Subsequently, the MIL tensor reflects this general agreement of isotropy of the distribution of material parallel to the x_1-x_2 plane. The MIL tensor coefficients for sample NS3 are plotted in Figure 9-36.

It is expected that the distribution of the orientations of the needle-like crystals is uniform across the plane parallel to the snow surface. However, due to the size of the crystals, a cross-sectional area of $5\,mm \times 5\,mm$ used for the microstructural sub volumes sometimes captures localized anisotropy in the distribution of surface crystals.

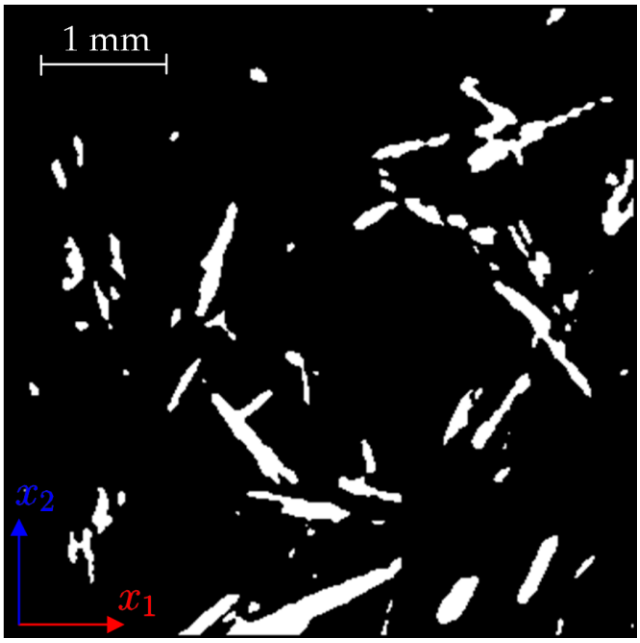


Figure 9-35: Needle-like crystal forms near the surface of experimental sample NS3 after 12 hours of recrystallization. The x_1-x_2 plane is shown here (parallel to the snow surface).

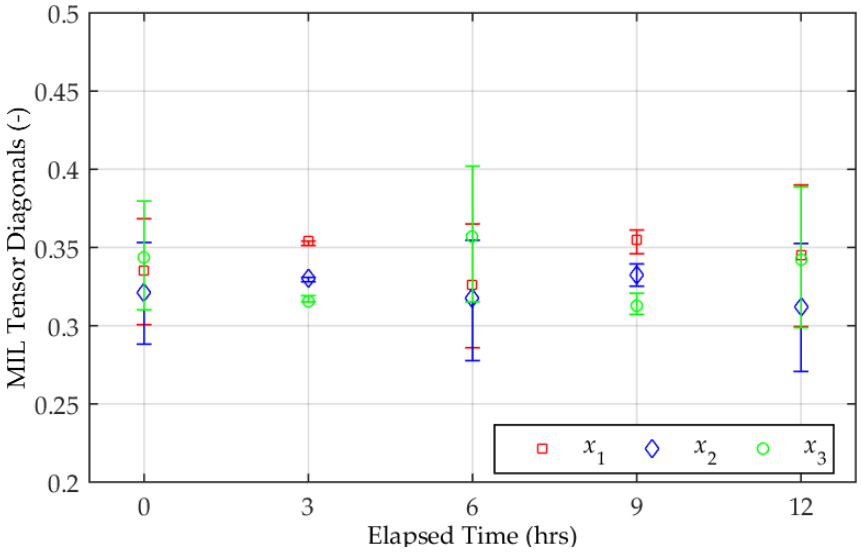


Figure 9-36: Principal MIL tensor coefficients for experimental sample NS3 demonstrating the coefficients in the x_1 and x_2 directions remain close to each other for the duration of the test.

Experimental sample 1W3 showed a strong preference for MIL tensor coefficients in the x_1 direction when radiation recrystallization concluded after 12 hours as seen in Figure 9-37. When examining the CT cross section near the surface of the sample, a majority of the crystals in question are oriented parallel with the x_1 axis. The cross-section of near surface needle-like crystals is shown in Figure 9-38. The remainder of the sample at depths below the surface does not show any obvious directional preference qualitatively. The sensitivity of the MIL tensor picked up on the local preference given by the surface crystals and assigns it to the entire volume analyzed.

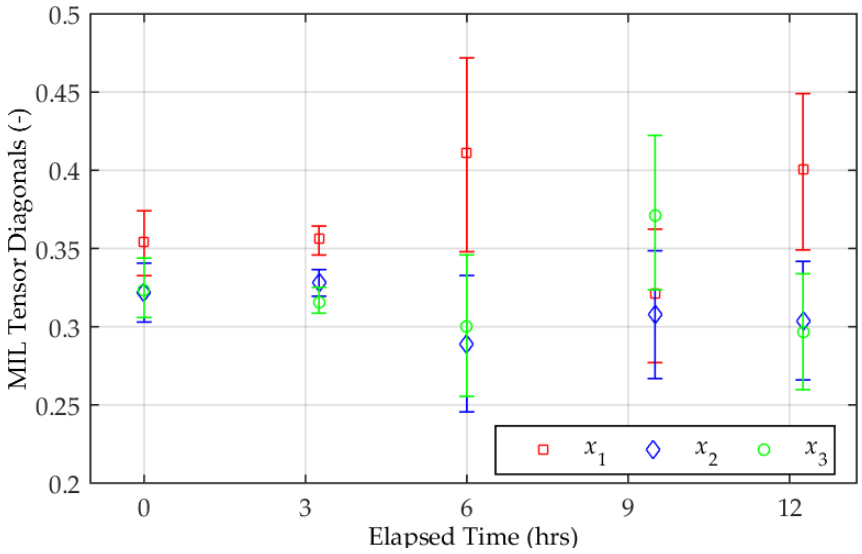


Figure 9-37: Principal MIL tensor coefficients for experimental sample 1W3 showing a clear preference to the x_1 direction at both 6 hours and 12 hours.

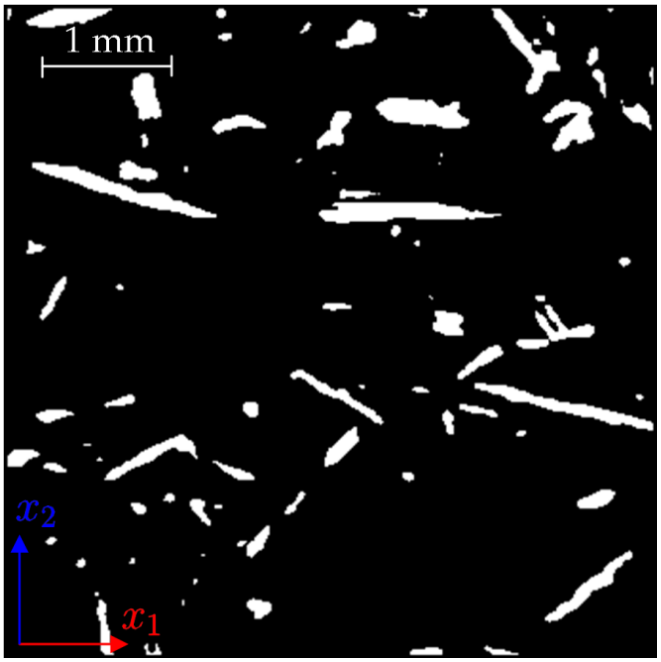


Figure 9-38: Needle-like crystal forms near the surface of experimental sample 1W3 after 12 hours of recrystallization. The x_1-x_2 plane is shown here (parallel to the snow surface).

This type of behavior was observed in 5 of the 7 experiments conducted in this study. The fact that the MIL tensor can be significantly affected by a small percentage of crystals in the volume suggests the volumes used for tensor analysis need to be bigger.

However, using bigger volumes can be problematic since larger volumes include multiple crystal morphologies. Including different crystal morphologies in a single analytical volume of interest provides an averaged result, potentially producing misleading results. As demonstrated in the previous chapter,

precision in selecting a region of interest is critical to properly analyzing mechanical features which exist in small stratified layers.

Volume Size Trouble. When analyzing the MIL tensor or the contact tensor, the volumes need to ideally be cubic in shape. For the MIL tensor analysis using the CTAn program, this condition is forced. When determining the coefficients of the MIL tensor, the MIL analysis actually operates on a virtual sphere fit inside the volume of interest. Since the MIL analysis is a line intersection counting technique, every grid of test lines at all orientations needs to be the same length. If performed on a non-cubic (non-spherical) volume, MIL values will be unequally weighted against different lengths of test lines. In contrast, the contact tensor is robust to volumes slightly skewed from cubes, however large deviations from a cubic volume can also cause problems.

For example, if analyzing a thin slice of a volume of snow shown in Figure 9-39, the contact tensor will always show a preference of bonds in the plane parallel to the slice since few if any bonds will be detected normal to the plane of the slice. When taken out of context from the volume from which the slice in Figure 9-39 came from, the results of the MIL tensor and contact tensor coefficients would be misleading. To successfully analyze the volume using either fabric tensor, a sub volume approximately cubic in shape would need to be

extracted to complete the analysis. In this situation, the extracted cubic volume would be large enough to only contain approximately one or two grains since the thickness of the slice is chosen to be approximately the average structure thickness. This would produce an invalid result since only a few grains out of thousands cannot statistically represent the full volume of grains.

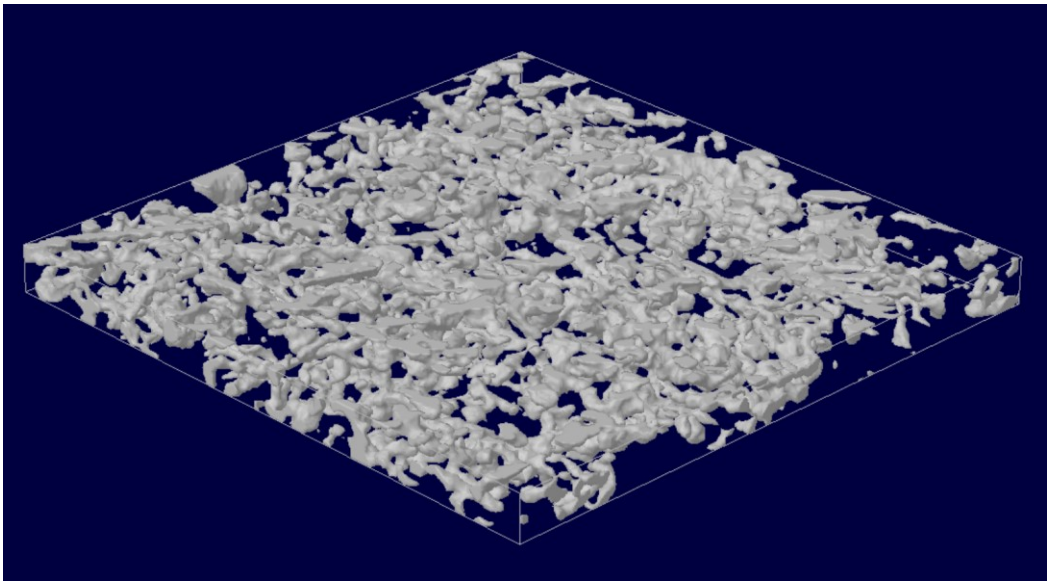


Figure 9-39: Thin slice of homogeneous snow where the contact tensor and MIL tensor cannot analyze.

This type of configuration is problematic since multiple zones containing different crystal morphologies exist within the sub volumes selected here for fabric tensor analysis. The details of the different morphologies are discussed in Chapter Eight. Macro scale mechanical testing is not of a high enough resolution to resolve localized strain within individual layers that exist inside the entire

radiation recrystallized layer. Regardless, isolating each general zone of crystal morphologies results in sub volumes that are too small for reliable or accurate analysis using a fabric tensor approach.

Other microstructures which do not exhibit such thin layers of crystal morphologies such as depth hoar or diurnal recrystallization may be better suited to investigate the feasibility of utilizing a fabric tensor approach to predicting the effective stiffness coefficients. Keep in mind, the primary goal of the original study by Shertzer was to investigate the anisotropic changes in thermal properties of depth hoar using a fabric tensor approach (Shertzer and Adams, 2011; Shertzer, 2011; Shertzer et al., 2010).

9.2.4 Tensor Analyses of Sub-Faceted Layer

The validity of the homogenization approach can still be evaluated by examining the microstructural evolution of the cohesive layer of rounded grains that develops immediately below the radiation recrystallized layer. Volumes from below the near surface faceted layers from three experiments (NS1, NS2, and 1W3) are analyzed using the homogenization approach. Experiment NS1 was tested in shear and exhibited the smallest increase in shear modulus in the snow immediately beneath the faceted layer. Sample NS2 is chosen since it is the only one to experience significant melt freeze below the faceted layer, resulting

in one of the largest increases in shear modulus of all of the experiments. Finally, experiment 1W3 was chosen to represent a sample physically tested in compression and representative of samples with aged surfaces (1 week old in this case).

Tensor Analysis of the Sub-Facet Layer of Sample NS1. Representative sub volumes from sample NS1 were analyzed temporally during the radiation recrystallization process from a layer below near surface facet development. This layer corresponds with a region at and below the warmest temperatures associated with the previously described "knee temperature gradient" that develops during temperature gradient metamorphism. This area supplies much of the vapor through sublimation for the kinetic metamorphism process occurring above this zone. In this region, equi-temperature metamorphism prevails resulting in a general rounding and coarsening of grains.

Without new crystal growth and rearrangement of grains in the region (only sintering), it could be reasonably expected that the original microstructural contact configuration should remain similar to the initial non-recrystallized configuration. Examining the evolution of the contact tensor for this region during metamorphism supports the concept of a minimally changing contact

configuration. The evolution of the contact tensor is illustrated below in Figure 9-40.

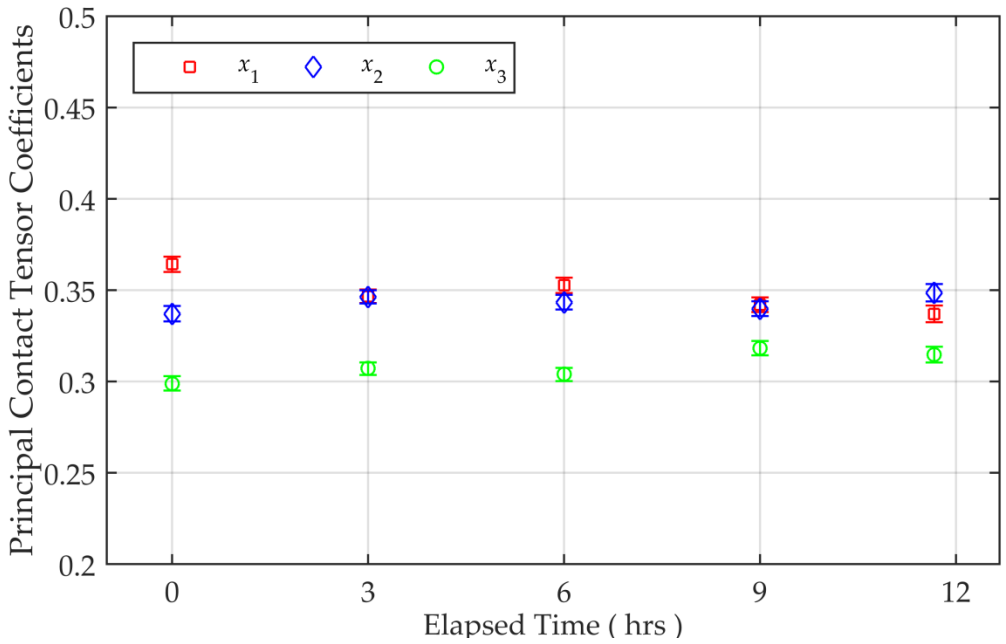


Figure 9-40: Contact tensor diagonal values for the coarsened layer of snow beneath the faceted layer of experimental sample NS1.

In contrast, as the anisotropic features of the fragmented stellar dendrites and small rounded grains degrade into a more uniform structure, the initially anisotropic MIL tensor is expected to converge toward isotropy since starting initially anisotropic. Examining the evolution of the MIL tensor coefficients mostly supports this idea. As seen in Figure 9-41, the MIL tensor coefficient averages converge toward an isotropic configuration with increasing confidence through 9 hours of recrystallization. The final time step at 12 hours decreases

significantly in confidence and shows a preference toward structures oriented in the vertical direction (x_3 axis). Examining the 3-D microstructural volume reveals a few abnormally large grains of ice that spilled out of the sieve during initial sample preparation which skew the confidence of the MIL tensor results for this particular volume. However, Figure 9-42 shows normal size grains and large inclusions with a slight vertical preference shown in the MIL tensor.

The movement of the tensor ratio coefficients followed closely with the significant changes to the MIL tensor. Tensor ratio coefficients (plotted in Figure 9-43) converge on isotropy through 9 hours with tightening confidence then diverge slightly as a result of the skewed MIL tensor at nearly 12 hours.

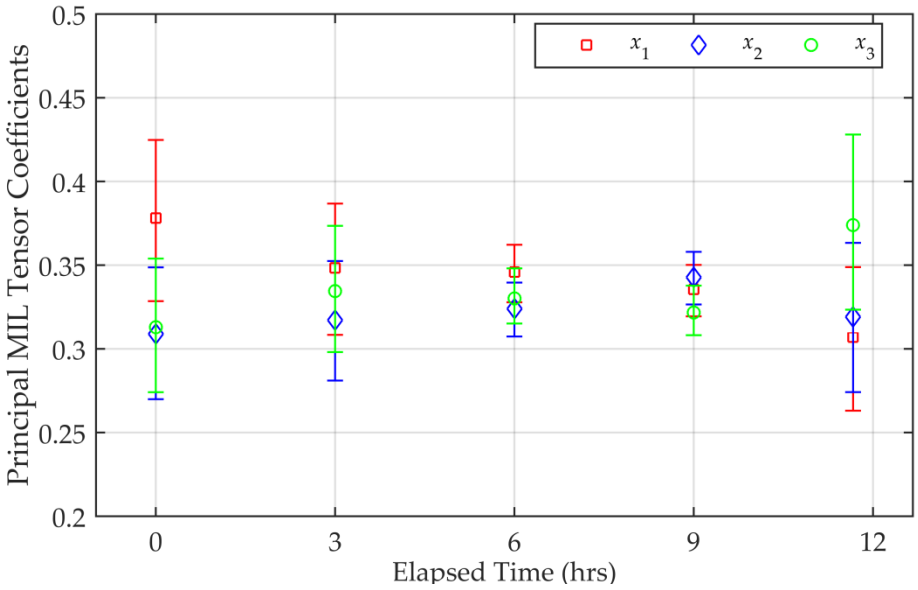


Figure 9-41: MIL tensor diagonal values for the coarsened layer of snow beneath the faceted layer of experimental sample NS1.

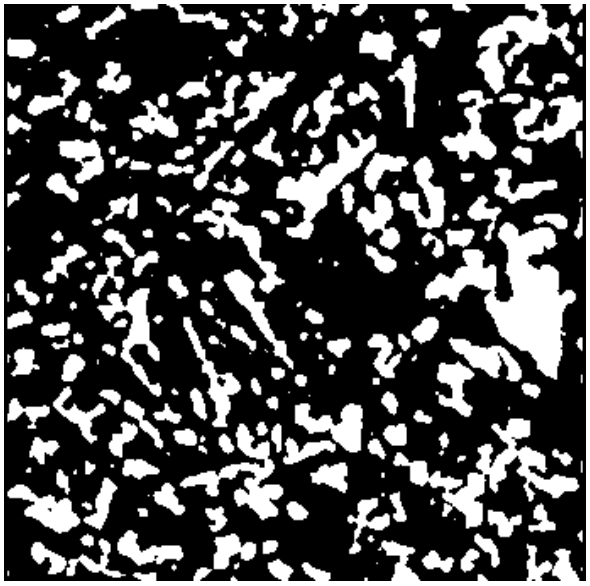


Figure 9-42: x_1-x_3 2-D cross section of coarse layer grains from experiment NS1 after 12 hours of metamorphism. Inclusions of large ice grains from sieve spillover during sample preparation occasionally skew microstructural results.

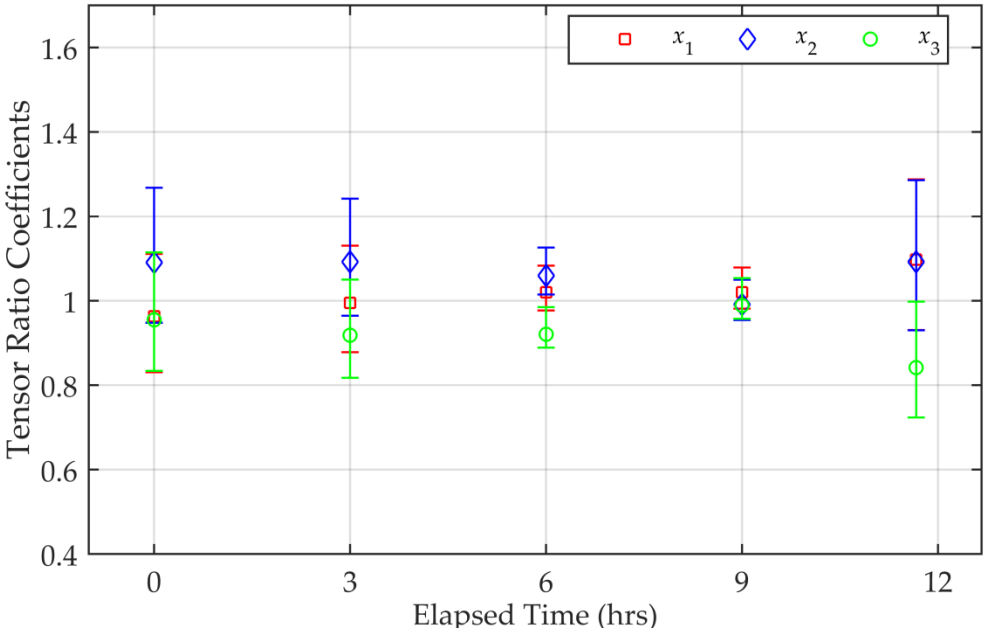


Figure 9-43: Tensor ratio coefficients for the coarsened layer of snow beneath the faceted layer of experimental sample NS1.

Computation of the effective stiffness coefficients resulted in reasonable approximations of the relative change of material properties between the initial state and final state of recrystallization. Recall from Table 8-2, the coarsened base layer below the faceted layer experienced a decrease in slope parallel shear modulus of +33.5%: initially 1.25 MPa up to 1.67 MPa measured via a physical mechanical test. Of all of the fabric tensors used to capture the anisotropic qualities of the snow microstructure, the tensor ratio performed the best in capturing the measured effective mechanical behavior.

The shear modulus coefficients as computed by the tensor ratio are illustrated in Figure 9-44 below. Again, the dashed line represents G^*, the computed scalar effective shear modulus and the labeled coefficients are modified by the employed fabric tensor. Variation in G^* is driven by a combination of changes in the mean 3-D coordination number (Figure 9-45) the bond-to-grain radius ratio (Figure 9-46). The volume fraction of this layer of snow remained unchanged throughout the duration of the experiment as the mean grain size and pore size changed in unison during the recrystallization experiment.

No discernable trend in the changes to the mean 3-D coordination number is observed in Figure 9-45. This random fluctuation is likely a result of the

statistical uncertainty of using representative volumes rather than identical volumes. Without multiple samples to average at each time interval, small variations in microstructural properties can combine to affect the computation of effective mechanical stiffness properties.

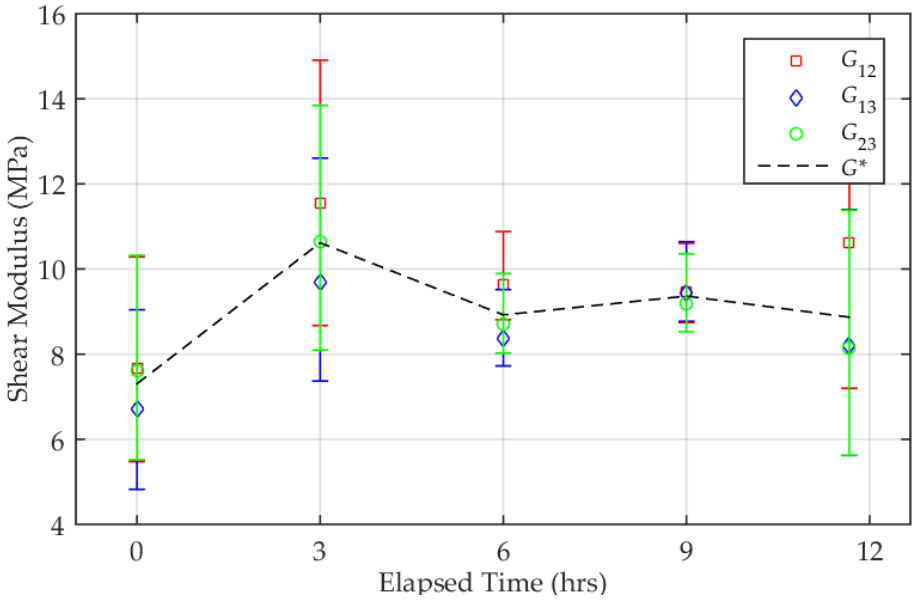


Figure 9-44: Computed effective shear moduli for the coarsened base layer below the near surface facets in sample NS1 using the tensor ratio for directional data.

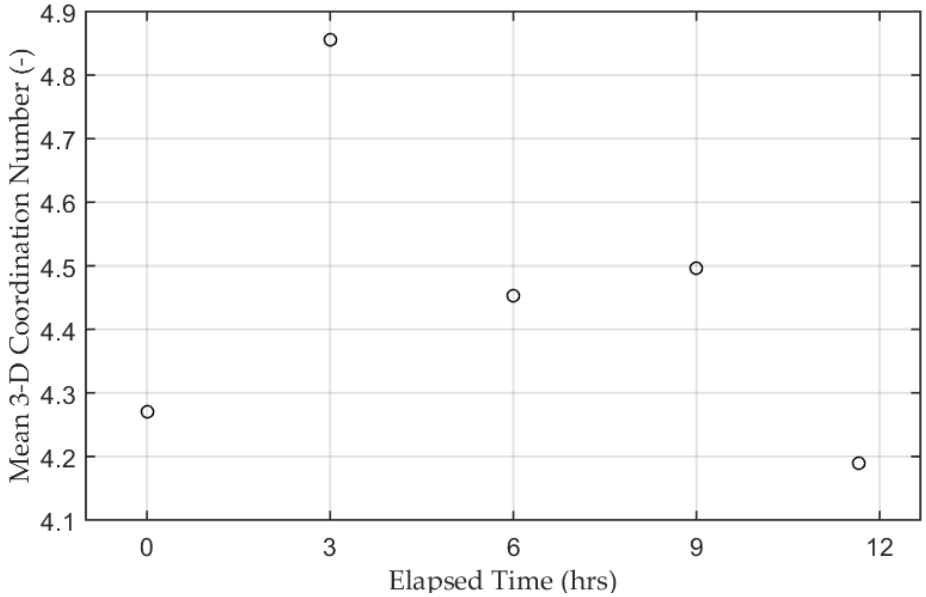


Figure 9-45: Mean 3-D coordination number for the coarsened base layer below the near surface facets in sample NS1.

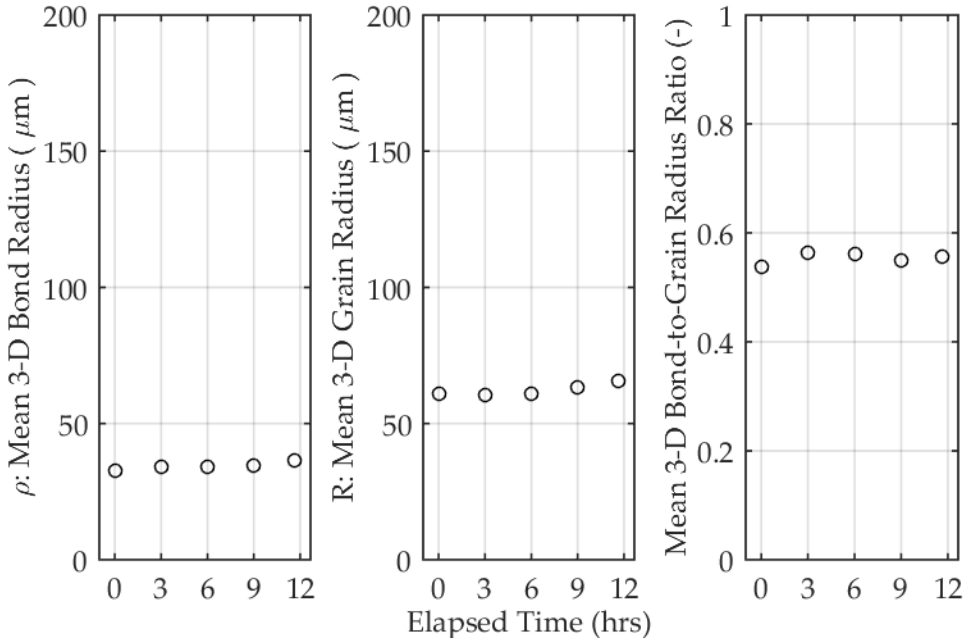


Figure 9-46: Mean 3-D bond radii and grain radii for the coarsened layer below the near surface facets of sample NS1.

The average calculated effective shear modulus G_{23} increased approximately 7% from the initial value of G_{23}. This corresponds to the minor change observed in the physical mechanical test for this particular experimental sample.

Significant directional microstructural changes were not expected for this layer and minimal changes to the stiffness properties were observed. These expectations and observations are reasonably reflected by the computation of effective properties using the tensor ratio for directional data.

Tensor Analysis of the Sub-Facet Layer of Sample NS2. Sample NS2 was unique from the other experiments conducted since it started with a significantly lower density and experienced subsurface melt-freeze in the later stages of the recrystallization experiment. Because of the development of the melt-freeze layer, the snow immediately beneath the near surface facet layer became significantly stiffer and more cohesive than the surrounding snow and initial snow. Recalling the physical results from Table 8-2, the measured shear modulus increased initially from 0.291 MPa to 1.97 MPa for the layer of snow immediately beneath the faceted layer. This was an increase of 579%.

Like the previous result in the sub-facet layer of sample NS1, it is expected the tensor-ratio coefficients will converge toward an isotropic configuration as

metamorphism progresses. Figure 9-47 shows the tensor ratio coefficients diverging slightly in the first few hours then converging toward isotropy by the end of the experiment.

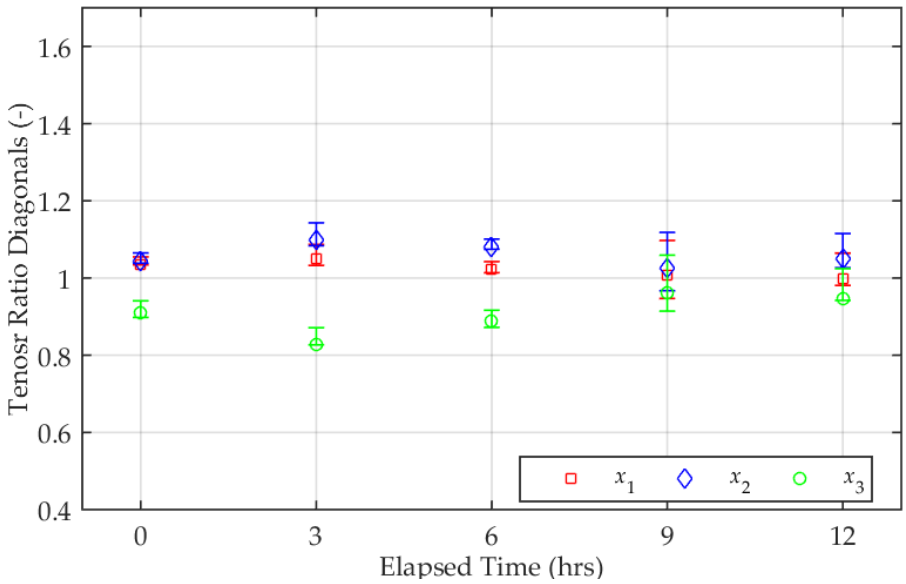


Figure 9-47: Tensor ratio coefficients for the sub-faceted layer of experimental sample NS2.

Changes to the mean 3-D coordination number and density of the sub-faceted layer contributed to a large upturn in the scalar shear modulus G^* toward the end of the test. In addition, the convergence of the tensor ratio toward isotropy also contributed to positive changes in the effective shear modulus. The computed effective shear moduli derived from the microstructure and the tensor ratio for the sub-faceted layer of experiment NS2 is illustrated in Figure 9-48.

The computed value of G_{23} started initially at 2.936 MPa and rose to 6.934 MPa by the end of the experiment – an increase of approximately 136%.

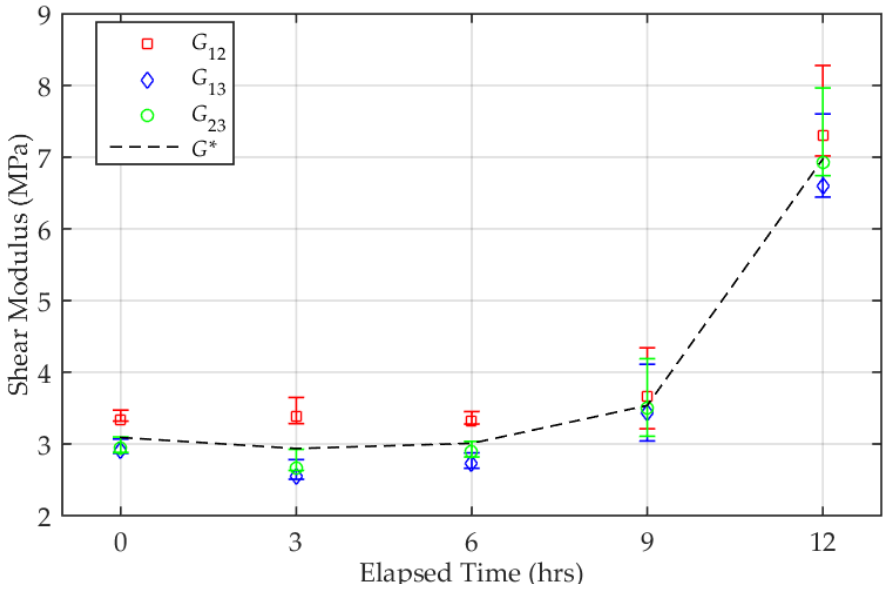


Figure 9-48: Computed effective shear moduli for the melt-freeze layer below the near surface facets in sample NS2 using the tensor ratio for directional data.

Here, as in other experiments, the effective stiffness properties still average 0.5-1 orders of magnitude higher than the measured values. Additionally, the relative increase in computed effective shear moduli did not match the magnitude of the relative increase in the physically measured shear; although it still marks a significant increase. Here, the input of appropriate material properties comes into question. As discussed previously, the input material stiffness for ice is taken for atmospherically formed ice (Kermani et al., 2008). This value is

approximately only 10% of reported values for freshwater ice formed from the liquid state (Petrenko and Whitworth, 1999). Here, if melt freeze conditions prevailed, some of the original microstructure would exhibit atmospheric ice qualities, and any new refrozen ice would exhibit much stiffer qualities of freshwater ice. The results reported in Figure 9-48 would provide a lower bound estimate of shear stiffness whereas multiplying the end result by approximately 9.3 (freshwater ice Young's modulus $E_{fresh,ice} = 9.3$ GPa) would provide an upper bound estimate of shear stiffness. Each of these cases would represent microstructures with purely atmospheric ice and purely freshwater ice respectively.

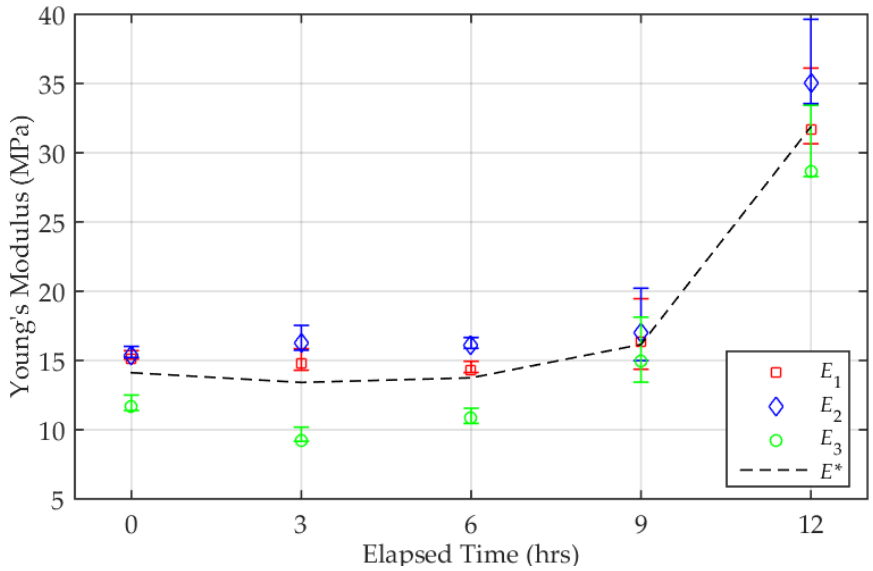


Figure 9-49: Computed effective Young's moduli for the melt-freeze layer below the near surface facets in sample NS2 using the tensor ratio for directional data.

Although not measured physically for this experimental sample, the computed effective Young's modulus also increased significantly as expected for the sub-facet cohesive layer. The computed effective Young's moduli using the tensor ratio are illustrated in Figure 9-49.

Tensor Analysis of the Sub-Facet Layer of Sample 1W3. The final sample re-examined for the snow microstructure underneath the faceted layer was sample 1W3. This sample had an initial snow surface set and left to sinter for 1 week prior to inducing near surface facet growth. This sample was also physically tested in compression to examine the changes to Young's modulus normal to the snow surface. Referencing the physical results tabulated in Table 8-4, the Young's modulus normal to the snow surface was measured initially at 2.28 MPa. Following radiation recrystallization, the layer below the faceted crystals experienced a 102% increase in measured Young's modulus from the initial state to 4.61 MPa.

Using the microstructural data and the tensor ratio, the effective Young's moduli are computed for this layer. The scalar Young's modulus E^* increased modestly in the latter half of the recrystallization experiment as shown in Figure 9-50 below. Using the tensor ratio to compute departures from isotropic E^*, the

effective Young's modulus in the vertical direction (E_3) rises from an initial value of 36.3 MPa to 40.7 MPa – a total increase of 12.2%.

As with the previous sub-facet layer samples examined, little change was observed in the contact tensor coefficients for this particular sample. The distribution was similar to sample NS1 shown in Figure 9-40. The MIL tensor converged toward isotropy after an initial divergence at the midpoint of the experiment. The MIL tensor coefficients are shown in Figure 9-51. Unlike the previously examined results for this layer (conducted on new snow samples), the configuration started off nearly isotropic in terms of the MIL tensor. This is an expectation of the microstructure following 1 week of sintering (equi-temperature metamorphism) prior to detailed analysis. Additionally, the tensor ratio coefficients behaved in similar nature to those of the previously examined sub-facet layer volumes analyzed here. The tensor ratio coefficients are plotted in Figure 9-52 below.

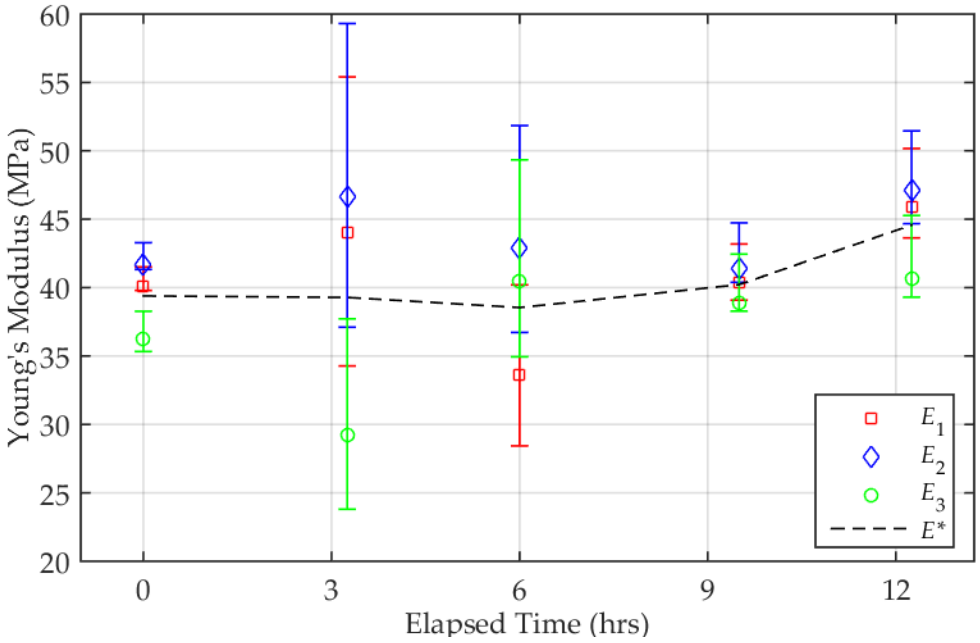


Figure 9-50: Computed effective Young's moduli for the cohesive layer below the near surface facets in sample 1W3 using the tensor ratio for directional data.

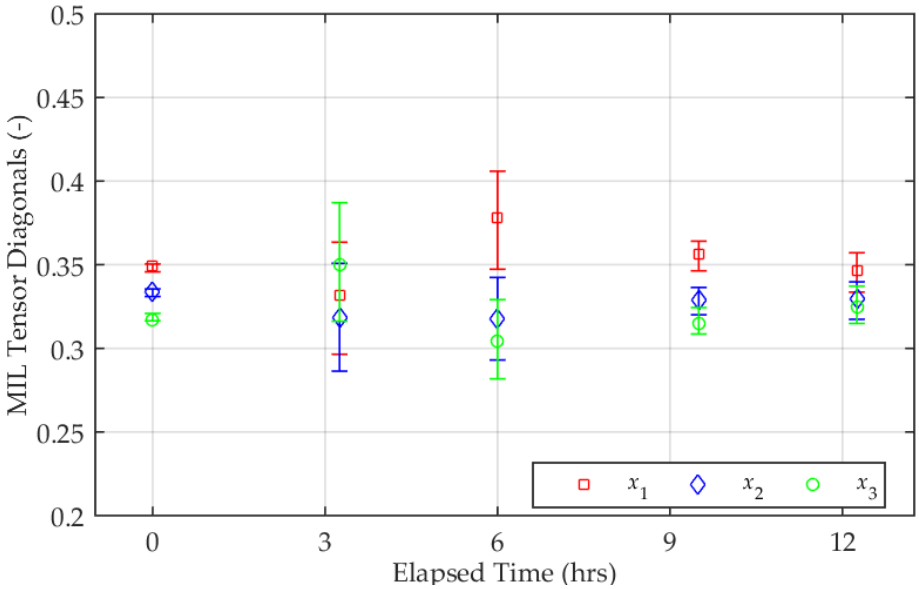


Figure 9-51: MIL tensor diagonal values for the coarsened layer of snow beneath the faceted layer of experimental sample 1W3.

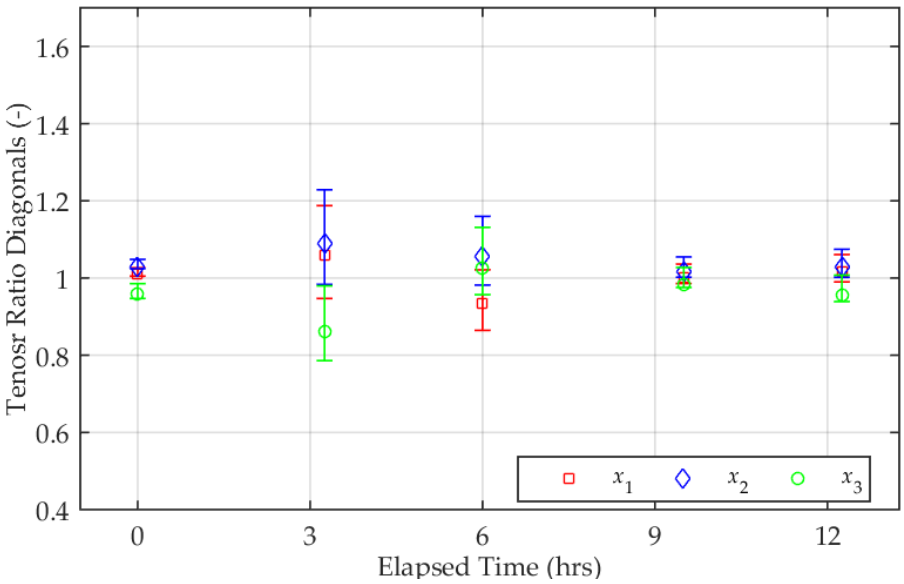


Figure 9-52: Tensor ratio coefficients for the sub-faceted layer of experimental sample 1W3.

Summary of Cohesive Layer Tensor Analysis. The homogenization approach utilizing the snow's microstructure in a layer of consistent texture performed reasonably well. Additional results are reported in Appendix E. In each of the cases analyzed above, the absolute value of the effective stiffness coefficients remained approximately 1 order of magnitude higher than those stiffness values computed from physical experimentation. Additionally, the absolute magnitude of the relative change between the initial configuration and the final configuration of the snow beneath the faceted layer was less than physically observed.

Of the three cases presented here, the homogenization approach with the tensor ratio did not contradict the physical results. Using sample NS1, minimal change was observed in the shear modulus between the initial and final state and the effective coefficients calculated using the tensor ratio reflected this. Sample NS2 experienced one of the largest observed increases in shear modulus and also experienced some melt-freeze in the layer examined. In this case, a significant upturn in effective shear modulus was computed using the tensor ratio approach. Lastly, a smaller increase in Young's modulus was physically observed for sample 1W3. This smaller response of the computed effective Young's moduli was reflected using the tensor ratio approach.

Examining just the texture of the microstructure using various metrics also matched expectations reasonably well. For the volumes analyzed, rounding and coarsening of the microstructure was expected in this region. Without rearrangement of the positions of grains within the microstructural ice network, the contact tensor distributions reflected this behavior by changing little throughout the process of recrystallization.

The MIL tensor showed significant convergence toward isotropy from an initially anisotropic state. Here, especially in the new snow volumes, as the initially elongated and dendritic structures degrade and evolve into more

rounded forms, the MIL tensor tracks these changes accurately. Initial anisotropic states of new snow were also observed in other research (Riche et al., 2013). In addition, the well-sintered one week old sample showed initial isotropy reflected by the initial rounded and sintered state. For this experiment in the region below the faceted crystals, the MIL tensor diverges toward anisotropy, potentially showing an early phase of microstructural rearrangement that occurs, before coming back to an isotropic configuration at the end.

The tensor ratio provided a good metric for balancing the changes in one textural measure (MIL tensor) to the steady unchanging characteristics of another textural measure (contact tensor). The mechanical response of the snow is partly dictated by both the geometric arrangement of ice grains and the arrangement of bonds between them. The tensor ratio captures this balance.

Using these volumes of snow containing a mostly consistent microstructural texture shows that the homogenization approach can reasonably reflect changes to the effective stiffness properties. Comparing the approach's effectiveness to the faceted layers previously described demonstrates the critical nature of selecting an appropriate RVE for analysis. For thin layers, an adequate volume may not be available which captures a single microstructural texture while also being significant enough in size.

9.3 Summary

Homogenization techniques were applied to the radiation recrystallized snow samples developed here in an attempt to accurately compute the effective stiffness coefficients. This method includes both scalar microstructural parameters and fabric tensors which describe the snow's changing microstructural texture.

Prior to use with snow, artificial 3-D binary volumes were generated with randomly sized and positioned spheres mimicking the 3-D voxel resolution of scanned microstructures. These volumes were used to evaluate the efficacy of the contact tensor and the MIL tensor using updated 3-D segmentation techniques. Like previous work by Shertzer and Adams (2011), the contact tensor required defining contact orientations by the vector connecting the centers of bonded grain pairs. For the volume sizes tested, the MIL tensor coefficients averaged near isotropy, as expected for randomly generated volumes, but suffered from significant uncertainty due to the small volume sizes.

Unfortunately, the application of the contact tensor, MIL tensor, and thus the tensor ratio is not feasible for radiation recrystallized layers due to the spatial scale associated with the faceted crystals. As highlighted in Chapter Eight, several unique crystal morphologies exist in a very narrow region (<10 mm).

Additionally, macroscale mechanical test results demonstrated the importance of precisely choosing spatial regions for subsequent mechanical analysis since averaging over too wide of an area can lead to misleading results.

In the case here with the fabric tensors, in order to capture a single zone of unique crystal morphology, the volumes become too small to compute accurate fabric tensor coefficients. In order to utilize a volume of sufficient size, several different crystal morphologies are included, thus producing an averaged and inaccurate result.

Fabric tensors were also evaluated for representative volumes in the transition zone between the faceted crystals and the well-sintered cohesive layer. In this region, evaluation of the efficacy of the tensor ratio is inconclusive since little change is observed in the contact tensor and MIL tensor coefficients. More conclusive evidence of the effect of the tensor ratio may be achieved by analyzing microstructures which develop significant uniform textural anisotropy over a larger spatial region (e.g. depth hoar).

The scalar stiffness coefficients (e.g. E^* and G^*) could still be evaluated since these terms do not suffer from the same volumetric limitations of the directional fabric tensors. The other scalar microstructural parameters originally included in the original formulation by Shertzer (2011) appropriately computed

the relative change in material properties of the recrystallized samples. However, while spherical grains are assumed in this formulation, the effective mechanical stiffness parameters were overestimated by close to two orders of magnitude.

A measurable scalar shape factor proposed here accounts for deviations away from the spherical grain assumption in the original formulation by Shertzer (2011). This factor improved computation of the effective stiffness coefficients by an order of magnitude. The relative change in macro-scale stiffnesses, from the initial state to the metamorphosed state, was reasonably computed when compared to the macro-scale mechanical test results presented in Chapter Eight. Even without accurate directional terms, the homogenization approach appropriately captured the significance of the microstructural properties on the macro-scale stiffness properties of snow. Homogenization provided similar relative difference in stiffness properties both at temporal scales and spatial scales.

CHAPTER TEN

FINITE ELEMENT MODEL RESULTS

"In the spirit of science, there really is no such thing as a 'failed experiment.' Any test that yields valid data is a valid test."
~ Adam Savage (Mythbusters)

CT scans obtained before radiation recrystallization and after the final recrystallized layer is buried by new snow are used to produce the geometry for a finite element model. The finite element model presented here, as with the fabric tensor calculations, computes effective stiffnesses. These are also compared to the real macroscale response tested experimentally. The setup and boundary conditions as detailed in Chapter Six are applied to accurately mimic the mechanical test performed in the laboratory: not necessarily the boundary conditions expected in a continuous mountain snowpack in a real avalanche scenario.

The results of the finite element analyses presented herein are first presented as is with comparisons to the original mechanical tests. Further explanation and discussion are provided later.

10.1 Finite Element Analysis Results

All samples, regardless of how they were physically tested in the lab, were simulated in both shear and compression. Shear displacements are imposed at the top of the sample parallel to the snow surface. Compressive displacements are applied normal to the snow surface. Further details regarding simulation boundary conditions are discussed in Chapter Six. All simulations are incremental static structural simulations. Therefore, no dynamic effects were considered.

The effective properties of the initial homogeneous finite element samples are computed from the displacement boundary conditions and the reaction forces on the fixed base. The nodal reaction forces on the fixed base are summed and divided by the total cross-sectional area of the total volume (here it is 5.06 mm × 5.06 mm) to produce an average macro-scale stress. Since no external loads are applied between the boundary conditions at the top and bottom edges, the average macroscale stress is constant for the entire height of the column, in particular the self-weight of the column was neglected. Nodal displacements from surface parallel planes at various elevations in the snow sample are averaged to compute the effective macroscale strain between selected planes (see Figure 10-1). For shear strain, this relationship is:

$$\gamma_{avg,13} = \gamma_{avg,23} = \tan^{-1}\frac{\delta_x}{h}, \tag{10.1}$$

where δ_x is the relative horizontal displacement between surface parallel planes h distance apart. Compressive strain in the x_3 direction utilizes a similar relationship:

$$\varepsilon_{avg,3} = \frac{\delta_z}{h}, \tag{10.2}$$

where δ_z is the relative vertical displacement between surface parallel planes separated by dimension h. A first order fit is performed on the elastic region of the resulting macro-scale stress and strain generated data. The slope of this fit defines either the shear modulus or Young's modulus (depending on the simulated mode of loading – shear or compression).

When analyzing the homogeneous samples, the microstructural geometry is expected to contain a consistent texture throughout the whole volume. Therefore, the whole height of the sample between the applied boundary conditions is utilized to examine the relative displacement for computation of the macroscale strains using either Equation (10.1) or Equation (2.9). However, the faceted samples require detailed refinement of locations for examining effective macro-scale strain resulting from the fine-structured layering of the radiation recrystallized faceted region. Restricting the region of interest to obtain accurate

effective stiffness measures for the faceted region originated from examining the physical test results and must be employed here for the simulated results.

Figure 10-1 shows an example finite element mesh of a buried radiation recrystallized layer. Average relative displacements are queried between the top and bottom planes of several different regions within the sample to examine differences in local effective macro-scale stiffness. The colored annotations illustrate the selected sub-regions for measuring relative displacements and correspond to the colors of the plotted and tabulated data in results presented further below. Displacements are queried for all nodes on the surface parallel plane (x-y plane in Figure 10-1) at z-locations defined by the top and bottom planes of the sections defined in Figure 10-1. The average displacement from the top edge of a region is subtracted from the bottom edge of a region to obtain the relative displacements (either δ_x or δ_z) for the selected sub-region. The difference in z-coordinate between the top edge and bottom edge of a region defines h. With relative displacements δ_x or δ_z and h defined for the selected sub-regions, Equation (10.1) or Equation (2.9) are used to define the strain in the sub-region of interest.

The sub-regions in Figure 10-1 are provided as a precise way of pinpointing strains occurring is specific zones within the buried radiation

recrystallized sample. The reduced section (depicted in red) omits new snow burying the old snow surface at the top, and the transition zone between faceted and rounded grains at the bottom. Although some scans contain the cohesive sub-faceted layer, it was not feasible to analyze these layers separately as they contained either incomplete data, or too small of a volume for adequate analysis.

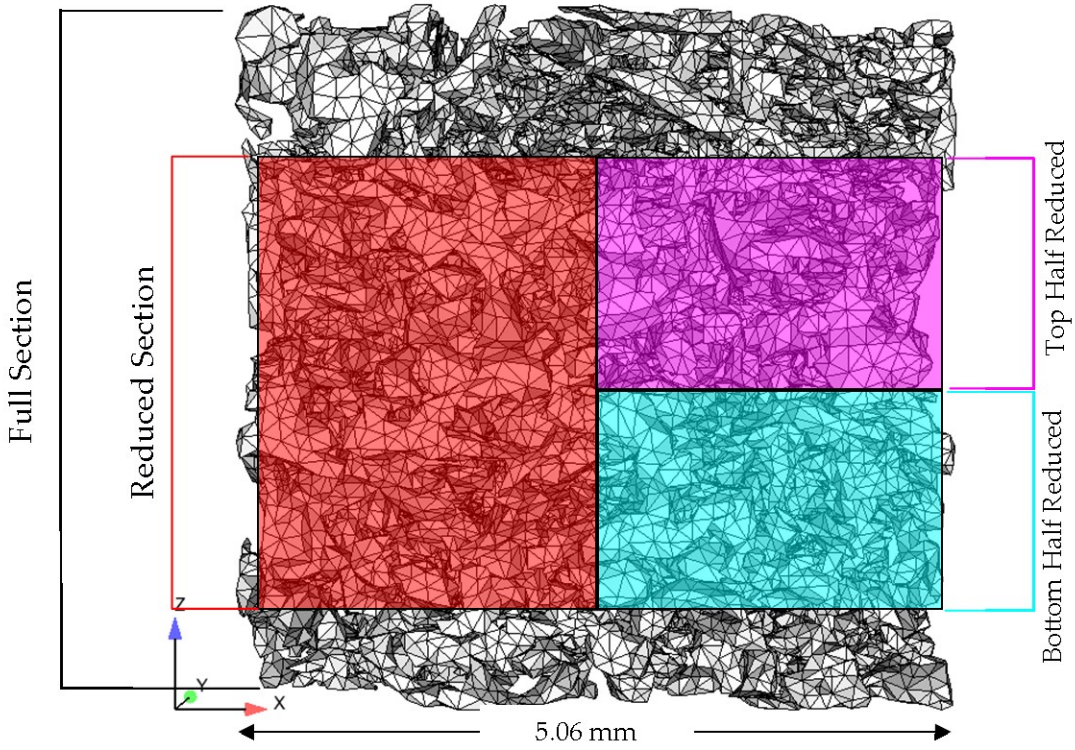


Figure 10-1: Regions used for examining relative displacements within local regions of the microstructure. Average displacements are computed at the top and bottom edges of the boundaries for the entire cross-sectional plane defined at that boundary. The different colored regions define the top and bottom boundaries of the regions utilized in the results presented in this chapter.

Representative results from each class of physical test conducted (new snow shear tests, aged snow surface shear tests, new snow compression test, and aged snow compression test) are presented in the following subsections. Full results are provided in Appendix F.

10.1.1 New Snow Shear Tests

Samples NS1 and NS2 were tested in shear experimentally. Only sample NS1 will be presented in detail here. Data from the samples not discussed here are shown in Appendix F. Referencing Table 8-2 for the physically measured results of sample NS1, the experimentally measured shear moduli of the initial snow sample and final faceted layer were 1.25 MPa and 0.417 MPa respectively. The faceted layer shear modulus decreased 66.6% relative to the initial snow sample.

The finite element analysis on the initial near surface snow microstructure (prior to faceting) produced an effective shear modulus of 1.72 MPa. This data is illustrated as the blue points in Figure 10-2. The slope of the line fit to the data is used to determine the effective macro-scale shear modulus from the simulation.

The same boundary conditions and material parameters are used to simulate the shear test on the radiation recrystallized sample. An initial examination of the effective shear modulus utilizes the whole height of the

radiation recrystallized sample. The full height includes a small portion of the new snow burying the faceted surface crystals and the transition area between faceted grains and rounded grains found at the bottom of the sample. Using this region, as described in Figure 10-1, the simulated effective shear modulus was 1.60 MPa – a small decrease but nowhere near the relative difference in the physical mechanical test. This data is represented by the black line and asterisk data in Figure 10-2.

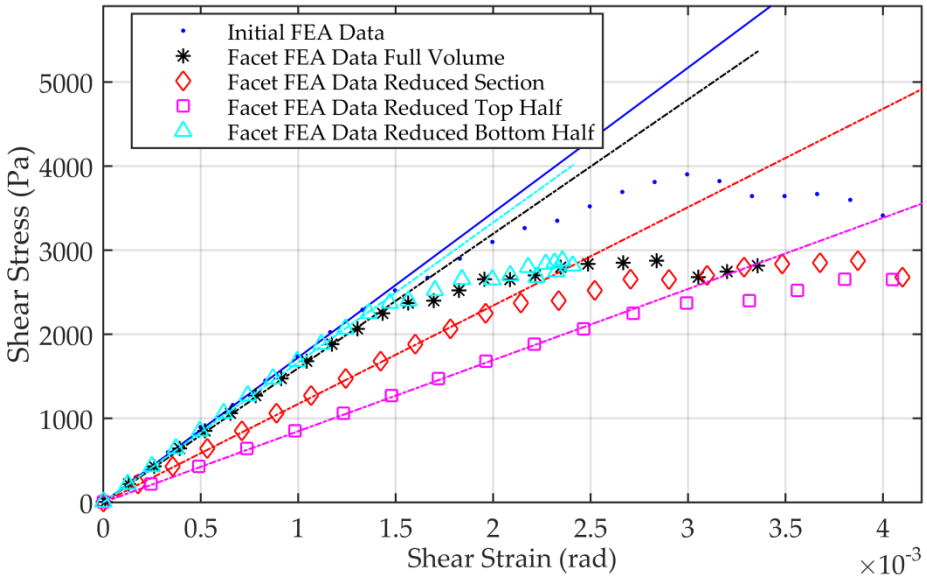


Figure 10-2: FEA simulated average shear stress and strain for the initial snow surface and the radiation recrystallized faceted layer of experimental sample NS1.

Reducing the volume to exclude the new snow at the top and the transition region at the bottom, the effective shear modulus was further reduced

to 1.17 MPa. The reduced section is plotted in red in Figure 10-2 (see Figure 10-1 for an illustration of the spatial definition of each colored curve). Splitting the reduced section into an upper half and lower half produced even more dramatic differences in simulated effective shear moduli. The top half, dominated by fewer and larger faceted grains, had an effective shear modulus of 0.846 MPa. The bottom half, composed of smaller and more numerous faceted grains, had an effective shear modulus of 1.66 MPa.

Another subtle feature of analyzing the strain in selective regions of interests reveals some information about the failure characteristics of the finite element model using the faceted sample. After macro-scale yield has occurred, the sample continues to increase in shear strain in the top half of the faceted sample while minimal shear strain is added to bottom half of the faceted sample. This could be indicative of macro-scale failure coalescing near the mid depth of the faceted layer. More obvious manifestations of this failure signature are presented later using other microstructural volumes and finite element simulations.

Although not physically tested in compression, FEA allows for unlimited loading scenarios. In this case, a compression test is simulated here on sample

NS1. Using the initial volume of non-recrystallized snow, the Young's modulus in the x_3 direction (vertical) was 8.53 MPa.

Switching to the faceted layer, the same regions of interest are utilized for computing Young's moduli for the whole sample and parts of the sample. All comparisons of simulated compressive stress and strain are shown in Figure 10-3. The effective Young's modulus simulated using the whole height of the volume was 5.02 MPa. The reduced section omitting the top and bottom edges of the sample came in with a Young's modulus of 4.54 MPa. Splitting the reduced section into a top half and bottom half resulted in Young's moduli of 3.14 MPa and 7.74 MPa respectively.

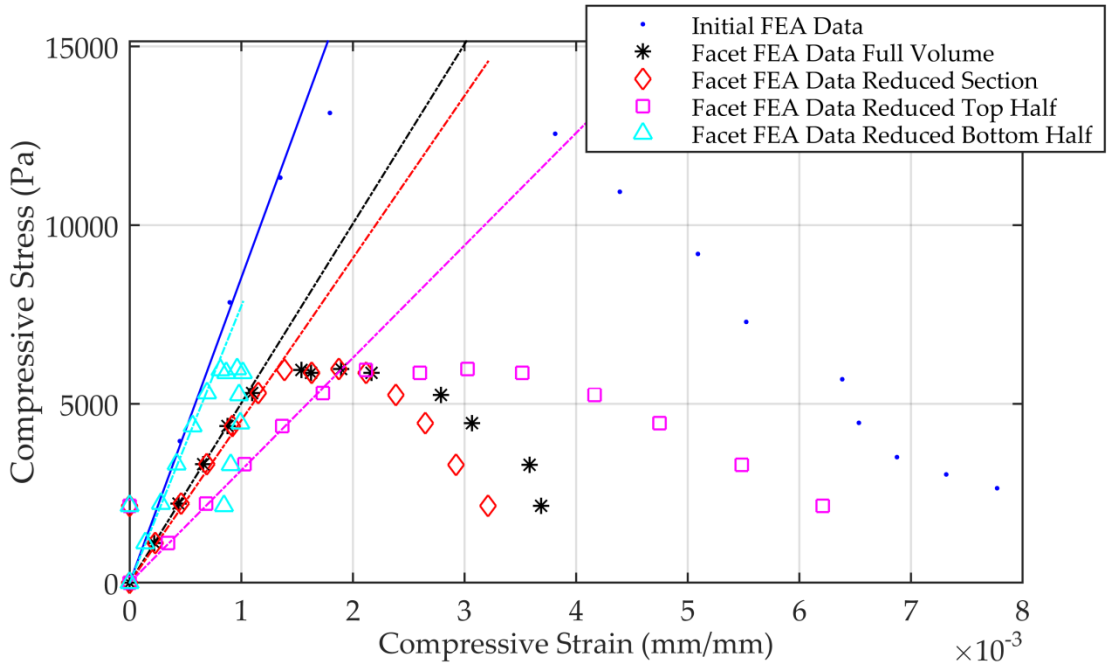


Figure 10-3: FEA simulated average compressive stress and strain for the initial snow surface and the radiation recrystallized faceted layer of experimental sample NS1.

Studying the strain distribution in the top and bottom half of the faceted region after reaching the peak stress shows a clear indication of macro-scale failure occurring in the middle of the faceted layer. The sample continues to accumulate compressive strain in the top half (magenta data) while the bottom half (cyan data) recovers some of the elastic portion of the strain. This post elastic behavior is observed in most other simulations using other faceted volumes.

10.1.2 New Snow Compression Test

A single compression test was performed experimentally at the macroscale. From the physical test results in Table 8-4, the Young's modulus normal to the snow surface from the initial state of experimental sample NS3 was measured as 1.39 MPa. The radiation recrystallized layer experimentally produced a decrease in Young's modulus by 61.7% to 0.530 MPa.

FEA simulations of the compression test on the initially homogeneous sample produced an effective Young's modulus of 15.5 MPa. The homogeneous layer properties are plotted in blue (points) in Figure 10-4 below. Compression of the homogeneous layer exhibited nearly brittle characteristics near the point of ultimate failure as noted by the minimal region of strain softening before reaching peak stress. The ultimate compressive strength of the homogeneous sample from the FEA simulations is calculated as 18.8 kPa.

Examining the faceted layer using isotropic material parameters for the ice in the finite element simulation produced consistent decreases in effective Young's modulus independent of the region examined. Starting with the full height of the volume, the simulated effective Young's modulus is 3.07 MPa. This data is denoted by the black points in Figure 10-4. This measure decreased relative to the initial simulated sample by 80.1%. Using smaller sub-regions

within the sample, which eliminates averaging strain from the new snow at the top of the sample and the more rounded grains at the bottom of the sample, calculating the effective Young's moduli yielded results between 2.42 MPa and 2.62 MPa denoted by the appropriate colored data in Figure 10-4.

This resulted in reductions in effective Young's modulus compared to the initial simulated resulted between 83.1% and 84.4%. The simulated ultimate compressive stress was 3.48 kPa for an overall decrease from the simulated homogeneous sample of 81.4%.

The microstructural volume from sample NS3 was also analyzed with simulated shear loads similar to the previous tests. Since this sample was physically tested in compression, there are no physical shear test results available for comparison with the simulated data. For the initial homogeneous sample, FEA simulations produced an effective shear modulus of 4.39 MPa. Using the full volume, the simulated effective shear modulus was reduced by 88.4% to 0.507 MPa. Examining the reduced section, which omits strain from the new snow at the top of the sample and the rounded grains at the bottom of the sample, produced further reductions in shear modulus to values between 0.400 MPa and 0.412 MPa as illustrated by the data presented in Figure 10-5.

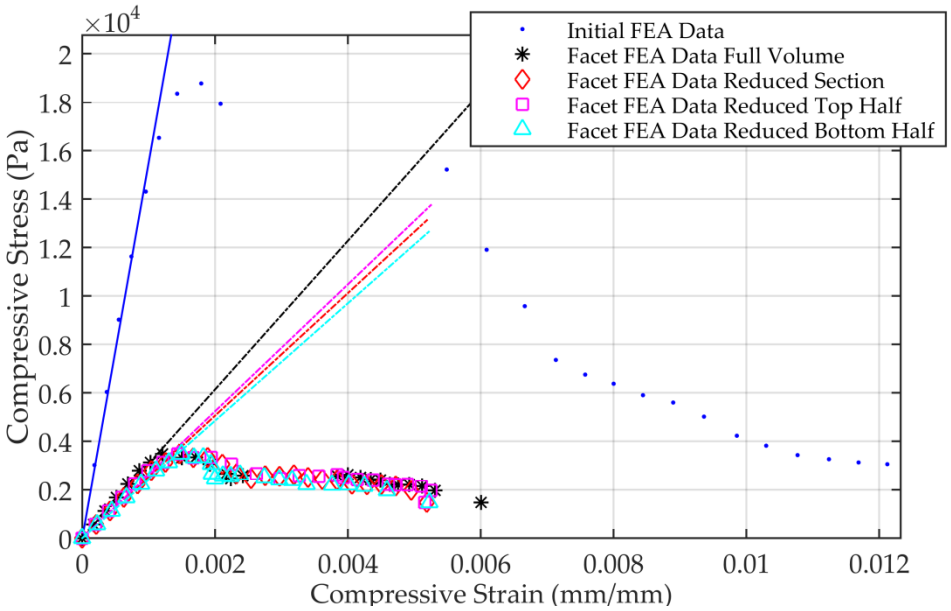


Figure 10-4: FEA simulated effective compressive stress and strain for the initial snow surface and the radiation recrystallized faceted layer of experimental sample NS3.

Although not representative of the effective shear strength of the model, the peak average shear stress computed by the simulation was reduced significantly. As seen in Figure 10-5, the initial homogeneous sample topped out with a volume average shear stress of nearly 12 kPa. This peak stress was reduced significantly to approximately 2 kPa using the faceted microstructure.

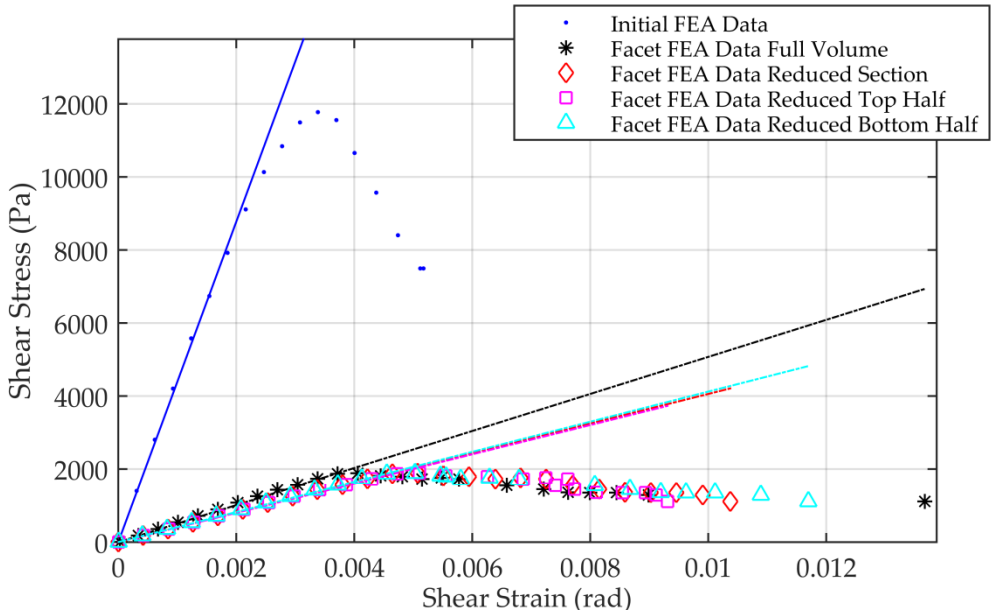


Figure 10-5: FEA simulated effective shear stress and strain for the initial snow surface and the radiation recrystallized faceted layer of experimental sample NS3.

Sample NS3 was the only new snow sample physically tested in compression which also included microstructural data for finite element simulations. Relative comparisons to other compression tests previously reported on can be made by examining the results in Table 8-7.

10.1.3 One Week Old Snow Shear Tests

Two physical shear tests were performed on the experimental samples that contained one week old snow surfaces. Only the physical and simulated results for sample 1W1 will be presented here. A compilation of simulated results for sample 1W2 is provided in Appendix F.

Referencing the physically measured results reported in Table 8-2, sample 1W1 decreased in shear stiffness by 33.8% from the initial snow surface to the faceted layer. The physically measured value of the shear modulus for the initial sample prior to recrystallization was 0.317 MPa. Following recrystallization, the shear modulus of the faceted layer was reduced to 0.209 MPa.

Using finite element analysis on the microstructure, the simulated effective shear modulus of the initial sample of snow was computed as 2.75 MPa. The initial shear modulus is computed using the slope of the blue linear fit line in Figure 10-6. Switching to the microstructural volume of faceted snow, several differences in effective shear modulus result, depending on the specific region examined within the faceted microstructure. If utilizing the full height of the volume (which includes new snow on the top and the transition region between rounded grains and facets on the bottom), the computed shear modulus remains relatively unchanged. This is illustrated by the black dashed linear fit line plotted nearly on top of the initial sample's linear fit line in Figure 10-6.

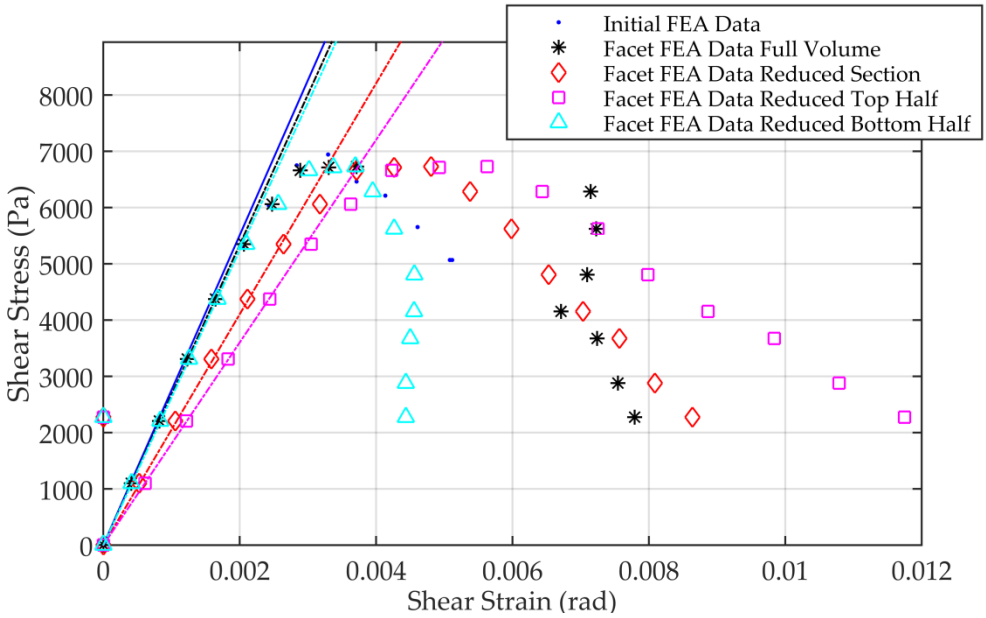


Figure 10-6: FEA simulated effective shear stress and strain for the initial snow surface and the radiation recrystallized faceted layer of experimental sample 1W1.

When examining the reduced section, which omits the new snow at the top of the sample, relative changes in simulated effective shear modulus are more significant. Here, referring to the red plotted data in Figure 10-6, the simulated effective shear modulus is 2.05 MPa – a relative change from the initially homogeneous sample of -25.5%.

Breaking the reduced section down even further into a top half (magenta data) and bottom half (cyan data) revealed significant spatial differences in effective shear stiffness within the faceted layer. The effective stiffness in the top half of the faceted region was further reduced to 1.80 MPa (relative change from initial -34.6%). This region consisted of mostly well-developed cup shaped facets

larger in size than the facets developing in the lower half of the reduced region. The effective shear modulus for the lower half of the reduced section reverted to nearly the same simulated effective shear stiffness as the initial sample.

Examining the simulated relative displacement of the sub-regions of this microstructural volume after achieving maximum average shear stress reveals an interesting result. The top half of the reduced section (magenta) in Figure 10-6 continues to strain as the top boundary continues to displace. However, the lower half of the reduced section (cyan) exhibits minimal additional strain. This indicates bulk macro-scale failure of the sample has occurred in the simulation somewhere in the middle of the faceted region. This result is supported by locating faceted crystals on either side of the fracture interface in the real physical results discussed previously in Section 8.3.5.

The initial and faceted microstructural volumes from experiment 1W1 were also analyzed using simulated compressive loads. Since the sample was physically tested in shear, the simulated results can only be compared relatively to other samples physically tested in compression. The initial homogeneous volume had a simulated effective Young's modulus normal to the snow surface of 8.24 MPa. The faceted microstructural sample's simulated effective Young's

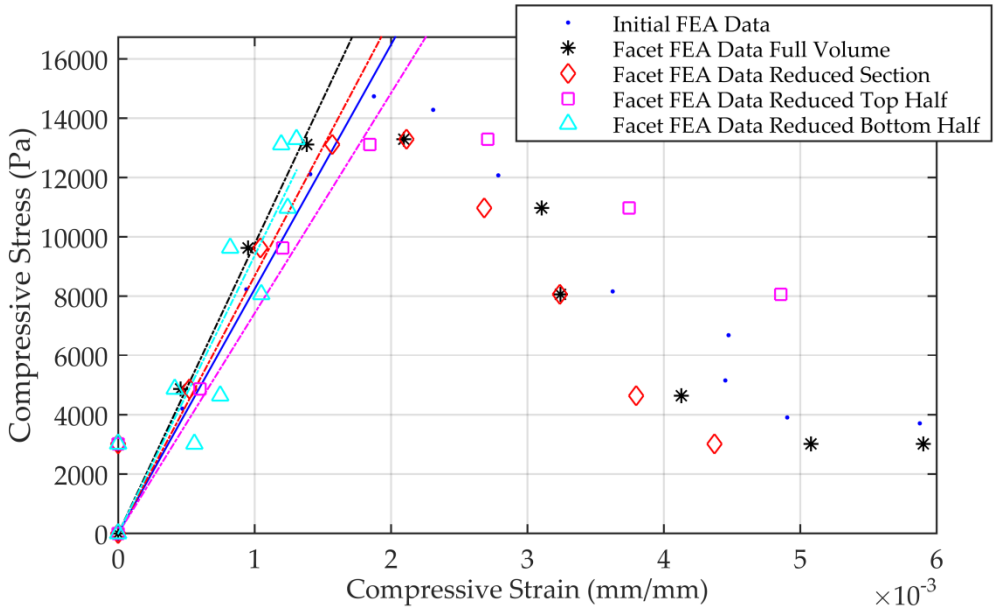


Figure 10-7: FEA simulated effective compressive stress and strain for the initial snow surface and the radiation recrystallized faceted layer of experimental sample 1W1.

modulus depended on the localized region examined within the total volume. Using the full height of the volume (black data in Figure 10-7), the computed Young's modulus increased slightly to 9.76 MPa. Reducing the section to exclude the new snow at the top of the sample (red data in Figure 10-7) brought the computed Young's modulus back closer to the initial simulated result at 8.68 MPa. Splitting the reduced section in half, like the shear results, showed significant differences in stiffness. The top half of the reduced section containing fewer and larger faceted grains resulted in a computed Young's modulus of 7.42 MPa: a reduction of 9.92% from the simulated initial sample modulus. The

bottom half however resulted in an increased computed value closer to that of the computed modulus for the full section.

In similar fashion to the simulated shear test, the simulated compression test also showed macro-scale failure occurring in the middle of the faceted layer. Taking a closer look at the cyan data in Figure 10-7, almost all of the strain recovers elastically after reaching peak stress. Strain continues to develop in the top half of the faceted region.

Detailed simulated data for sample 1W2 is presented in Appendix F. Overall the simulated results showed similar comparisons to the physical results as other tests discussed in this chapter. Additionally, the simulated macro-scale failure location could also be determined in sample 1W2 comparing the relative difference in plastic strain development in the top and bottom halves of the faceted layer.

10.1.4 One Week Old Snow Compression Test

Only one physical compression test was performed on the one week old snow surface before and after radiation recrystallization (experiment 1W3). Referencing the compressive experimental results in Table 8-4, the sample went from 2.28 MPa initially (in the 1 week old layer) to 0.494 MPa in the final

radiation recrystallized layer. This marked a relative change in the surface normal Young's modulus of −78.3%.

Starting with the finite element analysis results in compression, the computed effective Young's modulus normal to the snow surface for the initial non-recrystallized sample is calculated as 16.8 MPa. These are the blue data points in Figure 10-8.

Computation of the Young's modulus in the radiation recrystallized sample is slightly different from other simulated samples. This sample in its original dimensions proved difficult to generate a quality mesh while staying within the node and element limits – possibly due to the total thickness of the radiation recrystallized layer and individual grain and bond sizes. Instead, the new snow burying the faceted layer was omitted from the mesh. This meant simulated loads were directly applied to the faceted layer. Utilizing the full height of the reduced mesh sample, the effective macro-scale Young's modulus of the radiation recrystallized is computed as 4.32 MPa using finite element simulations. This data is represented by the black line and points in Figure 10-8. Reducing the section down to exclude the new snow at the top half of the faceted grains, the simulated macroscale Young's modulus came in slightly higher at 5.05 MPa. The lower half of the faceted crystals was nearly the same as seen by

the overlapping magenta and cyan data in Figure 10-8. The reduced section data excluded small sections of crystals near the boundary applied to the shortened mesh. This shows that inclusion of the new snow layer in the finite element simulations is important to generate a realistic response of the faceted layer to an externally applied load. Regardless, a significant lowering of the Young's modulus was shown in the faceted layer, similar to the physical test results.

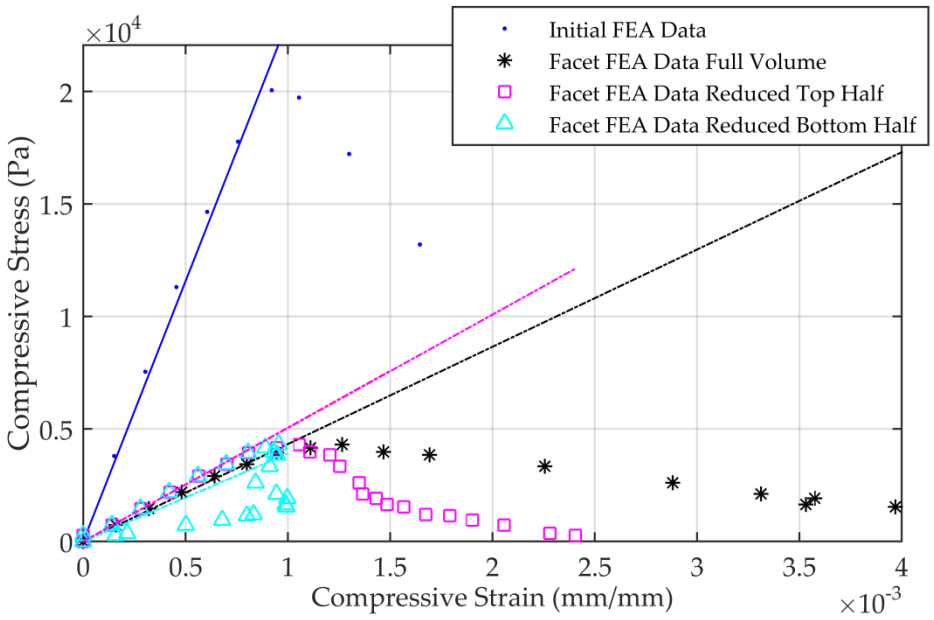


Figure 10-8: FEA simulated effective compressive stress and strain for the initial snow surface and the radiation recrystallized faceted layer of experimental sample 1W3.

Experimentally, the sample also produced usable compressive strength results. The ultimate compressive strength of sample 1W3 prior to recrystallization was 5.25 kPa. Following radiation recrystallization, the

compressive strength was reduced to 2.50 kPa. The relative change between the initial and final state of snow was −54.2%. The effective compressive stresses and strains from the FEA simulated tests are shown in Figure 10-8. The simulated compressive strength was reduced 78.6% from 20.1 kPa down to 4.31 kPa.

The simulations also showed macroscale failure of the sample occurred in the middle of the faceted layer. This is clearly indicated in Figure 10-8 by the recovery of elastic strain in the bottom half of the faceted layer after reaching peak stress. The top half of the sample continues to strain indicating almost full disconnection from the lower half of the sample.

The simulated shear test results also showed a significant decrease in effective shear modulus from the initial non-recrystallized volume to the final radiation recrystallized volume. The initial effective shear modulus of the simulated result was 3.43 MPa. The final effective shear modulus of the faceted layer, from the full height of the shortened mesh, decreased by 78.5% to 0.738 MPa. Splitting the volume into a top half and bottom half showed differences in the shear moduli from each region of the faceted layer. The simulated shear modulus from the top half of the faceted region was 0.550 MPa. The shear modulus from the bottom half was 1.19 MPa. The effective stress and strain

curves for the finite element analysis on volumes taken from experiment 1W3 are displayed in Figure 10-9.

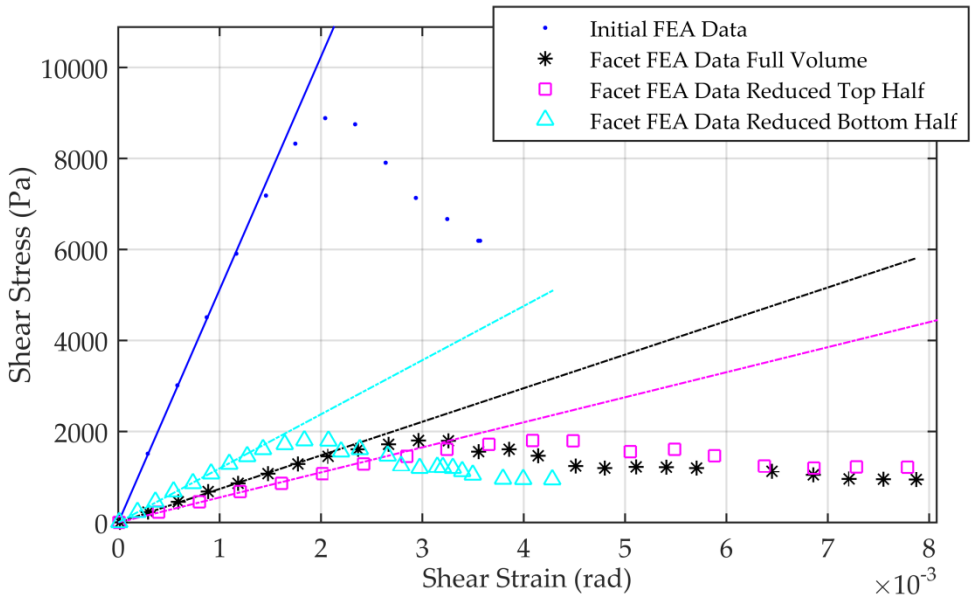


Figure 10-9: FEA simulated effective shear stress and strain for the initial snow surface and the radiation recrystallized faceted layer of experimental sample 1W3.

Shear strain after reaching peak stress in Figure 10-9 indicates a large degree of microstructural damage is simulated between the top and bottom half of the faceted region. Each point of stress and strain for the faceted data was taken from the same load step. The fact that the top half of the faceted sample strains significantly farther than the bottom half of the sample indicates large scale failure of elements near the middle of the sample. However complete separation has not occurred since there is no elastic recovery on the macroscale.

10.1.5 Two Weeks Old Snow Shear Test

Only one sample with a snow surface aged two weeks was prepared and tested experimentally. A physical shear test was performed on experimental sample 2W1 before and after radiation recrystallization. Referencing the previously reported mechanical test results listed in Table 8-2, the measured shear modulus started at 0.338 MPa initially. Following radiation recrystallization, the shear modulus in the faceted layer was reduced by 6.86% to 0.315 MPa.

Simulating the shear test on the initial non-radiation recrystallized volume produced an effective shear modulus of 7.96 MPa. The initial simulated shear stress and strain is the blue data in Figure 10-10. Effective shear moduli from simulations on the radiation recrystallized volume proved extremely sensitive to the size of the region examined. Using the full height of the volume, the computed shear modulus from the FEA simulation was 9.13 MPa – an increase from the initial sample. Using a reduced section which omits new snow at the top and rounded grains at the bottom, the simulated shear modulus was reduced slightly from the initial sample to 7.12 MPa. This data is illustrated as the red points in Figure 10-10.

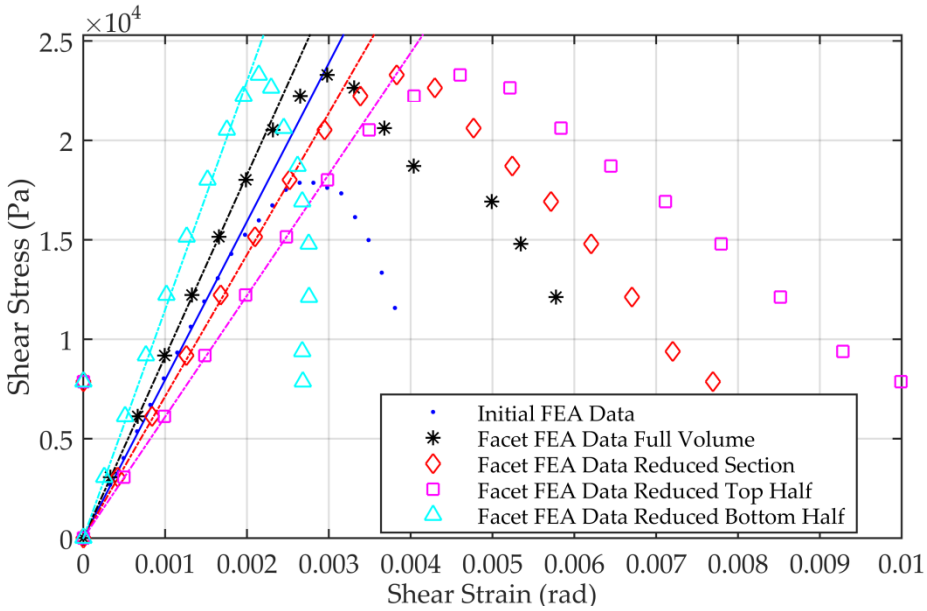


Figure 10-10: FEA simulated effective shear stress and strain for the initial snow surface and the radiation recrystallized faceted layer of experimental sample 2W1.

Splitting the reduced section in half highlights the differing stiffnesses in spatially small regions resulting from subtle changes in the microstructure. Focusing on the top half of the faceted region, where the faceted grains are larger and less in number, the shear modulus was reduced further to 6.10 MPa. Switching to the bottom half of the faceted region where grains tend to be smaller and more numerous resulted in a higher shear modulus of 11.5 MPa. The top and bottom half of the faceted data is represented by the magenta and cyan data respectively in Figure 10-10.

Consistent with the other tests, macroscale failure occurs near the midpoint of the height of the sample as indicated by the simulated strains

reported in Figure 10-10. The top half of the sample (magenta data) continues increase in strain after achieving peak stress, while the bottom half of the sample (cyan data) experiences insignificant additions to strain.

The same pair of volumes were also simulated in compression. The FEA simulation of compression on the initial volume yielded an effective Young's modulus of 34.3 MPa. Like the previous samples, the radiation recrystallized sample was split into specialized regions of interest. Using the full height of the radiation recrystallized volume, the simulated effective Young's modulus was 34.0 MPa. Using the same reduced volume as described for the simulated shear test, the reduced volume Young's modulus was 32.1 MPa. Splitting this reduced section even further into a top half and bottom half of the faceted region produces Young's moduli of 26.7 MPa and 49.5 MPa respectively. All of the stress and strain data from the finite element simulated compression tests are compared in Figure 10-11.

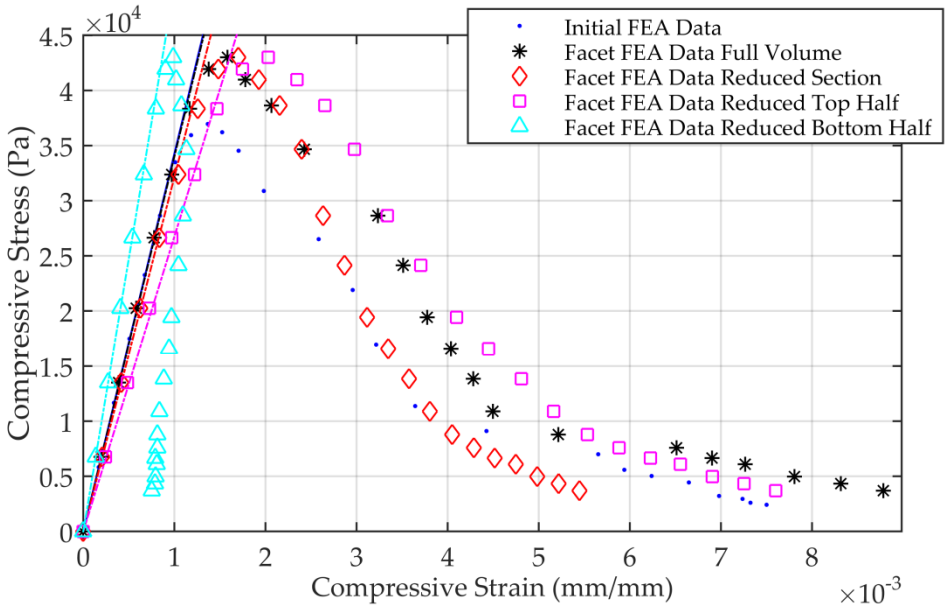


Figure 10-11: FEA simulated effective compressive stress and strain for the initial snow surface and the radiation recrystallized faceted layer of experimental sample 2W1.

Strain continued to develop in the top half of the sample after reaching peak stress while the bottom half of the sample recovered some strain as indicated by the cyan data in Figure 10-11. This simulated behavior is consistent with other simulations of other samples. Additionally the peak stress increased slightly in faceted sample when compared to the initial sample.

A summary of the finite element generated data presented in the preceding section is summarized below in Table 10-1. Table 10-1 also includes comparisons to the actual mechanical test result where available. Following afterward is a discussion of the results.

Table 10-1: Summary of finite element data for each experimental sample and actual experimental results where available. (Surface parallel shear modulus $= G_{23}$, surface normal Young's modulus $= E_3$, peak shear stress $= \tau_{peak}$, peak compressive axial stress $= \sigma_{peak}$). The colors correspond to the colored data points utilized in the presentation of the FEA simulated stress and strains shown above.

	FEA Data				Experimental Data			
NS1	G_{23}^{FEA} (MPa)	E_3^{FEA} (MPa)	τ_{peak}^{FEA}* (kPa)	σ_{peak}^{FEA} (kPa)	G_{23}^{Real} (MPa)	E_3^{Real} (MPa)	τ_{peak}^{Real}* (kPa)	σ_{peak}^{Real} (kPa)
Initial	1.72	8.53	3.90	13.1	1.25	-	1.93	-
Facets	1.60	5.02	2.87	5.98	0.417	-	0.601	-
Reduced	1.17	4.54						
Top ½	0.846	3.14						
Bot. ½	1.66	7.74						
NS2								
Initial	0.333	1.37	1.41	2.55	0.291	-	0.882	-
Facets	0.306	2.16	1.35	3.58	0.421	-	1.08	-
Reduced	0.212	1.91						
Top ½	0.254	2.34						
Bot. ½	0.166	1.52						
NS3								
Initial	4.39	15.5	11.8	18.8	-	1.39	-	3.83
Facets	0.507	3.07	1.89	3.48	-	0.530	-	2.50
Reduced	0.406	2.53						
Top ½	0.401	2.62						
Bot. ½	0.412	2.42						
1W1								
Initial	2.75	8.24	6.94	14.7	0.314	-	0.668	-
Facets	2.67	9.76	6.73	13.3	0.205	-	0.864	-
Reduced	2.05	8.68						
Top ½	1.80	7.42						
Bot. ½	2.62	9.37						

Table 10-1 continued…

	FEA Data				Experimental Data			
1W2	G_{23}^{FEA} (MPa)	E_3^{FEA} (MPa)	G_{23}^{FEA} (MPa)	E_3^{FEA} (MPa)	G_{23}^{FEA} (MPa)	E_3^{FEA} (MPa)	G_{23}^{FEA} (MPa)	E_3^{FEA} (MPa)
Initial	3.39	27.2	7.45	18.0	0.405	-	0.663	-
Facets	3.68	27.4	13.2	27.5	0.625	-	0.783	-
Reduced	3.31	22.5						
Top ½	3.00	21.1						
Bot. ½	3.79	24.5						
2W1								
Initial	7.96	34.3	17.9	37.0	0.338	-	0.657	-
Facets	9.13	34.0	23.3	43.0	0.315	-	0.969	-
Reduced	7.12	32.2						
Top ½	6.10	26.7						
Bot. ½	11.5	49.5						

*Peak shear stress values likely do not represent the shear strength. See discussion in Section 8.3.5 for details.

10.2 Discussion

With the exception a couple of experiments, most of the finite element results showed reasonable relative comparisons between initial and recrystallized layers of snow when compared to the macroscale experimental data reported earlier. In some cases like samples NS1 and NS2, the effective stiffnesses computed from the initial snow state matched well with the experimental data. However, less accurate absolute matching with the experimental results occurred in the faceted final state for both of these tests. In most of the remaining samples, although the absolute simulated effective

stiffnesses were approximately one order of magnitude higher than the recorded experimental values, the relative change from initial layer to radiation recrystallized layer was appropriate.

Keep in mind that all of the simulated results utilized the same material parameters across all experiments. FEA material parameters were not fit to any specific experimental test to better match results. The only component that changed from one experiment to the next was the microstructural geometry.

10.2.1 Damaged Microstructures

Not all simulated results matched the trend observed in the physical experiment. Sample 1W2 and sample 2W1 both had finite element results that produced much higher predictions of compressive Young's moduli and compressive strengths than any other sample collected (see Table 10-1). In addition, the simulated shear results did not appropriately capture the relative temporal change in the physically measured shear modulus before and after recrystallization. Physically, the shear modulus of sample 1W2 increased approximately 50% from the initial state to the faceted state. However the finite element result shows the opposite by recording a modest decrease in shear modulus between the initial and faceted samples when focusing on the reduced section (red) or the top half of the facets (magenta) in Table 10-1.

In similar fashion, experiment 2W1 physically had simulated Young's modulus values double or triple what other samples contained as well as higher compressive strengths. The shear modulus results when focused on the reduced section in the faceted layer seemed to agree well with the relative change in stiffness compared to the physical results. However, the simulated magnitudes of peak stress values in both shear and compression are much higher than their initial states of snow.

It is likely the microstructural integrity of the samples were damaged during the extraction process. Extracting buried radiation recrystallized samples for μCT imaging and subsequent microstructural analyses is an extremely delicate process. Extracting surface samples that are not buried by new snow is not as difficult since the delicate part of the sample is a free surface. However early on, radiation recrystallized layers were initially buried with new snow, allowed to sinter, then excavated in an attempt to extract an undamaged buried radiation recrystallized layer. The cohesiveness of the new layer of sintered snow made it difficult to cut samples small enough to fit in an imaging container without damaging the delicate radiation recrystallized microstructure. It was noted into laboratory notes that the two previously mentioned samples (1W2 and 2W1) likely contained damaged microstructures from the extraction process. A

finite amount of snow exists for microstructural sampling and once extracted and scanned, it is impossible to detect this damage after its occurrence. Samples prior to these were extracted successfully, but not easily.

It is plausible that a microstructural volume that collapsed as a result of extraction would exhibit a stiffer axial response normal to the plane of collapsed crystals. Also, with the weak crystals already having been fractured, the amount of stress it would take to cause bulk failure again should increase since the weakness of the faceted crystals had already been removed.

Following the likely damaged experiments, the extraction procedure of buried radiation recrystallized layers was revised. Later samples were successfully extracted in an easier fashion by first isolating the volume of interest containing a weak layer prior to sieving new snow over the top.

10.2.2 Deviations from Absolute Experimental Values

Boundary Conditions. Finite element models rely heavily on boundary conditions, material properties, and element formulations. The boundary conditions chosen to govern these analyses are thought to best replicate the circumstances of the laboratory mechanical test procedures, just scaled down to the microstructural level. Each finite element analysis setup will be sensitive to

the circumstances of the real world test being replicated. Here one assumption that deviates from reality is the lack of enforcement of contact between elements of failed grains. However, this parameter should only become significant after significant plastic strain is occurring, not during the elastic phase where the effective elastic stiffness coefficients are calculated. Additionally, due to the porous nature of the microstructure, it can reasonably be expected that failed bonds would physically occupy void spaces following failure in compression or shear, thus eliminating any significant contribution of contact following local failure. While element death does not match this assumption exactly, it still produces a similar effect: no contribution of contact forces between newly separated grains.

Material Properties. The second factor that affects performance of any finite element model is proper selection of material parameters. In this case, a wide range of options existed. Chandel et al. (2014) cited several sources producing a range of acceptable isotropic Young's moduli from 0.2 GPa to 9.5 GPa. In their study, the final input material model was refined to match the experimental result as close as possible (Chandel et al., 2014). Chandel et al. (2014) analyzed several sub volumes from a single homogeneous sample with a known macroscopically measured Young's modulus (Chandel et al., 2014). The

material properties selected for the model in this study are able to be refined to fit the experimental data since several independent samples of snow are not studied (Chandel et al., 2014).

As noted previously, an initial study by Schneebeli (2004) produced a range of effective stiffness values 3-100 times as large as experimentally measured values. Little detail is given in the Schneebeli study (2004) about the diversity of the samples tested. The only other study to approach finite element modeling on the microstructure in a similar fashion was a study by Hagenmuller et al. (2014). However, in this study, no comparison is ever made to experimentally measured stiffness properties (Hagenmuller et al., 2014). The reported values from the Hagenmuller et al. (2014) study are one to two orders of magnitude higher than those measured both experimentally and numerically in the present study. The broad applicability of the current finite element formulation conducted in the present study to compute effective stiffness values within one order of magnitude across several independent samples of homogeneous snow without adjusting the model's input material is encouraging.

In this particular study, the change to the microstructure is the primary emphasis for determining the relative change in stiffness and strength properties between non-faceted and radiation recrystallized faceted grains of snow. It is

shown here using finite element simulations that the microstructure does drive some of the macroscale changes observed in the macro-scale properties of the snow. However, this model also assumes homogeneous polycrystalline atmospherically formed ice as the material model for all of the microstructure.

A recent study by Riche et al. (2013) suggests persistent patterns of specific crystal orientations develop following kinetic growth metamorphism with crystallographic axes dictated by the temperature and vapor saturation environment. It is possible that individual crystal orientation, especially in highly structured layers developed as a result of kinetic metamorphism, could be significantly affected by an ordered arrangement of single ice crystals, in addition the overall geometry of the microstructure. The present study, however, did not have the ability to quantitatively analyze for crystal orientation patterns; however, some weak patterns were observed using qualitative methods. Chains of hexagonal crystals oriented with their c-axes in the direction of the vertical temperature gradient are apparent in optical images (Figure 8-21) and μCT volume renderings (Figure 10-12). In addition to c-axis growth, several a-axis forms are also present. Although not perfectly ordered or patterned, the formation of chains of facet growth should not be ignored.

Without the ability to quantify the preferred arrangement of individual crystals in the microstructure, it would not be feasible here to try to apply anisotropic single ice parameters to the microstructure volumes utilized here. However, it is conceivable that the crystallographic orientation of the crystals within a microstructure plays just as significant a role as the geometric orientation and connectivity of the ice network in determining the macroscale mechanical properties of snow. Its significance rises as the orientation of the microstructure diverges from a completely random, homogeneous arrangement.

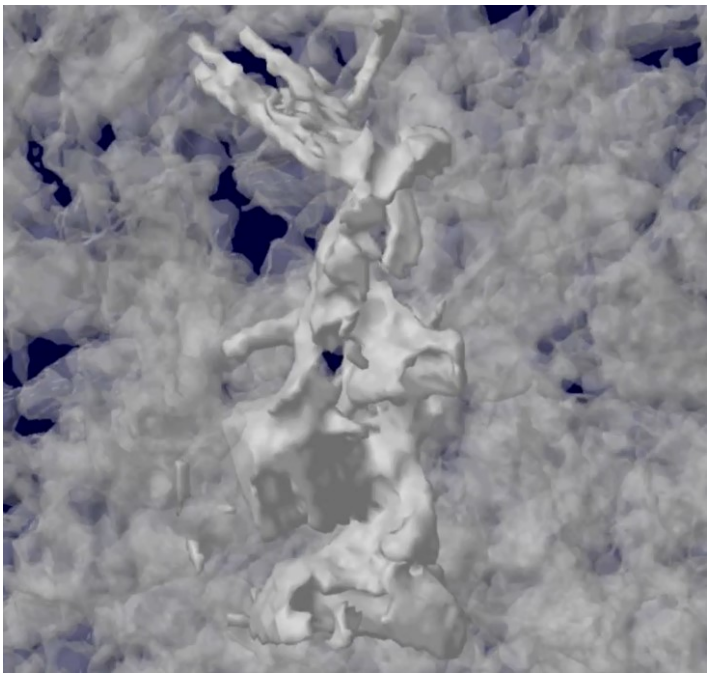


Figure 10-12: Volume rendering of a hexagonal cup/facet chain with the predominant crystal axis of the hexagonal cup oriented vertically – parallel to the macro-scale temperature gradient (adapted from Adams and Walters, 2014).

Accounting for crystal orientation patterns and preferences could also have significant impacts on the formulation of snow microstructure based constitutive models independent of numerical modeling.

Material Failure. The implementation of a failure theory was also utilized primarily to capture the strain softening behavior observed in many mechanical experiments before ultimate failure occurs. Mohr-Coulomb failure theory was selected since the difference in magnitude between tensile and compressive stresses varied by a significant amount (see Section 6.2.2). Implementing an iterative approach for detecting and killing failed element allows for progressive damage accumulation within the microstructural geometry. Utilizing the post peak stress strain data in several of the samples, bulk macroscale failure appears to have occurred near mid-height of the faceted sample.

The simulated shear stress and shear strain curves for sample 1W2 are plotted in Figure 10-13 below. Like the previous samples significant increases in strain occurred in the top half of the sample while the bottom half ceased to continue to strain. When viewed another way, the macro-scale failure plane becomes obvious. In Figure 10-14, the displacement in the x-direction is plotted over the top of the finite element mesh for the last computed load step. The colors indicate computed displacement values while the physical displacement

of the mesh is scaled 25x to make the displacement obvious. Some of the failed elements (which are still present but with zero stiffness) appear much bigger than usual as a consequence of this scaling. Units of displacement in Figure 10-14 are mm.

A steep displacement gradient exists near mid-height of the sample indicating an area of concentrated strain. This area is located in a region containing well developed cup shaped facets. This region exists spatially below the needle-like grains found on the previous surface of the snow, and above the transition region where smaller, fewer developed facets exists. Since fewer grains exists in the region where failure exists, fewer bonds are also likely in this region. Here, the critical number of bonds for macro-scale failure to occur is likely much less than other regions of the snow sample.

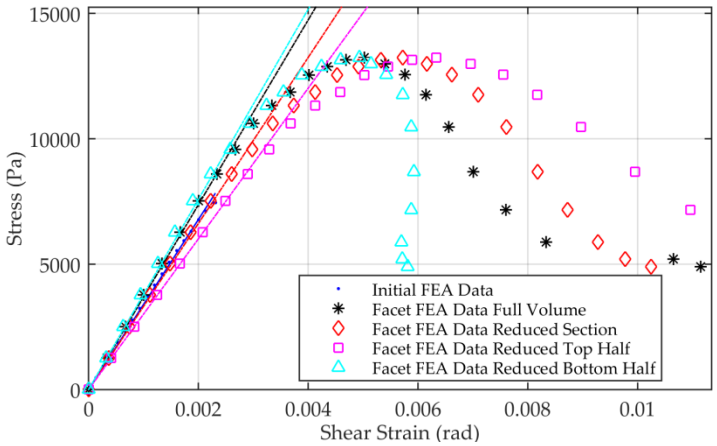


Figure 10-13: Simulated shear stress and strain of the initial and faceted volumes of experimental sample 1W2.

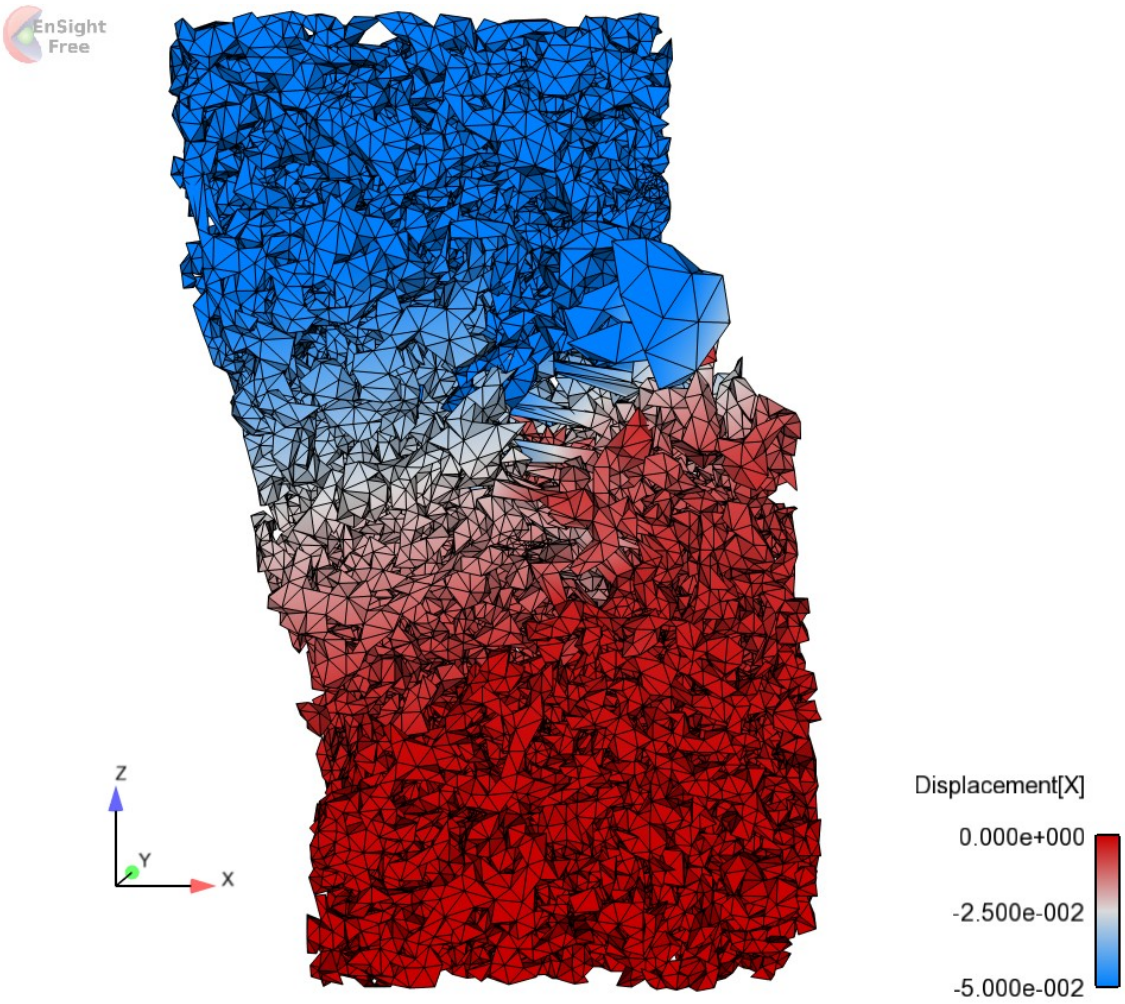


Figure 10-14: Displacement in the x-direction (mm) overlaid on the deformed mesh (25x displacement) during the final load step of the simulated shear test on the faceted volume of sample 1W2.

Element Formulation. Finite element analyses have a difficult time accurately measuring stress concentrations. This is especially true when stress concentrations are caused by abrupt changes to the geometry such as sharp corners, holes, and thin parts. The geometry of snow microstructure presents all of these problems that invite stress concentrations to form. The very nature of

how we think about deformation of the microstructure usually contends that stress concentrates at the bonded or "necked" regions of the microstructure. In preliminary reports, and other finite elements studies, it has been shown through finite element modeling that bonded regions of the snow microstructure exhibit the largest amount of stress in the entire volume (Chandel et al., 2014; Hagenmuller et al., 2014; Walters and Adams, 2014a).

When stress concentrations occur, mesh refinement around the area of interest is required to accurately reflect the magnitude and spatial scope of the stress concentration. In a two dimensional example shown in Figure 10-15, three separate mesh refinements are performed around two small corners of a part loaded in tension horizontally. In this example, mesh refinement not only more accurately computes the magnitude of stress, but also the proper spatial distribution of stress. Another benefit of mesh refinement is the decrease in stress and strain gradient in the elements. A high gradient of stress between elements indicates the need for more mesh refinement.

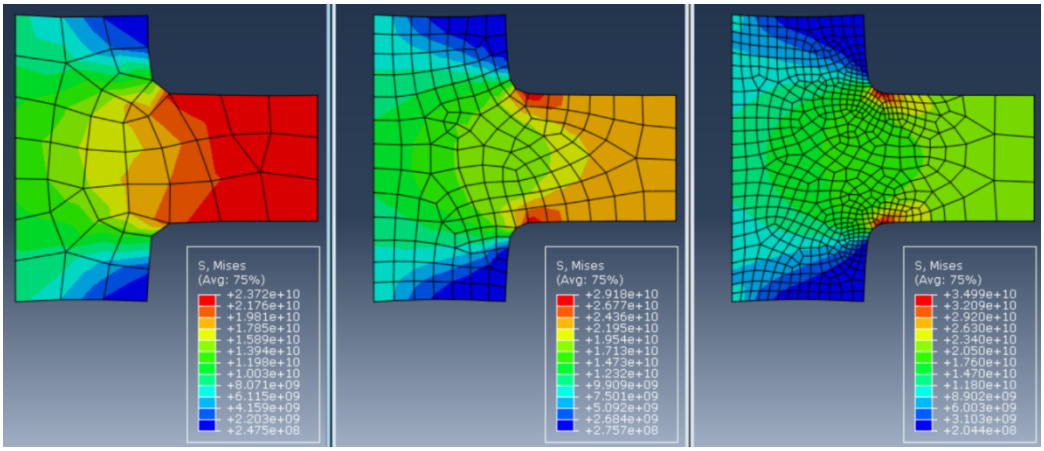


Figure 10-15: Two dimensional analysis of a part with two sharp corners loaded horizontally in tension. Mesh refinement around sharp changes in geometry results in more accurate computation and distribution of stress.

Examining the stress distribution within the snow microstructure reveals areas of the geometry that would benefit from mesh refinement. Figure 10-16 below shows the initial sample NS1 loaded in compression. The circled areas of the mesh indicate regions undergoing significant localized bending. This is indicated by the rapid change from tensile to compressive stress in the z-direction. This type of stress distribution is consistent with results seen in other studies (Hagenmuller et al., 2014).

Also visible in Figure 10-16 are areas where the stress gradient is high. These areas show quick transition from tension to compression in adjacent elements. To minimize the effects of abrupt geometry changes, element growth control is imposed to limit abrupt changes in element size around thin parts. However, it is apparent that the finite element models here would benefit from

additional mesh refinement to better approximate the effective mechanical response of the samples.

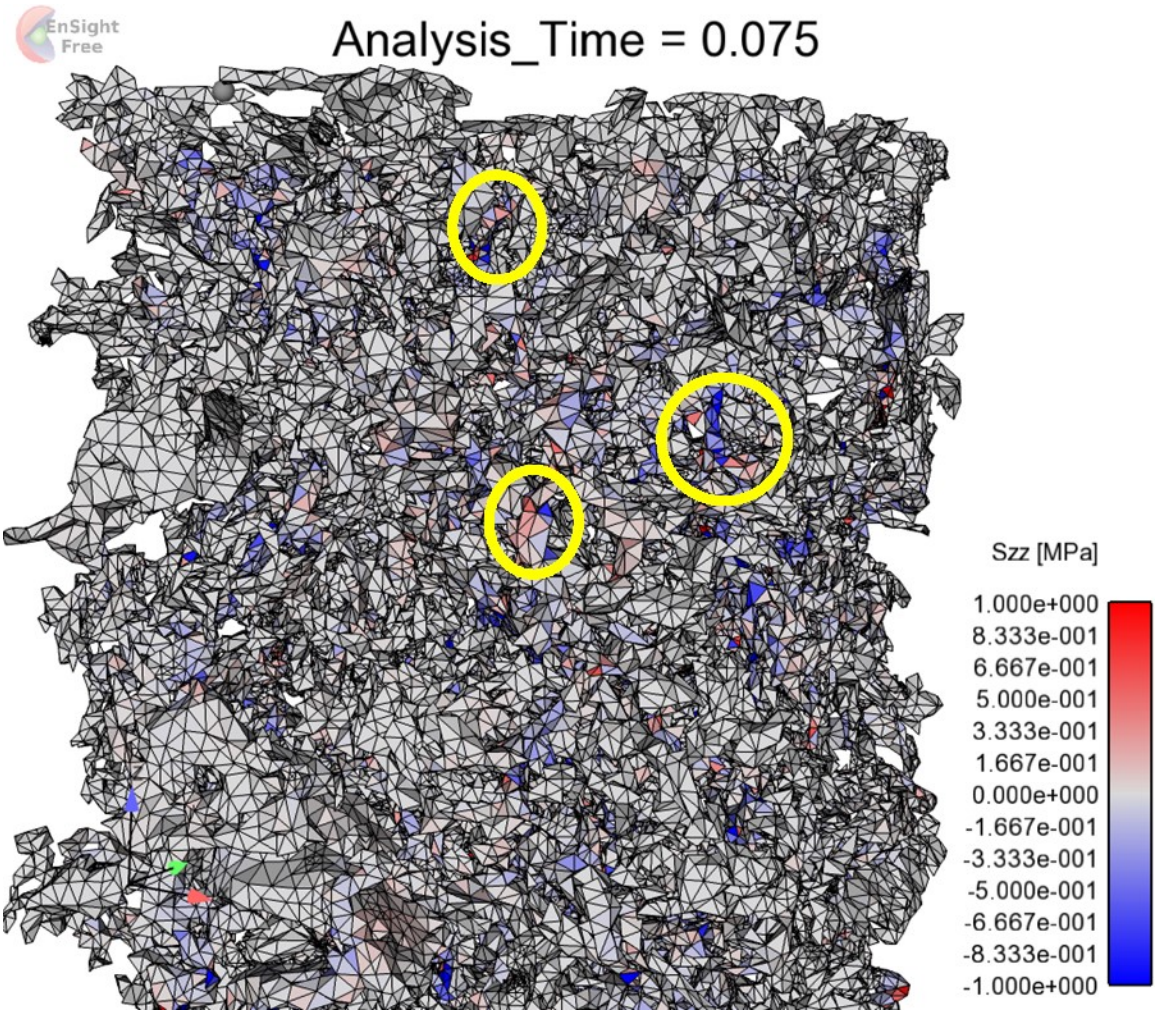


Figure 10-16: Sample NS1 with simulated compression load in the vertical direction. Circled elements show areas with significant flexural stress and high stress gradients.

Unfortunately, the computational resources are limited at the time of this study and model sizes are limited to 250k elements or nodes. All finite element

meshes utilized in this study have been refined by the maximum amount to stay within these limits. Increased mesh refinement has the ability to better capture the complex microstructure and would be expected to improve the simulated results to better match the experimental observations.

10.3 Summary

Pre and post radiation recrystallized snow samples were modeled successfully utilizing their microstructures as the input geometry. Through an iterative approach, element failure was utilized to approximate the location of the ultimate failure of the samples. Most modeled results were able to reasonably capture the relative change in material properties through changes in microstructural geometry observed temporally following radiation recrystallization metamorphism. In addition, most simulations on microstructural volumes containing faceted crystals re-emphasized the importance of the scale of regions of interest for examining results. Too large or too small of a scale can be misleading. Like the homogenization results in Chapter Nine however, the computed effective macro-scale stiffness coefficients were close to an order of magnitude higher than those measured in the physical tests presented in Chapter Eight.

The finite element models implemented here also helped investigate the location of the macro-scale failure within the faceted layer given a certain load with much higher detail than the physical tests. Using the physical tests, resolution of data only allowed for visualization of strain in the general area of the faceted layer with post failure analysis required to estimate the failure location within the faceted layer. In compression tests, this was impossible since the snow continued to compress in on itself. The finite element model provides an estimate of the possible failure modes within the microstructure itself. Rather than saying the faceted layer failed, FEA estimates where within the faceted layer macro-scale failure could have propagated.

Finite element results show the microstructure itself can be responsible for significant changes in the macroscale stiffness qualities of snow. However, material parameters which incorporate the anisotropic properties of single ice crystals could be utilized to further improve computation of the effective material properties to better match the absolute magnitudes observed experimentally. Implementation of anisotropic ice material models not only applies to numerical modeling, but should also be a consideration in constitutive modeling.

Additionally, the approach toward element failure utilizing a strength of materials approach (as employed here) may not accurately model local microstructural failure. New modeling techniques using a fracture mechanics approach and discrete element modeling shows promise toward accurately reflecting macro-scale effective mechanical properties. This approach is still under development and discussed as a personal communication with Anthony LeBaron at Montana State University in August 2016.

Additional mesh refinement is desired if the proper resources are available to achieve more accurate representation of stress concentrations throughout the sample. In addition, measurements on the distribution of individual crystal orientations within the microstructure could lead to more accurate applications of ice material properties within the microstructural volume.

CHAPTER ELEVEN

CONCLUSIONS AND RECOMMENDATIONS

"We choose to do these things, not because they are easy, but because they are hard!"
~ John F. Kennedy on going to the moon

11.1 Conclusions

Radiation recrystallized layers of faceted crystals can pose a serious hazard with regard to avalanche stability. From personal experience, these buried layers are difficult to detect in the field without prior knowledge of their formation. Through the study conducted in the lab, details about the fine structured layering were observed. Multiple layers of unique textures exist in the span of 5 to 10 mm. In the environmental temperatures tested in the laboratory, the growth of hexagonal cup shaped and rectangular faceted crystals were prevalent in the near surface morphologies that were observed. These crystals are akin to fine forms of depth hoar grains. After approximately 6 hours of growth, these faceted crystals appeared to form chains, again similar to well-developed depth hoar formations but on a much smaller scale. Simultaneous to facet chain development, slender elongated crystals begin to grow on the surface. The growth of these crystals can be explained by vapor moving up through the

snowpack and breaking free of the surface where radiative cooling induces crystal formation in surface hoar like growth. This scheme is similar to sublimation crystal growth observed in Antarctica (Gallet et al., 2014).

In addition to the weak faceted forms that grow near the surface and on the surface, sub surface crystals also undergo changes during the recrystallization process. Beneath the faceted layer, significant rounding and sintering of grains takes place resulting in the formation of a strong layer directly beneath the weakened faceted layer.

Mechanically, radiation recrystallization induces changes in mechanical stiffness and strength spatially in the near surface region of the snowpack. A pattern of changes to the shear modulus relative to the initial snow state was difficult to discern. Several factors including initial density and snowpack temperatures are thought to play a role. However, as previously stated, the snow immediately beneath the faceted layer generally became significantly stiffer than the original configuration. Spatially comparing the shear stiffness of the faceted layer and stiffer sub-faceted layer after metamorphism shows a consistent pattern. The faceted layer is usually 75%-80% less stiff than the sub-faceted layer following metamorphism. This drastic change in material properties at such a small scale creates mismatches of properties between the

interfaces that has the potential to focus long propagating fractures leading to bulk material failure.

In compression, similar weaknesses were observed. Here the compressive strength of the faceted layer was consistently reduced from its initial configuration while also decreasing in stiffness when compared to the initial configuration. Like the shear test results, the Young's moduli of the sub-faceted layer also gained significant stiffness following metamorphism.

Key to examining the stiffness properties of fine structured layers of snow is the appropriate selection of spatial boundaries. Results can be misleading if multiple snow textures are included in averaged results. Even without undertaking a microstructural analysis, understanding the spatial boundaries of key microstructural features is important to accurately analyzing the material properties of an easily metamorphosing material such as snow.

Examining the microstructural changes via homogenization techniques yielded mixed results. The initial model proposed by Shertzer (2011) consistently produced calculated effective stiffness coefficients two orders of magnitude over the measured values. The original model only considered spherical grains. Introducing a new measurable scalar shape factor, which describes crystals with an elliptical shape, improved computation of the effective

stiffness coefficients by an order of magnitude. Using the scalar microstructural parameters which include the scalar shape factor, distinct differences in elastic stiffness coefficients, similar to those observed in the physical mechanical tests, were computed using homogenization. However, the absolute magnitude of the computed effective stiffnesses were generally an order of magnitude higher than physically measured.

Fabric tensors are also a significant component of the homogenization approach. These are used to describe the textural anisotropy potentially present in the analyzed snow microstructures. As developed by Shertzer (2011) and Shertzer and Adams (2011) the contact tensor describes the overall orientation of the contact surface normal vector between bonded grains. Another useful fabric tensor is the MIL tensor used to describe the overall preferred orientation of the geometry. When analyzing the sub-faceted layers, the contact tensor showed little change from its original configuration throughout the metamorphism process. In contrast, the MIL tensor generally converged toward an isotropic configuration from an initially anisotropic configuration. Choosing either the contact tensor or MIL tensor would produce drastically different results in computing the individual anisotropic stiffness coefficients.

The introduction of the tensor ratio balances out the differences between the MIL tensor and the contact tensor. This ratio provides a directional factor which considers the significance of both types of directional quantities and replaces the directional data originally occupied by either the MIL tensor or the contact tensor.

The application of the tensor ratio, or even the MIL tensor, to the faceted layers proved to be problematic. The fine structured layering within this region made it difficult to select an RVE with a large enough volume to produce statistically significant results, yet only contain one consistent texture. The spatial scale of the unique crystal morphologies observed during and following metamorphism is prohibitive from utilizing the fully anisotropic form of homogenization for radiation recrystallized snow. This result reinforces the difficulty and importance of selecting an appropriate RVE for microstructural analysis.

However trivial, the tensor ratio generally remained isotropic for the sub-faceted region where RVE's of sufficient size could be selected which contained only one dominant microstructural texture. As stated previously, the effective isotropic coefficients reasonably estimated changes to the stiffness parameters associated with the sub-faceted region. After incorporating the scalar shape

factor, estimated effective stiffnesses were approximately one order of magnitude higher than those measured experimentally, similar to estimates from the faceted region.

In a separate approach, the finite element technique does not depend on capturing one consistent microstructural texture as long as the volume is of sufficient size. However, like the physical mechanical tests previously mentioned, isolating consistent textures while post-processing the results for simulated effective stiffness properties is important. This approach leverages similar techniques to previous studies investigating the feasibility of finite element studies operating directly on the 3-D microstructural geometry of the ice network (Chandel et al., 2014; Hagenmuller et al., 2014). Using the finite element technique, computed effective stiffnesses were generally 0.5 to 1 order of magnitude higher than the physically measured value. This is consistent with some FEA studies and improvements over others. In addition, the relative changes between the initial and final recrystallized state were captured reasonably with changes directly related to the changes in the microstructural geometry.

Here, input material parameters for ice remain constant for all simulations, regardless of the experimental sample utilized. This highlights the

significance of effect of the microstructural arrangement and shape of individual grains on the macroscale mechanical performance of snow layers. Additionally, some studies suggest material orientation also becomes significant during kinetic growth metamorphism (Riche et al., 2013), however no feasible means of quantifying patterns of single crystal orientation was available at the time of this study.

Additionally, the finite element model included an iterative process to model localized microstructural damage. This provided insight into effective strength values as well as dominant failure modes and locations within the microstructure. The implementation of a Mohr-Coulomb failure criteria produced reasonable estimations of strain softening prior to peak stress and macro-scale failure locations following peak stress. Here, failure locations consistently occurred within the region containing well developed, vertically oriented chains of facets. This is corroborated by examination of the failure surfaces from the physical mechanical tests.

Interestingly enough, both the homogenization technique (which includes scalar shape correction factors) and the finite element approach overestimate effective stiffnesses by close to an order of magnitude. This is consistent with other FEA modelling efforts which do not specifically fit ice material parameters

to fine tune model performance to better match physical testing. This raises important questions in microstructural modeling efforts on snow. Are isotropic polycrystalline ice material properties an appropriate assumption for modeling? Do the anisotropic characteristics of single ice crystals, even when positioned at random orientations, contribute significantly to local constitutive behavior? Although macro-scale strain rates modeled here assume purely elastic strain rates, are local microstructural strain rates small enough to need to consider viscous properties?

Overall, the analysis techniques employed here highlighted new details about the formation of radiation recrystallized layers and their potential effect on avalanches. Two techniques developed in this study (homogenization with scalar shape factors and finite element methods) performed reasonably well in some situations and have applicability to other types of snowpacks and weak layers. Some additional work could provide improvements in accuracy to the analytical tools provided here.

11.2 Recommendations

While the scope of this research was limited to investigating the micromechanical changes observed in radiation recrystallized snow, the methods

developed here have general application to all types of snow microstructure. Use and development of the tools in this study should be extended to operate on other forms of metamorphosed snow, especially those with more consistent microstructures across a broader spatial region.

The finite element approach to investigating the changing mechanical properties of radiation recrystallized snow performed reasonably well in describing the relative change of properties before and after metamorphism in most cases. However, like the homogenization technique, finite element methods fell short of matching the absolute magnitude of physically measured stiffnesses and were generally an order of magnitude too high.

It has been noted that in addition to changes to the microstructural geometry, ordered arrangements of single ice crystals could also contribute significantly to the macro-scale response of the snow. An appropriate extension of the current techniques would be devising a way to quantify single crystal orientation patterns in microstructures during metamorphism. This could be explored through sectioning techniques used by Riche et al (2013). Alternatively, developing an image processing/shape recognition algorithm to operate on μCT would enable leveraging the growing μCT data base in existence at Montana

State University. Anisotropic single crystal orientation could be incorporated into homogenization and FEA techniques.

In addition to mechanical studies, investigating the microstructural thermodynamic environment could be beneficial to understanding the physics driving certain crystal growth types and patterns observed in this study. Previous works by Miller et al. (2003) and Staron et al. (2014) could provide a foundation for this work as they investigate non-equilibrium thermodynamics and general temperature gradient metamorphism.

Further on, the work done here is just a brick in the foundation of other modeling efforts designed to predict changes to the snowpack affecting avalanche stability. Recent work has been completed by Curley (2015) improving spatial modeling of near surface thermal conditions making use of digital topography and modeled sky conditions. Extending this model to include a mapping of changing near surface snow properties, using the current research as a platform, could be beneficial in developing tools for forecasters and technicians to advance their abilities to operate in the field.

Other modeling efforts of the mechanical characteristics of layered snowpacks are ongoing at MSU. The results of the modeling work here can provide a complement as well as input parameters to separate modeling

techniques in use. This could apply to discrete element modeling of snow fracture or even dynamic modeling of layered snowpacks in response to explosive impulses.

Outside of snow, modeling techniques devised here have potential application in many other fields in which microstructural arrangement dictates the macro-scale thermo-mechanical response of a material.

"No man should escape our universities without knowing how little he knows."
~ Dr. J. Robert Oppenheimer

REFERENCES CITED

Abaqus 2016 Online Documentation, 2015. . Dassault Systèmes, Paris, France and Boston, MA.

Adams, E.E., Miller, D.A., 2003. Ice crystals grown from vapor onto an orientated substrate: application to snow depth-hoar development and gas inclusions in lake ice. J. Glaciol. 49, 8–12. doi:10.3189/172756503781830953

Adams, E.E., Sato, A., 1993. Model for effective thermal conductivity of a dry snow cover composed of uniform ice spheres. Ann. Glaciol. 18, 300–304.

Adams, E.E., Walters, D.J., 2014. Fine Structure Layering in Radiation Recrystallized Snow, in: International Snow Science Workshop. Banff, AB.

Akitaya, E., 1974. Studies on Depth Hoar. Contrib. from Inst. Low Temp. Sci. 26, 1–67.

Akitaya, E., Shimizu, H., 1987. Observations of weak layers in a snow cover. Low Temp. Sci., Ser. A 46, 67–75.

Alley, R.B., 1986. Three-dimensional coordination number from two-dimensional measurements: a new method. J. Glaciol. 32, 391–396.

ANSYS 14.5 APDL Element Reference, 2012. . ANSYS Inc., Canonsburg, PA.

ANSYS 14.5 APDL Structural Analysis Guide, 2012. . ANSYS Inc., Canonsburg, PA.

Armstrong, R., 1985. Metamorphism in a subfreezing, seasonal snow cover: The role of thermal and vapor pressure conditions (PhD thesis). University of Colorado.

Batchelor, G.K., O'Brien, R.W., 1977. Thermal or electrical conduction through a granular material. Proc. R. Soc. A Math. Phys. Eng. Sci. 355, 313–333.

Birkeland, K., Johnson, R., Schmidt, S., 1996. Near-surface faceted crystals: Conditions necessary for growth and contribution to avalanche formation, Southwest Montana, U.S.A., in: International Snow Science Workshop. Banff, AB, pp. 75–80.

Birkeland, K., Johnson, R.F., Schmidt, D.S., 1998. Near-surface facet crystals formed by dirunal recrystallization: A case study of weak layer formation in the mountain snowpack and its contribution to snow avalanches. Arct. Alp. Res. 30, 200–204.

Birkeland, K.W., 1998. Terminology and predominant processes associated with the formation of weak layers of near-surface faceted crystals in the mountain snowpack. Arct. Alp. Res. 30, 193–199.

Bohren, C.F., Barkstrom, B.R., 1974. Theory of Optical Properties of Snow. J. Geophys. Res. 79, 4527–4545.

Bones, J., Adams, E.E., 2009. Controlling Crystal Habit in a Small Scale Snowmaker, in: International Snow Science Workshop. Davos, SWITZERLAND, pp. 67–71.

Bruker-microCT, 2012. Morphometric parameters measured by Skyscan ™ CT - analyser software . Ref. Man. 1–49.

Cambou, B. (Ed.), 1998. CISM Courses and Lectures #385: Behaviour of Granular Materials. Springer-Verlag, New York, NY.

Cambou, B., Dubujet, P., 2001. Difficulties and limitation of statistical homogenization in granular materials. Lect. Notes Phys. 568, 205–214. doi:10.1007/3-540-44424-6_15

Cambou, B., Dubujet, P., Emeriault, F., Sidoroff, F., 1995. Homogenization for Granular Materials. Eur. J. Mech. A/Solids 14, 255–276.

Casteele, E. Van, Dyck, D. Van, Sijbers, J., Raman, E., 2004. A model-based correction method for beam hardening artefacts in X-ray microtomography. J. Xray. Sci. Technol.

Chandel, C., Srivastava, P.K., Mahajan, P., 2014. Micromechanical analysis of deformation of snow using X-ray tomography. Cold Reg. Sci. Technol. 101, 14–23. doi:10.1016/j.coldregions.2014.01.005

Chang, C.S., Chao, S.J., Chang, Y., 1995. Estimates of elastic moduli for granular material with anisotropic random packing structure. Int. J. Solids Struct. 32,

1989–2008. doi:10.1016/0020-7683(94)00225-L

Chang, C.S., Liao, C.L., 1994. Estimates of Elastic Modulus for Media of Randomly Packed Granules. Appl. Mech. Rev. 47, 197–206.

Chang, C.S., Lun, M., 1992. Elastic material constants for isotropic granular solids with particle rotation. Int. J. Solids Struct. 29, 1001–1018. doi:10.1016/0020-7683(92)90071-Z

Christoffersen, J., Mehrabadi, M.M., Nemat-Nasser, S., 1981. A Micromechanical Description of Granular Material Behavior. J. Appl. Mech. 48, 339. doi:10.1115/1.3157619

Colbeck, S.C., 1989. Snow-crystal growth with varying surface temperatures and radiation penetration. J. Glaciol. 35, 23–39. doi:10.3189/002214389793701536

Colbeck, S.C., 1983a. Theory of metamorphism of dry snow. J. Geophys. Res. Ocean. 88, 5475–5482. doi:10.1029/JC088iC09p05475

Colbeck, S.C., 1983b. Ice crystal morphology and growth rates at low supersaturations and high temperatures. J. Appl. Phys. 54, 2677. doi:10.1063/1.332290

Cook, R.D., Malkus, D.S., Plesha, M.E., Witt, R.J., 2002. Concepts and Applications of Finite Element Analysis, 4th ed. John Wiley & Sons, Inc.

Cooperstein, M.S., Birkeland, K.W., Hansen, K.J., 2004. The effects of slope aspect on the formation of surface hoar and diurnally recrystallized near-surface faceted crystals: Implications for avalanche forecasting, in: International Snow Science Workshop. Jackson Hole, WY, pp. 83–93.

Cowin, S.C., 1986. Wolff's Law of Trabecular Architecture at Remodeling Equilibrium. J. Biomech. Eng. 108, 83. doi:10.1115/1.3138584

Cowin, S.C., 1985. The relationship between the elasticity tensor and the fabric tensor. Mech. Mater. 4, 137–147. doi:10.1016/0167-6636(85)90012-2

Curl, H.J., Hardy, J.T., Ellemeier, 1972. Spectral Absorption of Solar Radiation in Alpine Snowfields. Ecol. Soc. Am. 53, 1189–1194.

Curley, P.G., 2015. The Influence of Solar Radiation in Snow on Near Surface Energy Balance in Complex Topography. MSc. Thesis Montana State University. doi:10.1017/CBO9781107415324.004

Curley, P.G., Adams, E.E., McKittrick, L.R., 2014. The Influence of Solar Radiation Attenuation in Snow on Near Surface Energy Balance in Complex Topography, in: International Snow Science Workshop. Banff, AB, pp. 567–573.

Eddins, S., 2002. The Watershed Transform: Strategies for Image Segmentation [WWW Document]. Mathworks Tech. Artic. Newsletters. URL http://www.mathworks.com/company/newsletters/articles/the-watershed-transform-strategies-for-image-segmentation.html (accessed 1.1.16).

Edens, M.Q., 1997. An experimental investigation of metamorphism-induced microstructure evolution in a " model " cohes ... Ph.D Dissertation, Montana State University.

Edens, M.Q., Brown, R.L., 1995. Measurement of microstructure of snow from surface sections. Def. Sci. J. 45, 107–116.

Emeriault, F., Cambou, B., 1996. Micromechanical modelling of anisotropic non-linear elasticity of granular medium. Int. J. Solids Struct. 33, 2591–2607. doi:10.1016/0020-7683(95)00170-0

Emeriault, F., Claquin, C., 2004. Statistical homogenization for assemblies of elliptical grains: effect of the aspect ratio and particle orientation. Int. J. Solids Struct. 41, 5837–5849. doi:10.1016/j.ijsolstr.2004.05.047

Eshelby, J.D., 1957. The Determination of the Elastic Field of an Ellipsoidal Inclusion, and Related Problems. Proc. R. Soc. A Math. Phys. Eng. Sci. 241, 376–396. doi:10.1098/rspa.1957.0133

Feldkamp, L.A., Davis, L.C., Kress, J.W., 1984. Practical cone-beam algorithm. J. Opt. Soc. Am. A 1, 612. doi:10.1364/JOSAA.1.000612

Fierz, C., 1998. Field observations and modeling of weak-layer evolution. Ann. Glaciol. 26, 7–13.

Fierz, C., Bakermans, L.A., Jamieson, J.B., Lehning, M., 2008. Modeling Short Wave Radiation Penetration in the Snowpack: What Can We Learn from Near-Surface Snow Temperatures, in: International Snow Science Workshop. Whistler, British Columbia, CANADA.

Fierz, C., Lehning, M., 2001. Assessment of the microstructure-based snow-cover model SNOWPACK : thermal and mechanical properties. Cold Reg. Sci. Technol. 33, 123–131. doi:doi:10.1016/S0165-232X(01)00033-7

Föhn, P.M.B., Camponovo, C., Krüsi, G., 1998. Mechanical and structural properties of weak snow layers measured in situ. Ann. Glaciol. 26, 1–6.

Fukuzawa, T., Akitaya, E., 1993. Depth-hoar crystal growth in the surface layer under high temperature gradient. Ann. Glaciol. 18, 39–45.

Fukuzawa, T., Narita, H., 1992. An experimental study on the mechanical behavior of a depth hoar layer under shear stress, in: International Snow Science Workshop. Breckenridge, Colorado, USA, pp. 171–175.

Gallet, J.-C., Domine, F., Savarino, J., Dumont, M., Brun, E., 2014. The growth of sublimation crystals and surface hoar on the Antarctic plateau. Cryosph. 8, 1205–1215. doi:10.5194/tc-8-1205-2014

Gammon, P.H., Kiefte, H., Clouter, M.J., Denner, W.W., 1983. Elastic Constants of Artificial and Natural Ice Samples by Brillouin Spectroscopy. J. Glaciol. 29, 433–460. doi:10.3198/1983JoG29-103-433-460

Garboczi, E.J., 1998. Finite Element and Finite Diierence Programs for Computing the Linear Electric and Elastic Properties of Digital Images of Random Materials. Build. Fire Res. Lab. Natl. Inst. Stand. Technol. U.S. Dep. Commer.

Gleason, A., 2006. Particle image velocimetry: A new technique to measure strain in loaded snow. Avalanche Rev. 24, 12.

Gray, D., Male, D., 1981. Handbook of Snow. Pergamon Press, Canada.

Greene, E., Atkins, D., Birkeland, K., Elder, K., Landry, C., Lazar, B., McCammon, I., Moore, M., Sharaf, D., Sterbenz, C., Tremper, B., Williams, K., 2010. Snow,

Weather, and Avalanches: Observation Guidelines for Avalanche Programs in the United States, 2nd ed. American Avalanche Association, Pagosa Springs, CO.

Grenfell, T.C., Perovich, D.K., 1981. Radiation Absorption Coefficients of Polycrystalline Ice from 400-1400 nm. J. Geophys. Res. 86, 7447–7450.

Habermann, M., Schweizer, J., Jamieson, J.B., 2008. Influence of snowpack layering on human-triggered snow slab avalanche release. Cold Reg. Sci. Technol. 54, 176–182. doi:10.1016/j.coldregions.2008.05.003

Hagenmuller, P., Theile, T.C., Schneebeli, M., 2014. Numerical simulation of microstructural damage and tensile strength of snow. Geophys. Res. Lett. 41, 86–89. doi:10.1002/2013GL058078

Hardy, D., Williams, M.W., Escobar, C., 2001. Near-surface faceted crystals, avalanches and climate in high-elevation, tropical mountains of Boliva. Cold Reg. Sci. Technol. 33, 291–302.

Harrigan, T.P., Mann, R.W., 1984. Characterization of microstructural anisotropy in orthotropic materials using a second rank tensor. J. Mater. Sci. 19, 761–767. doi:10.1007/BF00540446

Hill, R., 1963. Elastic properties of reinforced solids: some theoretical principles. J. Mech. Phys. Solids 11, 357–372.

Höller, P., 2004. Near-surface faceted crystals on a slope covered with stone pine trees, in: International Snow Science Workshop. Jackson Hole, WY, pp. 107–111.

Hollister, S.J., Kikuchi, N., 1992. A comparison of homogenization and standard mechanics analyses for periodic porous composites. Comput. Mech. 10, 73–95.

Hornung, U., 1997. Homogenization and Porous Media. Springer-Verlag, New York, NY.

Incropera, F.P., DeWitt, D.P., Bergman, T.L., Lavine, A.S., 2007. Fundamentals of Heat and Mass Transfer, 6th ed. John Wiley & Sons, Inc., Hoboken, NJ.

Jha, D., Sørensen, H.O., Dobberschütz, S., Feidenhans'l, R., Stipp, S.L.S., 2014. Adaptive center determination for effective suppression of ring artifacts in tomography images. Appl. Phys. Lett. 105, 143107. doi:10.1063/1.4897441

Kabel, J., van Rietbergen, B., Odgaard, A., Huiskes, R., 1999. Constitutive relationships of fabric, density, and elastic properties in cancellous bone architecture. Bone 25, 481–486. doi:10.1016/S8756-3282(99)00190-8

Kachanov, M., 1980. Continuum Model of Medium with Cracks. J. Eng. Mech. Div. 106, 1039–1051.

Kachanov, M., Sevostianov, I., 2005. On quantitative characterization of microstructures and effective properties. Int. J. Solids Struct. 42, 309–336. doi:10.1016/j.ijsolstr.2004.06.016

Kanatani, K.-I., 1984. Distribution of directional data and fabric tensors. Int. J. Eng. Sci. 22, 149–164. doi:10.1016/0020-7225(84)90090-9

Kermani, M., Farzaneh, M., Gagnon, R., 2008. Bending strength and effective modulus of atmospheric ice. Cold Reg. Sci. Technol. 53, 162–169. doi:10.1016/j.coldregions.2007.08.006

Kermani, M., Farzaneh, M., Gagnon, R., 2007. Compressive strength of atmospheric ice. Cold Reg. Sci. Technol. 49, 195–205. doi:10.1016/j.coldregions.2007.05.003

Kim, N.-H., Sankar, B. V., 2009. Introduction to Finite Element Analysis and Design. John Wiley & Sons, Inc., New York; Chichester; Weinheim; Brisbane; Singapore; Toronto.

Kry, P.R., 1975. The relationship between the visco-elastic and structural properties of fine-grained snow. J. Glaciol. 14, 479–500.

Labuz, J.F., Zang, A., 2012. Mohr–Coulomb Failure Criterion. Rock Mech. Rock Eng. 45, 975–979. doi:10.1007/s00603-012-0281-7

LaChapelle, E., 1970. Principles of avalanche forecasting, in: Gold, L., Williams, G. (Eds.), Ice Engineering and Avalanche Forecasting and Control. National Research Council of Canada, Associate Committee on Geotechnical

Research, Ottawa, pp. 106–112.

LaChapelle, E., Armstrong, R., 1977. Temperature patterns in an alpine snow cover and their influence on snow metamorphism. Inst. Arct. Alp. Res. Tech. Report. Univ. Color.

Lehning, M., Bartelt, P., Brown, B., Fierz, C., 2002. A physical SNOWPACK model for the Swiss avalanche warning. Cold Reg. Sci. Technol. 35, 169–184. doi:10.1016/S0165-232X(02)00072-1

Liao, C.-L., Chang, T.-P., Young, D.-H., Chang, C.S., 1997. Stress-strain relationship for granular materials based on the hypothesis of best fit. Int. J. Solids Struct. 34, 4087–4100. doi:10.1016/S0020-7683(97)00015-2

Libbrecht, K., 2003. The Snowflake, 1st ed. Voyager Press, St. Paul, MN.

Love, A.E.H., 1927. A Treatise on the Mathematical Theory of Elasticity. University Press, Cambridge, England.

Lubarda, V.A., Krajcinovic, D., 1993. Damage tensors and the crack density distribution. Int. J. Solids Struct. 30, 2859–2877. doi:10.1016/0020-7683(93)90158-4

Lundy, C.C., Edens, M.Q., Brown, R.L., 2002. Measurement of snow density and microstructure using computed tomography. J. Glaciol. 48, 312–316.

Mathworks, 2016. Matlab Documentation of “Watershed” Function.

McCabe, D., Munter, H., Catherine, D., Henninger, I., Cooperstein, M., Leonard, T., Adams, E.E., Slaughter, A.E., Staron, P.J., 2008. Near-surface faceting on south aspects in southwest Montana, in: International Snow Science Workshop. Whistler, British Columbia, Canada, pp. 147–154.

McClung, D., Schaerer, P., 2006. The avalanche handbook, 3rd ed. The Mountaineers Books, Seattle.

McClung, D.M., 1977. Direct simple shear tests on snow and their relation to slab avalanche formation. J. Glaciol. 19, 101–109.

Mehrabadi, M.M., Nemat-Nasser, S., 1982. On statistical description of stress and fabric in granular materials. Int. J. Numer. Anal. Methods Geomech. 6, 95–108.

Mellor, M., 1975. A review of basic snow mechanics, in: The International Symposium on Snow Mechanics. 114IAHS Publ., London, Grindelwald, Switzerland, pp. 251–291.

Meyer, F., 1994. Topographic distance and watershed lines. Signal Processing 38, 113–125. doi:10.1016/0165-1684(94)90060-4

Miller, D.A., Adams, E.E., Brown, R.L., 2003. A microstructural approach to predict dry snow metamorphism in generalized thermal conditions. Cold Reg. Sci. Technol. 37, 213–226. doi:10.1016/j.coldregions.2003.07.001

Morstad, B.W., 2004. Analytical and Experimental Study of Radiation-Recrystallized Near-Surface Facets in Snow (MSc. thesis). Mech. Eng. Montana State University.

Morstad, B.W., Adams, E.E., McKittrick, L.R., 2007. Experimental and Analytical Study of radiation-recrystallized near-surface facets in snow. Cold Reg. Sci. Technol. 47, 90–101.

Morstad, B.W., Adams, E.E., McKittrick, L.R., 2004. Experimental study of radiation-recrystallized near-surface facets in snow, in: International Snow Science Workshop. Jackson Hole, WY, pp. 124–132.

Nakamura, H., 1978. Apparatus Named “Shimo-bako” to Produce a Lot of Frost. J. Japanese Assoc. Snow Ice 40, 31–36.

Nakaya, U., 1954. Snow Crystals: Natural and Artificial. Harvard University Press, Cambridge, MA.

Navarre, J.P., Meyssonnier, J., Vagnon, A., 2007. 3D numerical model of snow deformation without failure and its application to cold room mechanical tests. Cold Reg. Sci. Technol. 50, 3–12. doi:10.1016/j.coldregions.2007.04.002

Nemat-Nasser, S., Hori, M., 1999. Micromechanics: Overall Properties of Heterogeneous Materials, 2nd ed. North Holland, Amsterdam; New York;

Nemat-Nasser, S., Mehrabadi, M., 1983. Stress and Fabric in Granular Masses, in: Studies in Applied Mechanics, Studies in Applied Mechanics. Elsevier, pp. 1–8. doi:10.1016/B978-0-444-42192-0.50007-4

Nicot, F., 2004. Constitutive modelling of snow as a cohesive-granular material. Granul. Matter 6, 47–60. doi:10.1007/s10035-004-0159-9

Oda, M., Iwashita, K. (Eds.), 1999. Mechanics of Granular Materials: An Introduction. A.A. Balkema, Rotterdam.

Oda, M., Nemat-Nasser, S., Konishi, J., 1985. Stress-induced anisotropy in granular masses. Soils Found. 25, 85–97.

Odgaard, A., 1997. Three-dimensional methods for quantification of cancellous bone architecture. Bone 20, 315–328. doi:10.1016/S8756-3282(97)00007-0

Odgaard, A., Kabel, J., van Rietbergen, B., Dalstra, M., Huiskes, R., 1997. Fabric and elastic principal directions of cancellous bone are closely related. J. Biomech. 30, 487–495. doi:10.1016/S0021-9290(96)00177-7

Paulson, T., 2001. In Avalanche Country, Thinnest of Defenses Hangs Tough: Poorly Funded Warning System Relies on a Coterie of Experts Able to Improvise. Seattle Post - Intell. Report.

Petrenko, V.F., Whitworth, R.W., 1999. Physics of Ice. Oxford University Press, New York.

Philpot, T., 2013. Mechanics of Materials: An Integrated Learning System, 3rd ed. Wiley, Hoboken, NJ.

Rahmoun, J., Kondo, D., Millet, O., 2009. A 3D fourth order fabric tensor approach of anisotropy in granular media. Comput. Mater. Sci. 46, 869–880. doi:10.1016/j.commatsci.2009.04.030

Reddy, J.N., 2008. An introduction to continuum mechanics: with applications. Cambridge University Press, New York, NY.

Reiweger, I., Schweizer, J., 2010. Failure of a layer of buried surface hoar. Geophys. Res. Lett. 37, L24501, 1–5. doi:10.1029/2010GL045433

Reiweger, I., Schweizer, J., Ernst, R., Dual, J., 2010. Cold Regions Science and Technology Load-controlled test apparatus for snow. Cold Reg. Sci. Technol. 62, 119–125. doi:10.1016/j.coldregions.2010.04.002

Reuss, A., 1929. Berechnung der Fließgrenze von Mischkristallen auf Grund der Plastizitätsbedingung für Einkristalle . ZAMM - J. Appl. Math. Mech. / Zeitschrift für Angew. Math. und Mech. 9, 49–58. doi:10.1002/zamm.19290090104

Riche, F., Montagnat, M., Schneebeli, M., 2013. Evolution of crystal orientation in snow during temperature gradient metamorphism. J. Glaciol. 59. doi:10.3189/2013JoG12J116

Satake, M., 1983. Mechanics of Granular Materials - New Models and Constitutive Relations, Studies in Applied Mechanics, Studies in Applied Mechanics. Elsevier. doi:10.1016/B978-0-444-42192-0.50008-6

Satyawali, P.K., Singh, A.K., Dewali, S.K., Kumar, P., Kumar, V., 2008. Time dependence of snow microstructure and associated effective thermal conductivity. Ann. Glaciol. 49, 43–50. doi:10.3189/172756408787814753

Scapozza, C., Bartelt, P.A., 2003. The influence of temperature on the small-strain viscous deformation mechanics of snow: a comparison with polycrystalline ice. Ann. Glaciol. 37, 90–96. doi:10.3189/172756403781815410

Schneebeli, M., 2004. Numerical simulation of elastic stress in the microstructure of snow. Ann. Glaciol. 38, 339–342.

Schneebeli, M., n.d. Producing Nature-Identical Snow [WWW Document]. Swiss Fed. Inst. For. Snow, Landsc. Res. URL http://www.wsl.ch/fe/schnee/projekte/nature_identical_snow/index_EN (accessed 1.28.16).

Schneebeli, M., Sokratov, S.A., 2004. Tomography of temperature gradient metamorphism of snow and associated changes in heat conductivity. Hydrol. Process. 18, 3655–3665. doi:10.1002/hyp.5800

Schulson, E.M., Duval, P., 2009. Creep and Fracture of Ice. Cambridge University Press, Cambridge, England.

Schweizer, J., 1999. Review of dry snow slab avalanche release. Cold Reg. Sci. Technol. 30, 43–57. doi:10.1016/S0165-232X(99)00025-7

Schweizer, J., 1998. Laboratory experiments on shear failure of snow. Ann. Glaciol. 26, 97–102.

Schwerdtfeger, P., Weller, G.E., 1971. Heat Transfer Processes in Snow and Ice. Meteorol. Stud. Plateau Station. Antarct. 25, 35–39.

Shames, I.H., Cozzarelli, F.A., 1997. Elastic and Inelastic Stress Analysis: Revised Printing. Taylor & Francis Ltd., Philadelphia.

Shertzer, R.H., 2011. Fabric tensors and effective properties of granular materials with applications to snow. Ph.D. thesis, Montana State University.

Shertzer, R.H., Adams, E.E., 2011. Anisotropic Thermal Conductivity Model for Dry Snow. Cold Reg. Sci. Technol. 69, 122–128. doi:10.1016/j.coldregions.2011.09.005

Shertzer, R.H., Adams, E.E., Schneebeli, M., 2010. Characterizing microstructural arrangement and effective properties of dry snow: thermal conductivity, in: International Snow Science Workshop. Lake Tahoe, CA, USA.

Sijbers, J., Postnov, A., 2004. Reduction of ring artefacts in high resolution micro-CT reconstructions. Phys. Med. Biol. 49, N247–53.

Slaughter, A.E., 2010. Numerical analysis of conditions necessary for near-surface snow metamorphism. Ph.D. thesis, Montana State University.

Slaughter, A.E., Adams, E.E., Staron, P.J., Shertzer, R.H., Walters, D.J., McCabe, D., Catherine, D., Henninger, I., Leonard, T., Cooperstein, M., Munter, H., 2011. Field investigation of near-surface metamorphism of snow. J. Glaciol. 57, 441–452.

Slaughter, A.E., McCabe, D., Munter, H., Staron, P.J., Adams, E.E., Catherine, D., Henninger, I., Cooperstein, M., Leonard, T., 2009. An investigation of radiation-recrystallization coupling laboratory and field studies. Cold Reg. Sci. Technol. 59, 126–132. doi:10.1016/j.coldregions.2009.07.002

Slaughter, A.E., Staron, P.J., Adams, E.E., McCabe, D., Munter, H., Catherine, D., Henninger, I., Cooperstein, M., Leonard, T., 2008. Laboratory simulations of radiation-recrystallization events in southwest montana, in: International Snow Science Workshop. Whistler, British Columbia, CANADA, pp. 139–146. doi:10.1029/2002JB002298.

Srivastava, P.K., Mahajan, P., Satyawali, P.K., Kumar, V., 2010. Observation of temperature gradient metamorphism in snow by X-ray computed microtomography: measurement of microstructure parameters and simulation of linear elastic properties. Ann. Glaciol. 50, 73–82.

Staples, M.J., 2008. Slope Scale Modeling of Snow Surface Temperature in Topographically Complex Terrain. Civ. Eng. MSc Thesis, Montana State University.

Staples, M.J., Adams, E.E., Slaughter, A.E., McKittrick, L.R., 2006. Slope Scale Modeling of Snow Surface Temperature in Topographically Complex Terrain, in: International Snow Science Workshop. Telluride, Colorado, USA, pp. 806–814.

Staron, P.J., Adams, E.E., Miller, D. a., 2014. Nonequilibrium thermodynamics of kinetic metamorphism in snow. Cold Reg. Sci. Technol. 97, 60–71. doi:10.1016/j.coldregions.2013.10.007

Staron, P.J., Adams, E.E., Miller, D.A., 2012. Formation of Depth Hoar Resulting from Thermal Optimization of Snow Microstructure, in: International Snow Science Workshop. Anchorage, Alaska, pp. 186–193.

Stoffel, L., Margreth, S., Schweizer, J., 2013. Artificial Avalanche Release and the Probability of Triggering Secondary Avalanches. Int. Snow Sci. Work. Grenoble – Chamonix Mont-Blanc - Oct. 07-11, 2013 779–782.

Stoffel, M., 2005. Numerical Modelling of Snow Using Finite Elements. Inst. Struct. Eng. (Department Civil, Environ. Geomat. Eng. Swiss Fed. Inst. Snow Avalanche Res. SLF. PhD Thesis, Swiss Federeal Institute of Technology Zürich, Zurich.

Stoffel, M., Bartelt, P., 2003. Modelling Snow Slab Release Using a Temperature-Dependent Viscoelastic Finite Element Model with Weak Layers. Surv.

Geophys. 24, 417–430. doi:10.1023/B:GEOP.0000006074.56474.43

Sturm, M., Holmgren, J., Konig, M., Morris, K., 1997. The thermal conductivity of seasonal snow. J. Glaciol. 43, 26–41.

Theile, T., Löwe, H., Theile, T.C., Schneebeli, M., 2011. Simulating creep of snow based on microstructure and the anisotropic deformation of ice. Acta Mater. 59, 7104–7113. doi:10.1016/j.actamat.2011.07.065

Tremper, B., 2001. Staying alive in avalanche terrain. The Mountaineers Books, Seattle.

Tresca, H., 1864. Memoire sur l'écoulement des solides à de forte pressions. Acad. Sci. Paris.

Turner, C.H., Cowin, S.C., 1987. Dependence of elastic constants of an anisotropic porous material upon porosity and fabric. J. Mater. Sci. 22, 3178–3184. doi:10.1007/BF01161180

Underwood, E.E., 1970. Quantitative Stereology, 2nd ed. Addison-Wesley Publishing Company, Reading, MA.

Vable, M., 2002. Mechanics of Materials, 1st ed. Oxford University Press, New York, NY.

Van Gompel, G., Van Slambrouck, K., Defrise, M., Batenburg, K.J., de Mey, J., Sijbers, J., Nuyts, J., 2011. Iterative correction of beam hardening artifacts in CT. Med. Phys. 38 Suppl 1, S36. doi:10.1118/1.3577758

Voigt, W., 1889. Über die Beziehung zwischen den Beiden Elasticitätsconstanten Isotroper Körper. Ann. Phys. 274, 573–587.

Voyiadjis, G.Z., Kattan, P.I., Taqieddin, Z.N., 2007. Continuum Approach to Damage Mechanics of Composite Materials with Fabric Tensors. Int. J. Damage Mech. 16, 301–329. doi:10.1177/1056789506064948

Walters, D.J., Adams, E.E., 2014a. Micromechanical applications to radiation recrystallized snow, in: International Snow Science Workshop. Banff, AB.

Walters, D.J., Adams, E.E., 2014b. Quantifying anisotropy from experimental testing of radiation recrystallized snow layers. Cold Reg. Sci. Technol. 97, 72–80. doi:10.1016/j.coldregions.2013.09.014

Walters, D.J., Adams, E.E., 2012. Directional mechanical properties of radiation recrystallized snow layers from experimental testing, in: International Snow Science Workshop. Anchorage, AK, pp. 201–208.

Walters, D.J., Adams, E.E., Staron, P.J., McKittrick, L.R., 2010. Shear deformation of radiation recrystallized near surface facets, in: International Snow Science Workshop. Lake Tahoe, CA, USA.

Walton, K., 1987. The effective elastic moduli of a random packing of spheres. J. Mech. Phys. Solids 35, 213–226.

Warren, S.G., Brandt, R.E., Grenfell, T.C., 2006. Visible and Near-Ultraviolet Absorption Spectrum of Ice from Transmission of Solar Radiation into Snow. Appl. Opt. 45, 5320–5334.

Whitehouse, W.J., 1974. The quantitative morphology of anisotropic trabecular bone. J. Microsc. 101, 153–168. doi:10.1111/j.1365-2818.1974.tb03878.x

Yuan, H., Lee, J.H., Guilkey, J.E., 2010. Stochastic reconstruction of the microstructure of equilibrium form snow and computation of effective elastic properties. J. Glaciol. 56, 405–414. doi:10.3189/002214310792447770

Zysset, P.K., Curnier, A., 1995. An alternative model for anisotropic elasticity based on fabric tensors. Mech. Mater. 21, 243–250. doi:10.1016/0167-6636(95)00018-6

APPENDICES

APPENDIX A

MECHANICAL TESTING DATA ACQUISITION SOFTWARE

The following material involves screenshots of the LabView virtual instrument setup utilized during the mechanical tests. The user interface contained a live preview of data as well as options for saving data files in a user selected directory. Sampling occurred at 1,000 Hz. The virtual instrument recorded readings from a load cell, LVDT, the excitation voltage of the load cell and LVDT, and the ARAMIS trigger for clock syncing.

Data files are exported in .tdms format, which is a proprietary binary format utilized by National Instruments LabView. Plugins for Microsoft Excel and Mathworks Matlab exist for importing data into their respective software suites.

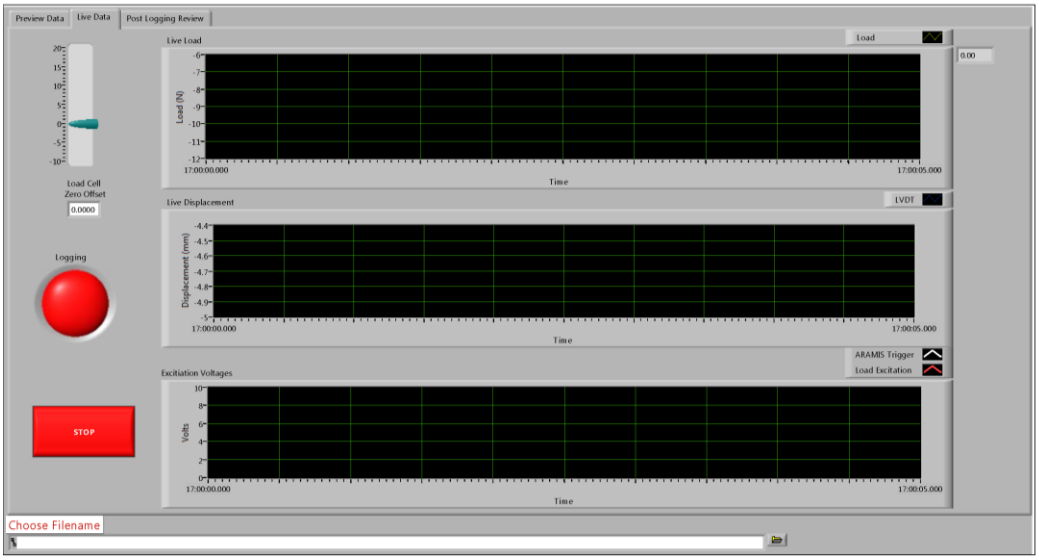


Figure A-1: User interface for activating the virtual instrument, selecting the data filename and directory, and panel for live preview of data.

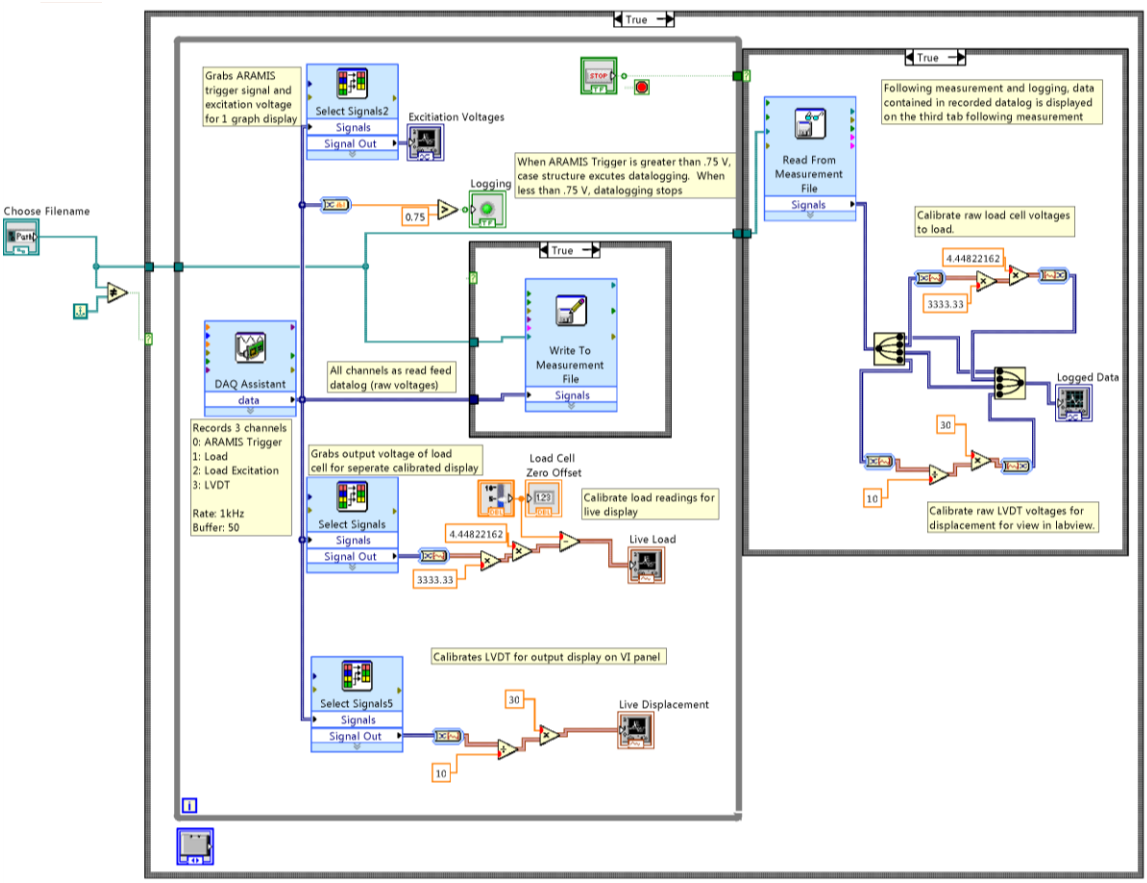


Figure A-2: Main internal block diagram for sampling data, producing the live previews, and recording the data to a measurement file.

APPENDIX B

3D WATERSHED SEGMENTATION MATLAB CODE

Matlab source code is provided here detailing the Watershed Segmentation routine. An outline of the code is provided first with details of each function following the outline.

RUNSEGMENTATION3D.m (Wrapper script for command line use)

+ Segmentation3D.m
  - BinStackImprt.m
  - WatershedSeg.m
  - InscribedSphere.m
  - GraphBuild2.m
    - NbrFind.m
    - multigrain.m
    - PlaneFit.m
  - FinalDataArray.m

RUNSEGMENTATION3D.m

```
% FileIO = {Image directory;
%             Bottom image name(with extension);
%             Top image name(with extension);
%             Output filename (no extension)}
```

```
FileIO = {'/home/david.walters/PhD Work/MicroMechanics/CT Images/2013-12-13 Shear
New/Radiation Recrystallized/Set2/0930/';
    '0930_rr_rec_tra_bin_v2_0510.bmp';
    '0930_rr_rec_tra_bin_v2_0850.bmp';
    '2013-12-13 0930 v2'};
sensitivity = 0.75;
% [Data]=Segmentation3D(runtype,imsize,FileIO,sensitivity,FileOutFlag,figflag)
[Data]=Segmentation3D('terminal',0,FileIO,sensitivity,1,0);

clear all
exit
```

Segmentation3D.m

```
function [Data]=Segmentation3D(runtype,imsize,FileIO,sensitivity,FileOutFlag,figflag)

% Function FabricTensor.m takes an image stack with cross sections parallel
% to the snow surface and performs 3-D segmentation finding bonds and grain
% pairs.
%
% INPUTS:
%   Code requires input of an image stack with sequential numbering of
%   binarized images exported from a CT Scan.  First and last images in the
%   sequence will be selected by the GUI.  The starting filepath is custom
%   and needs to be modified by the specfic user (see line 49: uigetfile)
%
%       runtype: specify either 'desktop' or 'terminal' to determine whether
%       graphical picking is enabled or not.  When running from a terminal
%       in a batch job, graphical picking and figures do not display.  This
%       also supresses all figures, regardless of the figflag input.
%
%       imsize: Specifies number of pixels in the [Y X] directions to analyze
%       on each cross section.  If the full cross section of the image is
%       desired, enter 0 here.
%
%       FileOutFlag: This specifies whether a .csv output file is created.
%       The output path of the file is customized.  See line 99 to change
%       file path to your specific needs (var = OutFilePath).
%               Specify 0 for no output (can omit if figflag is omitted)
%               Specify 1 for output
%
%       figflag: This specifies whether graphics of bond segmentation is
%       displayed or not.  When running on remote Linux server, graphics
%       generation can severely impact code performance
%               Specify 0 for no graphics (or omit all together)
%               Specify 1 for graphics
%
%       FileIO: This is a 4 element cell vector of strings containing the
%       required input and output file paths and names.  Format is as
%       specified below:
%               {'Binary image stack file path';
%                   'First binary image file name.ext';
%                   'Last binary image file name.ext';
%                   'Output file name' (no extension)}
%
%   OUTPUT:
%       Data is an array containing pertinent bond and grain information
%       for generating a contact tensor derived from 3-D volume
%       segmentation.  Column headers are as follows:
%       header=['Bond (ID), Bond X (pix), Bond Y (pix), Bond Z (pix)'...
%         ',Grain 1 (ID),Grain 1 X (pix), Grain 1 Y (pix), Grain 1 Z (pix)'...
%         ',Grain 2 (ID),Grain 2 X (pix), Grain 2 Y (pix), Grain 2 Z (pix)'...
%         ',Bond Area (pix^2),Bond Norm X (pix), Bond Norm Y (pix), Bond Norm Z (pix)'];
```

```
%
% Author: Anthony Lebaron, Montana State University
%   Edited by: David J. Walters, Montana State University
% matlabpool open 8
parpool(16)
if exist('figflag','var') == 0
    figflag = 0;
end
if exist('FileOutFlag','var') == 0
    FileOutFlag = 0;
end
% Starts with raw binary CT data

switch runtype
    case 'desktop'
        % Linux File Path
        [FirstFileName,FirstPathName] = uigetfile('/home/david.walters/PhD
Work/MicroMechanics/CT Images/*.*'...
            ,'Select First Image in Stack');

        % Windows File Path
        % [FirstFileName,FirstPathName] = uigetfile('C:\Doctoral Researach\Linux FTP
Mirror\PhD Work\MicroMechanics\CT Images\*.*'...
        %     ,'Select First Image in Stack');

        [LastFileName] = uigetfile([FirstPathName,'*.*'],'Select Last Image in Stack');
        [~,FirstInName,ext] = fileparts(FirstFileName);
        [~,LastImageName,~] = fileparts(LastFileName);
        FirstImageNum = str2num(FirstInName(end-3:end));
        LastImageNum = str2num(LastImageName(end-3:end));

        if FileOutFlag == 1
            OutFileName = input('Enter output file name (without suffix)\n','s');
        end
    case 'terminal'
        FirstPathName = FileIO{1}
        FirstFileName = FileIO{2}
        LastFileName = FileIO{3}
        [~,FirstInName,ext] = fileparts(FirstFileName);
        [~,LastImageName,~] = fileparts(LastFileName);
        FirstImageNum = str2num(FirstInName(end-3:end));
        LastImageNum = str2num(LastImageName(end-3:end));

        if FileOutFlag == 1
            OutFileName = FileIO{4}
        end
end
```

```
%% Import Images
fprintf('Begin image import.\n')
bw=BinStackImprt(FirstPathName,FirstInName(1:end-
4),'%04d',ext,FirstImageNum,imsize,LastImageNum); %Builds binary array from image stack
bw = logical(bw);
%bw=1;

fprintf('Image Import complete!\n')
fprintf('%s\n\n',datestr(now,'mmmm dd, yyyy HH:MM:SS AM'))
```

```
%% Perform Watershed Segmentation
fprintf('Begin watershed segmentation.\n')
[bonds,CCgrains,labelgrn,bw]=WatershedSeg(bw,figflag,sensitivity); %Performs watershed
segmentation, outputs bond and grain data
fprintf('Segmentation Complete!\n')
fprintf('%s\n\n',datestr(now,'mmmm dd, yyyy HH:MM:SS AM'))

clear bw
```

```
%% Calculate Effective Grain Radius for Individual Grains
fprintf('Begin grain radius calculation.\n')
GrainRadius = InscribedSphere(CCgrains);
fprintf('Grain radius calculation complete!\n')
fprintf('%s\n\n',datestr(now,'mmmm dd, yyyy HH:MM:SS AM'))
```

```
%% Build Graph
fprintf('Begin analyzing bond and grain sets.\n')
%Creates node-line graph from bond and grain data
[Area,normal,GrainBondSets,CCbonds]=GraphBuild2(bonds,CCgrains,labelgrn);
fprintf('Bond grain sets complete!\n')
fprintf('%s\n\n',datestr(now,'mmmm dd, yyyy HH:MM:SS AM'))
%Now have a current graph, but there are empty spaces in array where
%"floater" nodes (grains) existed. Graph should be cleaned up to eliminate
%nodes with no connections
% normal;
% Area;
% clear labelgrn
% clear bonds
```

```
%% Generate Final Data Array
fprintf('Create Data Array.\n')
[Data] = FinalDataArray(CCgrains,CCbonds,GrainBondSets,Area,normal,GrainRadius);
fprintf('Create Data Array Complete!\n')
fprintf('%s\n\n',datestr(now,'mmmm dd, yyyy HH:MM:SS AM'))

% Generates .csv output to specified folder in OutFilePath
if FileOutFlag == 1
%     Linux File Path
```

```
%    OutFilePath = '/home/david.walters/PhD Work/MicroMechanics/Matlab 3D Segmentation
Results/';
    OutFilePath = '/mnt/lustrefs/work/david.walters2/SegResults/';

%     Windows File Path
%     OutFilePath = 'C:\Doctoral Researach\Linux FTP Mirror\PhD
Work\MicroMechanics\Matlab 3D Segmentation Results\';
    header = ['Bond(Idx),BCx(pix),BCy(pix),BCz(pix)'...
        ',BA(pix^2),BNx(pix),BNy(pix),BNz(pix)'...
        ',G1(Idx),G1Cx(pix),G1Cy(pix),G1Cz(pix),G1Rad(pix)'...
        ',G1RCx(pix),G1RCy(pix),G1RCz(pix),G2(Idx),G2Cx(pix)'...
        ',G2Cy(pix),G2Cz(pix),G2Rad(pix),G2RCx(pix)'...
        ',G2RCy(pix),G2RCz(pix),Row(Idx)'];
    outid = fopen([OutFilePath,OutFileName,'.csv'], 'w');
    fprintf(outid, '%s\n', header);
    fclose(outid);
    dlmwrite ([OutFilePath,OutFileName,'.csv'],Data,'delimiter',',','-append');
    fprintf('Data successfully output to %s\n\n',[OutFilePath,OutFileName,'.csv'])
else
    fprintf('No data written to external file.  If desired, set FileOutFlag = 1\n\n')
end
% Data = [GrainBondSets,Area,normal];
% csvwrite('/home/david.walters/PhD Work/MicroMechanics/Edited
Code/Output/BondGrainData.csv',Data)

% matlabpool close
delete(gcp)

end
```

BinStackImprt.m

```
function [bw]= BinStackImprt(filepath,Imname,namedigits,suffix,firstim,imsize,lastim);
% Code to import a stack of binary snow images
% Filepath is a string variable to location of files and file prefixes
% namedigits is a code for the # of digits in your filenames
% suffix is '.bmp' or '.jpg' etc...be sure to include the period.

filepath=sprintf('%s',filepath); %file path for import

% lastim=firstim+imsize(3)-1; %Last image to use in stack

% IMPORT-General

for j=firstim:1:lastim
    filename=strcat(filepath,Imname,sprintf(namedigits,j),suffix);
    bwpart=imread(filename);
    if imsize == 0
        bw(:,:,j-firstim+1)=bwpart;
    else
```

```
        bw(:,:,j-firstim+1)=bwpart(1:imsize(1),1:imsize(2));
    end
end

end
```

WatershedSeg.m

```
function [bonds,CCgrains,labelgrn,bw]=WatershedSeg(bw,figflag,sensitivity)
% Anthony Lebaron
% Watershed Segmentation of objects (borrowed heavily from MATLAB help/webpage)
% http://www.mathworks.com/help/images/ref/watershed.html


%%Distance transform (from matlab help/example)

D = bwdist(~bw);


%%Complement distance transform, force nonobject pixels to be -Inf,
% then compute watershed transform

D=-D;
%D(~bw) = -Inf; %All nonobject pixels go to -infinity, therefore
%This creates a layer of 0 values on non-bond areas around objects after
%watershed segmentation. Problematic.


%%Perform Watershed Segmentation
% sprintf('Beginning Watershed Segmentation.')
L = watershed(imhmin(D,sensitivity)); %Adjust number after D for segmentation limit
%L=watershed(D);


%%Plotting for segmented objects- multicolor grains

% isosurface(L>=2,0.5) %Matlab seems to make boundaries =0 and nonobject pix =1
% %Each watershed has its own unique integer label, 2 through number of
% %grains
%
% axis equal
% title('Segmented objects')
% xlabel x, ylabel y, zlabel z
% %xlim(lims), ylim(lims), zlim(lims)
% view(3), camlight, lighting gouraud


%%Create bonds array- 1 where there is a bond voxel, 0 elsewhere
bonds=false(size(L));

for i=1:length(L(:,1,1)); %These 5 nested loops create an array of bonds in positions
```

```
where L=0 and bw=1
    for j=1:length(L(1,:,1));
        for k=1:length(L(1,1,:));
            if L(i,j,k)==0;
                if bw(i,j,k)==1;
                bonds(i,j,k)=1; %Binary bond array:
                end
            end
        end
    end
end
```

```
%%Plot bonds separately on their own array
% figure
% isosurface(bonds,0.5)
% axis equal
% title('Bonds')
% xlabel x, ylabel y, zlabel z
% xlim(lims), ylim(lims), zlim(lims)
% view(3), camlight, lighting gouraud
```

```
%%Create objects and grains arrays
%objects=bw+bonds; %Array of object voxels, where objects=1 is original objects,
objects=2 is a bond This array may only be useful for graphical output.
grains=bw-bonds;
```

```
%%Plot bonds in 1 color and grains in another
if figflag == 1
figure %Figure to show all grains in 1 color and all bonds in another
isosurface(grains,0.5)
isosurface(bonds,0.2)
axis equal
title('Segmented Objects')
end


CCgrains=bwconncomp(grains);
labelgrn=zeros(CCgrains.ImageSize); %Initialize labelgrn as zeros
%labelgrn=single(labelgrn); %Convert to single precision...a good idea, but
%then can't convert to sparse in GraphBuild2
for i=1:length(CCgrains.PixelIdxList); %For Each grain
    for j=1:length(CCgrains.PixelIdxList{i}); %For each voxel of each grain
        labelgrn(CCgrains.PixelIdxList{i}(j))=i; %Label each grain's voxel with number i
    end
end

% assignin('base','bwDebug',bw)
```

```
% assignin('base','CCgrainsDebug',CCgrains)
```

```
%%Plot multicolor grains
%
% isoval=0;
% for i=1:CCgrains.NumObjects
%     isosurface(labelgrn==i,isoval)
%     isoval=isoval+.015;
% end
%
%
% figure
% % isosurface(objects==1,0.5)
% isosurface(CCgrains,0.5)
% isosurface(bonds,0.2)
%
% axis equal
% title('Segmented objects')
% xlabel x, ylabel y, zlabel z
% %xlim(lims), ylim(lims), zlim(lims)
% view(3), camlight, lighting gouraud
% axis equal
```

InscribedSphere.m

```
function GrainRadius = InscribedSphere(CCgrains)
% Compute effective grain radius of segmented grains using the maximum
% distance transform.  This finds the size and location of the largest
% inscribed sphere within indivual grains
%
% David J. Walters
% Montana State University

GrainRadius = zeros(CCgrains.NumObjects,5);
parfor i = 1:CCgrains.NumObjects
    % Preallocate array so linear indexing has proper mapping
    Object = false(CCgrains.ImageSize);
    %Populate 3-D Array "Object" with only 1 seperate object at a time
    Object(CCgrains.PixelIdxList{i}) = 1;

    % Perform the distance transform on the singular object
    DObject = bwdist(~Object);

    %Calculate the value and position of the max distance transform
    [C1,I1] = max(DObject);
    [C2,I2] = max(C1);
    [C3,I3] = max(C2);
    I1small=squeeze(I1)
    Z = I3;
```

```
    X = I2(I3);
    Y = I1small(X,Z);

    % GrainRadius organizes data into neat data array
    % Format:
    % Grain #--Max Distance Transform(grain radius)--X--Y--Z (grain radius
    % center)
    GrainRadius(i,:) = [i,C3,X,Y,Z];
end
end
```

GraphBuild2.m

```
function [Area,normal,GrainBondSets,CCbonds]=GraphBuild2(bonds,CCgrains,labelgrn)
% Identify and label Discrete grains and bonds. Commented out b/c this is now done
externally
% Anthony LeBaron
% Montana State University

Size=size(bonds); %Size of array
% Six planes to erase bond voxels on edge of image. Prevents edge problems
% when analyzing neighborhoods. Could be improved?
bonds(1:2,:,:)=0;
bonds(:,1:2,:)=0;
bonds(:,:,1:2)=0;
bonds(Size(1)-1:Size(1),:,:)=0;
bonds(:,Size(2)-1:Size(2),:)=0;
bonds(:,:,Size(3)-1:Size(3))=0;

CCbonds=bwconncomp(bonds);%Lists voxels in each bond,
% GrnStat=regionprops(CCgrains,'Centroid'); %Stores centroids of each grain
% assignin('base','GrnStatDebug',GrnStat)
% assignin('base','CCbondsDebug',CCbonds) %Writes a copy of CCbonds to workspace in case
function doesn't finish
```

```
%%Identify neighbor grains of each bond and top/bottom relationship for flow directions
bondnum=1; %start a counter for the while loop

while bondnum<=CCbonds.NumObjects %For all bonds
    if rem(bondnum,1000) == 0;
        fprintf('Calculated %d bonds\n',bondnum)
        fprintf('%s\n\n',datestr(now,'mmmm dd, yyyy HH:MM:SS AM'))
    end
%     bondnum;
    [NbrGrains]=NbrFind(bondnum,labelgrn,Size,CCbonds);
       %Output displays grain idx number (from CCgrains) associated with
       %bond idx number (from CCbonds)
    %At this point, we have the numerical "names" of each grain touching
    %bond i. We assume flow from high z to low z.
```

```
    if length(NbrGrains)>2 %If a bond touches 3 or 4 grains, there is more work to be
done!
        %sprintf('multigrain routine triggered')
%         bondnum;
        [NbrGrains,CCbonds]=multigrain(bondnum,CCbonds,labelgrn);
        %NbrGrains=NbrGrains(1:2); %Temporary patch- not the best idea
    end

    if length(NbrGrains)<2 %If a bond has 1 or 0 neighbors, it is a floater and should be
eliminated...WHY WOULD THIS HAPPEN?!?!?! Probably due to trimming...
        fprintf('Bond detected with 0 or 1 neighbors\n')
        bondnum=bondnum+1
        continue
    end

    GrainPair = NbrGrains; %Grain Neighbors must be whittled down to pairs...add later
% GrainBondSets is an array where each column is a grain pair and
% associated bond.  The grain numbers are in rows 1 and 2 with the bond
% number in row 3.  The grain and bond numbers refer to the idx number
% associated with CCgrains and CCbonds.  From here, centroid dimensions can
% be extraceted.
    GrainBondSet(2:3,bondnum) = GrainPair;
    GrainBondSet(1,bondnum) = bondnum;

    [Area(bondnum),normal(bondnum,:)]=PlaneFit(bondnum,CCbonds);

    bondnum=bondnum+1;
end
GrainBondSets = GrainBondSet';

% Run routine that effectively deletes "floaters" from data array.  If left
% in the array, the bond number never gets removed from zero and could
% cause indexing issues later on.
b = 1;
while b <= size(GrainBondSets,1)
    if GrainBondSets(b,1) == 0
        GrainBondSets(b,:) = [];
        Area(b) = [];
        normal(b,:) = [];
        b = b;
    else
        b = b+1;
    end
end
Area = Area';
```

NbrFind.m

```
function [NbrGrains]=NbrFind(bondnum,labelgrn,Size,CCbonds)
% Function nested in GraphBuild, reports a bond's neighbors
% Anthony LeBaron

bondvox=CCbonds.PixelIdxList{bondnum}; %List of voxels in current bond
NbrGrains=[];
    for j=1:length(bondvox) %Goes through all voxels in bond to create array of
coordinates
        [x,y,z]=ind2sub(Size,bondvox(j)); %Coords of current bond voxel
        Nbrd=labelgrn(x-1:x+1,y-1:y+1,z-1:z+1); %Neighborhood in labeled grain array
        NbrGrains=vertcat(NbrGrains,unique(nonzeros(Nbrd))); %Only unique values of
neighbor grains are added to nbrs array

    end
    NbrGrains=unique(nonzeros(NbrGrains));
end
```

multigrain.m

```
function [GrainPair,CCbonds]=multigrain(bondnum,CCbonds,labelgrn)
% Function to separate bond areas in the case of >2 grains per continuous
% bond.
% If one continuous bond, as identified by watershed segmentation, touches
% more than 2 grains, this script identifies which bond voxels belong to
% which grains
% Anthony LeBaron
Separated=[0 0 0]; %Separated is a three column, multi-row array that will store bond
voxel index, 1st neighbor grain, and 2nd neighbor grain.

% Go through every voxel in the current bond, determine what each voxel's closest
neighbors are

for i=1:length(CCbonds.PixelIdxList{1,bondnum}) %For each bond voxel
    %bondnum %Display bond # for troubleshooting
    %i %Display bond voxel # in pixelidxlist
    dists=EucFromCent(5); %Euclidean distance of every voxel from center in a 5x5x5
neighborhood. This can be customized to search a closer or further neighborhood if
necessary.
    uniques=unique(dists); %List of unique distances in dists. Allows us to search
closest voxels first later on.
    [x,y,z]=ind2sub(CCbonds.ImageSize,CCbonds.PixelIdxList{1,bondnum}(i)); %Voxel
location x,y,z
    nbrd=labelgrn(x-2:x+2,y-2:y+2,z-2:z+2); %nbrd is the labeled grains surrounding the
current bond voxel

    Closest=0; %Empty array to store grains closest to current voxel
    Closest=nonzeros(Closest); %Make Closest a nonzero array
```

```
    for j=2:length(uniques) %For all nonzero distances from current bond voxel
(uniques(1)=0, so we start with j=2)

        Closest=unique(Closest); %Eliminates repeats from closest array

        Closest=unique(vertcat(Closest,unique(nonzeros(nbrd(dists==uniques(j)))))); %Find
all unique grains where distance from voxel is current value, add to current list of
closests

        if length(Closest)>=2 %If >=2 closest neighbors have been found, this loop will
assign 2 neighbors to that voxel. In the event of a three way tie, the bonds assigned are
arbitrary.

Separated=vertcat(Separated,[CCbonds.PixelIdxList{1,bondnum}(i),Closest(1),Closest(2)]);
%The first two neighbor grains are assigned to this voxel
            break %And we can stop going through neighbors of this voxel
        end
    end
end

% Now, we should have an array with one bond voxel index per row and its
% 2 closest grains. Column 1 is voxel index, column 2 is a closest
% neighbor grain, and column three is a closest neighbor grain

%Sort columns 2 and 3 in ascending order

for i=1:length(Separated(:,1)) %For all bond voxels
    Grain1=min(Separated(i,2:3));
    Grain2=max(Separated(i,2:3));
    Separated(i,2)=Grain1;
    Separated(i,3)=Grain2; %Sort all neighbor grains in ascending order
end

Separated(1,:)=[]; %Eliminates 1st row of zeros that was initially put in to enable the
vertcat command. Is there a better way to do this?

% Now there is a Separated array where each row looks like [bond vox
% index,Grain 1,Grain2. Sort by matching Grain1 and Grain2 values

Separated=sortrows(Separated,[2,3]); %Sort by 2nd then 3rd column

%The first NEW BOND voxels will replace bondnum in CCbonds
done=0; %Trigger to end function if done==1

newbond=Separated(1,1); %First voxel in Separated is assigned to array newbond
%assignin('base','SepDebug',Separated)
for i=1:length(Separated) %For all voxels in Separated

    if Separated(i,2:3)==Separated(1,2:3) %If voxel in row i of separated belongs to new
```

```
bond #1
        newbond=nonzeros(vertcat(newbond,Separated(i,1))); %newbond array is supplemented
with a new voxel
        if i==length(Separated(:,1))
            %sprintf('Only 1 bond existed, but multigrain was initiated...')
            done=1; %Trigger to break out of function
            break
        end
    else
        CCbonds.PixelIdxList{1,bondnum}=newbond; %Replace the current bond in CCbonds
with this first new bond
        GrainPair=Separated(1,2:3);
        lastpos=i; %Stores the last row in Separated that belongs to first bond
        %sprintf('1st new bond has been created')
        break %Exit for loop
    end
end

if done==1
    GrainPair=Separated(1,2:3);
    return
end

newbonds=0; %A counter to track the number of new entries to CCbonds
anustart=1; %A binary indicator to tell the for loop if it's starting a new bond. 1=yes,
0=no

for i=lastpos+1:length(Separated(:,1)) %For all remaining voxels in Separated


        if anustart==1 %If we are starting a new bond. This should trigger only after the
first bond from the previous for loop
            newbond=Separated(i,1); %The voxel in row i belongs to the new bond
            anustart=0;
            continue
        elseif Separated(i,2:3)==Separated(i-1,2:3) %If anustart!=1 and we're in the same
bond, then supplement the newbond array
            newbond=nonzeros(vertcat(newbond,Separated(i,1))); %newbond array is
supplemented with a new voxel
            if i==length(Separated(:,1))
            %sprintf('Final bond being written to CCbonds')
            newbonds=newbonds+1;
            CCbonds.PixelIdxList{1,CCbonds.NumObjects+1}=newbond; %Create a new bond in
CCbonds
            CCbonds.NumObjects= CCbonds.NumObjects+1; %Append the number of objects in
CCbonds
            %mulgrndone=1; %Not sure what this was all about
            end
```

```
        else %If anustart==0 and this row does not match the last row,
            %sprintf('New bond being written to CCbonds')
            newbonds=newbonds+1;
            CCbonds.PixelIdxList{1,CCbonds.NumObjects+1}=newbond; %Create a new bond in
CCbonds
            CCbonds.NumObjects= CCbonds.NumObjects+1; %Append the number of objects in
CCbonds
            newbond=Separated(i,1); %Start new bond


        end
end
end
```

PlaneFit.m

```
function [area,unorm]=PlaneFit(bondnum,CCbonds)
% Function to input bond voxels, output area of the best fit
% (least squares) plane
% Anthony LeBaron
%bondnum=1;

Bond=false(CCbonds.ImageSize);  %Preallocate zeros, logical array to save memory
for i=1:length(CCbonds.PixelIdxList{bondnum}) %Plot bond of interest from PIxel Id List
    Bond(CCbonds.PixelIdxList{bondnum}(i))=1;
end
%%Create X,Y,Z arrays of bond points
%In future, should reduce size of Bond to save memory. OK for now.
n=0; %counter set to 0
% Due to the index relationships to the x, y, and z coordinates, the x and
% y indices need to be flipped.  When referencing a coordinate direction in
% an array, the location should be array(Y,X,Z).  For this reason, the for
% statements are also flipped.


for y=1:CCbonds.ImageSize(1)
    for x=1:CCbonds.ImageSize(2)
        for z=1:CCbonds.ImageSize(3)
            if Bond(y,x,z)==1 %Creating X,Y,Z column arrays with coords of bond voxels
                n=n+1;
                X(n)=y;
                Y(n)=x;
                Z(n)=z;
            end
        end
    end
end
```

```
%%Find bond area based on geometry
if max(Y)==min(Y) %If plane is vertical, plane equation function doesn't work
    area=length(Y); %If plane vertical, area is # of voxels
    unorm=[0 1 0];
elseif max(Z)==min(Z) %If bond falls in constant z value, same
    area=length(Z);
    unorm=[0 0 1];
elseif max(X)==min(X) %If bond falls in constant X value, same
    area=length(X);
    unorm=[1 0 0];
else  %If plane is not neatly vertical/horizontal, bring out the big guns...Best Fit it!
    %Find plane A,B,C for equation z=Ax+By+C

ABC=[sum(X.*X),sum(X.*Y),sum(X);sum(X.*Y),sum(Y.*Y),sum(Y);sum(X),sum(Y),length(X)]\...
        [sum(X.*Z);sum(Y.*Z);sum(Z)]; %Least squares equation for a plane
    %Unit Normal
    normal=[-ABC(1)/sqrt(ABC(1)^2+ABC(2)^2+(-1)^2),...
        -ABC(2)/sqrt(ABC(1)^2+ABC(2)^2+(-1)^2),...
        1/sqrt(ABC(1)^2+ABC(2)^2+(-1)^2)]; %A normal to the plane
    %     normal = ABC; %Normal Vector
    %     unorm=normal/norm(normal); %Unit normal to the plane
    unorm = normal;

    %Thin the surface

    surface=Bond; %Surface array; some voxels will be eliminated
    for j=1:length(X)
        if max(abs(unorm))==abs(unorm(1)) %If max plane normal is in x direction
            %sprintf('Max Normal in X!')
            if surface(X(j)+1,Y(j),Z(j))==1 %If there is another bond in the x direction
                surface(X(j),Y(j),Z(j))=0; %Delete current voxel because it is redundant
for projection
                continue %Go to next iteration of for loop
            end
            if surface(X(j)-1,Y(j),Z(j))==1
                surface(X(j),Y(j),Z(j))=0; %Delete current voxel because it is redundant
for projection
                continue %Go to next iteration of for loop
            end
            continue
        end

        if max(abs(unorm))==abs(unorm(2)) %If max plane normal is in y direction
            %sprintf('Max Normal in Y!')
            if surface(X(j),Y(j)+1,Z(j))==1 %If there is another bond in the y direction
                surface(X(j),Y(j),Z(j))=0; %Delete current voxel because it is redundant
for projection
                continue %Go to next iteration of for loop
            end
```

```
            if surface(X(j),Y(j)-1,Z(j))==1
                surface(X(j),Y(j),Z(j))=0; %Delete current voxel because it is redundant
for projection
                continue %Go to next iteration of for loop
            end
            continue
        end

         if max(abs(unorm))==abs(unorm(3)) %If max plane normal is in z direction
             %sprintf('Max Normal in Z!')
            if surface(X(j),Y(j),Z(j)+1)==1 %If there is another bond in the z direction
                surface(X(j),Y(j),Z(j))=0; %Delete current voxel because it is redundant
for projection
                continue %Go to next iteration of for loop
            end
            if surface(X(j),Y(j),Z(j)-1)==1
                surface(X(j),Y(j),Z(j))=0; %Delete current voxel because it is redundant
for projection
                continue %Go to next iteration of for loop
            end
            continue
        end

    end

    %Now we have a 3D array of surface voxels (essentially a thinned
    %surface to work with Flin's algorithm)
    surfvox=nnz(surface); %# of surface voxels is equal to number of nonzero elements in
surface array
    %In the future, could only count surface voxels rather than create
    %new array, but for now will keep array for visualization.
    ratio=1/max(abs(unorm)); %Ratio of "true" surface area to area projected onto
functional plane (X,Y or Z)
    area=surfvox*ratio;
end
end
```

FinalDataArray.m

```
function [Data] = FinalDataArray(CCGrains,CCBonds,GrainBondSets,Area,Normal,GrainRadius)
% FinalDataArray.m organized bond and grain data into a single data array.
% The output column headers are as follows:
% header=['Bond (ID), Bond X (pix), Bond Y (pix), Bond Z (pix)'...
%         ',Grain 1 (ID),Grain 1 X (pix), Grain 1 Y (pix), Grain 1 Z (pix)'...
%         ',Grain 2 (ID),Grain 2 X (pix), Grain 2 Y (pix), Grain 2 Z (pix)'...
%         ',Bond Area (pix^2),Bond Norm X (pix), Bond Norm Y (pix), Bond Norm Z (pix)'];
%
% Author: David J. Walters, Montana State University
```

```
GrnStat = regionprops(CCGrains,'Centroid');
GrnCent = zeros(size(GrnStat,1),3);

parfor i=1:size(GrnStat,1)
    GrnCent(i,:) = GrnStat(i).Centroid;
end

BondStat = regionprops(CCBonds,'Centroid');
BondCent = zeros(size(BondStat,1),3);

parfor i=1:size(BondStat,1)
    BondCent(i,:) = BondStat(i).Centroid;
end

Data = zeros(size(GrainBondSets,1),25);
Data(:,1) = GrainBondSets(:,1); %List bond number
Data(:,9) = GrainBondSets(:,2); %List grain number 1 of pair bonded to associated bond
Data(:,17) = GrainBondSets(:,3); %List grain number 2 of pair bonded to associated bond
Data(:,5) = Area;              %List bond area
Data(:,6:8) = Normal;         %List bond noraml unit vector (x,y,z)
Data(:,25) = 1:size(Data,1);    %Generates listing of row number

for i=1:size(Data,1)
    Data(i,2:4) = BondCent(Data(i,1),:);        %Write centroid [x y z] in following
columns associated with bond number
    Data(i,10:12) = GrnCent(Data(i,9),:);       %Write centroid [x y z] in following
columns associated with grain number 1 of bond
    Data(i,18:20) = GrnCent(Data(i,17),:);      %Write centroid [x y z] in following
columns associated with grain number 2 of bond
    Data(i,13) = GrainRadius(Data(i,9),2);      %Write effective grain radius associated
with grain number 1 of bond
    Data(i,14:16) = GrainRadius(Data(i,9),3:5); %Write coordinates of center of grain
radius [x y z] of grain 1 of bond
    Data(i,21) = GrainRadius(Data(i,17),2);     %Write effective grain radius associated
with grain number 2 of bond
    Data(i,22:24) = GrainRadius(Data(i,17),3:5);%Write coordinates of center of grain
radius [x y z] of grain 2 of bond
end
% assignin('base','GrnCentDepug',GrnCent)
% assignin('base','BondCentDepug',BondCent)
end
```

APPENDIX C

TENSOR ASSEMBLY MATLAB CODE

Matlab source code is provided here detailing the computation of the contact tensor and tensor ratio. The MIL tensor is computed separately using advanced stereology operations in the program CTAn. This code detailed below imports these results for computation of the tensor ratio. An outline of the code is provided first with details of each function following the outline.

Two wrapper scripts are employed to invoke the functions that compute the fabric tensors. One operates on a single CT data set. The other operates on a series of datasets that utilize a specific file structure provided in the comments.

RunAllTensorsOnce.m –or– RunAllTensorsSeries.m

+AllTensors.m

- CTAnData3.m
- ContactTensor.m
  - MnDev.m
  - ConvgTest.m
  - padcat.m
  - ContactPlot.m
- TensorRatio.m
- MechModuli.m
- TensorRatioPlot.m
- MILTensorPlot.m
- MechModuliPlot.m

+SaveAllPlots.m (Quick function for saving workspace and figure windows in publication quality formats)

RunAllTensorsOnce.m

```
% Wrapper script for calling the function AllTensors.m for the one time
% step out of a series of timestamped radiation recrystallization
% experimental data
clear all; close all;
[PixSize,VolFrac,D,E,MeanStrucThick,MeanStucSep,idx,Tr,TrCi,MIL,MILCi,F2,F2Ci,...
    F4,F4Ci,bondRad,grainRad,meanBondRad,meanGrainRad,coordNum,shapeFac]...
    = AllTensors(1);
```

RunAllTensorsSeries.m

```
% Wrapper script for calling the function AllTensors.m for the entire time
% history series of a radiation recrystallization experimental run
clear all; close all; clc;
[PixSize,VolFrac,D,E,MeanStrucThick,MeanStrucSep,idx,Tr,TrCi,MIL,MILCi,F2,F2Ci,...
    F4,F4Ci,bondRad,grainRad,meanBondRad,meanGrainRad,coordNum,shapeFac]...
    = AllTensors(2);
```

AllTensors.m

```
function
[PixSize,VolFrac,D,E,MeanStrucThick,MeanStrucSep,idx,Tr,TrCi,MIL,MILCi,F2,F2Ci,...
    F4,F4Ci,bondRad,grainRad,meanBondRad,meanGrainRad,coordNum,shapeFac]...
    = AllTensors(FileIn)

% AllTensors.m
% [PixSize,VolFrac,D,E,MeanStrucThick,idx,CMILRatio,F2,F2Ci,...
%     F4,F4Ci,bondRad,grainRad,meanBondRad,meanGrainRad,coordNum,shapeFac]...
%     = AllTensors(FileIn)
% This function is utilized for post processing computed fabric tensors.
% This reads the inputs from the calculated CONTACT FABRIC TENSOR and the
% MIL FABRIC TENSOR from CTAn.
%
% INPUTS:
%       FileIn: specifies whether a single file is used or multiple files
%       chronologically ordered. 1 for single file, 2 for multiple files
%
% OUTPUTS:
%       PixSize: Outputs the pixel/voxel resolution of the CT Scan for
%       proper dimensional scaling.
%
%       VolFrac: Ice volume fraction computed for the volume of interest.
%
%       D: Eigen Values of the MIL Fabric Tensor reported from CTAn.
%
%       E: Eigen Vectors of the MIL Fabric Tensor reported from CTAn.
%
%       MeanStrucThick: The mean value of the structure thickness as
```

```
%       computed from CTAn.  This is produced by inscribing a sphere along
%       all voxels of the 3-D structures' skeleton.  The structure
%       thickness is the radius of that sphere.  In addition, a histogram
%       of the distribution of the computed structure thicknesses is
%       plotted.
%
%       F2(i,j,n): 2nd order contact tensor.  i and j reference the matrix
%       position within an individual tensor (i=1,2,3;j=1,2,3) and n
%       specifies the volume in chronological order with which the contact
%       tensor is associated.
%
%       F2Ci(i,j,n,b): Upper and lower bonds of the 95% confidence interval
%       of 2nd order contact tensor.  i, j, and n are the same as above.
%       b indicates the upper or lower bounds of the confidence interval.
%       1 indicates the lower bound, 2 indicates the upper bound.
%
%       F4(i,j,k,l,n): 4th order contact tensor. i,j,k,l are the indices of
%       the 4th order contact tensor (i,j,k,l=1,2,3). n specifies the
%       volume in chronological order with which the contact tensor is
%       associated.
%
%       F4Ci(i,j,k,l,n,b): Upper and lower bonds of the 95% confidence
%       interval of 2nd order contact tensor.  i,j,k,l,n are the same as
%       above.  b indicates the upper or lower bounds of the confidence
%       interval. 1 indicates the lower bound, 2 indicates the upper bound.
%
%       bondRad{n}: A vector of the distribution of bond radii contained
%       within a cell structure for time series data.
%
%       grainRad{n}: Same as bondRad except the distribution of grain
%       radii.
%
%       meanBondRad: Mean 3-D bond radius.  This assumes a circular contact
%       since it is based off the calculated bond area.
%
%       meanGrainRad: Mean 3-D grain radius based on the largest inscribed
%       sphere of each individual grain identified in 3-D segmentation
%
%       coordNum: Mean 3-D coordination number.  This number represents the
%       average number of contacts per grain.
%
%       shapeFac: A calculation of the scalar shape factor.  This is the
%       ratio of the spherical grain gradius (meanGrainRad) to the distance
%       of the grain center to bond center.
%
%       Tr: Tensor ratio
%
% Version: 1.0 - May 29, 2014
% Version: 2.0 - October 23, 2014
%   - Added ability to view all time series data for both segmentation
%   contact tensor data and MIL tensor data produced by CTAn.
```

```
% Version: 2.1 - October 28, 2014
%   - Added function for calculating the Tensor Ratio.  Inclusion of
%   mechanical properties is the next task.
% Version: 2.2 - October 29, 2015
%   - Changed how the MIL tensor is calculated
% AUTHOR: David J. Walters; Montana State University


%%Import data from CTAnData (external function)
[idx,PixSize,VolFrac,D,LD,UD,E,MeanStrucThick,StrucThickHist,...
    MeanStrucSep,StrucSepHist,RootPath]...
    = CTAnData3(FileIn);

%%Import data from Contact Tensor Segmentation Analysis
[F2,F2Ci,F4,F4Ci,bondRad,grainRad,meanBondRad,meanGrainRad,...
    coordNum,shapeFac,idx,endtime,spatialLabel]...
    = ContactTensor(FileIn,'geocenter2center',1,PixSize,RootPath);

%%Operate on Contact Fabric Tensor
for n = 1:length(idx)
    idx(n);
    % Generate an ellipsoid using the contact tensor to create a 3-D
    % visualization of of the distribution of bonds in the analyzed sample.
    % Generally assume contact tensor is in its principal orientation that is
    % concurrently alligned with the global coordinate system.
    %
    % To compare ellipsoids produced by the Contact Fabric Tensor, the MIL
    % Fabric Tensor, and an isotropic sphere, all volumes are normalize to one.
%     VCON(n) = (4/3)*pi*F2(1,1,n)*F2(2,2,n)*F2(3,3,n);
    %Generates an ellipsoid with the radii scaled such that the volume equals 1
%     CRad1(n) = F2(1,1,n)/(VCON(n)^(1/3));
%     CRad2(n) = F2(2,2,n)/(VCON(n)^(1/3));
%     CRad3(n) = F2(3,3,n)/(VCON(n)^(1/3));
    CRad1(n) = F2(1,1,n);
    CRad2(n) = F2(2,2,n);
    CRad3(n) = F2(3,3,n);


    [C1{n},C2{n},C3{n}]=ellipsoid(0,0,0,CRad1(n),CRad2(n),CRad3(n),30);


%%Operate on the MIL Fabric Tensor
    % Orient the MIL Fabric Tensor Ellipsoid with the Principal Axes
    % D(1,1),D(2,2), and D(3,3) are the Eigenvalues (dimensions of the
    % ellipsoid axes)
    % M1, M2, and M3 are the X, Y, and Z point clouds for producing a surface
    % mesh.
    % E is the EigenVector matrix as reported from CTAn.  Each column is the
    % EigenVector associated with each EigenValue M1,M2,and M3
%     VMIL(n) = (4/3)*pi*D(1,n)*D(2,n)*D(3,n);
    % Generates an ellipsoid with the radii scaled such that the volume equals 1
%     MILRad1(n) = D(1,n)/(VMIL(n)^(1/3));
```

```
%     MILRad2(n) = D(2,n)/(VMIL(n)^(1/3));
%     MILRad3(n) = D(3,n)/(VMIL(n)^(1/3));
    MILMatrix = D(:,n);
    MILRad1(n) = D(1,n)/sum(MILMatrix);
    MILRad2(n) = D(2,n)/sum(MILMatrix);
    MILRad3(n) = D(3,n)/sum(MILMatrix);

    [M1{n},M2{n},M3{n}]=ellipsoid(0,0,0,MILRad1(n),MILRad2(n),MILRad3(n),30);
    sz=size(M1{n});
    for x=1:sz(1)
        for y=1:sz(2)
            A=[M1{n}(x,y) M2{n}(x,y) M3{n}(x,y)]';
            A=E(:,:,n)'*A;
            M1{n}(x,y)=A(1);M2{n}(x,y)=A(2);M3{n}(x,y)=A(3);
        end
    end
```

```
    %%Compute volume of MIL Ellipsoid for equivalent isotropic sphere
%     rs = (3/4 / pi)^(1/3);
    rs = 1/3;

    [S1,S2,S3] = sphere(30);
    S1 = S1*rs;
    S2 = S2*rs;
    S3 = S3*rs;
    %%Calculate Aspect ratio of between the MIL and Contact Ellipsoids
    [Tr(:,n),TrCi(:,n,:),MIL(:,:,n),MILCi(:,:,n,:)] =
TensorRatio(F2(:,:,n),F2Ci(:,:,n,:),D(:,n),LD(:,n),UD(:,n),E(:,:,n));
```

```
    %%Calculate Mechanical Properties
    % Be sure to include outputs for the original contact tensor model, the
    % outputs for the model modified just by the grain aspect ratio, and
    % the outputs for the model modified by both the grain aspect ratio and
    % tensor ratio.

    [EStarRaw(n), GStarRaw(n), nuStarRaw(n), EStarAr(n), GStarAr(n), nuStarAr(n),...
        YoungsRaw(n), LYoungsRaw(n), UYoungsRaw(n),...
        YoungsAr(n), LYoungsAr(n), UYoungsAr(n),...
        YoungsArTr(n), LYoungsArTr(n), UYoungsArTr(n),...
        ShearRaw(n), LShearRaw(n), UShearRaw(n),...
        ShearAr(n), LShearAr(n), UShearAr(n),...
        ShearArTr(n), LShearArTr(n), UShearArTr(n),...
        PoissonRaw(n), LPoissonRaw(n), UPoissonRaw(n),...
        PoissonAr(n), LPoissonAr(n), UPoissonAr(n),...
        PoissonArTr(n), LPoissonArTr(n), UPoissonArTr(n),...
        SRaw(:,:,n), SAr(:,:,n), SArTr(:,:,n)] = ...
        MechModuli(VolFrac(n), coordNum(n), meanBondRad(n), meanGrainRad(n),...
        F2(:,:,n), F2Ci(:,:,n,:), shapeFac(n) , Tr(:,n), TrCi(:,n,:),...
        MIL(:,:,n), MILCi(:,:,n,:));
```

```
end
```

```
%% Plots
TensorRatioPlot(idx,Tr,TrCi,endtime);
MILTensorPlot(idx,MIL,MILCi,endtime);
% MILPlot(idx,C1,C2,C3,M1,M2,M3,S1,S2,S3,...
%     StrucThickHist,MeanStrucThick,StrucSepHist,MeanStrucSep,...
%     PixSize,spatialLabel,VolFrac,endtime);
MechModuliPlot( EStarRaw, GStarRaw, nuStarRaw, EStarAr, GStarAr, nuStarAr,...
    YoungsRaw, LYoungsRaw, UYoungsRaw,...
    YoungsAr, LYoungsAr, UYoungsAr,...
    YoungsArTr, LYoungsArTr, UYoungsArTr,...
    ShearRaw, LShearRaw, UShearRaw,...
    ShearAr, LShearAr, UShearAr,...
    ShearArTr, LShearArTr, UShearArTr,...
    PoissonRaw, LPoissonRaw, UPoissonRaw,...
    PoissonAr, LPoissonAr, UPoissonAr,...
    PoissonArTr, LPoissonArTr, UPoissonArTr,...
    SRaw, SAr, SArTr, endtime, idx);

end
```

CTAnData3.m

```
function [idx,PixSize,VolFrac,EigVals,LEigVals,UEigVals,EigVecs,...
    MeanStrucThick,StrucThickHist,MeanStrucSep,StrucSepHist,RootPath]...
    = CTAnData3(FileIn)
% CTAnData.m
% function [idx,PixSize,VolFrac,EigVals,EigVecs,...
%     MeanStrucThick,StrucThickHist,RootPath] = CTAnData(FileIn)
%
% This function reads in the data output from CTAn for a 3D volume analysis
% with adavanced anisotropy data turned on.  This produces the necessary
% variables for visualizing the Mean Intercept Length tensor as it relates
% to material texture (not to be confused with bonding texture).
%
% INPUTS:
%   FileIn: Enter either 1 or 2 to specify whether to read in a single file
%   (1) or multiple files (2).  In the former case, this allows you to
%   directly select the file to read in.  In the latter case, this allows
%   you to select a directory containing folders marked with the time of
%   the scan which contain the appropriate .txt files. E.g.:
%       >Time Lapse:
%           >0830
%               >0830Analysis_3D.txt
%               >0830Analysis_strucThick.txt
%           >1130
%               >1130Analysis_3D.txt
```

```
%               >1130Analysis_strucThick.txt
%           >1430
%               >1430Analysis_3D.txt
%               >1430Analysis_strucThick.txt
%        etc.
%
%
% OUTPUTS:
%       idx: Elapsed time identifier used to label plots and seperate data
%       based on time during experiment.  Derived from the folder stucture.
%       See help for subfunction FileImport in this file for the
%       appropriate folder structure to use with this function.
%
%       PixSize: Outputs the pixel/voxel resolution of the CT Scan for
%       proper dimensional scaling.
%
%       VolFrac: Ice volume fraction computed for the volume of interest.
%
%       EigVals: Eigen Values of the MIL Fabric Tensor reported from CTAn.
%
%       EigVecs: Eigen Vectors of the MIL Fabric Tensor reported from CTAn.
%
%       MeanStrucThick: The mean value of the structure thickness as
%       computed from CTAn.  This is produced by inscribing a sphere along
%       all voxels of the 3-D structures' skeleton.  The structure
%       thickness is the radius of that sphere.  In addition, a histogram
%       of the distribution of the computed structure thicknesses is
%       plotted.
%
%       StruckThickHist: Histogram data of structure thickness as computed
%       from CTAn.
%
%       RootPath: String variable containing the directory for starting
%       file selection in the correct folder.
%
% Version: 1.0 - October 23, 2014
% Version: 1.1 - Updated filepaths, October 29, 2015
% AUTHOR: David J. Walters; Montana State University


%%Import Files
switch FileIn
    case 1
%         LocalPath = 'C:\Doctoral Research\Mechanical Testing\Radiation
Recrystallization\Fabric Tensor and ANSYS\Matlab 3D Segmentation Results\';
%         LocalPath = 'C:\Users\David\Documents\MSU Research\Doctoral Work\Mechanical
Testing\Radiation Recrystallization\PhD Work\';
%         [CTAnStereoFile,CTAnStereoPath] = uigetfile(...
%             [LocalPath,'.txt'],'Select CTAn Stereology Data');
%         CTAnFullPath = [CTAnStereoPath,CTAnStereoFile];
        CTAnFullPath = 'C:\Users\David\Documents\MSU Research\Doctoral Work\Mechanical
```

```
Testing\Radiation Recrystallization\PhD Work\Spheres\Images\ThinSlice.batman.txt';
        [PixSize,VolFrac,EigVals,LEigVals,UEigVals,EigVecs,...
    MeanStrucThick,StrucThickHist{1},...
    MeanStrucSep,StrucSepHist{1}] = importCTAnAll(CTAnFullPath);
%         [PixSize,VolFrac,EigVals,LEigVals,UEigVals,EigVecs] =
importCTAnData(CTAnFullPath);
        EigVecs = EigVecs';
        VolFrac = VolFrac/100;

%         LocalPath = CTAnStereoPath;
%         [CTAnStrucThickFile,CTAnStrucThickPath] = uigetfile(...
%         [LocalPath,'.txt'],'Select CTAn Structure Thickness Data');
%         StrucThickFullPath = [CTAnStrucThickPath,CTAnStrucThickFile];
%         [MeanStrucThick,StrucThickHist{1}] = ...
%             importStruc(StrucThickFullPath,12);
%         [CTAnStrucSepFile,CTAnStrucSepPath] = uigetfile(...
%         [LocalPath,'.txt'],'Select CTAn Structure Seperation Data');
%         StrucSepFullPath = [CTAnStrucSepPath,CTAnStrucSepFile];
%         [MeanStrucSep,StrucSepHist{1}] = ...
%             importStruc(StrucSepFullPath,12);
        idx = 0;
        endtime = idx+1;
%         RootPath = LocalPath;
    case 2
        % Restrict local path for selecting data folder, and select file
        % from GUI selection
        LocalPath = 'C:\Doctoral Research\Mechanical Testing\Radiation
Recrystallization\Fabric Tensor and ANSYS\Matlab 3D Segmentation Results\';
        RootPath = uigetdir(LocalPath,...
            'Select root directory of segmentation results');
        % Get times from folders of specific tests
        TimeFolds = GetFolds(RootPath)

        % Loop through to get path for each data set and record the time
        for i = 1:length(TimeFolds)
            FilePath = fullfile(RootPath,TimeFolds{i});
            Files = dir(fullfile(FilePath,'*.txt'));
            if size(Files,1) > 3
                error('Cannot have more than three .txt file in results time folder.
Please reduce the number of .csv files to 1 in each time folder containing results')
            end
            CTAnFullPath1 = fullfile(FilePath,Files(1).name);
%             CTAnFullPath2 = fullfile(FilePath,Files(2).name);
%             CTAnFullPath3 = fullfile(FilePath,Files(3).name);
            [PixSize(i),VolFrac(i),EigVals(:,i),...
                LEigVals(:,i),UEigVals(:,i),EigVecs(:,:,i),...
    MeanStrucThick(i),StrucThickHist{i},...
    MeanStrucSep(i),StrucSepHist{i}] = importCTAnAll(CTAnFullPath1);
%
[PixSize(i),VolFrac(i),EigVals(:,i),LEigVals(:,i),UEigVals(:,i),EigVecs(:,:,i)] =
importCTAnData(CTAnFullPath1);
```

```
%             EigVecs(:,:,i) = (EigVecs{i})';
            VolFrac(i) = VolFrac(i)/100;

%             [MeanStrucThick(i),StrucThickHist{i}] = ...
%                 importStruc(CTAnFullPath2,12);
%
%             [MeanStrucSep(i),StrucSepHist{i}] = ...
%                 importStruc(CTAnFullPath3,12);

            t1{i} = datevec(TimeFolds{i},'HHMM');
            idx(i) = etime(t1{i},t1{1})/60^2;
        end
        endtime = idx(i)+1;
        days = 1;
end

if length(idx)>1
    PixSize = PixSize(1);
end

end
function [PixSize,VolFrac,EigVals,LEigVals,UEigVals,EigVecs,...
    MeanStrucThick,StrucThickHist,...
    MeanStrucSep,StrucSepHist] = importCTAnAll(filename)
fileID = fopen(filename);

% Open function
counter = 0;                                % line counter (sloppy but works)
```

```
%%Get Pixel Size
while 1                                     % infinite loop
    tline = fgetl(fileID);                     % read a line
    counter = counter + 1;                  % we are one line further
    if ischar(tline)                        % if the line is string
        U = strfind(tline, 'Pixel size,,'); % where the string start (if at all)
        if isfinite(U) == 1;                % if it is a number actually
            %             break                          % we found it, lets go home
            formatSpec = '%*s%*s%f%*s%[^\n\r]';
            delimiter = ',';
            % Read columns of data according to format string.
            % This call is based on the structure of the file used to generate this
            % code. If an error occurs for a different file, try regenerating the code
            % from the Import Tool.
            %             textscan(fileID, '%[^\n\r]', 'ReturnOnError', false)
            dataArray = textscan(tline, formatSpec, 'Delimiter', delimiter,
'ReturnOnError', false);
            PixSize = dataArray{:, 1};
            break
        end
    end
```

```
end
```

```
%%Get Volume Fraction
while 1                                    % infinite loop
    tline = fgetl(fileID);                    % read a line
    counter = counter + 1;                 % we are one line further
    if ischar(tline)                       % if the line is string
        U = strfind(tline, 'Percent object volume,'); % where the string start (if at
all)
        if isfinite(U) == 1;               % if it is a number actually
            %             break                           % we found it, lets go home
            formatSpec = '%*s%*s%f%*s%[^\n\r]';
            delimiter = ',';
            % Read columns of data according to format string.
            % This call is based on the structure of the file used to generate this
            % code. If an error occurs for a different file, try regenerating the code
            % from the Import Tool.
            %             textscan(fileID, '%[^\n\r]', 'ReturnOnError', false)
            dataArray = textscan(tline, formatSpec, 'Delimiter', delimiter,
'ReturnOnError', false);
            VolFrac = dataArray{:,1};
            break
        end
    end
end
```

```
%%Get Eigen Values
while 1                                    % infinite loop
    tline = fgetl(fileID);                    % read a line
    counter = counter + 1;                 % we are one line further
    if ischar(tline)                       % if the line is string
        U = strfind(tline, 'Principal MILs,'); % where the string start (if at all)
        if isfinite(U) == 1;               % if it is a number actually
            %             break                           % we found it, lets go home
            formatSpec = '%*s%*s%f%f%f%*s%[^\n\r]';
            delimiter = ',';
            % Read columns of data according to format string.
            % This call is based on the structure of the file used to generate this
            % code. If an error occurs for a different file, try regenerating the code
            % from the Import Tool.
            %             textscan(fileID, '%[^\n\r]', 'ReturnOnError', false)
            dataArray = textscan(tline, formatSpec, 'Delimiter', delimiter,
'ReturnOnError', false);
            EigVals = [dataArray{1:end-1}];
            EigVals = EigVals';
            break
        end
    end
```

```
end
```

```
%%Get Eigen Value Confidence Intervals
while 1                                     % infinite loop
    tline = fgetl(fileID);                     % read a line
    counter = counter + 1;                  % we are one line further
    if ischar(tline)                        % if the line is string
        U = strfind(tline, '95% Confidence intervals for principals:'); % where the
string start (if at all)
        if isfinite(U) == 1;                % if it is a number actually
            %             break                           % we found it, lets go home
            for i = 1:3
                tline = fgetl(fileID);
                counter = counter + 1;

                formatSpec = '%7f%*9c%7f%[^\n\r]';
                %             delimiter = ',';
                % Read columns of data according to format string.
                % This call is based on the structure of the file used to generate this
                % code. If an error occurs for a different file, try regenerating the
code
                % from the Import Tool.
                dataArray = textscan(tline, formatSpec);
                [LEigVals(i)] = dataArray{1, 1};
                [UEigVals(i)] = dataArray{1, 2};
            end

            break
        end
    end
end
```

```
%%Get Eigen Vectors
while 1                                     % infinite loop
    tline = fgetl(fileID);                     % read a line
    counter = counter + 1;                  % we are one line further
    if ischar(tline)                        % if the line is string
        U = strfind(tline, 'E-vector 1,'); % where the string start (if at all)
        if isfinite(U) == 1;                % if it is a number actually
            %             break                           % we found it, lets go home
            for i = 1:3
                formatSpec = '%*s%*s%f%f%f%*s%[^\n\r]';
                delimiter = ',';
                % Read columns of data according to format string.
                % This call is based on the structure of the file used to generate this
                % code. If an error occurs for a different file, try regenerating the
code
                % from the Import Tool.
                %             textscan(fileID, '%[^\n\r]', 'ReturnOnError', false)
```

```
                dataArray = textscan(tline, formatSpec, 'Delimiter', delimiter,
'ReturnOnError', false);
                [EigVecs(i,:)] = [dataArray{1:end-1}];
                tline = fgetl(fileID);
                counter = counter + 1;

            end
            EigVecs = EigVecs';

            break
        end
    end
end
```

```
%%Get Mean Structure Thickness
while 1                                 % infinite loop
    tline = fgetl(fileID);                  % read a line
    counter = counter + 1;              % we are one line further
    if ischar(tline)                    % if the line is string
        U = strfind(tline, 'Structure thickness,St.Th,'); % where the string start (if at
all)
        if isfinite(U) == 1;            % if it is a number actually
            %             break                       % we found it, lets go home
            formatSpec = '%*s%*s%f%*s%[^\n\r]';
            delimiter = ',';
            % Read columns of data according to format string.
            % This call is based on the structure of the file used to generate this
            % code. If an error occurs for a different file, try regenerating the code
            % from the Import Tool.
            %             textscan(fileID, '%[^\n\r]', 'ReturnOnError', false)
            dataArray = textscan(tline, formatSpec, 'Delimiter', delimiter,
'ReturnOnError', false);
            MeanStrucThick = [dataArray{1:end-1}];
            break
        end
    end
end
```

```
%%Get Structure Thickness Histogram
while 1                                 % infinite loop
    tline = fgetl(fileID);                  % read a line
    counter = counter + 1;              % we are one line further
    if ischar(tline)                    % if the line is string
        U = strfind(tline, 'Structure thickness distribution,St.Th'); % where the string
start (if at all)
        if isfinite(U) == 1;            % if it is a number actually
            startRow = counter+3;
            continue
        end
```

```
    end
    if ischar(tline)                        % if the line is string
        U = strfind(tline, 'Standard deviation of structure thickness'); % where the
string start (if at all)
        if isfinite(U) == 1;                % if it is a number actually
            endRow = counter-1;

            % Format string for each line of text:
            %   column2: double (%f)
            %  column4: double (%f)
            % For more information, see the TEXTSCAN documentation.
            formatSpec = '%*s%f%*s%f%[^\n\r]';
            delimiter = ',';
            % Read columns of data according to format string.
            % This call is based on the structure of the file used to generate this
            % code. If an error occurs for a different file, try regenerating the code
            % from the Import Tool.
            frewind(fileID);
            textscan(fileID, '%[^\n\r]', startRow(1),'Delimiter','\n', 'ReturnOnError',
false);
            dataArray = textscan(fileID, formatSpec, endRow(1)-startRow(1), 'Delimiter',
delimiter, 'ReturnOnError', false);
            for block=2:length(startRow)
                frewind(fileID);
                textscan(fileID, '%[^\n\r]', startRow(block)-1, 'ReturnOnError', false);
                dataArrayBlock = textscan(fileID, formatSpec, endRow(block)-
startRow(block)+1, 'Delimiter', delimiter, 'ReturnOnError', false);
                for col=1:length(dataArray)
                    dataArray{col} = [dataArray{col};dataArrayBlock{col}];
                end
            end

            % Create output variable
            StrucThickHist = [dataArray{1:end-1}];
            break
        end
    end
end
counter = endRow - 1;
```

```
%%Get Mean Structure Seperation
while 1                                     % infinite loop
    tline = fgetl(fileID);                     % read a line
    counter = counter + 1;                  % we are one line further
    if ischar(tline)                        % if the line is string
        U = strfind(tline, 'Structure separation,St.Sp,'); % where the string start (if
at all)
        if isfinite(U) == 1;                % if it is a number actually
            %             break                             % we found it, lets go home
            formatSpec = '%*s%*s%f%*s%[^\n\r]';
```

```
            delimiter = ',';
            % Read columns of data according to format string.
            % This call is based on the structure of the file used to generate this
            % code. If an error occurs for a different file, try regenerating the code
            % from the Import Tool.
            %            textscan(fileID, '%[^\n\r]', 'ReturnOnError', false)
            dataArray = textscan(tline, formatSpec, 'Delimiter', delimiter,
'ReturnOnError', false);
            MeanStrucSep = [dataArray{1:end-1}];
            break
        end
    end
end
```

```
%%Get Structure Seperation Histogram
while 1                                 % infinite loop
    tline = fgetl(fileID);                 % read a line
    counter = counter + 1;              % we are one line further
    if ischar(tline)                    % if the line is string
        U = strfind(tline, 'Structure separation distribution,St.Sp'); % where the string
start (if at all)
        if isfinite(U) == 1;            % if it is a number actually
            startRow = counter+3;
            continue
        end
    end
    if ischar(tline)                    % if the line is string
        U = strfind(tline, 'Standard deviation of structure separation'); % where the
string start (if at all)
        if isfinite(U) == 1;            % if it is a number actually
            endRow = counter-1;

            % Format string for each line of text:
            %   column2: double (%f)
            %  column4: double (%f)
            % For more information, see the TEXTSCAN documentation.
            formatSpec = '%*s%f%*s%f%[^\n\r]';
            delimiter = ',';
            % Read columns of data according to format string.
            % This call is based on the structure of the file used to generate this
            % code. If an error occurs for a different file, try regenerating the code
            % from the Import Tool.
            frewind(fileID);
            textscan(fileID, '%[^\n\r]', startRow(1),'Delimiter','\n', 'ReturnOnError',
false);
            dataArray = textscan(fileID, formatSpec, endRow(1)-startRow(1), 'Delimiter',
delimiter, 'ReturnOnError', false);
            for block=2:length(startRow)
                frewind(fileID);
```

```
                textscan(fileID, '%[^\n\r]', startRow(block)-1, 'ReturnOnError', false);
                dataArrayBlock = textscan(fileID, formatSpec, endRow(block)-
startRow(block)+1, 'Delimiter', delimiter, 'ReturnOnError', false);
                for col=1:length(dataArray)
                    dataArray{col} = [dataArray{col};dataArrayBlock{col}];
                end
            end

            % Create output variable
            StrucSepHist = [dataArray{1:end-1}];
            break
        end
    end
end
fclose(fileID);
end
```

ContactTensor.m

```
function [F2,F2Ci,F4,F4Ci,bondRad,grainRad,meanBondRad,meanGrainRad,...
    coordNum,shapeFac,idx,endtime,spatialLabel]...
    = ContactTensor(FileIn,BondVec,Plot,varargin)
% ContactTensor calculates the coefficients for the 2nd and 4th order
% contact tensor derived from 3-D segmentation data.  For 2-D stereology,
% refer to Dr. Rich Shertzer's code for analysis.
% Code also calculates confidence intervals via a bootstrap sampling method
% and also analyzes the statistical significance of the 2nd order tensor
% vs. the 4th order tensor.
%
%   INPUTS:
%       FileIn: specifies whether a single file is used or multiple files
%       chronologically ordered. 1 for single file, 2 for multiple files
%
%       BondVec: String input specifying method for calculating contact
%       tensor; options
%           'planenorm' - uses bond plane normal vector directly.  Caution
%           must be applied when using this value as bonds must be
%           sufficiently large to accurately define the plane.
%
%           'geocenter2center' - utilizes the vector connecting each grain
%           center (based on center of effective spherical grain radius)
%           in the grain-bond pair.  Can be used when 'planenorm' is not
%           giving accurate results
%
%           'masscenter2center' - utilizes the vector connecting each grain
%           center (mass centroid) in the grain-bond pair.  Can be used
%           when 'planenorm' is not giving accurate results.
%
%       Plot: Indicate 1 to include plots, 0 to exclude plots
%
```

```
%       varargin{1}: Optional input to specify the spatial pixel dimension in
%       micrometers (um).  If left blank, all spatial dimensions will be
%       based on per pixel rather than per micrometer.
%
%       varargin{2}: Optional input of the rootpath directory for starting
%       file selection in the correct folder.  This is used when function
%       is called in a higher level function where file selection is
%       already taking place.
%
%   OUTPUS:
%       F2(i,j,n): 2nd order contact tensor.  i and j reference the matrix
%       position within an individual tensor (i=1,2,3;j=1,2,3) and n
%       specifies the volume in chronological order with which the contact
%       tensor is associated.
%
%       F2Ci(i,j,n,b): Upper and lower bonds of the 95% confidence interval of
%       2nd order contact tensor.  i, j, and n are the same as above.  b
%       indicates the upper or lower bounds of the confidence interval. 1
%       indicates the lower bound, 2 indicates the upper bound.
%
%       F4(i,j,k,l,n): 4th order contact tensor. i,j,k,l are the indices of
%       the 4th order contact tensor (i,j,k,l=1,2,3). n specifies the
%       volume in chronological order with which the contact tensor is
%       associated.
%
%       F4Ci(i,j,k,l,n,b): Upper and lower bonds of the 95% confidence
%       interval of 2nd order contact tensor.  i,j,k,l,n are the same as
%       above.  b indicates the upper or lower bounds of the confidence
%       interval. 1 indicates the lower bound, 2 indicates the upper bound.
%
%       bondRad{n}: A vector of the distribution of bond radii contained
%       within a cell structure for time series data.
%
%       grainRad{n}: Same as bondRad except the distribution of grain
%       radii.
%
%       meanBondRad: Mean 3-D bond radius.  This assumes a circular contact
%       since it is based off the calculated bond area.
%
%       meanGrainRad: Mean 3-D grain radius based on the largest inscribed
%       sphere of each individual grain identified in 3-D segmentation
%
%       coordNum: Mean 3-D coordination number.  This number represents the
%       average number of contacts per grain.
%
%       shapeFac: A calculation of the scalar shape factor.  This is the
%       ratio of the spherical grain gradius (meanGrainRad) to the distance
%       of the grain center to bond center.
%
%       idx: Elapsed time identifier used to label plots and seperate data
%       based on time during experiment.  Derived from the folder stucture.
```

```
%       See help for subfunction FileImport in this file for the
%       appropriate folder structure to use with this function.
%
%       endtime: Variable listing the final elapsed time used in plotting
%       functions
%
%       spatialLabel: String variable set here to use in plotting functions
%       in other scripts and functions.
%
%   EXTERNAL FUNCTION CALLS:
%       MnDev.m
%       ConvgTest.m
%       padcat.m
%       errorbarwidth.m
%       GetFolds.m
%
%
% Author: David J. Walters, Montana State University
%
% Version 1.0 - Calculates contact tensor for a single file from 3-D
% segmentation data.  May 2, 2014
%
% Version 1.1 - Allows the import of timelapsed data from a directory of
% multiple segmentation data sets.  May 15, 2014
%
% Version 1.1.1 - Plots grain radius and bond radius distribution.
%
% Version 1.2 - Includes calculation of grain shape factor from the
% difference between spherical grain radius and the distance from spherical
% grain center to the bond center.  June 17, 2014
%
% Version 1.2.5 - Removed plots to seperate external function called
% ContactPlot.m.  October 22, 2014
%
% Version 1.3.0 - Added switch to how bond orientations are calculated.
% April 2, 2015
%
% Version 1.3.1 - Updated correct file paths
% October 29, 2015


%%Check Inputs
if isempty(varargin)
    pixdim = 1;
    spatialLabel = '( pix )';
    fprintf('All spatial dimensions are in pixels since no pixel dimension was
provided.\n')
    RootPath = 0;
elseif length(varargin) == 1
    pixdim = varargin{1};
    spatialLabel = '( \mum )';
```

```
    RootPath = 0;
elseif length(varargin) == 2
    pixdim = varargin{1};
    spatialLabel = '( \mum )';
    RootPath = varargin{2};
else
    error('Too many input arguments')
end
```

```
%%Initialize file input cases for either single analysis or a series of analyses
nboot = 1000;
[hdr,bonds,idx,endtime] = FileImport(FileIn,RootPath);   %Subfunction for importing files

% Create a waitbar to show progress of computation including a cancel
% button
h = waitbar(0,'Please wait...',...
    'Name','Calculating Contact Tensor...',...
    'CreateCancelBtn',...
    'setappdata(gcbf,''canceling'',1)');
setappdata(h,'canceling',0)
waitprev = 0;
for n = 1:length(idx)
    sprintf('idx(n)= %2.1f',idx(n))
    % Build data structure of output
    for i = 1:length(hdr{n}{1});
        % Searches for numerical position of the end of character string
        % before unit definition, i.e. rb(um), idx = 3 results in (data.rb)
        label = strfind(hdr{n}{1}{i},'(');
        data{n}.(hdr{n}{1}{i}(1:label-1)) = bonds{n}{i};
    end

    switch BondVec
        case 'planenorm'
            % Generates bond plane cell array directly from bond plane
            % normal vectors calculated during 3D segmentation
            BondPlanes{n} = [data{n}.BNx,data{n}.BNy,data{n}.BNz];

        case 'geocenter2center'
            % Generates bond plane cell array from the coordinates of the
            % centers of each grain in a grain-bond pair based on the
            % geometric center (grain radius center)

            % Calculate center to center vectors for all data at once
            BP = [data{n}.G2RCx - data{n}.G1RCx,...
                data{n}.G2RCy - data{n}.G1RCy,...
                data{n}.G2RCz - data{n}.G1RCz];

            %Need unit vectors.  These are generated here, one by one
            for i = 1:size(BP,1)
                BondPlanes{n}(i,:) = BP(i,:)/norm(BP(i,:));
```

```
            end
        case 'masscenter2center'
            % Generates bond plane cell array from the coordinates of the
            % centers of each grain in a grain-bond pair based on the
            % mass center (mass centroid)
            BP = [data{n}.G2Cx - data{n}.G1Cx,...
                data{n}.G2Cy - data{n}.G1Cy,...
                data{n}.G2Cz - data{n}.G1Cz];
            for i = 1:size(BP,1)
                BondPlanes{n}(i,:) = BP(i,:)/norm(BP(i,:));
            end
    end


    % Bootstrap sampling for confidence intervals
    for p = 1:nboot
        % Check for Cancel button press
        if getappdata(h,'canceling')
            delete(h)
            error('Canceled')
        end
        waitval = waitprev+((p/nboot)/3)/length(idx);
        waitbar(waitval,h,...
            sprintf('Bootstrap sampling in progress... Total progress
%12.1f%%',waitval*100))
        % Resample directional data before calculating tensor coefficients
        % Creates a random sample of bond numbers that is the has the
        % same length as the number of bonds, and selected with
        % replacement.
        SampRows = randsample(data{n}.Row,length(data{n}.Row),true);

        % Creates array of random sampled bond orientations based on
        % bonds identified in SampRows.
        for i = 1:length(SampRows)
            BPSamp(i,:) = BondPlanes{n}(SampRows(i),:);
        end

        F2Samp = zeros(3,3);
        F4Samp = zeros(3,3,3,3);
        for i = 1:3
            for j = 1:3
                for m=1:size(BPSamp,1)
                    F2Samp(i,j) = F2Samp(i,j) + BPSamp(m,i)*BPSamp(m,j);
                end
                for k = 1:3
                    for l = 1:3
                        for m = 1:size(BPSamp,1)
                            F4Samp(i,j,k,l) = F4Samp(i,j,k,l) + BPSamp(m,i)...
                                *BPSamp(m,j)*BPSamp(m,k)...
                                *BPSamp(m,l);
                        end
```

```
                    end
                end
            end
        end
        F2Samp = 1/length(data{n}.Bond)*F2Samp;
        F4Samp = 1/length(data{n}.Bond)*F4Samp;
        % Store each iteration of tensor coefficients for confidence
        % intervals
        F2TotSamp(:,:,p) = F2Samp;
        F4TotSamp(:,:,:,:,p) = F4Samp;

    end

    %Calculate the 95% confidence interval of the resampled tensor
    %coefficients.
    F2Ci(:,:,n,:) = prctile(F2TotSamp,[5 95],3);
    F4Ci(:,:,:,:,n,:) = prctile(F4TotSamp,[5 95],5);
    clear F2Samp
    clear F4Samp
    clear BPSamp
    clear SampRows
    clear F2TotSamp
    clear F4TotSamp
    % Calculate the 2nd order and 4th order contact tensors for the
    % entire sample of bonds.
    F2(:,:,n) = zeros(3,3);
    F4(:,:,:,:,n) = zeros(3,3,3,3);
    waitval2 = waitval;
    for i = 1:3
        waitval2 = waitval;
        for j = 1:3
            if getappdata(h,'canceling')
                delete(h)
                error('Canceled')
            end
            waitval = waitval2+(2/3)*(j/(3^2))/length(idx);
            waitbar(waitval,h,...
                sprintf('Calculating contact tensors... Total progress
%12.1f%%',waitval*100))
            for m=1:size(BondPlanes{n},1)
                F2(i,j,n) = F2(i,j,n) + BondPlanes{n}(m,i)*BondPlanes{n}(m,j);
            end
            for k = 1:3
                for l = 1:3
                    for m = 1:size(BondPlanes{n},1)
                        F4(i,j,k,l,n) = F4(i,j,k,l,n) + BondPlanes{n}(m,i)...
                            *BondPlanes{n}(m,j)*BondPlanes{n}(m,k)...
                            *BondPlanes{n}(m,l);
                    end
                end
            end
```

```
        end
    end

    F2(:,:,n) = 1/length(data{n}.Bond)*F2(:,:,n);
    F4(:,:,:,:,n) = 1/length(data{n}.Bond)*F4(:,:,:,:,n);
    if getappdata(h,'canceling')
        delete(h)
        error('Canceled')
    end
    waitval = waitprev+(7/8)/length(idx);
    waitbar(waitval,h,...
        sprintf('Finished calculating contact tensors... Total progress
%12.1f%%',waitval*100))
```

```
%%Calculate deviatoric part of contact tensors - required for N2 vs N4
    % Check for Cancel button press
    [D2,D4] = MnDev(F2(:,:,n),F4(:,:,:,:,n));   % External function

    %%Convergence of series approximations - statistical check
    alpha = 0.05;   % Significance of test - "95%"
    [zc,z2,z4] = ConvgTest(length(data{n}.Bond),3,D2,D4,alpha);   % External Function
    % Check for Cancel button press
    if getappdata(h,'canceling')
        delete(h)
        error('Canceled')
    end
    waitval = waitprev+(1/length(idx));
    waitbar(waitval,h,...
        sprintf('Testing significance... Total progress %12.1f%%',waitval*100))
    waitprev = waitval;
```

```
%%Calculate mean coordination number
    numBonds = length(data{n}.Bond);
    numGrains = length(unique([data{n}.G1 data{n}.G2]));
    coordNum(n) = 2*numBonds/numGrains;
```

```
%%Calculate mean bond radius to grain radius ratio
    bondRad{n} = (data{n}.BA./pi).^0.5;
    grainRad{n} = data{n}.G1Rad;

    meanBondRad(n) = mean(bondRad{n});
    meanGrainRad(n) = mean(grainRad{n});
```

```
%%Calculate non-spherical grain shape factor
    % Calculate the vector from the bond center to the grain radius center
    % of grain 1 of the bond.
    shapeVec{n} = [data{n}.BCx - data{n}.G1RCx,...
        data{n}.BCy - data{n}.G1RCy,...
        data{n}.BCz - data{n}.G1RCz];

    % Norm calculates the distance/magnitude of the vector.
    for i = 1:size(shapeVec{n},1)
        bondDistInd{n}(i) = norm(shapeVec{n}(i,:),2);
    end

    % Calculate the shape factor
    meanBondDist(n) = mean(bondDistInd{n});
    shapeFac(n) = meanGrainRad(n)/meanBondDist(n);


end

% Numbers of identified bonds and grains may vary if comparing more than
% one test.  Padcat is a function that pads arrays with "NaNs" when
% concatenating arrays together of different sizes.  The logic statements
% that follow allow for up to six analyses to be compared at once.  If more
% are needed, add more elseif statements following the syntax pattern found
% below.
if n == 1
    bondRad = bondRad{n};
    grainRad = grainRad{n};
elseif n == 2
    bondRad = padcat(bondRad{n-1},bondRad{n});
    grainRad = padcat(grainRad{n-1},grainRad{n});
elseif n == 3
    bondRad = padcat(bondRad{n-2},bondRad{n-1},bondRad{n});
    grainRad = padcat(grainRad{n-2},grainRad{n-1},grainRad{n});
elseif n == 4
    bondRad = padcat(bondRad{n-3},bondRad{n-2},bondRad{n-1},bondRad{n});
    grainRad = padcat(grainRad{n-3},grainRad{n-2},grainRad{n-1},grainRad{n});
elseif n == 5
    bondRad = padcat(bondRad{n-4},bondRad{n-3},bondRad{n-2},bondRad{n-1},bondRad{n});
    grainRad = padcat(grainRad{n-4},grainRad{n-3},grainRad{n-2},grainRad{n-
1},grainRad{n});
elseif n == 6
    bondRad = padcat(bondRad{n-5},bondRad{n-4},bondRad{n-3},bondRad{n-2},bondRad{n-
1},bondRad{n});
    grainRad = padcat(grainRad{n-5},grainRad{n-4},grainRad{n-3},grainRad{n-2},grainRad{n-
1},grainRad{n});
end

% Deletes the waitbar when complete
```

```
delete(h)
```

```
%%Plots & Figures

if Plot == 1
ContactPlot(F2,F2Ci,bondRad,grainRad,...
    meanBondRad,meanGrainRad,coordNum,shapeFac,...
    idx,pixdim,endtime,spatialLabel);
end
end

function [hdr,bonds,idx,endtime] = FileImport(FileIn,RootPath)
% FileImport is a function which imports 3-D segmentation data as produced
% by the Matlab function Segmentation3D run in a Linux environment.  This
% produces a .csv file containing bond and grain size, position, and
% orientation information.
%
% INPUTS:
%   FileIn: Enter either 1 or 2 to specify whether to read in a single file
%   (1) or multiple files (2).  In the former case, this allows you to
%   directly select the file to read in.  In the latter case, this allows
%   you to select a directory containing folders marked with the time of
%   the scan which contain the appropriate .csv files. E.g.:
%       >Time Lapse:
%           >0830
%               >0830Analysis.csv
%           >1130
%               >1130Analysis.csv
%           >1430
%               >1430Analysis.csv
%        etc.
%
% OUTPUTS:
%   hdr: Contains the header names of the imported data
%   bonds: Output array of the entire imported dataset
%   idx: Elapsed time of each scan.  This utilizes the name of the folder
%   to calculate time.
%   endtime: A variable that sets the maximum limit of time to be used on
%   any associated plots.
if RootPath == 0
    switch FileIn
        case 1
            LocalPath = 'C:\Doctoral Research\Mechanical Testing\Radiation
Recrystallization\Fabric Tensor and ANSYS\Matlab 3D Segmentation Results\';
            [FileName,FilePath] = uigetfile([LocalPath,'.csv'],'Select Segmentation
Data');
            FullPath = [FilePath,FileName];
            % Read files of segmentation data
            fid = fopen(FullPath, 'r');  %Open read only
```

```
            % Set headers and number of columns of data (24 columns currently)
            hdr{1} = textscan(fid, '%s',25,'delimiter',',');
            % Scan the numerical data (11 columns currently)
            bonds{1} = textscan(fid,
'%f%f%f%f%f%f%f%f%f%f%f%f%f%f%f%f%f%f%f%f%f%f%f%f%f%f%f'...
                ,'delimiter',',','HeaderLines',1);
            fclose(fid);
            idx = 0;
            endtime = idx+1;
        case 2
            % Restrict local path for selecting data folder, and select file
            % from GUI selection
            LocalPath = 'C:\Doctoral Research\Mechanical Testing\Radiation
Recrystallization\Fabric Tensor and ANSYS\Matlab 3D Segmentation Results\';
            RootPath = uigetdir(LocalPath,...
                'Select root directory of segmentation results');
            % Get times from folders of specific tests
            TimeFolds = GetFolds(RootPath);

            % Loop through to get path for each data set and record the time
            for i = 1:length(TimeFolds)
                FilePath = fullfile(RootPath,TimeFolds{i});
                Files = dir(fullfile(FilePath,'*.csv'));
                if size(Files,1) > 1
                    error('Cannot have more than one .csv file in results time folder.
Please reduce the number of .csv files to 1 in each time folder containing results')
                end
                FullPath = fullfile(FilePath,Files.name);
                fid = fopen(FullPath, 'r');  %Open read only
                % Set headers and number of columns of data (24 columns currently)
                hdr{i} = textscan(fid, '%s',25,'delimiter',',');
                % Scan the numerical data (11 columns currently)
                bonds{i} = textscan(fid...
                    ,'%f%f%f%f%f%f%f%f%f%f%f%f%f%f%f%f%f%f%f%f%f%f%f%f%f%f%f'...
                    ,'delimiter',',','HeaderLines',1);
                fclose(fid);
                t1{i} = datevec(TimeFolds{i},'HHMM');
                idx(i) = etime(t1{i},t1{1})/60^2;
            end
            endtime = idx(i)+1;
            days = 1;
    end
else
    switch FileIn
        case 1
%             LocalPath = 'C:\Doctoral Research\Mechanical Testing\Radiation
Recrystallization\Fabric Tensor and ANSYS\Matlab 3D Segmentation Results\';
%             [FileName,FilePath] = uigetfile([RootPath,'.csv'],'Select Segmentation
Data');
            Files = dir(fullfile(RootPath,'*.csv'));
```

```
            FullPath = fullfile(RootPath,Files.name);
%             FullPath = [RootPath,'VertEllipses.csv'];
            % Read files of segmentation data
            fid = fopen(FullPath, 'r');  %Open read only
            % Set headers and number of columns of data (24 columns currently)
            hdr{1} = textscan(fid, '%s',25,'delimiter',',');
            % Scan the numerical data (11 columns currently)
            bonds{1} = textscan(fid,
'%f%f%f%f%f%f%f%f%f%f%f%f%f%f%f%f%f%f%f%f%f%f%f%f%f%f%f'...
                ,'delimiter',',','HeaderLines',1);
            fclose(fid);
            idx = 0;
            endtime = idx+1;
        case 2
            % Restrict local path for selecting data folder, and select file
            % from GUI selection
%             LocalPath = 'C:\Doctoral Research\Mechanical Testing\Radiation
Recrystallization\Fabric Tensor and ANSYS\Matlab 3D Segmentation Results\';
%             RootPath = uigetdir(LocalPath,...
%                 'Select root directory of segmentation results');
            % Get times from folders of specific tests
            TimeFolds = GetFolds(RootPath)

            % Loop through to get path for each data set and record the time
            for i = 1:length(TimeFolds)
                FilePath = fullfile(RootPath,TimeFolds{i});
                Files = dir(fullfile(FilePath,'*.csv'));
                if size(Files,1) > 1
                    error('Cannot have more than one .csv file in results time folder.
Please reduce the number of .csv files to 1 in each time folder containing results')
                end
                FullPath = fullfile(FilePath,Files.name);
                fid = fopen(FullPath, 'r');  %Open read only
                % Set headers and number of columns of data (24 columns currently)
                hdr{i} = textscan(fid, '%s',25,'delimiter',',');
                % Scan the numerical data (11 columns currently)
                bonds{i} = textscan(fid...
                    ,'%f%f%f%f%f%f%f%f%f%f%f%f%f%f%f%f%f%f%f%f%f%f%f%f%f%f%f'...
                    ,'delimiter',',','HeaderLines',1);
                fclose(fid);
                t1{i} = datevec(TimeFolds{i},'HHMM');
                idx(i) = etime(t1{i},t1{1})/60^2;
            end
            endtime = idx(i)+1;
            days = 1;
    end
end
end
```

MnDev.m

```
function [Dev2,Dev4] = MnDev(F2,F4)
% This function computes the mean and deviatoric parts of the symmetric 2nd
% and 4th rank contact tensors (arrays)
% Richard Shertzer
%
%Input:
%   F2 - symmetric, 2nd order contact tensor
%   F4 - symmetric, 4th order contact tensor
%   fn - field names, "xy", "xz", "yz"
%   n - number of fields
%
%Output:
%   Mn - the scalar, mean value of input N2
%   Dev2 - the deviatoric part of N2, a 2nd rank tensor
%   Dev4 - the deviatoric part of N4, a 4th rank tensor

%%Intialize variables
dim = 3;
I = eye(dim);   % Define 2nd order identity/kronecker tensor

%%Calculate mean and deviatoric parts

% Calculate 2nd order mean
mn = trace(F2) / dim;
Mn = trace(F2);     %Density Distribution Mean is 1st invariant of N2

% Calculate 2nd order deviator
DevN = F2 - mn*I;

% Calculate 4th order deviator
for i = 1:dim

    for j = 1:dim
        for k = 1:dim
            for l = 1:dim
                K(i,j,k,l) = 1/3 * (I(i,j) * I(k,l) +...
                    I(i,k) * I(j,l )+...
                    I(i,l) * I(j,k));
                A(i,j,k,l) = 1/6 * (I(i,j) * F2(k,l) +...
                    I(k,l) * F2(i,j) +...
                    I(i,k) * F2(j,l) +...
                    I(i,l) * F2(j,k) +...
                    I(j,k) * F2(i,l) +...
                    I(j,l) * F2(i,k));
            end
        end
    end
end
```

```
% See Equations 2.20 and 2.21 in Shertzer's dissertation for
% explanation on the following.  See Kanatani (1984)
Dev2 = 15/2 * DevN;
Dev4= 315/8 * (F4 - 6/7*A + 3/35*K);


end
```

ConvgTest.m

```
function [zcrit,z2,z4] = ConvgTest(N,dim,D2,D4,alpha,fn,n)
% This function performs a hypothesis test to determine whether the higher
% rank tensors are required to more accurately describe the distribution
% density
%
% Richard Shertzer
% Input:
%   N - # of samples (contact normal vectors)
%   dim - dimension of individual tensors; 2 for 2-D problem, 3 for 3-D
%       problem
%   D2 - symmetric, 2nd rank deviatoric tensor
%   D4 - symmetric, 4th rank deviatoric tensor
%   alpha - user defined significance of hypothesis test
%   fn - field names of the three orthogonal planes: "xy", "xz", "yz"
%   n - dimension of problem, e.g. n = 3 for 3-D
%
% Output:
%   zcrit - critical value
%   z2 - test statistic for 2nd rank tensor
%   z4 - test statistic for 4th rank tensor
%
% Information
%   1.) Null hypothesis: true distribution has anisotropy characterized by
%           D2 or D4.
%
%   2.) Alternative hypothesis: true distribution is described by a lesser
%           order tensor -- D2 not required, scalar works, or D4 not
%           required, use D2
%
%   3.) Calculate test statistic: liklihood ratio --  Probability that data
%           comes from uniform distribution -or- probability that data
%           comes from a "D2" distribution


z2 = N/(dim^2) * sum(sum(D2.^2));
z4 = [];     %for now...

% Lookup critical value: liklihood ratio behaves according to
```

```
% Chi-square
zcrit = chi2inv(1-alpha,2);

% Compare test statistic to critical value and repeat for 4th rank if
% necessary
if z2 <= zcrit
    disp('D2 and D4 not required')
elseif z2 > zcrit
    disp(['** D2 Required ** - '])
    z4 = N/(dim^4) * sum(sum(sum(sum(D4.^2))));
    if z4 <= zcrit
        disp('D4 not required')
    elseif z4 > zcrit
        disp(['** D4 Required ** - '])
    end
end

end

%EOF
```

padcat.m

```
function [M, TF] = padcat(varargin)
% PADCAT - concatenate vectors with different lengths by padding with NaN
%
%   M = PADCAT(V1, V2, V3, ..., VN) concatenates the vectors V1 through VN
%   into one large matrix. All vectors should have the same orientation,
%   that is, they are all row or column vectors. The vectors do not need to
%   have the same lengths, and shorter vectors are padded with NaNs.
%   The size of M is determined by the length of the longest vector. For
%   row vectors, M will be a N-by-MaxL matrix and for column vectors, M
%   will be a MaxL-by-N matrix, where MaxL is the length of the longest
%   vector.
%
%   Examples:
%      a = 1:5 ; b = 1:3 ; c = [] ; d = 1:4 ;
%      padcat(a,b,c,d) % row vectors
%         % ->   1     2     3     4     5
%         %      1     2     3   NaN   NaN
%         %    NaN   NaN   NaN   NaN   NaN
%         %      1     2     3     4   NaN
%      CC = {d.' a.' c.' b.' d.'} ;
%      padcat(CC{:}) % column vectors
%         %      1     1   NaN     1     1
%         %      2     2   NaN     2     2
%         %      3     3   NaN     3     3
%         %      4     4   NaN   NaN     4
%         %    NaN     5   NaN   NaN   NaN
```

```
%
%   [M, TF] = PADCAT(..) will also return a logical matrix TF with the same
%   size as R having true values for those positions that originate from an
%   input vector. This may be useful if any of the vectors contain NaNs.
%
%   Example:
%       a = 1:3 ; b = [] ; c = [1 NaN] ;
%       [M,tf] = padcat(a,b,c)
%       % find the original NaN
%       [Vev,Pos] = find(tf & isnan(M))
%       % -> Vec = 3 , Pos = 2
%
%   This second output can also be used to change the padding value into
%   something else than NaN.
%
%       [M, tf] = padcat(1:3,1,1:4)
%       M(~tf) = 99 % change the padding value into 99
%
%   Scalars will be concatenated into a single column vector.
%
%   See also CAT, RESHAPE, STRVCAT, CHAR, HORZCAT, VERTCAT, ISEMPTY
%            NONES, GROUP2CELL (Matlab File Exchange)

% for Matlab 2008 and up (tested in R2011a)
% version 1.2 (oct 2011)
% (c) Jos van der Geest
% email: jos@jasen.nl

% History
% 1.0 (feb 2009) created
% 1.1 (feb 2011) improved comments
% 1.2 (oct 2011) added help on changing the padding value into something
%     else than NaN

% Acknowledgements:
% Inspired by padadd.m (feb 2000) Fex ID 209 by Dave Johnson

error(nargchk(1,Inf,nargin)) ;

% check the inputs
SZ = cellfun(@size,varargin,'UniformOutput',false) ; % sizes
Ndim = cellfun(@ndims,varargin) ; %

if ~all(Ndim==2)
    error([mfilename ':WrongInputDimension'], ...
        'Input should be vectors.') ;
end

TF = [] ; % default second output so we do not have to check all the time
```

```
% for 2D matrices (including vectors) the size is a 1-by-2 vector
SZ = cat(1,SZ{:}) ;
maxSZ = max(SZ) ;    % probable size of the longest vector
% maxSZ equals :
%  - [1 1] for all scalars input
%  - [X 1] for column vectors
%  - [1 X] for all row vectors
%  - [X Y] otherwise (so padcat will not work!)

if ~any(maxSZ == 1),  % hmm, not all elements are 1-by-N or N-by-1
    % 2 options ...
    if any(maxSZ==0),
        % 1) all inputs are empty
        M  = [] ;
        return
    else
        % 2) wrong input
        % Either not all vectors have the same orientation (row and column
        % vectors are being mixed) or an input is a matrix.
        error([mfilename ':WrongInputSize'], ...
            'Inputs should be all row vectors or all column vectors.') ;
    end
end

if nargin == 1,
    % single input, nothing to concatenate ..
    M = varargin{1} ;
else
    % Concatenate row vectors in a row, and column vectors in a column.
    dim = (maxSZ(1)==1) + 1 ;      % Find out the dimension to work on
    X = cat(dim, varargin{:}) ;    % make one big list

    % we will use linear indexing, which operates along columns. We apply a
    % transpose at the end if the input were row vectors.

    if maxSZ(dim) == 1,
        % if all inputs are scalars, ...
        M = X ;   % copy the list
    elseif all(SZ(:,dim)==SZ(1,dim)),
        % all vectors have the same length
        M = reshape(X,SZ(1,dim),[]) ;% copy the list and reshape
    else
        % We do have vectors of different lengths.
        % Pre-allocate the final output array as a column oriented array. We
        % make it one larger to accommodate the largest vector as well.
        M = zeros([maxSZ(dim)+1 nargin]) ;
        % where do the fillers begin in each column
        M(sub2ind(size(M), SZ(:,dim).'+1, 1:nargin)) = 1 ;
        % Fillers should be put in after that position as well, so applying
        % cumsum on the columns
```

```
        % Note that we remove the last row; the largest vector will fill an
        % entire column.
        M = cumsum(M(1:end-1,:),1) ; % remove last row

        % If we need to return position of the non-fillers we will get them
        % now. We cannot do it afterwards, since NaNs may be present in the
        % inputs.
        if nargout>1,
            TF = ~M ;
            % and make use of this logical array
            M(~TF) = NaN ; % put the fillers in
            M(TF)  = X ;   % put the values in
        else
            M(M==1) = NaN ; % put the fillers in
            M(M==0) = X ;   % put the values in
        end
    end

    if dim == 2,
        % the inputs were row vectors, so transpose
        M = M.' ;
        TF = TF.' ; % was initialized as empty if not requested
    end
end % nargin == 1

if nargout > 1 && isempty(TF),
    % in this case, the inputs were all empty, all scalars, or all had the
    % same size.
    TF = true(size(M)) ;
end
```

ContactPlot.m

```
function ContactPlot(F2,F2Ci,bondRad,grainRad,...
    meanBondRad,meanGrainRad,coordNum,shapeFac,...
    idx,pixdim,endtime,spatialLabel)
% This function reads the input from a seperate function, ContactTensor.m
% and plots the associated data for the production of useful figures and
% charts.  The inputs match the outputs of ContactTensor.m with the
% additional input of pixeldim to give real spatial resolution to the pixel
% based data.  The plots were originally inside of ContactTensor.m and have
% been moved to an external function for greater versatility.
%
% This function requires the use of errorbarwidth.m for appropriately
% sizing the error bars on the plots produced by this function.
%
% INPUTS
%       F2(i,j,n): 2nd order contact tensor.  i and j reference the matrix
%       position within an individual tensor (i=1,2,3;j=1,2,3) and n
%       specifies the volume in chronological order with which the contact
```

```
%       tensor is associated.
%
%       F2Ci(i,j,n,b): Upper and lower bonds of the 95% confidence interval of
%       2nd order contact tensor.  i, j, and n are the same as above.  b
%       indicates the upper or lower bounds of the confidence interval. 1
%       indicates the lower bound, 2 indicates the upper bound.
%
%       bondRad{n}: A vector of the distribution of bond radii contained
%       within a cell structure for time series data.
%
%       grainRad{n}: Same as bondRad except the distribution of grain
%       radii.
%
%       meanBondRad: Mean 3-D bond radius.  This assumes a circular contact
%       since it is based off the calculated bond area.
%
%       meanGrainRad: Mean 3-D grain radius based on the largest inscribed
%       sphere of each individual grain identified in 3-D segmentation
%
%       coordNum: Mean 3-D coordination number.  This number represents the
%       average number of contacts per grain.
%
%       shapeFac: A calculation of the scalar shape factor.  This is the
%       ratio of the spherical grain gradius (meanGrainRad) to the distance
%       of the grain center to bond center.
%
%       idx: Elapsed time identifier used to label plots and seperate data
%       based on time during experiment.  Derived from the folder stucture.
%       See help for subfunction FileImport in this file for the
%       appropriate folder structure to use with this function.
%
%       pixdim: Outputs the pixel/voxel resolution of the CT Scan for
%       proper dimensional scaling.
%
%       endtime: Variable listing the final elapsed time used in plotting
%       functions
%
%       spatialLabel: String variable set here to use in plotting functions
%       in other scripts and functions.
%
% Author: David J. Walters, Montana State University
% Version 1.0 - October 22, 2014
%   -Updated help file Oct. 23, 2014


%%Plot tensor coefficients
% Initialize plot parameters
font = 'Palatino Linotype';
fsize = 11;     % Font Size
msize = 5;      % Marker Size
```

```
% Initialize figure heading
figure('Name','3-D Tensor Diagonals','NumberTitle','off')

% Plot value and confidence interval of contact tensor coefficient F11
hE = errorbar(idx,F2(1,1,:),F2(1,1,:)-F2Ci(1,1,:,1),...
    F2Ci(1,1,:,2)-F2(1,1,:),'rsquare','MarkerSize',msize);

% Plot value and confidence interval of contact tensor coefficient F22
hold on
hE = errorbar(idx,F2(2,2,:),F2(2,2,:)-F2Ci(2,2,:,1),...
    F2Ci(2,2,:,2)-F2(2,2,:),'bdiamond','MarkerSize',msize+1);

% Plot value and confidence interval of contact tensor coefficient F33
hold on
hE = errorbar(idx,F2(3,3,:),F2(3,3,:)-F2Ci(3,3,:,1),...
    F2Ci(3,3,:,2)-F2(3,3,:),'go','MarkerSize',msize);

% Adjust format and appearance of contact tensor coefficient plot
grid
axis([-1 (endtime) 0.2 0.5])
y1 = ylabel('3-D Tensor Diagonals (-)');
x1 = xlabel('Elapsed Time ( hrs )');
set([y1 x1],'FontName',font,'FontSize',fsize)
legend('\it{x}\rm{_1}','\it{x}\rm{_2}','\it{x}\rm{_3}',...
    'Location','Northwest','Orientation','horizontal');
set(gca,'FontName',font,'FontSize',fsize,'XTick',0:3:endtime)


%%Plot distribution of bond radii
figure('Name','Bond Radii Distribution','NumberTitle','off')
hist(bondRad*pixdim,20)
y1 = ylabel('Number of Bonds');
x1 = xlabel(['\rho: 3-D Bond Radius ',spatialLabel]);
set([y1 x1],'FontName',font,'FontSize',fsize)


%%Plot distribution of grain radii
figure('Name','Grain Radii Distribution','NumberTitle','off')
hist(grainRad*pixdim,20)
y1 = ylabel('Number of Grains');
x1 = xlabel(['R: 3-D Grain Radius ',spatialLabel]);
set([y1 x1],'FontName',font,'FontSize',fsize)


%%Mean Bond and Grain Radii
figure('Name','Mean Bond and Grain Radii','NumberTitle','off')

% Plot mean bond radius on left of 3 subplots
ax(1) = subplot(1,3,1);
plot(idx,meanBondRad*pixdim,'ko','MarkerSize',msize);
grid
```

```
axis([-1 (endtime) 0 200])
y1(1) = ylabel(['\rho: Mean 3-D Bond Radius ',spatialLabel]);

% Plot mean grain radius on middle of 3 subplots
ax(2) = subplot(1,3,2);
plot(idx,meanGrainRad*pixdim,'ko','MarkerSize',msize);
grid
axis([-1 (endtime) 0 200])
y1(2) = ylabel(['R: Mean 3-D Grain Radius ',spatialLabel]);
x1 = xlabel('Elapsed Time (hrs)');

% Plot bond radius to grain radius ratio on right of 3 subplots
ax(3) = subplot(1,3,3);
plot(idx,meanBondRad./meanGrainRad,'ko','MarkerSize',msize);

% Adjust final appearance of plots
grid
axis([-1 (endtime) 0 1])
y1(3) = ylabel('Mean 3-D Bond-to-Grain Radius Ratio (-)');
set([y1 x1],'FontName',font,'FontSize',fsize)
set(ax,'FontName',font,'FontSize',fsize,'XTick',0:3:endtime)
```

```
%%3-D Coordination Number
figure('Name','Mean 3-D Coordination Number','NumberTitle','off')
plot(idx,coordNum,'ko','MarkerSize',msize);
grid
y1 = ylabel('Mean 3-D Coordination Number (-)');
x1 = xlabel('Elapsed Time (hrs)');
set([y1 x1],'FontName',font,'FontSize',fsize)
% axis([-1 (endtime) 1 3.5])
xlim([-1 (endtime)])
set(gca,'XTick',0:3:endtime)
end
```

TensorRatio.m

```
function [Tr,TrCi,MIL,MILCi] = TensorRatio(F2,F2Ci,MILVal,LMILVal,UMILVal,MILVec)
% TensorRatio.m
% Tr = TensorRatio(F2,MILVal,MILVec)
%
%   INPUTS:
%       F2(i,j,n): 2nd order contact tensor.  i and j reference the matrix
%       position within an individual tensor (i=1,2,3;j=1,2,3) and n
%       specifies the volume in chronological order with which the contact
%       tensor is associated.
%
%       MILVal: Eigen Values of the MIL Fabric Tensor reported from CTAn.
%
%       MILVec: Eigen Vectors of the MIL Fabric Tensor reported from CTAn.
```

```
%
%   OUTPUTS:
%       Tr: Tensor aspect ratio
%
%       MILRadVec: Vector containing MIL Values
%
% Version: 1.0 - October 28, 2014
%
% Version: 1.1 - Updated computation of the MIL tensor and reset the
% normaliztion parameters. October 29, 2015
%
% AUTHOR: David J. Walters; Montana State University
```

```
%%Ellipsoid Radii of Contact Tensor
% Generate an ellipsoid using the contact tensor to create a 3-D
% visualization of of the distribution of bonds in the analyzed sample.
% Generally assume contact tensor is in its principal orientation that is
% concurrently alligned with the global coordinate system.
%
% To compare ellipsoids produced by the Contact Fabric Tensor, the MIL
% Fabric Tensor, and an isotropic sphere, all volumes are normalize to one.
% Vcon = (4/3)*pi*F2(1,1)*F2(2,2)*F2(3,3);
%Generates an ellipsoid with the radii scaled such that the volume equals 1
% CRad1 = F2(1,1)/(Vcon^(1/3));
% CRad2 = F2(2,2)/(Vcon^(1/3));
% CRad3 = F2(3,3)/(Vcon^(1/3));
CRad1 = F2(1,1);
CRad2 = F2(2,2);
CRad3 = F2(3,3);

LCRad1 = F2Ci(1,1,1);
LCRad2 = F2Ci(2,2,1);
LCRad3 = F2Ci(3,3,1);

UCRad1 = F2Ci(1,1,2);
UCRad2 = F2Ci(2,2,2);
UCRad3 = F2Ci(3,3,2);

CRad = [CRad1; CRad2; CRad3];
LCRad = [LCRad1; LCRad2; LCRad3];
UCRad = [UCRad1; UCRad2; UCRad3];
```

```
%%Ellipsoid Radii of MIL Fabric Tensor

% Vmil = (4/3)*pi*MILVal(1)*MILVal(2)*MILVal(3);
%Generates an ellipsoid with the radii scaled such that the volume equals 1
% MILRad1 = MILVal(1)/(Vmil^(1/3));
% MILRad2 = MILVal(2)/(Vmil^(1/3));
% MILRad3 = MILVal(3)/(Vmil^(1/3));
```

```
MILRad1 = MILVal(1)/sum(MILVal);
MILRad2 = MILVal(2)/sum(MILVal);
MILRad3 = MILVal(3)/sum(MILVal);

LMILRad1 = LMILVal(1)/sum(LMILVal);
LMILRad2 = LMILVal(2)/sum(LMILVal);
LMILRad3 = LMILVal(3)/sum(LMILVal);

UMILRad1 = UMILVal(1)/sum(UMILVal);
UMILRad2 = UMILVal(2)/sum(UMILVal);
UMILRad3 = UMILVal(3)/sum(UMILVal);

% Adjust orientation of axes using the eigen vectors.  The Eigen Vector
% matrix should be 3x3 with the columns being individual vectors

MILRad1Vec = MILRad1 * MILVec(1,:);
MILRad2Vec = MILRad2 * MILVec(2,:);
MILRad3Vec = MILRad3 * MILVec(3,:);

LMILRad1Vec = LMILRad1 * MILVec(1,:);
LMILRad2Vec = LMILRad2 * MILVec(2,:);
LMILRad3Vec = LMILRad3 * MILVec(3,:);

UMILRad1Vec = UMILRad1 * MILVec(1,:);
UMILRad2Vec = UMILRad2 * MILVec(2,:);
UMILRad3Vec = UMILRad3 * MILVec(3,:);

MILRadVec = [MILRad1Vec;MILRad2Vec;MILRad3Vec];
LMILRadVec = [LMILRad1Vec;LMILRad2Vec;LMILRad3Vec];
UMILRadVec = [UMILRad1Vec;UMILRad2Vec;UMILRad3Vec];

MILSum = norm(MILRad1Vec) + norm(MILRad2Vec) + norm(MILRad3Vec);

% Tr(1) = CRad1/MILSum(1);
% Tr(2) = CRad2/MILSum(2);
% Tr(3) = CRad3/MILSum(3);

% Tr(1) = CRad1/norm(MILRad1Vec);
% Tr(2) = CRad2/norm(MILRad2Vec);
% Tr(3) = CRad3/norm(MILRad3Vec);

% Must match appropriate contact direction with oriented MIL direction
% since MIL Values 1, 2, and 3 don't necessarily point in the 1, 2, and 3
% directions.  The following loop figures out the orientation of each
% principal MIL value and matches it with the correct principal contact
% value.
Index_prev = 0;
for i=1:3
    [~,Index] = max(abs(MILRadVec(i,:)));
    if i > 1
```

```
        if Index_prev(i) == Index || Index_prev(i-1) == Index
            if Index == 1
                [~,Index] = max(abs(MILRadVec(i,2:3)));
                Index = Index + 1;
            elseif Index == 2
                [~,Index] = max(abs(MILRadVec(i,1:2:3)));
                if Index == 2
                    Index = Index + 1;
                end
            elseif Index == 3
                [~,Index] = max(abs(MILRadVec(i,1:2)));
            end
        end
    end
%     Tr(Index) = norm(MILRadVec(i,:))/CRad(Index)
%     Tr(Index) = CRad(Index)/norm(MILRadVec(i,:));
%     LTr(Index) = LCRad(Index)/norm(LMILRadVec(i,:));
%     UTr(Index) = UCRad(Index)/norm(UMILRadVec(i,:));

    MIL(Index,:) = abs(MILRadVec(i,:));
    LMIL(Index,:) = abs(LMILRadVec(i,:));
    UMIL(Index,:) = abs(UMILRadVec(i,:));
    Index_prev(i+1) = Index;
end
MIL = MIL/trace(MIL);
LMIL = LMIL/trace(MIL);
UMIL = UMIL/trace(MIL);

for i = 1:3
    Tr(i) = CRad(i)/MIL(i,i);
    LTr(i) = LCRad(i)/LMIL(i,i);
    UTr(i) = UCRad(i)/UMIL(i,i);
end


TrCi(:,:,1) = LTr;
TrCi(:,:,2) = UTr;
MILCi(:,:,:,1) = LMIL;
MILCi(:,:,:,2) = UMIL;
% Tr(1) = norm(MILRad1Vec)/CRad1;
% Tr(2) = norm(MILRad2Vec)/CRad2;
% Tr(3) = norm(MILRad3Vec)/CRad3;
```

MechModuli.m

```
function [EStarRaw, GStarRaw, nuStarRaw, EStarAr, GStarAr, nuStarAr,...
    YoungsRaw, LYoungsRaw, UYoungsRaw,...
    YoungsAr, LYoungsAr, UYoungsAr,...
    YoungsArTr, LYoungsArTr, UYoungsArTr,...
    ShearRaw, LShearRaw, UShearRaw,...
```

```
    ShearAr, LShearAr, UShearAr,...
    ShearArTr, LShearArTr, UShearArTr,...
    PoissonRaw, LPoissonRaw, UPoissonRaw,...
    PoissonAr, LPoissonAr, UPoissonAr,...
    PoissonArTr, LPoissonArTr, UPoissonArTr,...
    SRaw, SAr, SArTr] = ...
    MechModuli(phii, N3, rho_hat, R_hat, C, Unc,Ar,Tr,TrCi,...
        MIL, MILCi)
% MechModuli.m
% function [EStarRaw, GStarRaw, nuStarRaw, EStarAr, GStarAr, nuStarAr,...
%     YoungsRaw, LYoungsRaw, UYoungsRaw,...
%     YoungsAr, LYoungsAr, UYoungsAr,...
%     YoungsArTr, LYoungsArTr, UYoungsArTr,...
%     ShearRaw, LShearRaw, UShearRaw,...
%     ShearAr, LShearAr, UShearAr,...
%     ShearArTr, LShearArTr, UShearArTr,...
%     PoissonRaw, LPoissonRaw, UPoissonRaw,...
%     PoissonAr, LPoissonAr, UPoissonAr,...
%     PoissonArTr, LPoissonArTr, UPoissonArTr,...
%     SRaw] = ...
%     MechModuli(phii, N3, rho_hat, R_hat, C, Unc,Ar,Tr)
% This funtion calculates the effective Young's moduli and Shear Moduli of
% the sample.  These are calculated using stereologically determined
% isotropic constants (E* and G*) and the calculated contact tensor
% coefficients.
%
% INPUTS:
%   phii - Solid volume fraction from SkyScan CTAn.
%
%   N3 - 3-D Coordination number calculated from Edens' SSAnalyzer or
%   appropriate parameter from SkyScan CTAn software.
%
%   rho_hat - 3-D bond radius
%
%   R_hat - 3-D grain radius
%
%   C - Contact tensor coefficients.
%           Format: C(row,column,run number)
%           i.e. k = 3, run number = 3
%                   C = [F11,F12,F13;
%                        F21,F22,F23;
%                        F31,F32,F33]
%                   F22 = row 2, columnn 2, run 3 = C(2,2,3)
%
%   Unc - Confidence intervals for the contact tensor coefficients.
%           Format: Unc(row, column, run number, lower(1)/upper(2)
%           interval)
%
%   Ar - Grain shape factor aspect ratio
%
%   Tr - Tensor ratio (between MIL Tensor and Contact Tensor)
```

```
%
% OUTPUTS:
%   EStar(---) - Scalar Young's modulus calculated from measurable
%   microstructural parameters.
%       *Raw - Results produced by the original contact tensor model.
%       *Ar - Results as produced by incorporating only the scalar shape
%       factor aspect ratio, Ar.
%
%   GStar(---) - Scalar shear modulus calculated from measurable
%   microstructural parameters.
%
%   nuStar(---) - Scalar Poisson's ratio calculated from measurable
%   microstructural parameters.
%
%   Youngs(---) - A structure of anisotropic Young's moduli along each of the
%   principal directions of contact (i.e [E1,E2,E3]).
%       *Raw - Results as produced by the orginal contact tensor model.
%       *Ar - Results as produced by incorporating only the scalar shape
%       factor aspect ratio, Ar.
%       *ArTr - Results as produced by incorporating both the scalar shape
%       factor aspect ratio, Ar, and the tensor ratio, Tr.
%
%   LYoungs(---)/UYoungs(---) - Lower and upper confidence intervals for
%   Youngs---.
%
%   Shear(---) - A structure of anisotropic shear moduli along aligning with
%   the principal directions of contact (i.e. [G23,G13,G12]).
%
%   LShear(---)/UShear(---) - Lower and upper confidence intervals for
%   Shear(---).
%
%   Poisson(---) - A structure of anisotropic Poisson's ratio alignining with
%   the principal directions of contact (i.e. [nu23,nu13,nu12]).
%
%   LPossion(---)/UPoisson(---) - Lower and upper confidence intervals for
%   Poisson(---).
%
%   S(---) - A 6x6 array that represents the anisotropic compliance matrix.
%   Its maximum deviation from isotropy is orthotropic symmetry (9
%   independent coefficients) as restricted by the use of a 2nd order
%   contact tensor.
%
%   v1.0, June 17, 2013
%   v1.1, June 21, 2013, Added data for plotting moduli and confidence
%   intervals
%   v1.2, October 29, 2014, Added shape factor correction and appropriate
%   outputs for gains made by shape factors
% AUTHOR: David J. Walters; Montana State University
```

```
%%Initialize variables internal to function
% E_ice = 9330e6;     %Young's modulus ice (Petrenko and Whitworth 1999)
% G_ice = 3520e6;     %Shear modulus ice (Petrenko and Whitworth 1999)
E_ice = 1000e6;
G_ice = 377e6;
xi = G_ice/E_ice;   %Stiffness ratio
f = 1/3;            %Isotropic value of contact tensor


%%Calculate scalar (isotropic) moduli from stereological data
EStarRaw = (1/2) * (rho_hat/R_hat)^2 * phii * N3 * E_ice * (2+3*xi)/(4+xi);
GStarRaw = (1/40) * (rho_hat/R_hat)^2 * phii * N3 * E_ice * (2+3*xi);
nuStarRaw = (1-xi)/(4+xi);

EStarAr = EStarRaw * Ar;
GStarAr = GStarRaw * Ar;
nuStarAr = nuStarRaw;


%%Calculate anisotropic moduli as modified by the contact tensor

SRaw = zeros(6,6);
SAr = zeros(6,6);
SArTr = zeros(6,6);
LSRaw = zeros(6,6);
LSAr = zeros(6,6);
LSArTr = zeros(6,6);
USRaw = zeros(6,6);
USAr = zeros(6,6);
USArTr = zeros(6,6);
ERaw = zeros(3);
EAr = zeros(3);
EArTr = zeros(3);
LERaw = zeros(3);
LEAr = zeros(3);
LEArTr = zeros(3);
UERaw = zeros(3);
UEAr = zeros(3);
UEArTr = zeros(3);
nuRaw = zeros(3);
nuAr = zeros(3);
nuArTr = zeros(3);
LnuRaw = zeros(3);
LnuAr = zeros(3);
LnuArTr = zeros(3);
UnuRaw = zeros(3);
UnuAr = zeros(3);
UnuArTr = zeros(3);

% Work on upper left 3x3 corner of compliance matrix
```

```
k = 0;
for i = 1:3
    for j = 1:3
        if i == j % Diagonal values
            SRaw(i,j) = (1/EStarRaw) * (f/C(i,j,:))^2;
            SAr(i,j) = (1/EStarAr) * (f/C(i,j,:))^2;
%             SArTr(i,j) = (1/EStarAr) * (f/C(i,j,:))^2 * (1/Tr(i))^2;
            SArTr(i,j) = (1/EStarAr)  * (1/Tr(i))^2;

            LSRaw(i,j) = (1/EStarRaw) * (f/Unc(i,j,:,1))^2;  % Lower 95% CI
            LSAr(i,j) = (1/EStarAr) * (f/Unc(i,j,:,1))^2;
%             LSArTr(i,j) = (1/EStarAr) * (f/Unc(i,j,:,1))^2 * (1/Tr(i))^2;
            LSArTr(i,j) = (1/EStarAr) * (1/TrCi(i,:,1))^2;

            USRaw(i,j) = (1/EStarRaw) * (f/Unc(i,j,:,2))^2;  % Upper 95% CI
            USAr(i,j) = (1/EStarAr) * (f/Unc(i,j,:,2))^2;
%             USArTr(i,j) = (1/EStarAr) * (f/Unc(i,j,:,2))^2 * (1/Tr(i))^2;
            USArTr(i,j) = (1/EStarAr) * (1/TrCi(i,:,2))^2;

            ERaw(i) = SRaw(i,j)^(-1);
            EAr(i) = SAr(i,j)^(-1);
            EArTr(i) = SArTr(i,j)^(-1);

            LERaw(i) = LSRaw(i,j)^(-1);   % Lower 95% CI
            LEAr(i) = LSAr(i,j)^(-1);
            LEArTr(i) = LSArTr(i,j)^(-1);

            UERaw(i) = USRaw(i,j)^(-1);   % Upper 95% CI
            UEAr(i) = USAr(i,j)^(-1);
            UEArTr(i) = USArTr(i,j)^(-1);
        else
            SRaw(i,j) = (nuStarRaw/EStarRaw) * (f^2/(C(j,j,:)*C(i,i,:)));
            SAr(i,j) = (nuStarAr/EStarAr) * (f^2/(C(j,j,:)*C(i,i,:)));
%             SArTr(i,j) = (nuStarAr/EStarAr) * (f^2/(C(j,j,:)*C(i,i,:))) *
(1/(Tr(i)*Tr(j)));
            SArTr(i,j) = (nuStarAr/EStarAr) * (1/(Tr(i)*Tr(j)));

            LSRaw(i,j) = (nuStarRaw/EStarRaw) * (f^2/(Unc(j,j,:,1)*Unc(i,i,:,1)));
            LSAr(i,j) = (nuStarAr/EStarAr) * (f^2/(Unc(j,j,:,1)*Unc(i,i,:,1)));
%             LSArTr(i,j) = (nuStarAr/EStarAr) * (f^2/(Unc(j,j,:,1)*Unc(i,i,:,1))) *
(1/(Tr(i)*Tr(j)));
            LSArTr(i,j) = (nuStarAr/EStarAr) * (1/(TrCi(i,:,1)*TrCi(j,:,1)));

            USRaw(i,j) = (nuStarRaw/EStarRaw) * (f^2/(Unc(j,j,:,2)*Unc(i,i,:,2)));
            USAr(i,j) = (nuStarAr/EStarAr) * (f^2/(Unc(j,j,:,2)*Unc(i,i,:,2)));
%             USArTr(i,j) = (nuStarAr/EStarAr) * (f^2/(Unc(j,j,:,2)*Unc(i,i,:,2))) *
(1/(Tr(i)*Tr(j)));
            USArTr(i,j) = (nuStarAr/EStarAr) * (1/(TrCi(i,:,2)*TrCi(j,:,2)));

            if j > i
```

```
                k = k + 1;
            nuRaw(k) = SRaw(i,j)*ERaw(i);
            nuAr(k) = SAr(i,j)*EAr(i);
            nuArTr(k) = SArTr(i,j)*EArTr(i);

            LnuRaw(k) = LSRaw(i,j)*ERaw(i);
            LnuAr(k) = LSAr(i,j)*EAr(i);
            LnuArTr(k) = LSArTr(i,j)*EArTr(i);

            UnuRaw(k) = USRaw(i,j)*ERaw(i);
            UnuAr(k) = USAr(i,j)*EAr(i);
            UnuArTr(k) = USArTr(i,j)*EArTr(i);
            end
        end
    end
end

% Shear values
SRaw(4,4) = (1/(2*GStarRaw)) * (f^2/(C(2,2,:)*C(3,3,:)));
    LSRaw(4,4) = (1/(2*GStarRaw)) * (f^2/(Unc(2,2,:,1)*Unc(3,3,:,1)));
    USRaw(4,4) = (1/(2*GStarRaw)) * (f^2/(Unc(2,2,:,2)*Unc(3,3,:,2)));
SAr(4,4) = (1/(2*GStarAr)) * (f^2/(C(2,2,:)*C(3,3,:)));
    LSAr(4,4) = (1/(2*GStarAr)) * (f^2/(Unc(2,2,:,1)*Unc(3,3,:,1)));
    USAr(4,4) = (1/(2*GStarAr)) * (f^2/(Unc(2,2,:,2)*Unc(3,3,:,2)));
% SArTr(4,4) = (1/(2*GStarAr)) * (f^2/(C(2,2,:)*C(3,3,:))) * (1/(Tr(2)*Tr(3)));
%     LSArTr(4,4) = (1/(2*GStarAr)) * (f^2/(Unc(2,2,:,1)*Unc(3,3,:,1))) *
(1/(Tr(2)*Tr(3)));
%     USArTr(4,4) = (1/(2*GStarAr)) * (f^2/(Unc(2,2,:,2)*Unc(3,3,:,2))) *
(1/(Tr(2)*Tr(3)));
SArTr(4,4) = (1/(2*GStarAr)) * (1/(Tr(2)*Tr(3)));
    LSArTr(4,4) = (1/(2*GStarAr)) * (1/(TrCi(2,:,1)*TrCi(3,:,1)));
    USArTr(4,4) = (1/(2*GStarAr)) * (1/(TrCi(2,:,2)*TrCi(3,:,2)));

SRaw(5,5) = (1/(2*GStarRaw)) * (f^2/(C(1,1,:)*C(3,3,:)));
    LSRaw(5,5) = (1/(2*GStarRaw)) * (f^2/(Unc(1,1,:,1)*Unc(3,3,:,1)));
    USRaw(5,5) = (1/(2*GStarRaw)) * (f^2/(Unc(1,1,:,2)*Unc(3,3,:,2)));
SAr(5,5) = (1/(2*GStarAr)) * (f^2/(C(1,1,:)*C(3,3,:)));
    LSAr(5,5) = (1/(2*GStarAr)) * (f^2/(Unc(1,1,:,1)*Unc(3,3,:,1)));
    USAr(5,5) = (1/(2*GStarAr)) * (f^2/(Unc(1,1,:,2)*Unc(3,3,:,2)));
% SArTr(5,5) = (1/(2*GStarAr)) * (f^2/(C(1,1,:)*C(3,3,:))) * (1/(Tr(1)*Tr(3)));
%     LSArTr(5,5) = (1/(2*GStarAr)) * (f^2/(Unc(1,1,:,1)*Unc(3,3,:,1))) *
(1/(Tr(1)*Tr(3)));
%     USArTr(5,5) = (1/(2*GStarAr)) * (f^2/(Unc(1,1,:,2)*Unc(3,3,:,2))) *
(1/(Tr(1)*Tr(3)));
SArTr(5,5) = (1/(2*GStarAr)) * (1/(Tr(1)*Tr(3)));
    LSArTr(5,5) = (1/(2*GStarAr)) * (1/(TrCi(1,:,1)*TrCi(3,:,1)));
    USArTr(5,5) = (1/(2*GStarAr)) * (1/(TrCi(1,:,2)*TrCi(3,:,2)));

SRaw(6,6) = (1/(2*GStarRaw)) * (f^2/(C(1,1,:)*C(2,2,:)));
    LSRaw(6,6) = (1/(2*GStarRaw)) * (f^2/(Unc(1,1,:,1)*Unc(2,2,:,1)));
```

```
    USRaw(6,6) = (1/(2*GStarRaw)) * (f^2/(Unc(1,1,:,2)*Unc(2,2,:,2)));
SAr(6,6) = (1/(2*GStarAr)) * (f^2/(C(1,1,:)*C(2,2,:)));
    LSAr(6,6) = (1/(2*GStarAr)) * (f^2/(Unc(1,1,:,1)*Unc(2,2,:,1)));
    USAr(6,6) = (1/(2*GStarAr)) * (f^2/(Unc(1,1,:,2)*Unc(2,2,:,2)));
% SArTr(6,6) = (1/(2*GStarAr)) * (f^2/(C(1,1,:)*C(2,2,:))) * (1/(Tr(1)*Tr(2)));
%     LSArTr(6,6) = (1/(2*GStarAr)) * (f^2/(Unc(1,1,:,1)*Unc(2,2,:,1))) *
(1/(Tr(1)*Tr(2)));
%     USArTr(6,6) = (1/(2*GStarAr)) * (f^2/(Unc(1,1,:,2)*Unc(2,2,:,2))) *
(1/(Tr(1)*Tr(2)));
SArTr(6,6) = (1/(2*GStarAr)) * (1/(Tr(1)*Tr(2)));
    LSArTr(6,6) = (1/(2*GStarAr)) * (1/(TrCi(1,:,1)*TrCi(2,:,1)));
    USArTr(6,6) = (1/(2*GStarAr)) * (1/(TrCi(1,:,2)*TrCi(2,:,2)));

% Raw Outputs
YoungsRaw.x = ERaw(1);
    LYoungsRaw.x = LERaw(1);
    UYoungsRaw.x = UERaw(1);
YoungsRaw.y = ERaw(2);
    LYoungsRaw.y = LERaw(2);
    UYoungsRaw.y = UERaw(2);
YoungsRaw.z = ERaw(3);
    LYoungsRaw.z = LERaw(3);
    UYoungsRaw.z = UERaw(3);

ShearRaw.xy = SRaw(6,6)^(-1)/2;
    LShearRaw.xy = LSRaw(6,6)^(-1)/2;
    UShearRaw.xy = USRaw(6,6)^(-1)/2;
ShearRaw.xz = SRaw(5,5)^(-1)/2;
    LShearRaw.xz = LSRaw(5,5)^(-1)/2;
    UShearRaw.xz = USRaw(5,5)^(-1)/2;
ShearRaw.yz = SRaw(4,4)^(-1)/2;
    LShearRaw.yz = LSRaw(4,4)^(-1)/2;
    UShearRaw.yz = USRaw(4,4)^(-1)/2;

PoissonRaw.xy = nuRaw(1);
    LPoissonRaw.xy = LnuRaw(1);
    UPoissonRaw.xy = UnuRaw(1);
PoissonRaw.xz = nuRaw(2);
    LPoissonRaw.xz = LnuRaw(2);
    UPoissonRaw.xz = UnuRaw(2);
PoissonRaw.yz = nuRaw(3);
    LPoissonRaw.yz = LnuRaw(3);
    UPoissonRaw.yz = UnuRaw(3);

% Ar adjusted outputs
YoungsAr.x = EAr(1);
    LYoungsAr.x = LEAr(1);
    UYoungsAr.x = UEAr(1);
YoungsAr.y = EAr(2);
    LYoungsAr.y = LEAr(2);
```

```
    UYoungsAr.y = UEAr(2);
YoungsAr.z = EAr(3);
    LYoungsAr.z = LEAr(3);
    UYoungsAr.z = UEAr(3);

ShearAr.xy = SAr(6,6)^(-1)/2;
    LShearAr.xy = LSAr(6,6)^(-1)/2;
    UShearAr.xy = USAr(6,6)^(-1)/2;
ShearAr.xz = SAr(5,5)^(-1)/2;
    LShearAr.xz = LSAr(5,5)^(-1)/2;
    UShearAr.xz = USAr(5,5)^(-1)/2;
ShearAr.yz = SAr(4,4)^(-1)/2;
    LShearAr.yz = LSAr(4,4)^(-1)/2;
    UShearAr.yz = USAr(4,4)^(-1)/2;

PoissonAr.xy = nuAr(1);
    LPoissonAr.xy = LnuAr(1);
    UPoissonAr.xy = UnuAr(1);
PoissonAr.xz = nuAr(2);
    LPoissonAr.xz = LnuAr(2);
    UPoissonAr.xz = UnuAr(2);
PoissonAr.yz = nuAr(3);
    LPoissonAr.yz = LnuAr(3);
    UPoissonAr.yz = UnuAr(3);

% Ar and Tr adjusted outputs
YoungsArTr.x = EArTr(1);
    LYoungsArTr.x = LEArTr(1);
    UYoungsArTr.x = UEArTr(1);
YoungsArTr.y = EArTr(2);
    LYoungsArTr.y = LEArTr(2);
    UYoungsArTr.y = UEArTr(2);
YoungsArTr.z = EArTr(3);
    LYoungsArTr.z = LEArTr(3);
    UYoungsArTr.z = UEArTr(3);

ShearArTr.xy = SArTr(6,6)^(-1)/2;
    LShearArTr.xy = LSArTr(6,6)^(-1)/2;
    UShearArTr.xy = USArTr(6,6)^(-1)/2;
ShearArTr.xz = SArTr(5,5)^(-1)/2;
    LShearArTr.xz = LSArTr(5,5)^(-1)/2;
    UShearArTr.xz = USArTr(5,5)^(-1)/2;
ShearArTr.yz = SArTr(4,4)^(-1)/2;
    LShearArTr.yz = LSArTr(4,4)^(-1)/2;
    UShearArTr.yz = USArTr(4,4)^(-1)/2;

PoissonArTr.xy = nuArTr(1);
    LPoissonArTr.xy = LnuArTr(1);
    UPoissonArTr.xy = UnuArTr(1);
PoissonArTr.xz = nuArTr(2);
```

```
    LPoissonArTr.xz = LnuArTr(2);
    UPoissonArTr.xz = UnuArTr(2);
PoissonArTr.yz = nuArTr(3);
    LPoissonArTr.yz = LnuArTr(3);
    UPoissonArTr.yz = UnuArTr(3);

end
```

TensorRatioPlot.m

```
function TensorRatioPlot(idx,Tr,TrCi,endtime)
% This function reads the input from a seperate function, ContactTensor.m
% and plots the associated data for the production of useful figures and
% charts.  The inputs match the outputs of ContactTensor.m with the
% additional input of pixeldim to give real spatial resolution to the pixel
% based data.  The plots were originally inside of ContactTensor.m and have
% been moved to an external function for greater versatility.
%
% This function requires the use of errorbarwidth.m for appropriately
% sizing the error bars on the plots produced by this function.
%
% INPUTS
%       F2(i,j,n): 2nd order contact tensor.  i and j reference the matrix
%       position within an individual tensor (i=1,2,3;j=1,2,3) and n
%       specifies the volume in chronological order with which the contact
%       tensor is associated.
%
%       F2Ci(i,j,n,b): Upper and lower bonds of the 95% confidence interval of
%       2nd order contact tensor.  i, j, and n are the same as above.  b
%       indicates the upper or lower bounds of the confidence interval. 1
%       indicates the lower bound, 2 indicates the upper bound.
%
%       bondRad{n}: A vector of the distribution of bond radii contained
%       within a cell structure for time series data.
%
%       grainRad{n}: Same as bondRad except the distribution of grain
%       radii.
%
%       meanBondRad: Mean 3-D bond radius.  This assumes a circular contact
%       since it is based off the calculated bond area.
%
%       meanGrainRad: Mean 3-D grain radius based on the largest inscribed
%       sphere of each individual grain identified in 3-D segmentation
%
%       coordNum: Mean 3-D coordination number.  This number represents the
%       average number of contacts per grain.
%
%       shapeFac: A calculation of the scalar shape factor.  This is the
%       ratio of the spherical grain gradius (meanGrainRad) to the distance
%       of the grain center to bond center.
```

```
%
%       idx: Elapsed time identifier used to label plots and seperate data
%       based on time during experiment.  Derived from the folder stucture.
%       See help for subfunction FileImport in this file for the
%       appropriate folder structure to use with this function.
%
%       pixdim: Outputs the pixel/voxel resolution of the CT Scan for
%       proper dimensional scaling.
%
%       endtime: Variable listing the final elapsed time used in plotting
%       functions
%
%       spatialLabel: String variable set here to use in plotting functions
%       in other scripts and functions.
%
% Author: David J. Walters, Montana State University
% Version 1.0 - October 22, 2014
%   -Updated help file Oct. 23, 2014
```

```
%%Plot tensor coefficients
% Initialize plot parameters
ebwidth = 0.1;  % Errorbar cap width
font = 'Palatino Linotype';
fsize = 11;     % Font Size
msize = 5;      % Marker Size

%%Tensor Ratio
figure('Name','Tensor Ratio','NumberTitle','off')
% Plot value and confidence interval of contact tensor coefficient F11
hE = errorbar(idx,Tr(1,:),Tr(1,:)-TrCi(1,:,1),...
    TrCi(1,:,2)-Tr(1,:),'rsquare','MarkerSize',msize);

% Plot value and confidence interval of contact tensor coefficient F22
hold on
hE = errorbar(idx,Tr(2,:),Tr(2,:)-TrCi(2,:,1),...
    TrCi(2,:,2)-Tr(2,:),'bdiamond','MarkerSize',msize+1);

% Plot value and confidence interval of contact tensor coefficient F33
hold on
hE = errorbar(idx,Tr(3,:),Tr(3,:)-TrCi(3,:,1),...
    TrCi(3,:,2)-Tr(3,:),'go','MarkerSize',msize);

% Adjust format and appearance of contact tensor coefficient plot
grid
axis([-1 (endtime) 0.4 1.7])
y1 = ylabel('Tenosr Ratio Diagonals (-)');
x1 = xlabel('Elapsed Time (hrs)');
set([y1 x1],'FontName',font,'FontSize',fsize)
legend('\it{x}\rm{_1}','\it{x}\rm{_2}','\it{x}\rm{_3}',...
```

```
    'Location','best','Orientation','horizontal');
set(gca,'FontName',font,'FontSize',fsize,'XTick',0:3:endtime)
```

MILTensorPlot.m

```
function MILTensorPlot(idx,MIL,MILCi,endtime)
% This function reads the input from a seperate function, ContactTensor.m
% and plots the associated data for the production of useful figures and
% charts.  The inputs match the outputs of ContactTensor.m with the
% additional input of pixeldim to give real spatial resolution to the pixel
% based data.  The plots were originally inside of ContactTensor.m and have
% been moved to an external function for greater versatility.
%
% This function requires the use of errorbarwidth.m for appropriately
% sizing the error bars on the plots produced by this function.
%
% INPUTS
%       F2(i,j,n): 2nd order contact tensor.  i and j reference the matrix
%       position within an individual tensor (i=1,2,3;j=1,2,3) and n
%       specifies the volume in chronological order with which the contact
%       tensor is associated.
%
%       F2Ci(i,j,n,b): Upper and lower bonds of the 95% confidence interval of
%       2nd order contact tensor.  i, j, and n are the same as above.  b
%       indicates the upper or lower bounds of the confidence interval. 1
%       indicates the lower bound, 2 indicates the upper bound.
%
%       bondRad{n}: A vector of the distribution of bond radii contained
%       within a cell structure for time series data.
%
%       grainRad{n}: Same as bondRad except the distribution of grain
%       radii.
%
%       meanBondRad: Mean 3-D bond radius.  This assumes a circular contact
%       since it is based off the calculated bond area.
%
%       meanGrainRad: Mean 3-D grain radius based on the largest inscribed
%       sphere of each individual grain identified in 3-D segmentation
%
%       coordNum: Mean 3-D coordination number.  This number represents the
%       average number of contacts per grain.
%
%       shapeFac: A calculation of the scalar shape factor.  This is the
%       ratio of the spherical grain gradius (meanGrainRad) to the distance
%       of the grain center to bond center.
%
%       idx: Elapsed time identifier used to label plots and seperate data
%       based on time during experiment.  Derived from the folder stucture.
%       See help for subfunction FileImport in this file for the
%       appropriate folder structure to use with this function.
```

```
%
%       pixdim: Outputs the pixel/voxel resolution of the CT Scan for
%       proper dimensional scaling.
%
%       endtime: Variable listing the final elapsed time used in plotting
%       functions
%
%       spatialLabel: String variable set here to use in plotting functions
%       in other scripts and functions.
%
% Author: David J. Walters, Montana State University
% Version 1.0 - October 22, 2014
%   -Updated help file Oct. 23, 2014
```

```
%%Plot tensor coefficients
% Initialize plot parameters
font = 'Palatino Linotype';
fsize = 11;     % Font Size
msize = 5;      % Marker Size
```

```
%%MIL Tensor
figure('Name','MIL Tensor','NumberTitle','off')
% Plot value and confidence interval of contact tensor coefficient F11
hE = errorbar(idx,MIL(1,1,:),MIL(1,1,:)-MILCi(1,1,:,1),...
    MILCi(1,1,:,2)-MIL(1,1,:),'rsquare','MarkerSize',msize);

% Plot value and confidence interval of contact tensor coefficient F22
hold on
hE = errorbar(idx,MIL(2,2,:),MIL(2,2,:)-MILCi(2,2,:,1),...
    MILCi(2,2,:,2)-MIL(2,2,:),'bdiamond','MarkerSize',msize+1);

% Plot value and confidence interval of contact tensor coefficient F33
hold on
hE = errorbar(idx,MIL(3,3,:),MIL(3,3,:)-MILCi(3,3,:,1),...
    MILCi(3,3,:,2)-MIL(3,3,:),'go','MarkerSize',msize);

% Adjust format and appearance of contact tensor coefficient plot
grid
axis([-1 (endtime) 0.2 0.5])
y1 = ylabel('MIL Tensor Diagonals (-)');
x1 = xlabel('Elapsed Time (hrs)');
set([y1 x1],'FontName',font,'FontSize',fsize)
legend('\it{x}\rm{_1}','\it{x}\rm{_2}','\it{x}\rm{_3}',...
    'Location','best','Orientation','horizontal');
set(gca,'FontName',font,'FontSize',fsize,'XTick',0:3:endtime)
```

MechModuliPlot.m

```
function MechModuliPlot( EStarRaw, GStarRaw, nuStarRaw, EStarAr, GStarAr, nuStarAr,...
    YoungsRaw, LYoungsRaw, UYoungsRaw,...
    YoungsAr, LYoungsAr, UYoungsAr,...
    YoungsArTr, LYoungsArTr, UYoungsArTr,...
    ShearRaw, LShearRaw, UShearRaw,...
    ShearAr, LShearAr, UShearAr,...
    ShearArTr, LShearArTr, UShearArTr,...
    PoissonRaw, LPoissonRaw, UPoissonRaw,...
    PoissonAr, LPoissonAr, UPoissonAr,...
    PoissonArTr, LPoissonArTr, UPoissonArTr,...
    SRaw, SAr, SArTr, endtime, idx)
% MechModuliPlot.m
% function MechModuliPlot( EStarRaw, GStarRaw, nuStarRaw, EStarAr, GStarAr, nuStarAr,...
%     YoungsRaw, LYoungsRaw, UYoungsRaw,...
%     YoungsAr, LYoungsAr, UYoungsAr,...
%     YoungsArTr, LYoungsArTr, UYoungsArTr,...
%     ShearRaw, LShearRaw, UShearRaw,...
%     ShearAr, LShearAr, UShearAr,...
%     ShearArTr, LShearArTr, UShearArTr,...
%     PoissonRaw, LPoissonRaw, UPoissonRaw,...
%     PoissonAr, LPoissonAr, UPoissonAr,...
%     PoissonArTr, LPoissonArTr, UPoissonArTr,...
%     SRaw, SAr, SArTr )
%
% This function plots the results of the function MechModuli.m.  It should
% be able to appropriately handle time series data.
%
% INPUTS:
%   EStar(---) - Scalar Young's modulus calculated from measurable
%   microstructural parameters.
%       *Raw - Results produced by the original contact tensor model.
%       *Ar - Results as produced by incorporating only the scalar shape
%       factor aspect ratio, Ar.
%
%   GStar(---) - Scalar shear modulus calculated from measurable
%   microstructural parameters.
%
%   nuStar(---) - Scalar Poisson's ratio calculated from measurable
%   microstructural parameters.
%
%   Youngs(---) - A structure of anisotropic Young's moduli along each of the
%   principal directions of contact (i.e [E1,E2,E3]).
%       *Raw - Results as produced by the orginal contact tensor model.
%       *Ar - Results as produced by incorporating only the scalar shape
%       factor aspect ratio, Ar.
%       *ArTr - Results as produced by incorporating both the scalar shape
%       factor aspect ratio, Ar, and the tensor ratio, Tr.
%
%   LYoungs(---)/UYoungs(---) - Lower and upper confidence intervals for
%   Youngs---.
```

```
%
%   Shear(---) - A structure of anisotropic shear moduli along aligning with
%   the principal directions of contact (i.e. [G23,G13,G12]).
%
%   LShear(---)/UShear(---) - Lower and upper confidence intervals for
%   Shear(---).
%
%   Poisson(---) - A structure of anisotropic Poisson's ratio alignining with
%   the principal directions of contact (i.e. [nu23,nu13,nu12]).
%
%   LPossion(---)/UPoisson(---) - Lower and upper confidence intervals for
%   Poisson(---).
%
%   S(---) - A 6x6 array that represents the anisotropic compliance matrix.
%   Its maximum deviation from isotropy is orthotropic symmetry (9
%   independent coefficients) as restricted by the use of a 2nd order
%   contact tensor.
%
%   v1.0, October 30, 2014,
% AUTHOR: David J. Walters; Montana State University


%%Convert Structures to Arrays

for k = 1:length(idx)
    YoungsXRaw(k) = YoungsRaw(k).x;
    YoungsYRaw(k) = YoungsRaw(k).y;
    YoungsZRaw(k) = YoungsRaw(k).z;
    UYoungsXRaw(k) = UYoungsRaw(k).x;
    UYoungsYRaw(k) = UYoungsRaw(k).y;
    UYoungsZRaw(k) = UYoungsRaw(k).z;
    LYoungsXRaw(k) = LYoungsRaw(k).x;
    LYoungsYRaw(k) = LYoungsRaw(k).y;
    LYoungsZRaw(k) = LYoungsRaw(k).z;
    ShearXYRaw(k) = ShearRaw(k).xy;
    ShearXZRaw(k) = ShearRaw(k).xz;
    ShearYZRaw(k) = ShearRaw(k).yz;
    UShearXYRaw(k) = UShearRaw(k).xy;
    UShearXZRaw(k) = UShearRaw(k).xz;
    UShearYZRaw(k) = UShearRaw(k).yz;
    LShearXYRaw(k) = LShearRaw(k).xy;
    LShearXZRaw(k) = LShearRaw(k).xz;
    LShearYZRaw(k) = LShearRaw(k).yz;
    PoissonXYRaw(k) = PoissonRaw(k).xy;
    PoissonXZRaw(k) = PoissonRaw(k).xz;
    PoissonYZRaw(k) = PoissonRaw(k).yz;
    UPoissonXYRaw(k) = UPoissonRaw(k).xy;
    UPoissonXZRaw(k) = UPoissonRaw(k).xz;
    UPoissonYZRaw(k) = UPoissonRaw(k).yz;
    LPoissonXYRaw(k) = LPoissonRaw(k).xy;
    LPoissonXZRaw(k) = LPoissonRaw(k).xz;
```

```
      LPoissonYZRaw(k) = LPoissonRaw(k).yz;

      YoungsXAr(k) = YoungsAr(k).x;
      YoungsYAr(k) = YoungsAr(k).y;
      YoungsZAr(k) = YoungsAr(k).z;
      UYoungsXAr(k) = UYoungsAr(k).x;
      UYoungsYAr(k) = UYoungsAr(k).y;
      UYoungsZAr(k) = UYoungsAr(k).z;
      LYoungsXAr(k) = LYoungsAr(k).x;
      LYoungsYAr(k) = LYoungsAr(k).y;
      LYoungsZAr(k) = LYoungsAr(k).z;
      ShearXYAr(k) = ShearAr(k).xy;
      ShearXZAr(k) = ShearAr(k).xz;
      ShearYZAr(k) = ShearAr(k).yz;
      UShearXYAr(k) = UShearAr(k).xy;
      UShearXZAr(k) = UShearAr(k).xz;
      UShearYZAr(k) = UShearAr(k).yz;
      LShearXYAr(k) = LShearAr(k).xy;
      LShearXZAr(k) = LShearAr(k).xz;
      LShearYZAr(k) = LShearAr(k).yz;
      PoissonXYAr(k) = PoissonAr(k).xy;
      PoissonXZAr(k) = PoissonAr(k).xz;
      PoissonYZAr(k) = PoissonAr(k).yz;
      UPoissonXYAr(k) = UPoissonAr(k).xy;
      UPoissonXZAr(k) = UPoissonAr(k).xz;
      UPoissonYZAr(k) = UPoissonAr(k).yz;
      LPoissonXYAr(k) = LPoissonAr(k).xy;
      LPoissonXZAr(k) = LPoissonAr(k).xz;
      LPoissonYZAr(k) = LPoissonAr(k).yz;

      YoungsXArTr(k) = YoungsArTr(k).x;
      YoungsYArTr(k) = YoungsArTr(k).y;
      YoungsZArTr(k) = YoungsArTr(k).z;
      UYoungsXArTr(k) = UYoungsArTr(k).x;
      UYoungsYArTr(k) = UYoungsArTr(k).y;
      UYoungsZArTr(k) = UYoungsArTr(k).z;
      LYoungsXArTr(k) = LYoungsArTr(k).x;
      LYoungsYArTr(k) = LYoungsArTr(k).y;
      LYoungsZArTr(k) = LYoungsArTr(k).z;
      ShearXYArTr(k) = ShearArTr(k).xy;
      ShearXZArTr(k) = ShearArTr(k).xz;
      ShearYZArTr(k) = ShearArTr(k).yz;
      UShearXYArTr(k) = UShearArTr(k).xy;
      UShearXZArTr(k) = UShearArTr(k).xz;
      UShearYZArTr(k) = UShearArTr(k).yz;
      LShearXYArTr(k) = LShearArTr(k).xy;
      LShearXZArTr(k) = LShearArTr(k).xz;
      LShearYZArTr(k) = LShearArTr(k).yz;
      PoissonXYArTr(k) = PoissonArTr(k).xy;
      PoissonXZArTr(k) = PoissonArTr(k).xz;
      PoissonYZArTr(k) = PoissonArTr(k).yz;
```

```
    UPoissonXYArTr(k) = UPoissonArTr(k).xy;
    UPoissonXZArTr(k) = UPoissonArTr(k).xz;
    UPoissonYZArTr(k) = UPoissonArTr(k).yz;
    LPoissonXYArTr(k) = LPoissonArTr(k).xy;
    LPoissonXZArTr(k) = LPoissonArTr(k).xz;
    LPoissonYZArTr(k) = LPoissonArTr(k).yz;
end
```

```
%%Raw
% Plot tensor coefficients
% Initialize plot parameters
ebwidth = 0.1;  % Errorbar cap width
font = 'Palatino Linotype';
fsize = 11;     % Font Size
msize = 5;      % Marker Size

% Young's Modulus
% Initialize figure heading
figure('Name','3-D Youngs Moduli RAW',...
    'NumberTitle','off')
hold on

% Plot value and confidence interval of Young's modulus E1
hE = errorbar(idx,YoungsXRaw./10^6,(YoungsXRaw-LYoungsXRaw)./10^6,...
    (UYoungsXRaw-YoungsXRaw)./10^6,'rsquare','MarkerSize',msize);


% Plot value and confidence interval of Young's modulus E2
hE = errorbar(idx,YoungsYRaw./10^6,(YoungsYRaw-LYoungsYRaw)./10^6,...
    (UYoungsYRaw-YoungsYRaw)./10^6,'bdiamond','MarkerSize',msize+1);


% Plot value and confidence interval of Young's modulus E3
hE = errorbar(idx,YoungsZRaw./10^6,(YoungsZRaw-LYoungsZRaw)./10^6,...
    (UYoungsZRaw-YoungsZRaw)./10^6,'go','MarkerSize',msize);


% Plot value of scalar Young's Modulus E*
plot(idx,EStarRaw./10^6,'k--')

% Adjust format and appearance of Young's modulus plot
legend('\it{E}\rm{_1}','\it{E}\rm{_2}','\it{E}\rm{_3}','\it{E*}',...
    'Location','best');
grid, box on
x1 = xlabel('Elapsed Time (hrs)');
y1 = ylabel('Young''s Modulus (MPa)');
% axis([-1 (endtime) 200 500])
xlim([-1 (endtime)])
set([y1 x1],'FontName',font,'FontSize',fsize)
set(gca,'FontName',font,'FontSize',fsize,'XTick',0:3:endtime)
```

```
% Shear Modulus
% Initialize figure heading
figure('Name','3-D Shear Moduli RAW',...
    'NumberTitle','off')
hold on

% Plot value and confidence interval of shear modulus G12
hE = errorbar(idx,ShearXYRaw./10^6,(ShearXYRaw-LShearXYRaw)./10^6,...
    (UShearXYRaw-ShearXYRaw)./10^6,'rsquare','MarkerSize',msize);


% Plot value and confidence interval of shear modulus G13
hE = errorbar(idx,ShearXZRaw./10^6,(ShearXZRaw-LShearXZRaw)./10^6,...
    (UShearXZRaw-ShearXZRaw)./10^6,'bdiamond','MarkerSize',msize);


% Plot value and confidence interval of shear modulus G23
hE = errorbar(idx,ShearYZRaw./10^6,(ShearYZRaw-LShearYZRaw)./10^6,...
    (UShearYZRaw-ShearYZRaw)./10^6,'go','MarkerSize',msize);


% Plot value of scalar shear modulus G*
plot(idx,GStarRaw./10^6,'k--')

% Adjust format and appearance of shear modulus plot
legend('\it{G}\rm{_1_2}','\it{G}\rm{_1_3}','\it{G}\rm{_2_3}','\it{G*}');
grid, box on
x1 = xlabel('Elapsed Time (hrs)');
y1 = ylabel('Shear Modulus (MPa)');
% axis([-1 (endtime) 65 95])
xlim([-1 (endtime)])
set([y1 x1],'FontName',font,'FontSize',fsize)
set(gca,'FontName',font,'FontSize',fsize,'XTick',0:3:endtime)

% Poisson's Ratio
% Initialize figure heading
figure('Name','3-D Poissons Ratio',...
    'NumberTitle','off')

% Use subplots for better appearance
ax(1) = subplot(1,3,1);
hold on
% Plot value and confidence interval of Poisson's ratio nu12
hE = errorbar(idx,PoissonXYRaw,PoissonXYRaw-LPoissonXYRaw,...
    UPoissonXYRaw-PoissonXYRaw,'ko','MarkerSize',msize);

plot(idx,nuStarRaw,'r--')
legend('\it{\nu}\rm{_1_2}','\it{\nu*}');
grid, box on
y1 = ylabel('Poisson''s Ratio (-)');
```

```
axis([-1 (endtime) 0 0.5])

% Plot value and confidence interval of Poisson's ratio nu13
ax(2) = subplot(1,3,2);
hold on
hE = errorbar(idx,PoissonXZRaw,PoissonXZRaw-LPoissonXZRaw,...
    UPoissonXZRaw-PoissonXZRaw,'ko','MarkerSize',msize);

plot(idx,nuStarRaw,'r--')
legend('\it{\nu}\rm{_1_3}','\it{\nu*}');
grid, box on
x1 = xlabel('Elapsed Time (hrs)');
axis([-1 (endtime) 0 0.5])

% Plot value and confidence interval of Poisson's ratio nu23
ax(3) = subplot(1,3,3);
hold on
hE = errorbar(idx,PoissonYZRaw,PoissonYZRaw-LPoissonYZRaw,...
    UPoissonYZRaw-PoissonYZRaw,'ko','MarkerSize',msize);

plot(idx,nuStarRaw,'r--')
legend('\it{\nu}\rm{_2_3}','\it{\nu*}');
grid, box on
axis([-1 (endtime) 0 0.5])

set([y1 x1],'FontName',font,'FontSize',fsize)
set(ax,'FontName',font,'FontSize',fsize,'XTick',0:3:endtime)
```

```
%%Aspect Ratio, AR
% Plot tensor coefficients
% Initialize plot parameters
ebwidth = 0.1;  % Errorbar cap width
font = 'Palatino Linotype';
fsize = 11;     % Font Size
msize = 5;      % Marker Size

% Young's Modulus
% Initialize figure heading
figure('Name','3-D Youngs Moduli Ar',...
    'NumberTitle','off')
hold on

% Plot value and confidence interval of Young's modulus E1
hE = errorbar(idx,YoungsXAr./10^6,(YoungsXAr-LYoungsXAr)./10^6,...
    (UYoungsXAr-YoungsXAr)./10^6,'rsquare','MarkerSize',msize);


% Plot value and confidence interval of Young's modulus E2
hE = errorbar(idx,YoungsYAr./10^6,(YoungsYAr-LYoungsYAr)./10^6,...
    (UYoungsYAr-YoungsYAr)./10^6,'bdiamond','MarkerSize',msize+1);
```

```
% Plot value and confidence interval of Young's modulus E3
hE = errorbar(idx,YoungsZAr./10^6,(YoungsZAr-LYoungsZAr)./10^6,...
    (UYoungsZAr-YoungsZAr)./10^6,'go','MarkerSize',msize);


% Plot value of scalar Young's Modulus E*
plot(idx,EStarAr./10^6,'k--')

% Adjust format and appearance of Young's modulus plot
legend('\it{E}\rm{_1}','\it{E}\rm{_2}','\it{E}\rm{_3}','\it{E*}',...
    'Location','best');
grid, box on
x1 = xlabel('Elapsed Time (hrs)');
y1 = ylabel('Young''s Modulus (MPa)');
% axis([-1 (endtime) 200 500])
xlim([-1 (endtime)])
set([y1 x1],'FontName',font,'FontSize',fsize)
set(gca,'FontName',font,'FontSize',fsize,'XTick',0:3:endtime)

% Shear Modulus
% Initialize figure heading
figure('Name','3-D Shear Moduli Ar',...
    'NumberTitle','off')
hold on

% Plot value and confidence interval of shear modulus G12
hE = errorbar(idx,ShearXYAr./10^6,(ShearXYAr-LShearXYAr)./10^6,...
    (UShearXYAr-ShearXYAr)./10^6,'rsquare','MarkerSize',msize);


% Plot value and confidence interval of shear modulus G13
hE = errorbar(idx,ShearXZAr./10^6,(ShearXZAr-LShearXZAr)./10^6,...
    (UShearXZAr-ShearXZAr)./10^6,'bdiamond','MarkerSize',msize);


% Plot value and confidence interval of shear modulus G23
hE = errorbar(idx,ShearYZAr./10^6,(ShearYZAr-LShearYZAr)./10^6,...
    (UShearYZAr-ShearYZAr)./10^6,'go','MarkerSize',msize);


% Plot value of scalar shear modulus G*
plot(idx,GStarAr./10^6,'k--')

% Adjust format and appearance of shear modulus plot
legend('\it{G}\rm{_1_2}','\it{G}\rm{_1_3}','\it{G}\rm{_2_3}','\it{G*}');
grid, box on
x1 = xlabel('Elapsed Time (hrs)');
y1 = ylabel('Shear Modulus (MPa)');
% axis([-1 (endtime) 65 95])
```

```
xlim([-1 (endtime)])
set([y1 x1],'FontName',font,'FontSize',fsize)
set(gca,'FontName',font,'FontSize',fsize,'XTick',0:3:endtime)

% Poisson's Ratio
% Initialize figure heading
figure('Name','3-D Poissons Ratio',...
    'NumberTitle','off')

% Use subplots for better appearance
ax(1) = subplot(1,3,1);
hold on
% Plot value and confidence interval of Poisson's ratio nu12
hE = errorbar(idx,PoissonXYAr,PoissonXYAr-LPoissonXYAr,...
    UPoissonXYAr-PoissonXYAr,'ko','MarkerSize',msize);

plot(idx,nuStarAr,'r--')
legend('\it{\nu}\rm{_1_2}','\it{\nu*}');
grid, box on
y1 = ylabel('Poisson''s Ratio (-)');
axis([-1 (endtime) 0 0.5])

% Plot value and confidence interval of Poisson's ratio nu13
ax(2) = subplot(1,3,2);
hold on
hE = errorbar(idx,PoissonXZAr,PoissonXZAr-LPoissonXZAr,...
    UPoissonXZAr-PoissonXZAr,'ko','MarkerSize',msize);

plot(idx,nuStarAr,'r--')
legend('\it{\nu}\rm{_1_3}','\it{\nu*}');
grid, box on
x1 = xlabel('Elapsed Time (hrs)');
axis([-1 (endtime) 0 0.5])

% Plot value and confidence interval of Poisson's ratio nu23
ax(3) = subplot(1,3,3);
hold on
hE = errorbar(idx,PoissonYZAr,PoissonYZAr-LPoissonYZAr,...
    UPoissonYZAr-PoissonYZAr,'ko','MarkerSize',msize);

plot(idx,nuStarAr,'r--')
legend('\it{\nu}\rm{_2_3}','\it{\nu*}');
grid, box on
axis([-1 (endtime) 0 0.5])

set([y1 x1],'FontName',font,'FontSize',fsize)
set(ax,'FontName',font,'FontSize',fsize,'XTick',0:3:endtime)


%%Aspect Ratio and Tensor Ratio, Ar, Tr
% Plot tensor coefficients
```

```
% Initialize plot parameters
font = 'Palatino Linotype';
fsize = 11;     % Font Size
msize = 5;      % Marker Size

% Young's Modulus
% Initialize figure heading
figure('Name','3-D Youngs Moduli ArTr',...
    'NumberTitle','off')
hold on

% Plot value and confidence interval of Young's modulus E1
hE = errorbar(idx,YoungsXArTr./10^6,(YoungsXArTr-LYoungsXArTr)./10^6,...
    (UYoungsXArTr-YoungsXArTr)./10^6,'rsquare','MarkerSize',msize);


% Plot value and confidence interval of Young's modulus E2
hE = errorbar(idx,YoungsYArTr./10^6,(YoungsYArTr-LYoungsYArTr)./10^6,...
    (UYoungsYArTr-YoungsYArTr)./10^6,'bdiamond','MarkerSize',msize+1);


% Plot value and confidence interval of Young's modulus E3
hE = errorbar(idx,YoungsZArTr./10^6,(YoungsZArTr-LYoungsZArTr)./10^6,...
    (UYoungsZArTr-YoungsZArTr)./10^6,'go','MarkerSize',msize);


% Plot value of scalar Young's Modulus E*
plot(idx,EStarAr./10^6,'k--')

% Adjust format and appearance of Young's modulus plot
legend('\it{E}\rm{_1}','\it{E}\rm{_2}','\it{E}\rm{_3}','\it{E*}',...
    'Location','best');
grid, box on
x1 = xlabel('Elapsed Time (hrs)');
y1 = ylabel('Young''s Modulus (MPa)');
% axis([-1 (endtime) 200 500])
xlim([-1 (endtime)])
set([y1 x1],'FontName',font,'FontSize',fsize)
set(gca,'FontName',font,'FontSize',fsize,'XTick',0:3:endtime)

% Shear Modulus
% Initialize figure heading
figure('Name','3-D Shear Moduli ArTr',...
    'NumberTitle','off')
hold on

% Plot value and confidence interval of shear modulus G12
hE = errorbar(idx,ShearXYArTr./10^6,(ShearXYArTr-LShearXYArTr)./10^6,...
    (UShearXYArTr-ShearXYArTr)./10^6,'rsquare','MarkerSize',msize);
```

```
% Plot value and confidence interval of shear modulus G13
hE = errorbar(idx,ShearXZArTr./10^6,(ShearXZArTr-LShearXZArTr)./10^6,...
    (UShearXZArTr-ShearXZArTr)./10^6,'bdiamond','MarkerSize',msize);


% Plot value and confidence interval of shear modulus G23
hE = errorbar(idx,ShearYZArTr./10^6,(ShearYZArTr-LShearYZArTr)./10^6,...
    (UShearYZArTr-ShearYZArTr)./10^6,'go','MarkerSize',msize);


% Plot value of scalar shear modulus G*
plot(idx,GStarAr./10^6,'k--')

% Adjust format and appearance of shear modulus plot
legend('\it{G}\rm{_1_2}','\it{G}\rm{_1_3}','\it{G}\rm{_2_3}','\it{G*}');
grid, box on
x1 = xlabel('Elapsed Time (hrs)');
y1 = ylabel('Shear Modulus (MPa)');
% axis([-1 (endtime) 65 95])
xlim([-1 (endtime)])
set([y1 x1],'FontName',font,'FontSize',fsize)
set(gca,'FontName',font,'FontSize',fsize,'XTick',0:3:endtime)

% Poisson's Ratio
% Initialize figure heading
figure('Name','3-D Poissons Ratio',...
    'NumberTitle','off')

% Use subplots for better appearance
ax(1) = subplot(1,3,1);
hold on
% Plot value and confidence interval of Poisson's ratio nu12
hE = errorbar(idx,PoissonXYArTr,PoissonXYArTr-LPoissonXYArTr,...
    UPoissonXYArTr-PoissonXYArTr,'ko','MarkerSize',msize);

plot(idx,nuStarAr,'r--')
legend('\it{\nu}\rm{_1_2}','\it{\nu*}');
grid, box on
y1 = ylabel('Poisson''s Ratio (-)');
axis([-1 (endtime) 0 0.5])

% Plot value and confidence interval of Poisson's ratio nu13
ax(2) = subplot(1,3,2);
hold on
hE = errorbar(idx,PoissonXZArTr,PoissonXZArTr-LPoissonXZArTr,...
    UPoissonXZArTr-PoissonXZArTr,'ko','MarkerSize',msize);

plot(idx,nuStarAr,'r--')
legend('\it{\nu}\rm{_1_3}','\it{\nu*}');
grid, box on
x1 = xlabel('Elapsed Time (hrs)');
```

```
axis([-1 (endtime) 0 0.5])

% Plot value and confidence interval of Poisson's ratio nu23
ax(3) = subplot(1,3,3);
hold on
hE = errorbar(idx,PoissonYZArTr,PoissonYZArTr-LPoissonYZArTr,...
    UPoissonYZArTr-PoissonYZArTr,'ko','MarkerSize',msize);

plot(idx,nuStarAr,'r--')
legend('\it{\nu}\rm{_2_3}','\it{\nu*}');
grid, box on
axis([-1 (endtime) 0 0.5])

set([y1 x1],'FontName',font,'FontSize',fsize)
set(ax,'FontName',font,'FontSize',fsize,'XTick',0:3:endtime)
```

```
%%Plot All Together to Show Improvements of Each Model
% Plot tensor coefficients
% Initialize plot parameters
font = 'Palatino Linotype';
fsize = 11;     % Font Size
msize = 5;      % Marker Size

% Young's Modulus
% Initialize figure heading
figure('Name','3-D Youngs Moduli All Together',...
    'NumberTitle','off')
hold on
% Plot Raw Values First
% Plot value and confidence interval of Young's modulus E1
hE = errorbar(idx,YoungsXRaw./10^6,(YoungsXRaw-LYoungsXRaw)./10^6,...
    (UYoungsXRaw-YoungsXRaw)./10^6,'rsquare','MarkerSize',msize);


% Plot value and confidence interval of Young's modulus E2
hE = errorbar(idx,YoungsYRaw./10^6,(YoungsYRaw-LYoungsYRaw)./10^6,...
    (UYoungsYRaw-YoungsYRaw)./10^6,'rdiamond','MarkerSize',msize+1);


% Plot value and confidence interval of Young's modulus E3
hE = errorbar(idx,YoungsZRaw./10^6,(YoungsZRaw-LYoungsZRaw)./10^6,...
    (UYoungsZRaw-YoungsZRaw)./10^6,'ro','MarkerSize',msize);


% Plot value of scalar Young's Modulus E*
plot(idx,EStarRaw./10^6,'r--')

% Next Plot Ar adjusted values
% Plot value and confidence interval of Young's modulus E1
```

```
hE = errorbar(idx,YoungsXAr./10^6,(YoungsXAr-LYoungsXAr)./10^6,...
    (UYoungsXAr-YoungsXAr)./10^6,'gsquare','MarkerSize',msize);


% Plot value and confidence interval of Young's modulus E2
hE = errorbar(idx,YoungsYAr./10^6,(YoungsYAr-LYoungsYAr)./10^6,...
    (UYoungsYAr-YoungsYAr)./10^6,'gdiamond','MarkerSize',msize+1);


% Plot value and confidence interval of Young's modulus E3
hE = errorbar(idx,YoungsZAr./10^6,(YoungsZAr-LYoungsZAr)./10^6,...
    (UYoungsZAr-YoungsZAr)./10^6,'go','MarkerSize',msize);


% Plot value of scalar Young's Modulus E*
plot(idx,EStarAr./10^6,'g--')

% Plot ArTr adjusted Values
% Plot value and confidence interval of Young's modulus E1
hE = errorbar(idx,YoungsXArTr./10^6,(YoungsXArTr-LYoungsXArTr)./10^6,...
    (UYoungsXArTr-YoungsXArTr)./10^6,'bsquare','MarkerSize',msize);


% Plot value and confidence interval of Young's modulus E2
hE = errorbar(idx,YoungsYArTr./10^6,(YoungsYArTr-LYoungsYArTr)./10^6,...
    (UYoungsYArTr-YoungsYArTr)./10^6,'bdiamond','MarkerSize',msize+1);


% Plot value and confidence interval of Young's modulus E3
hE = errorbar(idx,YoungsZArTr./10^6,(YoungsZArTr-LYoungsZArTr)./10^6,...
    (UYoungsZArTr-YoungsZArTr)./10^6,'bo','MarkerSize',msize);


% Adjust format and appearance of Young's modulus plot
legend('\it{E}\rm{_1}\rm{^R^a^w}','\it{E}\rm{_2}\rm{^R^a^w}','\it{E}\rm{_3}\rm{^R^a^w}',.
..
    '\it{E*}\rm{^R^a^w}',...
    '\it{E}\rm{_1}\rm{^A^r}','\it{E}\rm{_2}\rm{^A^r}','\it{E}\rm{_3}\rm{^A^r}',...
    '\it{E*}\rm{^A^r}',...

'\it{E}\rm{_1}\rm{^A^r^T^r}','\it{E}\rm{_2}\rm{^A^r^T^r}','\it{E}\rm{_3}\rm{^A^r^T^r}',..
.
    'Location','best');
grid, box on
x1 = xlabel('Elapsed Time (hrs)');
y1 = ylabel('Young''s Modulus (MPa)');
% axis([-1 (endtime) 200 500])
xlim([-1 (endtime)])
set([y1 x1],'FontName',font,'FontSize',fsize)
set(gca,'FontName',font,'FontSize',fsize,'XTick',0:3:endtime)
```

```
% Shear Modulus
% Initialize figure heading
figure('Name','3-D Shear Moduli All Together',...
    'NumberTitle','off')
hold on

% Plot Raw Values First
% Plot value and confidence interval of shear modulus G12
hE = errorbar(idx,ShearXYRaw./10^6,(ShearXYRaw-LShearXYRaw)./10^6,...
    (UShearXYRaw-ShearXYRaw)./10^6,'rsquare','MarkerSize',msize);


% Plot value and confidence interval of shear modulus G13
hE = errorbar(idx,ShearXZRaw./10^6,(ShearXZRaw-LShearXZRaw)./10^6,...
    (UShearXZRaw-ShearXZRaw)./10^6,'rdiamond','MarkerSize',msize+1);


% Plot value and confidence interval of shear modulus G23
hE = errorbar(idx,ShearYZRaw./10^6,(ShearYZRaw-LShearYZRaw)./10^6,...
    (UShearYZRaw-ShearYZRaw)./10^6,'ro','MarkerSize',msize);


% Plot value of scalar Young's Modulus E*
plot(idx,EStarRaw./10^6,'r--')

% Next Plot Ar adjusted values
% Plot value and confidence interval of shear modulus G12
hE = errorbar(idx,ShearXYAr./10^6,(ShearXYAr-LShearXYAr)./10^6,...
    (UShearXYAr-ShearXYAr)./10^6,'gsquare','MarkerSize',msize);


% Plot value and confidence interval of shear modulus G13
hE = errorbar(idx,ShearXZAr./10^6,(ShearXZAr-LShearXZAr)./10^6,...
    (UShearXZAr-ShearXZAr)./10^6,'gdiamond','MarkerSize',msize+1);


% Plot value and confidence interval of shear modulus G23
hE = errorbar(idx,ShearYZAr./10^6,(ShearYZAr-LShearYZAr)./10^6,...
    (UShearYZAr-ShearYZAr)./10^6,'go','MarkerSize',msize);


% Plot value of scalar Young's Modulus E*
plot(idx,EStarAr./10^6,'g--')

% Plot ArTr adjusted Values
% Plot value and confidence interval of shear modulus G12
hE = errorbar(idx,ShearXYArTr./10^6,(ShearXYArTr-LShearXYArTr)./10^6,...
    (UShearXYArTr-ShearXYArTr)./10^6,'bsquare','MarkerSize',msize);
```

```
% Plot value and confidence interval of shear modulus G13
hE = errorbar(idx,ShearXZArTr./10^6,(ShearXZArTr-LShearXZArTr)./10^6,...
    (UShearXZArTr-ShearXZArTr)./10^6,'bdiamond','MarkerSize',msize+1);


% Plot value and confidence interval of shear modulus G23
hE = errorbar(idx,ShearYZArTr./10^6,(ShearYZArTr-LShearYZArTr)./10^6,...
    (UShearYZArTr-ShearYZArTr)./10^6,'bo','MarkerSize',msize);


% Adjust format and appearance of Young's modulus plot
legend('\it{G}\rm{_1_2}\rm{^R^a^w}','\it{G}\rm{_1_3}\rm{^R^a^w}','\it{G}\rm{_2_3}\rm{^R^a
^w}',...
    '\it{G*}\rm{^R^a^w}',...
    '\it{G}\rm{_1_2}\rm{^A^r}','\it{G}\rm{_1_3}\rm{^A^r}','\it{G}\rm{_2_3}\rm{^A^r}',...
    '\it{G*}\rm{^A^r}',...

'\it{G}\rm{_1_2}\rm{^A^r^T^r}','\it{G}\rm{_1_3}\rm{^A^r^T^r}','\it{G}\rm{_2_3}\rm{^A^r^T^
r}',...
    'Location','best');

grid, box on
x1 = xlabel('Elapsed Time (hrs)');
y1 = ylabel('Shear Modulus (MPa)');
% axis([-1 (endtime) 65 95])
xlim([-1 (endtime)])
ylim('Auto')
set([y1 x1],'FontName',font,'FontSize',fsize)
set(gca,'FontName',font,'FontSize',fsize,'XTick',0:3:endtime)

% Poisson's Ratio
% Initialize figure heading
figure('Name','3-D Poissons Ratio All Values',...
    'NumberTitle','off')

% Use subplots for better appearance
ax(1) = subplot(1,3,1);
hold on
% Plot value and confidence interval of Poisson's ratio nu12
hE = errorbar(idx,PoissonXYRaw,PoissonXYRaw-LPoissonXYRaw,...
    UPoissonXYRaw-PoissonXYRaw,'rsquare','MarkerSize',msize);

hE = errorbar(idx,PoissonXYAr,PoissonXYAr-LPoissonXYAr,...
    UPoissonXYAr-PoissonXYAr,'go','MarkerSize',msize);

hE = errorbar(idx,PoissonXYArTr,PoissonXYArTr-LPoissonXYArTr,...
    UPoissonXYArTr-PoissonXYArTr,'bdiamond','MarkerSize',msize+1);

plot(idx,nuStarRaw,'r--')
```

```
plot(idx,nuStarAr,'g--')
title('\it{\nu}\rm{_1_2}')

grid, box on
y1 = ylabel('Poisson''s Ratio (-)');
axis([-1 (endtime) 0 0.5])


% Plot value and confidence interval of Poisson's ratio nu13
ax(2) = subplot(1,3,2);
hold on
hE = errorbar(idx,PoissonXZRaw,PoissonXZRaw-LPoissonXZRaw,...
    UPoissonXZRaw-PoissonXZRaw,'rsquare','MarkerSize',msize);

hE = errorbar(idx,PoissonXZAr,PoissonXZAr-LPoissonXZAr,...
    UPoissonXZAr-PoissonXZAr,'go','MarkerSize',msize);

hE = errorbar(idx,PoissonXZArTr,PoissonXZArTr-LPoissonXZArTr,...
    UPoissonXZArTr-PoissonXZArTr,'bdiamond','MarkerSize',msize+1);

plot(idx,nuStarRaw,'r--')
plot(idx,nuStarAr,'g--')
title('\it{\nu}\rm{_1_3}')

grid, box on
x1 = xlabel('Elapsed Time (hrs)');
axis([-1 (endtime) 0 0.5])

% Plot value and confidence interval of Poisson's ratio nu23
ax(3) = subplot(1,3,3);
hold on
hE = errorbar(idx,PoissonYZRaw,PoissonYZRaw-LPoissonYZRaw,...
    UPoissonYZRaw-PoissonYZRaw,'rsquare','MarkerSize',msize);

hE = errorbar(idx,PoissonYZAr,PoissonYZAr-LPoissonYZAr,...
    UPoissonYZAr-PoissonYZAr,'go','MarkerSize',msize);

hE = errorbar(idx,PoissonYZArTr,PoissonYZArTr-LPoissonYZArTr,...
    UPoissonYZArTr-PoissonYZArTr,'bdiamond','MarkerSize',msize+1);

plot(idx,nuStarRaw,'r--')
plot(idx,nuStarAr,'g--')
title('\it{\nu}\rm{_2_3}')

legend('\it{\nu}\rm{^R^a^w}',...
    '\it{\nu}\rm{^A^r}',...
    '\it{\nu}\rm{^A^r^T^r}',...
    '\it{\nu*}\rm{^R^a^w}','\it{\nu*}\rm{^A^r}');
grid, box on
axis([-1 (endtime) 0 0.5])
```

```
set([y1 x1],'FontName',font,'FontSize',fsize)
set(ax,'FontName',font,'FontSize',fsize,'XTick',0:3:endtime)
end
```

SaveAllPlots.m

```
% Script saves all open figure windows to 3 file formats to the directory
% specified by the user.  (3 formats: .fig, .emf, .png)
% Author: David J. Walters
% Montana State University
hfigs = get(0,'children');  %Get list of figures

LocalPath = 'C:\Doctoral Research\Mechanical Testing\Radiation Recrystallization\Fabric
Tensor and ANSYS\Matlab 3D Segmentation Results\';
directory = uigetdir(LocalPath,...
    'Select  directory to save plots');
DataPath = fullfile(directory,'TensorData');
save(DataPath)

for i = 1:length(hfigs)
    % Set figure size and position on screen
    set(hfigs(i),'PaperUnits','inches')
    set(hfigs(i),'PaperPosition',[3,3,6,3.5])
    set(hfigs(i),'PaperPositionMode','manual')
end
for i = 1:length(hfigs)
    figure(hfigs(i))        %Bring figure to foreground
    filename = get(gcf,'name'); %Get window title for filename
    % If no special window title specified, give generic filename
    if isempty(filename)
        fname = sprintf('Figure %2.0f',i);
        filename = fname;
    end
    FilePath = fullfile(directory,filename);
    % Save figures to specified path
    print(hfigs(i),FilePath,'-dpng','-r300');
    saveas(hfigs(i),FilePath,'fig');
    print(hfigs(i),FilePath,'-dmeta');
end
```

APPENDIX D

MECHANICAL TESTING RESULTS

Stress and strain reports for all experimental samples are reported in this appendix. For tabulated stiffness values, refer to Tables 8-2 and 8-4. These values are derived from the slope of the single order fit plotted on stress strain curves here. Strain contours from ARAMIS are also included using the measure that best represents the mode of the teste (shear or compression).

D.1 New Snow 1 (NS1) Mechanical Shear Test Results

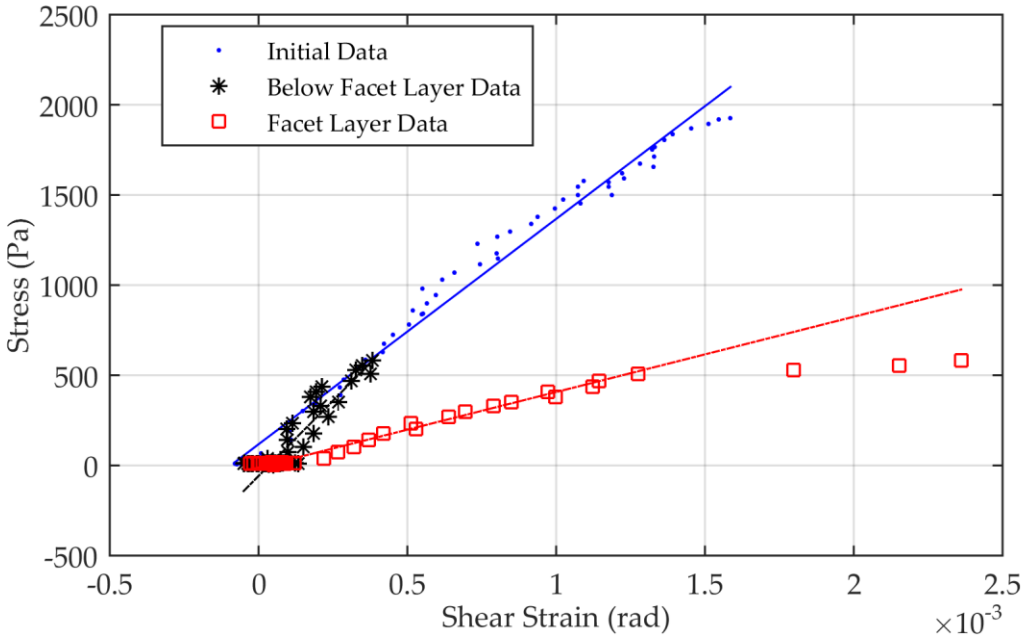


Figure D-1: Shear stress and strain from the physical shear test of sample NS1. Includes data from the initial snow sample prior to recrystallization (blue) and data post recrystallization within the faceted layer (red) and below the faceted layer (black). Best fit lines are plotted to compute the shear modulus.

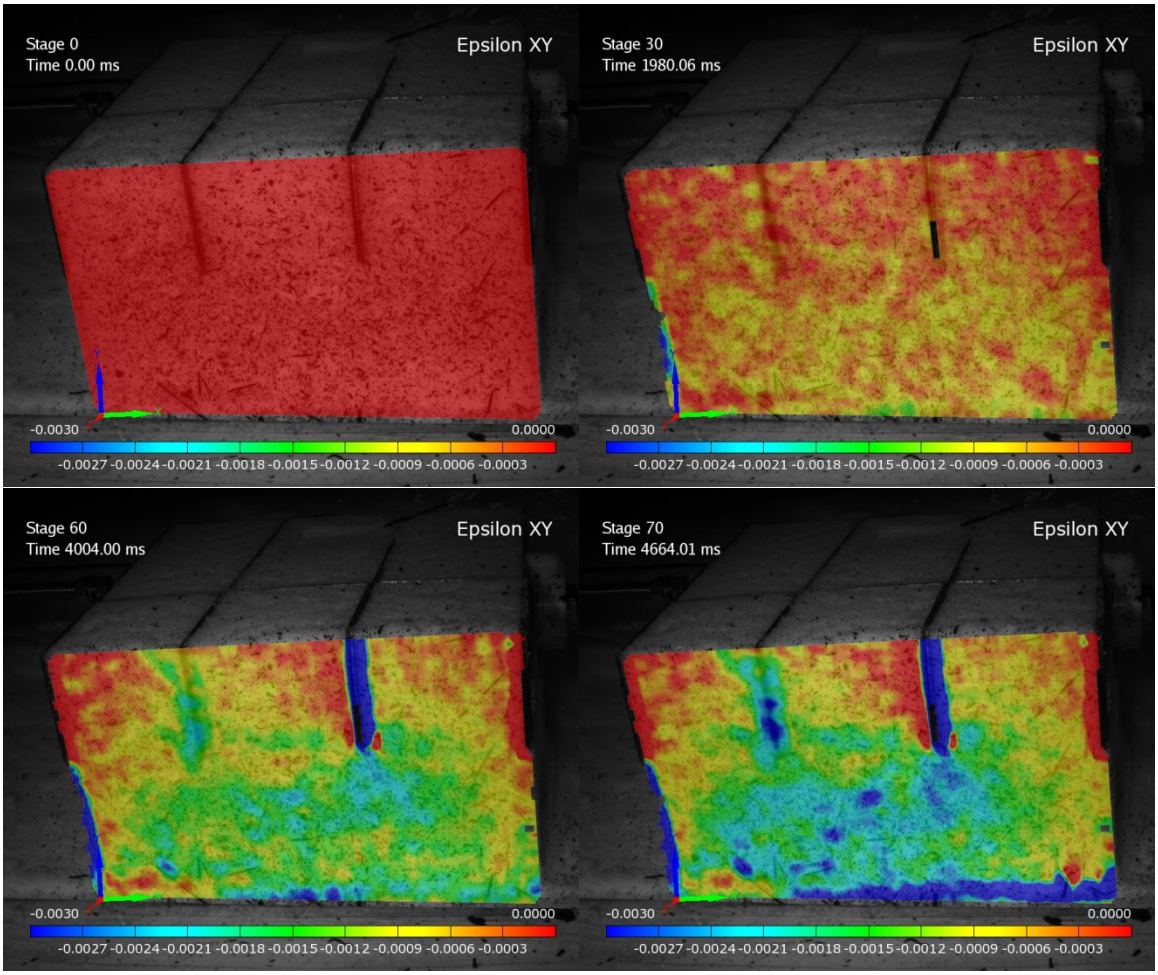


Figure D-2: Sequence of shear strain contours on sample NS1 of the initial non-recrystallized sample showing development of mostly uniform shear strain. Samples are loaded from right to left. The final image (Stage 70) is after failure of the sample has occurred.

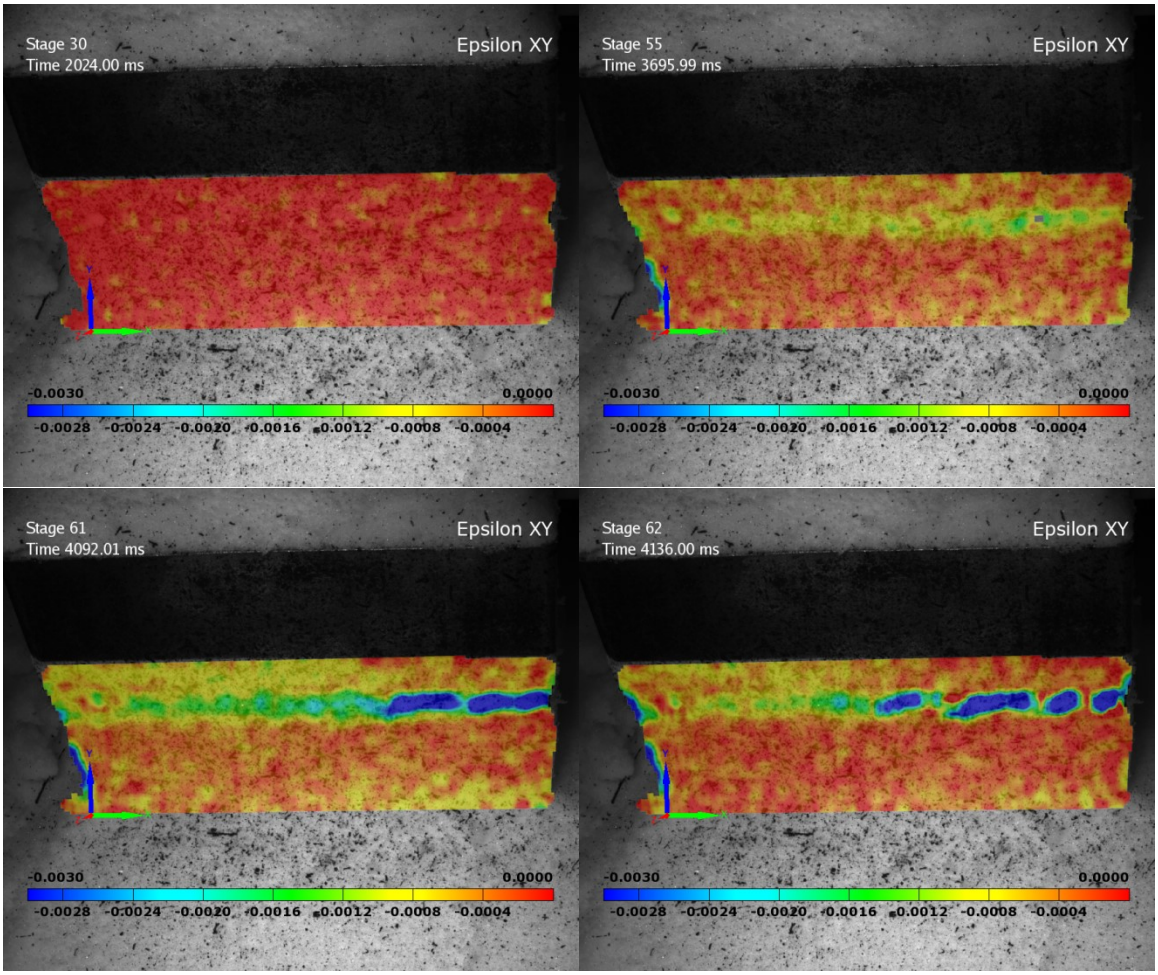


Figure D-3: Sequence of shear strain contours on sample NS1 of the radiation recrystallized sample showing development of localized shear strain in the faceted layer. Samples are loaded from right to left. The final image (Stage 62) is after partial failure of the sample has occurred. Failure continues across the plane defined by the area of increased shear strain.

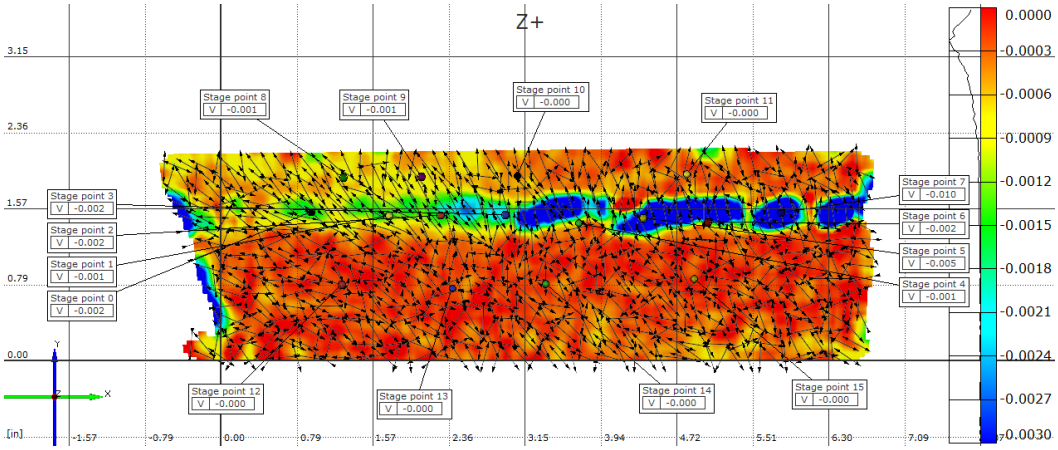


Figure D-4: Stage point locations used to query and average strain in regions of interest of sample NS1. Eight points (Stage point 0 through Stage point 7) are positioned within the faceted layer. Four points (Stage point 12 through Stage point 15) are positioned below the faceted layer.

D.2 New Snow 2 (NS2) Mechanical Shear Test Results

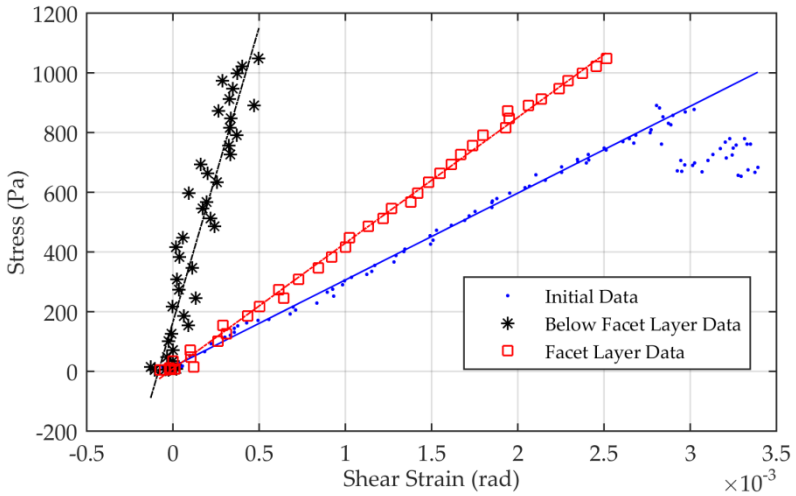


Figure D-5: Shear stress and strain from the physical shear test of sample NS2. Includes data from the initial snow sample prior to recrystallization (blue) and data post recrystallization within the faceted layer (red) and below the faceted layer (black). Best fit lines are plotted to compute the shear modulus.

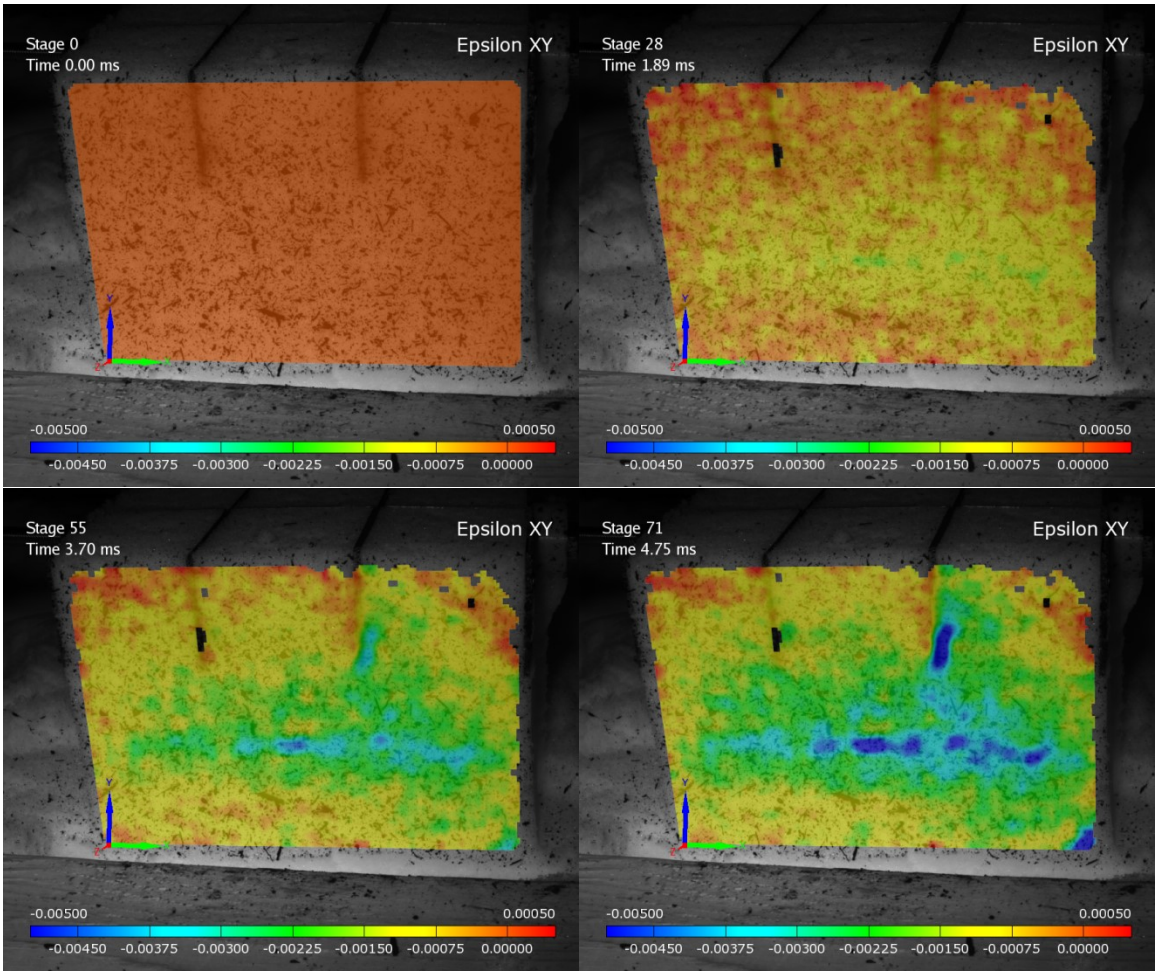


Figure D-6: Sequence of shear strain contours on sample NS2 of the initial non-recrystallized sample showing development of mostly uniform shear strain. Samples are loaded from right to left. The final image (Stage 71) is after failure of the sample has occurred. Although it appears a localized region of shear strain develops in the center, this is an artifact that became apparent after failure had occurred in the extreme lower right corner shown in Stage 71.

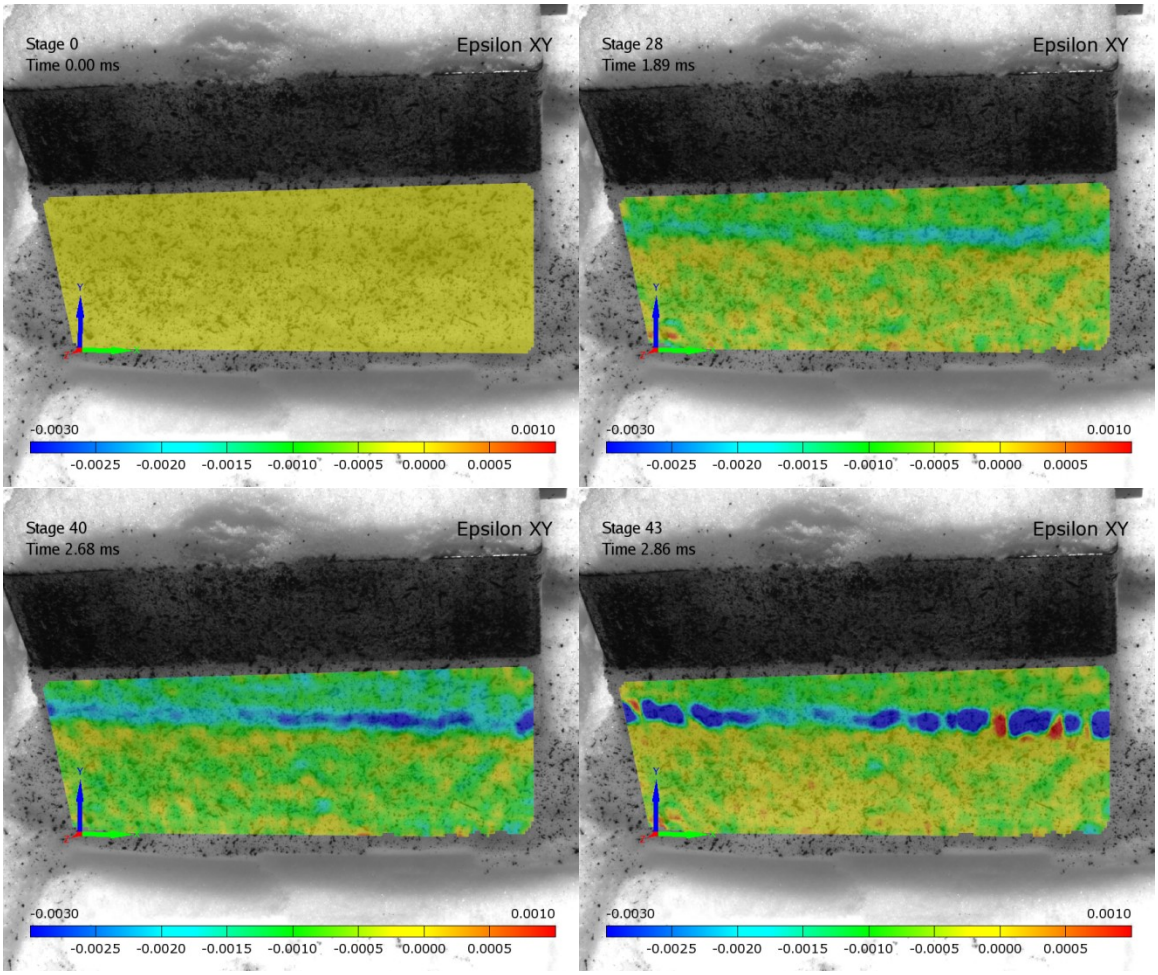


Figure D-7: Sequence of shear strain contours on sample NS2 of the radiation recrystallized sample showing development of localized shear strain in the faceted layer. Samples are loaded from right to left. The final image (Stage 43) is after failure of the sample has occurred. Failure occurred in a clean plane defined by the line of increased shear strain.

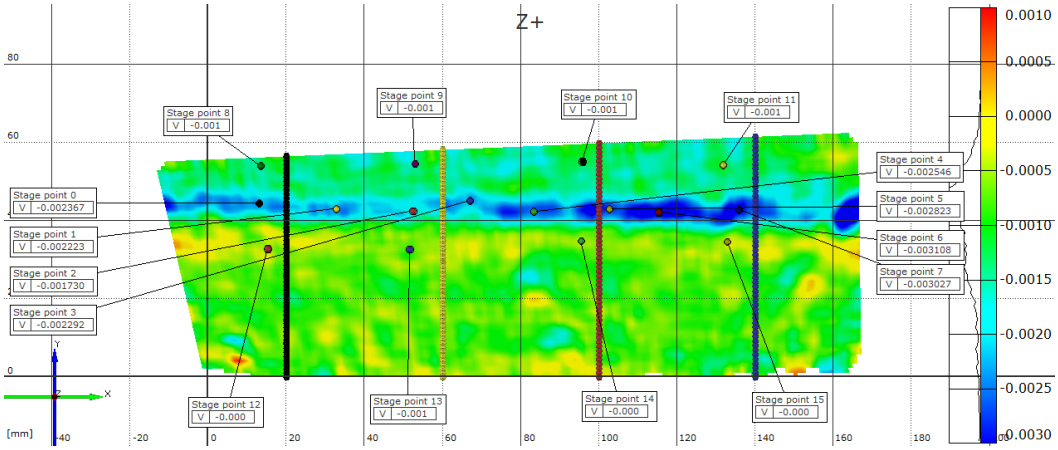


Figure D-8: Stage point locations used to query and average strain in regions of interest of sample NS2. Eight points (Stage point 0 through Stage point 7) are positioned within the faceted layer. Four points (Stage point 12 through Stage point 15) are positioned below the faceted layer.

D.3 New Snow 3 (NS3) Mechanical Compression Test Results

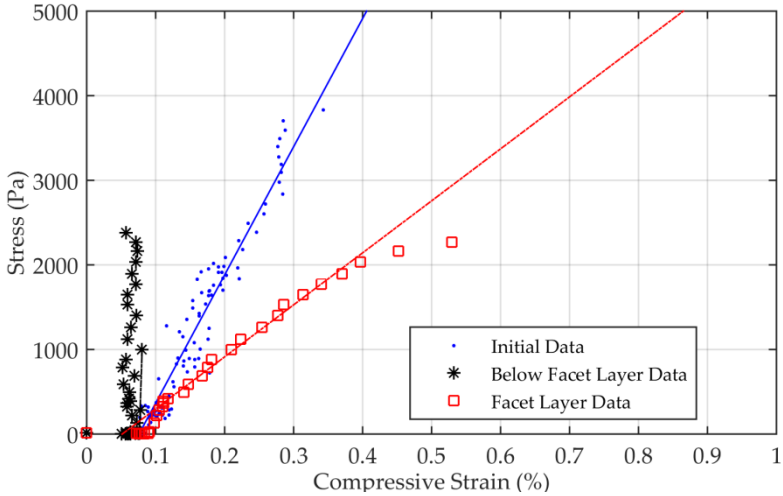


Figure D-9: Compressive stress and strain from the physical compression test of sample NS3. Includes data from the initial snow sample prior to recrystallization (blue) and data post recrystallization within the faceted layer (red) and below the faceted layer (black). Best fit lines are plotted to compute the Young's modulus.

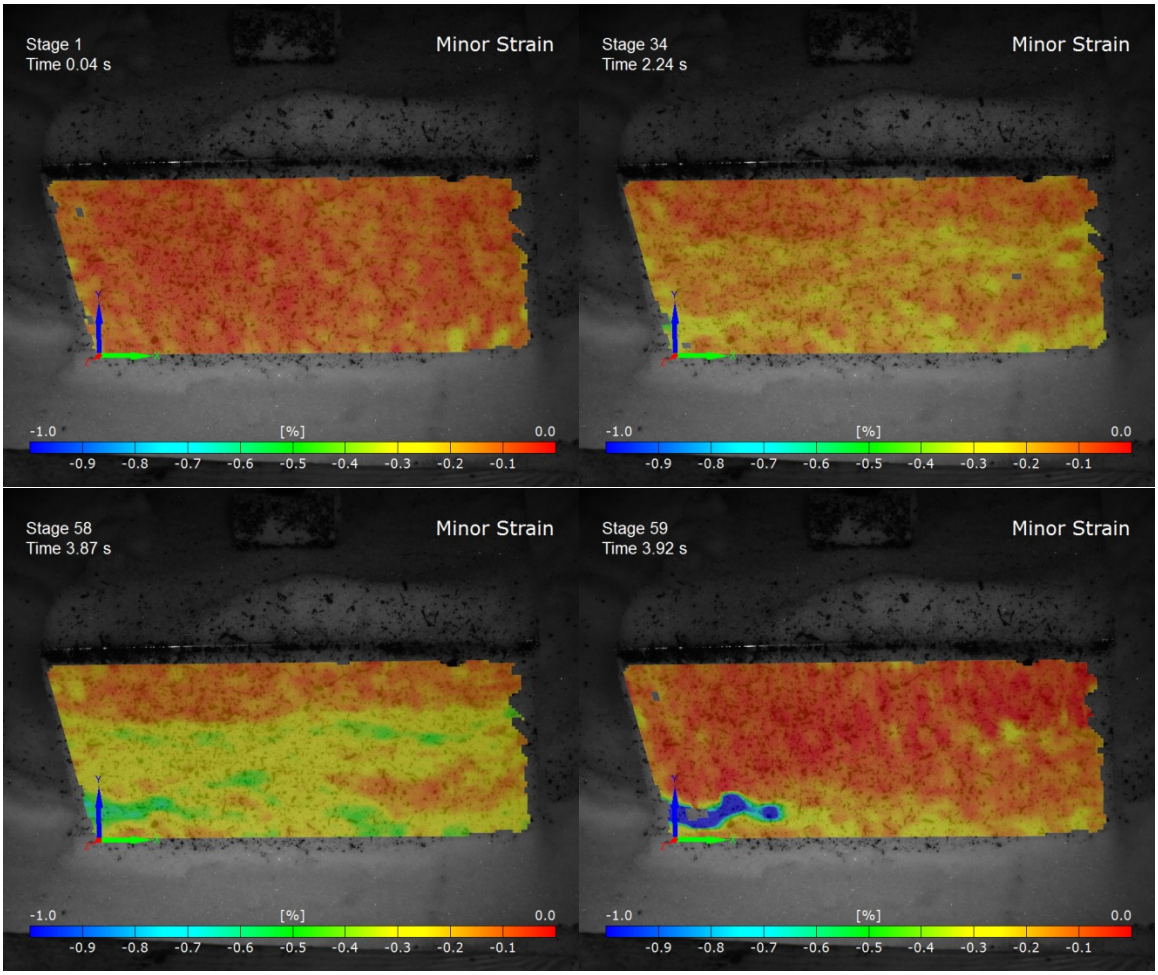


Figure D-10: Sequence of minor strain contours on sample NS3 of the initial non-recrystallized sample showing development of mostly uniform minor strain. Minor strain is the minimum principal value of strain. In these images, the minor strain directions are oriented vertically (blue y-axis in the images). Samples are loaded in compression from top to bottom. The final image (Stage 59) is after failure of the sample has occurred. The failure plane was non-planar and only manifested in measurable minor strain on a small portion of the exposed column. Elastic strain recovery is exhibited in other portions of the sample.

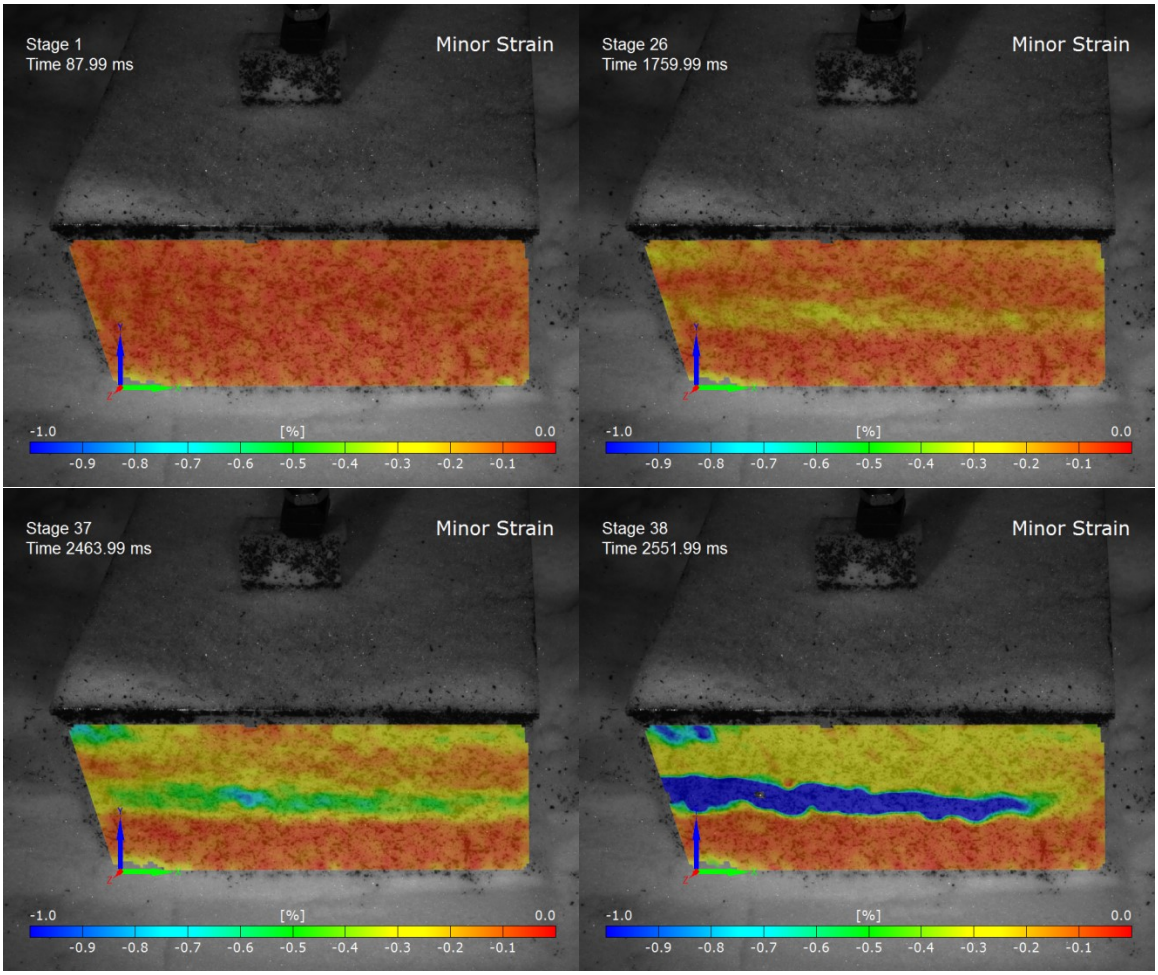


Figure D-11: Sequence of minor strain contours on sample NS3 of the radiation recrystallized sample showing development of minor strain in a localized region coincident with the faceted layer. Minor strain is the minimum principal value of strain. In these images, the minor strain directions are oriented vertically in areas of non-zero strain (blue y-axis in the images). Samples are loaded in compression from top to bottom. The final image (Stage 38) is after failure of the sample has occurred. The failure plane was planar and eventually propagated across the entire faceted layer.

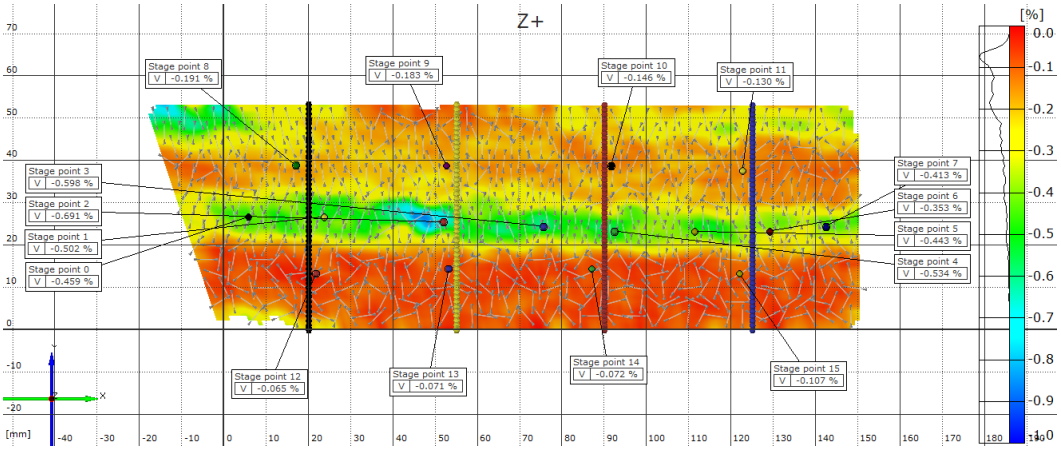


Figure D-12: Stage point locations used to query and average strain in regions of interest of sample NS3. Eight points (Stage point 0 through Stage point 7) are positioned within the faceted layer. Four points (Stage point 12 through Stage point 15) are positioned below the faceted layer.

D.4 1 Week Old 1 (1W1) Mechanical Shear Test Results

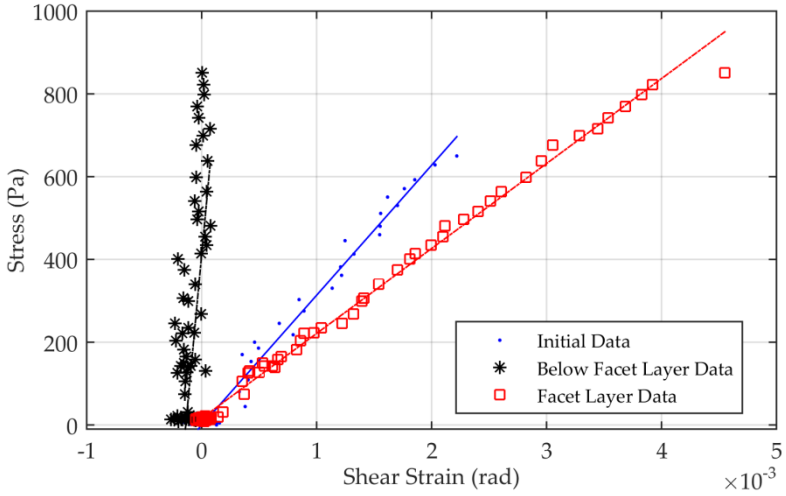


Figure D-13: Shear stress and strain from the physical shear test of sample 1W1. Includes data from the initial snow sample prior to recrystallization (blue) and data post recrystallization within the faceted layer (red) and below the faceted layer (black). Best fit lines are plotted to compute the shear modulus.

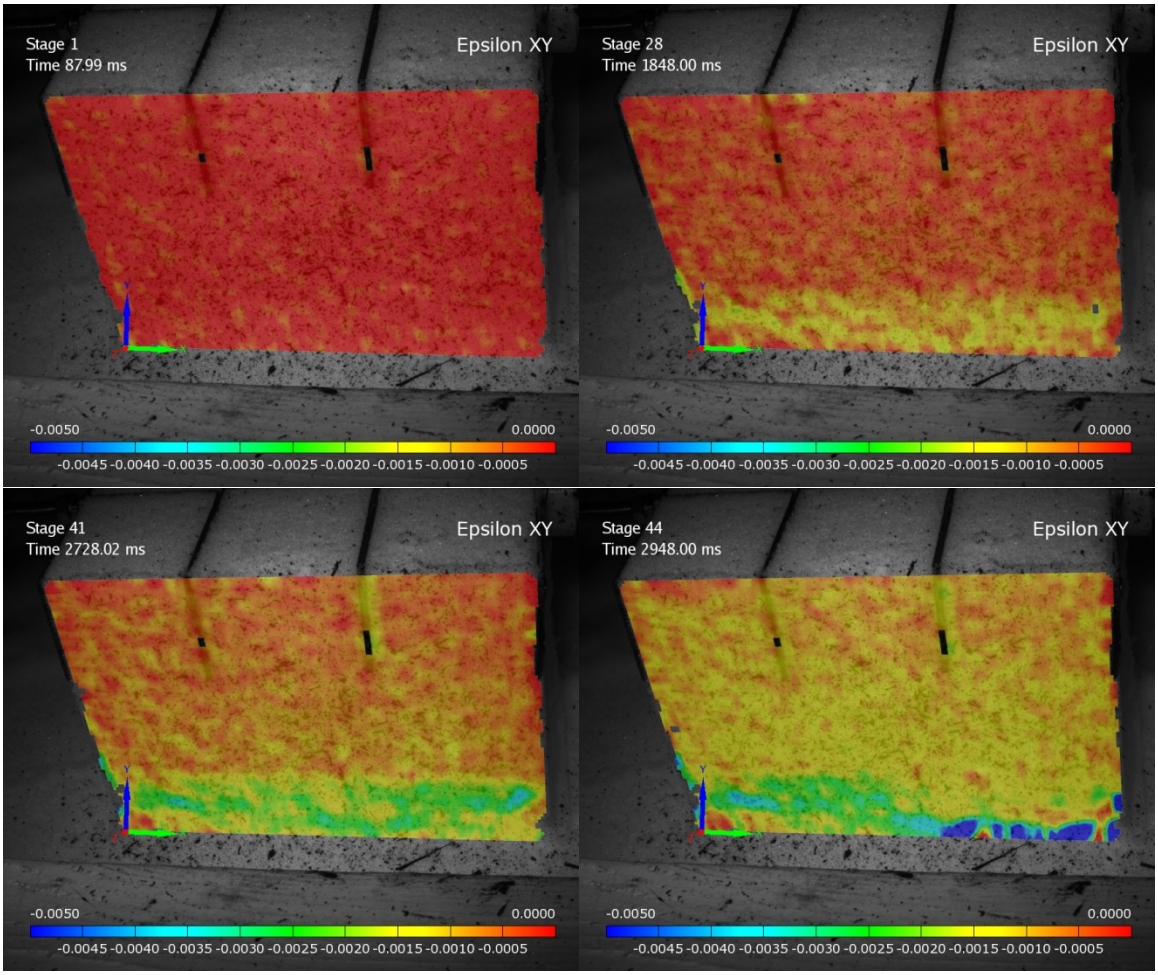


Figure D-14: Sequence of shear strain contours on sample 1W1 of the initial non-recrystallized sample showing development of differing levels shear strain in the 1 week old snow (lower region with increased strain) and the new snow burying it (upper two thirds of the contours). Samples are loaded from right to left. The final image (Stage 44) is after failure of the sample has occurred. Failure of this sample occurred within the 1 week old snow approximately 2 cm below the old snow/new snow interface.

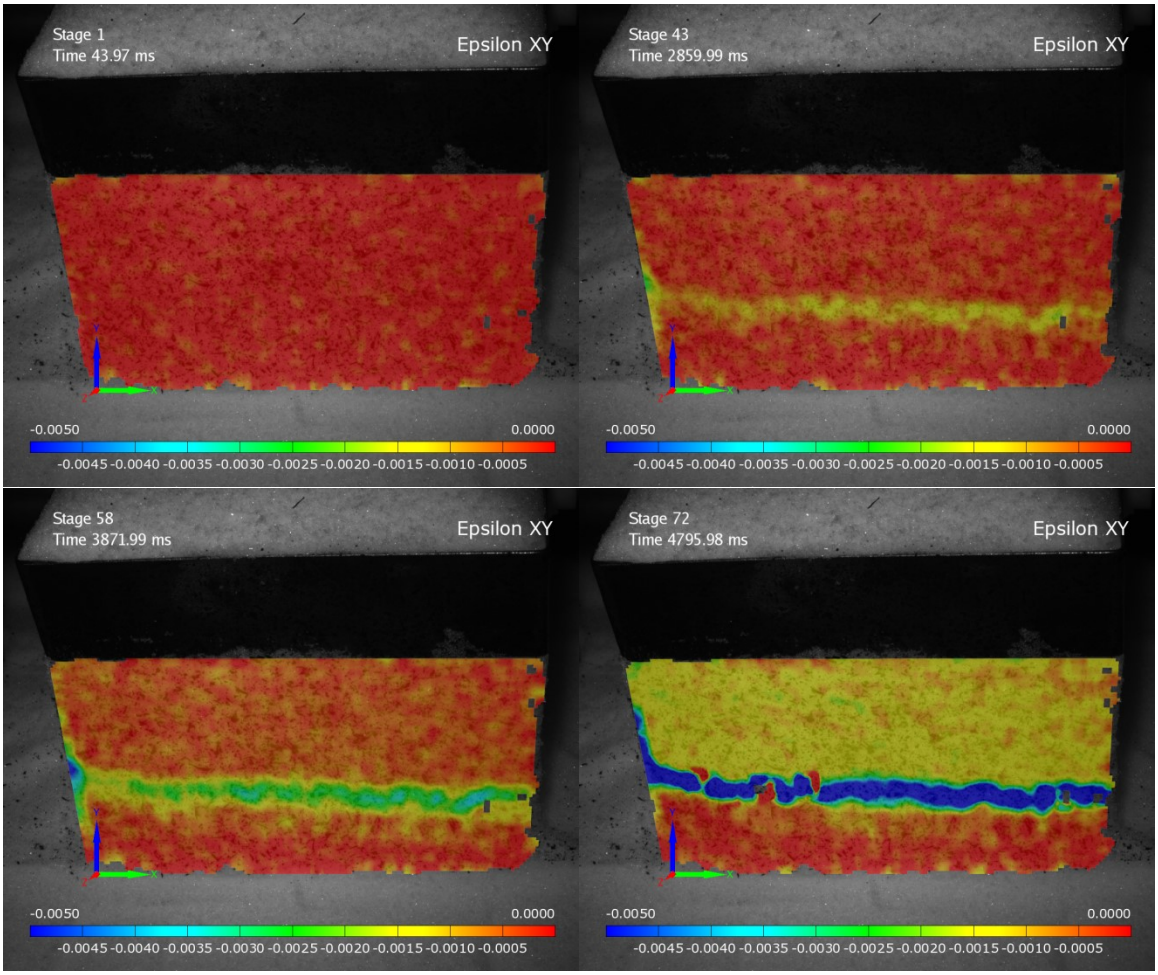


Figure D-15: Sequence of shear strain contours on sample 1W1 of the radiation recrystallized sample showing development of localized shear strain in the faceted layer. Samples are loaded from right to left. The final image (Stage 72) is after failure of the sample has occurred. Failure occurred along the plane defined by the area of increased shear strain. After separation, the upper slab seemed to get stuck and begin exhibiting increased uniform shear strain as the load actuator continued to push on the sample.

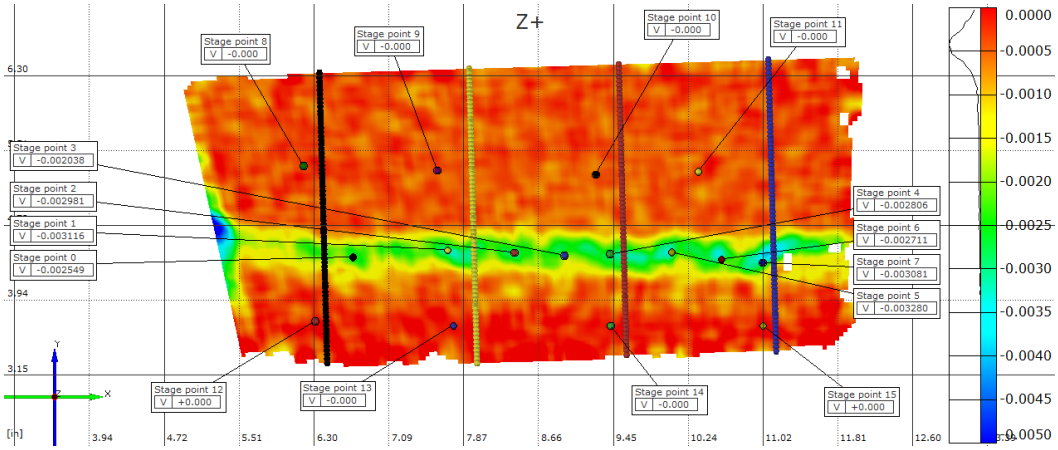


Figure D-16: Stage point locations used to query and average strain in regions of interest of sample 1W1. Eight points (Stage point 0 through Stage point 7) are positioned within the faceted layer. Four points (Stage point 12 through Stage point 15) are positioned below the faceted layer.

D.5 1 Week Old 2 (1W2) Mechanical Shear Test Results

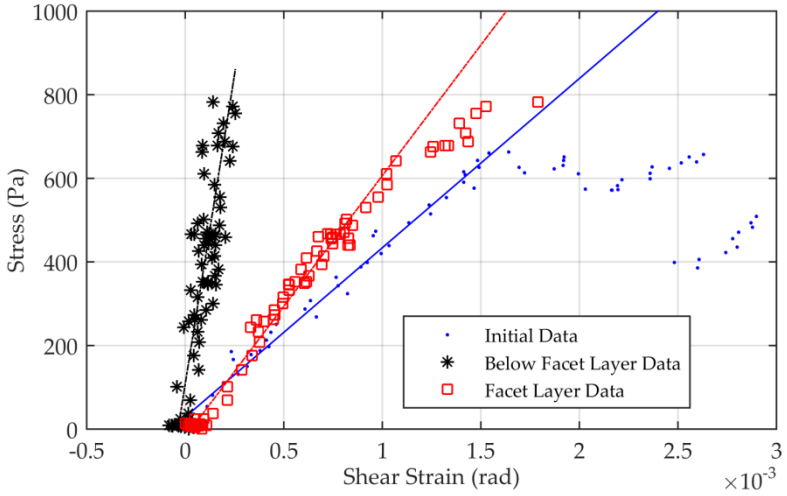


Figure D-17: Shear stress and strain from the physical shear test of sample 1W2. Includes data from the initial snow sample prior to recrystallization (blue) and data post recrystallization within the faceted layer (red) and below the faceted layer (black). Best fit lines are plotted to compute the shear modulus.

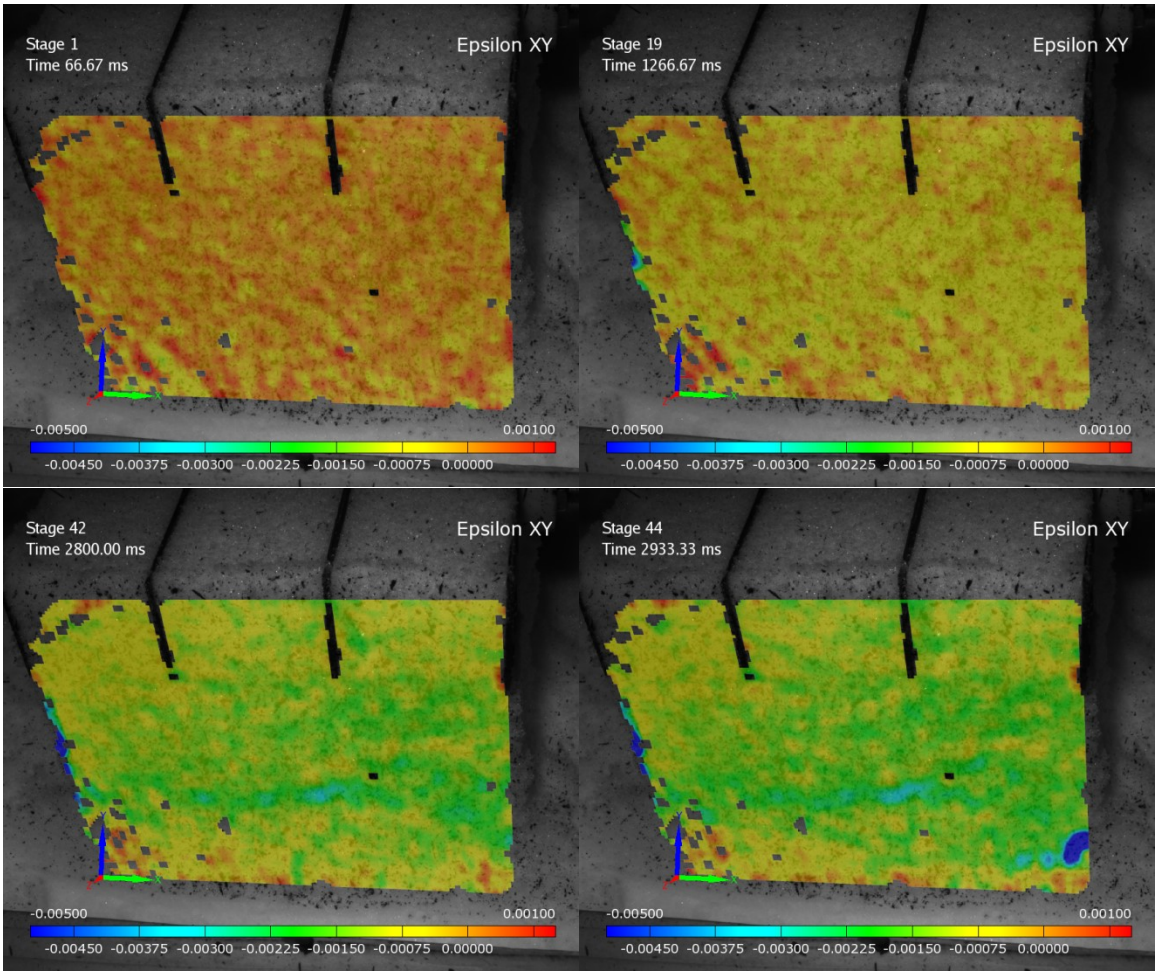


Figure D-18: Sequence of shear strain contours on sample 1W1 of the initial non-recrystallized sample showing development uniform levels shear strain. No discernable region in strain marks the interface between old snow and new snow. Samples are loaded from right to left. The final image (Stage 44) is after failure of the sample has occurred. Failure occurred at the base of the sample with the opening of a tensile crack in the lower right portion of the sample, similar to all other non-recrystallized shear tests.

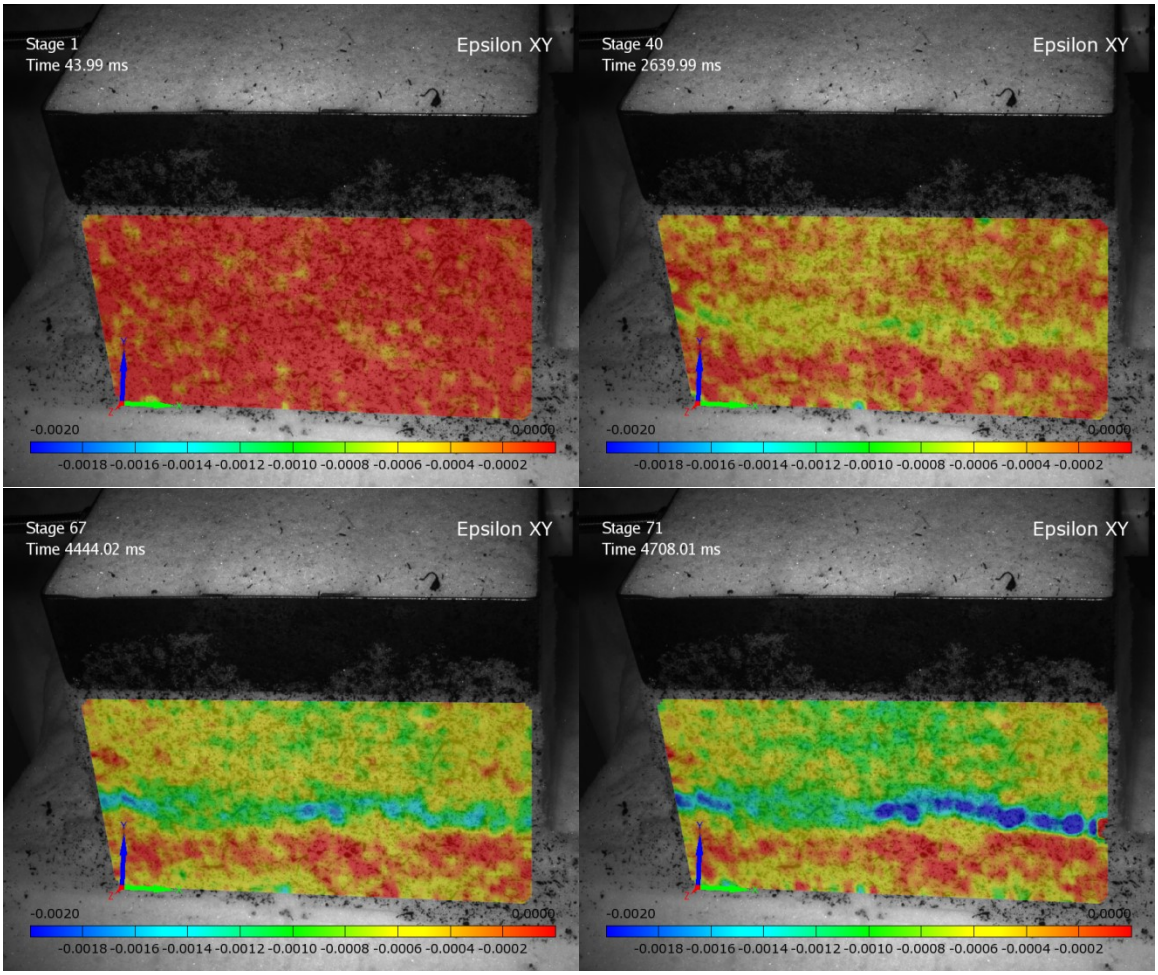


Figure D-19: Sequence of shear strain contours on sample 1W2 of the radiation recrystallized sample showing development of localized shear strain in the faceted layer. Samples are loaded from right to left. The final image (Stage 71) is after failure of the sample has occurred. Failure occurred along the plane defined by the area of increased shear strain.

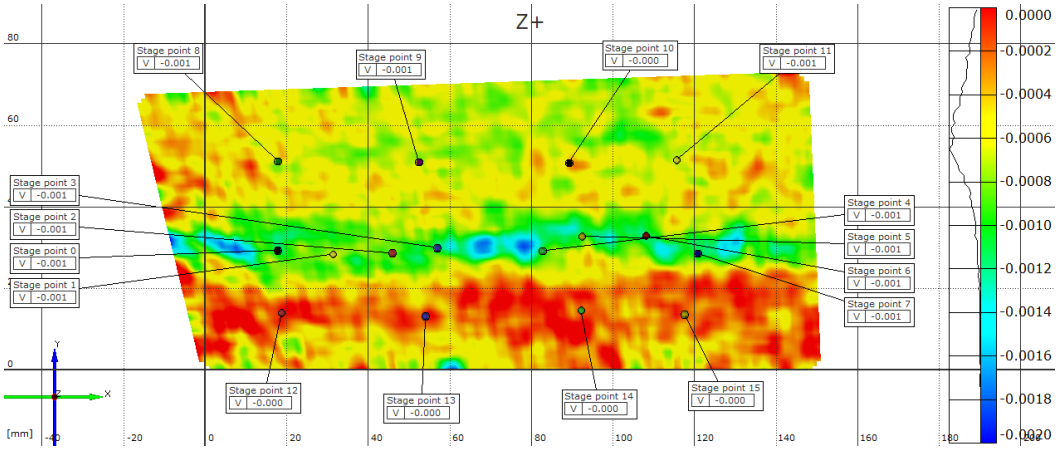


Figure D-20: Stage point locations used to query and average strain in regions of interest of sample 1W2. Eight points (Stage point 0 through Stage point 7) are positioned within the faceted layer. Four points (Stage point 12 through Stage point 15) are positioned below the faceted layer.

D.6 1 Week Old 3 (1W3) Mechanical Compression Test Results

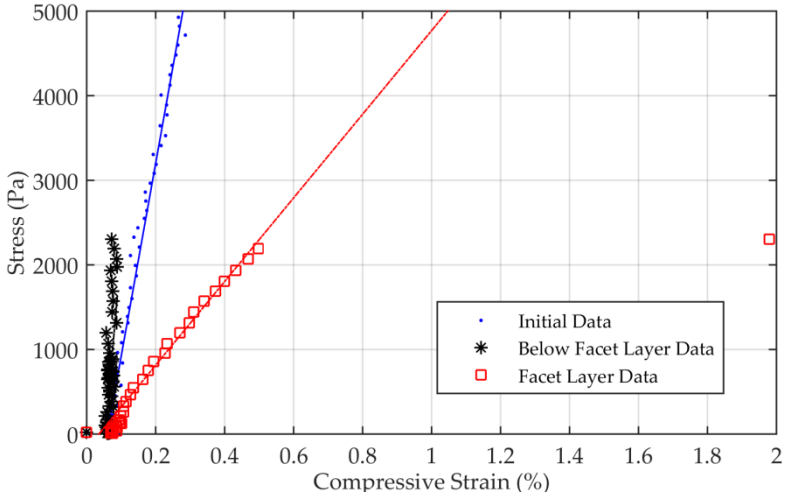


Figure D-21: Compressive stress and strain from the physical compression test of sample 1W3. Includes data from the initial snow sample before recrystallization (blue) and data post recrystallization within the faceted layer (red) and below the faceted layer (black). Best fit lines are plotted to compute Young's modulus.

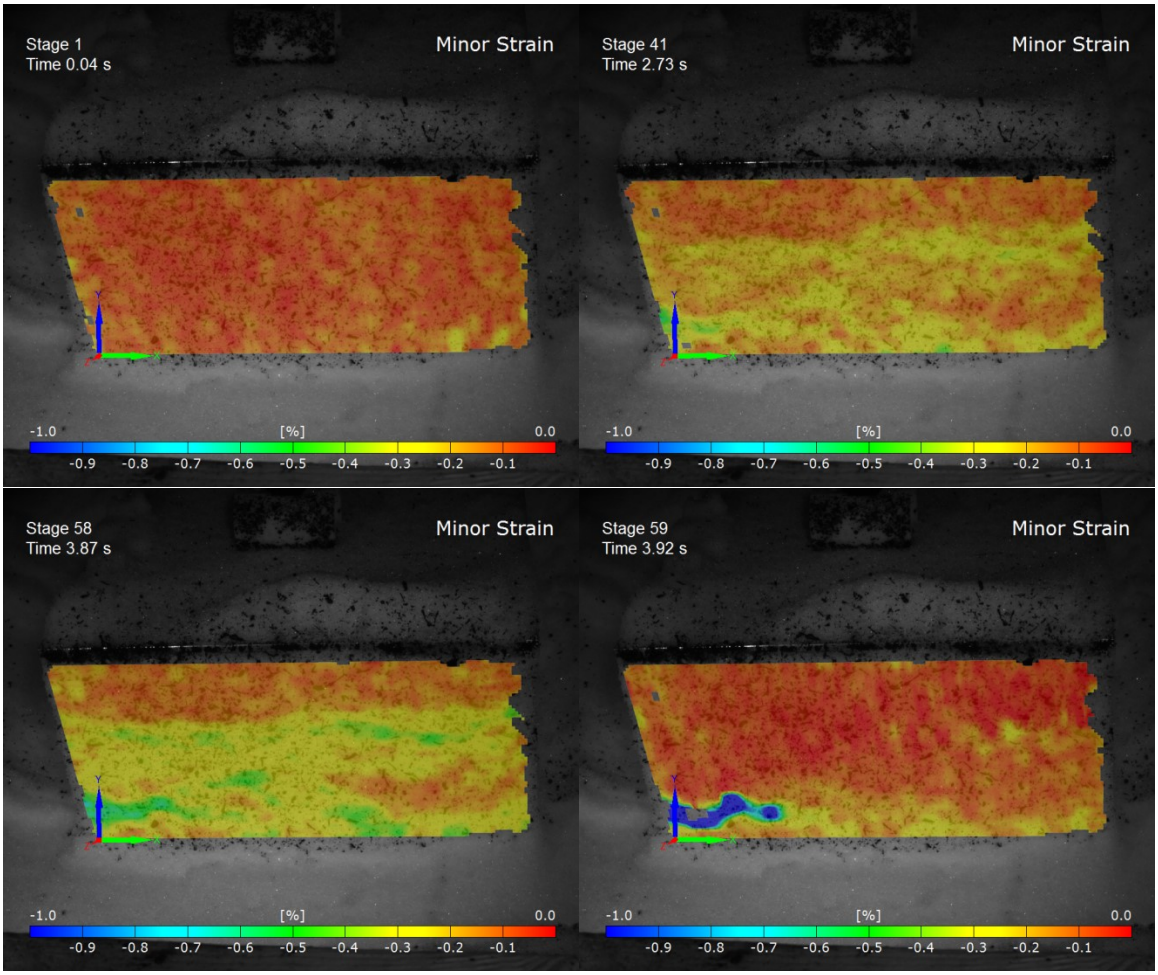


Figure D-22: Sequence of minor strain contours on sample 1W3 of the initial non-recrystallized sample showing development of differing levels shear strain in the 1 week old snow (lower region with increased strain) and the new snow burying it (upper region of the contours). Minor strain is the minimum principal value of strain. In these images, the minor strain directions are oriented vertically (blue y-axis in the images). Samples are loaded in compression from top to bottom. The final image (Stage 59) is after failure of the sample has occurred. Failure of this sample occurred within the 1 week old snow approximately 3 cm below the old snow/new snow interface. The failure plane was non-planar and only manifested in measurable minor strain on a small portion of the exposed column. Elastic strain recovery is exhibited in other portions of the sample.

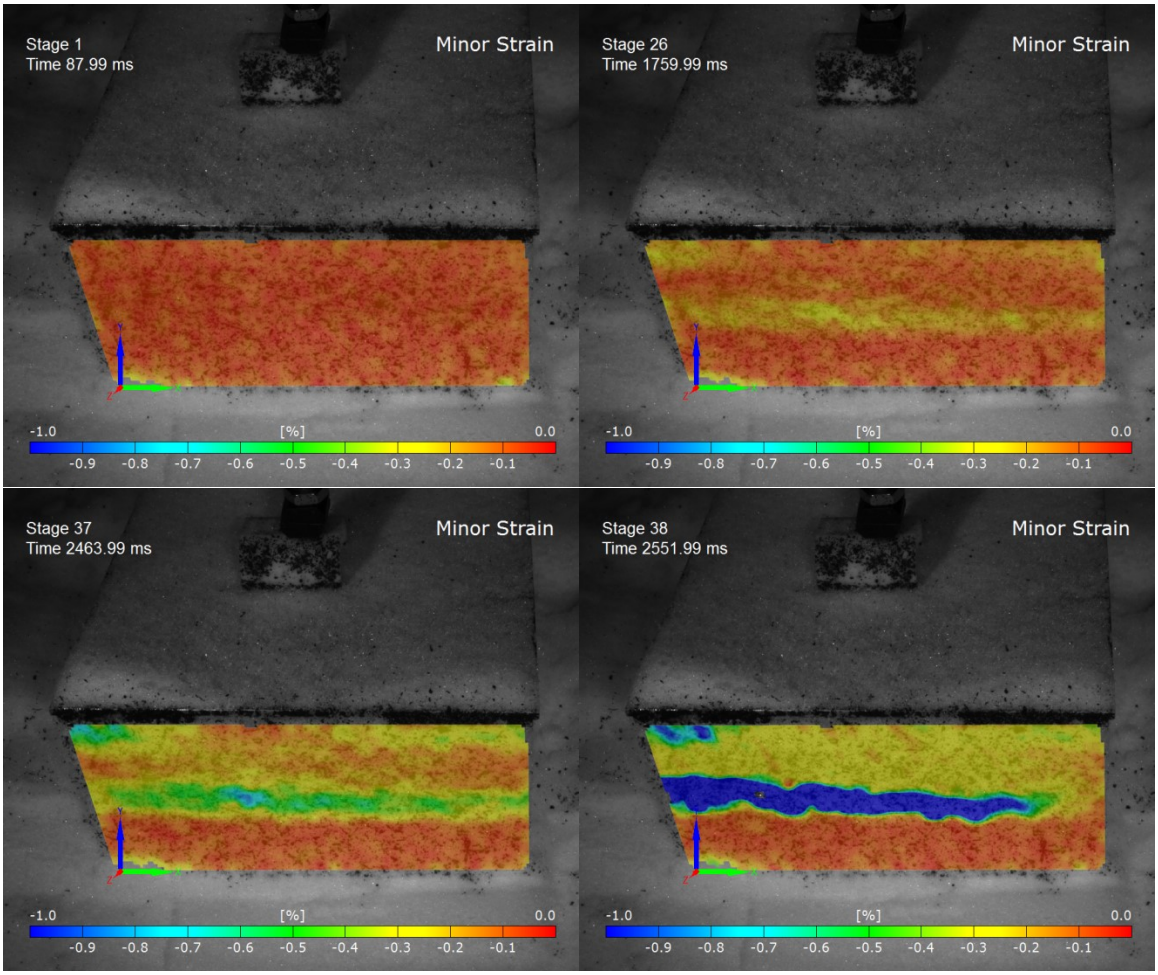


Figure D-23: Sequence of minor strain contours on sample 1W3 of the radiation recrystallized sample showing development of minor strain in a localized region coincident with the faceted layer. Minor strain is the minimum principal value of strain. In these images, the minor strain directions are oriented vertically in areas of non-zero strain (blue y-axis in the images). Samples are loaded in compression from top to bottom. The final image (Stage 38) is after failure of the sample has occurred. The failure plane was planar and eventually propagated across the entire faceted layer.

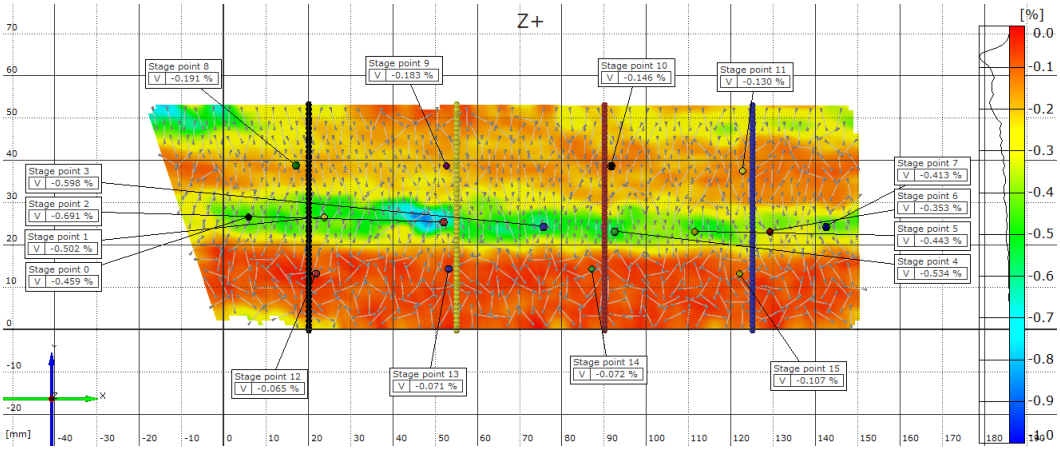


Figure D-24: Stage point locations used to query and average strain in regions of interest of sample 1W3. Eight points (Stage point 0 through Stage point 7) are positioned within the faceted layer. Four points (Stage point 12 through Stage point 15) are positioned below the faceted layer.

D.7 2 Weeks Old 1 (2W1) Mechanical Shear Test Results

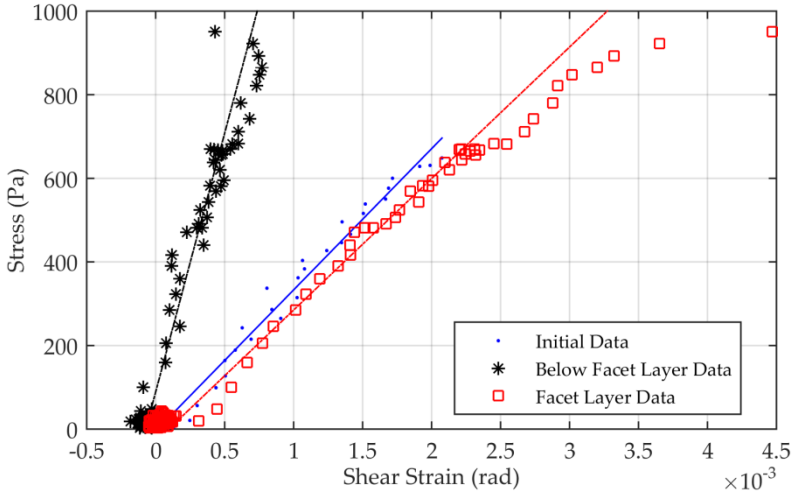


Figure D-25: Shear stress and strain from the physical shear test of sample 2W1. Includes data from the initial snow sample prior to recrystallization (blue) and data post recrystallization within the faceted layer (red) and below the faceted layer (black). Best fit lines are plotted to compute shear modulus.

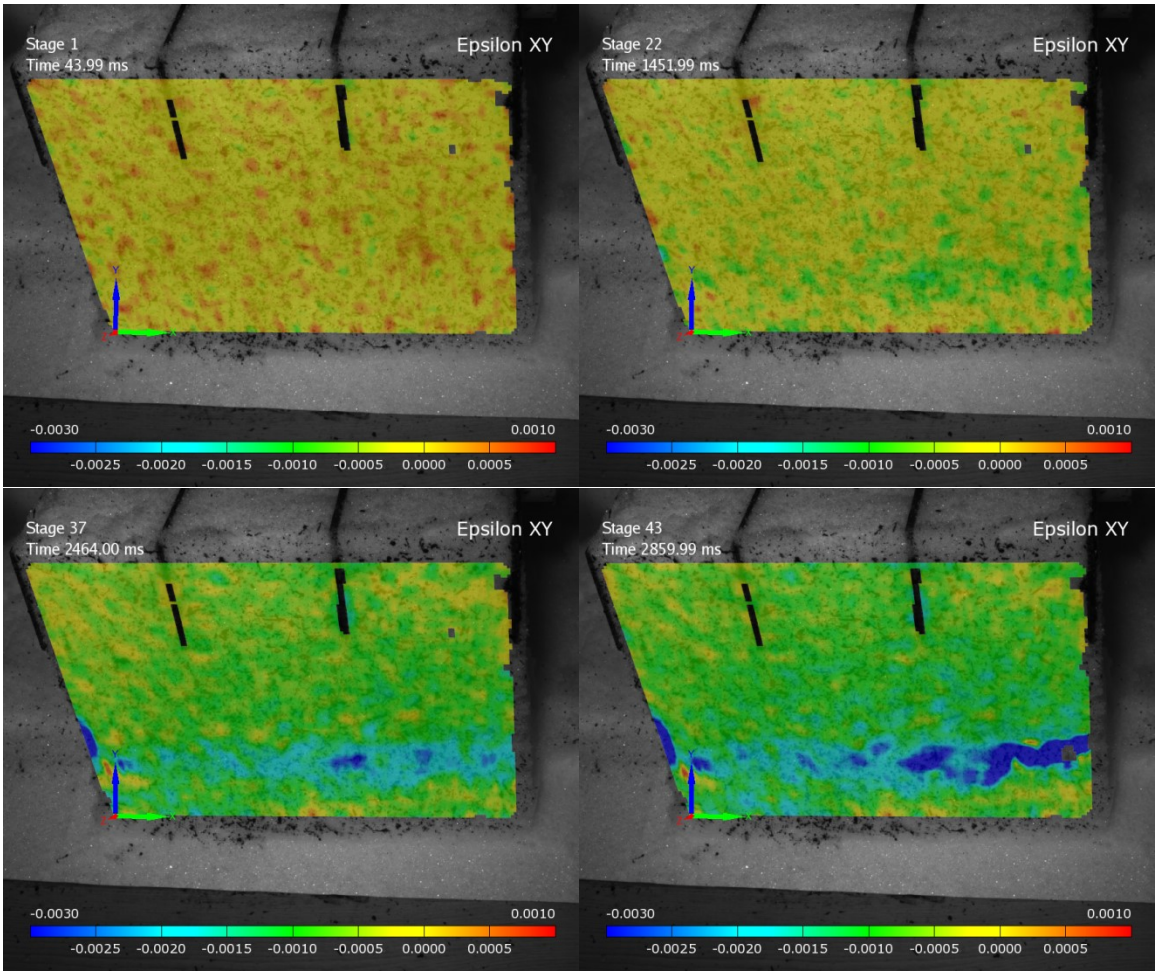


Figure D-26: Sequence of shear strain contours on sample 2W1 of the initial non-recrystallized sample showing development of differing levels shear strain in the 2 weeks old snow (lower region with increased strain) and the new snow burying it (upper two thirds of the contours). Concentration of strain occurs just below the new snow/old snow interface. Samples are loaded from right to left. The final image (Stage 43) is after failure of the sample has occurred. Failure of this sample occurred within the 2 weeks old snow approximately 1 cm below the old snow/new snow interface.

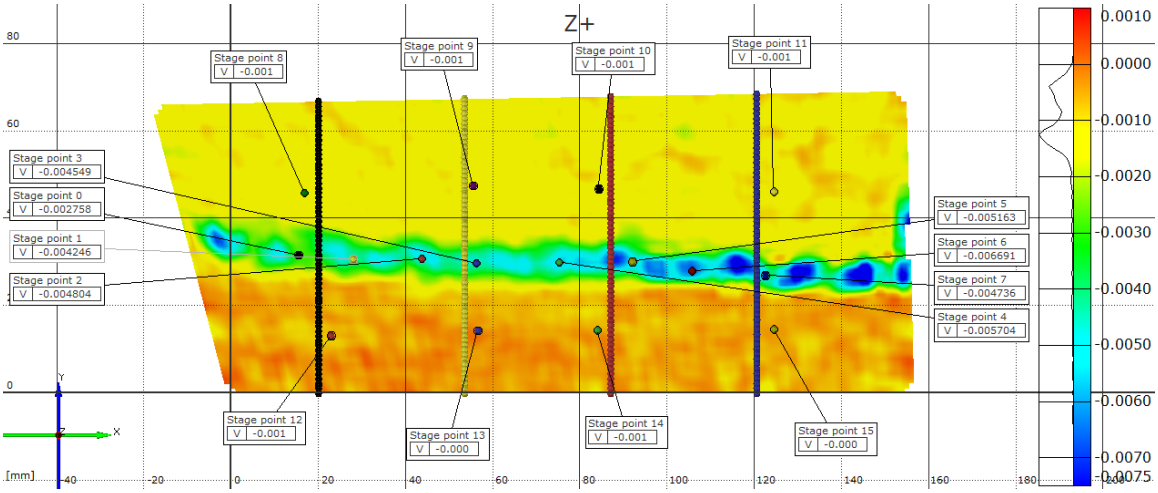


Figure D-27: Stage point locations used to query and average strain in regions of interest of sample 2W1. Eight points (Stage point 0 through Stage point 7) are positioned within the faceted layer. Four points (Stage point 12 through Stage point 15) are positioned below the faceted layer.

APPENDIX E

FABRIC TENSOR RESULTS

Computing effective stiffness properties using a homogenization approach relies on capturing and analyzing the snow's microstructure. Computing anisotropy of the material stiffness parameters requires measures of the materials' microstructural texture. The contact tensor mathematically describes the average orientations of the bond planes (contact planes) in a volume of snow. Independent of the contact tensor is the MIL tensor. The MIL tensor describes the overall geometric orientation of the material within a volume of snow. The tensor ratio is a numerical directional factor which combines the effects of both the contact tensor and the MIL tensor. All of these terms are described in Chapter Four and Chapter Five.

In order to fully assess the effective mechanical stiffness coefficients, scalar data representing the volume fraction, grain connectivity, grain size and shape, and bond size. All of these factors, directional and scalar, are evaluated at approximately 3 hour intervals using microstructural volumes collected during metamorphism of radiation recrystallized facets. These samples are scanned using micro Computed Tomography. The resulting 3-D data is processed and analyzed using procedures previously documented.

What follows are the analytical of each experimental sample to undergo radiation recrystallization. Representative volumes are analyzed in 2 different

spatial locations at each 3 hour interval: one coincident with the location of facet crystal growth, and the other in a region where grain become rounded and sinter into a cohesive layer. Detailed analyses of select samples are detailed in Chapter Nine. The raw data is presented here.

As a reminder, the scalar properties are computed using (3.21) and the directional properties are computed using relationships developed in Chapter Four and Chapter Five.

E.1 Fabric Tensor Results for Sample New Snow 1 (NS1)

E.1.1 Faceted Layer Results

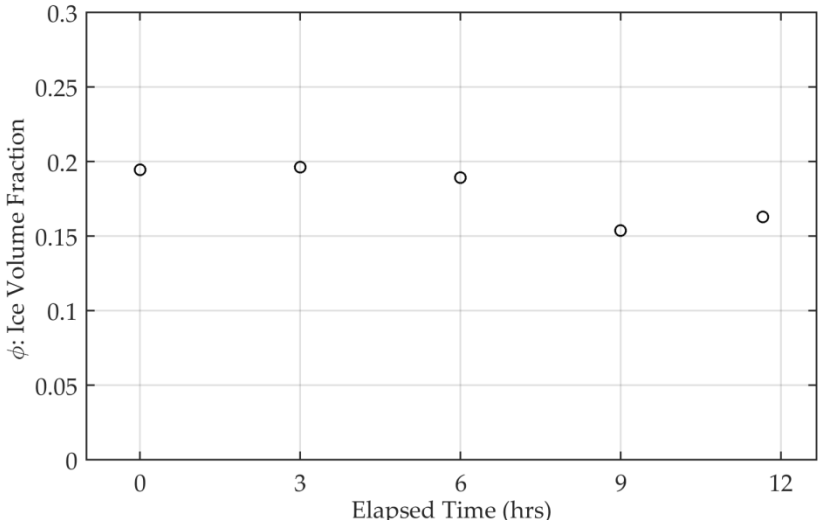


Figure E-1: Changes in volume fraction, ϕ, in the top 7.00 mm of sample NS1 associated with the faceted layer during the process of radiation recrystallization.

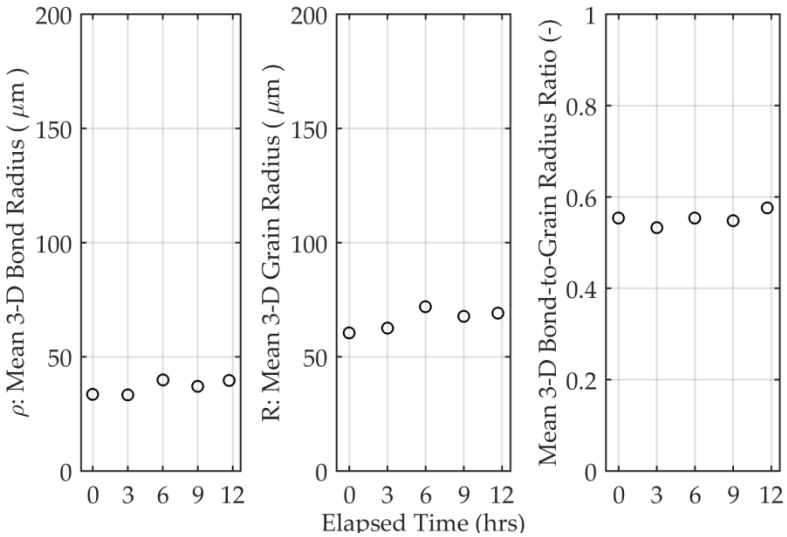


Figure E-2: Changes in mean bond radius, $\hat{\rho}$, and grain radius, $\hat{R}$, in the top 7.00 mm of sample NS1 associated with the faceted layer during the process of radiation recrystallization.

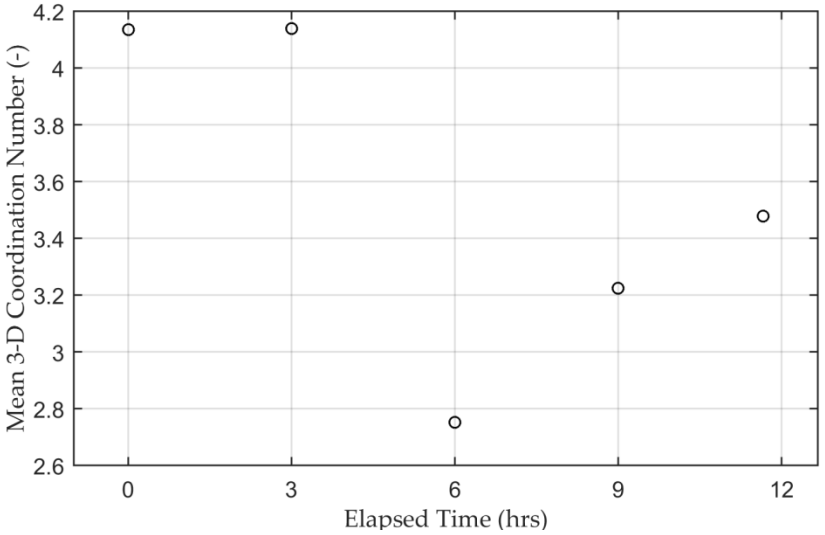


Figure E-3: Changes in mean 3-D coordination number, $\mathcal{N}$, in the top 7.00 mm of sample NS1 associated with the faceted layer during the process of radiation recrystallization.

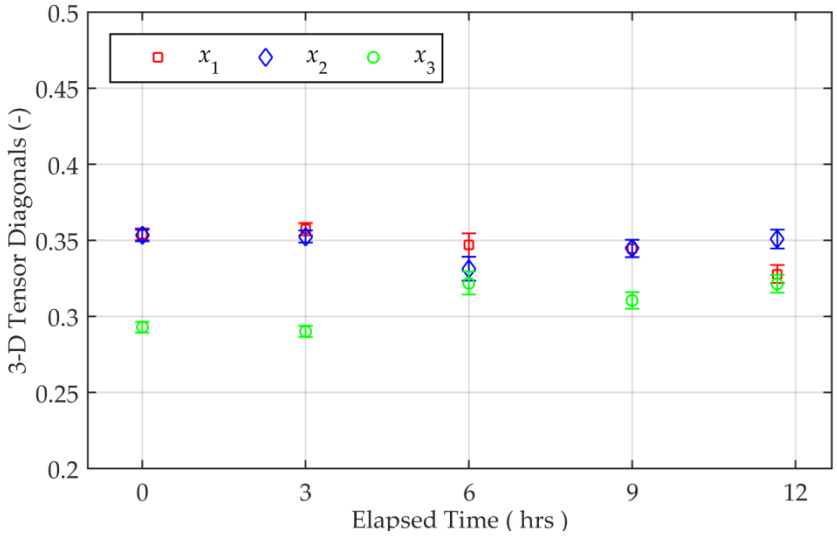


Figure E-4: Changes to the contact tensor diagonal coefficients aligned with the snow's coordinate system (x_3 is vertical, normal to the snow surface) in the top 7.00 mm of sample NS1 associated with the faceted layer during the process of radiation recrystallization.

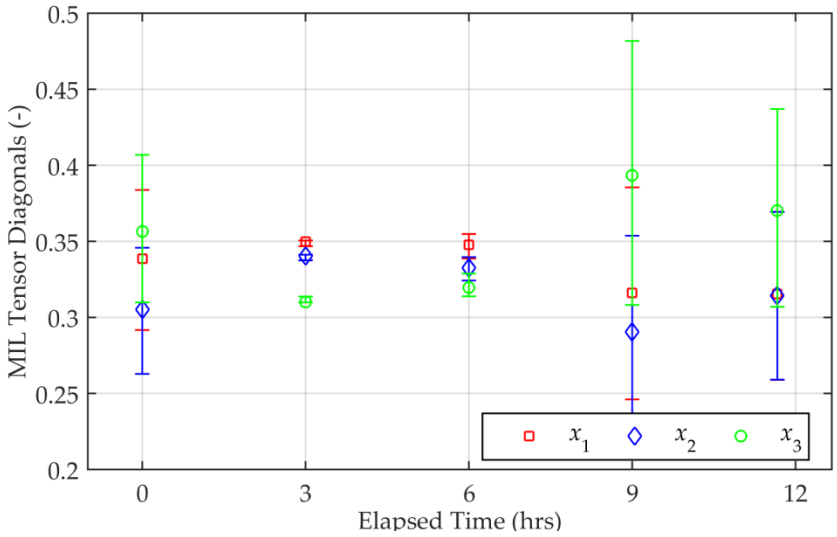


Figure E-5: Changes to the MIL tensor diagonal coefficients aligned with the snow's coordinate system (x_3 is vertical, normal to the snow surface) in the top 7.00 mm of sample NS1 associated with the faceted layer during the process of radiation recrystallization.

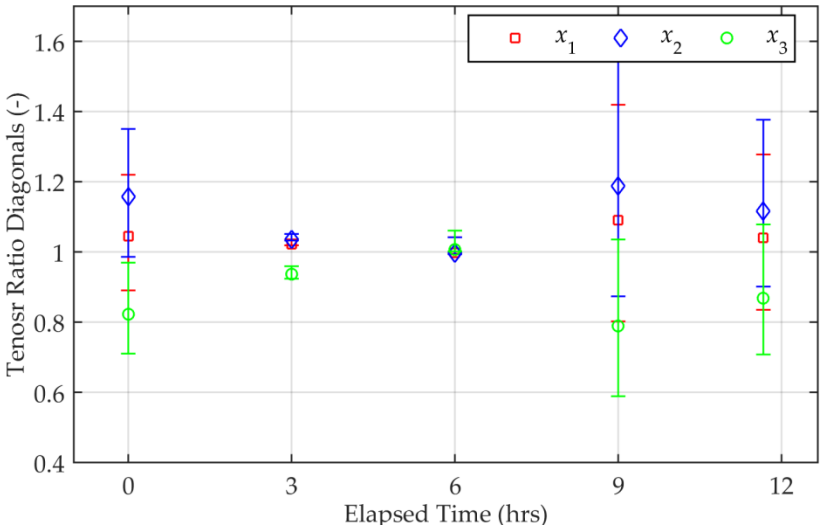


Figure E-6: Changes to the tensor ratio diagonal coefficients aligned with the snow's coordinate system (x_3 is vertical, normal to the snow surface) in the top 7.00 mm of sample NS1 associated with the faceted layer during the process of radiation recrystallization.

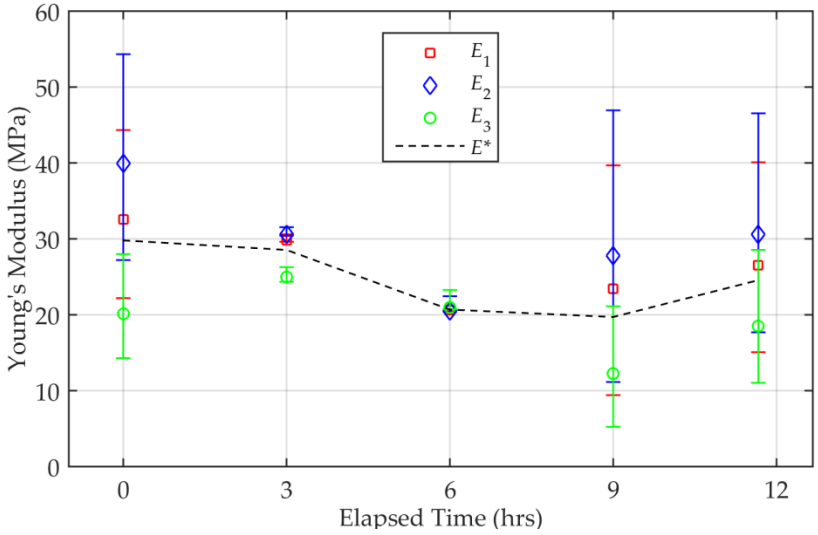


Figure E-7: Changes to the computed effective Young's moduli aligned with the snow's coordinate system in the top 7.00 mm of sample NS1 associated with the faceted layer during the process of radiation recrystallization. E^* represents the scalar computed effective Young's modulus.

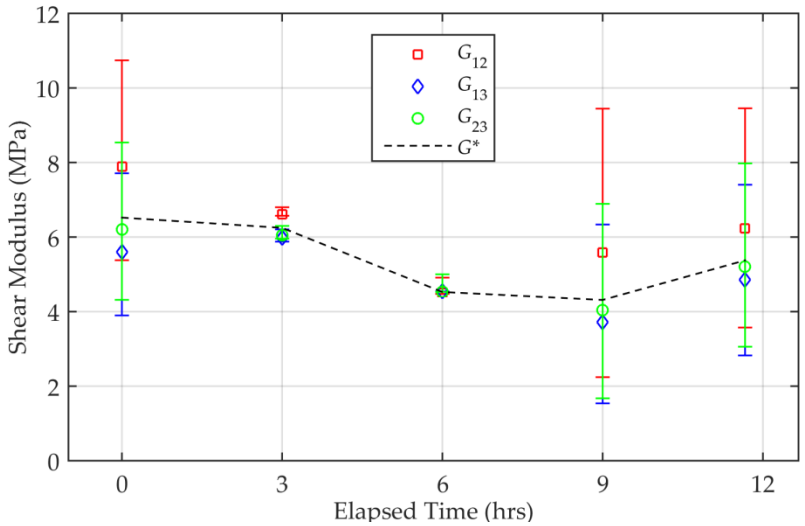


Figure E-8: Changes to the computed effective shear moduli aligned with the snow's coordinate system in the top 7.00 mm of sample NS1 associated with the faceted layer during the process of radiation recrystallization. G^* represents the scalar computed effective shear modulus.

E.1.2 Sub-Faceted Layer Results

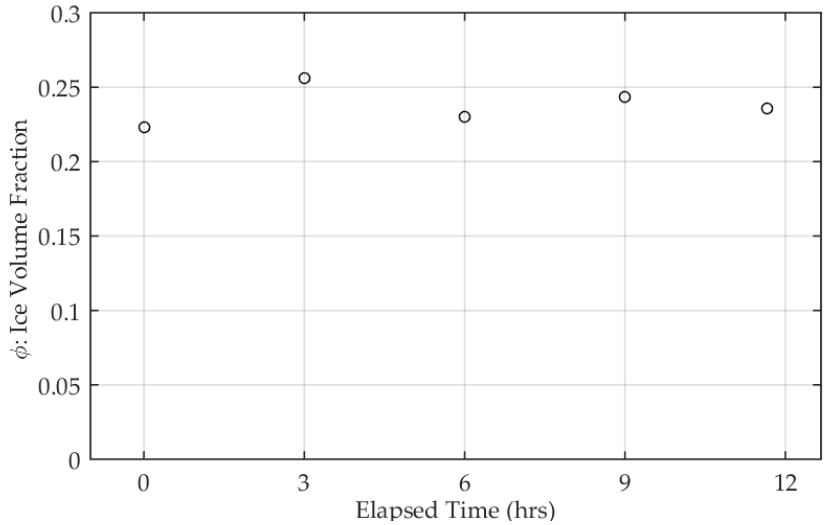


Figure E-9: Changes in volume fraction, ϕ, of sample NS1 associated with the layer below the faceted crystals during the process of radiation recrystallization.

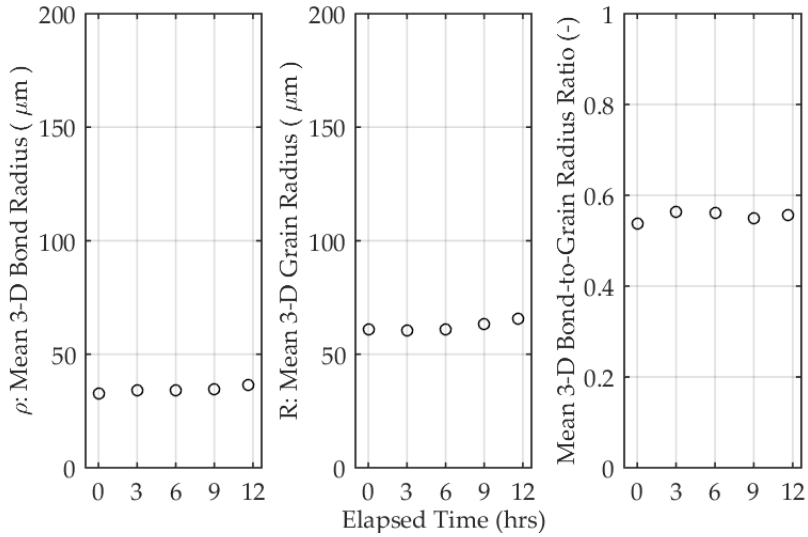


Figure E-10: Changes in mean bond radius, $\hat{\rho}$, and grain radius, $\hat{R}$, of sample NS1 associated layer below the faceted crystals during the process of radiation recrystallization.

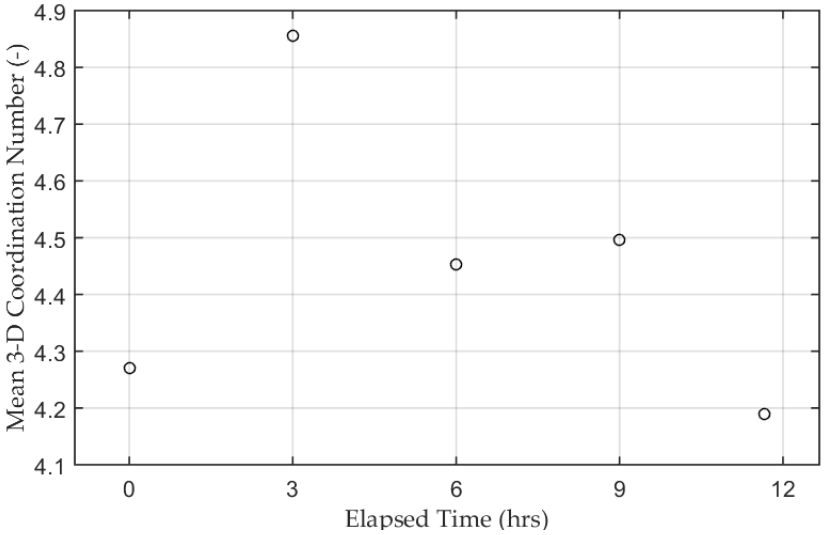


Figure E-11: Changes in mean 3-D coordination number, $\mathcal{N}$, of sample NS1 associated with the layer below the faceted crystals during the process of radiation recrystallization.

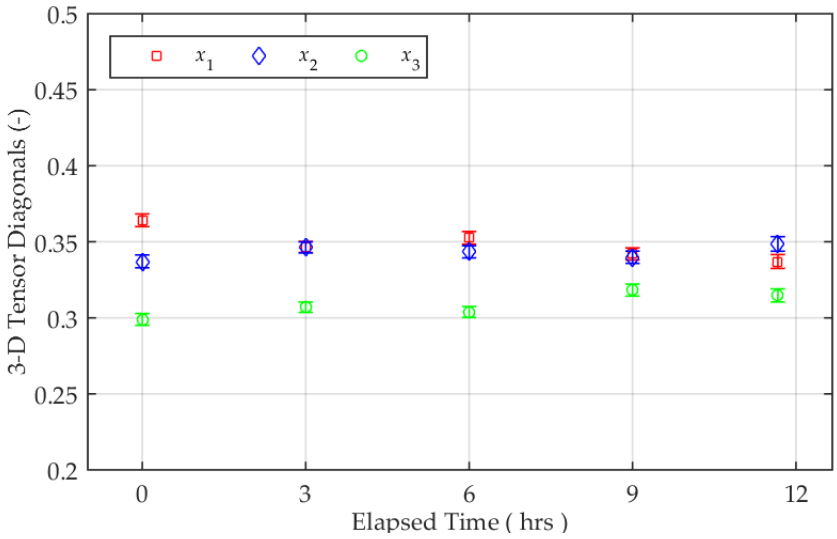


Figure E-12: Changes to the contact tensor diagonal coefficients aligned with the snow's coordinate system (x_3 is vertical, normal to the snow surface) of sample NS1 associated with the layer below the faceted crystals during the process of radiation recrystallization.

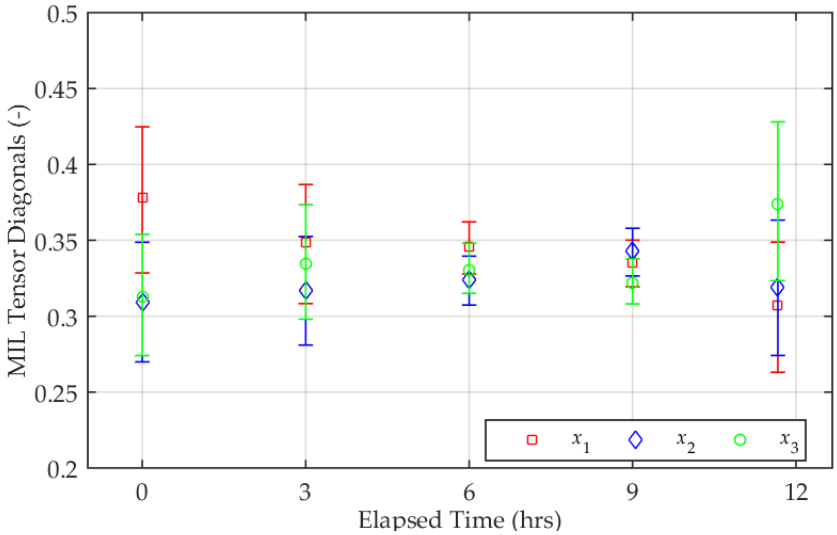


Figure E-13: Changes to the MIL tensor diagonal coefficients aligned with the snow's coordinate system (x_3 is vertical, normal to the snow surface) of sample NS1 associated with the layer below the faceted crystals during the process of radiation recrystallization.

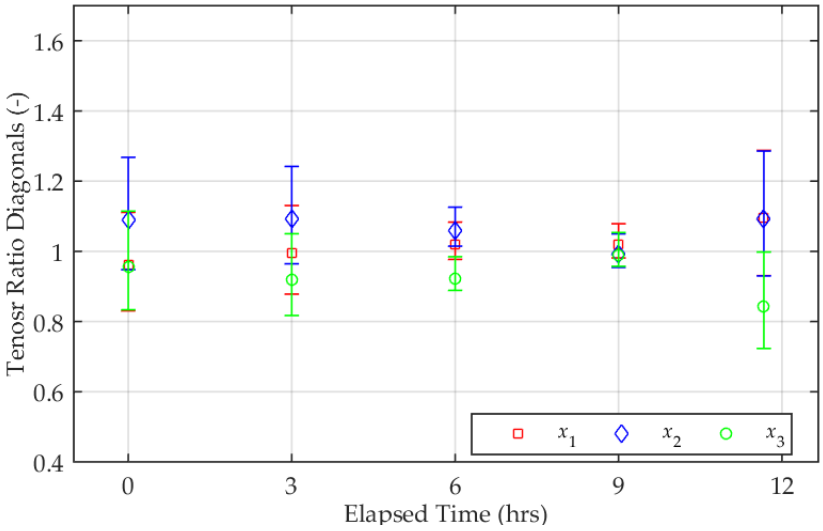


Figure E-14: Changes to the tensor ratio diagonal coefficients aligned with the snow's coordinate system (x_3 is vertical, normal to the snow surface) of sample NS1 associated with the layer below the faceted crystals during the process of radiation recrystallization.

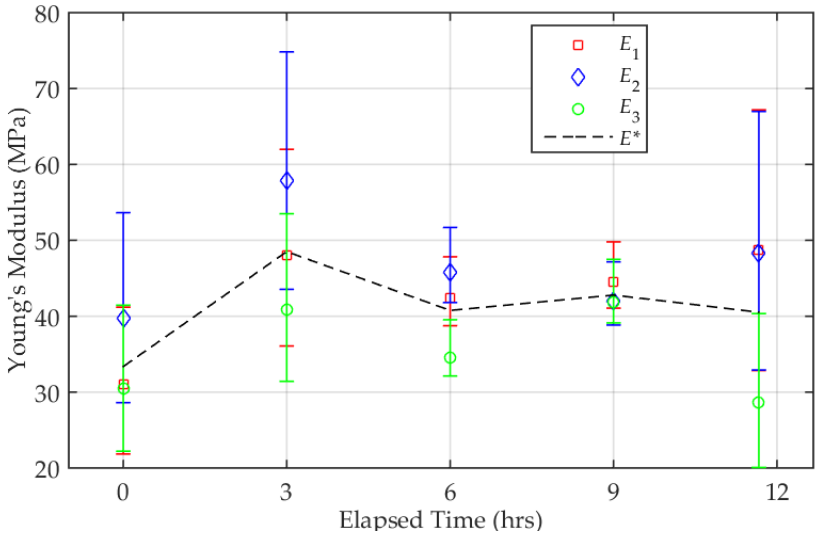


Figure E-15: Changes to the computed effective Young's moduli aligned with the snow's coordinate system of sample NS1 associated with the layer below the faceted crystals during the process of radiation recrystallization. E^* represents the scalar computed effective Young's modulus.

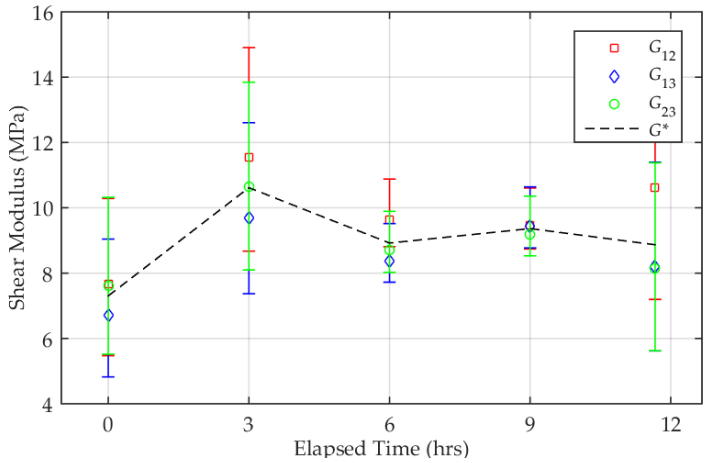


Figure E-16: Changes to the computed effective shear moduli aligned with the snow's coordinate system of sample NS1 associated with the layer below the faceted crystals during the process of radiation recrystallization. G^* represents the scalar computed effective shear modulus.

E.2 Fabric Tensor Results for Sample New Snow 2 (NS2)

E.2.1 Faceted Layer Results

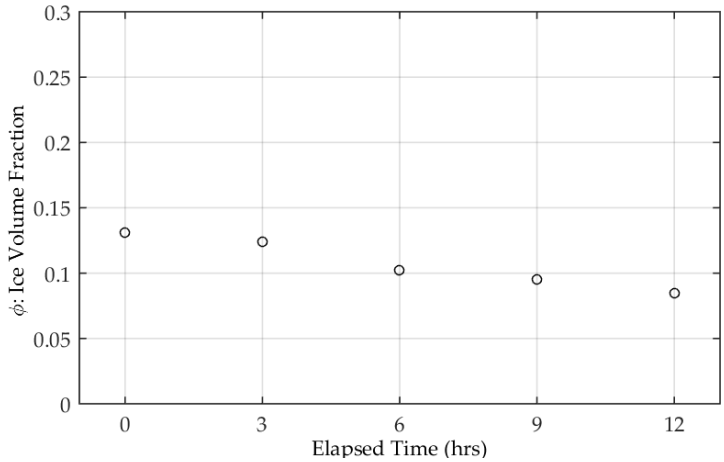


Figure E-17: Changes in volume fraction, ϕ, in the top 5.13 mm of sample NS2 associated with the faceted layer during the process of radiation recrystallization.

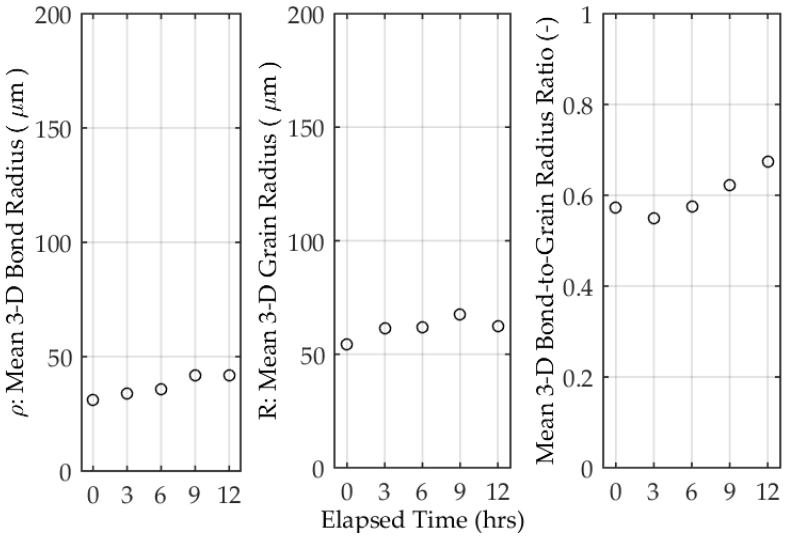


Figure E-18: Changes in mean bond radius, $\hat{\rho}$, and grain radius, $\hat{R}$, in the top 5.13 mm of sample NS2 associated with the faceted layer during the process of radiation recrystallization.

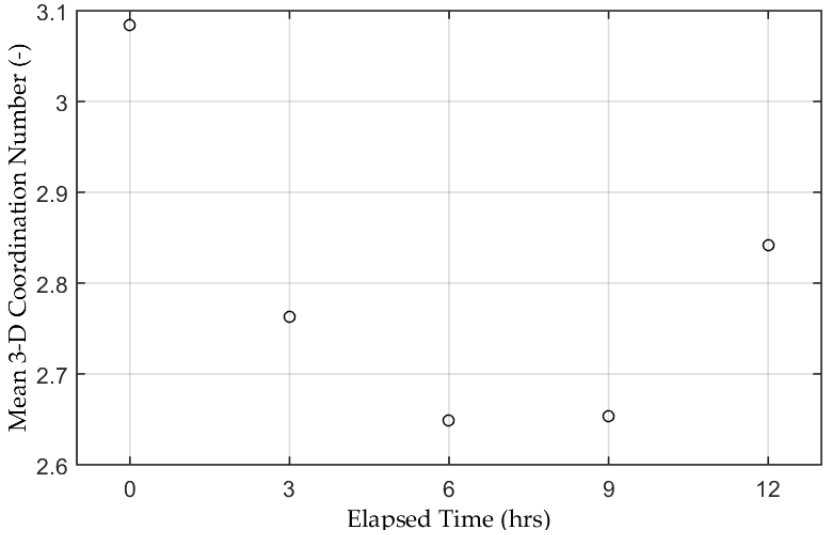


Figure E-19: Changes in mean 3-D coordination number, $\mathcal{N}$, in the top 5.13 mm of sample NS2 associated with the faceted layer during the process of radiation recrystallization.

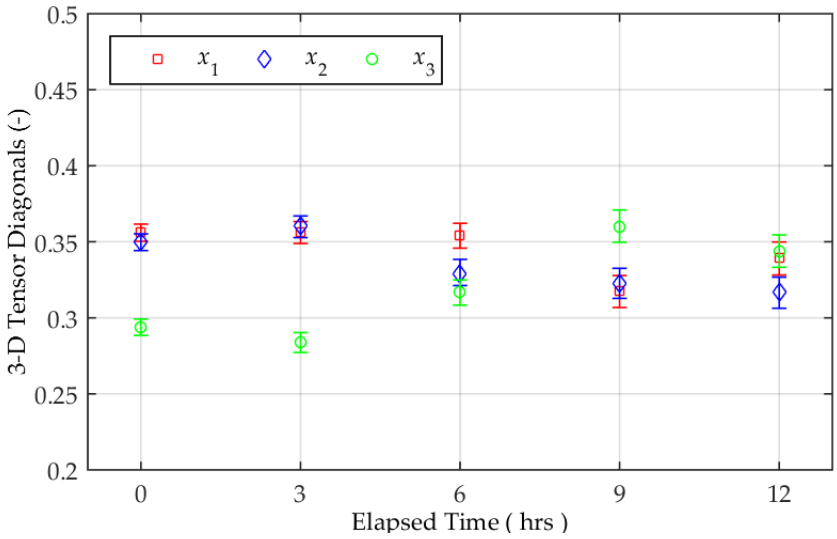


Figure E-20: Changes to the contact tensor diagonal coefficients aligned with the snow's coordinate system (x_3 is vertical, normal to the snow surface) in the top 5.13 mm of sample NS2 associated with the faceted layer during the process of radiation recrystallization.

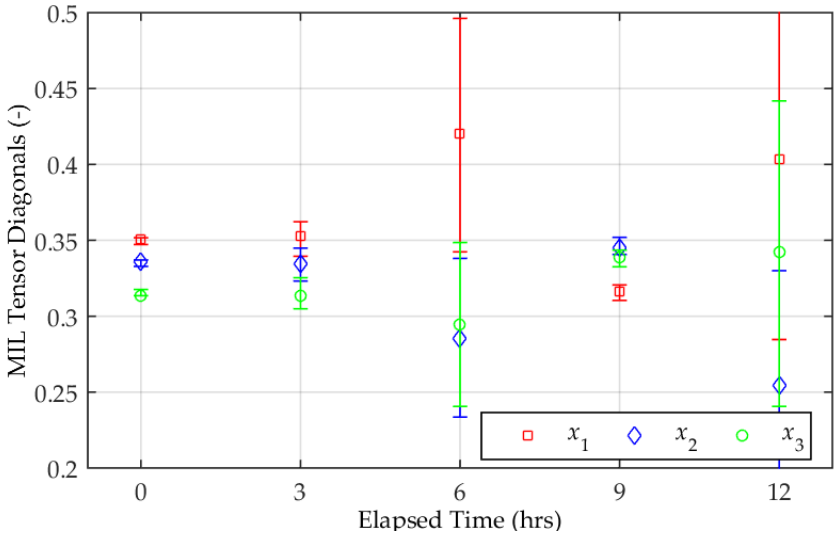


Figure E-21: Changes to the MIL tensor diagonal coefficients aligned with the snow's coordinate system (x_3 is vertical, normal to the snow surface) in the top 5.13 mm of sample NS2 associated with the faceted layer during the process of radiation recrystallization.

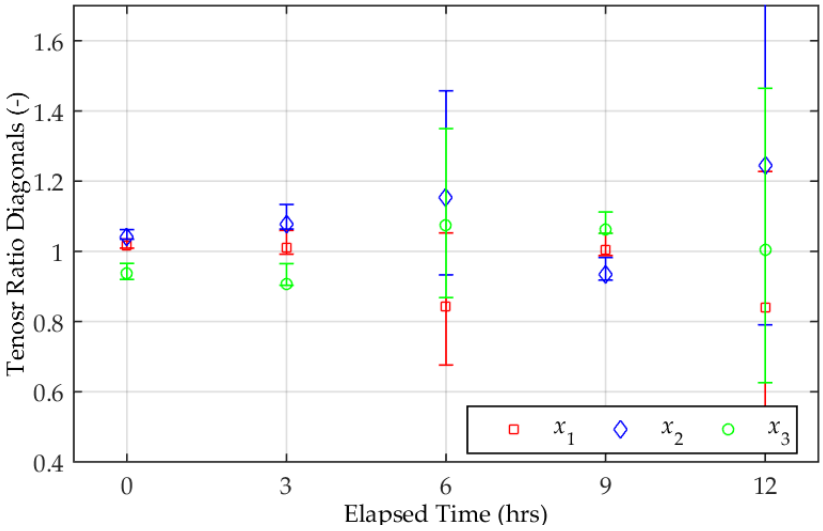


Figure E-22: Changes to the tensor ratio diagonal coefficients aligned with the snow's coordinate system (x_3 is vertical, normal to the snow surface) in the top 5.13 mm of sample NS2 associated with the faceted layer during the process of radiation recrystallization.

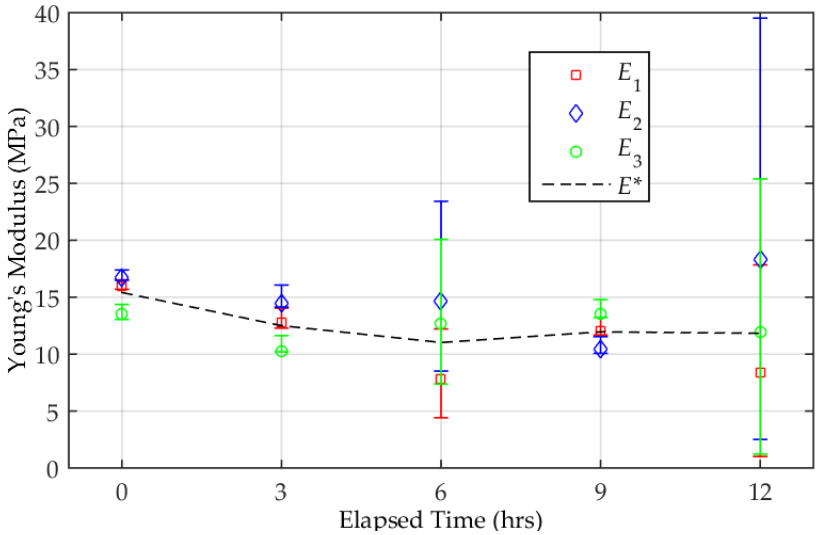


Figure E-23: Changes to the computed effective Young's moduli aligned with the snow's coordinate system in the top 5.13 mm of sample NS2 associated with the faceted layer during the process of radiation recrystallization. E^* represents the scalar computed effective Young's modulus.

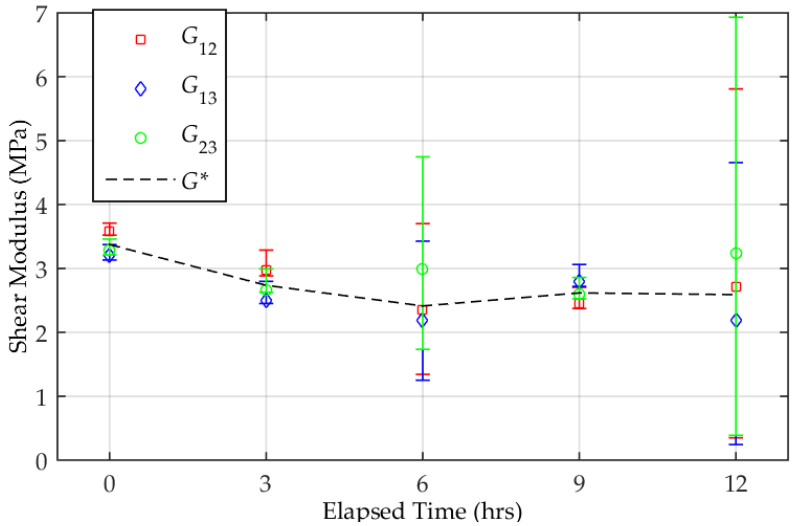


Figure E-24: Changes to the computed effective shear moduli aligned with the snow's coordinate system in the top 5.13 mm of sample NS2 associated with the faceted layer during the process of radiation recrystallization. G^* represents the scalar computed effective shear modulus.

E.2.2 Sub-Faceted Layer Results

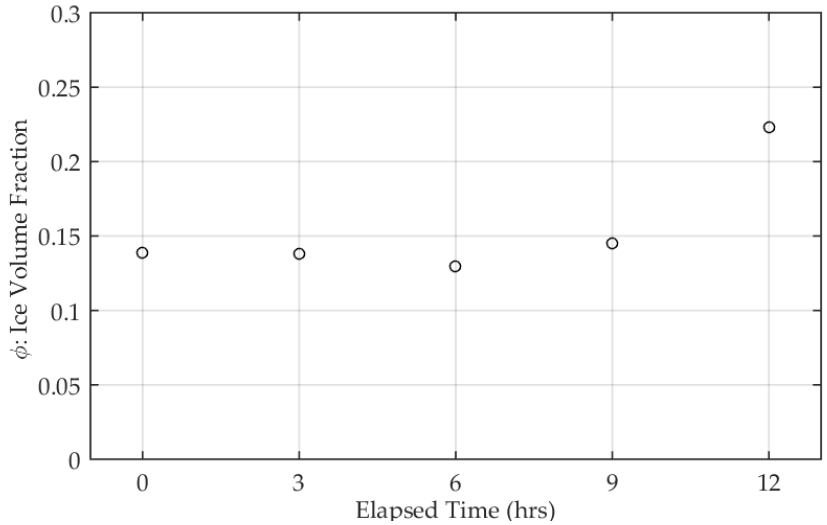


Figure E-25: Changes in volume fraction, ϕ, of sample NS2 associated with the layer below the faceted crystals during the process of radiation recrystallization.

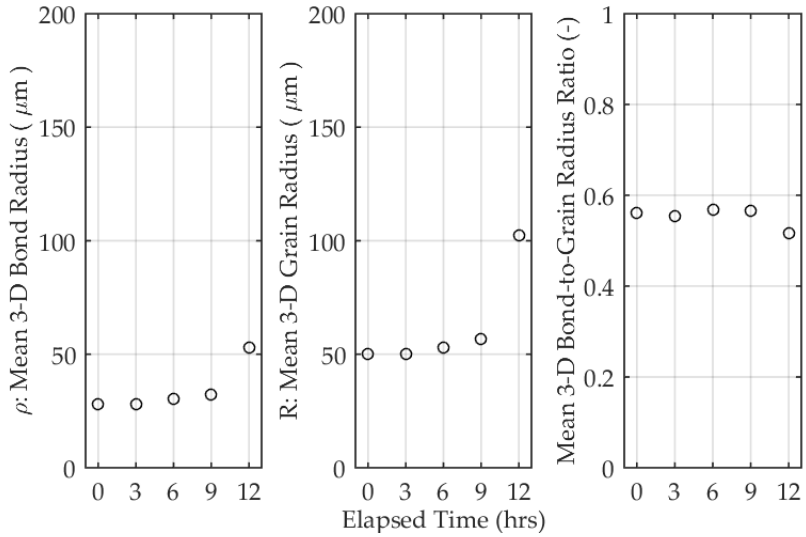


Figure E-26: Changes in mean bond radius, $\hat{\rho}$, and grain radius, $\hat{R}$, of sample NS2 associated layer below the faceted crystals during the process of radiation recrystallization.

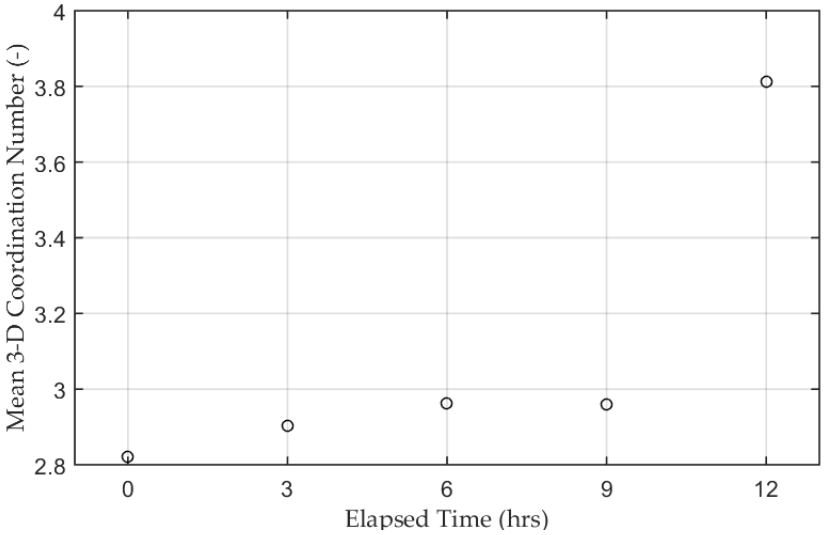


Figure E-27: Changes in mean 3-D coordination number, $\mathcal{N}$, of sample NS2 associated with the layer below the faceted crystals during the process of radiation recrystallization.

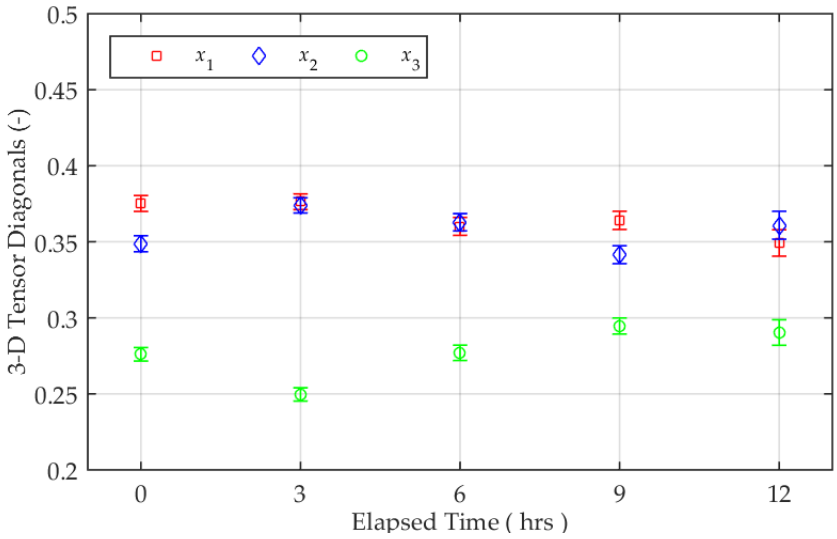


Figure E-28: Changes to the contact tensor diagonal coefficients aligned with the snow's coordinate system (x_3 is vertical, normal to the snow surface) of sample NS2 associated with the layer below the faceted crystals during the process of radiation recrystallization.

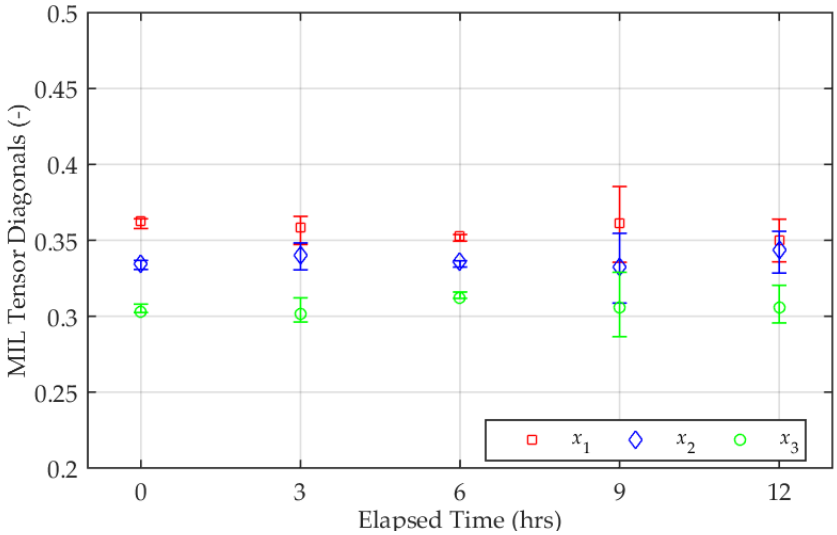


Figure E-29: Changes to the MIL tensor diagonal coefficients aligned with the snow's coordinate system (x_3 is vertical, normal to the snow surface) of sample NS2 associated with the layer below the faceted crystals during the process of radiation recrystallization.

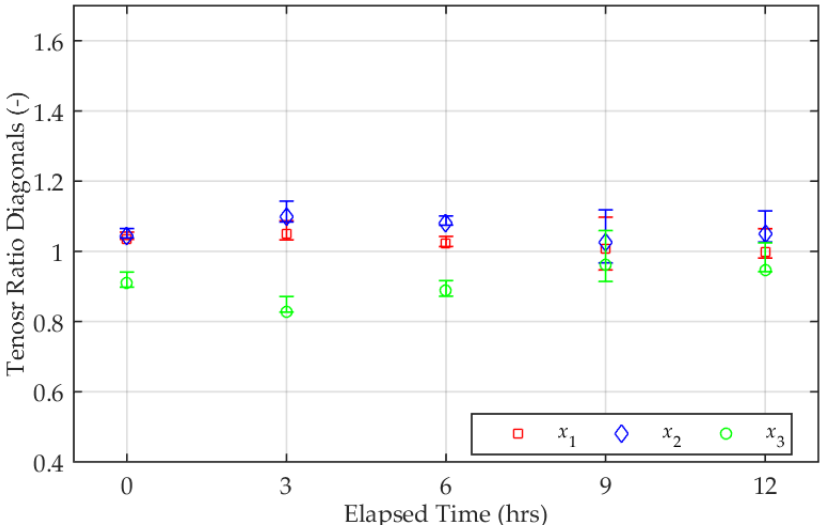


Figure E-30: Changes to the tensor ratio diagonal coefficients aligned with the snow's coordinate system (x_3 is vertical, normal to the snow surface) of sample NS2 associated with the layer below the faceted crystals during the process of radiation recrystallization.

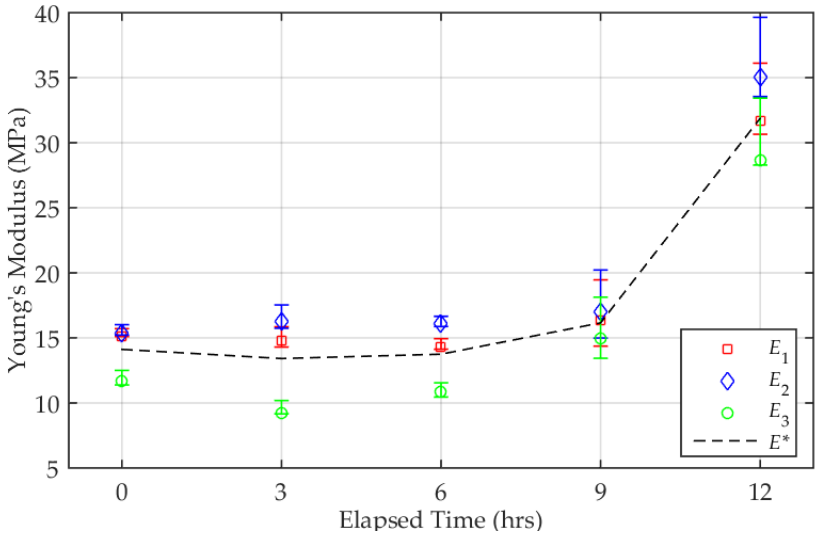


Figure E-31: Changes to the computed effective Young's moduli aligned with the snow's coordinate system of sample NS2 associated with the layer below the faceted crystals during the process of radiation recrystallization. E^* represents the scalar computed effective Young's modulus.

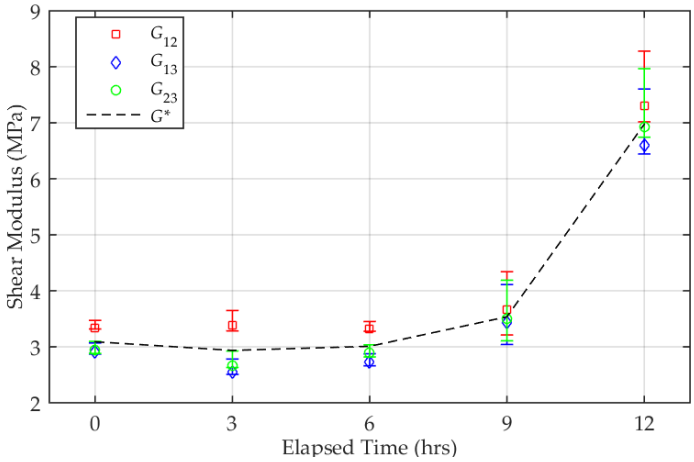


Figure E-32: Changes to the computed effective shear moduli aligned with the snow's coordinate system of sample NS2 associated with the layer below the faceted crystals during the process of radiation recrystallization. G^* represents the scalar computed effective shear modulus.

E.3 Fabric Tensor Results for Sample New Snow 3 (NS3)

E.3.1 Faceted Layer Results

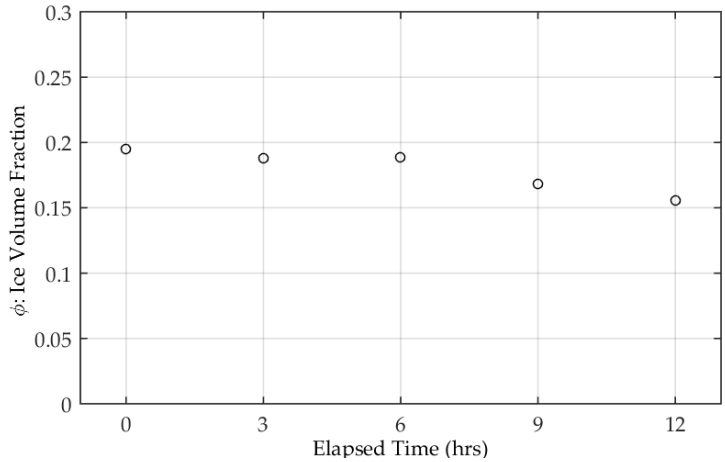


Figure E-33: Changes in volume fraction, ϕ, in the top 5.52 mm of sample NS3 associated with the faceted layer during the process of radiation recrystallization.

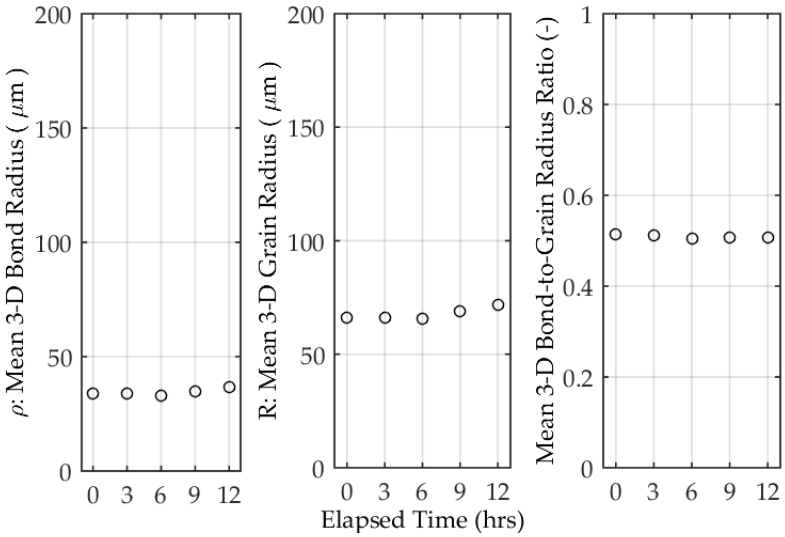


Figure E-34: Changes in mean bond radius, $\hat{\rho}$, and grain radius, $\hat{R}$, in the top 5.52 mm of sample NS3 associated with the faceted layer during the process of radiation recrystallization.

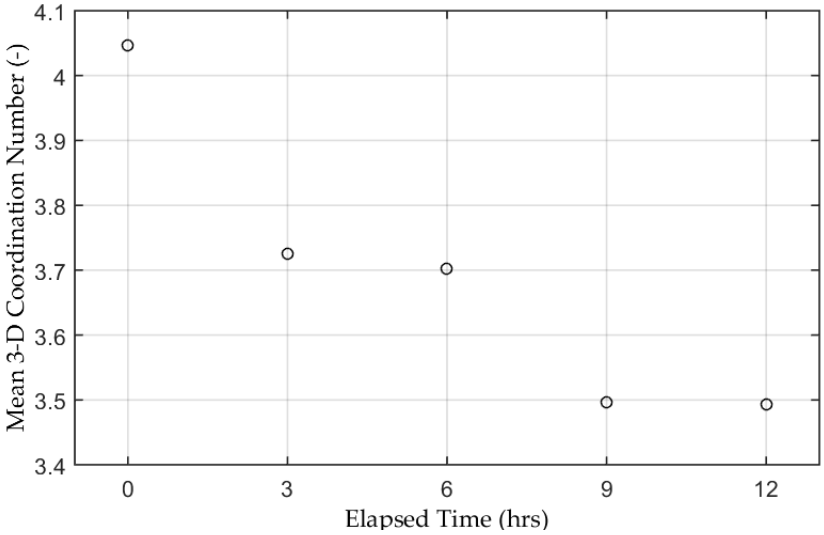


Figure E-35: Changes in mean 3-D coordination number, $\mathcal{N}$, in the top 5.52 mm of sample NS3 associated with the faceted layer during the process of radiation recrystallization.

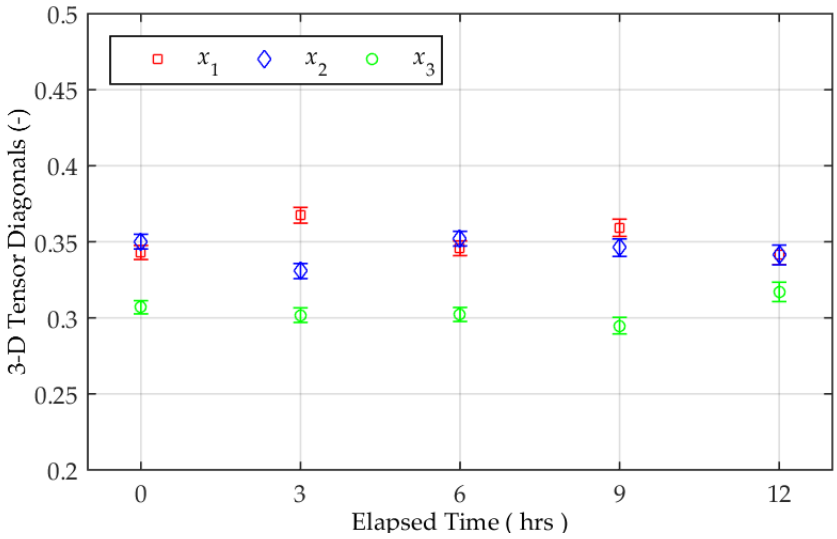


Figure E-36: Changes to the contact tensor diagonal coefficients aligned with the snow's coordinate system (x_3 is vertical, normal to the snow surface) in the top 5.52 mm of sample NS3 associated with the faceted layer during the process of radiation recrystallization.

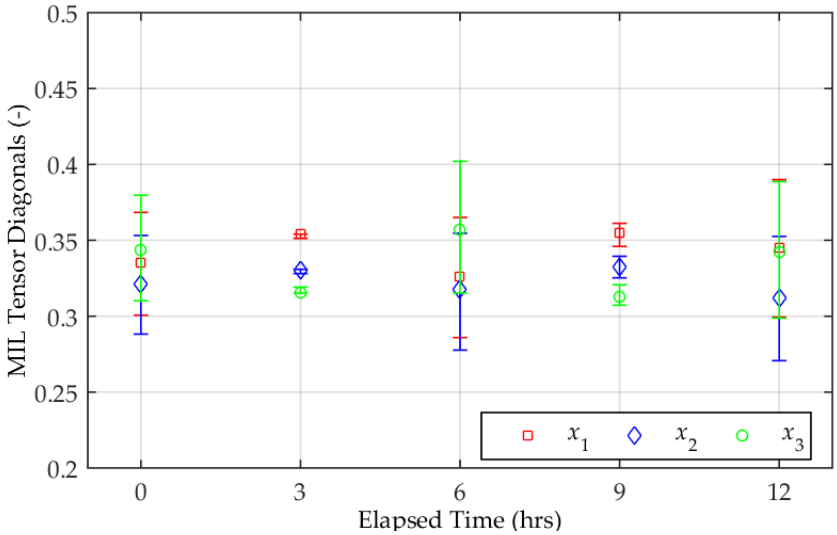


Figure E-37: Changes to the MIL tensor diagonal coefficients aligned with the snow's coordinate system (x_3 is vertical, normal to the snow surface) in the top 5.52 mm of sample NS3 associated with the faceted layer during the process of radiation recrystallization.

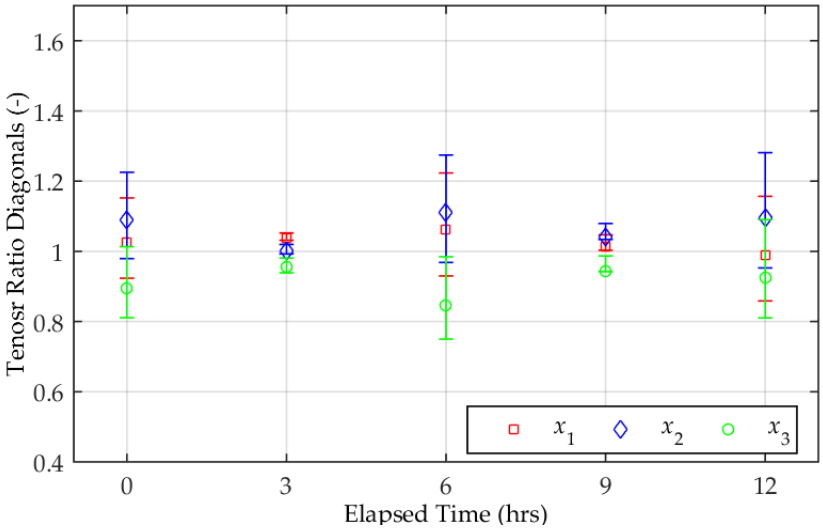


Figure E-38: Changes to the tensor ratio diagonal coefficients aligned with the snow's coordinate system (x_3 is vertical, normal to the snow surface) in the top 5.52 mm of sample NS3 associated with the faceted layer during the process of radiation recrystallization.

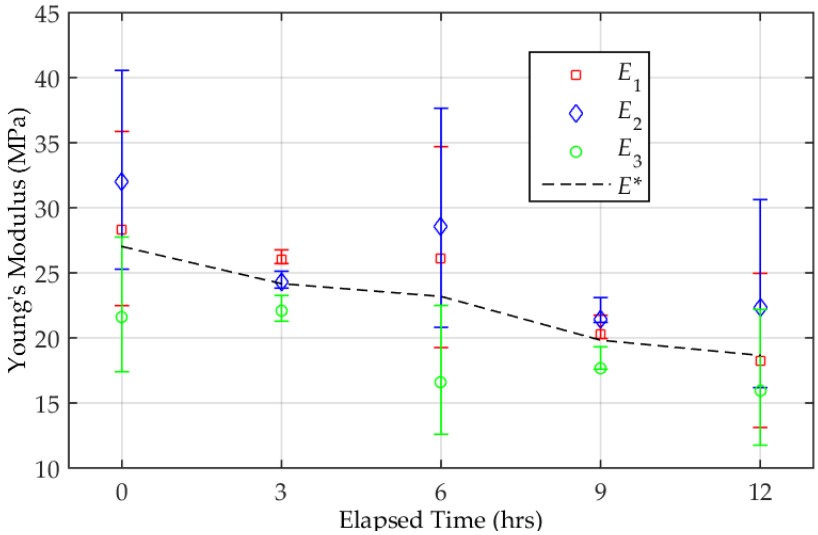


Figure E-39: Changes to the computed effective Young's moduli aligned with the snow's coordinate system in the top 5.52 mm of sample NS3 associated with the faceted layer during the process of radiation recrystallization. E^* represents the scalar computed effective Young's modulus.

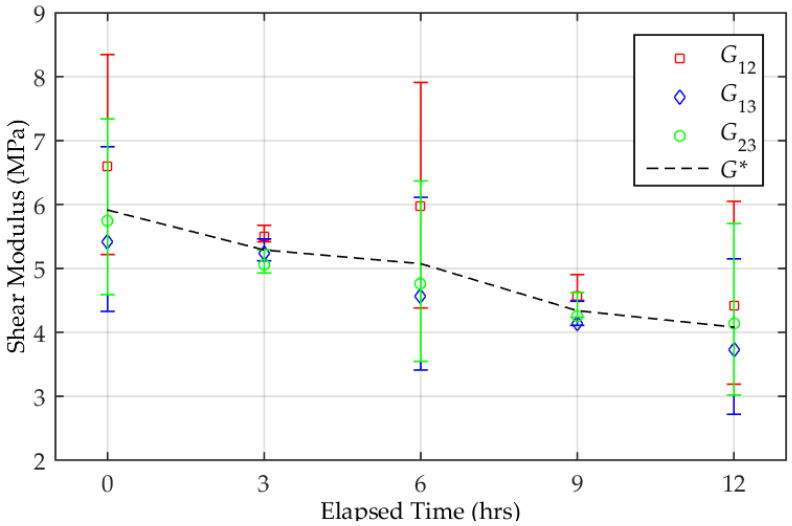


Figure E-40: Changes to the computed effective shear moduli aligned with the snow's coordinate system in the top 5.52 mm of sample NS3 associated with the faceted layer during the process of radiation recrystallization. G^* represents the scalar computed effective shear modulus.

E.3.2 Sub-Faceted Layer Results

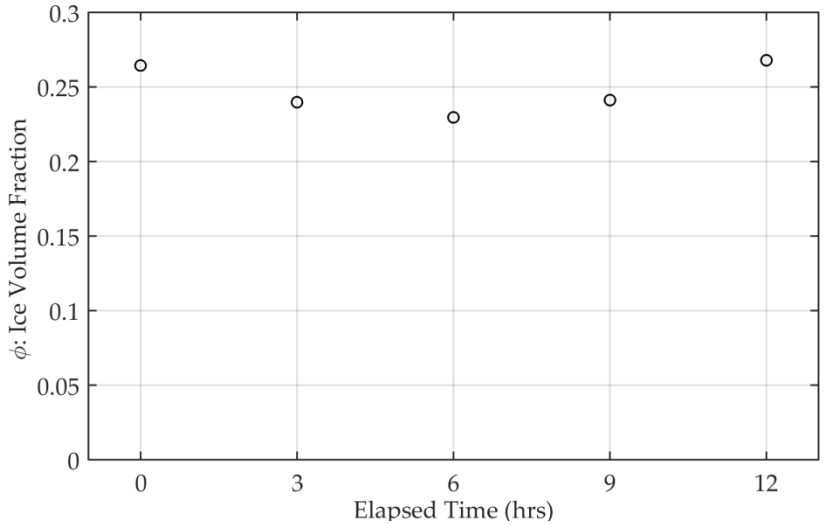


Figure E-41: Changes in volume fraction, ϕ, of sample NS3 associated with the layer below the faceted crystals during the process of radiation recrystallization.

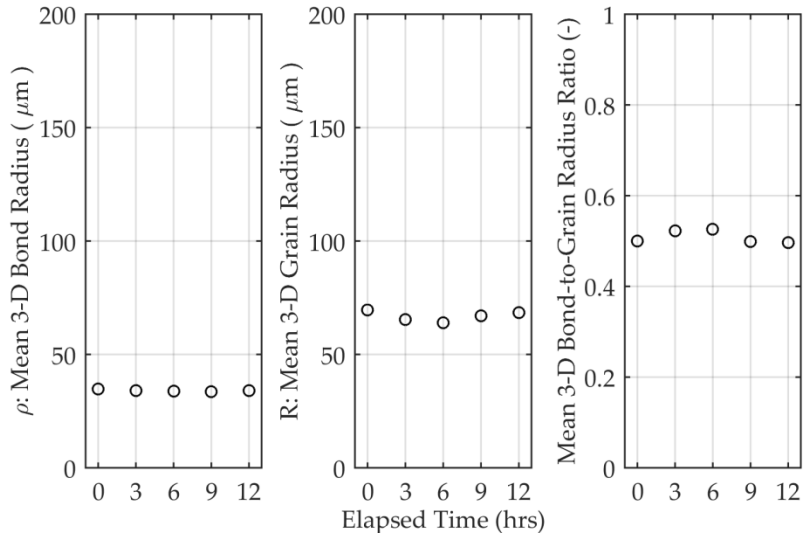


Figure E-42: Changes in mean bond radius, $\hat{\rho}$, and grain radius, $\hat{R}$, of sample NS3 associated layer below the faceted crystals during the process of radiation recrystallization.

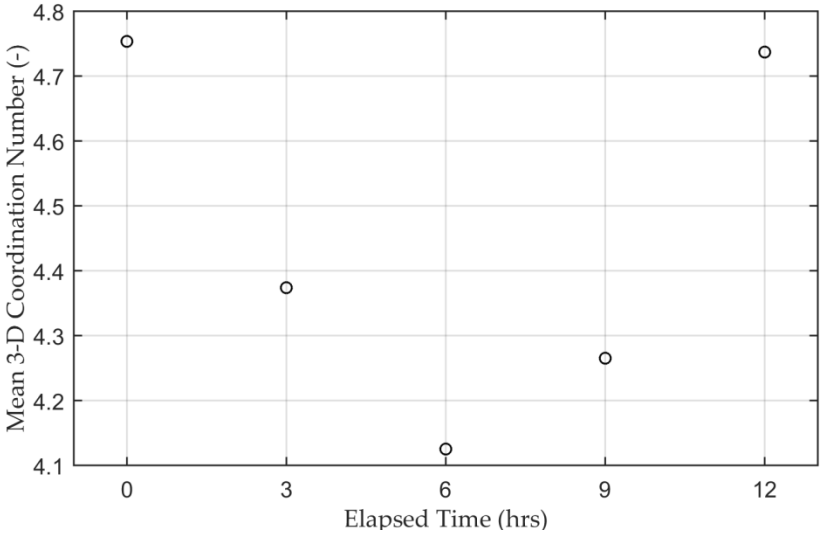


Figure E-43: Changes in mean 3-D coordination number, $\mathcal{N}$, of sample NS3 associated with the layer below the faceted crystals during the process of radiation recrystallization.

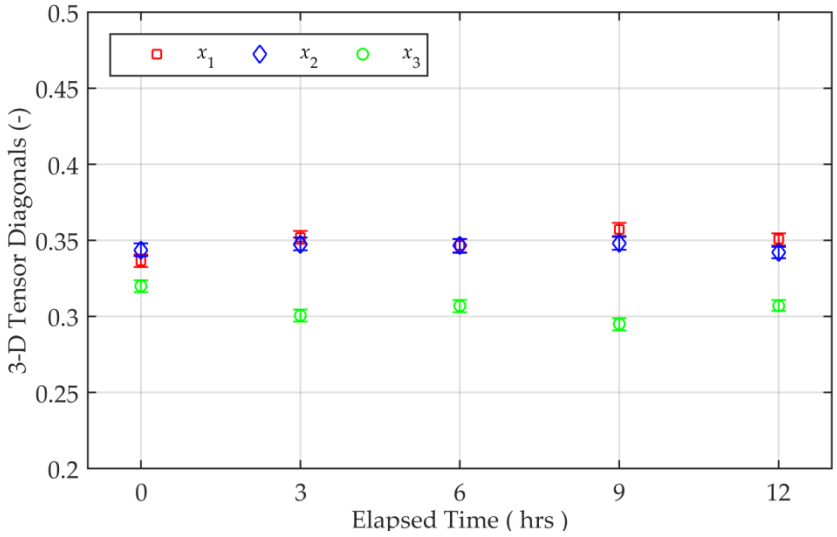


Figure E-44: Changes to the contact tensor diagonal coefficients aligned with the snow's coordinate system (x_3 is vertical, normal to the snow surface) of sample NS3 associated with the layer below the faceted crystals during the process of radiation recrystallization.

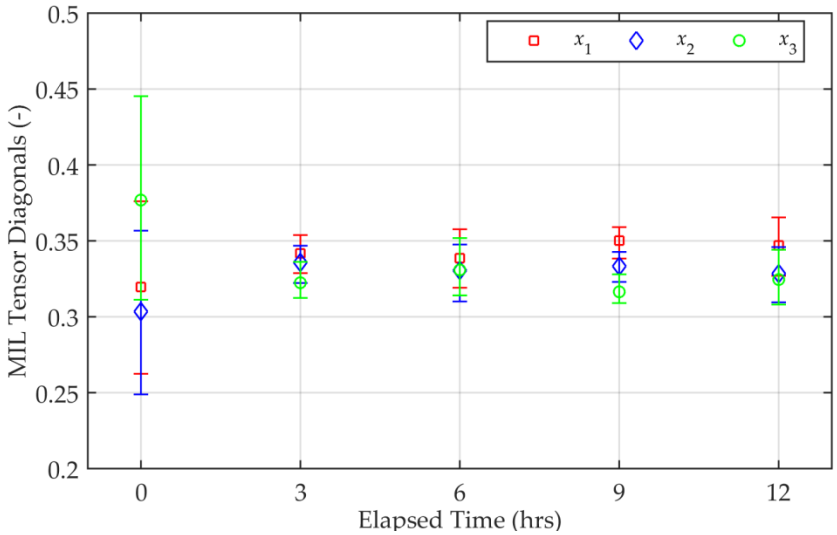


Figure E-45: Changes to the MIL tensor diagonal coefficients aligned with the snow's coordinate system (x_3 is vertical, normal to the snow surface) of sample NS3 associated with the layer below the faceted crystals during the process of radiation recrystallization.

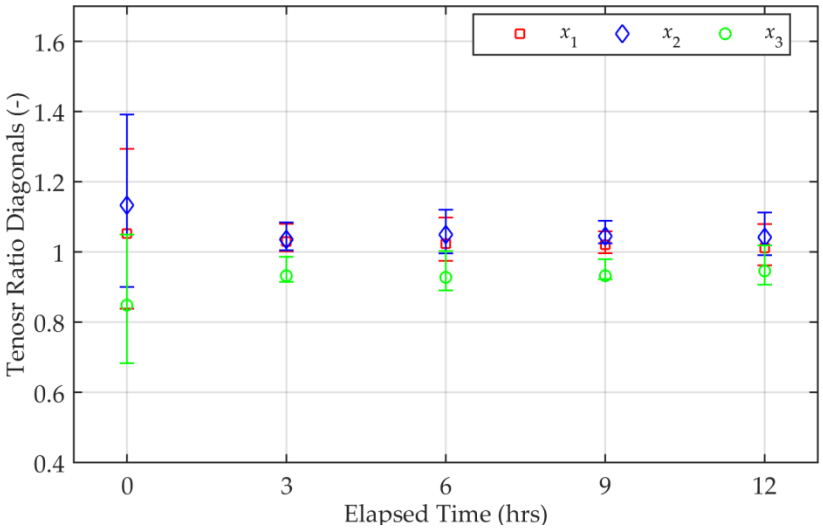


Figure E-46: Changes to the tensor ratio diagonal coefficients aligned with the snow's coordinate system (x_3 is vertical, normal to the snow surface) of sample NS3 associated with the layer below the faceted crystals during the process of radiation recrystallization.

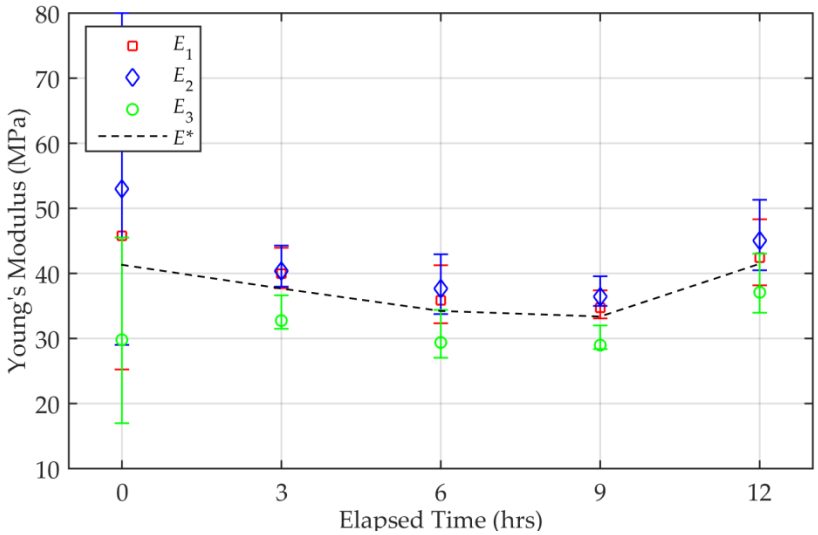


Figure E-47: Changes to the computed effective Young's moduli aligned with the snow's coordinate system of sample NS3 associated with the layer below the faceted crystals during the process of radiation recrystallization. E^* represents the scalar computed effective Young's modulus.

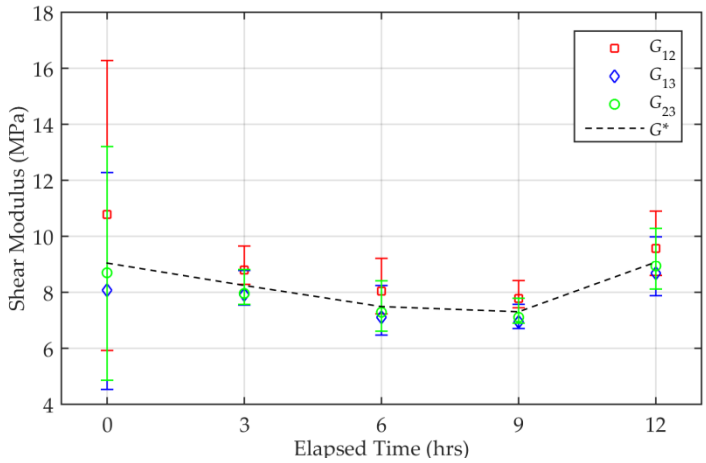


Figure E-48: Changes to the computed effective shear moduli aligned with the snow's coordinate system of sample NS3 associated with the layer below the faceted crystals during the process of radiation recrystallization. G^* represents the scalar computed effective shear modulus.

E.4 Fabric Tensor Results for Sample 1 Week Old 1 (1W1)

E.4.1 Faceted Layer Results

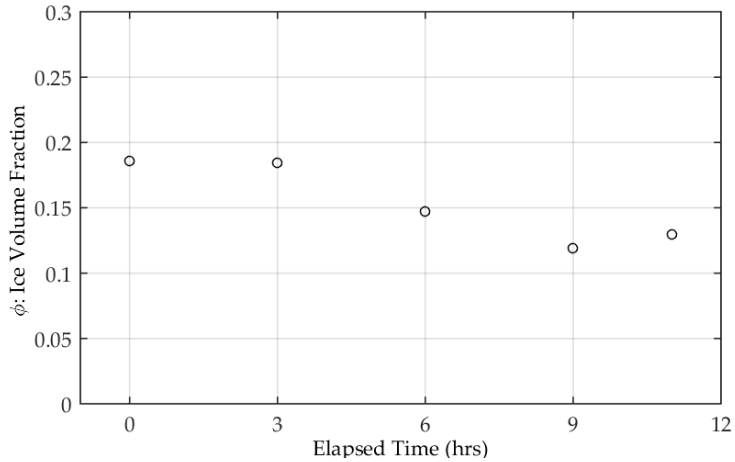


Figure E-49: Changes in volume fraction, ϕ, in the top 7.00 mm of sample 1W1 associated with the faceted layer during the process of radiation recrystallization.

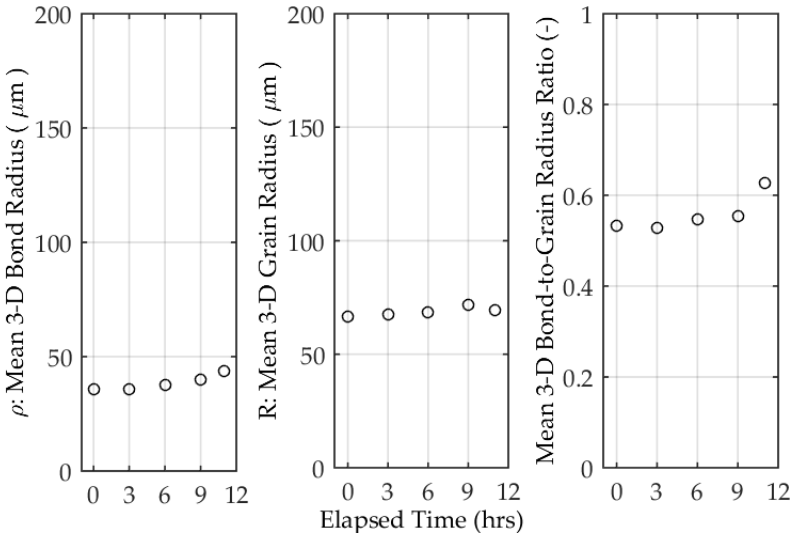


Figure E-50: Changes in mean bond radius, $\hat{\rho}$, and grain radius, $\hat{R}$, in the top 7.00 mm of sample 1W1 associated with the faceted layer during the process of radiation recrystallization.

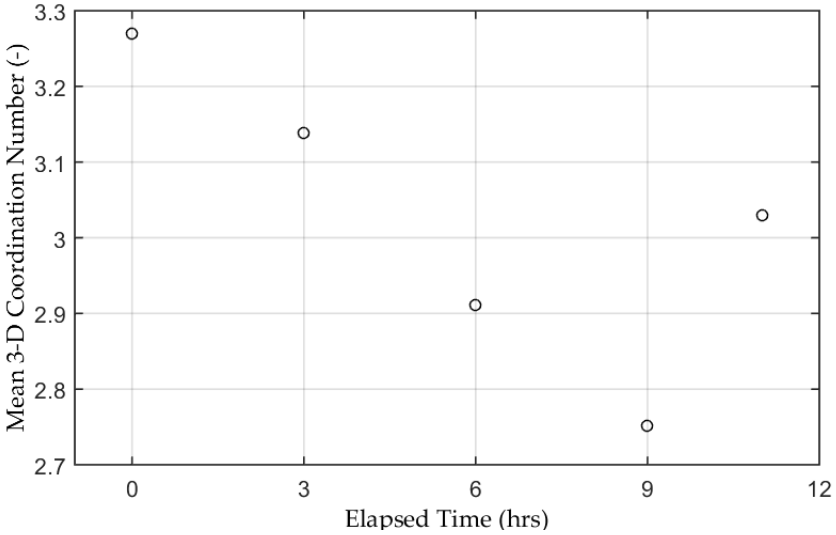


Figure E-51: Changes in mean 3-D coordination number, $\mathcal{N}$, in the top 7.00 mm of sample 1W1 associated with the faceted layer during the process of radiation recrystallization.

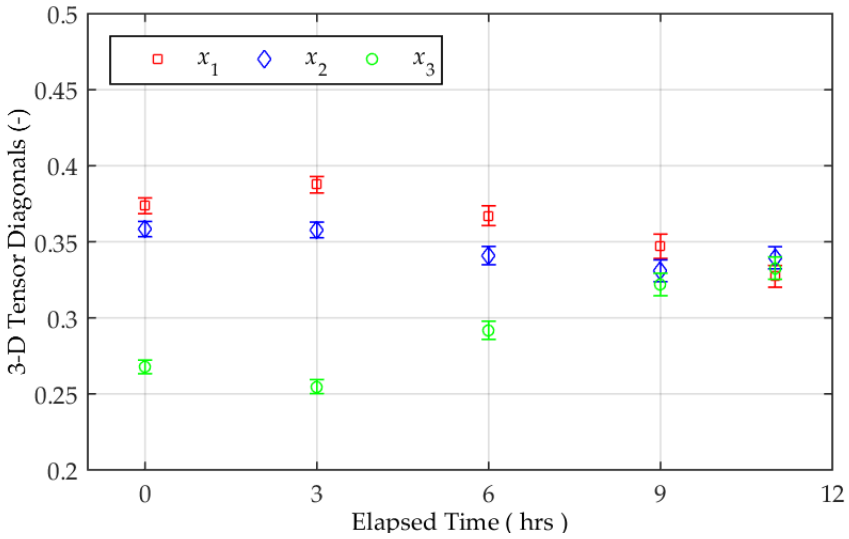


Figure E-52: Changes to the contact tensor diagonal coefficients aligned with the snow's coordinate system (x_3 is vertical, normal to the snow surface) in the top 7.00 mm of sample 1W1 associated with the faceted layer during the process of radiation recrystallization.

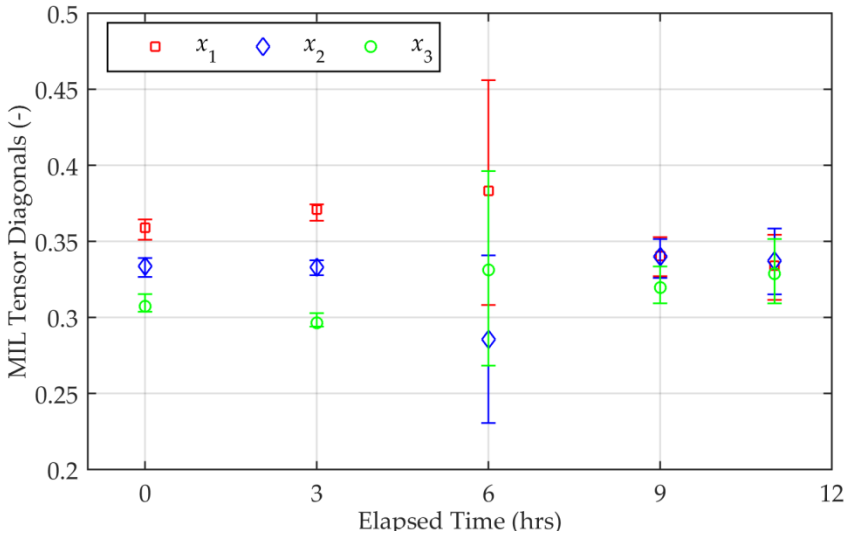


Figure E-53: Changes to the MIL tensor diagonal coefficients aligned with the snow's coordinate system (x_3 is vertical, normal to the snow surface) in the top 7.00 mm of sample 1W1 associated with the faceted layer during the process of radiation recrystallization.

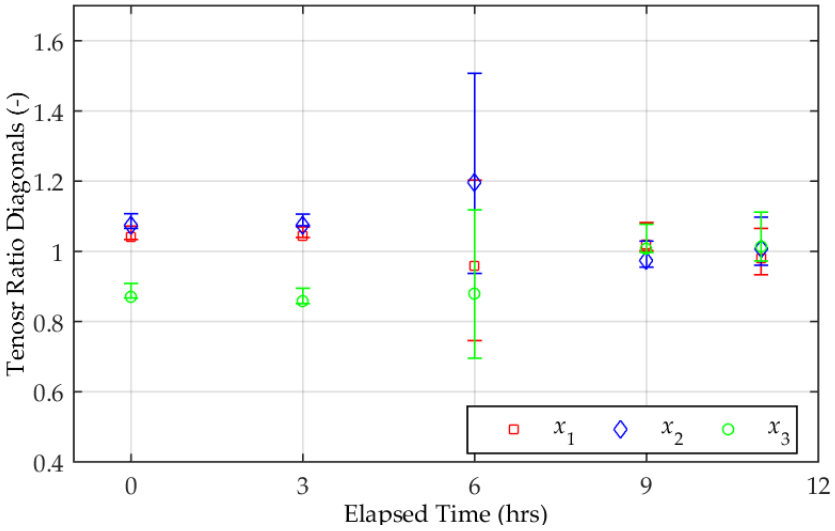


Figure E-54: Changes to the tensor ratio diagonal coefficients aligned with the snow's coordinate system (x_3 is vertical, normal to the snow surface) in the top 7.00 mm of sample 1W1 associated with the faceted layer during the process of radiation recrystallization.

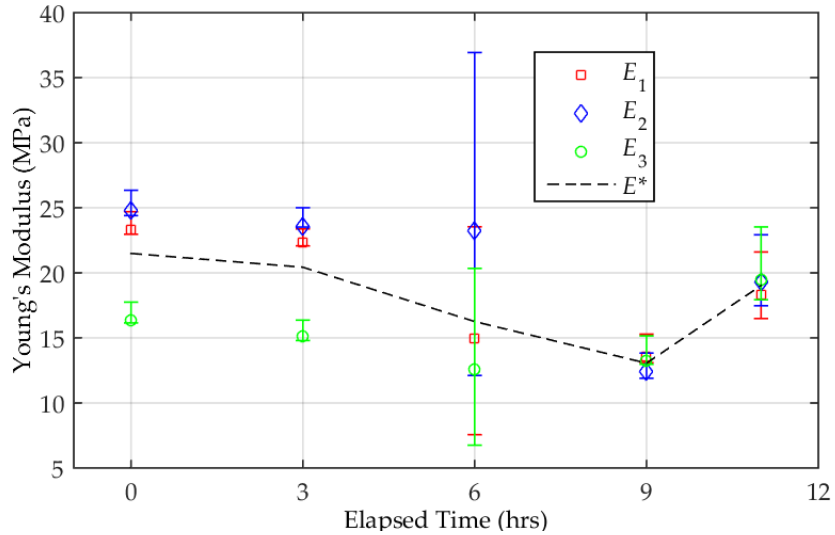


Figure E-55: Changes to the computed effective Young's moduli aligned with the snow's coordinate system in the top 7.00 mm of sample 1W1 associated with the faceted layer during the process of radiation recrystallization. E^* represents the scalar computed effective Young's modulus.

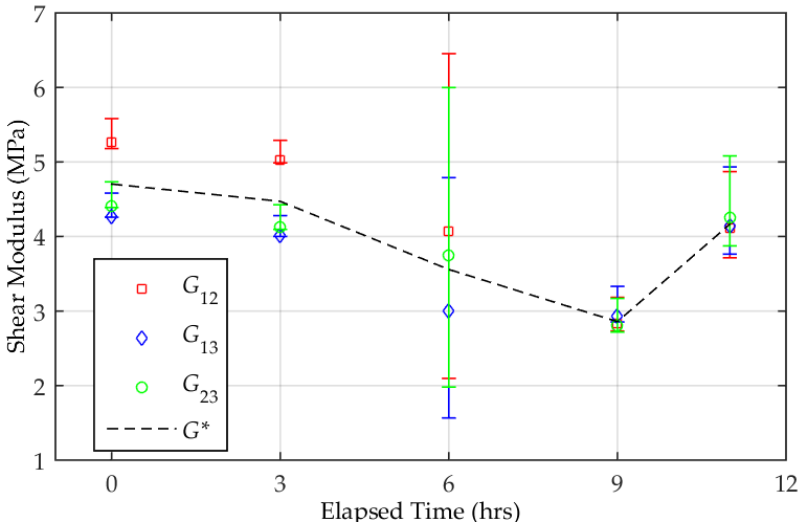


Figure E-56: Changes to the computed effective shear moduli aligned with the snow's coordinate system in the top 7.00 mm of sample 1W1 associated with the faceted layer during the process of radiation recrystallization. G^* represents the scalar computed effective shear modulus.

E.4.2 Sub-Faceted Layer Results

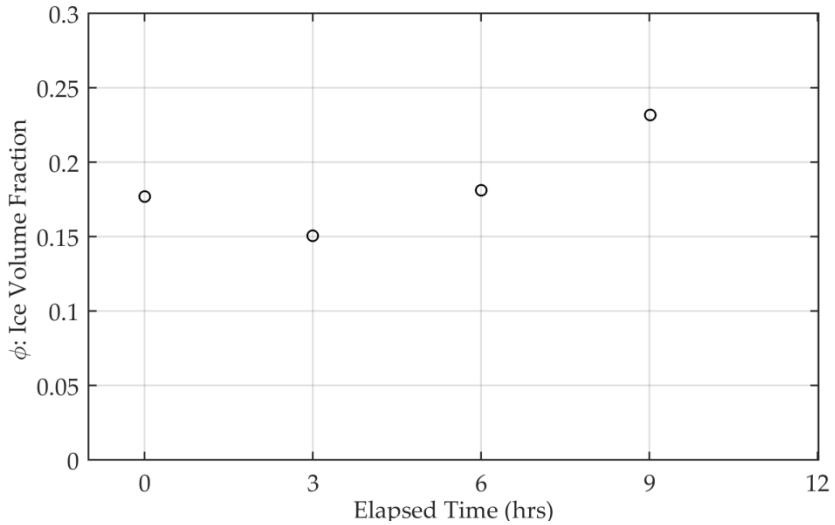


Figure E-57: Changes in volume fraction, ϕ, of sample 1W1 associated with the layer below the faceted crystals during the process of radiation recrystallization.

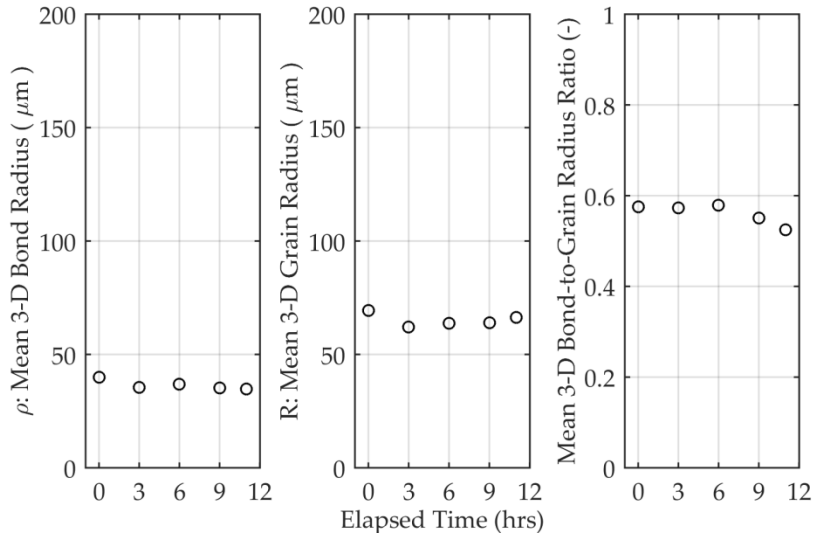


Figure E-58: Changes in mean bond radius, $\hat{\rho}$, and grain radius, $\hat{R}$, of sample 1W1 associated layer below the faceted crystals during the process of radiation recrystallization.

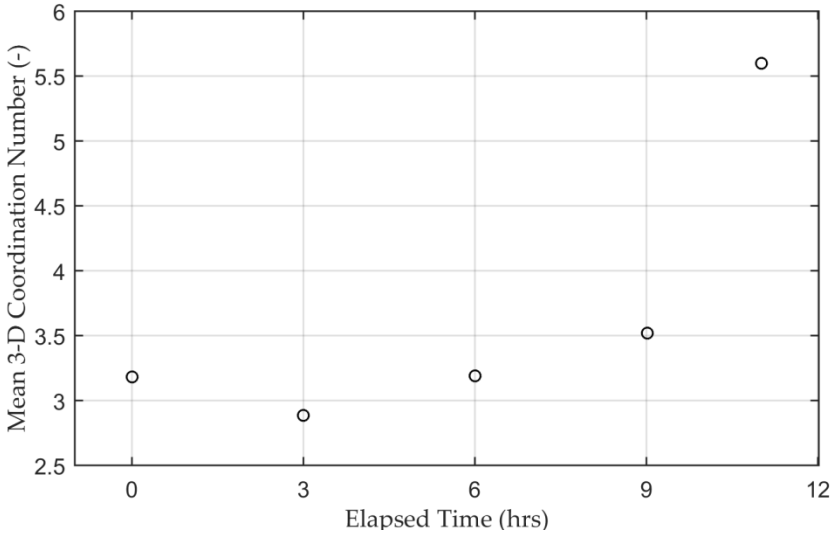


Figure E-59: Changes in mean 3-D coordination number, $\mathcal{N}$, of sample 1W1 associated with the layer below the faceted crystals during the process of radiation recrystallization.

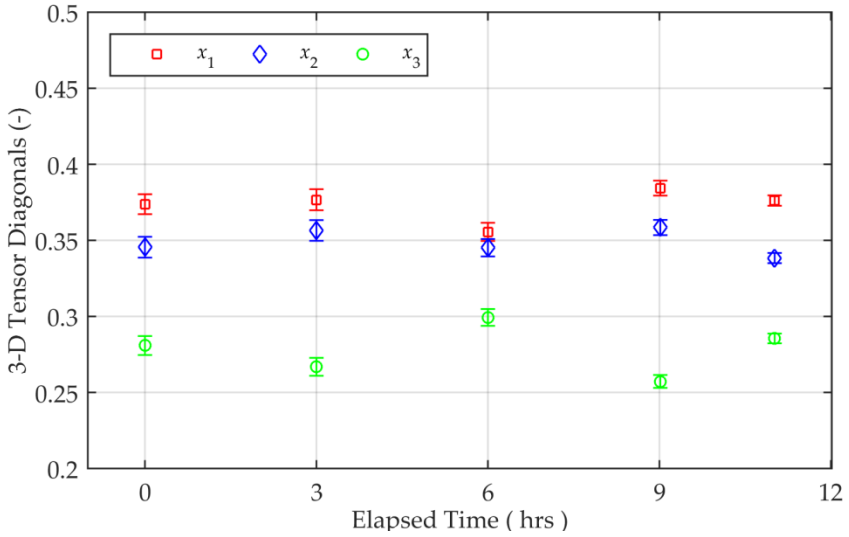


Figure E-60: Changes to the contact tensor diagonal coefficients aligned with the snow's coordinate system (x_3 is vertical, normal to the snow surface) of sample 1W1 associated with the layer below the faceted crystals during the process of radiation recrystallization.

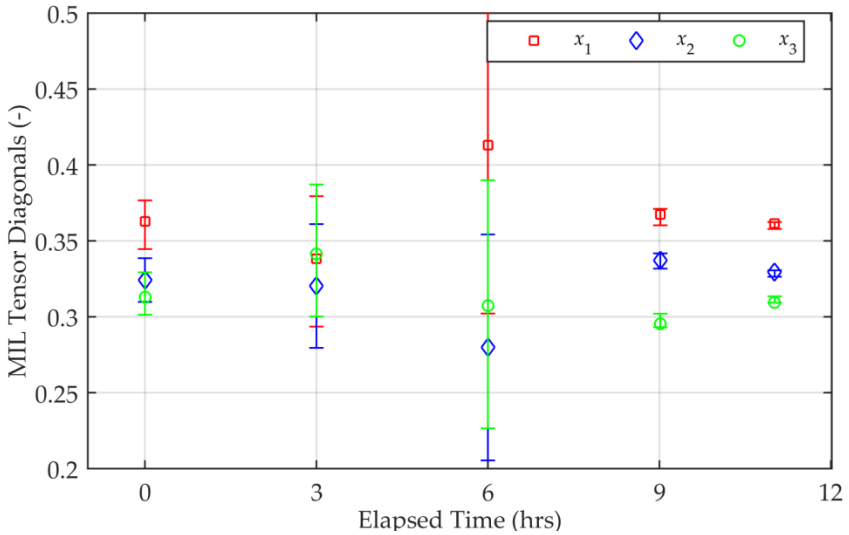


Figure E-61: Changes to the MIL tensor diagonal coefficients aligned with the snow's coordinate system (x_3 is vertical, normal to the snow surface) of sample 1W1 associated with the layer below the faceted crystals during the process of radiation recrystallization.

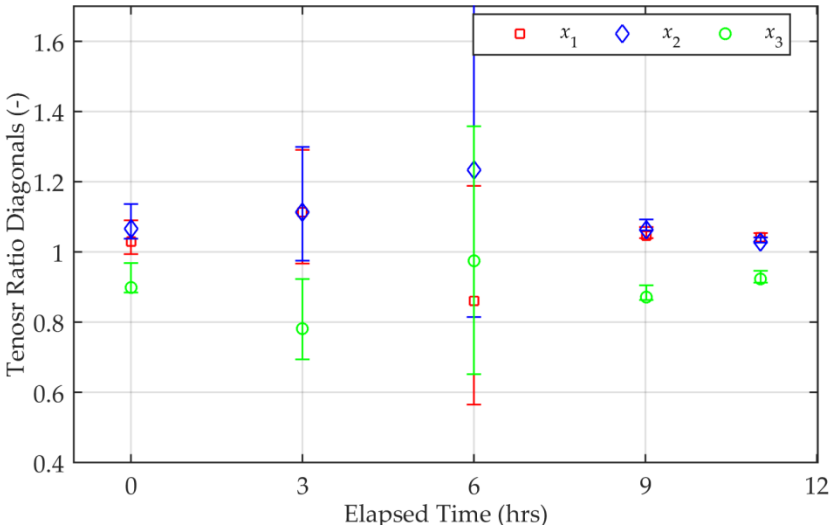


Figure E-62: Changes to the tensor ratio diagonal coefficients aligned with the snow's coordinate system (x_3 is vertical, normal to the snow surface) of sample 1W1 associated with the layer below the faceted crystals during the process of radiation recrystallization.

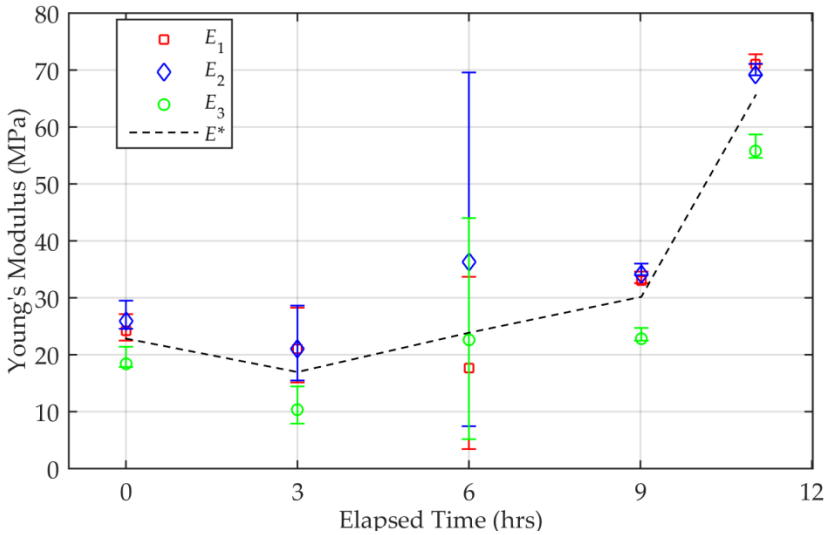


Figure E-63: Changes to the computed effective Young's moduli aligned with the snow's coordinate system of sample 1W1 associated with the layer below the faceted crystals during the process of radiation recrystallization. E^* represents the scalar computed effective Young's modulus.

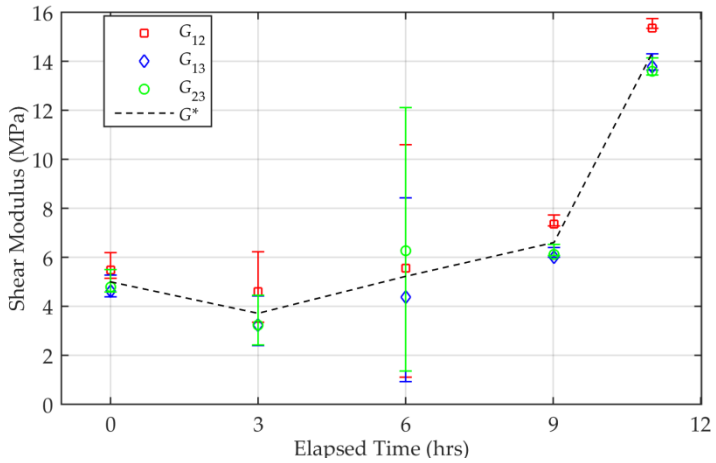


Figure E-64: Changes to the computed effective shear moduli aligned with the snow's coordinate system of sample 1W1 associated with the layer below the faceted crystals during the process of radiation recrystallization. G^* represents the scalar computed effective shear modulus.

E.5 Fabric Tensor Results for Sample 1 Week Old 2 (1W2)

E.5.1 Faceted Layer Results

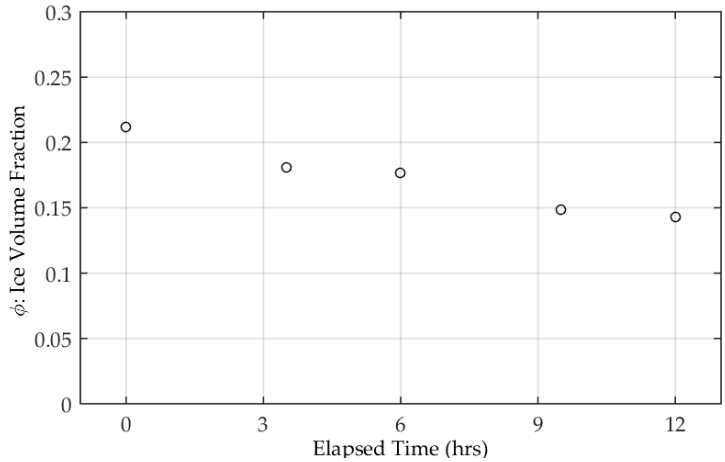


Figure E-65: Changes in volume fraction, ϕ, in the top 7.00 mm of sample 1W2 associated with the faceted layer during the process of radiation recrystallization.

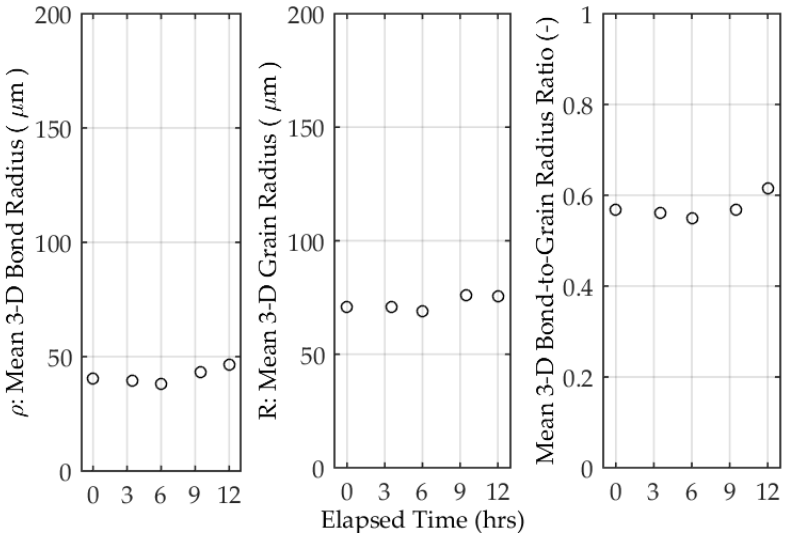


Figure E-66: Changes in mean bond radius, $\hat{\rho}$, and grain radius, $\hat{R}$, in the top 7.00 mm of sample 1W2 associated with the faceted layer during the process of radiation recrystallization.

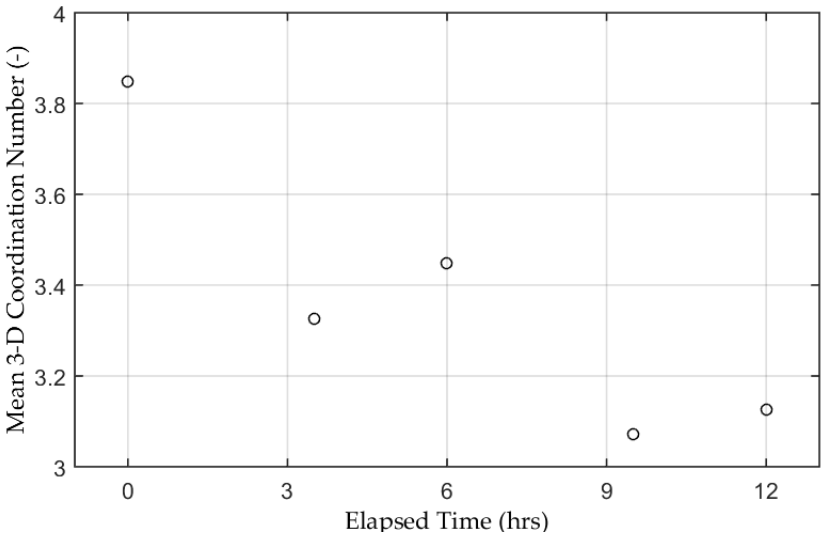


Figure E-67: Changes in mean 3-D coordination number, $\mathcal{N}$, in the top 7.00 mm of sample 1W2 associated with the faceted layer during the process of radiation recrystallization.

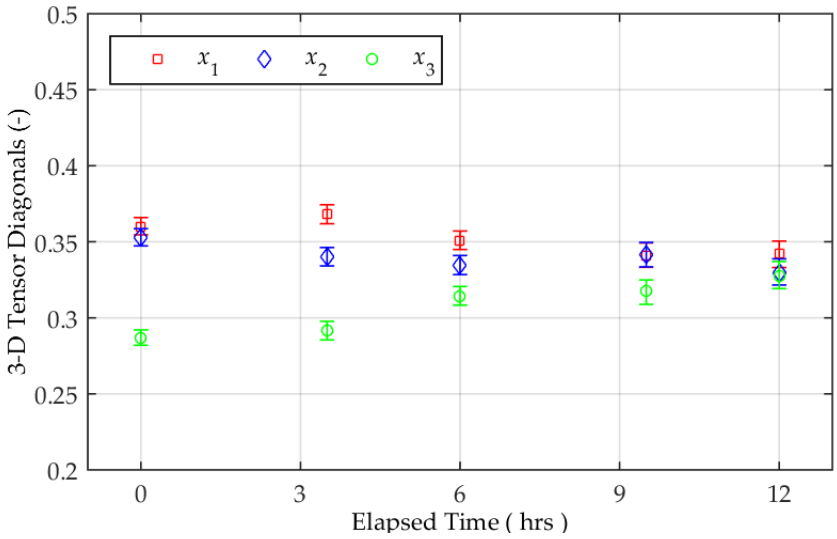


Figure E-68: Changes to the contact tensor diagonal coefficients aligned with the snow's coordinate system (x_3 is vertical, normal to the snow surface) in the top 7.00 mm of sample 1W2 associated with the faceted layer during the process of radiation recrystallization.

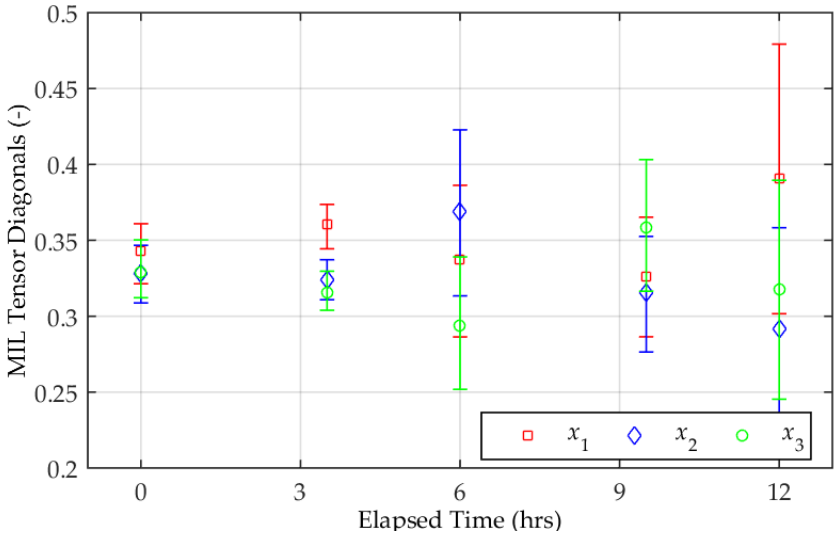


Figure E-69: Changes to the MIL tensor diagonal coefficients aligned with the snow's coordinate system (x_3 is vertical, normal to the snow surface) in the top 7.00 mm of sample 1W2 associated with the faceted layer during the process of radiation recrystallization.

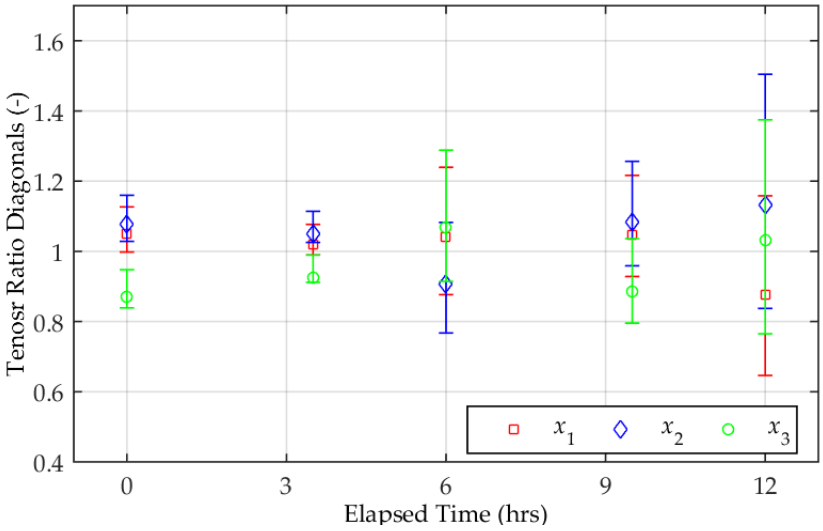


Figure E-70: Changes to the tensor ratio diagonal coefficients aligned with the snow's coordinate system (x_3 is vertical, normal to the snow surface) in the top 7.00 mm of sample 1W2 associated with the faceted layer during the process of radiation recrystallization.

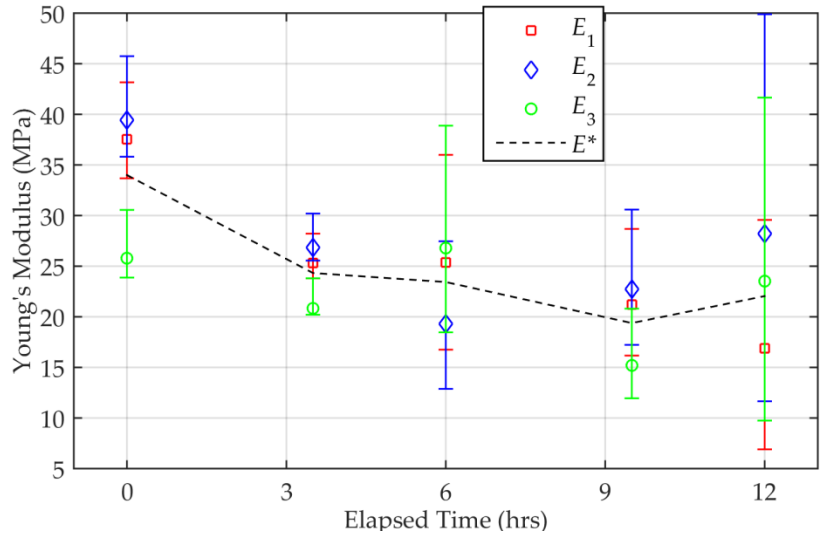


Figure E-71: Changes to the computed effective Young's moduli aligned with the snow's coordinate system in the top 7.00 mm of sample 1W2 associated with the faceted layer during the process of radiation recrystallization. E^* represents the scalar computed effective Young's modulus.

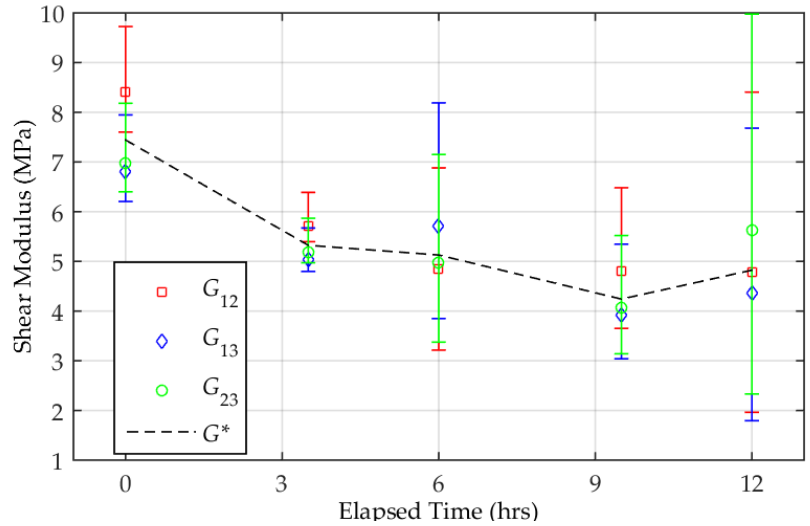


Figure E-72: Changes to the computed effective shear moduli aligned with the snow's coordinate system in the top 7.00 mm of sample 1W2 associated with the faceted layer during the process of radiation recrystallization. G^* represents the scalar computed effective shear modulus.

E.5.2 Sub-Faceted Layer Results

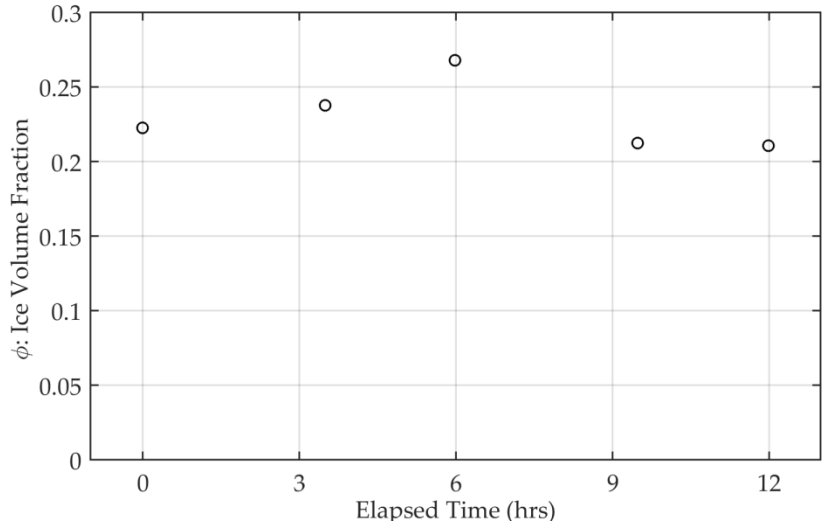


Figure E-73: Changes in volume fraction, ϕ, of sample 1W2 associated with the layer below the faceted crystals during the process of radiation recrystallization.

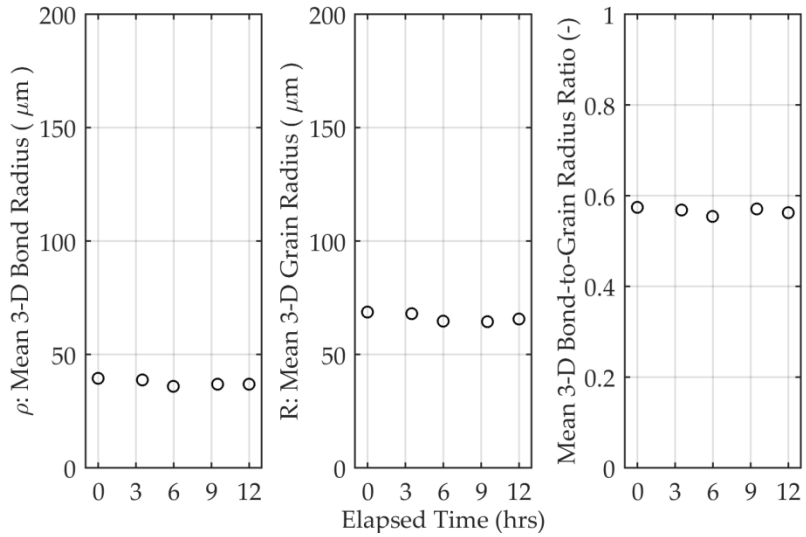


Figure E-74: Changes in mean bond radius, $\hat{\rho}$, and grain radius, $\hat{R}$, of sample 1W2 associated layer below the faceted crystals during the process of radiation recrystallization.

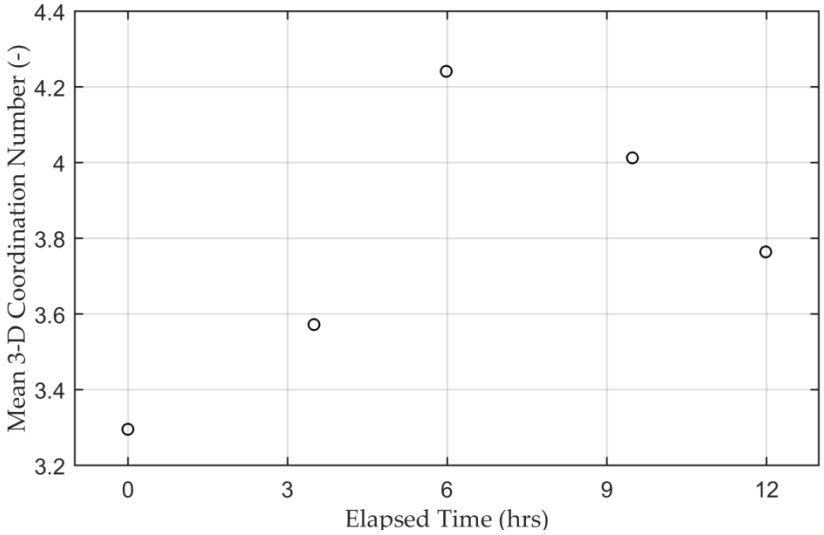


Figure E-75: Changes in mean 3-D coordination number, $\mathcal{N}$, of sample 1W2 associated with the layer below the faceted crystals during the process of radiation recrystallization.

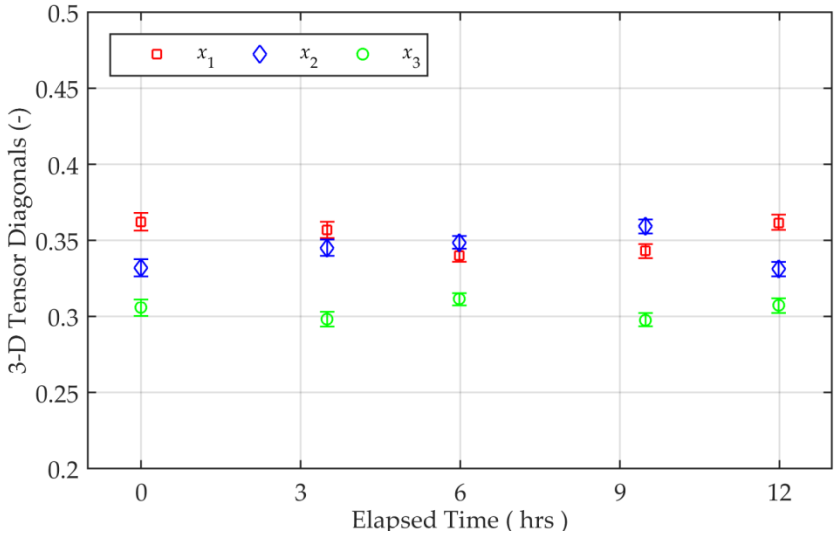


Figure E-76: Changes to the contact tensor diagonal coefficients aligned with the snow's coordinate system (x_3 is vertical, normal to the snow surface) of sample 1W2 associated with the layer below the faceted crystals during the process of radiation recrystallization.

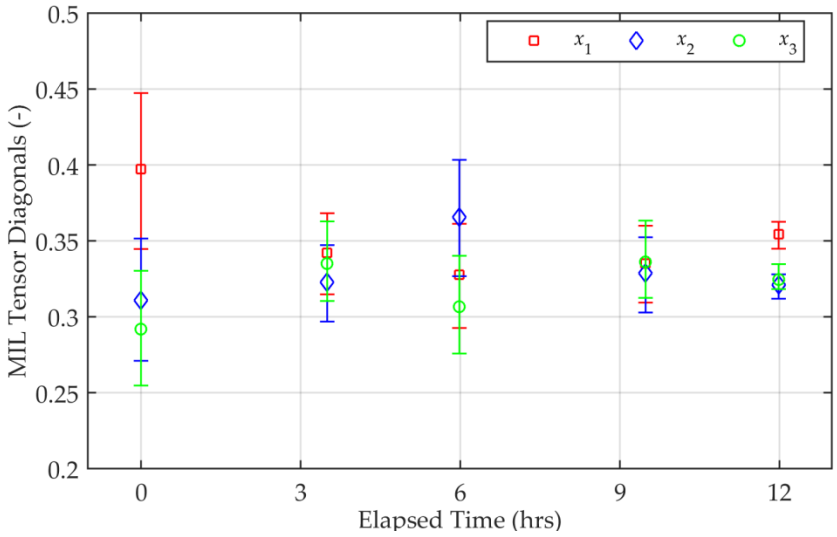


Figure E-77: Changes to the MIL tensor diagonal coefficients aligned with the snow's coordinate system (x_3 is vertical, normal to the snow surface) of sample 1W2 associated with the layer below the faceted crystals during the process of radiation recrystallization.

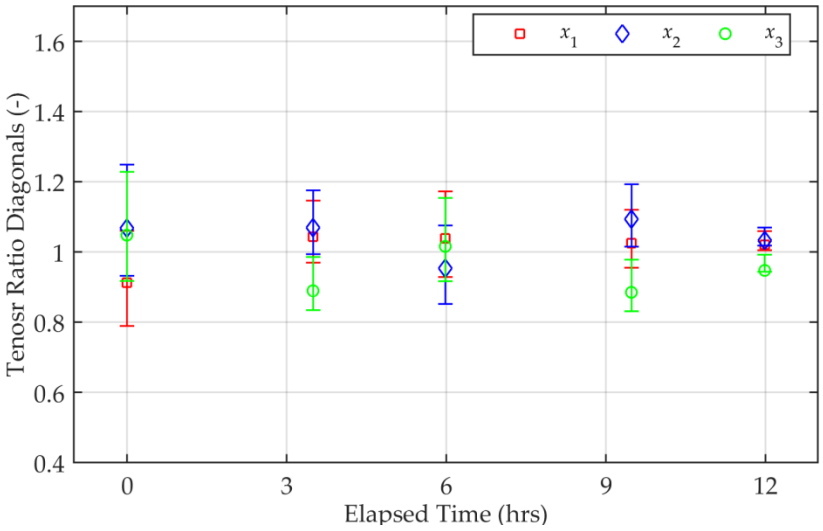


Figure E-78: Changes to the tensor ratio diagonal coefficients aligned with the snow's coordinate system (x_3 is vertical, normal to the snow surface) of sample 1W2 associated with the layer below the faceted crystals during the process of radiation recrystallization.

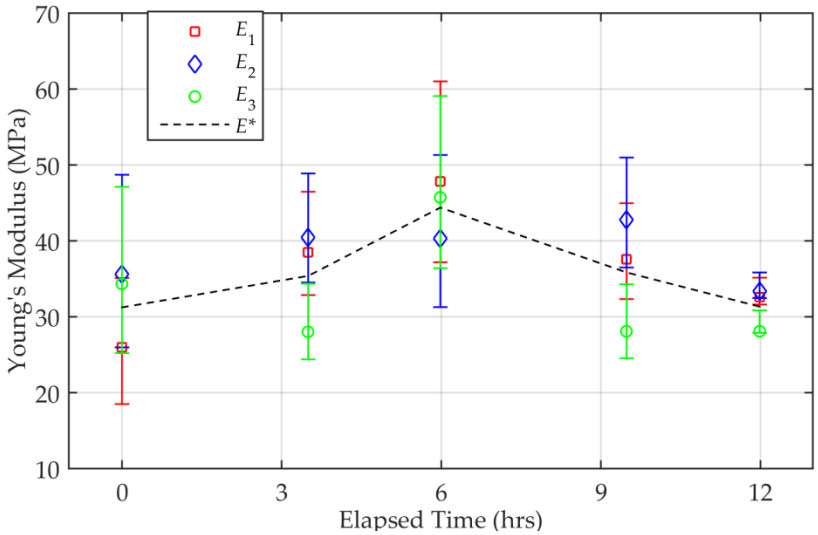


Figure E-79: Changes to the computed effective Young's moduli aligned with the snow's coordinate system of sample 1W2 associated with the layer below the faceted crystals during the process of radiation recrystallization. E^* represents the scalar computed effective Young's modulus.

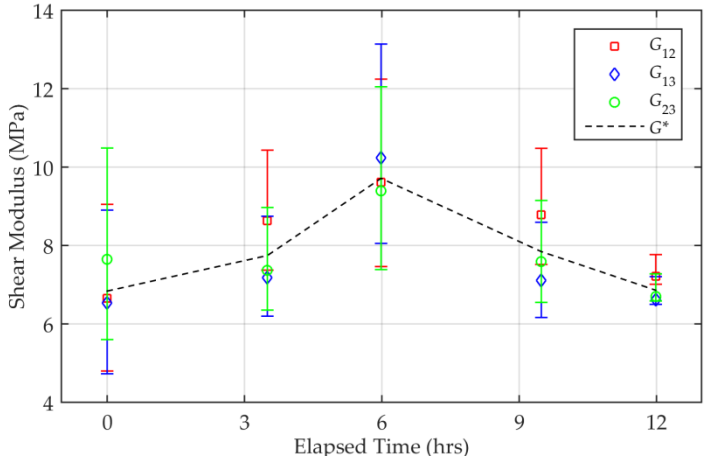


Figure E-80: Changes to the computed effective shear moduli aligned with the snow's coordinate system of sample 1W2 associated with the layer below the faceted crystals during the process of radiation recrystallization. G^* represents the scalar computed effective shear modulus.

E.6 Fabric Tensor Results for Sample 1 Week Old 3 (1W3)

E.6.1 Faceted Layer Results

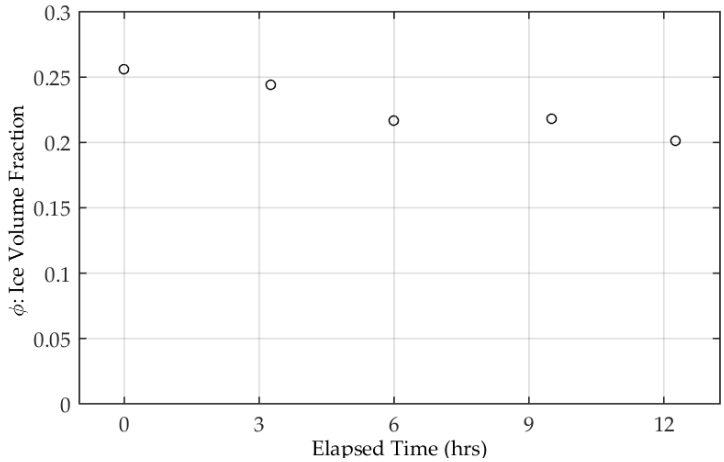


Figure E-81: Changes in volume fraction, ϕ, in the top 7.95 mm of sample 1W3 associated with the faceted layer during the process of radiation recrystallization.

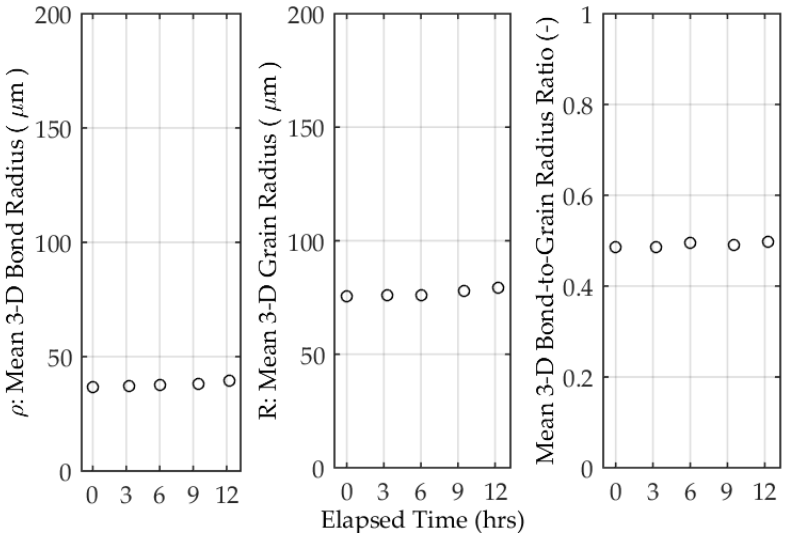


Figure E-82: Changes in mean bond radius, $\hat{\rho}$, and grain radius, $\hat{R}$, in the top 7.95 mm of sample 1W3 associated with the faceted layer during the process of radiation recrystallization.

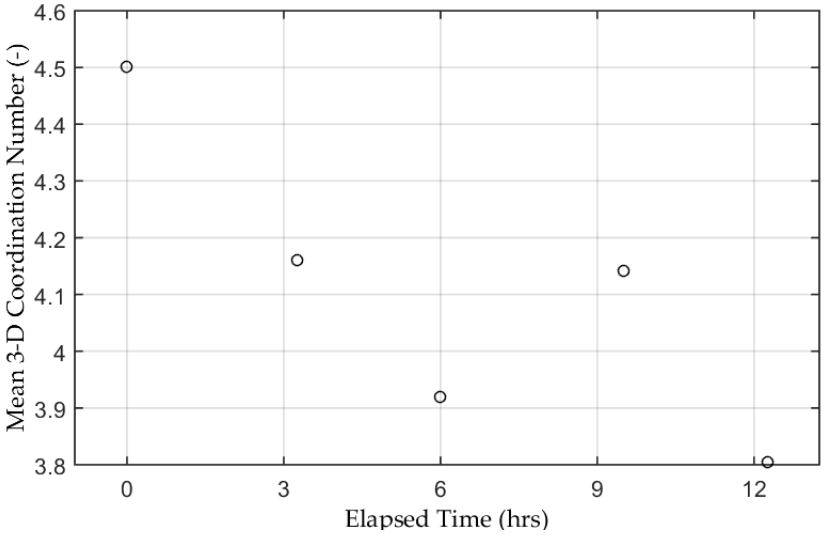


Figure E-83: Changes in mean 3-D coordination number, $\mathcal{N}$, in the top 7.95 mm of sample 1W3 associated with the faceted layer during the process of radiation recrystallization.

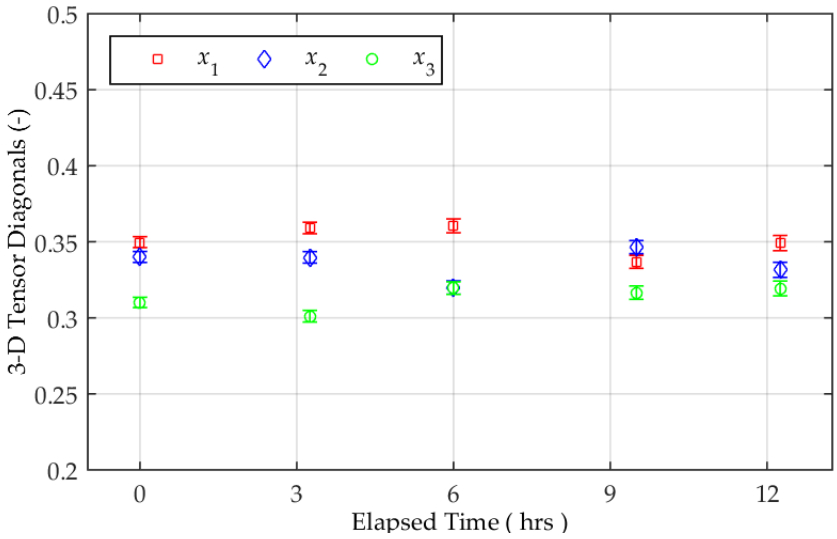


Figure E-84: Changes to the contact tensor diagonal coefficients aligned with the snow's coordinate system (x_3 is vertical, normal to the snow surface) in the top 7.95 mm of sample 1W3 associated with the faceted layer during the process of radiation recrystallization.

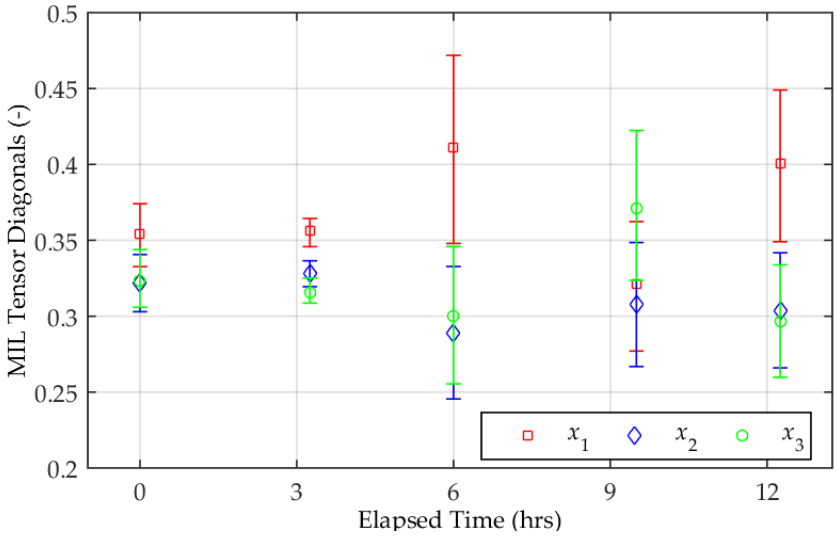


Figure E-85: Changes to the MIL tensor diagonal coefficients aligned with the snow's coordinate system (x_3 is vertical, normal to the snow surface) in the top 7.95 mm of sample 1W3 associated with the faceted layer during the process of radiation recrystallization.

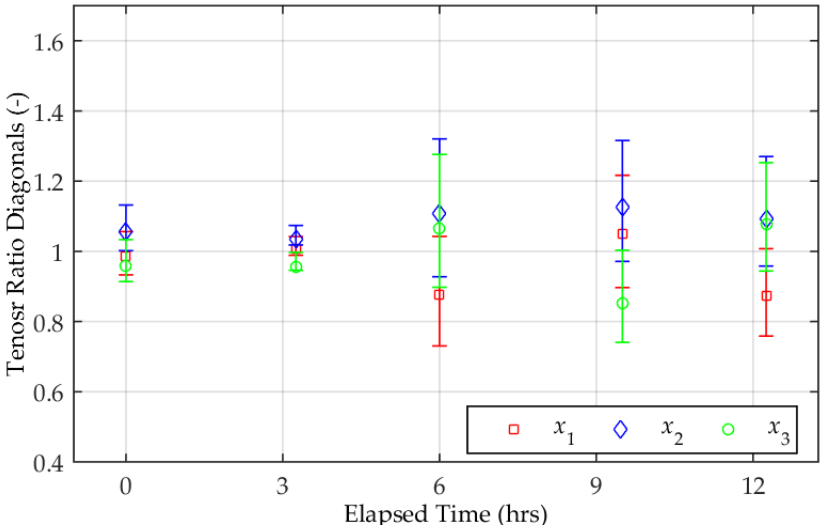


Figure E-86: Changes to the tensor ratio diagonal coefficients aligned with the snow's coordinate system (x_3 is vertical, normal to the snow surface) in the top 7.95 mm of sample 1W3 associated with the faceted layer during the process of radiation recrystallization.

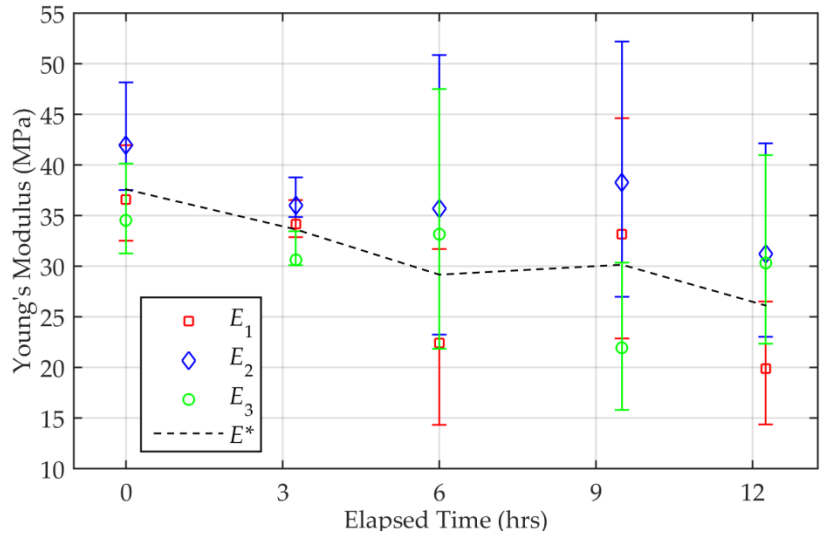


Figure E-87: Changes to the computed effective Young's moduli aligned with the snow's coordinate system in the top 7.95 mm of sample 1W3 associated with the faceted layer during the process of radiation recrystallization. E^* represents the scalar computed effective Young's modulus.

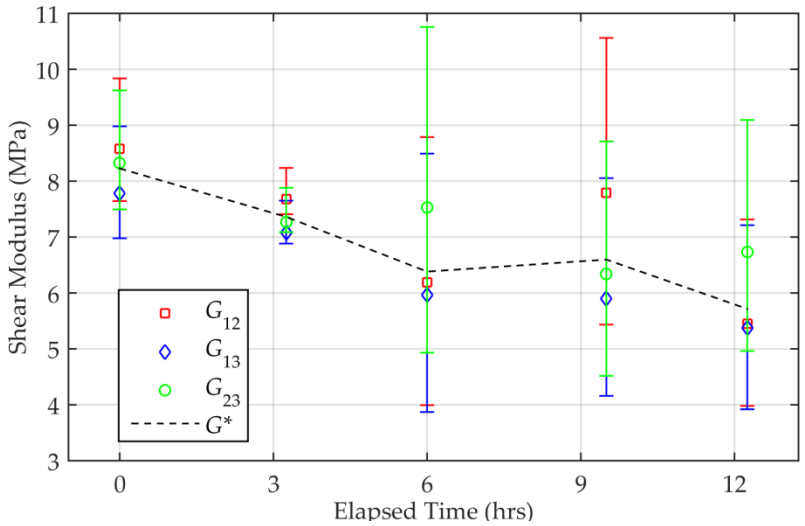


Figure E-88: Changes to the computed effective shear moduli aligned with the snow's coordinate system in the top 7.95 mm of sample 1W3 associated with the faceted layer during the process of radiation recrystallization. G^* represents the scalar computed effective shear modulus.

E.6.2 Sub-Faceted Layer Results

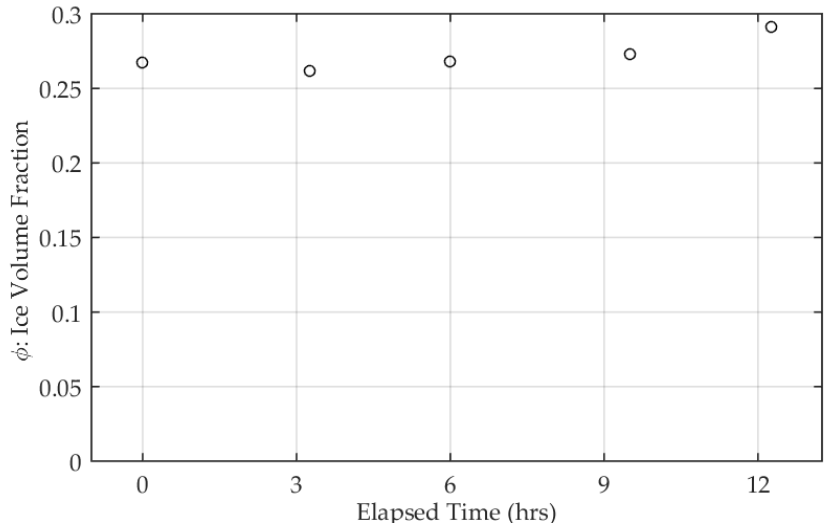


Figure E-89: Changes in volume fraction, ϕ, of sample 1W3 associated with the layer below the faceted crystals during the process of radiation recrystallization.

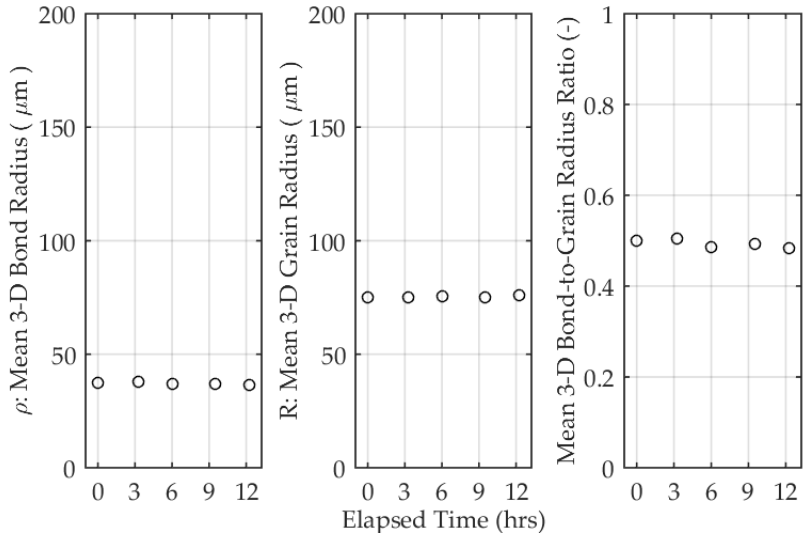


Figure E-90: Changes in mean bond radius, $\hat{\rho}$, and grain radius, $\hat{R}$, of sample 1W3 associated layer below the faceted crystals during the process of radiation recrystallization.

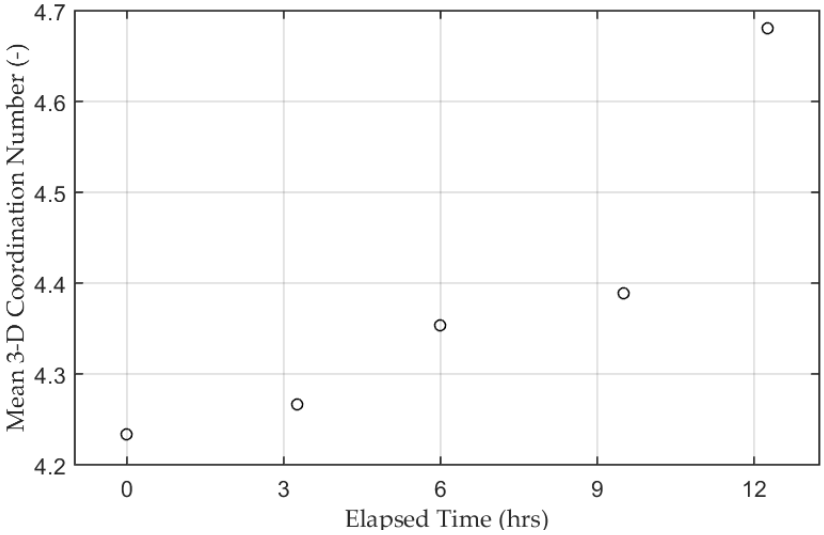


Figure E-91: Changes in mean 3-D coordination number, $\mathcal{N}$, of sample 1W3 associated with the layer below the faceted crystals during the process of radiation recrystallization.

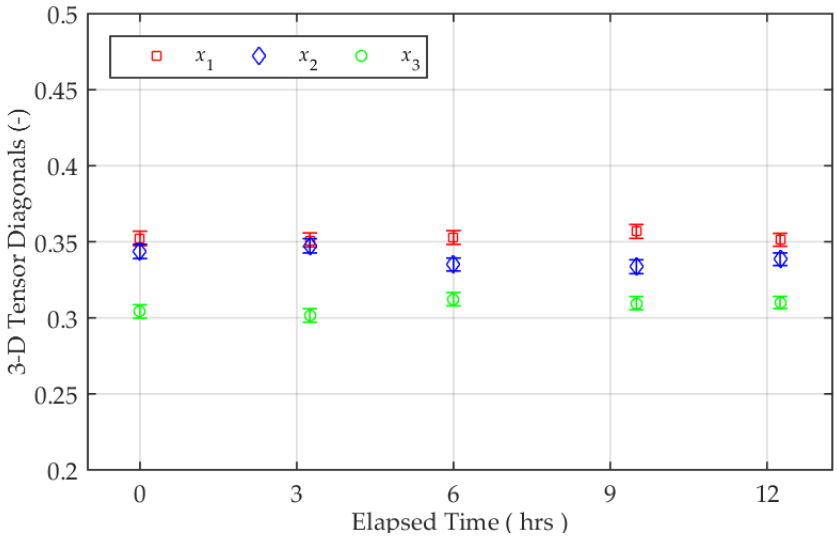


Figure E-92: Changes to the contact tensor diagonal coefficients aligned with the snow's coordinate system (x_3 is vertical, normal to the snow surface) of sample 1W3 associated with the layer below the faceted crystals during the process of radiation recrystallization.

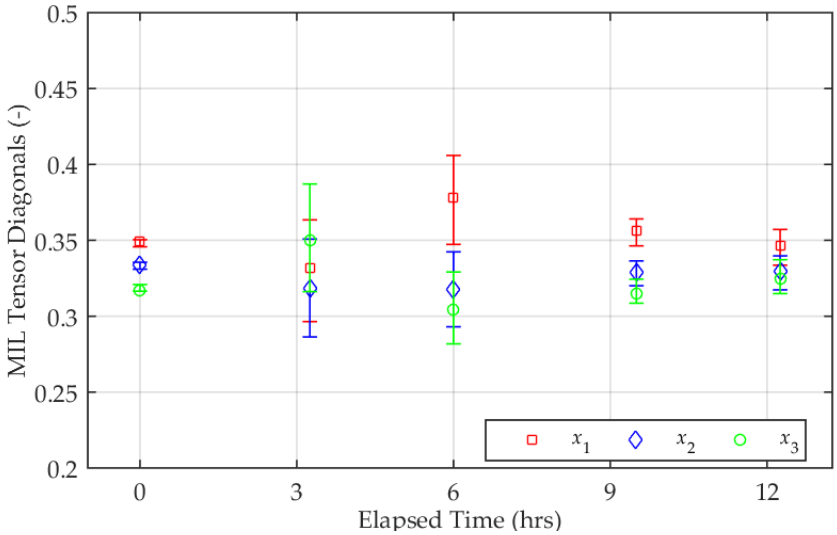


Figure E-93: Changes to the MIL tensor diagonal coefficients aligned with the snow's coordinate system (x_3 is vertical, normal to the snow surface) of sample 1W3 associated with the layer below the faceted crystals during the process of radiation recrystallization.

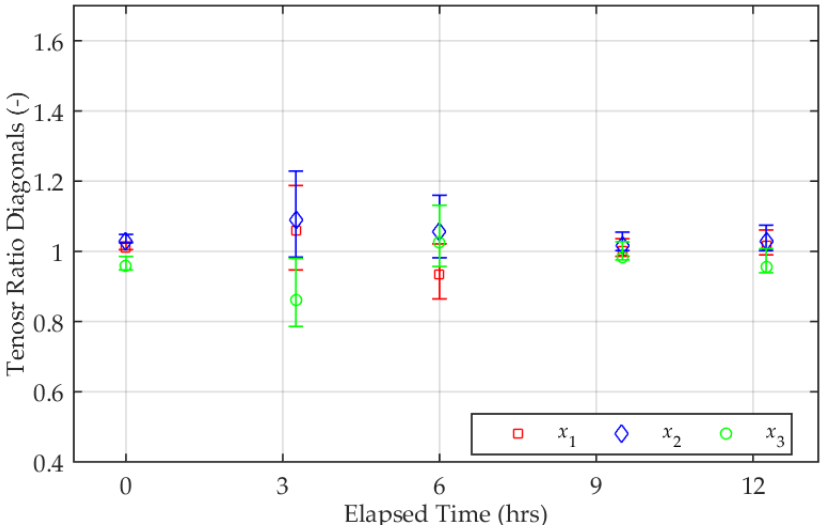


Figure E-94: Changes to the tensor ratio diagonal coefficients aligned with the snow's coordinate system (x_3 is vertical, normal to the snow surface) of sample 1W3 associated with the layer below the faceted crystals during the process of radiation recrystallization.

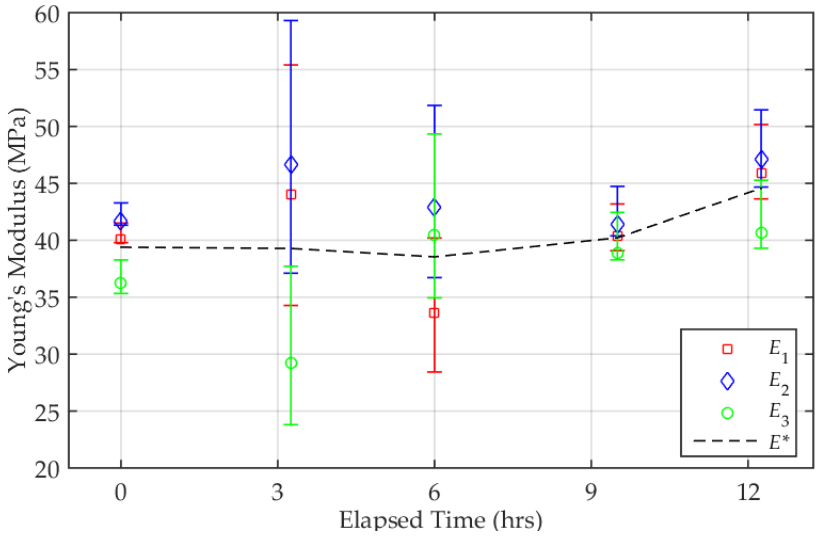


Figure E-95: Changes to the computed effective Young's moduli aligned with the snow's coordinate system of sample 1W3 associated with the layer below the faceted crystals during the process of radiation recrystallization. E^* represents the scalar computed effective Young's modulus.

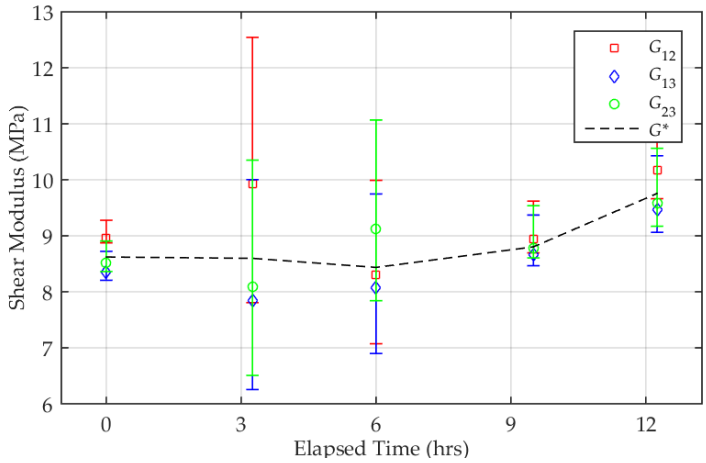


Figure E-96: Changes to the computed effective shear moduli aligned with the snow's coordinate system of sample 1W3 associated with the layer below the faceted crystals during the process of radiation recrystallization. G^* represents the scalar computed effective shear modulus.

E.7 Fabric Tensor Results for Sample 2 Weeks Old 1 (2W1)

E.7.1 Faceted Layer Results

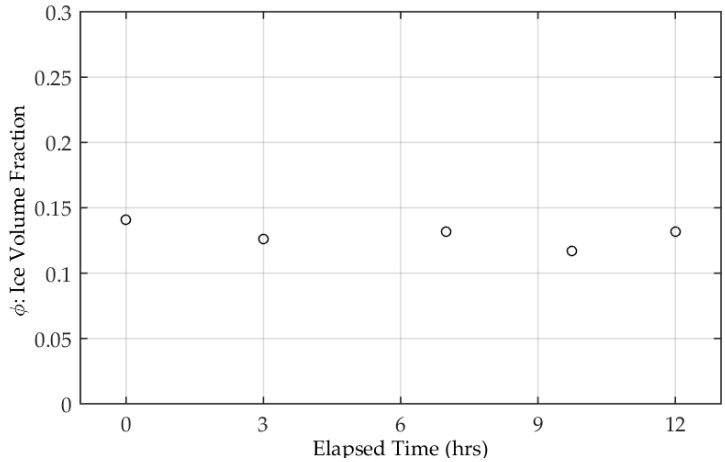


Figure E-97: Changes in volume fraction, ϕ, in the top 5.12 mm of sample 2W1 associated with the faceted layer during the process of radiation recrystallization.

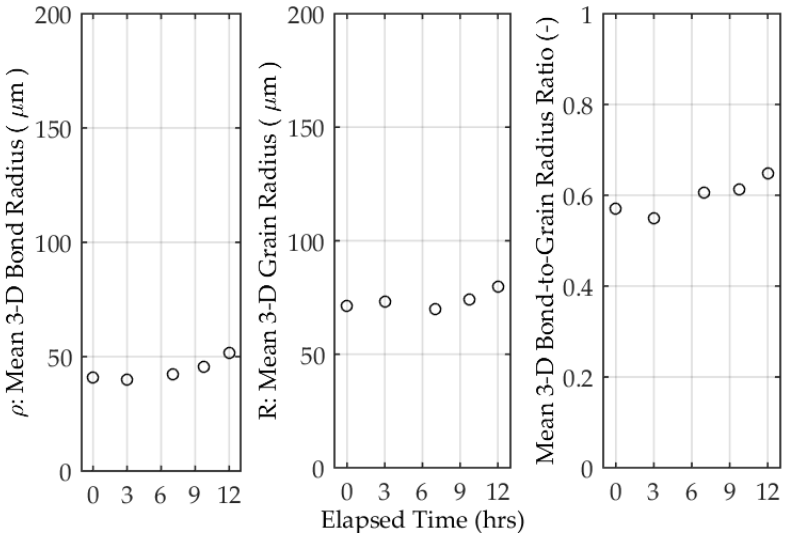


Figure E-98: Changes in mean bond radius, $\hat{\rho}$, and grain radius, $\hat{R}$, in the top 5.12 mm of sample 2W1 associated with the faceted layer during the process of radiation recrystallization.

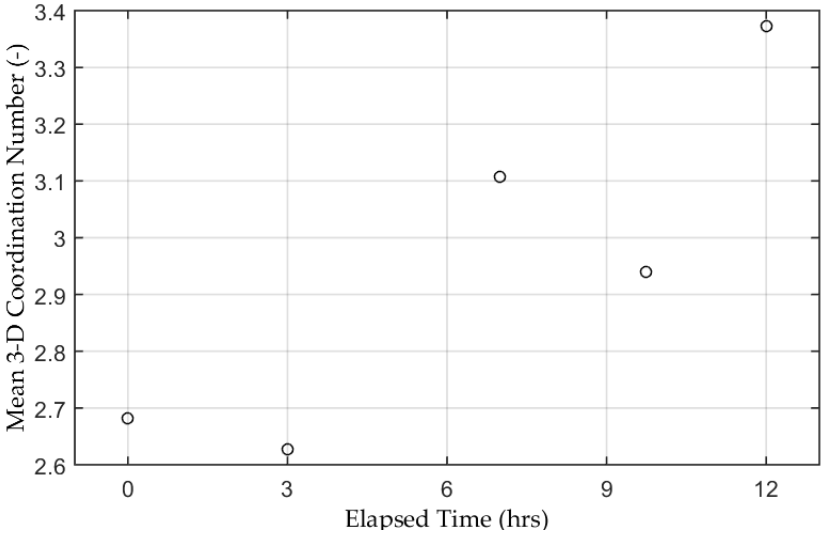


Figure E-99: Changes in mean 3-D coordination number, $\mathcal{N}$, in the top 5.12 mm of sample 2W1 associated with the faceted layer during the process of radiation recrystallization.

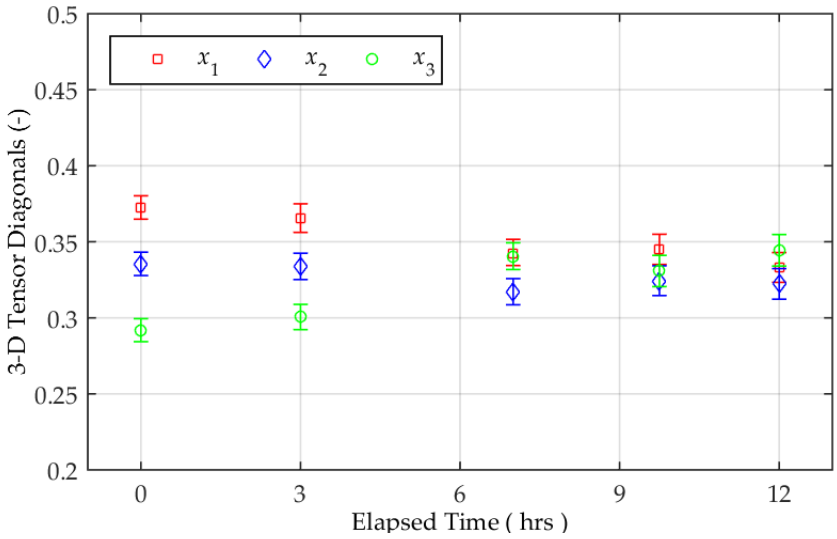


Figure E-100: Changes to the contact tensor diagonal coefficients aligned with the snow's coordinate system (x_3 is vertical, normal to the snow surface) in the top 5.12 mm of sample 2W1 associated with the faceted layer during the process of radiation recrystallization.

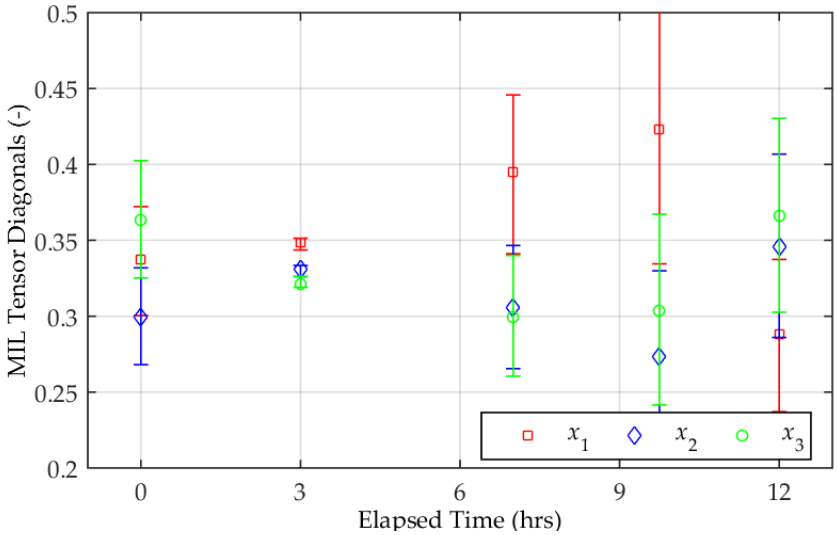


Figure E-101: Changes to the MIL tensor diagonal coefficients aligned with the snow's coordinate system (x_3 is vertical, normal to the snow surface) in the top 5.12 mm of sample 2W1 associated with the faceted layer during the process of radiation recrystallization.

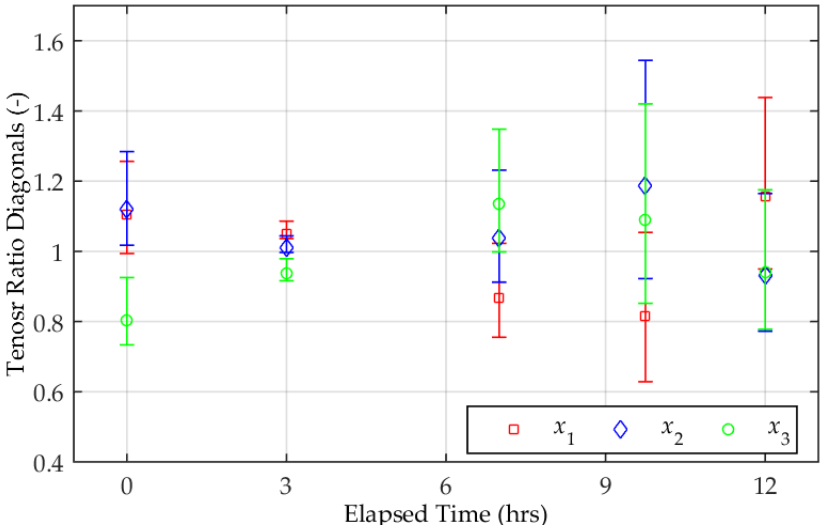


Figure E-102: Changes to the tensor ratio diagonal coefficients aligned with the snow's coordinate system (x_3 is vertical, normal to the snow surface) in the top 5.12 mm of sample 2W1 associated with the faceted layer during the process of radiation recrystallization.

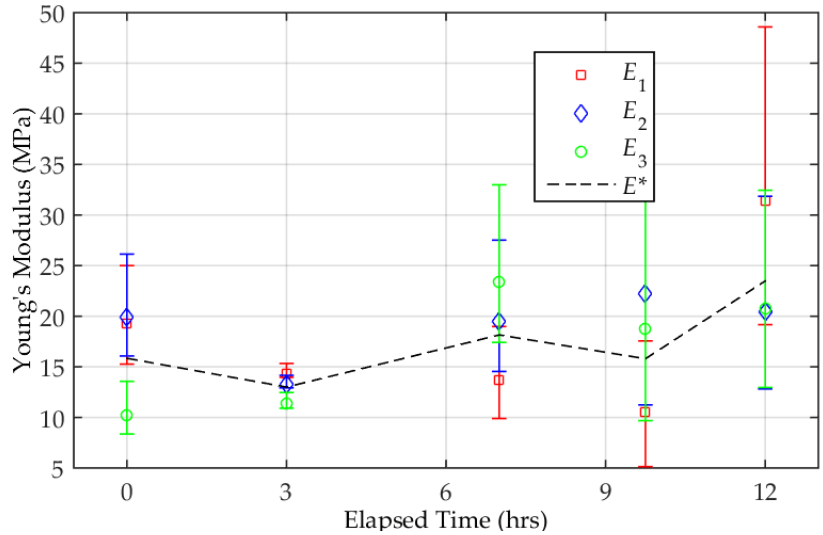


Figure E-103: Changes to the computed effective Young's moduli aligned with the snow's coordinate system in the top 5.12 mm of sample 2W1 associated with the faceted layer during the process of radiation recrystallization. E^* represents the scalar computed effective Young's modulus.

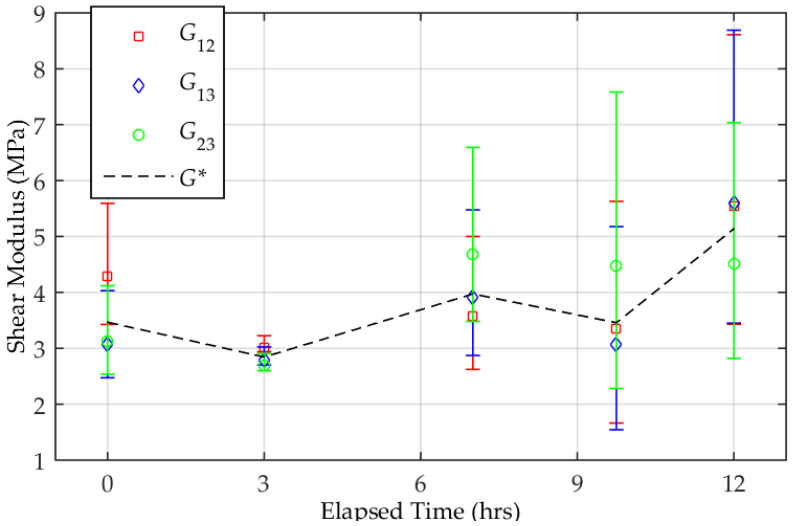


Figure E-104: Changes to the computed effective shear moduli aligned with the snow's coordinate system in the top 5.12 mm of sample 2W1 associated with the faceted layer during the process of radiation recrystallization. G^* represents the scalar computed effective shear modulus.

E.7.2 Sub-Faceted Layer Results

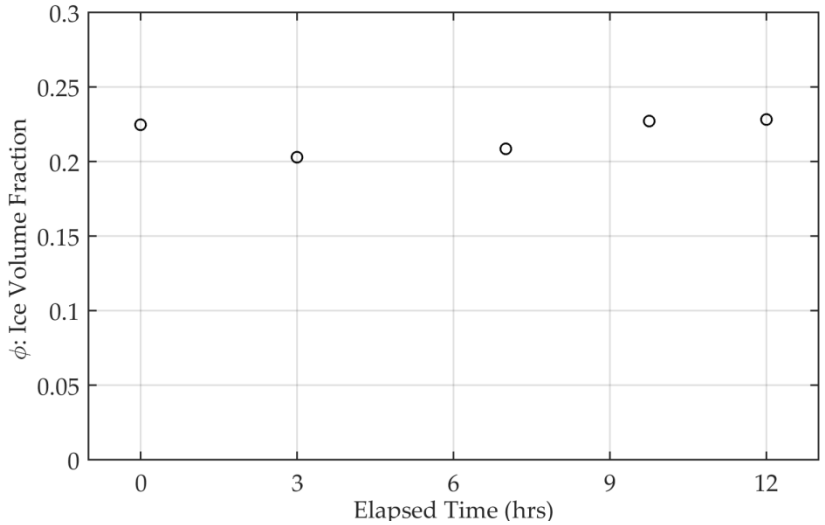


Figure E-105: Changes in volume fraction, ϕ, of sample 2W1 associated with the layer below the faceted crystals during the process of radiation recrystallization.

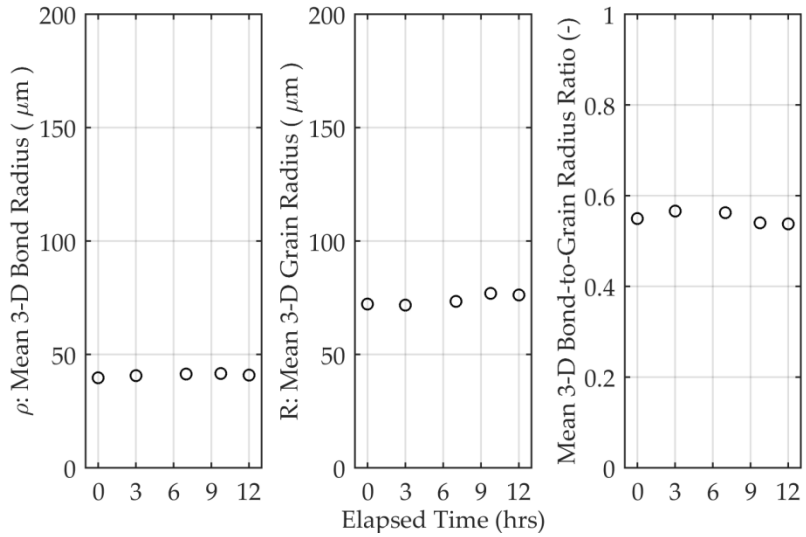


Figure E-106: Changes in mean bond radius, $\hat{\rho}$, and grain radius, $\hat{R}$, of sample 2W1 associated layer below the faceted crystals during the process of radiation recrystallization.

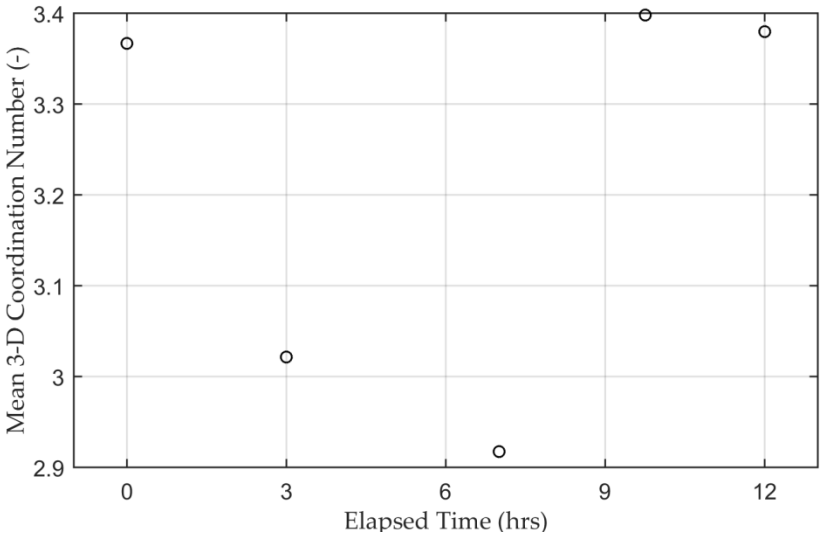


Figure E-107: Changes in mean 3-D coordination number, $\mathcal{N}$, of sample 2W1 associated with the layer below the faceted crystals during the process of radiation recrystallization.

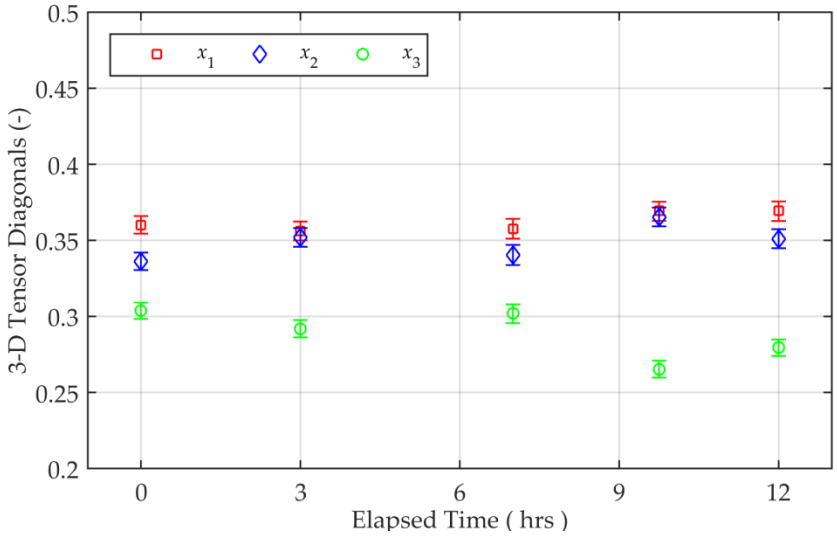


Figure E-108: Changes to the contact tensor diagonal coefficients aligned with the snow's coordinate system (x_3 is vertical, normal to the snow surface) of sample 2W1 associated with the layer below the faceted crystals during the process of radiation recrystallization.

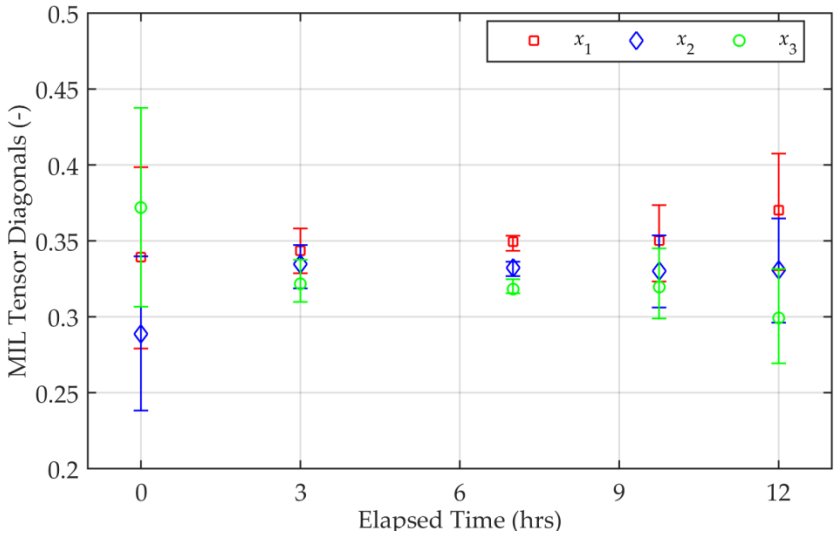


Figure E-109: Changes to the MIL tensor diagonal coefficients aligned with the snow's coordinate system (x_3 is vertical, normal to the snow surface) of sample 2W1 associated with the layer below the faceted crystals during the process of radiation recrystallization.

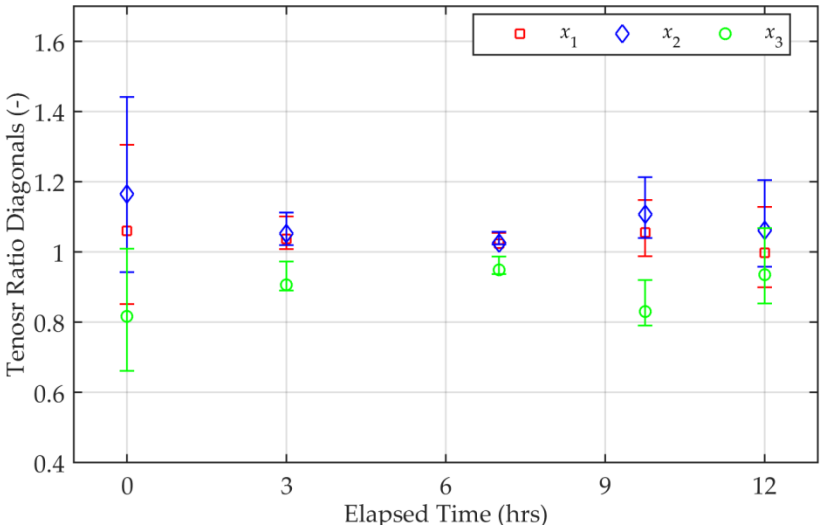


Figure E-110: Changes to the tensor ratio diagonal coefficients aligned with the snow's coordinate system (x_3 is vertical, normal to the snow surface) of sample 2W1 associated with the layer below the faceted crystals during the process of radiation recrystallization.

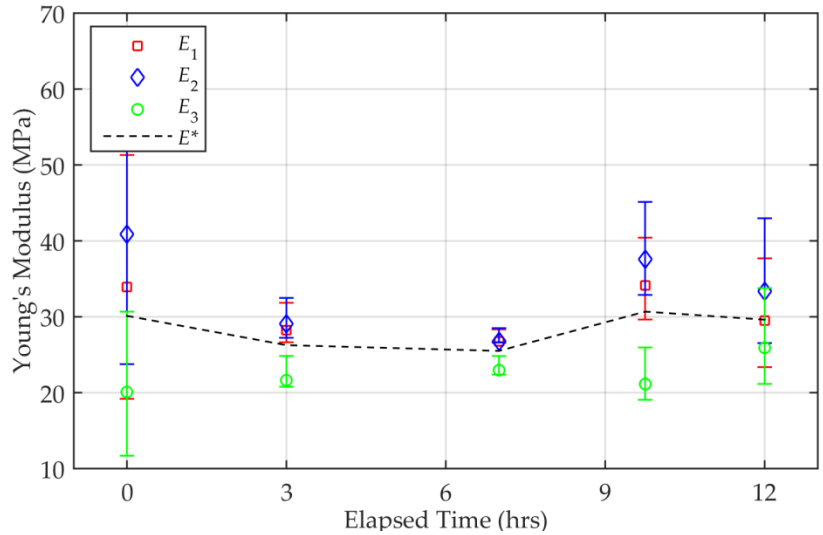


Figure E-111: Changes to the computed effective Young's moduli aligned with the snow's coordinate system of sample 2W1 associated with the layer below the faceted crystals during the process of radiation recrystallization. E^* represents the scalar computed effective Young's modulus.

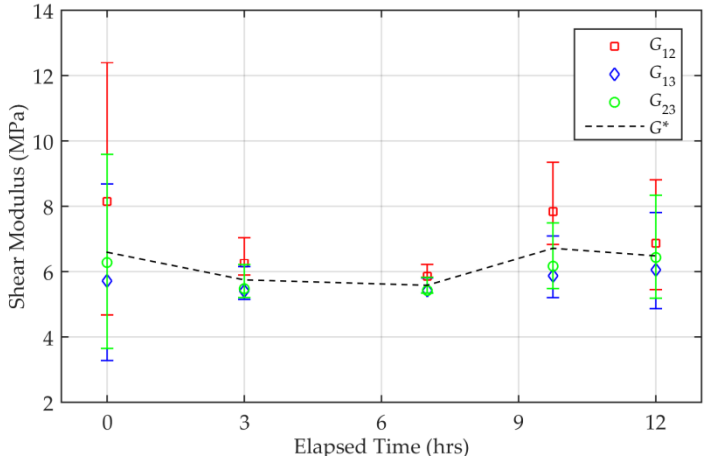


Figure E-112: Changes to the computed effective shear moduli aligned with the snow's coordinate system of sample 2W1 associated with the layer below the faceted crystals during the process of radiation recrystallization. G^* represents the scalar computed effective shear modulus.

APPENDIX F

FINITE ELEMENT ANALYSIS RESULTS

Finite element analyses were conducted utilizing μCT imaging of the microstructure of the snow. The representative volumes from both the non-recrystallized volumes and buried radiation recrystallized volumes are converted to finite element meshes such that structural loads can be simulated directly on the ice network making up snow. Either compressive or shear loads are applied using a displacement boundary condition. Isotropic material parameters are assigned to both volumes using values for polycrystalline ice. Post-processing of the results includes measuring reaction forces at the bottom of the representative volume, and average nodal displacements from various elevations throughout the sample. Since external forces are only applied at the top and bottom of the samples, constant average cross-sectional stresses are expected using the full volume of the sample. Strain is computed using the relative displacements between the top and bottom nodes on the initial, non-recrystallized volume and between planes defined by the sections illustrated in Figure 10-1 on the buried radiation recrystallized volume.

The simulated results in shear and compression are compiled below for all of the microstructural volumes collected for this study. The line and data colors for the faceted sample results correspond to the regions shown in Figure 10-1.

F.1 FEA Results for Sample New Snow 1 (NS1)

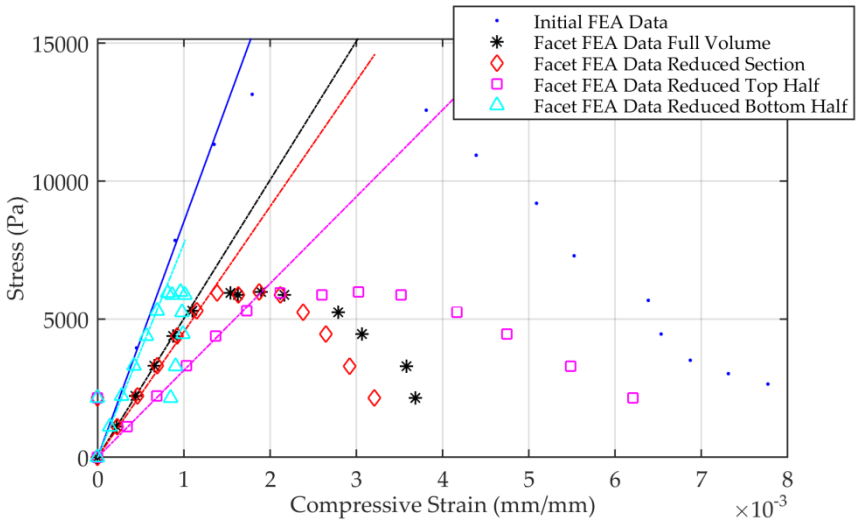


Figure F-1: FEA simulated average compressive stress and strain for the initial snow surface and the radiation recrystallized faceted layer of experimental sample NS1.

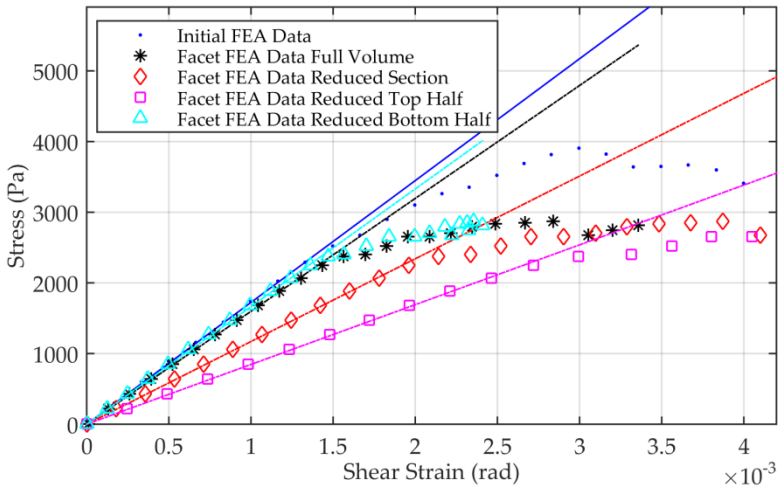


Figure F-2: FEA simulated average shear stress and strain for the initial snow surface and the radiation recrystallized faceted layer of experimental sample NS1.

F.2 FEA Results for Sample New Snow 2 (NS2)

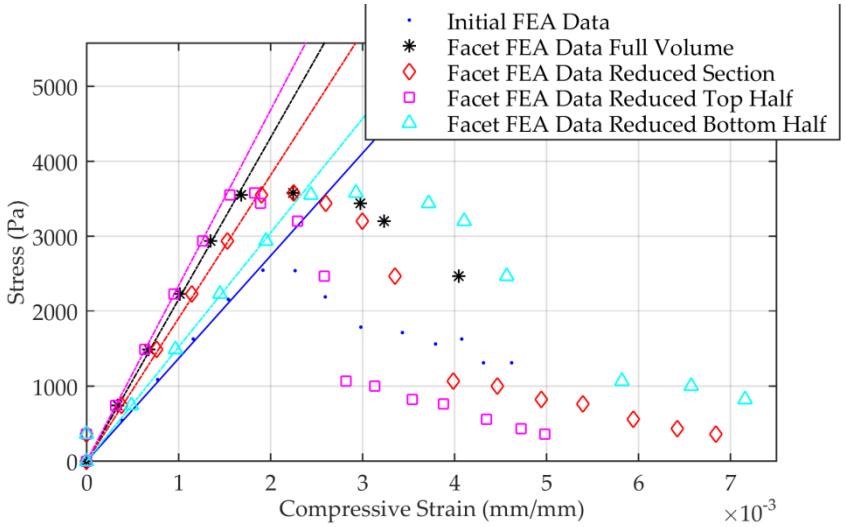


Figure F-3: FEA simulated average compressive stress and strain for the initial snow surface and the radiation recrystallized faceted layer of experimental sample NS2.

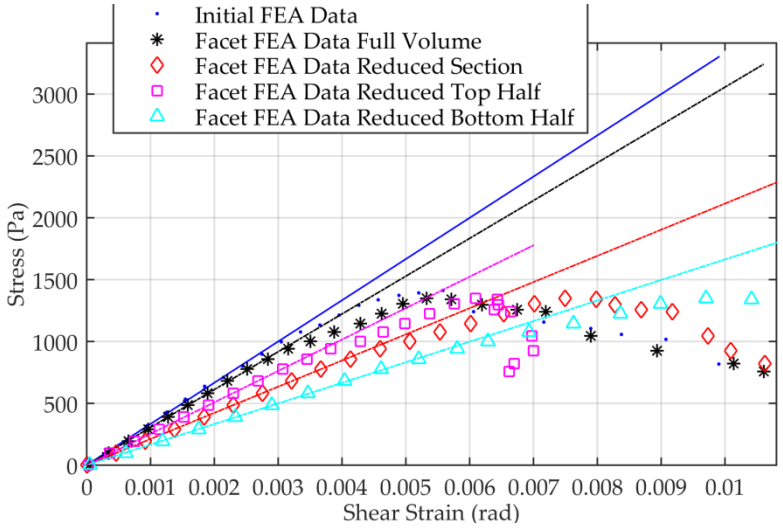


Figure F-4: FEA simulated average shear stress and strain for the initial snow surface and the radiation recrystallized faceted layer of experimental sample NS2.

F.3 FEA Results for Sample New Snow 3 (NS3)

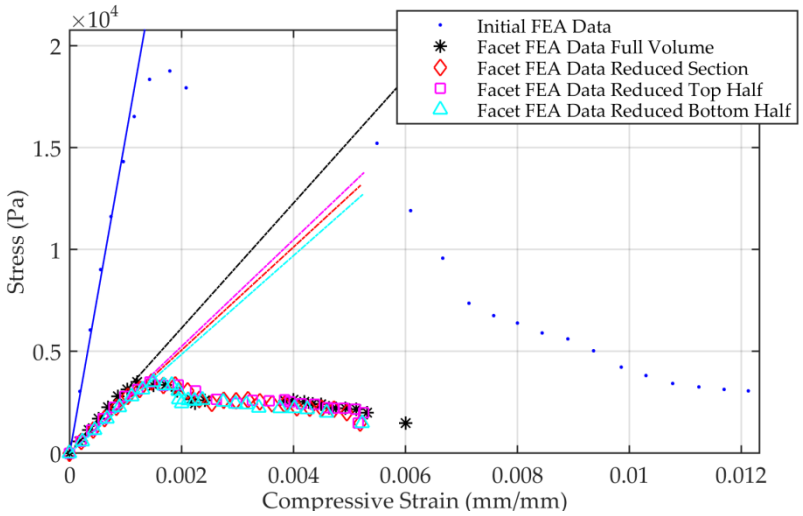


Figure F-5: FEA simulated average compressive stress and strain for the initial snow surface and the radiation recrystallized faceted layer of experimental sample NS3.

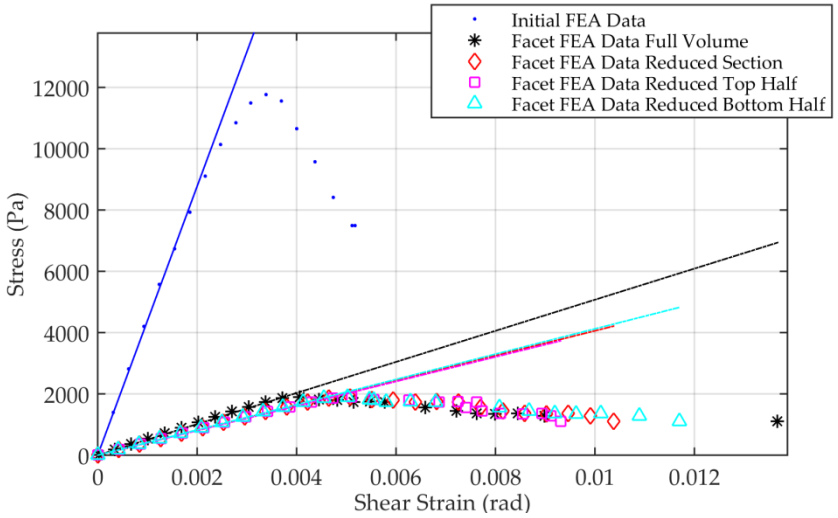


Figure F-6: FEA simulated average shear stress and strain for the initial snow surface and the radiation recrystallized faceted layer of experimental sample NS3.

F.4 FEA Results for Sample 1 Week Old Snow 1 (1W1)

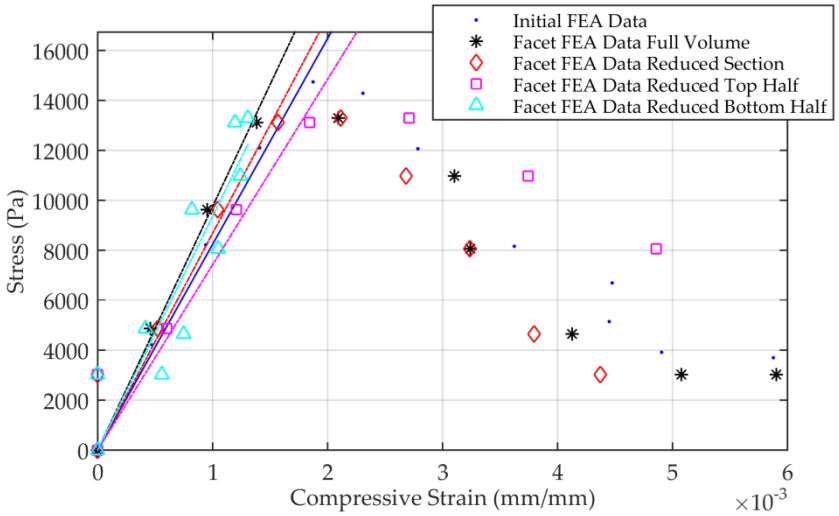


Figure F-7: FEA simulated average compressive stress and strain for the initial snow surface and the radiation recrystallized faceted layer of experimental sample 1W1.

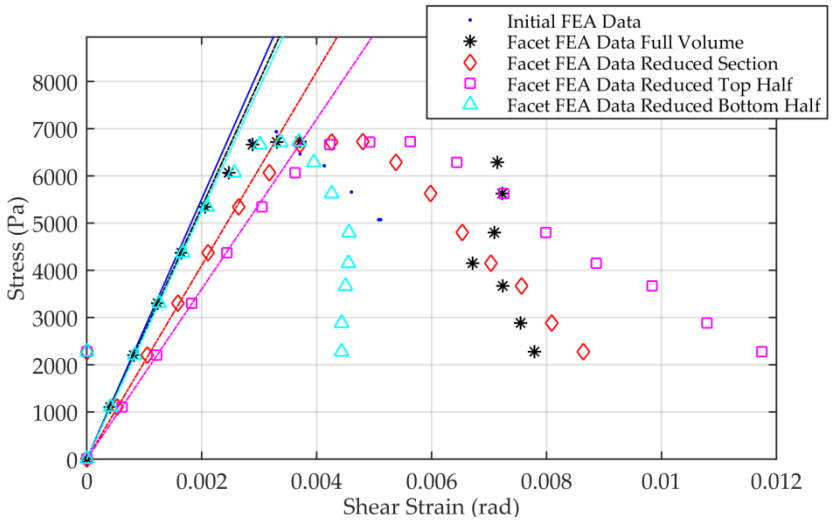


Figure F-8: FEA simulated average shear stress and strain for the initial snow surface and the radiation recrystallized faceted layer of experimental sample 1W1.

F.5FEA Results for Sample 1 Week Old Snow 2 (1W2)

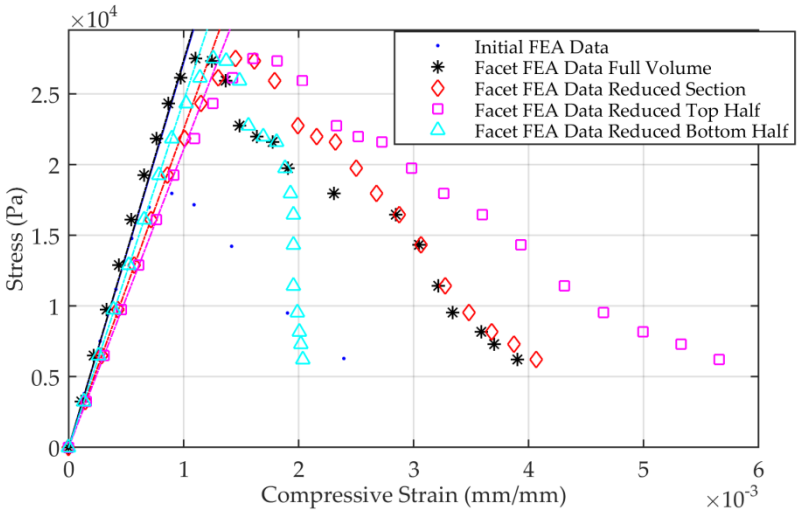


Figure F-9: FEA simulated average compressive stress and strain for the initial snow surface and the radiation recrystallized faceted layer of experimental sample 1W2.

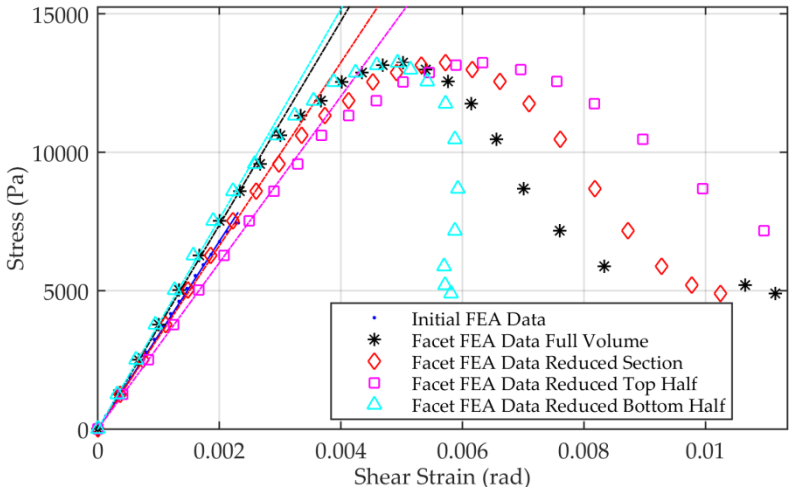


Figure F-10: FEA simulated average shear stress and strain for the initial snow surface and the radiation recrystallized faceted layer of experimental sample 1W2.

F.6FEA Results for Sample 1 Week Old Snow 3 (1W3)

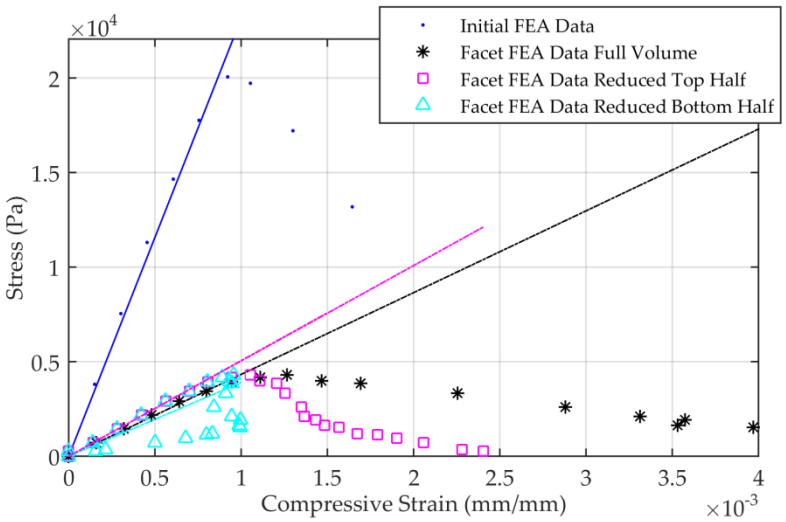


Figure F-11: FEA simulated average compressive stress and strain for the initial snow surface and the radiation recrystallized faceted layer of experimental sample 1W3.

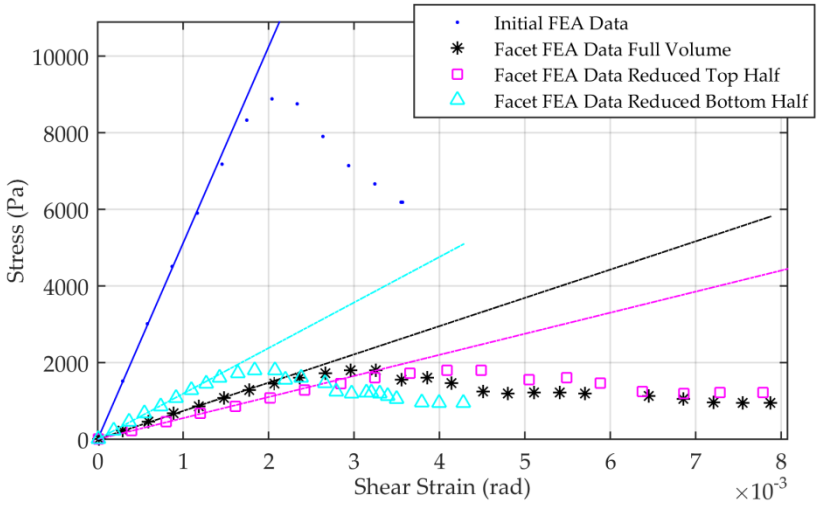


Figure F-12: FEA simulated average shear stress and strain for the initial snow surface and the radiation recrystallized faceted layer of experimental sample 1W3.

F.7FEA Results for Sample 2 Weeks Old Snow 1 (2W1)

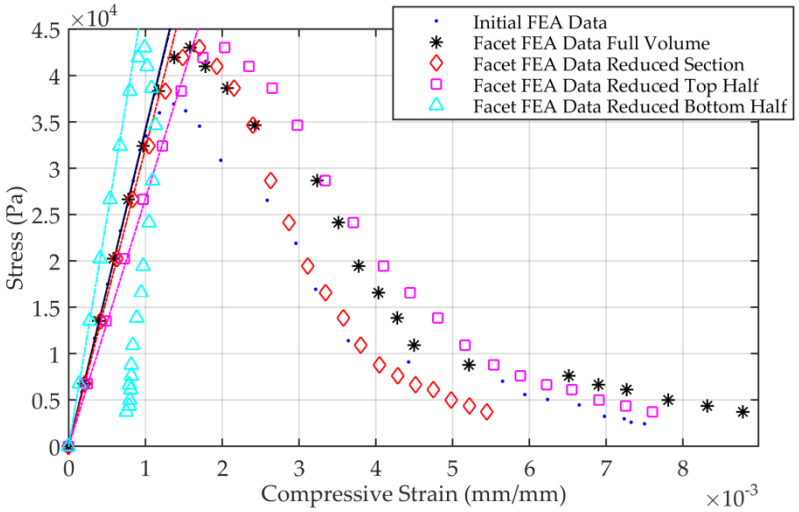


Figure F-13: FEA simulated average compressive stress and strain for the initial snow surface and the radiation recrystallized faceted layer of experimental sample 2W1.

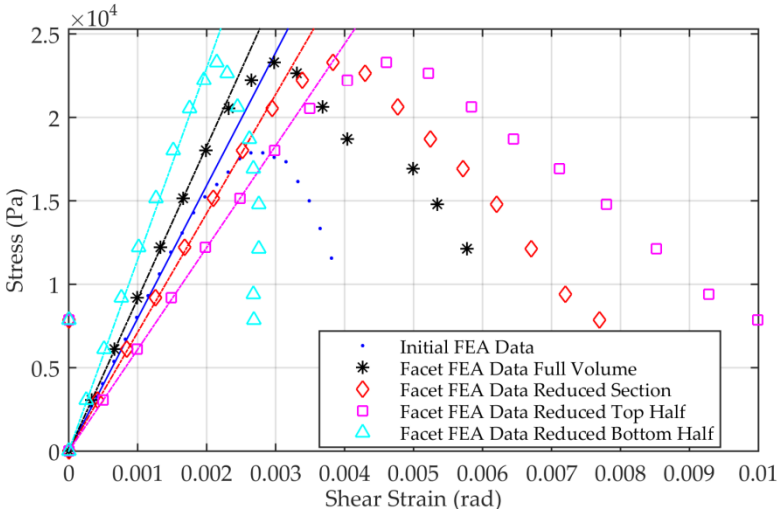


Figure F-14: FEA simulated average shear stress and strain for the initial snow surface and the radiation recrystallized faceted layer of experimental sample 2W1.